

A Novel Way for Designing Bifocal Reflector Antennas

A. N. Plastikov and B. L. Kogan

National Research University “Moscow Power Engineering Institute”
Krasnokazarmennaya Str. 14, Moscow 111250, Russia

Abstract— A new approach to the problem of calculating the reflectors surfaces of offset bifocal antennas by the raytracing procedure is presented. The use of this approach allows us to obtain analytical expressions for reflector surfaces in the form of functions of two variables and simplify the classical iterative process of determining the sequence of points two reflectors. A 43° field-of-view reflector antenna with 60×60 -wavelength aperture is presented as an example.

1. INTRODUCTION

Today, the development of multi-beam reflector antennas (MBRAs), which can operate (i.e., receive or transmit the information) simultaneously through several rays (directions of plane waves), is an important area of antenna technology for both ground and space systems. An obvious advantage of MBRAs over a single-beam reflector antennas is the usage of a single aperture (i.e., one main reflector) to form multiple beams, which allows a single MBRA to “replace” a certain number of “ordinary” reflector antennas.

Bifocal two-reflector antennas have two exact foci and allow aberration-free focusing of the field arriving from two different directions. For the first time, problems of the theory of design of three-dimensional bifocal reflector antennas (BFRAs) were studied in the 1980s in the works of C. M. Rappaport [1–3], B. E. Kinber [4–6] and others. In these publications, iterative algebra has been used to derive the set of reference points on reflector and subreflector surfaces. As far as we know, over the past two decades any other approaches to solving this problem have not been proposed. To form a continuous smooth surface, it was necessary to fulfill the conditions of smooth interpolation between adjacent points. It seems that these MBRAs are not widely used because of the difficulty of obtaining reflector smooth profiles by solving the synthesis problem.

In this paper, a new approach to the problem of calculating the reflector surfaces of offset BFRAs is presented. The use of this approach allows one to obtain analytical expressions for profiles of two reflectors in the form of parametric functions of two variables. The latter is also important because modern electronically controlled machines make it possible to manufacture rather complicated reflector profiles with satisfactory accuracy in the case when these surfaces are defined analytically.

2. DESCRIPTION OF THE SYNTHESIS PROCEDURE

Let us consider an antenna system whose plane of symmetry coincides with the vertical XZ plane. The beams of the antenna pattern scan in the horizontal XY plane. The main idea of the proposed approach to the BFRA synthesis problem is as follows: for each of two beams that ensures exact focusing it is necessary to ensure the most efficient (in terms of GO rays) illumination of the main reflector with illumination of only a half of the subreflector for each of these two beams. Thus, it is possible to provide relatively effective illumination of the whole main reflector, while the “spot” of the currents induced on the subreflector moves from one side of the subreflector to the other when the beam moves between two required scanning directions.

The initial data can be specified by the following parameters:

- angle α of deflection of the reference rays from the plane of symmetry (the required scan angle);
- subreflector cross section in the symmetry plane, $z_0(x)$, with the initial point equal to the origin of the coordinates, i.e., $z_0(0) = 0$;
- the coordinates of the focus;
- length of the optical path from the focus to the point in the aperture plane, which passes through the origin of coordinates.

In this case, the reflector surfaces are calculated from the requirement of ensuring the constant value of the optical path length for all rays leaving the focus. The rays are calculated taking into account Snell’s law.

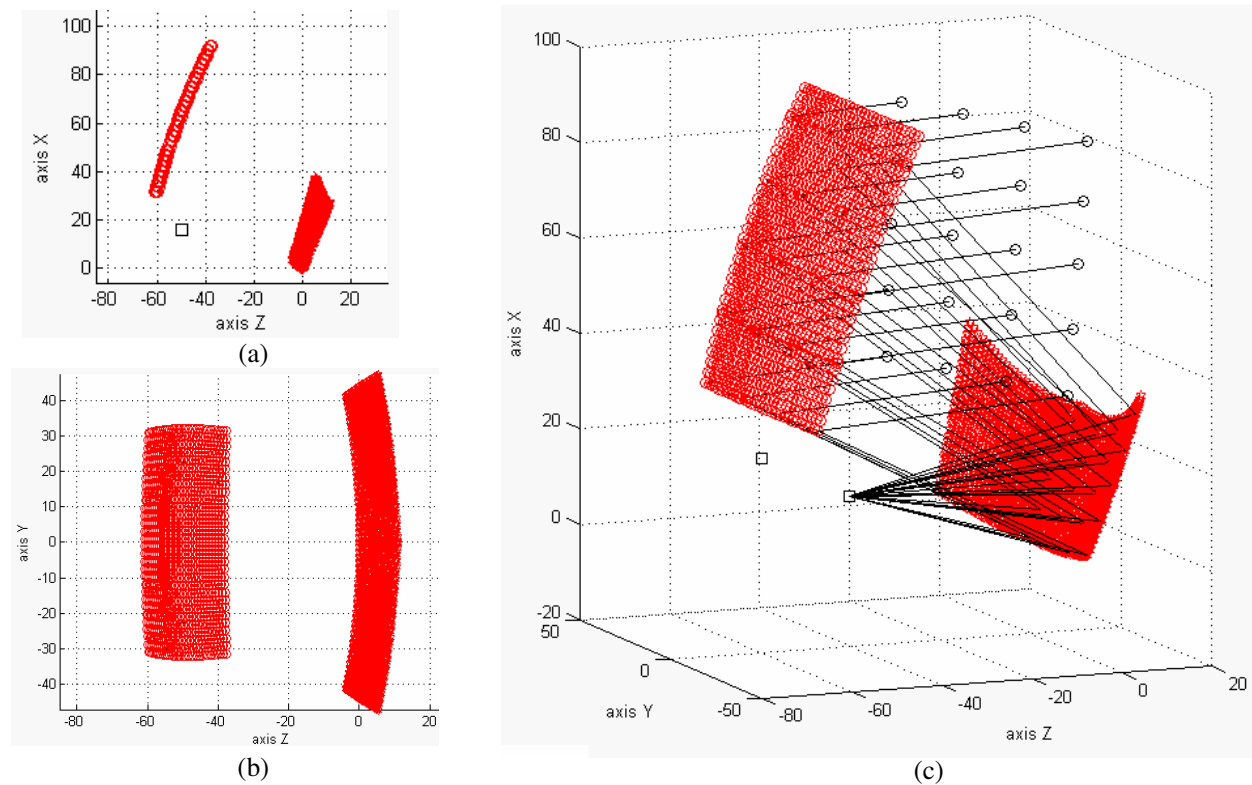


Figure 1: (a), (b) Cross-section views of the BFRA designed for the scan angle $\alpha = 17^\circ$. (c) The perspective view of the BFRA with a set of GO rays coming from the focus. All dimensions are given in wavelengths.

Based on the initial data, we can calculate the coordinates of points on the lateral edges of the main reflector and normals to the outer surface for these points. These points are symmetrical with respect to the vertical XZ plane. The surface of the main reflector is formed as a set of curves, which pass through symmetric pairs of reference points and are orthogonal to the normals. The curves can be selected in the form of canonical second-order curves. This feature is an additional degree of freedom for the synthesis problem, which allows one to optimize the antenna efficiency. Surface points corresponding to one half of the subreflector then can be calculated taking into account the reference points on the main reflector surface. The second half of the subreflector is symmetrical with respect to the first one. As a result of the synthesis procedure, we can determine the reflector surfaces as a functions of two parametric variables. One of them is the X -axis coordinate of a point on the subreflector in the symmetry plane, the other one is the normalized coordinate along the curve connecting the edge points of the main reflector.

The numerical studies have shown that it is possible to classify several different types of synthesized BFRA with different reflector arrangement and patterns of GO rays.

3. AN EXAMPLE OF THE DESIGN OF A BIFOCAL REFLECTOR ANTENNA

The antenna shown in Figure 1 is a synthesized BFRA with aperture dimensions of about 60×60 wavelengths. The antenna is designed for the required scan angle $\alpha = 17^\circ$; however, the multibeam performance of this BFRA allows one to exceed the $2 \cdot \alpha$ field of view. The subreflector cross section in the symmetry plane is defined as a quadratic polynomial; the shapes of the main reflector curves are defined as circular arcs. The subreflector dimension in the horizontal plane is about 100 wavelengths.

Far-field patterns of the BFRA were computed with the use of a physical optics method code from ICARA (Induced Current Analysis of Reflector Antennas) software package [7]. The feed was modeled as a point source with an axisymmetric radiation pattern in the form of the $(\cos \theta)^q$ function with vertically polarized field. Figure 2 shows the current distributions on the reflector surfaces for the central beam and the beam corresponding to the required scan angle. Figure 3 shows the co- and cross-polarization radiation patterns in the vertical plane for three different beams. A 3-dB beamwidth is about 1.1° . The aperture efficiency (AE) for the beam deflected

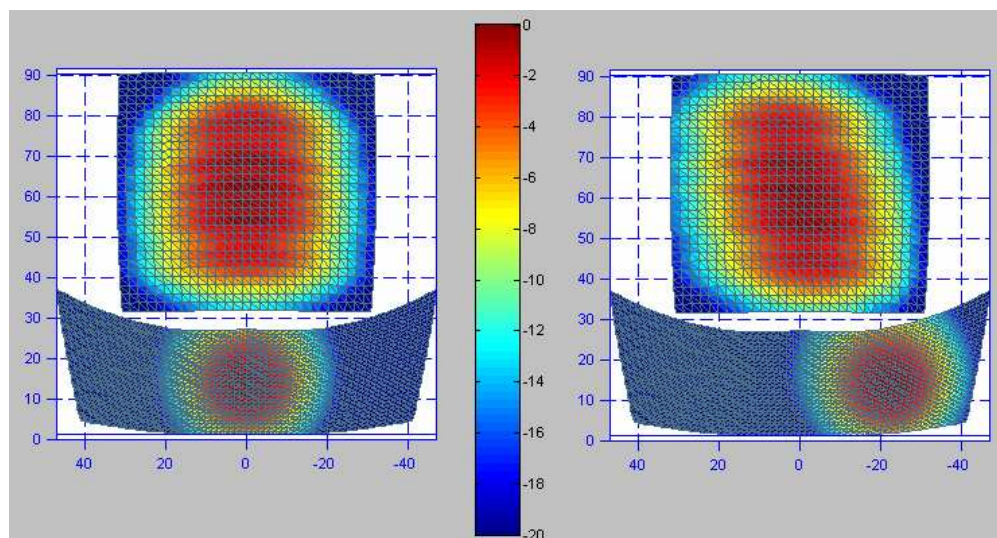


Figure 2: Simulated distribution of normalized currents on the surfaces of the BFRA for the central beam and the beam deflected through an angle of 17° (on a logarithmic scale).

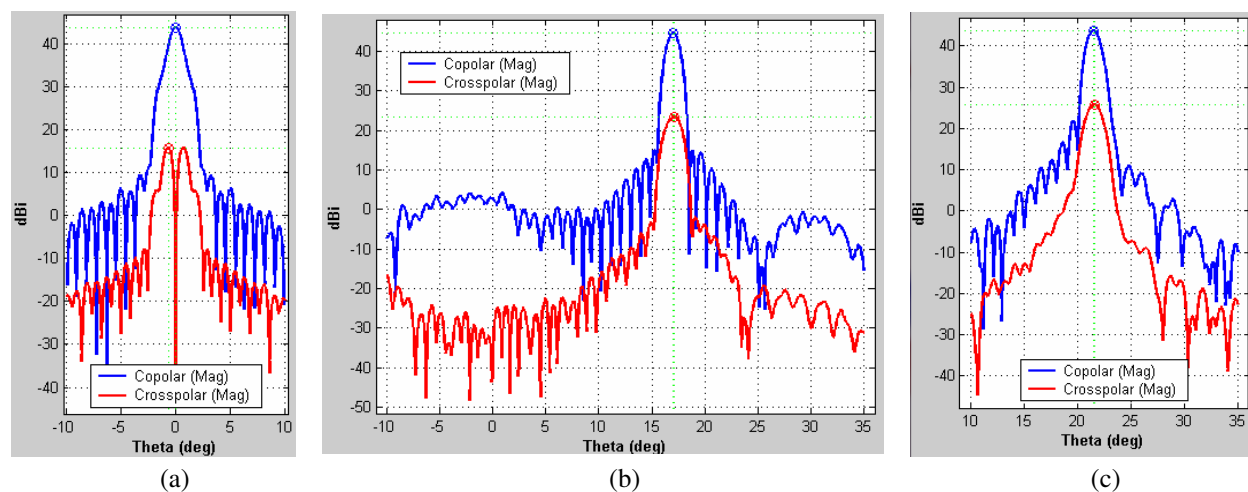


Figure 3: Simulated radiation patterns of the BFRA with $\alpha = 17^\circ$ for three different scan angles: (a) 0° , (b) 17° , and (c) 21.5° .

through the angle $\alpha = 17^\circ$ is 62.5%. The AEs for the central beam and the beam deflected through an angle of 21.5° are both about 50%. In this case, the AE values are determined from the expression [8]

$$AE = \frac{D_{AS}}{D_{id}} = \frac{D_{AS}}{4\pi \cdot S/\lambda^2}, \quad (1)$$

where D_{AS} is the calculated antenna directivity, D_{id} is the directivity of the perfect aperture with uniform amplitude and phase distribution, and S is the area of the aperture of the main reflector.

Thus, the field of view is 43° or is about 39 3-dB beamwidths for $AE \geq 50\%$. The usage of a feed with asymmetric far field allows an approximately 0.5 dB improvement of the co-polarization directivity component.

4. CONCLUSIONS

A novel method for the synthesis of BFRA reflector surfaces is briefly discussed. An example of the antenna design with an aperture of 60×60 wavelengths can provide a 43° -wide field of view with an antenna efficiency of above 50%.

At the conference, we plan to present the results of calculation and optimization of another BFRA designs.

REFERENCES

1. Rappaport, C. M., “The offset bifocal reflector antenna,” *Int. IEEE APS Symp. Digest*, 265–268, 1982.
2. Rappaport, C. M., “An offset bifocal reflector antenna design for wide-angle beam scanning,” *IEEE Trans. Antennas and Propaga.*, Vol. 32, 1196–1204, 1984.
3. Lorenzo, M. E., C. M. Rappaport, and A. G. Pino, “An offset bifocal reflector antenna with gregorian configuration,” *Antennas and Propagation Society/URSI Symposium Digest*, 1655–1658, 1997.
4. Kinber, B. E., V. I. Klassen, and V. I. Steblin, “Theory of three-dimension bifocal antennas,” *Journal of Communications Technology and Electronics*, No. 8, 1509–1517, 1983 (in Russian).
5. Kinber, B. E., *Reflector Antenna Theory Inverse Problems — Geometrical Optics Approach*, Preprint No. 38, 410, Institute of RE RAS, Moscow, 1984 (in Russian).
6. Vaaz, I. L. and B. E. Kinber, “Polyfocal systems — a consistent mapping method,” *Communications Technology and Electronics*, No. 8, 1507–1515, 1986.
7. ICARA, Induced Current Analysis of Reflector Antennas-software, www.com.uvigo.es.
8. Milligan, T. A., *Modern Antenna Design*, 2nd Edition, Wiley-IEEE Press, 2005.

The Effects of the Tube Characteristics on the Performance of a Plasma Monopole Antenna

F. Sadeghikia¹, F. Hodjat-Kashani¹, J. Rashed-Mohassel², and S. J. Ghayoomeh-Bozorgi¹

¹Department of Electrical Engineering, Iran University of Science and Technology
P. O. Box 16846-13114, Farjam, Narmak, Tehran, Iran

²Center of Excellence on Applied Electromagnetic Systems, ECE Department
University of Tehran, P. O. Box 14395-515, Tehran, Iran

Abstract— This theoretical study examines the effects of the radius of the plasma tube and its thickness on the input impedance, radiation pattern, efficiency and gain of a surface wave driven plasma monopole antenna using finite difference time domain (FDTD) simulation. We have demonstrated that more broadband characteristics can be obtained by increasing the diameter of the plasma tube. Moreover, the imaginary part of the input impedance of the plasma antenna can be eliminated by making the total length of the antenna approximately less than $\lambda/5$, where λ is the wavelength, and decreases while the ratio L/r decreases. Theoretical modeling of the plasma antenna with different thicknesses shows that the least thickness can cause a more efficient antenna while minimizing its bandwidth.

1. INTRODUCTION

Plasma antennas are constructed from insulating tubes filled with low pressure gases. Unique properties of plasma, such as variable impedance, frequency and phase shifting, broadband matching and the ability for switching on and off in a short time, may lead us to novel antennas [1, 2]. Reported experimental results have shown that the plasma antenna can have radiation efficiencies high enough [3–6]. It has been demonstrated that plasma antenna generates sufficiently low noise in HF/VHF communications [3]. However, the flexibility of the physical experiment is often limited. Numerical simulation is a powerful tool with the maximum flexibility and minimal cost to evaluate the performance of plasma antennas. Although simulations of plasma antennas by different numerical and computational methods have already been performed [1, 2, 7, 8], a full set of antenna characteristics has not been extensively studied yet. To the best of our knowledge, there has been not enough report on the tube properties of plasma antennas and its effect on radiation characteristics so far. Hence, in this paper, the finite difference time domain (FDTD) method is employed to simulate the performance of the plasma tube on the antenna parameters. We have presented radiation characteristics, gain and efficiency of a monopole plasma antenna at different plasma tube radii and thicknesses.

2. FDTD FORMULATION FOR PLASMA

In this section, we briefly explain the FDTD algorithm used in this research. In this investigation the direct integration method (DI) is applied to simulate isotropic cold plasma with a fixed uniform electron density [9]. In this method, Maxwell's equations are coupled to an auxiliary ordinary differential equation modeling the response of the polarization current density, \vec{J} , to the field, \vec{E} . The field equations for non magnetized cold plasma are given by [9]:

$$\nabla \times \vec{E} = -\mu_0 \frac{\partial \vec{H}}{\partial t}, \quad (1)$$

$$\nabla \times \vec{H} = \varepsilon_0 \frac{\partial \vec{E}}{\partial t} + \vec{J}, \quad (2)$$

$$\frac{\partial \vec{J}}{\partial t} + \nu \vec{J} = \varepsilon_0 \omega_p^2 \vec{E}, \quad (3)$$

where, \vec{H} is the magnetic field, μ_0 is the permeability and ε_0 is the free space permittivity. Furthermore, $\omega_p = 2\pi f_p = \sqrt{Ne^2/m\varepsilon_0}$, in which f_p is the plasma resonant frequency (Hz), and N is the electron density (m^{-3}), ν is the average collision frequency (Hz), m and e are the electron mass (kg) and charge (C) respectively. Equation (3) is the auxiliary equation for accounting the effect of

plasma. By performing backward differencing approximation to (1)–(3), a second order approximation for numerical simulation can be derived for Yee’s FDTD formulation. After discretizing \vec{E} , \vec{H} and \vec{J} in spatial discretization, Δx , Δy , Δz and the time step Δt , the electromagnetic wave propagation is simulated in time domain. For the details of FDTD methodology, the reader is referred to [10, 11]. To obtain the far-zone radiated field, we use near to far zone transformation on the boundary of the FDTD domain. Detailed procedure can be found in [10–12]. The FDTD approach allows the impedance evaluation simply by calculating the input voltage and current associated with the excitation point where the field is applied. These time-domain results are subsequently converted to frequency domain using FFT.

A schematic of the simulation setup for a surface wave generated plasma column is shown in Fig. 1. In this setup, a 600 mm long plasma column with a radius of 12.5 mm and the thickness of 0.5 mm with $\varepsilon_r = 3$ is inserted in a metallic box with the dimensions of $300 \times 300 \times 53 \text{ mm}^3$ under a metallic plate with $500 \times 500 \times 3 \text{ mm}^3$ as a ground plane. A copper ring, with a thickness and a height of 3 mm and 30 mm, placed, 10 mm below the ground plane, around the tube and is used as a coupling sleeve to apply the electric field between the ring and the box. The excitation voltage is applied through a coaxial structure to the coupling sleeve. The FDTD problem space has $100 \times 100 \times 250$ cells. Perfectly matched layer (PML) boundaries were used at the surfaces of the FDTD domain to simulate the far zone radiated field. The waveform of the source is a modulated Gaussian pulse.

3. NUMERICAL RESULTS AND DISCUSSION

In a surface wave driven plasma monopole antenna, similar to a conventional metallic antenna [13], one method to widen the acceptable operational bandwidth will be to decrease the L/r ratio, where L is the length of the plasma antenna and r is the radius of the tube. It has been observed that for a given length of a plasma column, its impedance variations become less sensitive as a function of frequency as L/r decreases. Thus, more broadband characteristics can be obtained by increasing the diameter of the plasma tube, similar to metallic conventional antennas. To demonstrate this, in Fig. 2(a), we have plotted, as a function of frequency, the input resistance and reactance of plasma monopole antenna with $L/r = 70, 34$ and 23 which correspond to $\Omega = 10, 8.5$ and 7.6 as the thickness parameter defined by $\Omega = 2 \ln(2L/r)$.

When the plasma frequency is twice larger than the excitation frequency, the imaginary part of the input impedance of the plasma antenna can be eliminated by making the total length, L , of the antenna less than $\frac{\lambda}{4}$, where λ is the wavelength. Numerical investigation of a plasma column, with a plasma frequency of 7500 MHz and the collision frequency of 400 MHz, as shown in Fig. 2(b), indicates that the first resonant length of the antenna is approximately $0.185\lambda F'$, where $F' = \frac{L/r}{1+L/r}$. This value increases by increasing the plasma frequency and consequently the conductivity of the plasma. However, for the plasma frequency of 20 GHz in the column the resonant length becomes $0.195\lambda F'$. The resonant length is reported as $0.24\lambda F'$ in [13] for a conventional metallic antenna. The resonant length of the plasma antenna is a function of the radius of the plasma tube as well as the plasma frequency, as shown in Fig. 2(c). Increasing the radius of the tube decreases the resonant length of the antenna. Investigation on the antenna efficiency and gain of a plasma element with the plasma frequency of 7500 MHz, as shown in Figs. 2(d) and 2(e), reveals that increasing Ω , decreases considerably the antenna gain and efficiency. Furthermore, it seems nearly the same

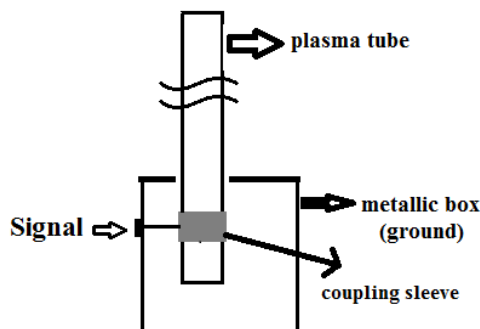


Figure 1: Geometry of surface wave driven plasma monopole antenna for simulation.

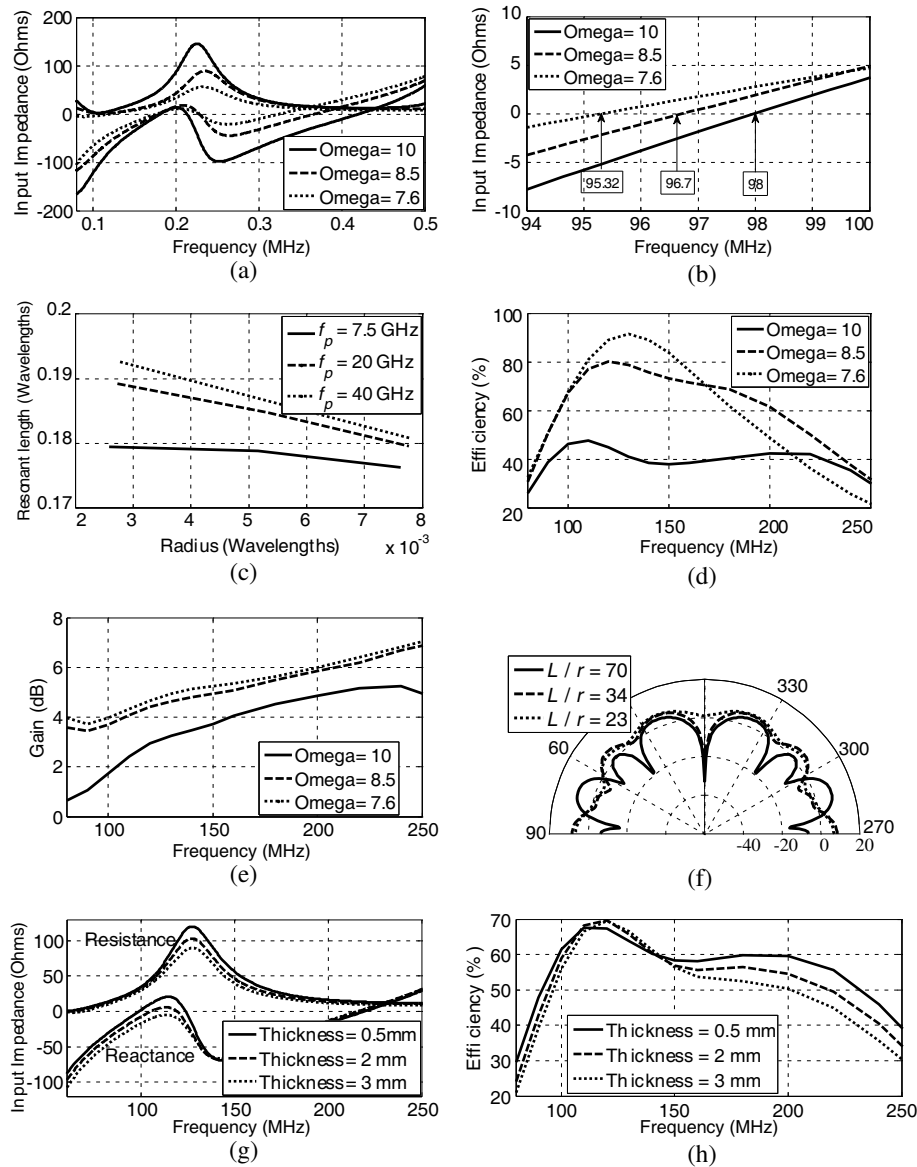


Figure 2: The effects of the plasma tube radii for plasma frequency of 7500 MHz and collision frequency of 400 MHz on the antenna parameters: (a) input impedance, (b) input reactance, (c) resonant length, (d) efficiency, (e) gain, (f) radiation pattern, (g) the effects of the tube thickness on the input impedance, and (h) efficiency.

for Ω values of 8.5 and 7. The radiation pattern is essentially unaffected by the thickness of the plasma tube in regions of intense radiation. However, as the radius of the tube increases, the minor lobes diminish in intensity and the nulls are replaced by low level radiation as shown in Fig. 2(f).

Because of an insulating outer envelope around the plasma column, the radiation characteristics of the plasma antenna will be affected by its thickness. The results of the numerical investigation have shown that increasing the thickness, from 0.5 mm to 3 mm in a constant permittivity, decreases the peak input impedance of the antenna as well as the antenna efficiency and widens the bandwidth, as shown in Fig. 2(g) and Fig. 2(h). The dielectric tube behaves like a capacitor in the excitation point between the coupling sleeve and plasma.

4. CONCLUSION

This investigation has established a number of characteristics of the discharge tube of a SWD plasma monopole antenna with a constant plasma frequency. It has been shown that the larger the diameter of the plasma tube is, more broadband characteristics can be obtained. Moreover, the L/r ratio of 34 can be considered as an optimum value to achieve a compromise between the maximum

gain and bandwidth of the antenna. It has also been observed that decreasing the thickness of the plasma tube decreases the bandwidth of the antenna. However, using a higher thickness of the tube is not a very efficient technique to broadband the plasma antenna.

ACKNOWLEDGMENT

This work is sponsored by Iran telecommunication research center (ITRC). The authors would like to appreciate their kindly supports.

REFERENCES

1. Sadeghikia, F., F. Hodjat-Kashani, J. Rashed-Mohassel, and J. Ghayoomeh-Bozorgi, "Characterization of a surface wave driven plasma monopole antenna," *Journal of Electromagnetic Waves and Applications*, Vol. 26, Nos. 2–3, 239–250, 2012.
2. Sadeghikia, F., F. Hodjat-Kashani, J. Rashed-Mohassel, and J. Ghayoomeh-Bozorgi, "A yagi-uda plasma monopole array," *Journal of Electromagnetic Waves and Applications*, Vol. 26, No. 7, 885–894, 2012.
3. Rayner, J. P., A. P. Wichello, and A. D. Cheetham, "Physical characteristics of plasma antennas," *IEEE Trans. Plasma Sci.*, Vol. 32, No. 1, 269–281, 2004.
4. Cerri, G., R. D. Leo, V. M. Primiani, and P. Russo, "Measurement of the properties of a plasma column used as a radiating element," *IEEE Trans. Instrumentation and Measurement*, Vol. 57, No. 2, 242–247, Feb. 2008.
5. Anderson, T., E. Alexeff, E. Farshi, and N. Karnam, "An operating intelligent plasma antenna," *16th IEEE International Conference on Pulsed Power*, 353–356, Albuquerque, New Mexico, USA, Jun. 2007.
6. Kumar, R. and D. Bora, "Experimental study of parameters of a plasma antenna," *Plasma Sci. and Tech.*, Vol. 12, No. 5, 592–600, 2010.
7. Lee, Y. and S. C. Ganguly, "Analysis of a plasma column antenna using FDTD method," *Mic. and Opt. Tech. Letters*, Vol. 46, No. 3, 252–259, 2005.
8. Qian, Z. H., K. W. Leung, R. S. Chen, and D. X. Wang, "FDTD analysis of plasma whip antenna," *Antennas and Propag. Society Int. Symposium IEEE*, 166–169, Washington DC, USA, Jul. 2005.
9. Nickisch, L. J. and P. M. Franke, "Finite difference time domain solution of Maxwell's equations for the dispersive ionosphere," *IEEE Antennas and Propagation Magazine*, Vol. 34, No. 5, 33–39, Oct. 1992.
10. Kunz, K. S. and R. J. Luebbers, *The Finite Difference Time Domain Method for Electromagnetics*, CRC Press, Boca Raton, FL, 1993.
11. Toflove, A., *Computational Electromagnetics: The Finite Difference Time Domain Method*, Artech House, Boston, FL, 1995.
12. Luebbers, R. J., K. S. Kunz, M. Schneider, and F. Hansberger, "A finite difference time domain near to far zone transformation," *IEEE Trans. Antennas and Propagation*, Vol. 39, No. 4, 429–433, Apr. 1991.
13. Balanis, A., *Antenna Theory, Analysis and Design*, John Wiley & Sons Inc., New Jersey, Apr. 2005.

Characteristics of Plasma Antennas under Radial and Axial Density Variations

F. Sadeghikia¹, F. Hodjat-Kashani¹, J. Rashed-Mohassel², and S. J. Ghayoomeh-Bozorgi¹

¹Department of Electrical Engineering, Iran University of Science and Technology
P. O. Box 16846-13114, Farjam, Narmak, Tehran, Iran

²Center of Excellence on Applied Electromagnetic Systems, ECE Department
University of Tehran, P. O. Box 14395-515, Tehran, Iran

Abstract— This paper examines the characteristics of a surface wave driven argon plasma monopole antenna with an excitation power of 60 W and gas pressure of 0.4 mb using finite difference time domain method. The knowledge of the plasma density distribution as a function of radial and axial variations in the plasma tube is one of the most important aspects of the plasma antennas. To this end, a numerical model of the pre-ionized plasma tube is investigated under different radial distribution functions as well as linear axial variations. The model completely characterizes the radiation characteristics of a plasma monopole antenna considering its input impedance, efficiency and radiation pattern using finite difference time domain (FDTD) simulation. The results show that non-uniform radial distribution leads to a considerable reduction in the antenna gain and a minor shift in the resonant frequency.

1. INTRODUCTION

Plasma antennas can be used in many applications [1] and are particularly suitable for wireless terrestrial or aeronautical communication systems. The physical properties of plasma antennas were investigated experimentally [1, 2], showing the relationship between the plasma density and the applied power. Numerical simulations of a plasma column antenna and an array of Yagi-Uda plasma monopole array were previously reported [3, 4]. In almost all reported simulations of plasma column antennas, the density of plasma in the column has been considered constant [5, 6] or linear [3, 4]; however plasma density varies along the column in radial directions as well as the axial one [7, 8]. There are some different ideas on the radial distribution function of the plasma density [9].

In the present work, our major task is computing the plasma antenna parameters and its radiation characteristics after excitation, while the axial plasma density is considered linear and the radial profile is considered different functions such as zero order Bessel, cosine and parabolic. This paper is organized as follows: In Section 2, the simulation setup and FDTD numerical method for a monopole plasma antenna are briefly discussed and then the plasma density in the radial and axial positions are described in Section 3. The numerical results are presented in Section 4 and we summarize this investigation in Section 5.

2. OVERVIEW OF THE SIMULATION SETUP

A surface wave driven plasma antenna is employed in this investigation, using the arrangement shown in Fig. 1. The antenna consists of a 1 m long fluorescent tube with a radius of 13 mm and

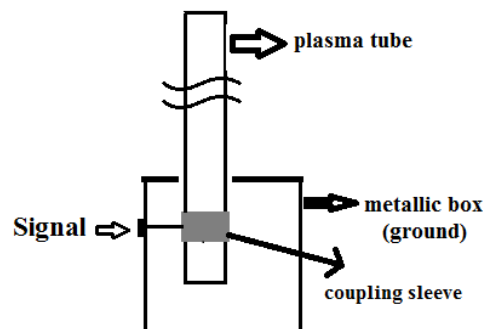


Figure 1: Geometry of surface wave driven plasma monopole antenna.

a thickness of 1 mm from quartz, filled with argon at a nominal pressure of 0.4 mb. The plasma is pre ionized using a surface wave launcher at a power of 60 W in the frequency of 500 MHz. RF signal launcher consists of a copper collar of length 32 mm and the thickness of 2 mm mounted 3 mm below a circular hole cut on the top of a grounded box. A coaxial cable is directly connected to the collar. The outer and inner radii of the coaxial cable are 2 mm and 4.6 mm, respectively. The FDTD simulation space is $100 \times 100 \times 250 \text{ mm}^3$. In this investigation, the direct integration method (DI) is used [10, 11] for the simulation of the the plasma column. Plasma is a type of Debye dispersive media [11]. So, at any particular \vec{E} observation point, where \vec{E} is the electric field, Ampere's law in the time domain can be expressed as shown in Eq. (1).

$$\frac{\partial \vec{J}}{\partial t} + \nu \vec{J} = \varepsilon_0 \omega_p^2 \vec{E} \quad (1)$$

where \vec{J} is the plasma polarization current density, $\omega_p = 2\pi f_p = \sqrt{Ne^2/m\varepsilon_0}$ in which f_p is the plasma resonant frequency (Hz), N is the electron density (m^{-3}), m and e are the electron mass (Kg) and charge, respectively and ν is the collision frequency (Hz). The auxiliary Eq. (1) accounts for the effects of the plasma. This numerical method was completely introduced before in [3, 4]. After discretizing of \vec{E} , \vec{H} and \vec{J} in spatial discretization Δx , Δy , Δz and the time step Δt , the electromagnetic wave propagation is simulated in time domain by performing backward differencing approximation to that equation. As in the classic Yee algorithm, the electromagnetic quantities are calculated in a staggered grid and in an iterative way by a leapfrog time stepping [11]. More details of the FDTD methodology is found in [10, 11]. The plasma density in the column is a function of axial and radial distributions of free electrons. In the next section we discuss the exact value of density in the simulation setup.

3. PLASMA DENSITY

When surface wave carries sufficient power, it can sustain the plasma column along the propagation axis. However, the electron density steadily decreases from the launcher because the power flux of the wave decreases axially as power is gradually transferred to the discharge. Consequently, the plasma column is axially non uniform [1–4, 7, 8] which will result in a non uniform conductivity along the column. The plasma density decreases along the antenna from a high density n_0 in the position of excitation to the critical density $n_{critical}$ at the far end of the antenna, i.e.,

$$n_0 = A(p)\sqrt{P_0}, \quad (2)$$

$$n_{critical} = \frac{4\pi^2 \varepsilon_0 m_e}{e^2} f^2 (1 + \varepsilon_d), \quad (3)$$

where, P_0 , is the applied RF power, $A(p)$ is a constant for a given pressure, f is the excitation frequency and ε_d is the permittivity of the dielectric tube. The evaluation of these equations are not reported here and readers interested in this subject can refer to [1, 7, 8]. Following the analysis of [1], the length of a plasma antenna is $h = \frac{n_0 L_0}{n_{critical}} - L_0$, where, $L_0 = \frac{n_{critical}}{kv}$ and k is a constant value for a given pressure. Considering the antenna along z axis, the plasma density is stated as:

$$n(z, p) = n_{critical} + kv(h - z). \quad (4)$$

There are no experimental measurement reports on the radial density distribution. Examinations of scientists [7–9] reveal that as βR becomes larger than one, the wave field increasingly concentrates radially at the plasma-dielectric interface. $\beta = 2\pi/\lambda$ is the phase coefficient, λ is the wavelength and R is the radius of the plasma column. So, the electron density value at or close to the tube wall is lower than the cross sectional average density. The radial profile of electron density, $n(r)/n(0)$, where r is the radial position, is determined by two factors. The first factor is the global movement of particles toward the wall, which depends essentially on the vessel configuration and dimensions. The second factor is the radial variations of ionization rate. Ferreira's modeling [9] shows that $n(r)/n(0)$ is flatter than the Bessel function $J_0(2.4r/R)$. Moreover, Trivelpiece [7] approximated the radial density distribution of the plasma by a parabolic profile as $n(r)/n(0) = [1 - K(r/R)^2]$. In addition, K is the rate of parabolic decrease and the angular plasma frequency, ω_p , corresponds to the average cross sectional electron density expressed in Eq. (5).

$$\omega_p = \sqrt{\frac{4\pi \langle n \rangle e^2}{m}}. \quad (5)$$

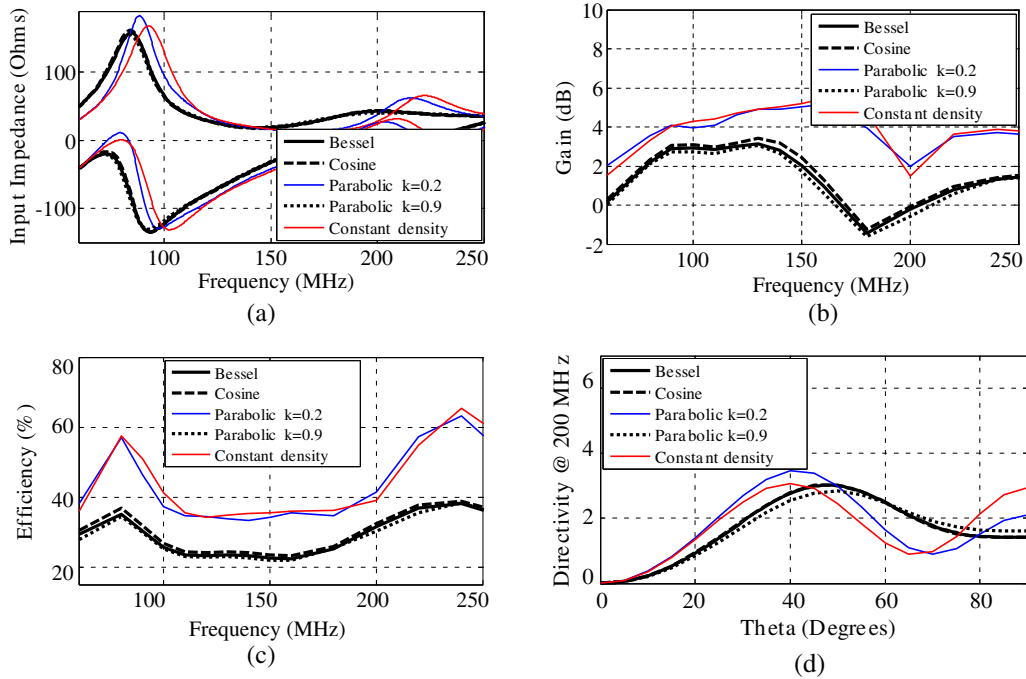


Figure 2: The effects of radial and axial density distributions in the plasma column on the antenna parameters: (a) input impedance, (b) gain, (c) efficiency, (d) directivity at 200 MHz.

where, $\langle n \rangle$, is the average cross sectional electron density and is given by:

$$\langle n \rangle = \frac{2}{R^2} \int_0^R n(r) r dr. \quad (6)$$

Since in this investigation, the typical pressure of 0.4 mb is assumed in the tube filled with argon, k and ν are 5×10^9 and 5×10^8 Hz respectively [1]. The initial values of the numerical simulation are characterized by the following parameters:

- $f_d = 500$ MHz, $\epsilon_d = 3.75$, $R = 12$ mm,
- $p = 0.4$ mb, $A(p) = 0.28 \times 10^{18} \text{ m}^{-3} \text{ W}^{1/2}$, $P_0 = 60$ W,
- $k = 5 \times 10^9$, $\nu = 5 \times 10^8$ Hz, $h = 861.77$ mm.

4. NUMERICAL RESULTS

The numerical FDTD program is validated before in [3,4]. Having now established the plasma column's radial and axial distributions, we will investigate their effects on the antenna's radiation characteristics. FDTD simulation results of a SWD plasma antenna in the pressure of 0.4 mb and 500 MHz excitation frequency at the excitation power of 60 W and the radial density distributions as Bessel function, cosine function, and parabolic function are presented in Fig. 2. The rate of parabolic K values are considered as 0.2, and 0.9 and the axial density distribution is linear.

It is observed that the variations of radial density with a parabolic function of $K = 0.9$, cosine and Bessel functions leads to the same input impedance and radiation characteristics. Moreover, the results of the constant radial densities and the $K = 0.2$ parabolic one follow the same trend. However, there are observed some differences between these two categories. The difference in the radiation characteristics is because the average radial densities are not the same. Therefore, the consideration of the constant radial density causes a little deviation in the resonant frequency of the antenna, as shown in Fig. 2(a), while increases in some extent the antenna gain and efficiency, as in Figs. 2(b) and 2(c). These deviations may lead us to a non accurate radiation characteristics of a plasma antenna. The directivity of a plasma antenna may be found from the far zone radiated fields. Fig. 2(d) shows the directivity of a plasma antenna at the operating frequency of 200 MHz. It is observed that the main lobe direction differs between these two groups. Whether or not the

plasma radial density is a significant factor affects the radiation characteristics of a plasma antenna. So, it is a crucial issue when considering the radiation characteristics of a plasma antenna. Bessel function can be considered as the most general radial density distribution.

5. CONCLUSION

Since Plasma columns are, in general, axially and radially non uniform, different radial density distributions such as Bessel, cosine and parabolic functions have been considered in this investigation. We have shown that the radial non uniformity of the plasma has some, though limited, influence on the antenna radiation characteristics. Bessel function distribution of the radial density, which follows the same trend with cosine and parabolic function with $K = 0.9$, represents a more general distribution. Radial density distribution considering is inevitable when βR becomes larger.

REFERENCES

1. Rayner, J. P., A. P. Wichello, and A. D. Cheetham, "Physical characteristics of plasma antennas," *IEEE Trans. Plasma Sci.*, Vol. 32, No. 1, 269–281, 2004.
2. Kumar, R. and D. Bora, "A reconfigurable plasma antenna," *Journal of Applied Physics*, Vol. 107, 2010.
3. Sadeghikia, F., F. Hodjat-Kashani, J. Rashed-Mohassel, and S. J. Ghayoomeh-Bozorgi, "Characterization of a surface wave driven plasma monopole antenna," *Journal of Electromagnetic Waves and Applications*, Vol. 26, Nos. 2–3, 239–250, 2012.
4. Sadeghikia, F., F. Hodjat-Kashani, J. Rashed-Mohassel, and S. J. Ghayoomeh-Bozorgi, "A Yagi-Uda plasma monopole array," *Journal of Electromagnetic Waves and Applications*, Vol. 26, No. 7, 885–894, 2012.
5. Lee, Y. and S. C. Ganguly, "Analysis of a plasma column antenna using FDTD method," *Microwave and Optical Technology Letters*, Vol. 46, No. 3, 252–259, June 2005.
6. Qian, Z. H., R.-S. Chen, K. W. Leung, and H. W. Yang, "FDTD analysis of microstrip patch antenna covered by plasma sheath," *Progress In Electromagnetics Research*, Vol. 52, 173–183, 2005.
7. Moisan, M., A. Shivorava, and A. W. Trivelpiece, "Experimental investigation of the propagation of surface waves along a plasma column," *Plasma Physics*, Vol. 24, No. 11, 1331–1400, 1982.
8. Oleg, A. P., *High Density Plasma Sources: Design, Physics and Performance*, Noyes Publication, Park Ridge, New Jersey, 1995.
9. Ferrira, C. M., "Modeling of a low-pressure plasma column sustained by a surface wave," *J. Phys. D: Appl. Phys.*, No. 16, 1673–1685, 1983.
10. Kunz, K. S. and R. J. Luebbers, *The Finite Difference Time Domain Method for Electromagnetics*, CRC Press, Boca Raton, FL, 1993.
11. Toflove, A., *Computational Electromagnetics: The Finite Difference Time Domain Method*, Artech House, Boston, FL, 1995.

Mathematical Modeling of Plane Chiral Waveguide Using Mixed Finite Elements

A. N. Bogolyubov, Yu. V. Mukhartova, J. Gao, and N. A. Bogolyubov
Faculty of Physics, Moscow State University, Russia

Abstract— This work presents the investigation of a plane waveguide with perfectly conducting walls, containing a chiral insertion. The distribution of electrical field inside the chiral insertion, excited by an incident normal wave of the waveguide, is calculated. The full vector statement of a problem is considered. The method of mixed finite elements, that prevents spurious modes appearance, is used for numerical solution of the problem.

1. INTRODUCTION

Metamaterials are the artificial media, which interaction with electromagnetic field differs significantly from interaction with ordinary natural media. Among modern metamaterials bi-anisotropic, bi-isotropic and negative index materials are of a special interest.

Bi-isotropic medium is the most general type of linear isotropic medium. The main difference between ordinary dielectrics or magnetics and bi-isotropic media is that the electric or magnetic field, applied to them, produces both electric and magnetic polarization:

$$\vec{D} = \varepsilon\vec{E} + \xi\vec{H}, \quad \vec{B} = \varsigma\vec{E} + \mu\vec{H},$$

where $\xi = (\kappa - i\chi)$, $\varsigma = (\kappa + i\chi)$. In these expressions ε is the permittivity of the medium, μ is a permeability, κ is Tellegen parameter, and χ is a chirality parameter. Constitutive relations are formulated in frequency domain for harmonic time dependence ($e^{-i\omega t}$).

The important subclass of bi-isotropic media are chiral media with $\kappa \equiv 0$. Chirality is a geometrical property of an object not to coincide with its reflection in a plane mirror. The macroscopically uniform material is assumed chiral, if it is constructed of chiral objects, natural (molecules) or artificial.

2. THE STATEMENT OF THE PROBLEM

Consider a plane waveguide with perfectly conducting walls, situated at a distance a from each other. The waveguide contains an insertion of chiral material (Figure 1). The insertion is located in the area $z \in [0, z_0]$. Let the parameters of the insertion be ε , μ , χ , and the parameters of the waveguide filling outside the insertion be ε_0 and μ_0 .

The following numerical algorithm for calculating electrical field inside the chiral insertion, excited by an incident normal wave or a combination of normal waves, can be proposed. First of all we reduce Maxwell's equations with perfectly conducting boundary conditions to the boundary problem for electric field vector in the finite area $z \in [0, z_0]$, using partial radiation conditions:

$$\text{rot} \frac{1}{\mu} \text{rot} \vec{E} + \frac{\omega}{c} \text{rot} \frac{\chi}{\mu} \vec{E} + \frac{\omega \chi}{c \mu} \text{rot} \vec{E} - \frac{\omega^2}{c^2} \left(\varepsilon - \frac{\chi^2}{\mu} \right) \vec{E} = 0, \quad x \in (0, a), \quad z \in (0, z_0), \quad (1)$$

$$\left[\vec{e}_z, \vec{E} \right] \Big|_{z=0} = \left[\vec{e}_z, \vec{E}^{ext} \right] \Big|_{z=0}, \quad \left[\vec{e}_z, \vec{E} \right] \Big|_{z=z_0} = \left[\vec{e}_z, \vec{E}^{ext} \right] \Big|_{z=z_0}, \quad (2)$$

$$E_y|_{x=0} = E_y|_{x=a} = 0, \quad E_z|_{x=0} = E_z|_{x=a} = 0. \quad (3)$$

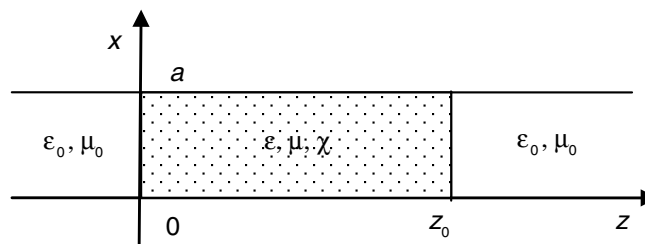


Figure 1: The scheme of the waveguide.

Here $\{\vec{E}^{ext}, \vec{H}^{ext}\}$ is the field outside the insertion:

$$\vec{E}^{ext} = \sum_{n=1}^{\infty} \left\{ R_n^m \vec{E}_{n,-}^m + R_n^e \vec{E}_{n,-}^e \right\} + \vec{E}_+^{ins}, \quad \vec{H}^{ext} = \sum_{n=1}^{\infty} \left\{ R_n^m \vec{H}_{n,-}^m + R_n^e \vec{H}_{n,-}^e \right\} + \vec{H}_+^{ins} \quad (4)$$

for $z < 0$ and

$$\vec{E}^{ext} = \sum_{n=1}^{\infty} \left\{ T_n^m \vec{E}_{n,+}^m + T_n^e \vec{E}_{n,+}^e \right\}, \quad \vec{H}^{ext} = \sum_{n=1}^{\infty} \left\{ T_n^m \vec{H}_{n,+}^m + T_n^e \vec{H}_{n,+}^e \right\} \quad (5)$$

for $z > z_0$, where $\{\vec{E}_{n,\pm}^e, \vec{H}_{n,\pm}^e\}$ and $\{\vec{E}_{n,\pm}^m, \vec{H}_{n,\pm}^m\}$ are the normal waves of electric and magnetic type respectively, and $\{\vec{E}_+^{ins}, \vec{H}_+^{ins}\}$ is the incident field.

The generalized statement of the problem is the following: we must find a vector $\vec{E} \in H(\text{rot}, D)$, that satisfies the equation

$$\begin{aligned} & \int_0^a \int_0^{z_0} \frac{1}{\mu} \left\{ \frac{\partial E_y^*}{\partial z} \frac{\partial E_y}{\partial z} + \frac{\partial E_y^*}{\partial x} \frac{\partial E_y}{\partial x} + \frac{\partial E_x^*}{\partial z} \frac{\partial E_x}{\partial z} + \frac{\partial E_z^*}{\partial x} \frac{\partial E_z}{\partial x} - \frac{\partial E_x^*}{\partial z} \frac{\partial E_z}{\partial x} - \frac{\partial E_z^*}{\partial x} \frac{\partial E_x}{\partial z} \right\} dx dz \\ & + \frac{\omega}{c} \int_0^a \int_0^{z_0} \frac{\chi}{\mu} \left\{ -\frac{\partial E_y^*}{\partial z} E_x + \left(\frac{\partial E_x^*}{\partial z} + \frac{\partial E_x^*}{\partial x} \right) E_y + \frac{\partial E_y^*}{\partial x} E_z - \frac{\partial E_y}{\partial z} E_x^* + E_y^* \left(\frac{\partial E_x}{\partial z} - \frac{\partial E_z}{\partial x} \right) + E_z^* \frac{\partial E_y}{\partial x} \right\} dx dz \\ & - \frac{\omega^2}{c^2} \int_0^a \int_0^{z_0} \left(\varepsilon - \frac{\chi^2}{\mu} \right) \vec{E}^* \vec{E} dx dz - \frac{2ik_0^2}{\mu_0 a} \sum_{n=1}^{\infty} \frac{1}{\gamma_n} \int_0^a E_x^*(x, z_0) \cos \frac{\pi n x}{a} dx \int_0^a E_x(x, z_0) \cos \frac{\pi n x}{a} dx \\ & - \frac{2ik_0^2}{\mu_0 a} \sum_{n=1}^{\infty} \frac{1}{\gamma_n} \int_0^a E_x^*(x, 0) \cos \frac{\pi n x}{a} dx \int_0^a E_x(x, 0) \cos \frac{\pi n x}{a} dx \\ & - \frac{2i}{\mu_0 a} \sum_{n=1}^{\infty} \gamma_n \int_0^a E_y^*(x, z_0) \sin \frac{\pi n x}{a} dx \int_0^a E_y(x, z_0) \sin \frac{\pi n x}{a} dx \\ & - \frac{2i}{\mu_0 a} \sum_{n=1}^{\infty} \gamma_n \int_0^a E_y^*(x, 0) \sin \frac{\pi n x}{a} dx \int_0^a E_y(x, 0) \sin \frac{\pi n x}{a} dx \\ & = -\frac{1}{\mu_0} \left\{ \int_0^a E_x^*(x, 0) \cdot \left(\frac{\partial E_x^{ins}}{\partial z} - \frac{\partial E_z^{ins}}{\partial x} \right) \Big|_{z=0} dx + \int_0^a E_y^*(x, 0) \frac{\partial E_y^{ins}}{\partial z} \Big|_{z=0} dx \right\} \\ & - \frac{2ik_0^2}{\mu_0 a} \sum_{n=1}^{\infty} \frac{1}{\gamma_n} \int_0^a E_x^*(x, 0) \cos \frac{\pi n x}{a} dx \int_0^a E_x^{ins}(x, 0) \cos \frac{\pi n x}{a} dx \\ & - \frac{2i}{\mu_0 a} \sum_{n=1}^{\infty} \gamma_n \int_0^a E_y^*(x, 0) \sin \frac{\pi n x}{a} dx \int_0^a E_y^{ins}(x, 0) \sin \frac{\pi n x}{a} dx. \end{aligned} \quad (6)$$

for any vector $\vec{E}^* \in H(\text{rot}, D)$, satisfying boundary conditions (3).

3. NUMERICAL SOLUTION OF THE PROBLEM

The finite-element method is a powerful method of analysis of waveguide boundary problems, but it has a drawback. For a full-vector statement of a problem this method can give nonphysical, spurious solutions that satisfy the finite-element equations, but not the original boundary problem. So the method of mixed finite elements, that prevents spurious modes appearance, is used for numerical solution of the problem.

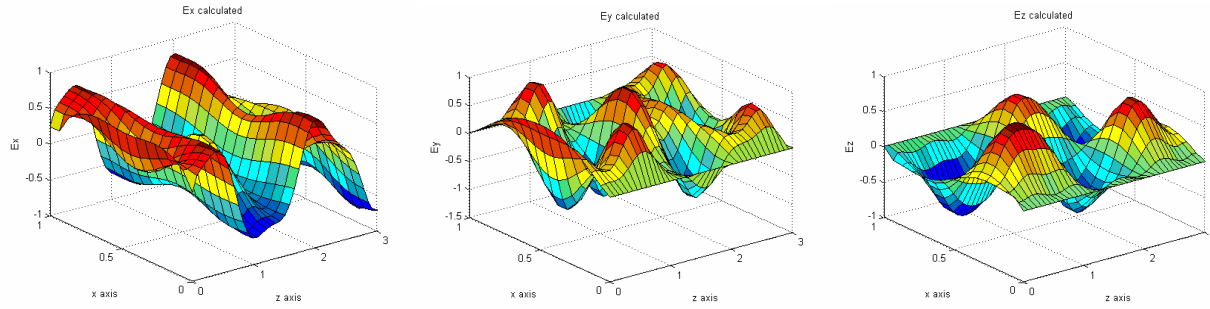


Figure 2: Components of the field inside the insertion for incident wave of fundamental TE-type.

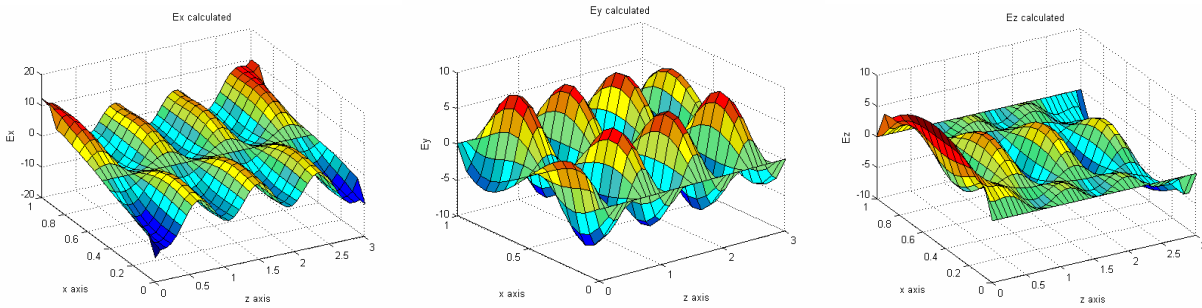


Figure 3: Components of the field inside the insertion for incident wave of fundamental TM-type.

Consider the lattice $z^j = j \cdot \Delta z$, $x^i = i \cdot \Delta x$ and basic functions:

$$N_i(\xi) = \begin{cases} \frac{\xi_{i+1} - \xi}{\xi_{i+1} - \xi_i}, & \xi \in [\xi_i, \xi_{i+1}], \\ \frac{\xi - \xi_{i-1}}{\xi_i - \xi_{i-1}}, & \xi \in [\xi_{i-1}, \xi_i], \\ 0, & \xi \in (-\infty, \xi_{i-1}) \cup (\xi_{i+1}, +\infty) \end{cases} \quad P_{i,i+1}(\xi) = \begin{cases} 1, & \xi \in [\xi_i, \xi_{i+1}], \\ 0, & \xi \in (-\infty, \xi_i) \cup (\xi_{i+1}, +\infty). \end{cases} \quad (7)$$

The numerical solution of the problem we are searching in the form:

$$N_i(\xi) = \begin{cases} E_x(x, z) = \sum_{i=0}^{I-1} \sum_{j=0}^J E_x^{i,j} N_j(z) P_{i,i+1}(x), \\ E_y(x, z) = \sum_{i=1}^{I-1} \sum_{j=0}^J E_y^{i,j} N_j(z) N_i(x), \\ E_z(x, z) = \sum_{i=1}^{I-1} \sum_{j=0}^{J-1} E_z^{i,j} P_{j,j+1}(z) N_i(x). \end{cases} \quad (8)$$

The unknown coefficients $E_x^{i,j}$, $E_y^{i,j}$, $E_z^{i,j}$ can be found as a solution of algebraic system of equations, obtained after substitution (8) for E_x , E_y , E_z in the Equation (6), and taking

- 1) $\vec{E}^*(x, z) = \{N_j(z) P_{i,i+1}(x)\} \vec{e}_x$, $i = \overline{0, (I-1)}$, $j = \overline{0, J}$;
- 2) $\vec{E}^*(x, z) = \{N_j(z) N_i(x)\} \vec{e}_y$, $i = \overline{1, (I-1)}$, $j = \overline{0, J}$;
- 3) $\vec{E}^* = \{P_{i,i+1}(z) N_j(x)\} \vec{e}_z$, $i = \overline{1, (I-1)}$, $j = \overline{0, (J-1)}$.

The algorithm proposed was tested on empty waveguide and used for modeling electric field inside the chiral insertion for different values of chirality parameter and for incident waves of TM and TE types. The results for the case $\omega/c = 5$, $a = 1$, $z_0 = 3$, $\varepsilon_0 = \mu_0 = 1$, $\chi = 0.8$ are presented in Figures 2 and 3.

4. CONCLUSIONS

Computations made illustrate that the field inside the chiral insertion present a result of interference of different mode types. So we can conclude that this system with appropriate parameters may be used for transformation of one type of normal waves to another.

The method proposed can be generalized for anisotropic filling of a waveguide and for a three dimensional case. It is also suitable for solving inverse synthesis problem of a waveguide with desirable features.

REFERENCES

1. Lindell, I. V., A. H. Sihvola, S. A. Tretyakov, and A. J. Viitanen, *Electromagnetic Waves in Chiral and Bi-Isotropic Media*, Artech House, Boston, MA, 1994.
2. Bogolyubov, A. N., N. A. Mosunova, and D. A. Petrov, *Mathematical Modeling*, Vol. 19, No. 5, 3, 2007.
3. Bogolyubov, A. N., J. Gao, and Yu. V. Mukhartova, "The excitation of electromagnetic oscillations in the aria with chiral filling," *Journal of Computational Mathematics and Mathematical Physics*, Vol. 51, No. 9, 1721, 2011.
4. Bogolyubov, A. N., A. L. Delitsyn, A. V. Krasilnikova, D. V. Minaev, and A. G. Sveshnikov, "Foreign radioelectronics," *Progress in Modern Radioelectronics*, No. 5, 39, 1998.
5. Bogolyubov, A. N. and A. L. Delitsyn, *Moscow University Physics Bulletin*, No. 1, 9, 1996.
6. Raviart, P. A. and J. M. Thomas, *Mathematics of Computation*, Vol. 31, No. 138, 391, 1977.
7. Bogolyubov, A. N. and A. V. Lavrenova, "The mixed finite element method as applied to waveguide diffraction problem," *Moscow University Physics Bulletin*, Vol. 62, No. 4, 221, 2007.

Avoiding Diffraction Order Singularity in Scattering Matrix Approach Used for Grating Modelling

A. A. Petukhov¹, M. K. Trubetskov², and A. N. Bogolyubov¹

¹Faculty of Physics, Moscow State University, Russia

²Research Computing Center, Moscow State University, Russia

Abstract— The problem of wave diffraction on a multilayer grating is considered. Numerical technique based on a combination of the incomplete Galerkin method and scattering matrix method is applied. The problem of scattering matrix singularity in the case when a new diffraction order appears is treated in detail and the singularity-free expressions for the scattering matrix are introduced.

1. INTRODUCTION

Diffraction grating problems, particularly those for multilayer diffraction gratings, require rigorous stable methods, which can provide fast and efficient computations of the grating properties. One of the most efficient numerical techniques is based on a combination of the incomplete Galerkin method [1] and matrix formalism such as transfer matrix method, scattering matrix method etc. [2, 3]. Within this approach a grating is approximated by a set of inhomogeneous layers irrespective of the grating groove shape. The structure can also include a stack of homogeneous layers. The diffracted wave field is decomposed into discrete set of plane waves, each of them corresponding to a certain diffraction order. The set of Maxwell equations is reduced to one second-order or a system of two first-order matrix differential equations. The layered structure of the grating makes it reasonable to apply matrix methods.

Being rather convenient in implementation, transfer matrix method turns out to be numerically unstable due to possible overflows during computations [2, 3]. The existence of evanescent diffraction orders results in large positive arguments of exponents for thick gratings or for metallic structures, and the calculations are therefore impossible. Scattering matrix approach [3] was suggested as a stable alternative method instead of transfer matrix technique. By implementing the scattering matrix formalism numerical overflows are avoided. However, scattering matrix method has some problems connected with singularity of a scattering matrix in the case when a new diffraction order appears in one of the grating layers, in the incident medium or in the substrate. The wave vector for this diffraction order is exactly parallel to the layer interface and has zero component in the direction perpendicular to the interface. Treated directly this requires inversion of the propagation matrix, which has a zero eigenvalue.

In this paper, we suggest a rigorous and physically consistent approach to avoid the singularities of this type. Specific expressions for the scattering matrix are given, which are free of diffraction order singularity. Generalizations for lossy gratings are also discussed.

The paper is organized as follows. In Section 2, we present the physical and mathematical description of a multilayer diffraction grating. In Section 3, we describe the numerical algorithm based on incomplete Galerkin method and scattering matrix method. In Section 4, we present particular expressions for a scattering matrix, which are free of diffraction order singularity. In Section 5, we discuss the physical consistency of the algorithm and the case of lossy gratings. Section 6 gives conclusions.

2. PROBLEM STATEMENT

Let us consider a multilayer one-dimensional periodic diffraction grating (Fig. 1). The whole structure includes the substrate (represented as a light brown area in Fig. 1), the grating itself (yellow area in Fig. 1), and generally (however it is not mandatory) a set of regular homogeneous layers between them (green and light green layers in Fig. 1). The grating is periodic along the x axis with a period d . The z axis is perpendicular to the grating boundaries. The groove shape may be different (binary, triangular, sinusoidal gratings etc.), however this does not affect the method formulation. For definiteness let us consider triangular gratings (Fig. 1). For further numerical treatment the grating profile is approximated as a set of inhomogeneous layers as shown in Fig. 1.

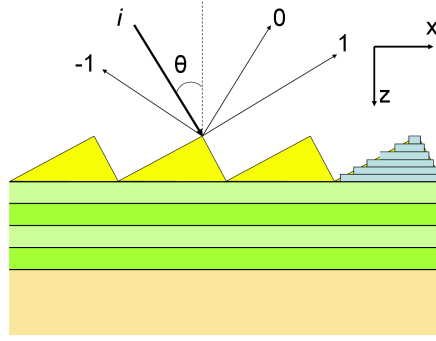


Figure 1: Multilayer grating structure. In one period the grating profile is approximated by a set of layers.

Thus the grating is represented as a set of homogeneous and inhomogeneous layers between two semi-infinite media — the incident medium and the substrate.

A wave with a wavelength λ is considered to be incident on a grating at some given angle θ (direction $\langle i \rangle$ in Fig. 1) and diffracted into discrete directions (diffraction orders). Within this paper we will consider waves with *TE*-polarization, i.e., waves with electric field vector perpendicular to the plane of incidence. There are only three non-zero field components E_y, H_x, H_z in this case and the Maxwell equations for them look like as follows [4]:

$$\begin{cases} \frac{\partial H_x}{\partial z} - \frac{\partial H_z}{\partial x} = -jk_0 \varepsilon(x, z) E_y; \\ \frac{\partial E_y}{\partial z} = -jk_0 H_x; \\ \frac{\partial E_y}{\partial x} = jk_0 H_z, \end{cases} \quad (1)$$

where $\varepsilon(x, z)$ is a dielectric permittivity distribution in the grating region, $k_0 = 2\pi/\lambda$ is a vacuum wave number of the incident wave and $j^2 = -1$. The time dependence is chosen as $e^{-j\omega t}$ with $\omega = k_0 c$, where c is the velocity of light in free space. By elimination the H_z component, the Maxwell equations can be rewritten in the form

$$\begin{cases} \frac{\partial E_y}{\partial z} = -jk_0 H_x; \\ \frac{\partial H_x}{\partial z} = -jk_0 \varepsilon(x, z) E_y + \frac{1}{jk_0} \frac{\partial^2 E_y}{\partial x^2}. \end{cases} \quad (2)$$

The set of Maxwell equations is complemented by the continuity boundary conditions for the tangential field components E_x and H_y at each interface. The incident wave is given in the form

$$E_y^{inc} = e^{jk_{x,0}x + jk_{z,0}^{(I)}z}, \quad (3)$$

where $k_{x,0} = n_I k_0 \sin \theta$, $k_{z,0}^{(I)} = n_I k_0 \cos \theta$ are x - and z -components respectively of the wave vector of the incident wave, n_I is a refractive index of an incident medium (usually the incident medium is air and thus $n_I = 1$).

3. NUMERICAL ALGORITHM

The numerical algorithm for treating the structure under consideration is primarily based on the incomplete Galerkin method [1]. As the grating is periodic along the x axis with a period d we can introduce a set of periodic functions

$$Y_n(x) = \sqrt{\frac{1}{d}} \exp(jk_{x,n}x), \quad n = 0, \pm 1, \pm 2, \dots, \quad (4)$$

where $k_{x,n} = k_0(n_I \sin \theta - n\lambda/d)$, $n = 0, \pm 1, \pm 2, \dots$ are propagation constants for the diffraction orders along the x axis and are obtained from the classical grating equation [5]. The functions $\{Y_n\}$

form an orthonormal basis in the L^2 -space on a segment $[0; d]$. According to the the principle ideas of the incomplete Galerkin method [1], we will look for the approximate solution in the form of a truncated series in terms of the given basis

$$E_y^{(N)}(x, z) = \sum_{n=1}^N U_n(z) Y_n(x), \quad (5)$$

or in matrix form

$$E_y^{(N)}(x, z) = \mathbf{\Phi}(x) \mathbf{U}(z), \quad (6)$$

where $\mathbf{\Phi}(x) = (Y_1(x), Y_2(x), \dots, Y_N(x))$ represents a row-vector of the first N basis functions and a column-vector of z -dependent coefficients is given by $\mathbf{U}(z) = (U_1(z), U_2(z), \dots, U_N(z))^T$. Plugging the solution in the form (6) into Maxwell Equation (2), eliminating the H_x component, multiplying by $\mathbf{\Phi}(x)^*$ and integrating over the grating period we get the equation for the vector of coefficients $\mathbf{U}(z)$:

$$\mathbf{U}''(z) + \left(k_0^2 \int_0^d \mathbf{\Phi}^*(x) \varepsilon(x, z) \mathbf{\Phi}(x) dx - \mathbf{M}^2 \right) \mathbf{U}(z) = 0. \quad (7)$$

Equation (7) is a second-order linear matrix-vector differential equation with constant coefficients in each grating layer. Here \mathbf{M} is a diagonal matrix

$$\mathbf{M} = \begin{pmatrix} k_{x,0} & 0 & \dots & 0 \\ 0 & k_{x,1} & \dots & 0 \\ \vdots & \vdots & \ddots & \vdots \\ 0 & 0 & \dots & k_{x,N} \end{pmatrix}. \quad (8)$$

For obtaining the solution in the grating region and determining the wave amplitudes of all retained diffraction orders the generalization of matrix technique can be applied, which is used for treating homogeneous layered media [6]. Equation (7) can be solved in each grating layer and afterwards the solutions are coupled by the continuity boundary conditions resulting from the boundary conditions for the tangential field components E_y and H_x . The vector of coefficients $\mathbf{U}(z)$ and its z -derivative must be continuous at the each layer interface. Among the most prominent matrix techniques there are transfer matrix method and scattering matrix method. The transfer matrix method is more convenient in implementation, however it is numerically unstable due to possible overflows during calculations (3). The scattering matrix method helps to overcome this difficulty providing numerical stability for calculations. However, the scattering matrix becomes singular in the case when a new diffraction order appears in one of the grating layers, in the incident medium or in the substrate. The wave vector for this diffraction order is exactly parallel to the layer interface and has zero component in the direction perpendicular to the interface.

4. SINGULARITY-FREE SCATTERING MATRIX CALCULATION

The scattering matrix [3] links the incoming and outgoing wave amplitudes in the following manner. Suppose \mathbf{A}_1 is a amplitude vector of a wave incident on the grating. In our case $\mathbf{A}_1(z) = (1, 0, 0, \dots, 0)^T$. The amplitude vectors of the reflected and transmitted waves are denoted as \mathbf{B}_1 and \mathbf{A}_3 respectively. The vector \mathbf{B}_3 denotes the possible incoming waves from the substrate (it is a zero-vector in our case, however it should be kept for a general description of the method). All the amplitude vectors are given in terms of the diffraction orders. The scattering matrix \mathbf{S} is defined by the equation

$$\begin{pmatrix} \mathbf{A}_3 \\ \mathbf{B}_1 \end{pmatrix} = \mathbf{S} \begin{pmatrix} \mathbf{A}_1 \\ \mathbf{B}_3 \end{pmatrix}. \quad (9)$$

Similarly the scattering matrix can be defined for an interface, for a layer or for a set of layers. The scattering matrix for the whole structure can be calculated iteratively. The general formulas for the scattering matrix calculations can be found for example in [3]. However the specific expressions for the interface scattering matrix are not presented in [3]. Furthermore, the problem rising up when a new diffraction order appears exhibits exactly in the interface scattering matrix calculations. Therefore we will give a closer look at this problem and give singularity-free expressions.

The solution of Equation (7) in the k -th layer is given by the following expression:

$$\mathbf{U}_k(z) = \mathbf{Q}_k e^{j\mathbf{\Gamma}_k(z-z_{k-1})} \mathbf{A}_k(z_{k-1}) + \mathbf{Q}_k e^{-j\mathbf{\Gamma}_k(z-z_{k-1})} \mathbf{B}_k(z_{k-1}), \quad (10)$$

where \mathbf{Q}_k is a matrix of eigenvectors and $\mathbf{\Gamma}_k$ is a diagonal matrix of eigenvalues of the matrix $\mathbf{K}(z) = k_0^2 \int_0^d \mathbf{\Phi}^*(x) \varepsilon(x, z) \mathbf{\Phi}(x) dx - \mathbf{M}^2$ in Equation (7) and z_{k-1} is a z -coordinate of the interface between layers k and $(k-1)$. Similar expression can be written for the solution in the layer $(k-1)$. At the interface the amplitude vectors must be coupled under the continuity conditions for $\mathbf{U}(z)$ and $\partial \mathbf{U} / \partial z$ (see Section 3). This gives:

$$\begin{aligned} \mathbf{Q}_k [\mathbf{A}_k(z_{k-1}) + \mathbf{B}_k(z_{k-1})] &= \mathbf{Q}_{k-1} [\mathbf{A}_{k-1}(z_{k-1}) + \mathbf{B}_{k-1}(z_{k-1})]; \\ \mathbf{Q}_k \mathbf{\Gamma}_k [\mathbf{A}_k(z_{k-1}) - \mathbf{B}_k(z_{k-1})] &= \mathbf{Q}_{k-1} \mathbf{\Gamma}_{k-1} [\mathbf{A}_{k-1}(z_{k-1}) - \mathbf{B}_{k-1}(z_{k-1})]. \end{aligned} \quad (11)$$

The interface scattering matrix \mathbf{S}_{k-1}^{int} is defined in the following way:

$$\begin{pmatrix} \mathbf{A}_k(z_{k-1}) \\ \mathbf{B}_{k-1}(z_{k-1}) \end{pmatrix} = \mathbf{S}_{k-1}^{int} \begin{pmatrix} \mathbf{A}_{k-1}(z_{k-1}) \\ \mathbf{B}_k(z_{k-1}) \end{pmatrix}. \quad (12)$$

The expression for the interface scattering matrix \mathbf{S}_{k-1}^{int} is obtained through inverting the matrices \mathbf{Q}_k , \mathbf{Q}_{k-1} , $\mathbf{\Gamma}_k$ and $\mathbf{\Gamma}_{k-1}$. The matrices of eigenvectors \mathbf{Q}_k , \mathbf{Q}_{k-1} are well-conditioned and can be inverted without problems, while the matrices of eigenvalues $\mathbf{\Gamma}_k$, $\mathbf{\Gamma}_{k-1}$ can in definite cases be non-invertible. The eigenvalues represent the propagation constants (along the z axis) for the waves corresponding to different diffraction orders in the grating layer (the same is true for the incident medium of the substrate as well). Diffraction orders can generally be propagating or evanescent and under some conditions (change in wavelength, angle of incidence etc.) evanescent orders can become propagating and vice-versa. At the moment when a new diffraction order appears in the layer k , its z -propagation constant is exactly equal to zero (if there are no losses). Therefore the matrix \mathbf{K} has a zero eigenvalue and the matrix $\mathbf{\Gamma}_k$ cannot be inverted. This can happen for any grating layer including the incident medium and the substrate. However, it is possible to omit the inversion of the matrices $\mathbf{\Gamma}_k$, $\mathbf{\Gamma}_{k-1}$.

To obtain the expression for the interface scattering matrix we must eliminate sequentially $\mathbf{B}_{k-1}(z_{k-1})$ and $\mathbf{A}_k(z_{k-1})$ from Equation (11). To eliminate $\mathbf{B}_{k-1}(z_{k-1})$, instead of multiplying the first equation in (11) by \mathbf{Q}_{k-1}^{-1} and the second one by $(\mathbf{Q}_{k-1} \mathbf{\Gamma}_{k-1})^{-1}$, we modify only the first equation, multiplying it by $\mathbf{Q}_{k-1} \mathbf{\Gamma}_{k-1} \mathbf{Q}_{k-1}^{-1}$, and then sum the modified first equation with the second one. The similar procedure is repeated for eliminating $\mathbf{A}_k(z_{k-1})$. The interface scattering matrix is obtained afterwards in a block form:

$$\begin{aligned} \mathbf{S}_{11}^{int,(k-1)} &= 2 [\mathbf{Q}_k \mathbf{\Gamma}_k + \mathbf{Q}_{k-1} \mathbf{\Gamma}_{k-1} \mathbf{Q}_{k-1}^{-1} \mathbf{Q}_k]^{-1} \mathbf{Q}_{k-1} \mathbf{\Gamma}_{k-1}; \\ \mathbf{S}_{12}^{int,(k-1)} &= [\mathbf{Q}_k \mathbf{\Gamma}_k + \mathbf{Q}_{k-1} \mathbf{\Gamma}_{k-1} \mathbf{Q}_{k-1}^{-1} \mathbf{Q}_k]^{-1} [\mathbf{Q}_k \mathbf{\Gamma}_k - \mathbf{Q}_{k-1} \mathbf{\Gamma}_{k-1} \mathbf{Q}_{k-1}^{-1} \mathbf{Q}_k]; \\ \mathbf{S}_{21}^{int,(k-1)} &= [\mathbf{Q}_{k-1} \mathbf{\Gamma}_{k-1} + \mathbf{Q}_k \mathbf{\Gamma}_k \mathbf{Q}_k^{-1} \mathbf{Q}_{k-1}]^{-1} [\mathbf{Q}_{k-1} \mathbf{\Gamma}_{k-1} - \mathbf{Q}_k \mathbf{\Gamma}_k \mathbf{Q}_k^{-1} \mathbf{Q}_{k-1}]; \\ \mathbf{S}_{22}^{int,(k-1)} &= 2 [\mathbf{Q}_{k-1} \mathbf{\Gamma}_{k-1} + \mathbf{Q}_k \mathbf{\Gamma}_k \mathbf{Q}_k^{-1} \mathbf{Q}_{k-1}]^{-1} \mathbf{Q}_k \mathbf{\Gamma}_k. \end{aligned} \quad (13)$$

The interface scattering matrix is obtained therefore without direct inversion of the matrices $\mathbf{\Gamma}_k$ and $\mathbf{\Gamma}_{k-1}$ and possible singularity of the scattering matrix is abandoned.

5. DISCUSSION

The appearing diffraction order is characterized by the wave vector that is exactly parallel to the layer interface. It is in some sense neither evanescent nor propagating, as the propagation constant along the z axis is equal to zero and has no imaginary part (suppose there are no losses). The calculations show that the amplitude of the wave diffracted in this order is generally non-zero. At the same time the wave amplitude is not decaying and therefore this order should take some energy from the incident wave. However it turns out that such an order does not really affect the energy redistribution between reflection and transmission diffraction orders. The energy is carried in this case in the direction exactly parallel to the grating boundaries, and the grating is considered to be periodic and infinite in the x -direction. For better understanding consider three neighbouring grating sections (periods) and suppose the wave diffracted into the new order carries some amount

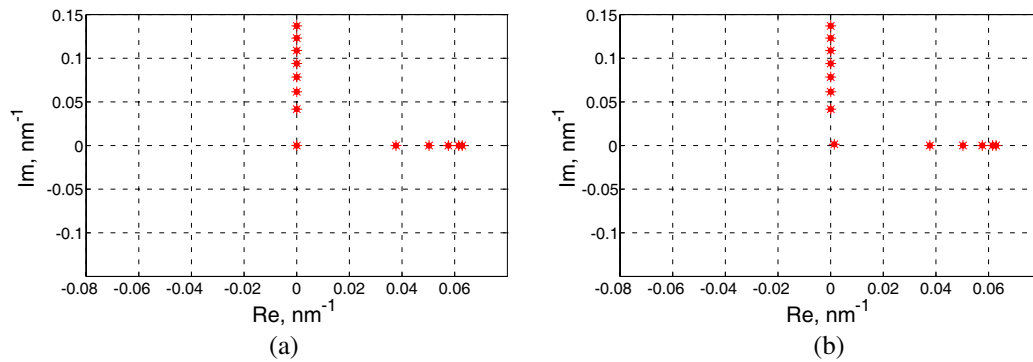


Figure 2: Diffraction order propagation constants for a grating layer: (a) non-lossy grating; (b) lossy grating.

of energy from the middle section to the right one. As the grating is periodic and infinite (however, this is in some sense the model restriction), exactly the same amount of energy is brought from the left section to the middle one, and the energy is locally conserved. These reasoning gives physical consistency for the energy conservation in the case when a new diffraction order appears.

Another crucial point is generalization of the obtained results to the case of lossy gratings. However, this singularity problem in most cases does not appear if the absorption is introduced. A non-zero imaginary part of the refractive index immediately shifts the propagation constant from the zero point (Fig. 2).

6. CONCLUSION

Within this paper, we considered numerical techniques based on incomplete Galerkin method and scattering matrix method applied to diffraction grating modeling. We showed that the singularity of the scattering matrix in case of a new diffraction order is abandoned by modifying the analytical expressions. Specific expressions for the interface scattering matrix were presented. The approach is quite general and the results can be generalized to the case of *TM*-polarization and conical mount, as well as two-dimensional biperiodic gratings.

REFERENCES

1. Sveshnikov, A. G., "Incomplete Galerkin's method," *RAS USSR*, Vol. 236, No. 5, 1076–1079, 1977.
2. Moharam, M. G., D. A. Pommet, E. B. Grann, and T. K. Gaylord, "Stable implementation of the rigorous coupled-wave analysis for surface-relief gratings: Enhanced transmittance matrix approach," *J. Opt. Soc. Am. A*, Vol. 12, No. 5, 1077–1086, 1995.
3. Li, L., "Formulation and comparison of two recursive matrix algorithms for modeling layered diffraction gratings," *J. Opt. Soc. Am. A*, Vol. 13, No. 5, 1024–1035, 1996.
4. Ilyinskii, A. S., V. V. Kravtsov, and A. G. Sveshnikov, *Mathematical Models of Electrodynamics*, Visshaya Shkola, Moscow, 1991 (in Russian).
5. Palmer, C. and E. Loewen, *Diffraction Grating Handbook*, Newport Corporation, 2005.
6. Born, M. and E. Wolf, *Principles of Optics*, Cambridge University Press, Cambridge, 1999.

Projective Methods in Problems of Waveguide with Singularity

A. N. Bogolubov, A. I. Erokhin, and I. E. Mogilevsky
Faculty of Physics, M. V. Lomonosov Moscow State University, Russia

Abstract— A vectorial mathematical model of electromagnetic irregular waveguides with reentrant edges in their surfaces is proposed. The existence and uniqueness of the exact solution is proved. Numerical research is provided using different projective methods. The existence, uniqueness, and convergence of numerical solution to exact one are proved.

1. INTRODUCTION

Electromagnetic waveguides with reentrant edges are generally used in microwave devices as filters or their tuning elements [1–3]. This geometrical singularity also appears in cases where several waveguides are connected. Reentrant edges can serve as a model of different scratches in waveguide's surface or as a model of electromagnetic probe.

To study such irregular systems, a vectorial mathematical model is proposed. The existence and uniqueness of exact solution is proved. Numerical research is provided using different projective methods.

Approximate solution of the problem is sought by applying incomplete Galerkin method as one of projective methods. As a basis set of vectors is constructed using Laplacian eigen functions for irregular waveguide's cross-section with reentrant corners. This eigen-value problem doesn't have analytical solution. To calculate the last one, finite element method is used as a projective-grid method.

Using technique proposed in [4], asymptotic by smoothness of the solution of eigen-value problem is found where singularities are additively singled out. Taking these singularities as test functions in finite element method the rate of convergence of numerical solution of eigen-value problem to exact one is estimated.

Convergence of approximate solution of the problem constructed with the help of numerically searched solutions of the eigen-value problem is proved.

Existence and uniqueness in appropriate spaces of approximate solution of the problem is proved.

2. STATEMENT OF THE PROBLEM

Let us consider an infinite circular cylinder with a finite part of length a which has reentrant edges so its cross-section has reentrant corners (Fig. 1).

Let the n_0 -th normal wave of electrical type with an amplitude A^e be propagating rightward. Let us define $\tilde{\varphi}_n, \tilde{\lambda}_n$ as eigen functions and eigen values of Laplacian with Dirichle boundary conditions, $\hat{\psi}_n, \hat{\lambda}_n$ — as eigen functions and eigen values of Laplacian with Neyman boundary conditions for cross-section S of regular part of the waveguide, that is a cycle, \vec{e}_n, \vec{h}_n — as a basis for representation of waves in the cross-section S , constructed with help of eigen functions of the cross-section [5]. Taking into account Maxwell equations, partial radiation conditions [5] and continuity of the solution and its derivative on the boundary between regular and irregular parts of the waveguide we come to the following problem in the bounded domain for the description of

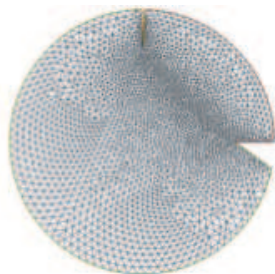


Figure 1: A cross-section of irregular part of waveguide with two reentrant edges.

waves propagating in the irregular part of the waveguide:

$$\left\{ \begin{array}{l} \operatorname{rot} \vec{H}(M, z) = -ik_0 \varepsilon \vec{E}(M, z), \quad M \in S_z, \quad z \in (0; a), \\ \operatorname{rot} \vec{E}(M, z) = ik_0 \mu \vec{H}(M, z), \\ [n, \vec{E}] \Big|_{\Sigma} = 0, \\ \frac{\partial \vec{E}_{\tau}}{\partial z} \Big|_{z=0} = 2i\tilde{\gamma}_{n0} A^e \vec{e}_{n0}^e e^{i\tilde{\gamma}_{n0} z} - \sum_n i\gamma_n (\vec{E}_{\tau}, \vec{e}_n) \Big|_{S_0} \vec{e}_n, \\ \frac{\partial \vec{H}_{\tau}}{\partial z} \Big|_{z=0} = 2i\tilde{\gamma}_{n0} A^e \vec{h}_{n0}^e e^{i\tilde{\gamma}_{n0} z} - \sum_n i\gamma_n (\vec{H}_{\tau}, \vec{h}_n) \Big|_{S_0} \vec{h}_n, \\ \frac{\partial \vec{E}_{\tau}}{\partial z} \Big|_{z=a} = \sum_n i\gamma_n (\vec{E}_{\tau}, \vec{e}_n) \Big|_{S_a} \vec{e}_n, \\ \frac{\partial \vec{H}_{\tau}}{\partial z} \Big|_{z=a} = \sum_n i\gamma_n (\vec{H}_{\tau}, \vec{h}_n) \Big|_{S_a} \vec{h}_n, \end{array} \right. \quad (1)$$

where k_0 is a wave number, $\gamma_n = \sqrt{k_0^2 - \lambda_n}$ — a propagation constant, ε — a permittivity of irregular part of the waveguide, $\operatorname{Im} \varepsilon > 0, \operatorname{Re} \varepsilon > 0, \mu = 1$ — a magnetic permeability, \vec{n} — an external normal vector to the surface of the waveguide, S_z — a cross-section of the irregular part with reentrant corners, Σ — a surface of the irregular part.

Define V as a volume of the irregular part of the waveguide and W as a following space:

$$W = \{w = (\vec{E}, \vec{H}) : E_i \in L_2(V), \quad H_i \in L_2(V), \quad \frac{\partial \vec{E}_{\tau}}{\partial z} \in L_2(V) \times L_2(V), \quad \frac{\partial \vec{H}_{\tau}}{\partial z} \in L_2(V) \times L_2(V),$$

$$\text{where } \|w\|_W = \sum_{i=1}^3 \left(\|E_i\|_{L_2(V)} + \|H_i\|_{L_2(V)} \right) + \left\| \frac{\partial \vec{E}_{\tau}}{\partial z} \right\|_{L_2(V)} + \left\| \frac{\partial \vec{H}_{\tau}}{\partial z} \right\|_{L_2(V)}.$$

Using technique proposed in [5] it is proved that the solution of the problem (1) is unique and belongs to the space W .

3. SOLUTION OF THE PROBLEM

An approximate solution of the problem (1) is sought by applying incomplete Galerkin method, i.e., in the form

$$\vec{E}_{\tau}^N = \sum_{n=1}^{2N} A_n(z) \vec{p}_n(M), \quad \vec{H}_{\tau}^N = \sum_{n=1}^{2N} B_n(z) \vec{q}_n(M), \quad (2)$$

where \vec{p}_n, \vec{q}_n is a basis constructed for representation of fields in the irregular part of the waveguide using eigen functions for Laplacian with Dirichlet and Neyman conditions for the cross-section S_z with reentrant corners.

Using the same technique [5] it is proved that the approximate solution exists in the space W , is unique and converges in the space W to the exact solution of the problem (1).

With restriction to the third order of smoothness, the asymptotics near the reentrant corner of the solutions of Dirichlet and Neyman eigen-value problems have the following forms in polar coordinates respectively

$$\varphi(r, \varphi) = \sum_{j: 0 < j\pi\omega_0^{-1} < 2} C_j r^{j\pi\omega_0^{-1}} \sin j\pi\omega_0^{-1} \varphi + \mathfrak{R}(r, \varphi), \quad (3)$$

$$\psi(r, \varphi) = D_0 + \sum_{j: \delta < j\pi\omega_0^{-1} < \delta+2} D_j r^{j\pi\omega_0^{-1}} \cos j\pi\omega_0^{-1} \varphi + \tilde{\mathfrak{R}}(r, \varphi), \quad (4)$$

where C_j, D_j — constants, $0 < \delta < 1$ — a constant, ω_0 — an angle of the reentrant corner, $\mathfrak{R}, \tilde{\mathfrak{R}} \in H^3$ — smooth remainders. Singled out singularities can be used as test functions in finite element method so singular part of the solution can be described exactly. Considering appropriate finite elements for describing smooth remainders it is possible to estimate a rate of convergence of the approximate solution of eigen-value problems. These results can be used to estimate an approximate solution of the problem (1).

4. CONCLUSIONS

A vectorial model is proposed to study the irregular waveguide with reentrant edges. Existence and uniqueness of the solution of the problem is proved in appropriate space. An approximate solution is constructed using projective methods which converges to the exact one in the same space.

One of the results of mathematical modeling of such structures is a presentation of selective mode propagation through irregular part of the waveguide. It can be explained by the absence of energetical interaction between different modes of the waveguide. The effect has been already demonstrated using scalar model for description of such systems [6]. The result of the investigation can be used for the development of mode filters.

REFERENCES

1. Schiff, B. and Z. Yosibash, “Eigenvalues for waveguides containing re-Entrant corners by a finite-element method with superelements,” *IEEE Trans. Microwave Theory Tech.*, Vol. 48, No. 2, 214–220, 2000.
2. Yahia, M., J. W. Tao, H. Benzina, and M. N. Abdelkrim, “Ridged waveguide filter optimization using the neural networks and a modified simplex method,” *International Journal of Innovation, Management and Technology*, Vol. 1, No. 3, 259–263, 2010.
3. Cogollos, S., S. Marini, V. E. Boria, P. Soto, A. V. H. Esteban, J. V. Morro, and B. Gimeno, “Efficient modal analysis of arbitrarily shaped waveguides composed of linear, circular, and elliptical arcs using the BI-RME method,” *IEEE Trans. Microwave Theory Tech.*, Vol. 51, No. 12, 2378–2389, 2003.
4. Nazarov, S. A. and B. A. Plamenevskiy, *Elliptic Problems in Domains with Piecewise Smooth Boundaries*, Walter de Gruyter & Co, Berlin, 1994.
5. Sveshnikov, A. G. and I. E. Mogilevsky, *Matematicheskie Zadachi Teorii Difrakcii*, Faculty of Physics of MSU, Moscow, 2010.
6. Bogolubov, A. N., A. I. Erokhin, and I. E. Mogilevsky, “Matematicheskoe modelirovanie cilindricheskogo volnovoda s deformaciey bokovoy poverkhnosti,” *Vestnic MGU, Series 3. Physics, Astronomy*, No. 6, 127–130, 2011.

Wavelet Approximation of Discontinuous Solutions in EHD Model of Charged Jet Flow

Oleg Kravchenko^{1,2} and Dmitriy Churikov²

¹Bauman Moscow State Technical University, Moscow, Russia

²Kotel'nikov Institute of Radio Engineering and Electronics
Russian Academy of Sciences, Moscow, Russia

Abstract— In present work, a mathematical two-fluid Electrohydrodynamics (EHD) model of charged jet flow is investigated numerically in 1D case. The system of nonlinear partial differential equations (PDE) is transformed into Burgers equation with a constant source. Afterwards, an ordinary differential wave equation is considered. Such kind of equation doesn't have an explicit solution, that is why it is investigated numerically with help of wavelet Haar method (WHM) [4]. The initial value problem (IVP) is taken into consideration and the corresponding wavelet approximation is used according to [5].

1. INTRODUCTION

The problems of stability of charged jet flow occupy the central place in EHD. But the fluid equations are difficult to handle because of their nonlinearity and mathematical complexity as a result. One of the approaches consists of studying the influence of an electric field on a velocity field. This approach has been introduced by V. I. Pustovoit [1]. It also has been introduced by E. Moreau and O. Vallee in [2] independently. Such approach allows to reduce a system of nonlinear PDEs into one nonlinear Burgers type equation with a constant source.

Wavelet methods are successfully applied to numerical approximation of boundary-value problems (BVPs) [4] and IVPs as well [5].

In present work, we consider a static case of Burgers type, i.e., ordinary differential equation (ODE) and present a discontinuous solutions governed by conservation law according to [3]. We employ WHM to construct a wavelet approximation of ODE and well known Runge-Kutta (RGK) numerical method to verify a wavelet approximation.

2. EHD MODEL OF CHARGED JET FLOW

In [1, 2] a simple EHD model is considered and it regards the following two-fluid model:

$$\begin{cases} en\vec{E} + \nabla p + mn\nu(\vec{v}_e - \vec{v}_i) = 0, \\ \frac{\partial}{\partial t}n + \frac{\partial}{\partial x}(n\vec{v}_e) = 0, \\ \varepsilon_0\nabla\vec{E} = -4\pi(n_e - n_i). \end{cases} \quad (1)$$

Here $\vec{v}_e = \vec{v}_e(t, x)$, $\vec{E} = \vec{E}(x, t)$, and $n_e = n_e(x, t)$ are unknown functions (characteristics of electron fluid). The following scalar system:

$$\begin{cases} enE + kT\frac{\partial}{\partial x}n + mn\nu(v_e) = 0, \\ \frac{\partial}{\partial t}n + \frac{\partial}{\partial x}(nv_e) = 0, \\ \varepsilon_0\frac{\partial}{\partial x}E = -4\pi(n_e - n_i) \end{cases} \quad (2)$$

is the projection of (1) on x direction under general assumption

$$v_e(t, x) \equiv \text{const}, \quad v_i(t, x) \equiv 0. \quad (3)$$

It can be demonstrated that in the dimensionless variables [1] the following nonlinear equation for the dimensionless electric field can be derived from [2]:

$$\frac{\partial y}{\partial \tau} = \frac{1}{2}\frac{\partial^2 y}{\partial \xi^2} - y\left(\frac{\beta^2}{2} - \frac{\partial y}{\partial \xi}\right), \quad (4)$$

here $y(\xi, \tau)$ is a dimensionless electric field, ξ is a dimensionless space variable and τ is a dimensionless time variable respectively. Equation (4) is Burgers type equation with elasting term

$-y\beta^2/2$ [1, 2]. It was shown in [1] that Equation (4) with $\beta = 0$ have the following discontinuous wave solution:

$$y(\xi - \gamma\tau) = \frac{C_1 Ai'(\xi - \gamma\tau) + C_2 Bi'(\xi - \gamma\tau)}{C_1 Ai(\xi - \gamma\tau) + C_2 Bi(\xi - \gamma\tau)}. \quad (5)$$

If we consider a general case with $\beta \neq 0$, then wave equation of Equation (4) (for argument $\xi - \gamma\tau$) is the following:

$$y'' + 2y'(y - \gamma) - \beta^2 y = 0. \quad (6)$$

There is no explicit solution of Equation (6). The major purpose of present work is to investigate a wave Equation (6) numerically. We employ RGK and WHM methods according to [4, 5]. The IVP consists of Equation (6) and initial conditions

$$y(0) = \alpha_1, \quad y'(0) = \beta_1. \quad (7)$$

3. WAVELET HAAR METHOD

The Haar wavelet family for $x \in [0, 1)$ according to [4] is defined as

$$\psi_i^0(x) = \begin{cases} 1 & \text{for } x \in [\alpha, \beta), \\ -1 & \text{for } x \in [\beta, \gamma), \\ 0 & \text{elsewhere,} \end{cases} \quad \begin{matrix} \alpha = k/m, \\ \beta = (k + 0.5)/m, \\ \gamma = k + 1/m. \end{matrix} \quad (8)$$

The integer $m = 2^j$, $j = \overline{0, J}$ indicates the level of wavelet and integer $k = \overline{0, m - 1}$ is the translation parameter. The maximum level of resolution is J . The index i in Equation (8) is calculated as $i = m + k + 1$. For $i = 1$ the function $h_1(x)$ the scaling function for Haar wavelet family which is defined as

$$h_1(x) = \begin{cases} 1 & \text{for } x \in [0, 1), \\ 0 & \text{elsewhere.} \end{cases}$$

The following notations are introduced:

$$\psi_i^1(x) = \int_0^x \psi_i^0(s) ds, \quad \psi_i^{n+1}(x) = \int_0^x \psi_i^n(s) ds, \quad n = 1, 2, \dots \quad (9)$$

$$\psi_i^1(x) = \begin{cases} x - \alpha & \text{for } x \in [\alpha, \beta), \\ \gamma - x & \text{for } x \in [\beta, \gamma), \\ 0 & \text{elsewhere,} \end{cases} \quad (10)$$

$$\psi_i^2(x) = \begin{cases} \frac{(x - \alpha)^2}{2} & \text{for } x \in [\alpha, \beta), \\ \frac{1}{4m^2} - \frac{(\gamma - x)^2}{2} & \text{for } x \in [\beta, \gamma), \\ \frac{1}{4m^2} & \text{for } x \in [\gamma, 1), \\ 0 & \text{elsewhere.} \end{cases} \quad (11)$$

Following [5] we assume that

$$y''(x) = \sum_{i=1}^{2M} c_i \psi_i^0(x). \quad (12)$$

We consider the collocation points

$$x_j = \frac{j - 0.5}{2M}, \quad j = \overline{1, 2M}. \quad (13)$$

The expressions of $y(x)$, $y'(x)$ and $y''(x)$ are substituted in the given differential equation and discretization is applied by means of collocation points Equation (13) resulting into a $2M \times 2M$

nonlinear system. For initial conditions Equation (7) the approximate solution $y(x)$ and its first derivative can be expressed as

$$y'(x) = y'(0) + \int_0^x \sum_{i=1}^{2M} c_i \psi_i^0(s) ds = \sum_{i=1}^{2M} c_i \psi_i^1, \quad (14)$$

$$y(x) = y(0) + \int_0^x \sum_{i=1}^{2M} c_i \psi_i^1(s) ds = \sum_{i=1}^{2M} c_i \psi_i^2. \quad (15)$$

Substituting these values of $y(x)$, $y'(x)$ and $y''(x)$ in the Equation (6) we obtain nonlinear system of equations

$$\left(\alpha_1 + x_j \beta_1 + \sum_{i=1}^{2M} c_i \psi_i^2(x_j) \right) \left(2\beta_1 + 2 \sum_{i=1}^{2M} c_i \psi_i^1(x_j) - \beta^2 \right) + \sum_{i=1}^{2M} c_i \psi_i^0(x_j) = 0, \quad j = \overline{1, 2M}. \quad (16)$$

Solving this system we get unknown Haar coefficients c_i , $i = \overline{1, 2M}$.

4. NUMERICAL EXAMPLE

In this section, we test the Haar wavelet collocation algorithm on benchmark problems. The accuracy of the algorithm is assessed in terms of the Chebyshev norm $L_\infty = \max_j |y_j^e - y_j^a|$ where y_j^e is the exact solution and y_j^a is the numerical solution.

Problem 1. Consider a IVP problem Equations (6), (7) with

$$\gamma = 0, \quad \beta^2 = 0, \quad \alpha_1 = 0, \quad \beta_1 = -1.$$

The exact discontinuous solution is given by $y(\xi) = -\tan(\xi)$. All computations we made are carried out with the use of MATLAB. We use standard `ode45` function as RGK solver. The level of resolution is $J = 3$ and the number of collocation points is $2M = 2^{J+1} = 16$. The L_∞ error RGK method is 0.093225 whereas the L_∞ error of WHM is 0.0038597. The L_∞ error between RGK and WHM is 0.097084. Comparison of the exact versus WHM and RGK solutions is shown in Fig. 1.

Problem 2. Consider a IVP problem Equations (6), (7) with

$$\gamma = 0, \quad \beta^2 = 2, \quad \alpha_1 = 0, \quad \beta_1 = -1.$$

There is no exact solution, so we compare WHM method with RGK technic only. The L_∞ error between RGK and WHM is 0.21825 for $2M = 16$. For $2M = 32$ and $2M = 64$ the L_∞ error between RGK and WHM is 0.1176 and 0.061194 respectively. Comparison of the WHM versus RGK solution is shown in Fig. 2.

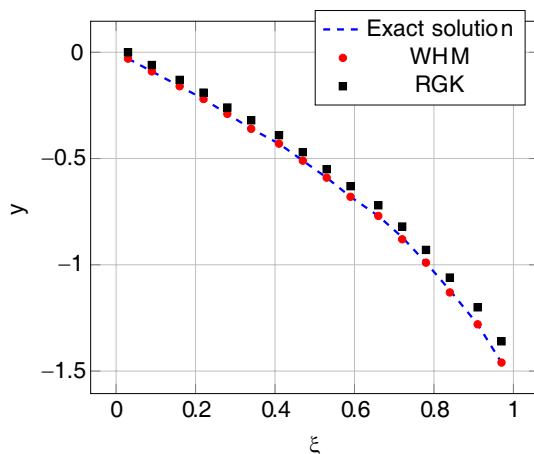


Figure 1: Comparison of the Haar solution with the exact solution of problem 1 with $\gamma = 0$ and $\beta^2 = 0$.

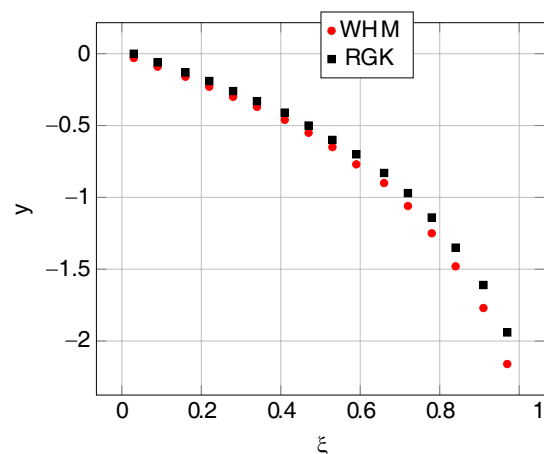


Figure 2: Comparison of the WHM with the RGK solution of problem 2 with $\gamma = 0$ and $\beta^2 = 2$.

5. CONCLUSION

In present work, a simple nonlinear ODE relative to two-fluid plasma model is investigated numerically by means of WHM and RGK method. The wavelet Haar method shows better accuracy on a small number of collocation point in benchmark problem 1 with an exact solution. In problem 2 with no exact solution the differences between RGK and WHM methods tend to zero with an increase in collocation point number.

ACKNOWLEDGMENT

This study was supported by the Federal Program “Kadry” (contract P780) and by the Russian President’s State encouragement of leading scientific groups under Contract NSh — 4705.2012.9.

REFERENCES

1. Pustovoit, V. I., “Mechanism of lightning discharge,” *Journal of Communications Technology and Electronics*, Vol. 51, No. 8, 937–943, 2006.
2. Moreau, E. and O. Vallee, “Connection between the Burgers equation with an elastic forcing term and a stochastic process,” *Phys. Rev. E*, Vol. 73, 016112-4, 2006.
3. Sapogin, V. G., “On compensation of coulomb Interaction of charges by beam’s self-consistent field (model of isothermal equilibrium with homogeneous temperature),” *Proceedings 1st IEEE International Conference on Circuits and Systems for Communications*, 408–411, St. Petersburg, Russia, 2002.
4. Siraj-ul-Islam, I. Aziz, and B. Šarler, “The numerical solution of second-order boundary-value problems by collocation method with the Haar wavelets,” *Mathematical and Computer Modelling*, Vol. 52, Nos. 9–10, 1577–1590, 2012.
5. Bishnupriya, S., “A study on solution of differential equations using Haar wavelet collocation method,” MSc Thesis, 2012.

The Scanning Reflective Antenna with an Impedance Conformal Reflector in the Form of Laminated Structure the Semiconductor-dielectric-metal with Photonic Control

A. A. Prilutskiy

JSC Distant Radio Communication Scientific Research Institute
d.12/11, 1-ya Str. Buhvostova, Moscow 107258, Russia

Abstract— Possibility of creation of the conformal scanning reflective antenna with photonic control is investigated. The antenna reflector is executed in the form of the multilayered medium consisting of alternating dielectric layers and semiconductor films on the metal emulsion carrier which conductivity changes under the influence of optical bombarding radiation. Depending on a condition of semi-conductor films on a reflector surface of the reflective antenna the cylindrical front of an incident wave is converted to flat front of the reflected. The mathematical model of the reflective antenna in the Kirchhoff approximation is gained. Radiation patterns are resulted at scanning in wide sector of angles.

1. INTRODUCTION

Antenna array with phase shifters with photonic control have a number of advantages if the photo detector photonics pair is a component of a design or a material of an electrodynamic part of the antenna. A role of a such photo detector various photo spending semiconductor films and photo dielectric, changing under the influence of light can carry out the dielectric permeability. In works [1, 2] the effect of change of a phase of factor of reflexion of a wave is investigated at inclined falling on layered structure of alternating layers of semiconductor films (software) and dielectrics on a metal substrate at influence of optical radiation in approach of infinite reradiating structure. It has been shown, that the layered structure depending on a condition of conductivity of software provides phase shift of the reflected wave. It has been noticed, that properties of such layered structures can be used at construction of antenna systems of a cent metric and mill metric wave band. As one of applied application of layered structures of software and dielectric layers on a metal substrate creation of a reflector of the reflective antenna is. Such antennas can be not only low profile, but also can possess conformal properties, that is have geometrical interface to a surface, for example flying or a space vehicle.

2. FORMULATION OF THE PROBLEM

We investigate possibility of creation scanning conformal the reflective antenna with photonic control. The antenna reflector is executed in the form of the multilayered environment consisting of alternating dielectric layers and semiconductor films. The problem geometry is represented on Fig. 1. Let the cylindrical curvilinear surface of the reflective antenna, infinite along axis Z (forming the cylinder), is irradiated with cylindrical wave E or H -polarization. A source of radiation for the E -polarization wave is the thin thread with an electric current, and in case of H -polarization — a thread of a magnetic current.

The diagramme of an orientation of a thread with a current is defined by necessary distribution of a current to surfaces of a reflector of the antenna. For calculation of a field reflected from an antenna reflector we will take advantage of the approached method of Kirchhoff diffraction [3]. In this method for calculation of a diffraction field for a basis not indignant value of a primary field of a wave following from geometrical optics falling on a boundary surface undertake. This method yields satisfactory results for a diffraction field in a forward hemisphere provided that a surface of a reflector of much more wave length.

Let's assume that everyone the geometrical optics beam is locally flat wave of corresponding polarization falling under the set corner on a boundary surface. The complex factor of reflexion of a beam corresponds to factor of reflexion of a flat wave from an infinite surface with a certain superficial impedance. The conclusion of factor of reflexion has been resulted in work [1, 2]. Thus, field distribution on a reflector in Kirchhoff method will be defined reflected by geometrical optics beams in each local point of a surface, which is field tangents in each local point correspond to fields in a problem of reflexion of a flat wave from an infinite surface.

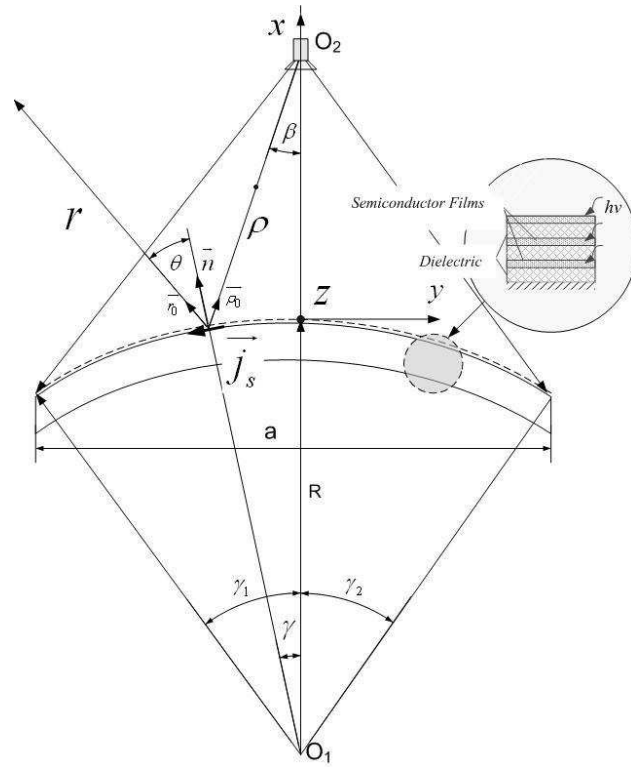


Figure 1.

According to a principle of equivalence of Shelkunov S. A. [4], tangents components magnetic and electric field on a boundary surface are equivalent to corresponding density of a magnetic and electric superficial current.

$$\begin{cases} \vec{J}_s^e = -[\vec{n}\vec{H}] \\ \vec{J}_s^\mu = [\vec{n}\vec{E}] \end{cases} \quad (1)$$

The antenna field in an infinite point will be expressed in the form of Kirchoff integral from distribution of density of currents on a surface of a curvilinear reflector. Incident wave field for E -polarization

$$E_z^i = E_0 [\vec{n}\vec{e}_0] F(\beta) H_0^{(2)}(k\rho) \quad (2)$$

for H -polarization

$$H_z^i = H_0 [\vec{n}\vec{e}_0] F(\beta) H_0^{(2)}(k\rho) \quad (3)$$

Field of the reflected wave from local point of a surface ∂l in a polar frame $-R, \beta$

$$E_z^r = E_0 [\vec{n}[\vec{r}_0\vec{\rho}_0]] \gamma^e F(\beta) H_0^{(2)}(k\rho) \frac{e^{-ikr}}{\sqrt{r}} \quad (4)$$

$$H_z^r = H_0 [\vec{n}[\vec{r}_0\vec{\rho}_0]] \gamma^\mu F(\beta) H_0^{(2)}(k\rho) \frac{e^{-ikr}}{\sqrt{r}} \quad (5)$$

where \vec{n} — normal vector to a reflector surface, $\vec{\rho}_0$ — a direction unit vector on an irradiator, \vec{r}_0 — a direction unit vector in an observation point.

In (4), (5) γ^e and γ^μ — reflectivity's from a antenna surface in the local point ∂l , expressed through transmission matrixes element of layered structure for E and H -polarization [3]

$$\gamma^e = \frac{(t_{12}^e + t_{22}^e)}{(t_{11}^e + t_{21}^e)} \quad (6)$$

$$\gamma^\mu = \frac{(t_{12}^\mu + t_{22}^\mu)}{(t_{11}^\mu + t_{21}^\mu)} \quad (7)$$

The reflected field in infinitely remote point for E and H -polarization

$$E_z = \int_l E_0 [\vec{n} [\vec{r}_0 \vec{\rho}_0]] \gamma^e(\theta) F(\beta) H_0^{(2)}(k\rho) e^{-ik \sin(\theta)y - ik \cos(\theta)x} dl \tag{8}$$

$$H_z = \int_l H_0 [\vec{n} [\vec{r}_0 \vec{\rho}_0]] \gamma^\mu(\theta) F(\beta) H_0^{(2)}(k\rho) e^{-ik \sin(\theta)y - ik \cos(\theta)x} dl \tag{9}$$

3. THE RESULTS OF THE SIMULATION

Numerical modeling reflective antenna was spent, both for flat, and for a cylindrical reflector with a symmetric and asymmetrical disposition of an irradiator for H and E -polarization of a field of excitation of a reflector for frequency of 10 GHz. The layered structure consisted of 3 stratum of semiconductor films on dielectric substrates and took places on the metal screen. At calculations the size of a flat reflector was equal 0.4 m. Has been investigated: - behavior of amplitude-phase distribution (APD) of a reradiated field; - antennas radiation patterns at excitation by field H or E -polarization for various position of an irradiator — on an antenna axis (a symmetric disposition), and carried out in antenna edge (asymmetrical); - antenna performances are investigated at scanning in wide sector of angles up to 72° (a deviation from a normal).

At the antenna radiation patterns modeling it was normalized to patterns the ideal antenna with APD defined by an irradiator in the absence of amplitude and phase errors at transformation of wave front.

On Figs. 2, 3 schedules APD for the ideal antenna with discrete change of a phase and the antenna with a layered reflector are resulted. It is obvious, that reflective antenna with layered structure has the big peak and phase errors in comparison with the ideal antenna. It leads to

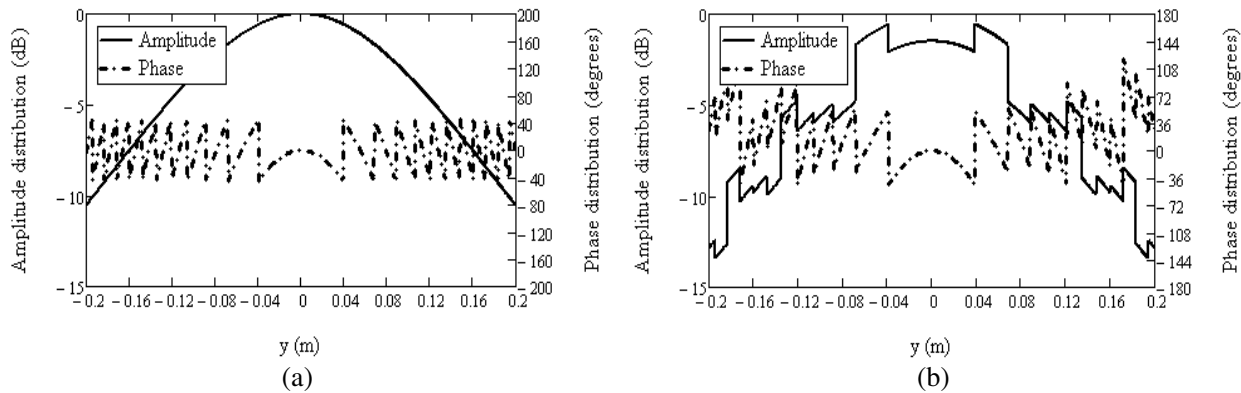


Figure 2. APD of the reflected front of a wave for reflective antenna with a flat reflector and a symmetric arrangement of an irradiator at normal radiation (H -polarization). (a) APD of the ideal antenna. (b) APD of the layered structure antenna.

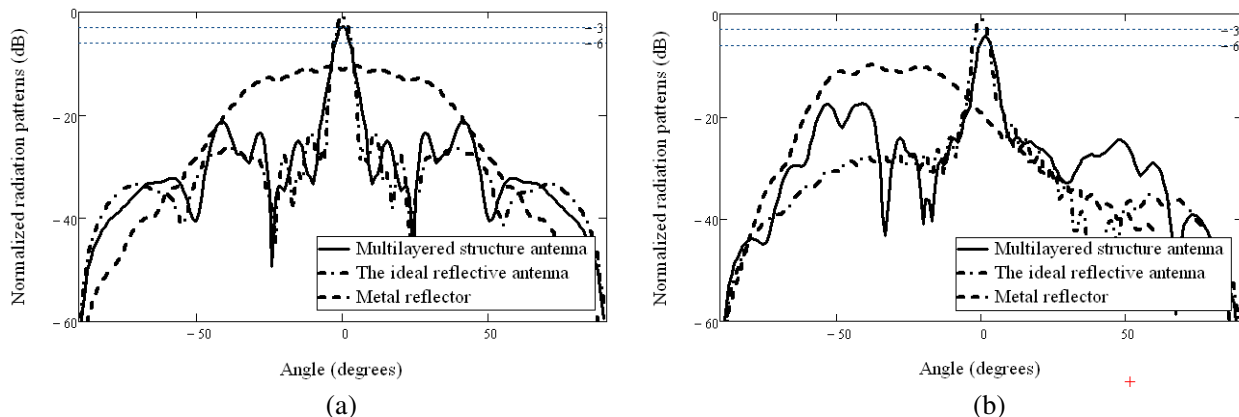


Figure 3. Normalized radiation patterns of the reflective antenna with a flat reflector (H -polarization). (a) Symmetric arrangement of an irradiator. (b) Asymmetric arrangement of an irradiator ($y_0 = a/2$).

additional decrease in operating ratio of a surface, hence, and directivity. Phase errors increase with increase in a corner of an irradiation of a reflector surface, but also the amplitude of a field thus decreases at an irradiation of edge of a reflector, which smoothes increase in phase errors a little. Besides the layered structure brings additional ohmic losses, at the expense of losses in software which reach 2 . . . 2.5 dB at some angles of an irradiation.

On Fig. 3 results of calculation radiation patterns reflective antenna with a flat reflector are resulted at symmetric Fig. 3(a) and an asymmetrical arrangement of an irradiator Fig. 3(b). The Focal length is chosen equal to half of reflector size. At asymmetrical position of irradiator antenna the increase in level of lateral radiation in a mirror direction to 18 dB is marked.

4. CONCLUSION

The mathematical model of the scanning reflective antenna with a cylindrical reflector with photonic control of phase front of the reradiated wave with use of layered structure consisting of semiconductor films on dielectric substrates is developed. For change of a condition of layered structure the photo effect in semiconductor films is used at external illumination.

REFERENCES

1. Prilutskiy, A. A., “Interaction of microwave radiation with multilayered metal-dielectric-semiconductor structures (MDS),” *Uspehi Sovremennoy Elektroniki*, No. 9, 74–80, 2009 (in Russian).
2. Prilutskiy, A. A., “Inclined falling of a flat wave of E -polarization on a reflective periodic array from wave guides with slabs in the form of structure — A semiconductor film-dielectric-metal,” *XVI Research Symposium “Radiolocation Navigation Connect”(RLNC 2010) Proceedings*, Russia, Voroneg City, 2010 (in Russian).
3. Kun, R., *Microwave Antennas*, 132–137, Izdatelstvo Sudostroenie, 1967 (in Russian).
4. Fradin, A. Z., *Antennas-Feeders Devices*, 440, Moscow, Izdatelstvo Sviyz, 1977 (in Russian).

A New Type of Wilkinson Power Divider with Triple-band Response Based on Dual Transmission Line

Pu-Hua Deng, Wen-Chian Lai, Li-Chi Dai, Yu-Ta Chen, and Sung-Yen Juang

Department of Electrical Engineering, National University of Kaohsiung, Taiwan

Abstract— The conventional single uniform transmission line can be equivalent to the dual transmission line, which has been proposed in the previous literature. Because this equivalence is usually not a narrow bandwidth, each transmission line section of conventional tri-band Wilkinson power divider using three-section transmission-line transformers may be replaced by the dual transmission line. Based on this equivalence, a new type of triple-band Wilkinson power divider composed of six dual transmission lines and three resistors between the two transmission paths is presented in this paper. To reduce the total circuit size, the proposed triple-band Wilkinson power divider is implemented by using meandering dual transmission lines. Furthermore, the simulated results are in good agreement with the circuit models of the proposed divider and conventional tri-band Wilkinson power divider using three-section transmission-line transformers, and the simulated comparison also provides in this study to support our design concept. To verify the proposed design, a new triple-band Wilkinson power divider is carefully examined and fabricated on a substrate with a thickness of 3.2 mm, a relative dielectric constant of 3.55, and a loss tangent of 0.0065.

1. INTRODUCTION

Wilkinson power dividers are important passive microwave components used for power dividing. The conventional Wilkinson power divider [1] can only be designed for single band. In wireless communication system, multi-band application is a new trend and multi-band Wilkinson power divider may be an interest topic of investigation. Recently, dual-band Wilkinson power dividers have been widely developed. For example, [2–5] and [6] were designed for dual-band and tri-band applications, respectively.

In [6], the divider used three section transmission line transformers in each path and three isolation resistors for achieving tri-band response. The proposed tri-band Wilkinson power divider uses dual transmission-line section, as suggested by [7] and [8], to replace each single transmission line of [6].

2. THE PROPOSED TRI-BAND WILKINSON POWER DIVIDER

Figure 1 displays the equivalence circuit of an arbitrary electrical length transmission line with dual transmission lines [7]. Based on the $ABCD$ matrix equivalence, as suggested by [7] or similar

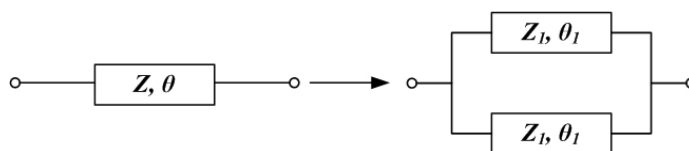


Figure 1: Equivalent circuit of an arbitrary wavelength transmission line with dual transmission line.

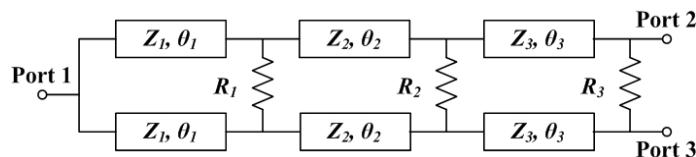


Figure 2: Conventional tri-band Wilkinson power divider.

analysis of [8], the design equations can be written as

$$Z_1 = Z \frac{\sin \theta (\cos \theta_2 - \sin \theta_1)}{\sin \theta_1 (\cos \theta_2 - \cos \theta_1)} \quad (1)$$

$$Z_2 = Z \frac{\sin \theta (\cos \theta_2 - \sin \theta_1)}{\sin \theta_2 (\cos \theta - \cos \theta_1)} \quad (2)$$

where Z_i and θ_i , $i = 1$ or 2 , are the characteristic impedances and electrical lengths of dual transmission lines, respectively; Z and θ are the characteristic impedance and electrical length of an arbitrary electrical length transmission line, respectively; the electrical lengths have a restriction $\theta_2 < \theta < \theta_1$.

Figure 2 shows the conventional tri-band Wilkinson power divider using three-section transmission-line transformers [6], and the related design parameters are $Z_1 = 85.2 \Omega$, $Z_2 = 70.7 \Omega$, $Z_3 = 58.8 \Omega$, $\theta_1 = 65.1^\circ$, $\theta_2 = 34.7^\circ$, $\theta_3 = 65.6^\circ$, $R_1 = 243 \Omega$, $R_2 = 176 \Omega$, and $R_3 = 124 \Omega$, where Z_i , θ_i , and R_i , $i = 1, 2$ or 3 are the characteristic impedance, electrical length, and resistors of each transmission line section, respectively.

To verify the proposed design, Figure 3 shows the proposed tri-band Wilkinson power divider which each transmission line section of Figure 2 may be replaced by the dual transmission-line section because the equivalence of Figure 1 is usually not a narrow bandwidth. The related design

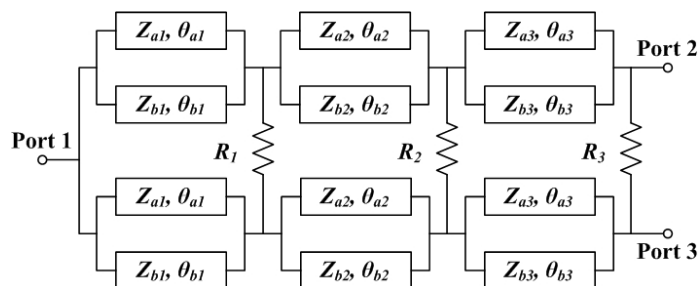


Figure 3: Proposed tri-band Wilkinson power divider using dual transmission lines structure.

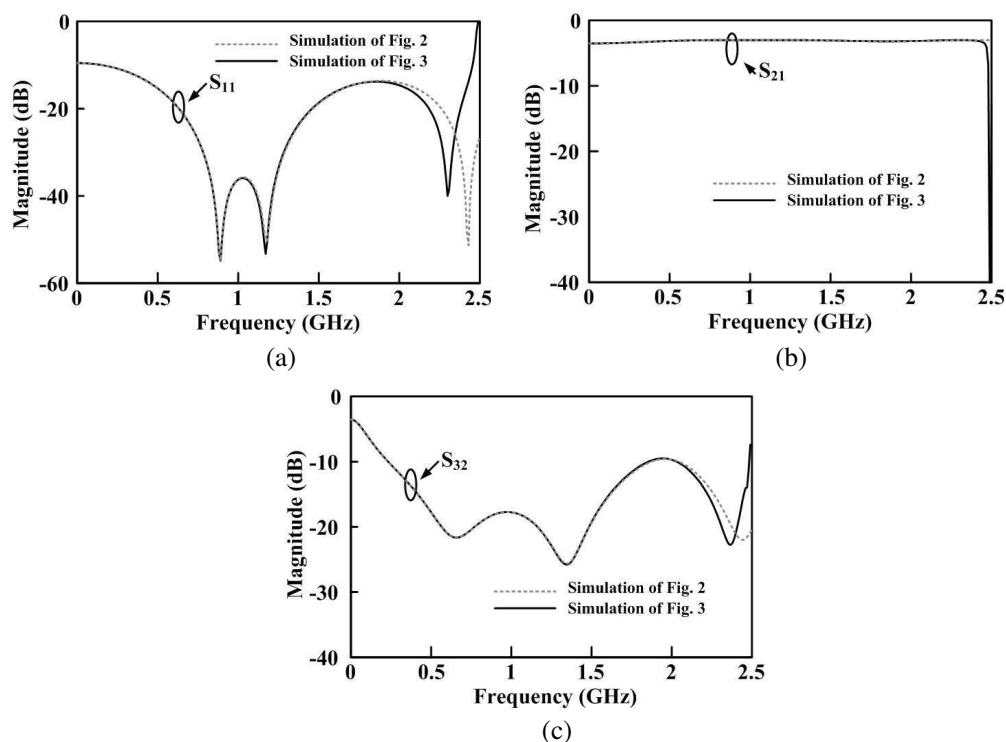


Figure 4: Simulated comparisons between the proposed divider and conventional tri-band Wilkinson power divider using three-section transmission-line transformers. (a) $|S_{11}|$. (b) $|S_{21}|$. (c) $|S_{32}|$.

parameters of tri-band Wilkinson power divider, as shown in Figure 3, are $Z_{a1} = 168.63 \Omega$, $Z_{b1} = 172.78$, $Z_{a2} = 142.66 \Omega$, $Z_{b2} = 143.46 \Omega$, $Z_{a3} = 103.6 \Omega$, $Z_{b3} = 137.41 \Omega$, $\theta_{a1} = 68.1^\circ$, $\theta_{b1} = 62.1^\circ$, $\theta_{a2} = 40^\circ$, $\theta_{b2} = 30^\circ$, $\theta_{a3} = 70^\circ$, $\theta_{b3} = 60^\circ$, $R_1 = 243 \Omega$, $R_2 = 176 \Omega$, and $R_3 = 124 \Omega$, where Z_{ai} , Z_{bi} , θ_{ai} , θ_{bi} , and R_i , $i = 1, 2$ or 3 are the characteristic impedance, electrical length, and resistors in each section in dual transmission line, respectively. Figure 4 shows the good agreement results between the proposed divider and conventional tri-band Wilkinson power divider using three-section transmission-line transformers which may be a wideband equivalence.

Specifically, each dual transmission line section of the proposed divider can be realized by two high characteristic impedance transmission lines. Therefore, the two high impedance lines are easily implemented by meander transmission lines for the purpose of compact circuit size. A new triple-band Wilkinson power divider, as shown in Figure 5, is fabricated on the substrate which

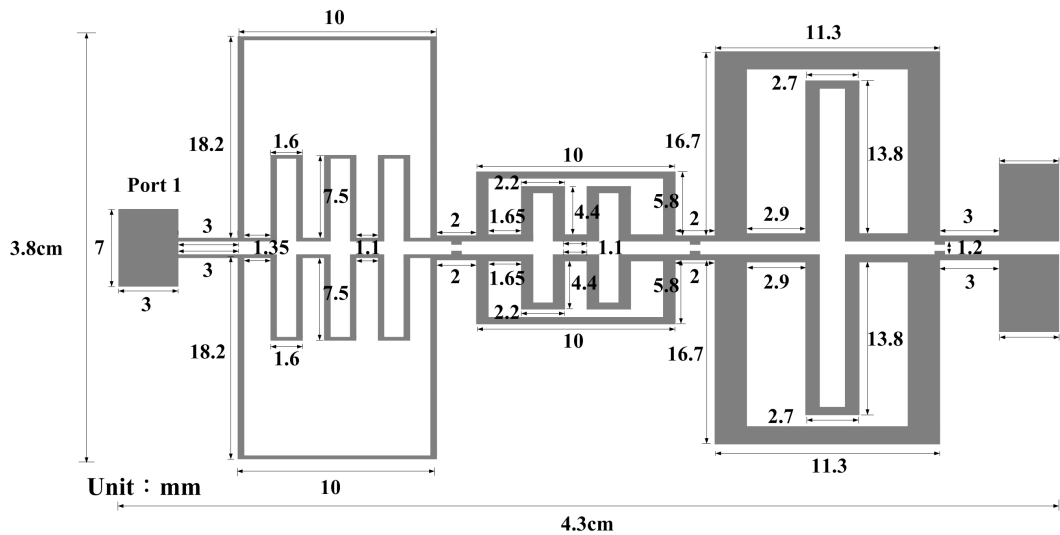


Figure 5: Layout of proposed divider.

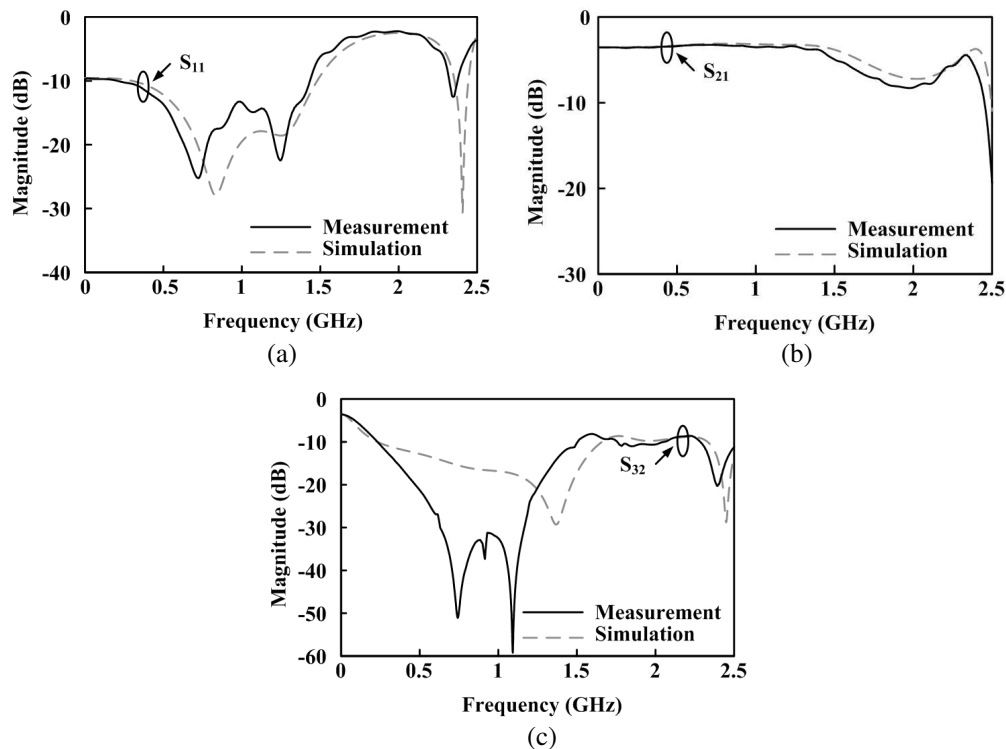


Figure 6: The simulated and measured responses of Figure 5. (a) $|S_{11}|$. (b) $|S_{21}|$. (c) $|S_{32}|$.

has thickness of 3.2 mm, a relative dielectric constant of 3.55, and a loss tangent of 0.0065, and the total circuit size is 3.8 cm \times 4.3 cm.

Figure 6 shows the comparison of the simulated and measured results. The center frequency, minimal insertion, and maximal isolation of the first band are approximately 0.72 GHz, 3.238 dB ($-|S_{21}|$), and 49.8 dB ($-|S_{32}|$), respectively. The center frequency, minimal insertion, and maximal isolation of the second band are approximately 1.245 GHz, 3.413 dB ($-|S_{21}|$), and 55.5 dB ($-|S_{32}|$), respectively. The center frequency, minimal insertion, and maximal isolation of the third band are approximately 2.341 GHz, 4.438 dB ($-|S_{21}|$), and 20 dB ($-|S_{32}|$), respectively.

3. CONCLUSION

The new type of triple-band Wilkinson power divider using dual transmission lines is proposed. The main purpose of this study is used meandering dual transmission-line section to replace each single transmission-line transformer of the conventional tri-band Wilkinson power divider for reducing circuit size. The simulated and measured results are also carefully examined and shown in this paper.

ACKNOWLEDGMENT

This work was supported by the National Science Council of Taiwan under Grant NSC 98-2221-E-390-041, Grant NSC 99-2221-E-390-007, and Grant NSC 100-2221-E-390-027. Besides, we are also grateful to the National Center for High-performance Computing for computer time and facilities.

REFERENCES

1. Pozar, D. M., *Microwave Engineering*, 2nd Edition, Chapters 7–8, New York, Wiley, 1998.
2. Wu, L., Z. Sun, H. Yilmaz, and M. Berroth, “A dual-frequency Wilkinson power divider,” *IEEE Trans. Microw. Theory Tech.*, Vol. 54, No. 1, 278–284, Jan. 2006.
3. Kawai, T., Y. Nakashima, Y. Kokubo, and I. Ohta, “Dual-band Wilkinson power dividers using a series RLC circuit,” *IEICE Transactions on Electronics*, Vol. E91-C, No. 11, 1793–1797, Nov. 2008.
4. Wang, X. and I. Sakagami, “Generalized dual-frequency Wilkinson power dividers with a series/parallel RLC circuit,” *IEEE MTT-S Int. Microw. Symp. Dig.*, 1–4, Jun. 2011.
5. Park, M. J., “Two-section cascaded coupled line Wilkinson power divider for dual-band applications,” *IEEE Microw. Wireless Compon. Lett.*, Vol. 19, No. 4, 188–190, Apr. 2009.
6. Chongcheawchamnan, M., S. Patisang, M. Krairiksh, and I. D. Robertson, “Tri-band Wilkinson power divider using a three-section transmission-line transformer,” *IEEE Microw. Wireless Compon. Lett.*, Vol. 16, No. 8, 452–454, Aug. 2006.
7. Guo, J. H., L. C. Dai, and P. H. Deng, “A new dual-band Wilkinson power divider using arbitrary-length dual transmission lines,” *IEEE Electronics Packaging Technology Conference*, 452–454, 2011.
8. Tang, C. W., M. G. Chen, and C. H. Tsai, “Miniaturization of microstrip branch-line coupler with dual transmission lines,” *IEEE Microw. Wireless Compon. Lett.*, Vol. 18, No. 3, 185–187, Mar. 2008.

Equivalent Network Extraction of a Coplanar Waveguide

Rizwan Masood¹ and S. A. Mohsin²

¹National Engineering and Scientific Commission, Islamabad, Pakistan

²The University of Faisalabad, Faisalabad, Pakistan

Abstract— The lumped element equivalent network of a Coplanar Waveguide (CPW) is proposed in this paper. The equivalent network for CPW was obtained by curve-fitting the scattering parameters with that of a lumped element N-section ladder network using Method of Moment (MOM) and then verified by Finite Integration Technique (FIT) using a Spice compatible touchstone export. Accuracy and validity considerations of the equivalent network are also discussed. The generated SPICE model is passive and hence stable and suitable for embedding into larger structure, simulation or CAD applications etc.

1. INTRODUCTION

A coplanar waveguide (CPW) is the preferred choice for High frequency structure-design and MMIC applications. This is because of the superb advantages CPW offers in fabrication owing to its uniplanar construction; e.g., surface mounting of active and passive devices in shunt or series. Furthermore on a CPW, the ground planes (semi-infinite) lie on the same side of the substrate and hence no need of wraparound, via holes etc.

A CPW can be conventional or conductor-backed (CBCPW). The former has no bottom ground plane whereas the latter has a bottom ground plane in addition to the top semi-infinite ground planes. The lower ground plane not only provides mechanical support to the substrate but also acts as heat sink for CPW based active devices [1]. Furthermore, a CPW can be on a single substrate or on a multilayer dielectric substrate with or without a ground plane. And finally the propagation characteristics (Z_0 , ϵ_{eff} , etc.) would also vary based on finite or infinite ground planes and can be studied in [2].

The CPW supports a quasi-TEM mode of operation and there is no low frequency cut-off. For Microwave Integrated Circuits (MICs) and Monolithic Microwave Integrated Circuits (MMICs), its great advantage in circuit design if CPW can be replaced by an equivalent network, i.e., the CPW sections can be replaced by a lumped element network for circuit design and CAD applications. And if CPW can be replaced by a lumped element network then the CPW based discontinuities can also be replaced by well formulated equivalent networks following the same approach. The CPW open end, short end, series gap, step change in the width of center conductor and the bend are some of such discontinuities.

The lumped element equivalent models for the CPW series open and short stubs can be found in [3]. The analysis of these stubs has been discussed in [4, 5].

Different authors have discussed the equivalent models for different scenarios concerning CPW [6–13]. This work proposes lumped element equivalent networks for a supported CPW, i.e., a CPW on a dielectric substrate with another supporting substrate at the bottom. There was no bottom ground plane and semi-infinite ground planes were assumed. The top substrate considered was Rogers RT 6010 ($\epsilon_r = 10.2$, $h = 0.635$ mm) and the bottom dielectric substrate was RT 5880 ($\epsilon_r = 2.2$, $h = 1.575$ mm).

The scattering parameters of the CPW were obtained by Method of Moments (MOM) [14] using commercially available simulator [15]. Firstly an N-section ladder network equivalent for the CPW is proposed by curve-fitting the scattering parameters already obtained. Then a cascaded lumped Pi network model is proposed by the method of Finite Integration Technique (FIT) using a commercially available CAD program [16]. Finally, a more accurate equivalent network model is proposed by Model Order Reduction technique of the FIT program. This is done by doing a CAD export from MOM tool to FIT program and generating a SPICE compatible touchstone.

2. THEORY AND SIMULATION

The layout of the structure used for model parameter extraction is shown in Figure 1. “ S ” is the width of metallization strips whereas “ W ” is the separation between the center strip conductor and the semi-infinite ground planes. “ t ” is the metallization thickness. ϵ_{r1} is equal to 2.2 for the

substrate RT 5880 and ϵ_{r2} equals 10.2 for the substrate Rogers RT 6010. Finally $h2 = 0.635$ mm and $h1 = 0.635$ mm + 1.575 mm = 2.21 mm.

The analysis of such a structure can be done by conformal mapping assuming a quasi-static TEM mode of propagation along the line and can be found in [1, 2, 17–24].

The characteristic impedance can be calculated from ϵ_{eff} and elliptic integral using the following formula

$$Z = \frac{30\pi}{\sqrt{\epsilon_{eff}}} \frac{K(k'_0)}{K(k_0)} \quad (1)$$

where ϵ_{eff} is the effective dielectric constant, $K(k_0)$ and $K(k'_0)$ represent the modulus of complete elliptic integral and its complement.

The separation w as shown in Figure 1 was taken to be $225 \mu\text{m}$ and the width S of the metalization was taken to be $450 \mu\text{m}$ for simulation purpose. The scattering parameters for the CPW structure computed by the Method of Moments are shown in Figure 2.

The lumped element Ladder network equivalent for the CPW was then obtained by curve-fitting the S -parameters obtained by MOM above. The proposed network is shown in Figure 3. XX' and YY' represent the input and output ports respectively for the CPW. For a network equivalent of a CPW discontinuity structure these would be reference planes (beyond which the field excitations caused by the discontinuity have decayed to zero). The scattering parameters of the equivalent network are shown in Figure 4 compared with those of the CPW.

The structure being symmetric, all the inductance values are equal and likewise all the capacitance values as well. This remarkably simplifies complex circuit simulations where a CPW is to be replaced by such a lumped element ladder network equivalent. But the comparison of curves in Figure 4 shows that such model is not very suitable for applications requiring high accuracy.

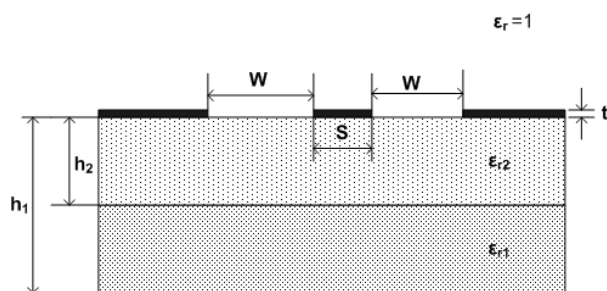


Figure 1: A coplanar waveguide with supported substrate (placed in air $\epsilon_r = 1$).

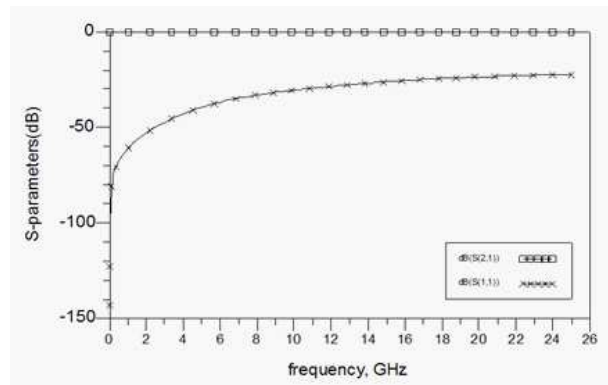


Figure 2: Scattering parameters of the CPW obtained by MOM.

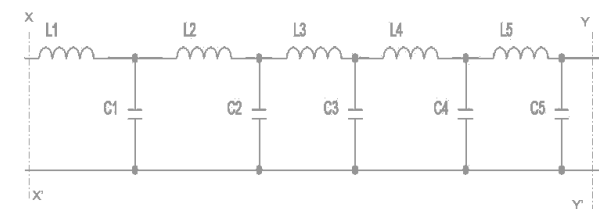


Figure 3: Equivalent lumped element ladder network for the CPW ($N = 5$) ($L1 = L2 = L3 = L4 = L5 = 0.0766$ nH, $C1 = C2 = C3 = C4 = C5 = 0.020$ pF).

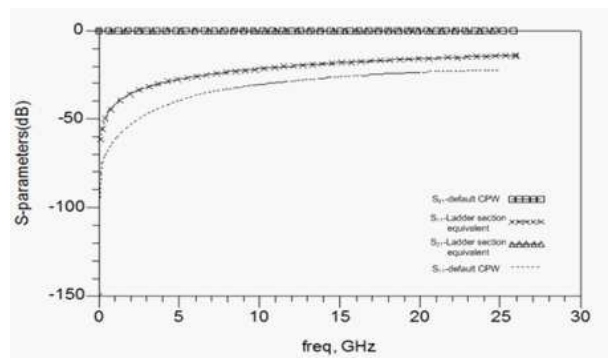


Figure 4: Scattering parameters of the five section Ladder network equivalent compared to the scattering parameters of CPW.

The reflection (indicated by S_{11}) particularly is high for the network equivalent compared to the CPW. Though, the error goes on decreasing with increasing frequency. The equivalent network in this case is composed of five sections. However, increasing the number of sections will improve the accuracy of curve-fitting at an expense of increasing complexity. Better network equivalents are to be proposed in the following.

The equivalent network model is now obtained using FIT using simulation program [16]. This was done by performing a Spice touchstone Import from the FIT tool [16] to the MOM tool [15] and then extracting the equivalent network. The methodology is shown in Figure 5.

The equivalent network thus obtained is shown in Figure 6 which is actually the cascade of four lumped PI networks. The comparison of the equivalent network with that of CPW structure is shown in Figure 7.

Again the equivalent network is symmetric owing to the symmetry of CPW. The comparison of the scattering parameters shows that the lumped element PI section equivalent provides a very good network equivalent to the CPW and the accuracy goes on improving with increasing frequency. So the network equivalent is valid for high frequency applications also. The network is composed of four PI sections. Accuracy can be enhanced further by increasing the number of sections at the cost of increasing complexity.

Finally the equivalent network is proposed based on the Model Order reduction (MOR) technique of FIT tool [16]. This method is based on evaluating system poles to remodel the S -parameters with a SPICE compatible network. However this method provides a complex equivalent network composed of controlled sources and hence is not passive. The scattering parameters of the equivalent network obtained by MOR are shown in Figure 8.

A SPICE-compatible Netlist was generated by FIT program which consists of resistors, capac-

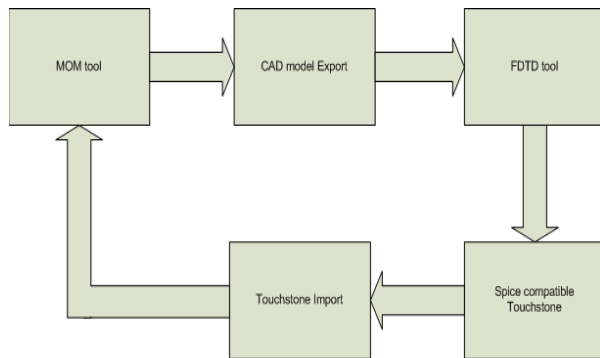


Figure 5: Methodology of equivalent network extraction based on FIT tool.

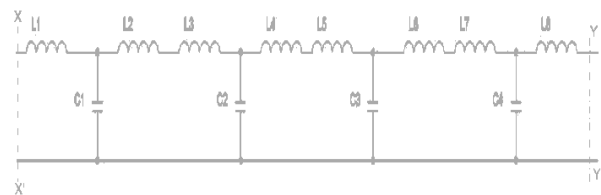


Figure 6: Equivalent lumped element network obtained by FIT which is a cascade of four PI networks ($L1 = L2 = L3 = L4 = L5 = L6 = L7 = L8 = 49.48 \mu\text{H}$, $C1 = C2 = C3 = C4 = 314.66 \text{ pF}$).

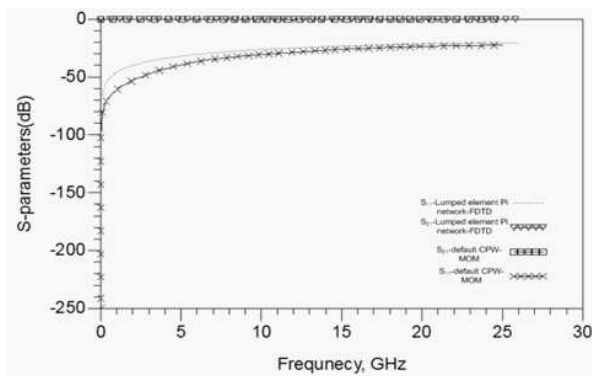


Figure 7: Scattering parameters of the lumped element PI network equivalent (FIT) compared to the scattering parameters of CPW obtained by MOM.

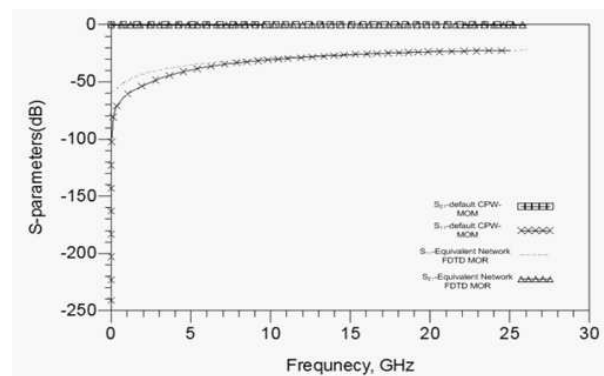


Figure 8: Scattering parameters of the network equivalent obtained by Model Order Reduction method of FIT tool.

itors, inductors and controlled sources. Such a netlist can be imported in a SPICE manager, e.g., Berkeley SPICE [25] and an equivalent network can be generated easily.

3. CONCLUSION

The lumped element network equivalent models were proposed for a supported CPW. The equivalent network models were obtained by curve-fitting the scattering parameters with those of CPW. The equivalent network models would remarkably reduce the complexity and CPU time for CPW based circuit simulators and CAD applications.

REFERENCES

1. Simons, R. N., *Coplanar Waveguide Circuits, Components and Systems*, Wiley Interscience, 2001.
2. Wolff, I., *Microwave Integrated Circuits*, Wiley Interscience, 2006.
3. Dib, N., L. Katehi, G. Ponchak, and R. Simons, "Theoretical and experimental characterization of coplanar waveguide discontinuities for filter applications," *IEEE Trans. on Microwave Theory and Techniques*, 873–882, May 1991.
4. Masood, R. and S. A. Mohsin, "Optimization of the S -parameter response of a coplanar waveguide series short stub for broadband applications," *ICCE*, Nha Trang, 2010.
5. Masood, R., S. A. Mohsin, and D. Ahmed, "A novel analysis of a coplanar waveguide series open stub for broadband applications," *IBCAST*, Islamabad, 2011.
6. Hu, J. and L. Sun, "EC-ANN models for CPW discontinuities," *IEE Proc. Microw. Antennas Propag.*, Vol. 152, No. 5, 292–297, Oct. 2005.
7. Simons, R. N. and G. E. Ponchak, "Modeling of some coplanar waveguide discontinuities," *IEEE Trans. on Microwave Theory and Techniques*, Vol. 36, 1796–1803, Dec. 1988.
8. Li, X., Y. Shi, and Y. Ding, "Model and performance analysis of coplanar waveguide based on different oxide structure HR-Si substrate," *PIERS Proceedings*, 489–492, Xi'an, China, Mar. 2010.
9. Gevorgian, S., L. J. Peter Linner, et al., "CAD models for shielded multilayered CPW," *IEEE Trans. on Microwave Theory and Techniques*, Vol. 43, No. 4, 772–779, Apr. 1995.
10. Radišić, D. Hjelme, A. Horrigan, Z. Popović, and A. Mickelson, "Experimentally verifiable modeling of coplanar waveguide discontinuities," *IEEE Trans. on Microwave Theory and Techniques*, Vol. 41, Special Issue on Modeling and Design of Coplanar Monolithic Microwave and Millimeter-Wave Integrated Circuits, 1524–1533, Sep. 1993.
11. Liu, G., H. Nakano, and K. Honjo, "Compact accurate scalable model for millimeter wave InP CPW with under-bridge," *IEICE Electron. Express*, Vol. 5, No. 2, 74–80, 2008.
12. Dib, N., J. Ababneh, and A. Omar, "CAD modeling of coplanar waveguide interdigital capacitor," *International Journal of RF and Microwave Computer-Aided Engineering*, Vol. 15, No. 6, 551–559, Nov. 2005.
13. Nached, M. and I. Wolff, "Equivalent capacitances of coplanar waveguide discontinuities and interdigitated capacitors using a three-dimensional finite difference method," *IEEE Trans. on Microwave Theory and Techniques*, Vol. 38, No. 12, Dec. 1990.
14. Harrington, R. F., *Field Computation by Moment Methods*, Macmillan, New York, 1968.
15. Agilent ADS, Momentum, <http://www.agilent.com/find/eesof-ads>.
16. CST Microwave Studio, <http://www.cst.com/>.
17. Veyres, C. and V. Fouad-Hanna, "Extension of the application of conformal mapping techniques to coplanar lines with finite dimensions," *Int. J. Electronics*, Vol. 48, No. 1, 47–56, 1980.
18. Collin, R. E., *Foundations for Microwave Engineering*, 2nd Edition, Mc Graw-Hill, New York, 1992.
19. Gupta, K. C., R. Garg, I. J. Bahl, and P. Bhartia, *Microstrip Lines and Slotlines*, 2nd Edition, Artech House, Inc., 1996.
20. Fouad-Hanna, V., "Finite boundary corrections to coplanar stripline analysis," *Electronics Lett.*, Vol. 16, No. 15, 604–606, 1980.
21. Ghione, G. and C. Naldi, "Parameters of coplanar waveguides with lower ground plane," *Electronics Lett.*, Vol. 19, No. 18, 734–735, 1983.
22. Kitazawa, T. and Y. Hayashi, "Variational method for coplanar waveguide with anisotropic substrates," *IEE Proc. H — Microwaves, Optics and Antennas*, Vol. 134, No. 1, 7–10, 1987.

23. Hilber, W., “From approximation to exact relations for characteristic impedances,” *IEEE Trans. on Microwave Theory and Techniques*, Vol. 17, 259–265, 1969.
24. Gevorgian, S., L. J. P. Linner, and E. L. Kollberg, “CAD models for shielded multilayered CPW,” *IEEE Trans. on Microwave Theory and Techniques*, Vol. 43, No. 4, 772–779, Apr. 1995.
25. Berkeley SPICE, <http://bwrc.eecs.berkeley.edu/classes/icbook/spice/>.

Grounded CPW-WR12 Transition Design for 1.55 μm Photodiode Based E-band Transmitter

Merih Palandöken¹, Sascha Lutzmann¹, Vitaly Rymanov², Andreas Stöhr², and Tolga Tekin¹

¹Technische Universität Berlin, Gustav-Meyer-Allee 25, Berlin 13355, Germany

²Universität Duisburg-Essen, Lotharstr. 55, Duisburg 47057, Germany

Abstract— In this paper, an RF transition from a grounded coplanar waveguide (CPW) to a rectangular waveguide is proposed as a millimeter wave component in wireless E-band applications. One side of coplanar waveguide is loaded with a circular slot line in the form of short-circuited broadband termination. The other side is tapered linearly in order for the resulting slot line to match with the wave impedance of H₁₀ fundamental mode of rectangular waveguide. The proposed transition design provides easy fabrication in a planar form. Due to the grounded CPW line, the transition can be quite precisely positioned inside the waveguide with any dielectric/metallic material under the ground plane. The transition has smaller than 0.3 dB insertion loss in the frequency band of 64–78 GHz with the minimum value of 0.1 dB at 68.87 GHz. The return loss is larger than 15 dB in the same frequency band with the maximum value of 43 dB at 68.9 GHz. The effects of geometrical parameters in the transition design in terms of input impedance are additionally discussed in order to verify the design approach and determine the critical design parameters for the optimum design.

1. INTRODUCTION

Due to the continuous growth in wireless communications with rising demand for higher data-rates, new technologies and design strategies have to be developed. A promising method to multi-Gbps wireless communication is to use mm-wave frequencies where very large bands of frequency spectrum are available for different modulation schemes. However, there are important challenges to be overcome such as higher air-link loss (e.g., about 30 dB higher at 60 GHz than at 2.4 GHz), and reduced device performance and lower power efficiency. In addition, the wide channel bandwidth means higher noise power and reduced SNR [1–3]. Therefore, RF transmission has to be accomplished through high bandwidth and gain antennas with low loss. In order for these antennas to be operated in an optimum manner, the feeding network from mm-wave circuit to the antenna has to be carefully designed. The waveguide transitions are therefore important microwave components to obtain optimum coupling from microwave circuits to waveguide feeding networks of high gain transmitting antenna arrays.

In recent years, various types of coplanar waveguide-to-rectangular waveguide transitions are proposed [4–8]. Ponchak, et al. proposed a coplanar waveguide-to-rectangular waveguide transition by using a gradually tapered ridge in one of the broad walls of the waveguide and a nonradiating slot in the opposite wall [4]. The advantage of the transition is no need of bonding wires to suppress the slot line mode of the CPW in this design, but the fabrication cost is high due to precise machining. Although this transition can also be applied at a higher frequency using micromachining techniques, the cost is still high [5]. In order to reduce the cost, planar types of transition circuits are developed to integrate more easier with standard rectangular waveguides [6–8]. In [6], an open-ended planar probe is fed by an asymmetric CPW.

Because the length of the monopole antenna, which is formed from the exciting probe has to be sufficiently long to couple the probe E field on E -plane of the waveguide, it results the feeding CPW line to be highly asymmetric. This could result the exciting CPW to couple with the housing due to slot line mode. Air bridges are therefore needed to suppress the radiating odd mode of the CPW generated by the asymmetric discontinuity. Besides, a broadband coplanar waveguide-to-rectangular waveguide transition can be achieved with a slot line radial stud loaded to the CPW, which is formed on the trenches of a metal block [7]. The transition circuit has the form of tapered fin-line without any air bridges with the disadvantage of electrically large area due to fin-line. A coplanar waveguide-to-rectangular waveguide transition based on tapered slot antenna with E -plane probe coupling and a slotline to CPW matching section [8]. The need of an intermediate CPW to slotline transition occupies an additional area in the transition. Also, air bridges are needed in order to ensure the even mode operation of the CPW. Further transition designs with integrated

end-fire antennas are applied in the design of the coplanar waveguide to rectangular waveguide transition [9–11].

In this paper, a grounded CPW to waveguide transition in E-band is studied. The important design parameters are indicated to figure out their effect on the input impedance. These parameters are sufficient to obtain an easy design for higher frequency bands.

2. TRANSITION DESIGN

The grounded CPW-waveguide transition is shown in Fig. 1 along with the geometric model. In the transition geometry, the transmission line length from the field excitation point upto the broadband load, L_1 is 2.4 mm. The broadband load is designed in a form of a circular aperture in the short-circuited signal line and ground plane to obtain a low Q resonator. The radius of circular slot is 0.18 mm. The starting distance of the linear taper, L_2 is 3.6 mm. The ground length is 3.3 mm. This is an important design parameter, which determines the degree of field coupling from the circular broadband load to the slot line for the efficient waveguide excitation. The radius and separation distance of vias are 65 μm and 0.3 mm respectively. The vias are used in order to suppress the slot line mode (odd mode), which could be excited due to the material inhomogeneity along the field propagation direction. The separation distance between the vias and field excitation point, L_4 is 1.435 mm. They are located with a distance of $D_1 = 0.26$ mm from the outer metal sides. The slot line is extended linearly to be coupled to the fundamental H10 mode of waveguide. The tapering distance is important to design a broadband transition. Therefore, the angle between the extended slot line arms has to be small enough with a disadvantage of electrically large transition length. The signal and gap width are set as 0.35 mm and 0.1 mm to obtain 50Ω impedance. The substrate is Rogers 5880 with the relative permittivity and loss tangent of 2.2 and 0.0009, respectively. The substrate thickness is 130 μm . The transition design approach is to compensate any reactive impedance obtained from the waveguide impedance transformation through linearly tapered slot line with an inductance or capacitance resulting from the slot resonator smaller than or larger than the resonance frequency, respectively.

In that term, the whole transition can be regarded as a broadband balun for unbalanced CPW line to the balanced slot line at the transition end. Because the transition has to be inserted into the waveguide with high precision, the metal block underneath is necessary to locate the tapered slot line at the middle of waveguide as in Fig. 1(a). The waveguide size is 1.55 mm \times 3.1 mm.

3. NUMERICAL RESULTS

The numerically calculated transmission and reflection parameters are shown in Fig. 2. The insertion loss is smaller than 0.3 dB with the minimum value of 0.1 dB at 68.87 GHz in the frequency band of 64 GHz and 78 GHz. The return loss is larger than 15 dB at the same frequency band with the minimum value of 43 dB at 68.9 GHz. In the transition design, two different geometrical parameters are investigated to optimize RF performance. The radius of circular slot is the first parameter to be optimized as shown in Fig. 3. The larger radius has the effect of broader impedance bandwidth with low Q . The larger impedance bandwidth can be deduced from the higher magnetic coupling from the circular slot to the slot line transition due to small separation distance inbetween.

In other words, the high field concentration in the circular slot load leads the resonator field to be better coupled with another shunt load formed by the slot line-waveguide transition. However, the larger radius increases the real part of input impedance with an additional capacitive reactance

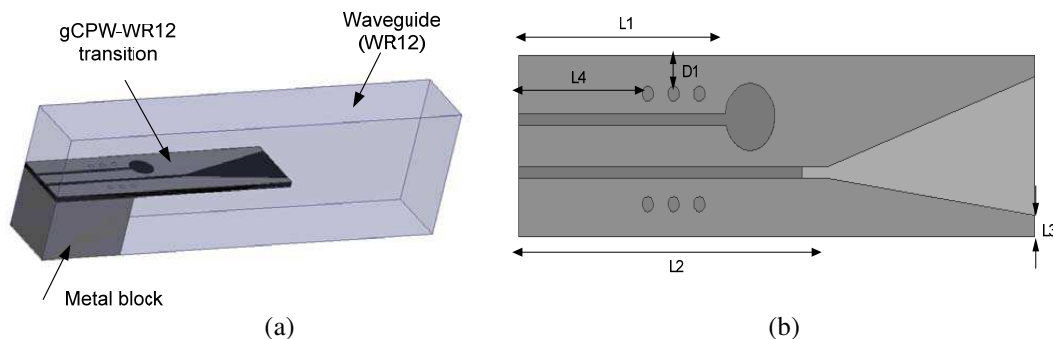


Figure 1: (a) Schematic view and (b) geometric model of grounded CPW-waveguide transition.

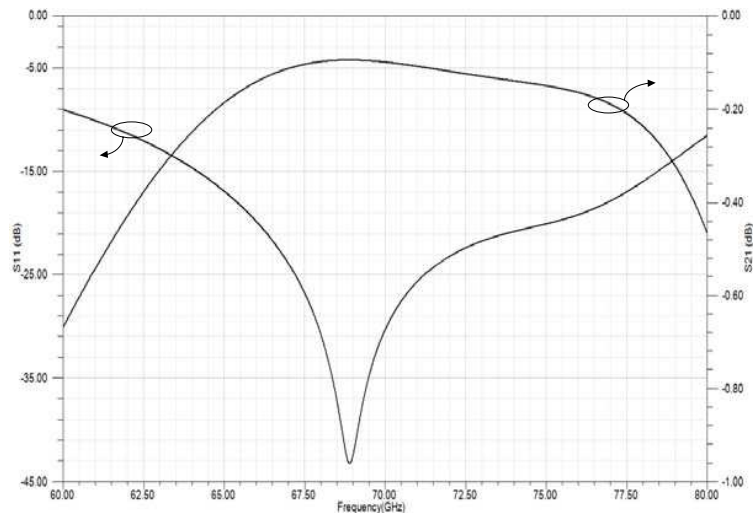


Figure 2: The transmission and reflection parameter of grounded CPW-waveguide transition.

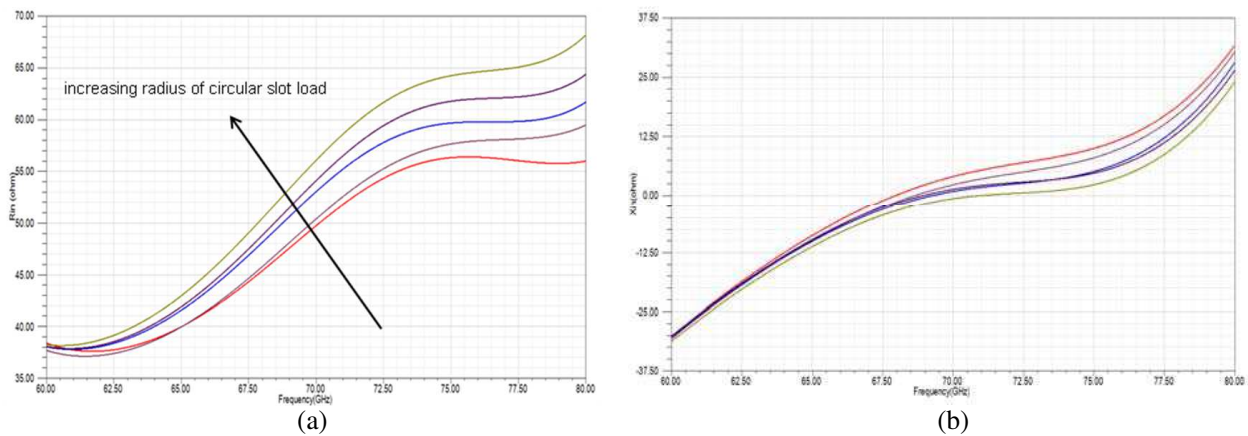


Figure 3: (a) Real and (b) imaginary part of input impedance with various circular slot load radius.

due to narrower signal line width as shown in Fig. 3(b). The ground plane length is the second parameter to be optimized. The larger ground length has the effect of circular slot load to have higher Q . This results in turn the real part of line impedance to be larger with larger inductive part. However, the larger ground length degrades the insertion loss due to screening the field lines on both sides of linear taper to excite the waveguide.

The length of metal block is another parameter for the determination of how long it has to be as a support material. As it is used to locate the transition precisely inside the waveguide, it has to have negligible effect on RF performance. The numerical calculations indicate small effect on the input impedance upto the ground length due to no field coupling from the signal line. For the larger block length, the near field coupling from the linear slot line transition to the metallic block is higher, which degrades the transmission parameter due to low field coupling to the waveguide mode. Therefore, especially for the substrates with small thickness, this has to be investigated not to influence the slot line impedance.

4. CONCLUSION

In this paper, a grounded CPW to E-band waveguide transition is proposed. The effect of radius of circular slot line and ground plane length on the input impedance are studied. The proposed transition design can be easily fabricated and precisely positioned inside the waveguide with any material under the ground plane. The transition has smaller than 0.3 dB insertion loss in the frequency band of 64–78 GHz with 20% 15-dB fractional bandwidth.

REFERENCES

1. Wells, J., “Faster than fiber: The future of multi-Gb/s wireless,” *IEEE Microw. Mag.*, Vol. 10, No. 3, 104–112, May 2009.
2. Ng’oma, A., D. Fortusini, D. Parekh, W. Yang, M. Sauer, S. Benjamin, W. Hofmann, M. C. Amann, and C. J. Chang-Hasnain, “Performance of a multi-Gb/s 60 GHz radio over fiber system employing a directly modulated optically injection-locked vcsel,” *Journal of Lightwave Technology*, Vol. 28, No. 16, 2436–2444, 2010.
3. Park, C. and T. S. Rappaport, “Short-range wireless communications for next-generation networks: UWB, 60 GHz millimeter-wave WPAN, and ZigBee,” *IEEE Wireless Commun.*, Vol. 14, No. 4, 70–78, Aug. 2007.
4. Ponchak, G. E. and R. N. Simons, “A new rectangular waveguide to coplanar waveguide transition,” *Proc. IEEE MTT-S Int. Microw. Symp. Dig.*, Vol. 1, 491–492, Dallas, USA, May 1990.
5. Li, Y., B. Pan, J. P. Becker, J. R. East, and L. P. B. Katehi, “Fully micromachined finite-ground coplanar line-to-waveguide transitions for W-band applications,” *IEEE Trans. Microw. Theory Tech.*, Vol. 52, No. 3, 1001–1007, Mar. 2004.
6. Möttönen, V. S. and A. V. Räisänen, “Novel wide-band coplanar waveguide-to-rectangular waveguide transition,” *IEEE Trans. Microw. Theory Tech.*, Vol. 52, No. 8, 1836–1842, Aug. 2004.
7. Möttönen, V. S., “Wideband coplanar waveguide-to-rectangular waveguide transition using fin-line taper,” *IEEE Microw. Wireless Compon. Lett.*, Vol. 15, No. 2, 119–121, 2005.
8. Lin, T.-H. and R.-B. Wu, “CPW to waveguide transition with tapered slotline probe,” *IEEE Microw. Wireless Compon. Lett.*, Vol. 11, No. 7, 314–316, Jul. 2001.
9. Kaneda, N., Y. Qian, and T. Itoh, “A broadband CPW-to-waveguide transition using quasi-Yagi antenna,” *Proc. IEEE MTT-S Int. Microw. Symp. Dig.*, Vol. 2, 617–620, Boston, USA, Jun. 2000.
10. Fang, R.-Y. and C.-L. Wang, “A broadband coplanar waveguide to rectangular waveguide transition using a truncated bow-tie antenna,” *Proc. 37th Eur. Microw. Conf.*, 468–471, Amsterdam, The Netherlands, Oct. 2008.
11. Fang, R.-Y., J.-K. Chuang, and C.-L. Wang, “Coplanar waveguide-to-rectangular waveguide transition using meander slotline,” *Proceedings of the Asia-Pacific Microwave Conference*, 2011.

Integrating Equal-split Wilkinson Power Dividers and Coupled-line Bandpass Filters

P. H. Deng, L. C. Dai, and Y. D. Chen

Department of Electrical Engineering, National University of Kaohsiung
No. 700, Kaohsiung University Road, Nan-Tzu District, Kaohsiung 81148, Taiwan, R.O.C.

Abstract— Conventional equal-split Wilkinson power dividers usually demonstrate poor selectivity. By cascading an additional bandpass filter before the input or after each output port of the conventional equal-split Wilkinson power divider, the band selection of each transmission path can be enhanced substantially. However, the selectivity has been increased at the cost of a large circuit area by connecting an additional filter. Therefore, integrating bandpass filters and conventional equal-split Wilkinson power dividers may provide a solution for reducing the total circuit size. This paper presents a novel type of divider with favorable selectivity using two coupled-line bandpass filters to replace two quarter-wavelength ($\lambda/4$) transformers of a conventional Wilkinson power divider. Specifically, two crucial design conditions should be met for each coupled-line bandpass filter. The first condition requires fitting a system impedance of $70.7\ \Omega$ for each filter when the termination impedances at all ports of the divider are set at $50\ \Omega$. The second condition requires selecting an even-order coupled-line bandpass filter, because the filter order may significantly affect the performance of the divider. Notably, the selectivity of the proposed divider is similar to that of the conventional equal-split Wilkinson power divider with an additional filter placed before the input port or after each output port. Nevertheless, the proposed type of divider can avoid two $\lambda/4$ transformers, which are usually used in the conventional Wilkinson power divider. For demonstration, two equal-split Wilkinson power dividers with high-quality band selection are proposed in this study, achieving favorable agreement with simulated and measured responses.

1. INTRODUCTION

Wilkinson power divider is popularly used to split the power due to the easy theoretical analysis, low loss, and extremely good isolation between two output ports. For the practical purpose, several types of Wilkinson power divider has been studied in [1–14]. Some investigations have been utilized different coupled-line structures to design novel power divide for various purpose as shown in [1–8]. For instance, a pair of parallel coupled lines constructed on defected ground structure was employed for harmonic suppression [1].

In general, the $\lambda/4$ transmission lines are utilized as impedance transformers in conventional Wilkinson power divider, but the poor selectivity in each transmission path is a main drawback. Intuitively, the selectivity can be improved by adding extra higher order bandpass filter before the input or after each output port of the divider, but the large total circuit may be a terrible problem. In [11] and [12], they integrated two bandpass filters with Wilkinson power dividers for improving the selectivity and relaxing the large circuit size issue.

In [13], the unequal-split Wilkinson power divider proposed a method to integrate high-order parallel coupled-line bandpass filter transformers, which can achieve the favorable selectivity and high isolation. Based on the integrating filter transformer concept of [13], this paper presents two new equal-split Wilkinson power dividers with favorable selectivity in each transmission path. The proposed structure integrates conventional equal-split Wilkinson power divider with two even-order parallel coupled-line bandpass filter transformers, and the desired selectivity in each output signal can be easily achieved.

2. DESIGN OF THE PROPOSED WILKINSON POWER DIVIDER

Figure 1(a) illustrates a conventional Wilkinson power divider structure [14] consisted of two $\lambda/4$ transmission lines (X_A and X_B) and an isolated resistor R . A power divider in equal-split division can be designed by following design parameters: $Z_1 = Z_2 = Z_3 = Z_0$, $Z_{0A} = Z_{0B} = \sqrt{2}Z_0$, and $R = 2Z_0$, where the Z_1 , Z_2 , and Z_3 are the load impedance at each port; Z_0 is the system impedance; Z_{0A} and Z_{0B} are the characteristic impedances of the $\lambda/4$ transformers; R is a resistor for isolation.

Because conventional power divider suffers from poor selectivity in each transmission path, an additional filter can be increased before the input or after each output port of the divider to

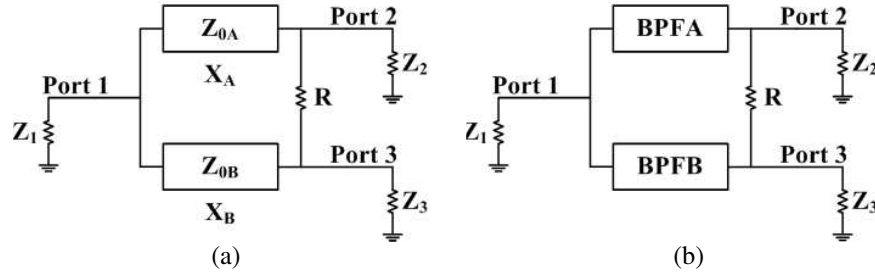


Figure 1: (a) Conventional Wilkinson power divider structure. (b) Proposed Wilkinson power divider with two embedded bandpass filter transformers.

improve this situation. However, large circuit area is an inevitable problem. Therefore, to integrate bandpass filters into equal-split Wilkinson power divider, as shown in Fig. 1(b), may be a better solution for increasing selectivity and reducing total circuit size. The method of using higher-order coupled-line filter to replace $\lambda/4$ transformer [13] can be utilized in the proposed equal-split Wilkinson power divider with favorable selectivity. The coupled-line filter design equations of the proposed divider [14] can be written as

$$\begin{aligned} Z_{0ei} &= Z_{cf} \left[1 + Z_{cf} J_i + (Z_{cf} J_i)^2 \right] \\ Z_{0oi} &= Z_{cf} \left[1 - Z_{cf} J_i + (Z_{cf} J_i)^2 \right] \\ i &= 1, 2, \dots, N + 1 \end{aligned} \quad (1a)$$

$$Z_{cf} J_1 = \sqrt{\frac{\pi FBW}{2g_1}} \quad (1b)$$

$$Z_{cf} J_n = \frac{\pi FBW}{2\sqrt{g_{n-1}g_n}}, \quad n = 2, 3, \dots, N \quad (1c)$$

$$Z_{cf} J_{n+1} = \sqrt{\frac{\pi FBW}{2g_N g_{N+1}}} \quad (1d)$$

where Z_{0ei} and Z_{0oi} are the even- and odd-mode characteristic impedances of each coupled-line section; Z_{cf} and FBW are the system impedance and the 3-dB fractional bandwidth of the filter; J_i , $i = 1, 2, \dots, N + 1$, are the admittance inverters (J-inverters); g_i , $i = 1, 2, \dots, N + 1$, are the lumped element values for low-pass filter prototype. In the conventional equal-split Wilkinson power divider, the characteristic impedance of each $\lambda/4$ transformer (X_A or X_B in Fig. 1(a)) is $\sqrt{2}Z_0$. Therefore, each $\lambda/4$ transformer in Fig. 1(a) can be replaced by even-order coupled-line bandpass filter when the system impedance of the filter is $\sqrt{2}Z_0$, which design concept has been discussed in the unequal-split Wilkinson power dividers [13].

3. TWO EQUAL-SPLIT WILKINSON POWER DIVIDERS WITH FAVORABLE BAND SELECTION

The purpose of this paper is to integrate the conventional Wilkinson power divider with higher-order coupled-line filter transformers, which can improve the divider selectivity and replace two $\lambda/4$ transformers in the conventional Wilkinson power divider. However, the order of the coupled-line filter transformer need to select evenorder for achieving the impedance matching requirement, as discussed in [13]. For demonstration, two equal-split Wilkinson power dividers with different even-order Butterworth-type bandpass filter responses are proposed in this study. The first divider is used two second-order Butterworth-type coupled-line bandpass filter transformers where Z_{0ei}/Z_{0oi} , $i = 1, 2$, or 3, is the even-/odd-mode characteristic impedance of each coupled-line section between input port (Port 1) and output ports (Port 2 and Port 3) as shown in Fig. 2(a). This study fabricates all of the circuits on the FR4 substrate with a dielectric constant of 4.4, a thickness of 1.6 mm, and a loss tangent of 0.02. Fig. 2(b) demonstrates the circuit layout of Fig. 2(a) (the proposed equal-split Wilkinson power divider with two integrating second-order Butterworth-type bandpass filter transformers). The Z_{cf} and R are 70.7Ω and 100Ω , respectively, when Z_0 is equal to 50Ω .

The center frequency and 3-dB fractional bandwidth of each filter transformer (BPF A or BPF B) are around 1.5 GHz and 15%, respectively. The corresponding design parameters of each filter transformer are $g_1 = 1.4142$, $g_2 = 1.4142$, $g_3 = 1$, $J_1 = 0.005772$, $J_2 = 0.002356$, $J_3 = 0.005772$, $Z_{0e1} = 111.35 \Omega$, $Z_{0e2} = 84.45 \Omega$, $Z_{0e3} = 111.35 \Omega$, $Z_{0o1} = 53.63 \Omega$, $Z_{0o2} = 60.89 \Omega$, and $Z_{0o3} = 53.63 \Omega$. The simulated and measured responses of Fig. 2(b) are shown in Fig. 3. The measured minimal insertion loss ($-|S_{21}|$ or $-|S_{31}|$) is approximately 5.5 dB; the measured isolation ($-|S_{32}|$) is better than 24 dB around the desired band; the measured 3-dB fractional bandwidth and center frequency of each filter transformer are approximately 14.9 % and 1.502 GHz, respectively.

Figure 4(a) shows an equal-split Wilkinson power with two fourth-order Butterworth-type band-pass filter transformers, which can provide a better band selection for each transmission path than that of Fig. 2(b). The layout of Fig. 4(a) is shown in Fig. 4(b). The Z_{cf} and R are 70.7Ω and 100Ω , respectively, when Z_0 is set to be 50Ω . The center frequency and 3-dB fractional bandwidth of each filter transformer (BPF A or BPF B) are around 1.5 GHz and 15%, respectively. The corresponding design parameters of each filter transformer are $g_1 = 0.7654$, $g_2 = 1.8478$, $g_3 = 1.8478$, $g_4 = 0.7654$, $g_5 = 1$, $J_1 = 0.007846$, $J_2 = 0.002802$, $J_3 = 0.001803$, $J_4 = 0.002802$, $J_5 = 0.007846$, $Z_{0e1} = 131.71 \Omega$, $Z_{0e2} = 87.5 \Omega$, $Z_{0e3} = 80.88 \Omega$, $Z_{0e4} = 87.5 \Omega$, $Z_{0e5} = 131.71 \Omega$, $Z_{0o1} = 53.25 \Omega$, $Z_{0o2} = 59.48 \Omega$, and $Z_{0o3} = 62.84 \Omega$, $Z_{0o4} = 59.48 \Omega$, and $Z_{0o5} = 53.25 \Omega$. The simulated and measured responses of Fig. 4(b) are shown in Fig. 5. The measured minimal insertion loss ($-|S_{21}|$ or $-|S_{31}|$) is 6.8 dB; the measured isolation ($-|S_{32}|$) is better than 24 dB around the desired band; the measured 3-dB fractional bandwidth and center frequency of each filter transformer are approximately 15.2% and 1.502 GHz, respectively.

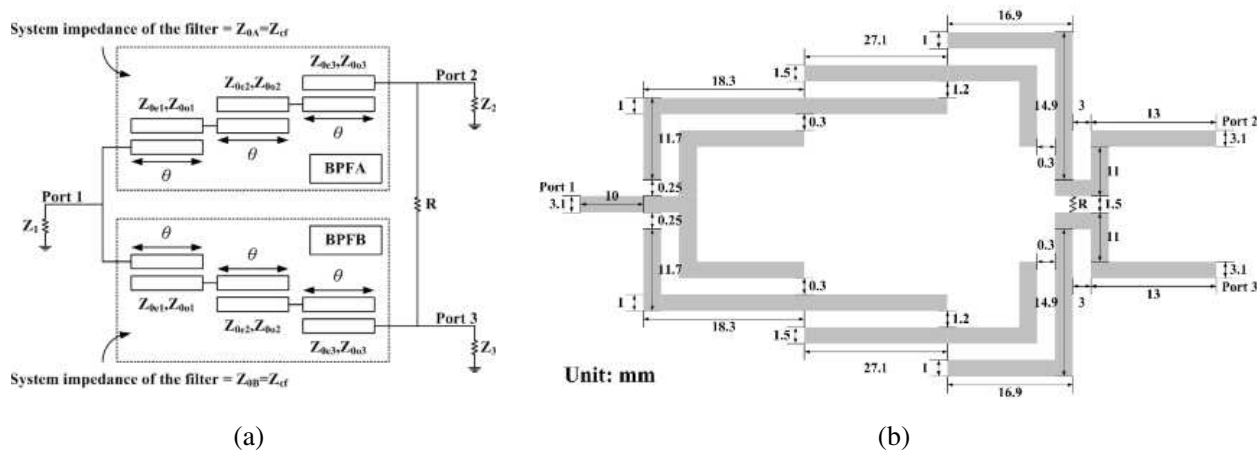


Figure 2: (a) Circuit models and (b) layout of the proposed equal-split Wilkinson power divider with two integrating second-order Butterworth-type bandpass filter transformers.

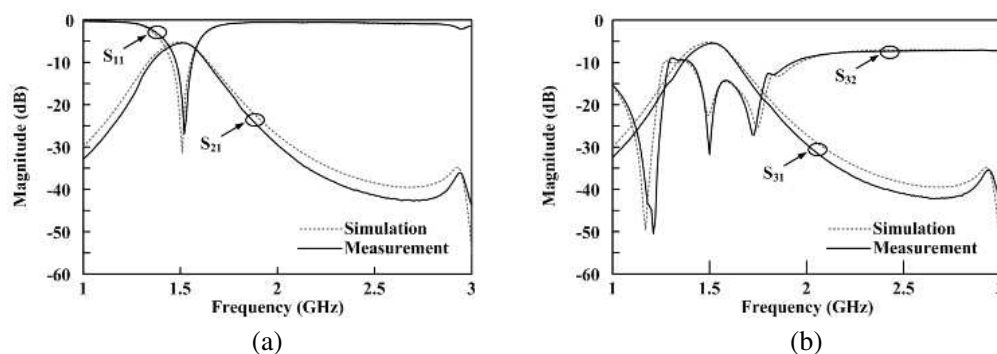


Figure 3: Simulated and measured frequency responses of Fig. 2(b). (a) $|S_{11}|$ and $|S_{21}|$. (b) $|S_{31}|$ and $|S_{32}|$.

5. Lee, D. H., Y. B. Park, and Y. Yun, “Highly miniaturised Wilkinson power divider employing π -type multiple coupled microstrip line structure,” *Electron. Lett.*, Vol. 42, No. 13, 763–765, Jun. 2006.
6. Tang, X. and K. Mouthaan, “Analysis and design of compact two-way Wilkinson power dividers using coupled-line,” *Proc. Asia-Pacific Microwave Conference*, 1319–1322, Dec. 2009.
7. Chiu, J. C., J. M. Lin, and Y. H. Wang, “A novel planar three-way power divider,” *IEEE Microwave Wireless Compon. Lett.*, Vol. 16, No. 8, 449–451, Aug. 2006.
8. Tang, X. and K. Mouthaan, “Compact dual-band power divider with single allpass coupled-line sections,” *Electron. Lett.*, Vol. 46, No. 10, 688–689, May 2010.
9. Park, M. J. and B. Lee, “A dual-band Wilkinson power divider,” *IEEE Microwave Wireless Compon. Lett.*, Vol. 18, No. 2, 85–87, Feb. 2008.
10. Avrillon, S., I. Pele, A. Chousseaud, and S. Toutain, “Dual-band power divider based on semiloop stepped-impedance resonators,” *IEEE Trans. Microw. Theory Tech.*, Vol. 51, No. 4, 1269–1273, Apr. 2003.
11. Singh, P. K., S. Basu, and Y. H. Wang, “Coupled line power divider with compact size and bandpass response,” *Electron. Lett.*, Vol. 45, No. 17, 892–894, Aug. 2009.
12. Shao, J. Y., S. C. Huang, and Y. H. Pang, “Wilkinson power divider incorporating quasi-elliptic filters for improved out-of-band rejection,” *IET Electronics Letters*, Vol. 47, No. 23, 1288–1289, 2011.
13. Deng, P. H. and L. C. Dai, “Unequal Wilkinson power dividers with favorable selectivity and high-isolation using coupled-line filter transformers,” *IEEE Trans. Microw. Theory Tech.*, Vol. 60, No. 6, 1520–1529, Jun. 2012.
14. Pozar, D. M., *Microwave Engineering*, 2nd Edition, Chapters 7–8, Wiley, New York, 1998.

Full-wave Modeling of Open Subwavelength Resonator with Metamaterial

A. P. Smirnov, A. N. Semenov, D. O. Ignatyeva, and A. P. Sukhorukov
Lomonosov Moscow State University, Moscow, Russia

Abstract— The properties of an open Fabry-Perot nano resonator containing a layer of metamaterial with a negative refractive index are investigated. Numerical simulation of this cavity is performed using an EMWSolver3D solver based on the FDTD scheme, with Drude model for the frequency dependent media and the UPML absorbing boundary conditions for open region simulations. It demonstrates that waveguide eigenmodes with arbitrary profiles exist in such a cavity and the metamaterial layer considerably lowers diffraction losses. It was shown that even though diffraction theory is not formally applicable on nano scales, waveguide modes with an arbitrary distribution of amplitude can be excited if the effective diffraction length is zero.

1. INTRODUCTION

Artificial composite media that can have properties fundamentally different from those of well-known substances — called metamaterials — are of great interest now. Among other factors, such media can have negative refraction indices in case when the effective magnetic permeability and dielectric permittivity are negative. The problem of negative refraction was studied in such works as [2, 3] and the media with negative material parameters were presented by V. Veselago in 1967 [1]. Since metamaterials with dielectric permittivity and effective magnetic permeability were discovered first in microwave frequency range [4] and later at optical frequencies [5, 6], interest in such media rapidly grew.

Due to metamaterials one is allowed to produce different devices that have fundamentally new properties. For example, because of negative refraction at its boundary, a plane-parallel layer of metamaterial can serve as an ideal super-lens not only focusing that not only focuses the far field components but also amplifies and focuses the near-field components that contain information on a source with a size of less than one wavelength [7]. One can also use a periodic sequence of plane-parallel layers of a metamaterial alternating with layers of a dielectric to produce an analogue of a lens line preventing the diffraction spreading of a wave beam [8]. New waveguide and dispersive properties can be produced after placing a metamaterial layer inside an open cavity, compared to cavities without a filler. Compact microcavities of size less than half a wavelength can be produced in case when the space shift of a plane wave inside of cavity with metamaterial can be equal to zero [9].

The description of the profiles and conditions for the stability of waveguide modes, the diffraction theory of a cavity with metamaterials and its eigen frequencies can be found in [10, 11]. The main difference between a dielectric cavity and a cavity with metamaterial is the presence of waveguide modes in a Fabry-Prot cavity. Meanwhile, these modes can have arbitrary profiles. The cavity diffraction theory for the cavity with metamaterial for the case of rather large cavities (relative to wavelength) was formulated in the above works. However, practically the case of a microcavity with characteristic sizes comparable to the order of one wavelength is important to study from a practical point of view.

2. NUMERICAL SIMULATION OF MICRORESONATOR

We can use numerical solutions for Maxwell equations in differential form for investigating the dynamics and stationary process in an open cavity. The use of the FDTD (Finite Difference Time Domain) method [12] allows us to study the dynamics of propagation and diffraction of electromagnetic waves and the formations of waveguide modes in a composite cavity.

The dispersion of metamaterials is used to be described by the following model:

$$\varepsilon(\omega) = \varepsilon_0 \left(1 - \frac{\omega_{pe}^2}{\omega^2 - i\omega\gamma_e} \right) \quad (1)$$

$$\mu(\omega) = \mu_0 \left(1 - \frac{\omega_{pm}^2}{\omega^2 - i\omega\gamma_m} \right) \quad (2)$$

where ω_{pe} , ω_{pm} are the electric and magnetic plasma frequencies, and γ_e , γ_m characterize the electromagnetic losses in metamaterial. The solutions for Maxwell equations in dispersive materials with second order accuracy in terms of time and space are allowed to be obtained using this model [13].

As an open cavity belongs to the mathematical class of indefinite systems the boundary conditions are important to be set properly for correct simulations in a selected computation domain. The key factor here is that external boundaries must not add substantial distortions to the initial solution. In this work, a layer of artificial anisotropic absorbing media that does not generate reflections restricts the computation domain. The use of UPML absorbing boundary conditions allows to obtain numerical solutions for open problems [14], in our case, for an open cavity. The second order accuracy $O(h^2 + \tau^2)$ of the FDTD method is ensured by selecting the optimum width and shape of the layer's loss profile. We developed a software complex based on these methods for numerical solution of solving Maxwell equations by means of FDTD method taking into account material dispersion and UPML absorbing boundary conditions.

When considering the model of a two-dimensional open cavity shown in Fig. 1. The cavity is restricted by two mirrors considered ideal within the model (reflection coefficient $R = 1$, achieved numerically by zeroing the tangential components of the electric field). The central part of the mirror with width d that is partially transparent (transmittance coefficient = 0.02) is used to introduce electromagnetic radiation into the cavity. A quasimonochromatic wave beam with the width a is used as the external source. The resonator contains two layers: a vacuum $\varepsilon = \mu = 1$ and metamaterial with negative dielectric permittivity and magnetic permeability $\varepsilon = \mu = -1$ without losses ($\omega_{pe} = \omega_{pm} = \sqrt{2}\omega$ and $\gamma_e = \gamma_m = 0$). An absorbing layer (UPML) restricting the computation domain from the top and bottom simulates the boundary conditions at infinity.

3. PROPERTIES OF MICRORESONATOR WITH METAMATERIAL

The properties of a Fabry-Perot cavity that contains a layer of metamaterial with a negative refraction index is considered. A quasioptic theory in approximation of an indefinite aperture of mirrors and greater width of beams relative to wavelength was presented in [10]. The presence of waveguide modes of arbitrary profile under the condition of a zero effective diffraction length of the longitudinal mode is the unique property of the composite cavity:

$$L_{eff} = \sum_j l_j/n_j = 0 \quad (3)$$

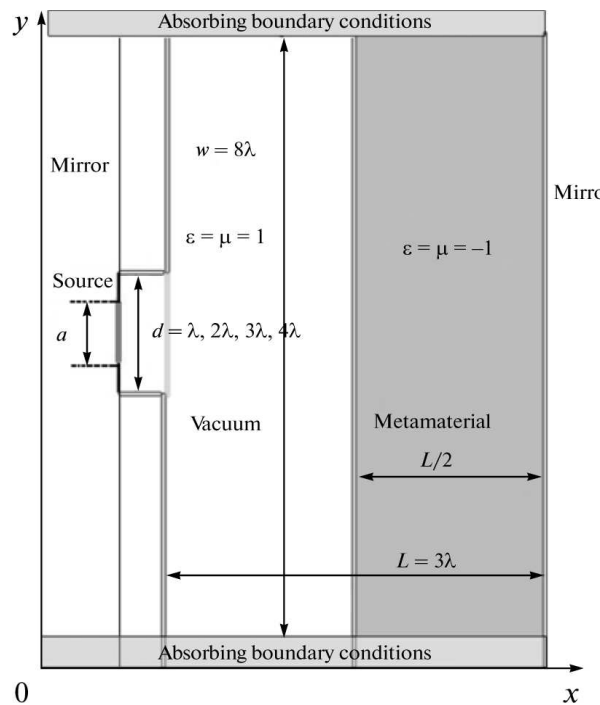


Figure 1: Scheme of model of microresonator with a layer of metamaterial.

There is no difference between the properties of the TE and TM modes in the above quasi-optic cavity theory. However, as the resonator length is reduced, the cavity properties change substantially in dependence on the polarization of a wave. Particularly, it is shown below that the resonators TE modes have higher quality factor, and the distribution of the wave amplitudes in the cavity differ as well.

The fact that, as in case of wide beams, micro-beams with arbitrary transversal profiles are the eigenmodes of the cavity if the effective diffraction length is zero, is confirmed by our numerical experiments.

The excitation of beams with a Gaussian profile $\vec{E}(x) = \vec{E}_0 \exp(-x^2/a^2)$ and a profile in the form of a hyperbolic secant $\vec{E}(x) = \vec{E}_0 \operatorname{sech}(x/a)$ with different beam widths a was studied. The amplitude distribution of components for a TE wave is shown in Figure 2. The superwide spatial beam spectrum leads to the appearance of longitudinal components of a waves electromagnetic field.

The diffraction spreading is compensated by the metamaterial in the microresonator, but part of the radiation goes beyond the resonator and is scattered because of the mirrors' finite sizes and dielectric and metamaterial layers. Let us estimate diffractive losses q associated with the transverse sizes of the cavity. This quantity is assumed to be equal to the ratio of energy lost through diffraction spreading of beam W_{dif} and the energy accumulated in cavity W_{res} :

$$q = \frac{W_{res}}{W_{dif}} \quad (4)$$

Let us estimate this quantity for a cavity containing two layers of media with refraction indices identical in modulus, $n_1 = n_2 = 1$. We assume that the cavity is excited by an external Gaussian source with width, and that the width of the mirrors and the layers of dielectric and metamaterial is w . Diffraction loss q can then be estimated as the ratio of energy of the part of the beam outside the cavity and the initial beam energy:

$$q = \frac{\int_0^w A_1^2(x) dx}{\int_0^w A_0^2(x) dx}, \quad (5)$$

where A_0 , a_0 is the amplitude and width of the beam on the first mirror, A_1 ; a_1 is the amplitude and width of the beam at the boundary of the metamaterial; and w is the half-width of the mirror.

Diffraction loss q in the microresonator for different widths of the external source was calculated during numerical simulations of the microresonator:

$$q = \frac{2\pi f_0 W}{P}, \quad (6)$$

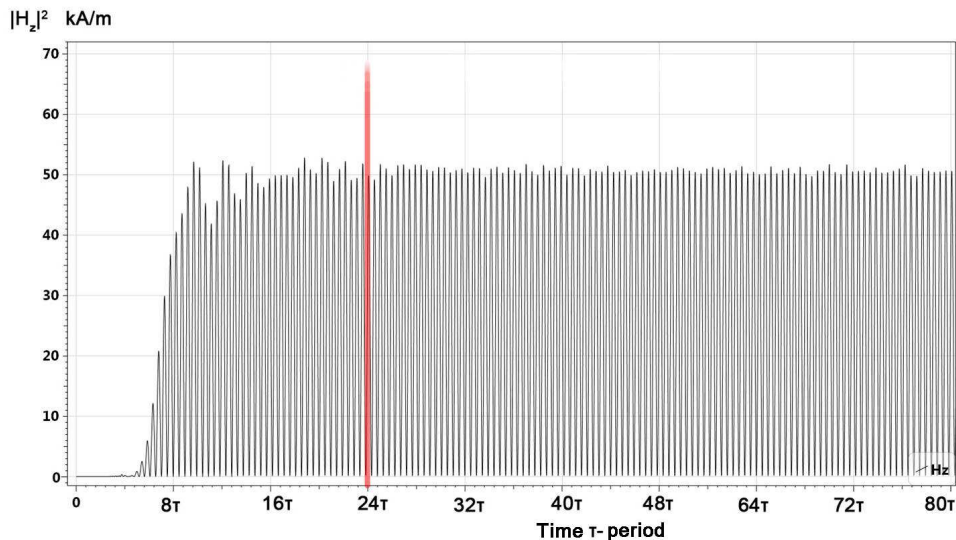


Figure 2: Intensity distribution of H_z components of the electromagnetic field of a beam with width $a = 2\pi$ at moment $t = 100\tau$ from the moment of source switching-on, where τ is the oscillation period of the source.

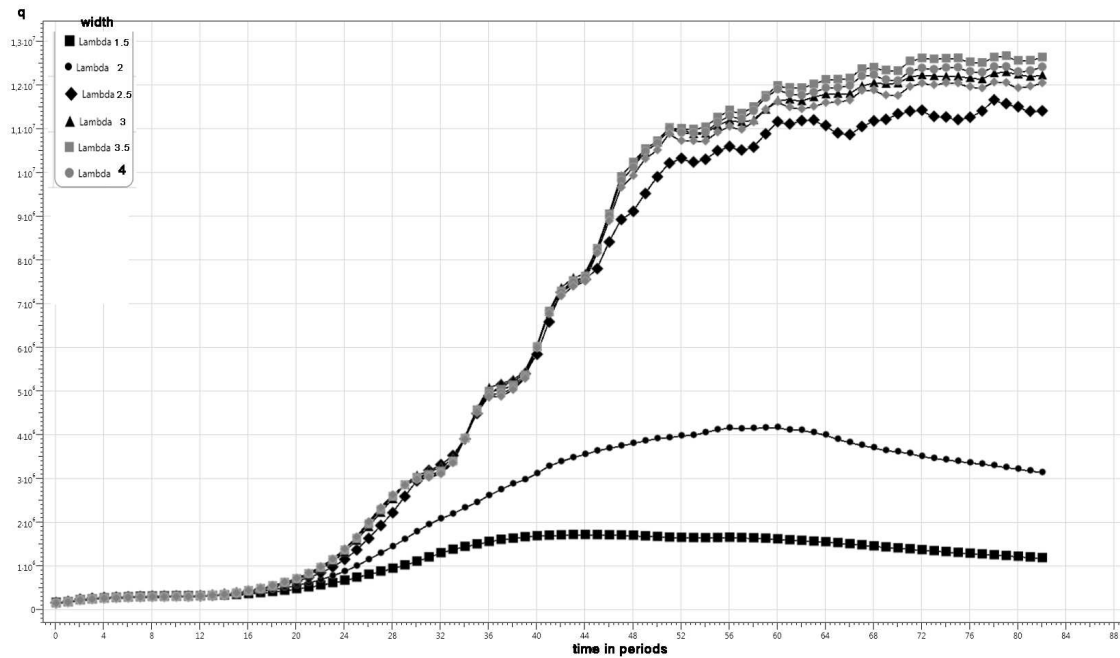


Figure 3: Dependence of diffraction losses on time for different width of source.

where f_0 is the resonant frequency, W is the accumulated energy, and $P = dW/dt$ is the scattering power. The dependence of diffraction losses on the beam width shown in Fig. 3 can be explained as follows: the considerable losses at narrow widths are due to the strong diffraction spreading of the beam. Increasing the initial beam width reduces diffraction, but the beam width becomes comparable to that of the mirrors and metamaterial, also leading to a considerable scattering of energy.

4. CONCLUSION

Numerical simulations of a microresonator with metamaterial were performed. Although the similar resonator was considered in earlier works, its sizes considerably exceeded radiation wavelengths; therefore it was interesting if microresonator possess the same unique properties as the properties described in [10, 11].

Our numerical simulation of microresonators with metamaterial was performed using FDTD method subject to the frequency dispersion of media with UPML absorbing boundary conditions.

Even though diffraction theory is not formally applicable on such scales, some of our conclusions were shown to be true for microresonators. In particular, in case when the effective diffraction length is zero waveguide modes with an arbitrary distribution of amplitude can be excited.

ACKNOWLEDGMENT

This study was partially supported by Russian Foundation for Basic Research, grant Nos. 11-02-00681 and 12-02-01119. D. O. Ignatyeva also thanks the non-profit Dynasty Foundation.

REFERENCES

1. Veselago, V. G., *Usp. Fiz. Nauk*, Vol. 92, No. 3, 517, 1967.
2. Schuster, A., *An Introduction to the Theory of Optics*, E. Arnold, London, 1904.
3. Mandel'shtam, L. I., "Lektsii po optike, teorii otноситel'nosti i kvantovoi mekhanike (Lectures on Optics, Relativity Theory and Quantum Mechanics)," Nauka, Moscow, 1972.
4. Smith, D. R., W. J. Padilla, and D. C. Vier, *Phys. Rev. Lett.*, Vol. 84, No. 3, 4184, 2000.
5. Shalaev, V. M., *Nature Photon*, Vol. 1, 41–48, 2007.
6. Xiao, S., U. K. Chettiar, and A. V. Kildishev, *Opt. Lett.*, Vol. 34, No. 22, 3478–3480, 2009.
7. Pendry, J. B., *Phys. Rev. Lett.*, Vol. 85, 3966, 2000.
8. Panfilova, N. O., D. O. Sapparina, and A. P. Sukhorukov, *BRAS: Physics*, Vol. 70, No. 12, 1722, 2006.
9. Engheta, N., *IEEE Ant. Wireless Pro. Lett.*, Vol. 1, No. 1, 10, 2002.

10. Saparina, D. O. and A. P. Sukhorukov, *Izv. Vyssh. Uchebn. Zaved., Prikl. Nelinein. Dinam.*, Vol. 17, No. 3, 3–16, 2009.
11. Saparina, D. O. and A. P. Sukhorukov, *Laser Phys.*, Vol. 19, No. 5, 1125–1130, 2009.
12. Taflove, A. and S. C. Hagness, *Computational Electrodynamics: The Finite Difference Time-domain Method*, Norwood, 2000.
13. Zhao, Y., P. Belov, and Y. Hao, *Phys. Rev. E*, Vol. 75, No. 37, 602, 2006.
14. Gedney, S. D., *IEEE Trans. Antennas Prop.*, Vol. 44, 1630–1639, 1996.
15. Semenov, A. N., A. P. Smirnov, D. O. Ignatyeva, and A. P. Sukhorukov, *BRAS: Physics*, Vol. 75, No. 12, 1741–1744, 2011.

A K-band Low Noise and High Gain Down-conversion Mixer

Chia-Yang Huang and Yen-Chung Chiang

National Chung Hsing University, Taiwan

Abstract— A down-converting mixer implemented in the TSMC 0.18- μm RF-CMOS process technology for applications in the K band is presented in this paper. Based on the conventional Gilbert cell topology, a dynamic current bleeding technique is adopted to suppress the flicker noise generated by the switch stage and thus to improve the noise figure (NF) of the mixer. Besides, an inductor for resonating the parasitic capacitances at the output of the transconductance (G_m) stage is utilized to increase the conversion gain and the linearity of the mixer. The chip size of the proposed mixer is $1.06 \times 0.98 \text{ mm}^2$. The measured peak power conversion gain (CG) for the proposed K-band mixer is 9.05 dB and the measured noise figure (NF) is 10.64 dB, respectively, at 22 GHz. And the measured 1 dB compression point (P1 dB) and IIP3 are -7.4 dBm and 0.5 dBm , respectively, at 24 GHz. The core circuit of the proposed mixer draws a 3.14 mA dc current from the 1.8 V voltage supply.

1. INTRODUCTION

Due to its low cost and easy integration capability with digital baseband, CMOS technology has become a strong candidate for wireless communication. Meanwhile, the growing demand of data transfer via the wireless communication systems pushes the operating frequency band higher. Some systems operating above 20 GHz, including the vehicle crash prevention radars, wireless local area networks, local multipoint distribution service (LMDS), and other ISM band applications, have been proposed. In those systems, the RF front-end circuits are crucial and the design trend is with low chip cost and low power consumption, thus the CMOS technology is now widely used in the design of such applications. One of the critical RF front-end circuits is the mixer which converts the incoming RF signal to the intermediate frequency (IF) signal. The mixer in general is the second or third stage, and it is required to provide a sufficient conversion gain (CG) with low noise figure (NF) and high linearity.

Figure 1 shows a conventional double-balanced mixer (Gilbert cell) for transceivers which has less even-order distortion and low LO-IF feedthrough. The noise figure is an important specification for a mixer and is influenced by many factors, including the noises from the G_m stage, the switch stage, and the load. The detailed analysis of the noise effect in a mixer design can be found in previous works [1, 2]. Among those noise sources, a noise cancellation technique has been proposed to diminish the noise from the switch stage [3]. For a direct conversion receiver, the flicker noise deeply affects the mixer's noise performance in the close-in frequencies, and it is reported that using current bleeding circuit with resonating inductor can overcome drawbacks introduced in the switch stage [4, 5]. In this paper, we adopt the PMOS dynamic current bleeding technique with one resonating inductor and design a K-band mixer in the 0.18 μm RF-CMOS process technology.

2. CIRCUIT DESIGN

The conventional double-balanced mixer (Gilbert cell) is as shown in Figure 1. It consists of the transconductance (G_m) stage (formed by M_1 and M_2), the switch stage (formed by $M_3 \sim M_6$), and load resistors (R_1 and R_2). In the mixer design, the specifications to be achieved are high gain, high linearity, low noise and low power consumption. However, these performances are difficult to achieve simultaneously. For example, we may achieve a higher gain at the cost of larger power consumption. Another example is that larger current in the G_m stage can provide higher gain and suppress noise, but also generate larger noise in the switch stage. In addition, larger current will also diminish the voltage headroom due to the cascode structure, thus the linearity is getting worse.

Noise is presented in all components including transistors and resistors. For a direct conversion receiver, the RF signal is down-converted directly to the DC. Because the flicker noise has a spectrum density distribution proportional to $1/f$, its contribution to overall system becomes significant at close-in frequencies. As indicated in [1], the flicker noises of mixers are primarily determined by LO switch pair devices, because the noise directly leaks to the output in process of frequency translation. As explained in [1], the flicker noise from the switch devices can be reduced by either decreasing the dc current I through the switch devices or increasing the slope of the LO signal.

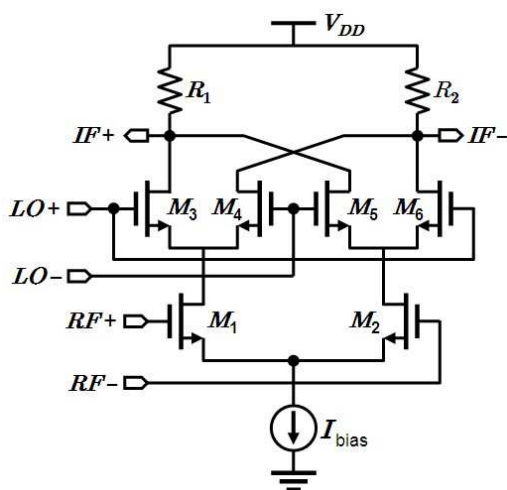


Figure 1. Schematic of a conventional double-balanced mixer.

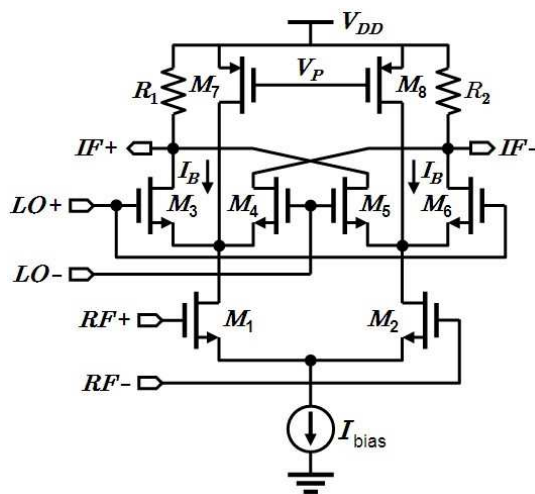


Figure 2. Gilbert mixer with current injection (current bleeding).

It is found that increasing the bias current of the Gm stage can suppress the noise contribution, while decreasing the dc current of the switch stage can also reduce the flicker noise. Therefore a current bleeding technique was proposed to improve overall noise performance [6], in which fixed currents I_B are injected into source terminals of LO switch transistors. The current bleeding technique can be implemented by using PMOS current source because the PMOS brings lower flicker noise. Using PMOS M_7 and M_8 as current sources, the current bleeding technique is as shown in Figure 2. With the help of the bleeding current I_B , the dc bias currents through switch transistors $M_3 \sim M_6$ are reduced and thus flicker noises are also decreased. Meanwhile, load resistances of the mixer can be chosen larger, and a higher conversion gain can be obtained without additional power consumption. Smaller currents through load resistances and switch transistors also relax the voltage headroom condition and the switching transistors can be operated at smaller over drive voltage.

Although it can benefit from the current bleeding technique, however, the current bleeding technique still suffers some drawbacks which limit its improvement on the mixer. First, there exist parasitic capacitances at the node between Gm stage and switch stage, which will shunt the RF current from the Gm stage to the ground node. The current bleeding circuit will produce additional parasitic capacitances at that node, and it leads to more loss of the RF signal. Therefore, the conversion gain will drop down and the noise figure will increase. Secondly, the current bleeding circuit consists of active devices which also produce noises and make the NF of the mixer worse. For these reasons, the improvement by using the primitive current bleeding technique is not significant. As addressed in [5], the success of the current bleeding technique depends on three important conditions. First, the output impedance of the bleeding current sources I_B must be high enough compared with the input impedance seen at the injection node. Second, all transistors should be operated in saturation region. Third, the output impedance of the Gm stage should be high impedance. Since the additional parasitic capacitances introduced by the current bleeding circuit are the main factor diminishing its benefit, thus it was proposed to resonate out the parasitic capacitances by adding one inductor between the current injection nodes [4, 5]. The advantages of this modification include not only improving flicker noises but also enhancing the conversion gain.

Compared to NMOS devices, using PMOS devices to provide bleeding current generates less flicker noises, however, the current bleeding circuitry still contributes additional noises. It is reported that using PMOS transistors to form cross-coupled pair as the current bleeding circuit can cancel the noises [3]. Such technique can also generate negative resistance at the output of the Gm stage which boosts the small signal voltage gain. In this work, we combine the cross-coupled pair technique with the inductor mentioned above and design a mixer for K-band applications as shown in Figure 3. The inductor L_5 is used for resonating out the parasitic capacitances and PMOS M_7 and M_8 form the cross-coupled pair for providing the bleeding current. Inductors L_1 , L_2 , L_3 , and L_4 are used for input matching of the RF port, and this matching method also take the noise figure into account. Since inductors L_3 and L_4 are also used as inductive source-degeneration, it can thus

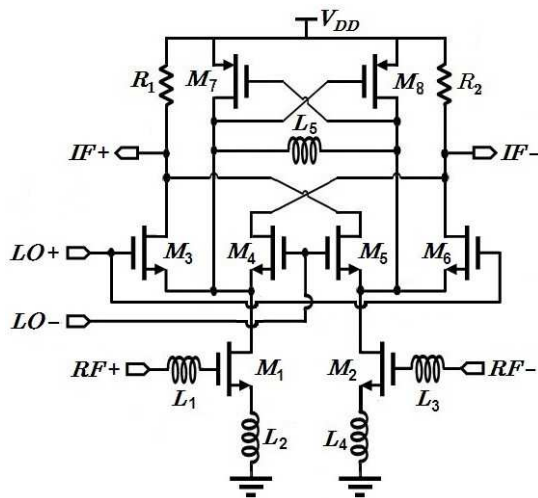


Figure 3. Schematic of the proposed mixer.

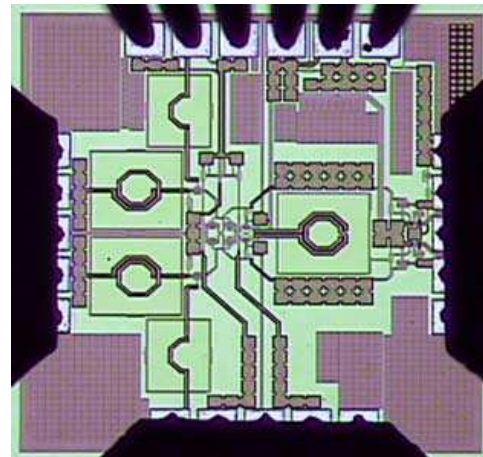


Figure 4. Micrograph of the proposed mixer.

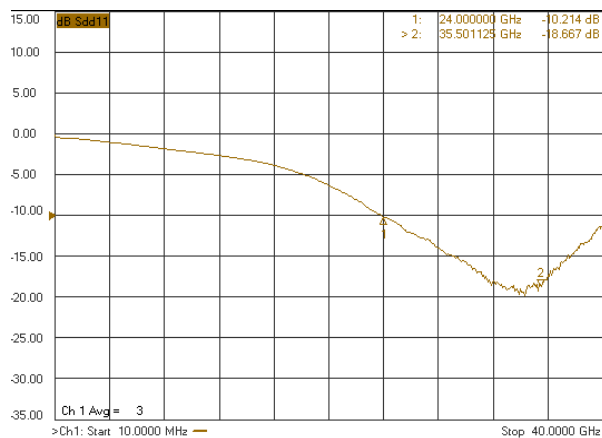


Figure 5. Measured S_{11} (RF port) of the proposed K-band mixer.

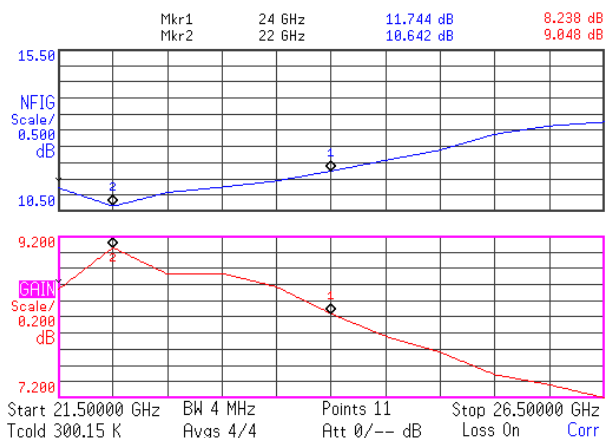


Figure 6. Measured NF and CG of the proposed mixer.

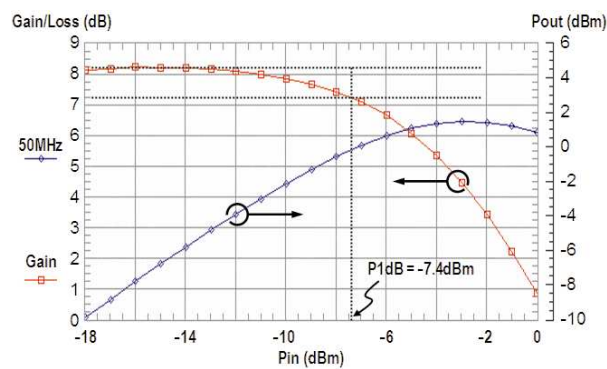


Figure 7. Measured P1 dB of the K-band mixer.

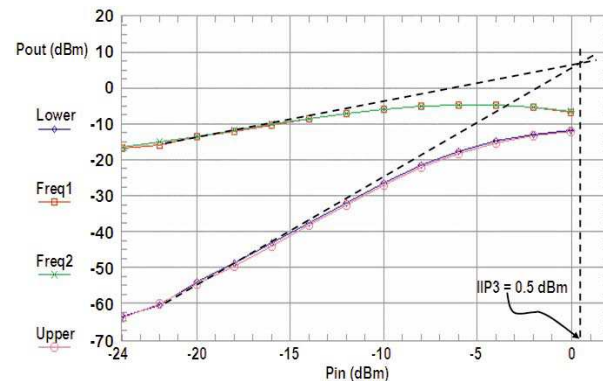


Figure 8. Measured IIP3 of the K-band mixer.

help the linearity performance. Figure 4 shows the chip micrograph of the proposed mixer which is implemented in $0.18 \mu\text{m}$ RF-CMOS process technology and the chip size is $1.06 \times 0.98 \text{ mm}^2$.

3. MEASURED RESULTS

The core circuit of the proposed mixer draws a 3.14 mA dc current from a 1.8 V power supply. We choose the LO signal power level as -2 dBm for all the measurements. Figure 5 shows the

Table 1.

	This work	[7]	[8]	[9]
Process	0.18 μm	0.18 μm	0.18 μm	0.13 μm
Frequency (GHz)	22	24	23–25	22–29
Conversion Gain (CG; dB)	9.05	9.12	10	1
NF (dB)	10.64	10.5	23	9
IIP3 (dBm)	0.5	−1.4 ^a	0	−3
DC Power (mW)	5.652	16.2	8.3	6.9
FOM ^b	16.613	11.265	2.81	11.911

$${}^a\text{obtained from P1 dB} + 9.6 \text{ dB}, \quad {}^b\text{FOM} = 10 \log \left(\frac{10^{G/20} \cdot 10^{\text{IIP3}/20}}{10^{NF/10} \cdot P} \right),$$

in which P = DC power consumption in W.

measured S_{11} (RF port matching) and it is shown that the input range is from 24 GHz to 40 GHz. Figure 6 shows the measured NF and CG versus the RF frequency under the condition that the IF is fixed at 50 MHz. It can be shown that the NF is 10.64 dB and CG is 9.05 dB for the RF frequency being 22 GHz. Due to the effect of the inductor L_5 in Figure 3, the CG of the proposed mixer has a peak at 22 GHz. It is also seen that the NF and CG will become 13.25 dB and 7.2 dB, respectively, at 26.5 GHz of RF input. Figure 7 shows the measured P1 dB and it reads −7.4 dBm, while Figure 8 shows the measure IIP3 and it reads 0.5 dBm under 24 GHz of RF frequency. A summary of the performance of the proposed mixer is listed in Table 1 and some results of previous works for K-band applications [7–9] are also given in this table. For a fair comparison, we adopt the figure of merit (FOM) formula given in [10] as shown below the Table 1. It can be seen that the performances of our mixer are superior to those in [7–9].

4. CONCLUSIONS

We have presented a direct down conversion Gilbert mixer with the dynamic current bleeding technique and an inductor for resonating parasitic capacitances. The circuit is implemented in the 0.18 μm RF-CMOS process technology. The core circuit draws a 3.14 mA dc current from the 1.8-V power supply. The measured conversion gain is 9.05 dB and the measured NF is 10.64 dB for the RF frequency being 22 GHz. The measured P1 dB and IIP3 are −7.4 dBm and 0.5 dBm, respectively. The overall performance of the proposed mixer shows its superiority by comparing with previous works for K-band applications.

ACKNOWLEDGMENT

This work was supported in part by the Ministry of Education, Taiwan, R.O.C. under the ATU plan and by the National Science Council of the Republic of China under Grant NSC 99-2221-E-005-114 and NSC100-2221-E-005-057. The authors would like to thank the National Chip Implementation Center (CIC) in Taiwan for the chip fabrication, measurement and other technical supports.

REFERENCES

1. Darabi, H. and A. A. Abidi, “Noise in RF-CMOS mixers: A simple physical model,” *IEEE J. Solid-State Circuits*, Vol. 35, No. 1, 15–25, 2000.
2. Terrovitis, M. T. and R. G. Meyer, “Noise in current-commutating CMOS mixers,” *IEEE J. Solid-State Circuits*, Vol. 34, No. 6, 772–783, 1999.
3. Darabi, H. and J. Chiu, “A noise cancellation technique in active RF-CMOS mixers,” *IEEE J. Solid-State Circuits*, Vol. 40, No. 12, 2628–2632, 2005.
4. Park, J., C.-H. Lee, B.-S. Kim, and J. Laskar, “Design and analysis of low flicker-noise CMOS mixers for direct-conversion receivers,” *IEEE Trans. Microw. Theory Tech.*, Vol. 54, No. 12, 4372–4380, 2006.
5. NacEachern, L. A. and T. Manku, “A charge-injection method for Gilbert cell biasing,” *Proc. IEEE Canadian Conf. Elect. Comp. Eng.*, Vol. 1, 365–368, Waterloo, Canada, May 24–28, 1998.
6. Sansen, W. M. C. and R. G. Meyer, “Distortion in bipolar transistor variable-gain amplifiers,” *IEEE J. Solid-State Circuits*, Vol. 8, No. 4, 275–282, 1973.

7. Ahn, D., D.-W. Kim, and S. Hong, “A K-band high-gain down-conversion mixer in 0.18 μm CMOS technology,” *IEEE Microw. Wireless Compon. Lett.*, Vol. 19, No. 4, 227–229, 2009.
8. Bae, H., C. Cho, J. Lee, and J. Kim, “A 24 GHz dual-gate mixer using sub-harmonic in 0.18 μm CMOS technology,” *Proc. 2009 Asia Pacific Microwave Conference (APMC 2009)*, 1739–1742, Dec. 2009.
9. Verma, A., G. Li, K. O. Kenneth, and J. Lin, “A K-band down-conversion mixer with 1.4-GHz bandwidth in 0.13- μm CMOS technology,” *IEEE Microw. Wireless Compon. Lett.*, Vol. 15, No. 8, 493–495, 2005.
10. Vidojkovic, V., J. van der Tang, A. Leeuwenburgh, and A. H. M. van Roermund, “A low-voltage folded-switching mixer in 0.18- μm CMOS,” *IEEE J. Solid-State Circuits*, Vol. 40, No. 6, 1259–1264, 2005.

Multidimensional S -parameters: Modeling, Measurement, Identification and Computer-aided Design of Nonlinear Microwave Circuits

S. M. Nikulin, A. A. Terentyev, and I. P. Shishkina
Aleksiev's Nizhny Novgorod State Technical University, Russia

Abstract— In this paper, we propose a mathematical model of nonlinear circuits in the form of multidimensional S -parameters. There are obtained some relations to describe the nonlinear properties of a three-stage cascade connection. In this paper, we propose the original way to measure and identify the model parameters using the method of remote load. At the end, the perspectives of computer-aided design, based on identification of multidimensional S -parameters using the method of harmonic balance and linear multi-frequency analysis of nonlinear microwave circuits, are discussed.

1. INTRODUCTION

In recent years, in theory and technique of measurement, as well as in modeling and computer-aided design of nonlinear RF and microwave devices, there were achieved some practically useful results. For example, the most sophisticated vector network analyzers with two internal signal sources and built-in or external amplifier providing a measurement of “Hot- S_{22} ” parameters of microwave power amplifiers; the Agilent’s PNA-X NVNA provided the X -parameters definition of nonlinear components. These parameters, as the authors say, are the most accurate and extended version of the wave scattering parameters (S -parameters) which can be used in modeling and computer-aided design of nonlinear RF and microwave devices [1].

However, X -parameters are characterized by structural imperfections, excessive redundancy of information, and this type of measurement didn’t correspond to the optimal criterion of price/performance, and therefore encouraged to develop any alternative solutions.

2. MULTIDIMENSIONAL S -PARAMETERS

The term multidimensional S -parameters is typically used, when the higher types of waves may spread in transmission lines that connect linear or nonlinear devices (components). However, in practice, such a line is selected (the cross-sectional geometry, materials) in which the higher types of waves that occur at inhomogeneities, are local and do not apply. Although the natural existence of higher order modes in the vicinity of the analyzed components requires the right restriction of the region of surrounding space, beyond which their influence is not manifests itself.

When applying constant supply voltage and/or currents to the nonlinear component (transistor or diode) or to the device (amplifier, frequency multiplier, mixer) and when it’s excited by the large enough amplitude incident wave there are reflected and transmitted waves at a frequency of the fundamental tone, its higher and combination frequencies. These waves, including persistent currents and voltages, don’t have any obstacles to the spread in the supplying transmission lines and, therefore, for the simulating of nonlinear circuits behavior should be using the multidimensional block matrix. The model indubitably provides the complete description of the nonlinear properties. In case of the one-tone excitation it has the form of a block ($N \times N$) linear equations system:

$$\begin{bmatrix} B_0 \\ B_1 \\ * \\ B_K \end{bmatrix} = \begin{bmatrix} S_{00} & S_{01} & * & S_{0K} \\ S_{10} & S_{11} & * & S_{1K} \\ * & * & * & * \\ S_{K0} & S_{K1} & * & S_{KK} \end{bmatrix} \times \begin{bmatrix} A_0 \\ A_1 \\ * \\ A_K \end{bmatrix} \quad (1)$$

The order N is determined by the number of harmonics K in the spectrum of scattered waves: $N = K + 1$. Each block S_{kl} of the multidimensional S -matrix for the quadripole (2-port network) is a 2×2 matrix, and the blocks of the complex amplitudes of the reflected B_k and falling A_l waves are the column matrices:

$$S_{kl} = \begin{bmatrix} S_{11}^{kl} & S_{12}^{kl} \\ S_{21}^{kl} & S_{22}^{kl} \end{bmatrix}, \quad B_k = \begin{bmatrix} b_{1k} \\ b_{2k} \end{bmatrix}, \quad A_l = \begin{bmatrix} a_{1l} \\ a_{2l} \end{bmatrix}, \quad k, l = 0, 1, 2, \dots, K$$

Here the index 1 corresponds to the input and the index 2 — to the output of the nonlinear circuit; the indices l and k are the numbers of harmonics (including $l = 0$ and $k = 0$ for DC) of the fundamental tone, respectively, for the incident and reflected (past) waves. The diagonal blocks of the index S_{kk} are responsible for the relationship between the incident and reflected waves at constant current ($k = 0$), the fundamental tone ($k = 1$) and its harmonics ($k \neq 1$), and the nondiagonal blocks S_{kl} — for the up- and down-converting of the frequency.

Linear S -parameters are the complex functions of the frequency of the electromagnetic waves oscillation that excite the analyzed object (Device under test, DUT). In the case of nonlinear DUT the multidimensional S -parameters are functions and the incident wave amplitude $|a_{11}|$. The amplitude a_{11} determined by the source power, its internal resistance and input resistance of nonlinear DUT. The nonlinear DUT input resistance depends not only on the S -parameters of a nonlinear DUT, but also on the impedance of the output load. The choose of the analytical model of nonlinear DUT S -parameters as a function of frequency f and amplitude a_{11} should be based on the properties of the cascade connection with the linear circuits.

3. NONLINEAR PROPERTIES OF THE CASCADE CONNECTIONS

Nonlinear properties of cascade consisting of an input A, output B and of a nonlinear circuit are a key link in the nonlinear devices measurement and computer-aided design problem solving. This three-stage compound is typical for the power amplifier and frequency multiplier; it can be extended to the case of frequency conversion when the non-linear component is excited by signals of two independent sources. All these devices convert the vector of input signals into output signals. The input action is given by the DC power mode through α_{10} , α_{20} and by the complex amplitude α_{11} of the incident wave; the output signal vector is formed by the complex amplitudes of the scattered waves at the input and output of the device at constant current, on the fundamental frequency ($k = 1$) and its harmonics ($k = 2, 3, \dots$) (Fig. 1). Note that the power mode and the DC reaction function of the nonlinear circuit are described by the real numbers and functions.

Multidimensional S -parameters (1) of the linear circuits A and B are the diagonal matrices. For the simplification of the formulas this matrices are denoted by the letters A and B:

$$\begin{aligned} \begin{bmatrix} B_0 \\ B_1 \\ * \\ B_K \end{bmatrix} &= \begin{bmatrix} A_{00} & 0 & * & 0 \\ 0 & A_{11} & * & 0 \\ * & * & * & * \\ 0 & 0 & * & A_{KK} \end{bmatrix} \times \begin{bmatrix} A_0 \\ A_1 \\ * \\ A_K \end{bmatrix} \\ \begin{bmatrix} B_0 \\ B_1 \\ * \\ B_K \end{bmatrix} &= \begin{bmatrix} B_{00} & 0 & * & 0 \\ 0 & B_{11} & * & 0 \\ * & * & * & * \\ 0 & 0 & * & B_{KK} \end{bmatrix} \times \begin{bmatrix} A_0 \\ A_1 \\ * \\ A_K \end{bmatrix} \end{aligned} \quad (2)$$

Scattering matrix $[\Sigma]$ of the cascade connection in the frequency conversion mode can be simply obtained from (1), (2) using methods, developed for multiterminal networks. As an example, we can simply derive the approximate analytical formulas for the reflection and transmission coefficients

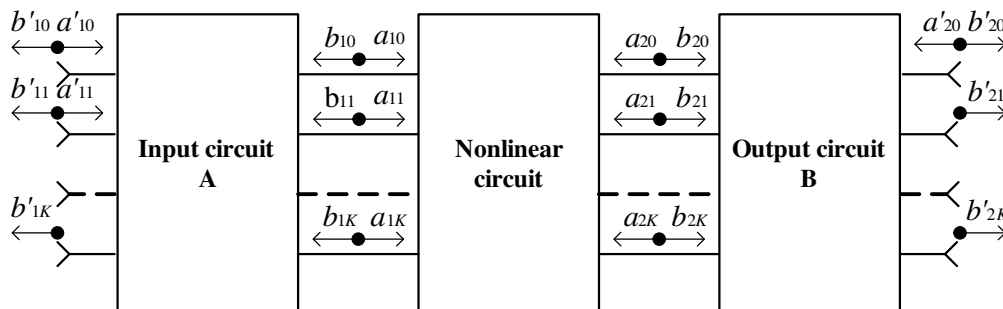


Figure 1: Nonlinear cascade connection.

for the fundamental tone:

$$\begin{aligned} \Sigma_{11}^{11} &\approx A_{11}^{11} + \frac{A_{12}^{11} A_{21}^{11} \left[S_{11}^{11} + \frac{S_{12}^{11} B_{11}^{11} S_{21}^{11}}{1 - S_{22}^{11} B_{11}^{11}} + \frac{S_{11}^{12} A_{22}^{22} S_{11}^{21}}{1 - S_{11}^{22} A_{22}^{22}} + \frac{S_{12}^{12} B_{11}^{22} S_{21}^{21}}{1 - S_{22}^{22} B_{11}^{22}} \right]}{1 - A_{22}^{11} \left[S_{11}^{11} + \frac{S_{12}^{11} B_{11}^{11} S_{21}^{11}}{1 - S_{22}^{11} B_{11}^{11}} + \frac{S_{11}^{12} A_{22}^{22} S_{11}^{21}}{1 - S_{11}^{22} A_{22}^{22}} + \frac{S_{12}^{12} B_{11}^{22} S_{21}^{21}}{1 - S_{22}^{22} B_{11}^{22}} \right]} \\ \Sigma_{21}^{11} &\approx \frac{A_{21}^{11} B_{21}^{11} \frac{S_{21}^{11} + \frac{S_{21}^{21} S_{12}^{12} B_{11}^{22}}{1 - S_{22}^{22} B_{11}^{22}} + \frac{S_{21}^{21} S_{12}^{12} A_{22}^{22}}{1 - S_{11}^{22} A_{22}^{22}}}{1 - B_{11}^{11} \left[S_{22}^{11} + \frac{S_{22}^{21} S_{12}^{12} B_{11}^{22}}{1 - S_{22}^{22} B_{11}^{22}} - \frac{S_{12}^{21} S_{21}^{12} A_{22}^{22}}{1 - S_{11}^{22} A_{22}^{22}} \right]}}{1 - A_{22}^{11} \left[S_{11}^{11} + \frac{S_{12}^{11} B_{11}^{11} S_{21}^{11}}{1 - S_{22}^{11} B_{11}^{11}} + \frac{S_{11}^{12} A_{22}^{22} S_{11}^{21}}{1 - S_{11}^{22} A_{22}^{22}} + \frac{S_{12}^{12} B_{11}^{22} S_{21}^{21}}{1 - S_{22}^{22} B_{11}^{22}} \right]} \end{aligned} \quad (3)$$

and for the frequency conversion from fundamental tone to the second harmonic mode:

$$\begin{aligned} \Sigma_{11}^{21} &\approx \frac{A_{12}^{22} A_{21}^{11} \left[\frac{S_{11}^{21} + S_{21}^{11} S_{12}^{21} B_{11}^{11} / (1 - S_{22}^{11} B_{11}^{11})}{1 - S_{11}^{22} A_{22}^{22}} \right]}{1 - A_{22}^{11} \left[S_{11}^{11} + \frac{S_{12}^{11} B_{11}^{11} S_{21}^{11}}{1 - S_{22}^{11} B_{11}^{11}} + \frac{S_{11}^{12} A_{22}^{22} S_{11}^{21}}{1 - S_{11}^{22} A_{22}^{22}} + \frac{S_{12}^{12} B_{11}^{22} S_{21}^{21}}{1 - S_{22}^{22} B_{11}^{22}} \right]} \\ \Sigma_{21}^{21} &\approx \frac{A_{21}^{11} B_{21}^{22} \frac{S_{21}^{21} + \frac{S_{22}^{21} S_{21}^{11} B_{11}^{11}}{1 - S_{11}^{11} B_{11}^{11}} + \frac{S_{21}^{21} S_{12}^{22} A_{22}^{22}}{1 - S_{11}^{22} A_{22}^{22}}}{1 - S_{22}^{22} B_{11}^{22} - \frac{S_{22}^{21} S_{12}^{12} B_{11}^{11} B_{11}^{22}}{1 - S_{11}^{11} B_{11}^{11}} + \frac{S_{12}^{21} S_{21}^{12} B_{11}^{11} A_{22}^{22}}{1 - S_{11}^{22} A_{22}^{22}}}}{1 - A_{22}^{11} \left[S_{11}^{11} + \frac{S_{12}^{11} B_{11}^{11} S_{21}^{11}}{1 - S_{22}^{11} B_{11}^{11}} + \frac{S_{11}^{12} A_{22}^{22} S_{11}^{21}}{1 - S_{11}^{22} A_{22}^{22}} + \frac{S_{12}^{12} B_{11}^{22} S_{21}^{21}}{1 - S_{22}^{22} B_{11}^{22}} \right]} \end{aligned} \quad (4)$$

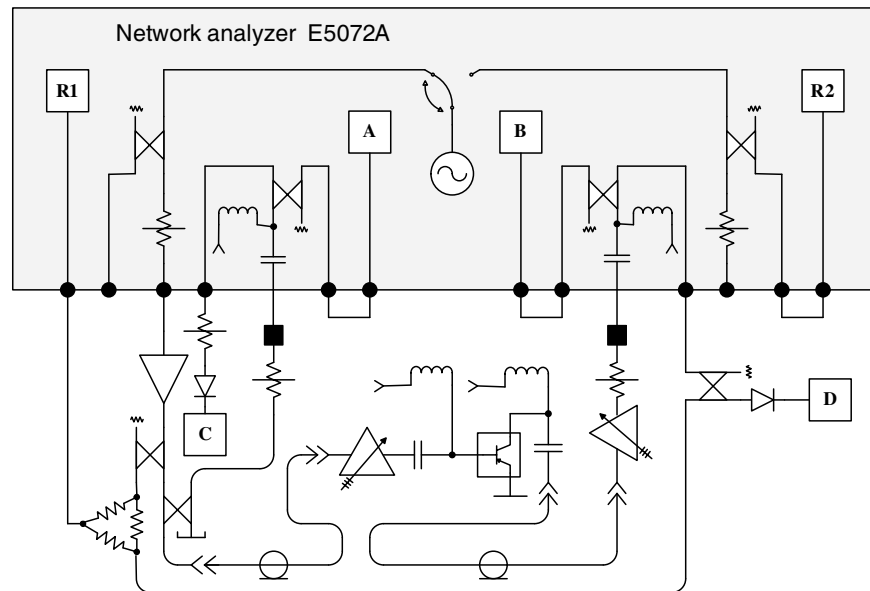
From these relations it is clear that in addition to the four parameters of the fundamental tone S_{11}^{11} , S_{21}^{11} , S_{12}^{11} , S_{22}^{11} , which is called in the literature large-signal parameters, we should take into account the others parameters describing the interconversion of the fundamental tone and the second harmonic. For a more accurate simulation of nonlinear circuits we must take into account the conversion of the fundamental tone to its higher harmonics and DC.

Formulas (3), (4) have a clear physical interpretation and allow the solving of the problem of the nonlinear microwave circuits measurement and computer-aided design.

4. MEASUREMENT AND IDENTIFICATION OF MULTIDIMENSIONAL S -PARAMETERS

For the S -parameter nonlinear circuit by measuring of the complex reflection and transmission coefficients at the fundamental mode and in the frequency conversion mode is necessary to use the input and output linear circuits with variable parameters. Such a circuits providing electronic tuning of the parameters in a wide frequency range are called tuners or variable loads. Various tuners are designed for example by Maury Microwave Corporation and Focus Microwaves. Tuners can transform the input and output impedances of transistors to a standard impedance of 50 Ohm. The results of measurements with the tri-state tuners give a redundant system of 12 equations for determining the unknown parameters at a fixed frequency. However, the variation of the input power absorbing by the nonlinear circuit due to changes in the input impedance of the cascade connection must be taken into account. Therefore, it is advisable to carry out all measurements varying the input signal amplitude. This way, we can get only those resulting data set that correspond to a fixed value of the absorbed power. Thus, after the data-processing we can generate two-dimensional S -parameters table of a nonlinear circuit with the following parameters: frequency f , the absorbed power P_a . Measurements of reflection and transmission coefficients at the fundamental frequency and it's harmonics can be carried out with 4-port vector network analyzer series PNA-X, focused on such measurements. However, you can use the less expensive device ENA E5072A series with direct receiver access. Block diagram for transistor S -parameters measuring is shown in (Fig. 2).

Power transistor must be mounted in a coaxial channel with a special contact device. The supply voltage is supplied through a DC adapter. The input circuit of a cascade connection consists of a


 Figure 2: Measuring the power transistor S -parameters using E5072A.

coaxial cable, input tuner, adapter, and the input circuit of the contact device; the output circuit of a cascade connection consists of the output circuit of the contact device, the output adapter, coaxial cable, tuner, and a variable attenuator. S -parameters of the input and output circuits must be defined during the preliminary calibration using the stripe calibration set instead of the transistor for every state of tuners.

The measured nonlinear cascade of circuits is excited using the E5072A internal generator with the frequency tuning from F_1 to F_2 with the step ΔF . The amplitude of the input signal is set by an external amplifier and built-in variable attenuator. The coefficients of reflection \sum_{11}^{11} and transmission \sum_{21}^{11} at the fundamental frequency are obtained by measuring using the reference receiver R1 and test receivers A, B, and in frequency conversion mode from fundamental frequency to its higher harmonics — by measuring the signal from diode detectors with analog-to-digital converters C, D. An important feature of the proposed solution is that the signal at the input of the measuring receiver A and at the input detector is separated using the directional coupler with the short-circuiting of its secondary channel. This coupler serves as a non-directional coupler (probe), sensitive to the magnitude and phase of reflection coefficients. Sensitivity of the detectors to the harmonics of the fundamental tone is provided in mode of input signal frequency tuning by the interference of incident and reflected waves in the coaxial cables. Interference of waves in the output cable is caused by reflections from the variable capacitor and from the output impedance of the cascade connection.

The usage of the coaxial cables gives the opportunity to find the nonlinear circuit S -parameters as an analytical function of input signal frequency. The presence of cables leads to a rapid change of complex frequency depended functions: B_{11}^{11} , B_{21}^{11} , B_{11}^{22} , B_{22}^{22} . It allows you to restore the S -parameters of linear chains as the slow complex function of the frequency using different ways of filtering of spatial harmonics. An effective way of solving the problem is to identify the model parameters using window function in the frequency-domain:

$$|S_{ij}^{kl}(f)| = q_1 + q_2(f - f_1) + q_3(f - f_1)^2 + \dots$$

$$\arg[S_{ij}^{kl}(f)] = g_1 + g_2(f - f_1) + g_3(f - f_1)^2 + \dots$$

5. COMPUTER-AIDED DESIGN

Multidimensional S -parameters of nonlinear circuits can be obtained not only using tools methods, but also with the help of circuit modeling method (harmonic balance and Volterra series methods). Construction of a nonlinear model (1) is realized by software simulation and optimization (identification) using formulas (3), (4). Construction of models, based both on measurements and analysis of the nonlinear circuit models, requires a sufficiently long time. Therefore the S -models library for nonlinear electronic components must be developed.

S -models allow you to quickly carry out the simulation, configuration and optimization of the devices for various functional purposes: microwave power amplifiers, frequency multipliers, mixers, etc. More importantly, the simulation and optimization of nonlinear circuits using multidimensional S -parameters is reduced to the analysis of cascade connection of multiterminal linear circuits. Furthermore, analysis using S -parameters provides not only higher speed of obtaining the information, but also it provides the better completeness of this information. In contrast to the harmonic balance method and Volterra series method, not only output reflection coefficients are available, but also the reverse transmission coefficients and the frequency conversion coefficients.

6. CONCLUSION

In this paper we consider an alternative method of modeling, measurement and computer-aided design of nonlinear microwave devices. In our opinion, the attractiveness of S -parameters for engineering practice is not only the natural simplicity of the mathematical description of the nonlinear properties of electronic components, assemblies and modules, but also the possibility of obtaining the information using cheaper hardware. Due to the limited scope and novelty of the material, the article does not purport to be comprehensive. Some aspects of the problem formulated at the level of ideas, and require detailed study by means of simulation and experiment.

REFERENCES

1. Root, D. E., J. Horn, L. Betts, C. Gillease, and J. Verspecht, “ X -parameters: The new paradigm for measurement, modeling, and design of nonlinear RF and microwave components,” *Microwave Engineering Europe*, December 2008.

Analysis of Embedded-silicon-substrate Impact on CiSP Design

Jang-Hoon Lee, Jinho Song, Jae-Kyung Wee, and In-Chae Song
School of Electronics, Soongsil University, Korea

Abstract—This paper suggests routing design guides which help the lossy effect of an embedded silicon substrate be reduced in a chip-in-substrate package (CiSP). These guidelines are applied for determining optimal design of signal and power line. In order to achieve this purpose, the losses of a coplanar waveguide (CPW) line over an embedded silicon substrate and a ground plane are analyzed according to different position and length of the line. Also, via hole closed an embedded silicon substrate is analyzed with various height and distance to the embedded silicon substrate.

1. INTRODUCTION

Nowadays, packaging technologies are rapidly challenged and diverged due to new mobile product requirements such as multi-functions and a small packaging volume. Especially, the mainstream of packaging technologies in mobile products are focused on realization of the small and thin outlines, several GHz operation frequencies, and mixed system in one module. According to increasing these requirements, a new packaging concept has been developed of the Chip-in-Substrate Package (CiSP) technology as another choice of SoP. CiSP has merits of a small and thin outline, embedding one or multiple passive and active devices into the built-up dielectric layers on an organic substrate. CiSP technology not only can shrink a size of an electronic package or system size but also provide a better electronic performance for the high frequency application [1]. So, a lot of studies about CiSP technology have been reported. Although these are mainly focused on process and material technologies of CiSP[2, 3], but the design studies about CiSP are relatively little and mainly focused on insertion loss, return loss, and characteristic impedance of lines crossover the embedded silicon [4]. However, the effect of an embedded silicon substrate on signal and power integrities are not sufficiently evaluated about. Also, the loss characteristics of via hole around the embedded silicon substrate are not clear for tradeoff of package area and electrical performances in CiSP.

In this paper, the design guide for silicon-loss-aware line routing is presented, mainly considered on performance improvements without sacrificing the area. For this purpose, attenuation constants according to positions of CPW lines are analyzed for CPW lines over embedded silicon substrate and ground plane. Moreover, various line patterns with respect to different line lengths and geometries under a CPW line are simulated in order to determine the minimum loss. Secondly, via holes with various distances to an embedded silicon substrate are simulated with three heights of via holes. Also, the losses of via holes with and without ground guard between an embedded silicon substrate and a via hole are analyzed and compared for loss reduction.

2. STRUCTURE AND DESIGN ISSUES OF CiSP

Figure 1 shows the CiSP designed with stack up of 6 Layers. In the CiSP, some active ICs or passive capacitors are embedded in a core layer (3rd and 4th metal layer). So, there are many cavities by these embedded devices on 3rd and 4th metal layer. Build-up layers (1st, 2nd, 5th and 6th metal layer) are stacked on the core layer to upper and lower side. Most of signal and power lines are routed on build-up layers than on core layer because the core layer has small routable area since the lines should be placed through many cavities and with design constraints like minimum line widths or spaces between line and cavity. Moreover, there are many via holes in the core layer in order to connect lines and planes between 3rd and 4th metal layers. In the CiSP, the first design issue is the loss of signal and power line happened from an embedded IC, and the second design issue is the loss of a via hole placed beside the embedded IC. Therefore, the losses of these lines and via holes affected by an embedded silicon substrate are analyzed, and then a design guide of optimal line and position of via hole is determined with considering these losses in Sections 3 and 4.

3. LOSS OF TRANSMISSION LINE IN CiSP

3.1. Attenuation Constant of CPW over Silicon Substrate and Ground

A cavity breaks the return current path of a transmission line running crossover itself. In order to prevent this problem, the line is often designed as CPW line type. In this case, the CPW line

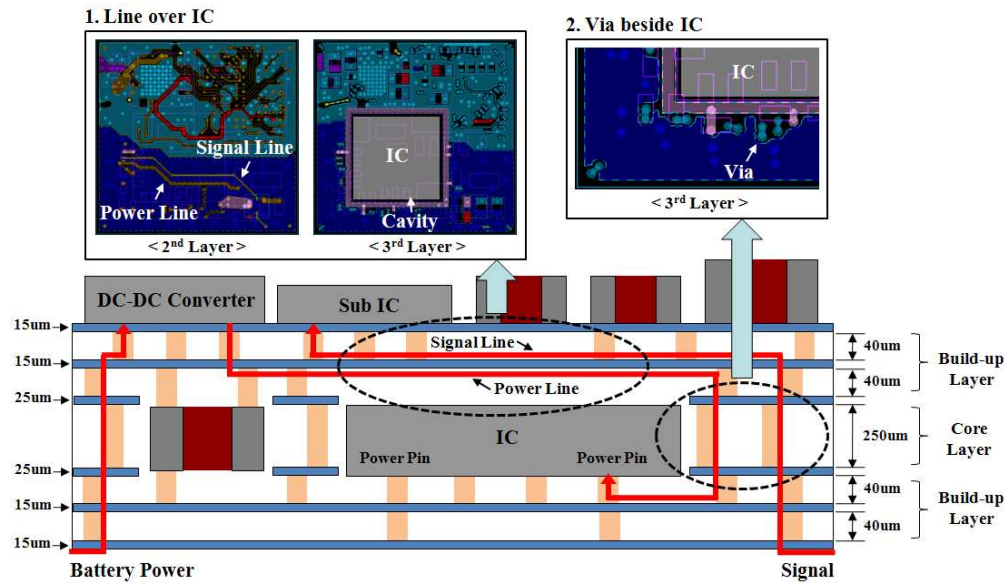


Figure 1: 6 metal layer CiSP structure and two design issues.

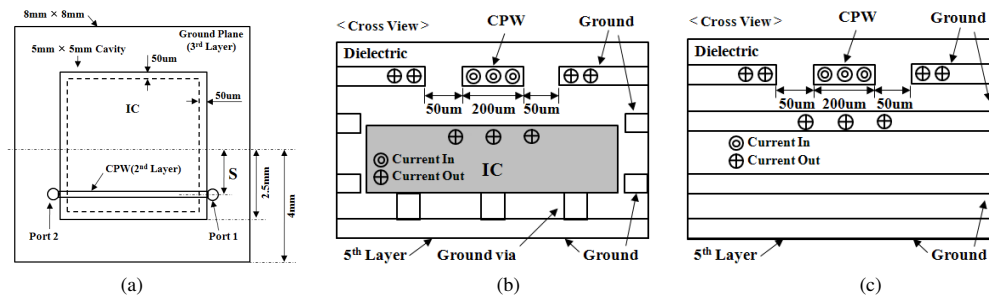


Figure 2: Geometry of CPW line in CiSP: (a) position of CPW line with space S , (b) cross view of CPW line when $S = 0$ mm, (c) cross view of CPW line when $S = 3$ mm.

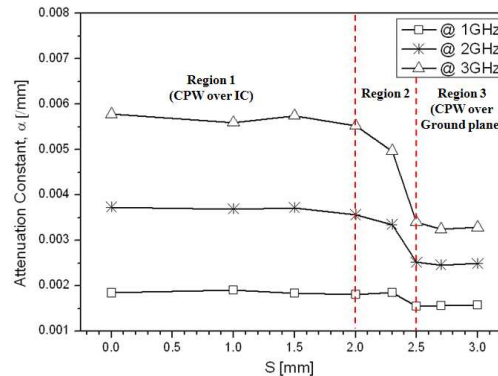


Figure 3: Attenuation constant per unit length with respect to space S and frequencies.

routed on 2nd Layer has two structures as shown in Figure 2. Figure 2(a) shows CPW lines with space S from the center of an embedded silicon substrate to a line. Figures 2(b) and 2(c) show the cross view of CPW lines with spaces S of 0 mm and 3 mm. The CPW line is placed over the silicon substrate at space S of 0 mm, while it is placed over ground plane at S of 3 mm.

In order to analyze the loss characteristic of a CPW line according to its position, attenuation constants per unit length of CPW line are extracted with various spaces S using the pattern in Figure 2(a). Figure 3 shows the attenuation constants based on S -parameter [5] at frequencies of 1 GHz, 2 GHz, and 3 GHz. In Figure 3, losses of the CPW line can be classified to three parts

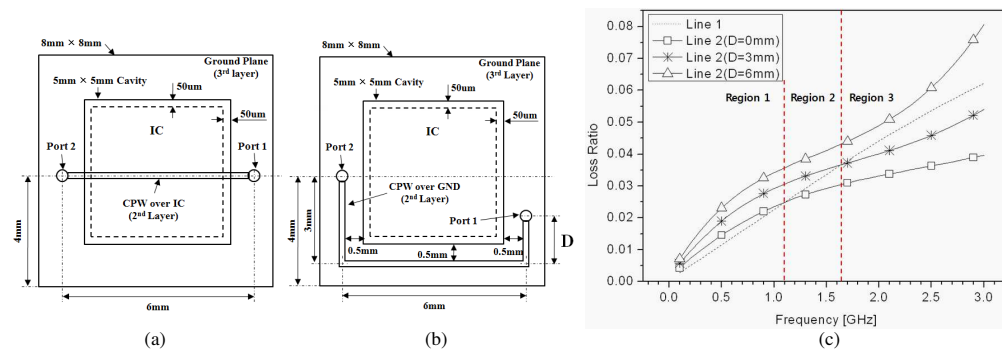


Figure 4: Geometries of two different lines according to routing method: (a) Line 1, (b) Line 2 with distance D , (c) loss ratio of Line 1 and Line 2 with distance D of 0 mm, 3 mm, and 6 mm with respect to frequencies.

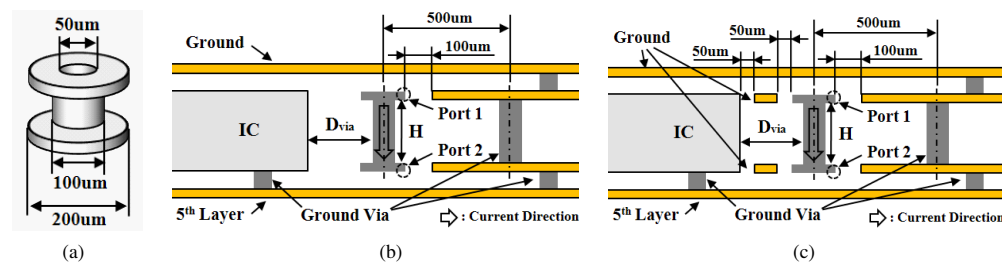


Figure 5: Geometries of test patterns for via hole with distance D_{via} and height H in CiSP: (a) dimension of a via hole, (b) test pattern without ground gourd, (c) test pattern with ground gourd.

according to space S . The attenuation constants keep constant levels in both Regions 1 and 3, although they in each Regions 1 and 3 show the different levels due to different loss characteristics of silicon and metal planes. The CPW line over the silicon substrate has greater loss than it over the ground plane due to silicon loss. Also the loss is largely increased as the frequency on line is increased. On the other hand, the attenuation constants in Region 2 are changed according to space S neighbored between the silicon substrate and ground plane. It means that the loss of the CPW line depends on both silicon substrate and ground plane in Region 2.

3.2. Optimization of Transmission Line

Generally, the optimal design is obtained from selection of the line which has the minimum total loss. But, it is needed to consider the total line length as well as the silicon substrate, because extended line length can have more loss than added loss by substrate. Therefore, two different lines are proposed as shown in Figure 4 in order to select an optimal line for low total loss. Line 1 has minimum line length of 6 mm, overcrossing the silicon substrate as shown in Figure 4(a). The total loss of Line 1 includes the loss from the silicon substrate. Line 2 has a different line path running on ground plane as shown in Figure 4(b). The whole loss of Line 2 is added with the loss of extended line length. The total length of Line 2 is given as 9 mm, 12 mm, and 15 mm when distance D is 0 mm, 3 mm, and 6 mm, respectively. Equation (1) shows the relative loss ratio as follows,

$$loss\ ratio = \frac{P_{loss}}{P_{in}} = 1 - (|S_{11}|^2 + |S_{21}|^2) \quad (1)$$

where P_{in} is an incident power into a line, P_{loss} is a dissipative power on a line, S_{11} is a reflection coefficient, and S_{21} is a transfer coefficient. Loss ratio means the relative magnitude of a dissipative power during an incident power. Figure 4(c) shows a loss ratio of Line 1 and Line 2's having distances D of 0 mm, 3 mm, and 6 mm. This figure provides useful information to optimize the total loss of signal and power line in CiSP. Firstly, Line 1 has smaller loss ratio than Line 2 with distance D of 3 mm in Regions 1 and 2, but Line 1 has greater loss ratio than Line 2 with distance D of 3 mm in Region 3. This is explained as loss of the CPW lines over the silicon substrate is rapidly increased than that of the CPW line over ground plane as frequency increases. Therefore, it means that the loss by extended line length is dominant at relatively low frequencies, and the loss by the effect of the silicon substrate becomes dominant for higher frequency range. Secondly,

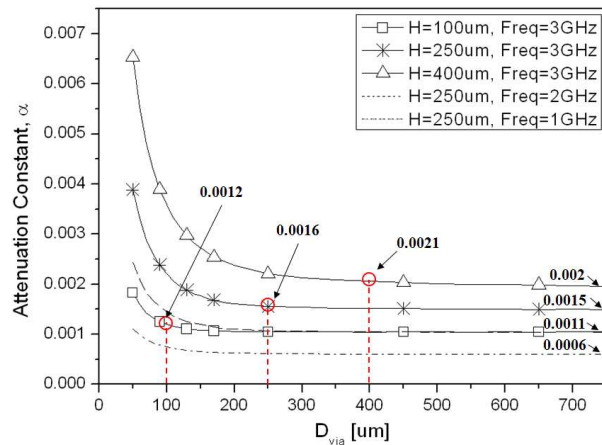


Figure 6: Attenuation constant per via hole with respect to height H , distance D_{via} , and frequencies.

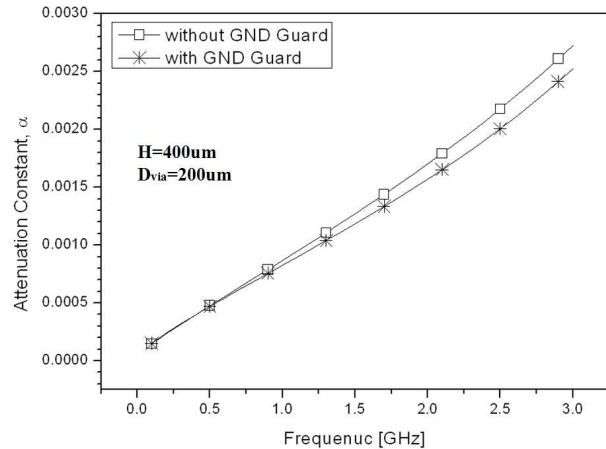


Figure 7: Attenuation constant per via hole with/without ground guard.

Line 1 has greater loss ratio than Line 2 with distance D of 0 mm only in Region 2, but both 0 mm and 3 mm in Region 3. It means that the loss by extended line length becomes dominant until higher frequency as line length is longer. If the total length of Line 2 is much longer than Line 1 as case of Line 2 with distance D of 6 mm, the loss by extended line length will always become dominant regardless of frequencies. These results show that it is needed to consider total length of signal and power lines as well as the effect by silicon substrate and frequencies.

4. LOSS OF VIA IN CiSP

A via hole closed to an embedded silicon substrate can have large loss which varies with distance to the silicon substrate, height of the via hole, and ground guard between the via hole and the silicon substrate. The via holes used for the loss analysis have the same dimensions of via pad, inner via hole, and outer hole except height as shown in Figure 5(a). Figure 5(b) shows the structure with variations of D_{via} and H : D_{via} is a distance between the via hole and silicon substrate and H is a height of the via hole. Figure 5(c) is the structure with ground guard between the via hole and silicon substrate in the same geometrical condition of Figure 5(b). Figure 6 shows attenuation constants per via hole according to various geometries of height H and distance D_{via} and frequencies. In the result, attenuation constants of the via hole decrease with an increase of distance D_{via} in all cases with various heights H and frequencies. Also, they are constant wherever distance D_{via} is greater than height H in all cases. These phenomena mean that the effect of the silicon substrate is not dominant; i.e., distance D_{via} is greater than height H . Therefore, loss of a via hole by an embedded silicon substrate can be reduced enough in case of further distance from the silicon substrate than height of the via hole. Figure 7 shows curves of attenuation constants for a via hole with and without ground guard where their via geometries are given as height H of 400 μm and distance D_{via} of 200 μm . In the results, the ground guard nearby a via hole reduces the loss by preventing the silicon substrate loss. Also, the EM field is crowded from silicon substrate into the ground guard for reduction of impedances because inductive impedance is extremely increased as frequency increases. Therefore, the ground guard can effectively prevent the loss from silicon substrate for high frequencies.

5. CONCLUSIONS

In CiSP, the losses of transmission lines and via holes are increased by the effect of an embedded silicon substrate. In case of transmission lines, it is needed to consider both the loss effect of added line length and the effect of the silicon substrate. Generally, it is recommended to route the line as firstly it has the shortest length regardless of existence of the silicon substrate for low frequency and secondly it should not be permitted crossover the silicon substrate for high frequency. In case of via holes, it is needed to locate via holes further longer distance from the silicon substrate than length of height of the via holes. Also, a ground guard between via holes and the silicon substrate reduces the losses of via holes by the effect of the silicon substrate, especially for more high frequencies.

ACKNOWLEDGMENT

This work was supported by the National Research Foundation of Korea (NRF) grant funded by the Korea government (MEST) (No. 2009-0086631).

REFERENCES

1. Ko, C., S. Chen, C. Chiang, T. Kuo, Y. Shih, and Y. Chen, “Embedded active device packaging technology for next-generation chip-in-substrate package, CiSP,” *Electronic Components and Technology Conference*, 322–329, San Diego, USA, May 2006.
2. Lee, B., V. Sundaram, S. Kennedy, D. Baars, and R. Tummala, “Novel chip-last method for embedded actives in organic packaging substrates,” *IEEE Trans. Components, Packaging, and Manufacturing Technology*, Vol. 2, No. 1, 63–70, 2012.
3. Kim, J. W., H. S. Park, S. C. Lee, Y. K. Chung, S. M. Choi, and S. Yi, “Development of lamination process for chip-in-substrates,” *Electronic Materials and Packaging*, 1–6, Daejeon, Korea, Nov. 2007.
4. Sankaran, N., B. Lee, V. Sundaram, E. Engin, and M. Iyer, “Electrical characterization and design optimization of embedded chip in substrate cavities,” *Electronic Components and Technology Conference*, 992–999, Reno, USA, May 2007.
5. Eisenstadt, W. R. and Y. Eo, “S-parameter-based IC interconnect transmission line characterization,” *IEEE Trans. Components, Hybrids, and Manufacturing Technology*, Vol. 15, No. 4, 483–490, 1992.

Ferromagnetic Microwire Usage for Magnetic Tags

S. Gudoshnikov^{1,2}, N. Usov^{1,2}, A. Ignatov³, V. Tarasov³, A. Zhukov^{2,4,5}, and V. Zhukova^{2,4}

¹Pushkov Institute of Terrestrial Magnetism, Ionosphere and Radio Wave Propagation (IZMIRAN), Troitsk, Moscow Region, Russia

²Ltd. “Magnetic and Cryoelectronic Systems”, Troitsk, Moscow Region, Russia

³National University of Science and Technology “MISiS”, Moscow, Russia

⁴Dpto. de Fisica de Materiales, Fac. Químicas, Universidad del Pais Vasco, San Sebastián, Spain

⁵IKERBASQUE, Basque Foundation for Science, Bilbao, Spain

Abstract— The amplitudes of the electromagnetic harmonics of magnetic tags made from bistable Fe-Co-Si-B amorphous microwire with positive magnetostriction are studied as a function of the distance between the tag and the receiving coils. It is shown that the electromotive force signals generated by the magnetic tags of length 3–5 cm with magnetic core diameter 90–100 μm can be detected at the distances up to 50 cm from the receiving coils. The dependence of the amplitudes of the electromagnetic harmonics on the size of the receiving coil is investigated theoretically.

1. INTRODUCTION

Amorphous and nanocrystalline ferromagnetic microwires exhibit a number of unusual magnetic properties suitable for various technical applications [1–3]. In particular, Fe-based microwires [4] with positive magnetostriction and high magnetic response have been considered as new tags for Electronic article surveillance (EAS) applications [5]. It is well known [6] that Fe-based microwires having magnetic core diameter $d = 10\text{--}20\ \mu\text{m}$ and total diameter $D = 15\text{--}30\ \mu\text{m}$ show bistable magnetic behavior under the influence of uniform external magnetic field. The bistable behavior of these microwires has been interpreted as a magnetization reversal of a large magnetic domain in a single Barkhausen jump. This phenomenon looks quite attractive for EAS applications. In our previous work [7] it was demonstrated that the electromagnetic response of the pieces of Fe-based microwires with diameter $D = 15\text{--}30\ \mu\text{m}$ and several centimeter length can be detected at a distance more than 20 cm from the wire. The aim of the present paper is to investigate the properties of thicker Fe-based glass covered microwires with magnetic core diameter of the order of $d \sim 100\ \mu\text{m}$. It is shown experimentally that the electromagnetic response of these microwires can be detected at higher distances, up to 40 cm from the microwire. Theoretical calculations of the amplitudes of electromagnetic harmonics generated by magnetic tag as a function of the distance from the receiving coils are in reasonable agreement with the experimental data. The calculations are based on the model described in Ref. [7].

2. EXPERIMENTAL

2.1. Microwire Characterization

The amorphous ferromagnetic Fe-Co-Si-B microwires obtained by means of Taylor-Utilovsky method were procured from TAMAG Iberica S. L.. The magnetic core diameter of the microwires is given by $d \sim 100\ \mu\text{m}$. The modified Sixtus-Tongs method [6, 8] has been used to study the magnetic properties of the microwire. The dynamics of head-to head domain walls (DW) has been investigated in long pieces ($\sim 30\ \text{cm}$ length) of microwire under the influence of uniform external magnetic field. Using the technique developed [6] one can determine the stationary DW velocity, V , the DW nucleation field, H_n , the wire saturation magnetization, M_s , the value of the total DW magnetic charge, Q . The geometrical and magnetic parameters of the microwire studied are given in the Table 1. For magnetic tag preparation short pieces of the microwire with length $l = 3\text{--}5\ \text{cm}$ have been attached within thin plastic holders.

2.2. Tag Response Detection Installation

To study the electromagnetic response of the magnetic tags in applied alternating magnetic field the installation shown in Fig. 1(a) has been developed. In contrast to the previously used scheme [7], in the present installation two square coils with opposite connection were used as receivers. The receiving coils with a side of $a = 20\ \text{cm}$ were made of 20 turns of thin copper wire. The low noise band amplifier with an amplification ~ 100 and the transmission band in the range of frequencies

Table 1: Microwire characteristics.

Microwire	Core diameter d , μm	Total diameter D , μm	Saturation magnetization M_s , emu/cm^3	DW velocity V , cm/sec	Nucleation field H_n , Oe	DW magnetic charge Q , emu/cm
MW-100	97	158	710	460	1.5	0.11

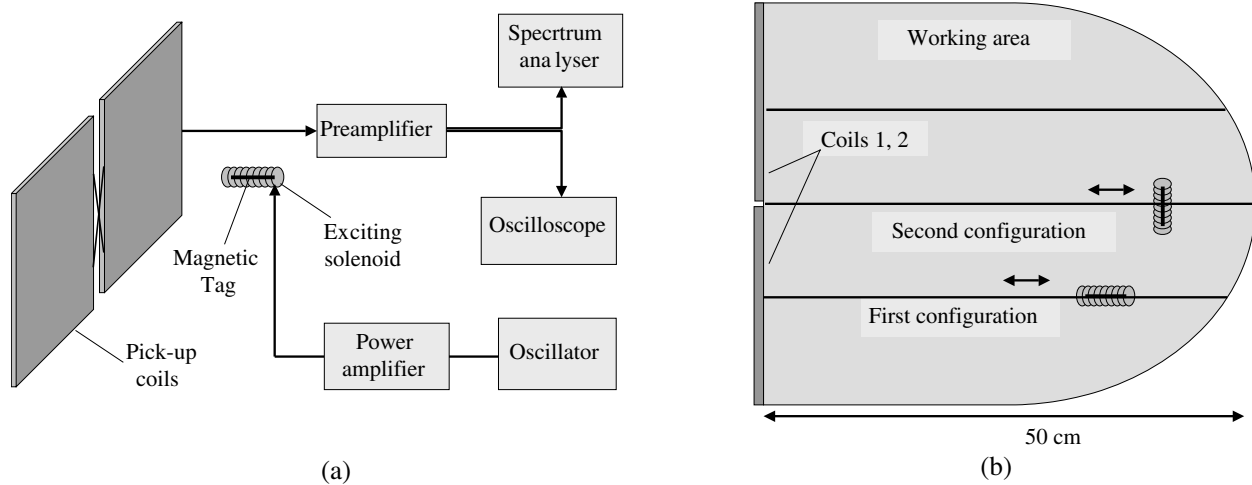


Figure 1: (a) Scheme of the installation to record the EMF signals of magnetic tags; (b) Geometry of the working area near the receiving coils.

500 Hz–12 kHz has been used to amplify the electromotive force signals (EMF) generated in the receiving coils. The low frequency spectrum analyser CF 5210 and digital oscilloscope were used to record the EMF signals. A small solenoid with a length 5 cm has been used to excite the magnetic tags by alternating magnetic field with a frequency $f = 327$ Hz and amplitude $H_0 = 5$ Oe. In the absence of the magnetic tag within the solenoid the EMF signal contains the components at the exciting frequency and its second and third harmonics, as well as the harmonics of the power supply at 50 Hz. The noise voltage at a frequency higher than 1 kHz was around $\sim 20 \mu\text{V}/\text{Hz}^{1/2}$. However, when the magnetic tag is placed within the solenoid its electromagnetic response can be observed by means of digital oscilloscope as a series of short positive and negative impulses. The corresponding EMF signal contains a number of harmonics up to the frequencies higher than 10 kHz.

3. RESULTS AND DISCUSSION

During the experiments performed the amplitudes of 5-th, 7-th and 11-th harmonics of the exciting frequency averaged over the 5 seconds time interval were measured as a function of the distance between the magnetic tag and the receiving coil plane. As Fig. 1(b) shows, the magnetic tag can be moved within a working area along the guiding line perpendicular to the coil plane and fixed at a desirable angle with respect to the coil plane in any point between 0 (point near the receiving coils) and 50 cm far from the coil plane. Two configurations were studied in the experiment. In the first configuration the guiding line starts at the center of one of the receiving coil and the solenoid with the magnetic tag is oriented along the guiding line, perpendicular to the coil plane. In the second configuration the origin of the guiding line is located in the middle between the receiving coil centers, however the solenoid with magnetic tag is oriented horizontally and parallel to the receiving coil plane. Figs. 2(a), 2(b) show the characteristic spectra of the EMF signals for the first tag configuration recorded at the distances Z equal 46 cm and 30 cm from the coil plane in the frequency range $f = 5$ Hz–5 kHz. It is found that for the distances $z \leq 30$ cm the main contributions to the measured signals were the harmonics generated by the magnetic tag during its magnetization reversal. However, the measured spectra contain also the contribution at the frequency 50 Hz and its odd harmonics up to 2 kHz.

In Fig. 3(a) solid squares show the dependence of the 7-th harmonics of the magnetic tag EMF signal ($f_7 = 2289$ Hz) as a function of the distance from the coil plane. Theoretical calculations for

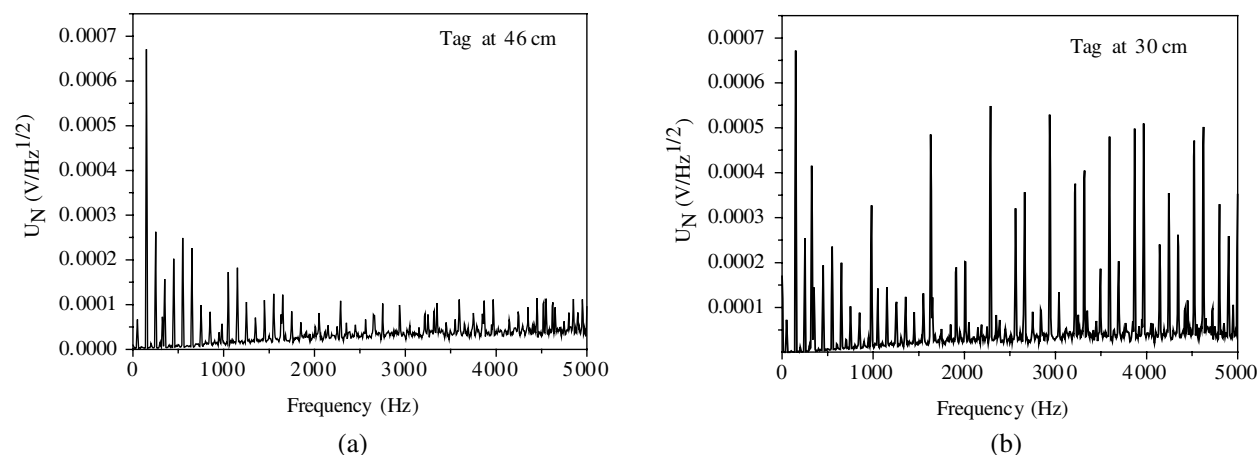


Figure 2: Spectra of the magnetic tag EMF signals recorded at the distances (a) $z_1 = 46$ cm and (b) $z_2 = 30$ cm far from the coil plane in the frequency range $f = 5$ Hz–5 kHz.

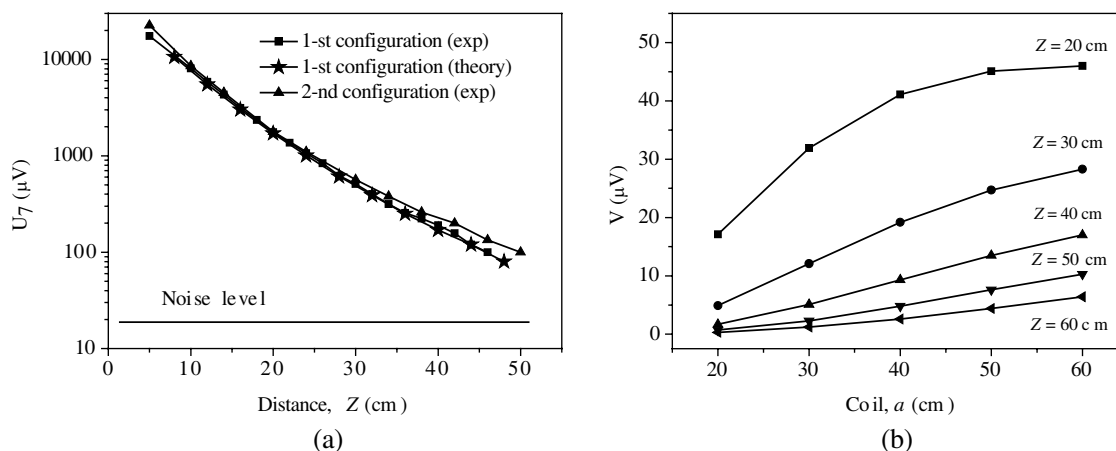


Figure 3: (a) The measured amplitude of 7-th harmonics of the magnetic tag EMF signals as a function of the distance of the tag from the receiving coil plane for the cases when the tag is oriented perpendicular (squares) or parallel (triangles) to the coil plane. The stars show the result of the theoretical calculation for the first tag configuration. (b) Theoretical calculation of the amplitude of 7-th harmonics as a function of the receiving coil size a for various distances Z of the magnetic tag from the receiving coil plane.

the amplitude of the 7-th harmonics are shown in Fig. 3(a) by stars. They are based on the model described in Ref. [7] and are in reasonable agreements with the experimentally measured data. One can see that even at the distance $z = 46$ cm the signal level is given by $\sim 90 \mu\text{V}$, that is 4 times higher than the noise level at this frequency. Similar data were obtained also for 11-th harmonics of the EMF signal at $f = 3597$ Hz. The results obtained were identical also for the case when the guiding line starts at the center of the second receiving coil. On the other hand, the signal level for the first tag configuration decreases considerably if the guiding line is shifted from the coil center to the point located in the middle between the receiving coil centers.

For the second configuration the dependence of the amplitude of the 7-th harmonics on the tag distance from the coil plane is shown in Fig. 3(a) by the closed triangles. For this case the magnetic tag response can be confidently detected up to 50 cm from the coil plane.

One can see therefore, that for the given size of the receiving coils the magnetic tag having $\sim 100 \mu\text{m}$ magnetic core diameter can be detected at the distances higher than 45 cm, irrespective of the magnetic tag orientation with respect to the receiving coil plane. However, at certain tag positions and orientations the EMF signal decreases considerably. One way to increase the sensitivity of the installation developed is to enlarge the sizes of the receiving pick-up coils.

The theoretical model developed [7] to estimate the EMF signals generated in receiving coils during tag magnetization reversals in external alternating magnetic field was used to study the influence of the receiving coil geometry on the amplitude of the EMF signals detected. Fig. 3(b)

shows the results of the calculations of the amplitude of the 7-th harmonics of the EMF coil's signal performed for magnetic tag with length $l = 3$ cm and magnetic core diameter $d = 100 \mu\text{m}$ in the first tag configuration for various distances Z of the magnetic tag from the receiving coil plane. One can see in Fig. 3(b) that for confident detection of the magnetic tag EMF signals at the distances up to 50 cm for the receiving coil plane it is desirable to use the receiving square coils with sizes $a = 30\text{--}40$ cm.

4. CONCLUSIONS

In the given paper, the amplitudes of electromagnetic harmonics of the short pieces of the bistable Fe-based amorphous microwire was measured as a function of the distance between the wire and the receiving coils. It is shown that the EMF signals of the magnetic tags with length 3–5 cm having magnetic core diameter $d \sim 100 \mu\text{m}$ can be detected at the distance more than 45 cm from the coil plane at the signal to noise ratio higher than 4. The theoretical estimation shows that the sizes of the receiving coils have to be enlarged to increase further the signal to noise ratio.

REFERENCES

1. Jiles, D. C., "Recent advances and future directions in magnetic materials," *Acta Materialia*, Vol. 51, 5907–5939, 2003.
2. Gudoshnikov, S. A., B. Y. Ljubimov, P. S. Palvanov, Y. V. Prokhorova, N. A. Usov, and A. V. Torcunov, "Possible origin of hysteresis loops with finite remanence for Co-rich amorphous microwires," *Phys. Status Solidi A*, Vol. 206, No. 4, 625–629, 2009.
3. Vazquez, M., H. Chiriac, A. Zhukov, L. Panina, and T. Uchiyama, "On the state-of-the-art in magnetic microwires and expected trends for scientific and technological studies," *Phys. Status Solidi A*, Vol. 208, 493–501, 2011.
4. Rodionova, V., M. Ipatov, M. Ilyn, V. Zhukova, N. Perov, J. Gonzalez, and A. Zhukov, "Tailoring of magnetic properties of magnetostatically-coupled glass-covered magnetic microwires," *J. Supercond. Nov. Magn.*, Vol. 24, Nos. 1–2, 541–547, 2011.
5. Han, M., D. F. Liang, and L. J. Deng, "Sensors development using its unusual properties of Fe/Co-based amorphous soft magnetic wire," *J. Mat. Science*, Vol. 40, 5573–5580, 2005.
6. Gudoshnikov, S. A., Y. B. Grebenshchikov, B. Y. Ljubimov, P. S. Palvanov, N. A. Usov, M. Ipatov, A. Zhukov, and J. Gonzalez, "Local nucleation field and characteristic width of head to head domain wall in Fe-rich amorphous microwire," *Phys. Status Solidi A*, Vol. 206, No. 4, 613–617, 2009.
7. Gudoshnikov, S., N. Usov, A. Zhukov, V. Zhukova, P. Palvanov, B. Ljubimov, O. Serebryakova, and S. Gorbunov. "Evaluation of use of magnetically bistable microwires for magnetic labels," *Phys. Status Solidi A*, Vol. 208, No. 3, 526–529, 2011.
8. Gudoshnikov, S. A., B. Y. Ljubimov, P. S. Palvanov, and N. A. Usov, "A device for measuring the characteristics of amorphous ferromagnetic microwires," Utility Patent Number 84587, Application No. 2008148482/22, Priority of the Utility Model on December 10, 2008.

Tailoring of Frequency and Magnetic Field Dependence of Giant Magnetoimpedance Effect in Thin Wires

A. Zhukov^{1,2}, M. Ipatov¹, and V. Zhukova¹

¹Dpto. de Física de Materiales, Fac. Químicas, UPV/EHU, San Sebastián 20018, Spain

²IKERBASQUE, Basque Foundation for Science, Bilbao, Spain

Abstract— We present our results on studies of soft magnetic properties and GMI effect in thin microwires at elevated frequencies paying special attention to tailoring the GMI effect and achievement of high GMI effect with low hysteretic behavior. We measured magnetic field dependence of real part, of the longitudinal wire impedance up to frequency, f , 4 GHz in Co-rich microwires. We observed that the GMI magnetic field dependence can be tailored either controlling magnetoelastic anisotropy of as-prepared microwires or by heat treatment.

1. INTRODUCTION

Amorphous soft magnetic materials continue playing important role in many technological applications [1]. Among different families of soft amorphous magnetic materials, magnetically soft thin wires (with typical diameters from 1 to 120 μm) attract considerable interest owing to unusual magnetic properties exhibiting by amorphous ferromagnetic wires such as magnetic bistability and giant magneto-impedance, GMI, effect [1–3]. These properties are especially attractive for the magnetic sensor applications.

One of the recent tendencies in the field of magnetic sensor applications is their miniaturization. Therefore reduction of diameters of magnetically soft wires keeping soft magnetic properties is one of the priority tasks in this field of applied magnetism. Therefore, studies of magnetically soft thin wires attract considerable attention [4–8]. The advantage of the Taylor-Ulitovsky method allowing the fabrication of glass-coated metallic microwires consists of controllable fabrication of long (up to few km long continuous microwire) and homogeneous thin composite wires.

The GMI effect has been successfully explained in the terms of classical electrodynamics through the influence of magnetic field on penetration depth of electrical current flowing through the magnetically soft conductor [9, 10]. The highest GMI effect and soft magnetic properties are observed for nearly-zero magnetostrictive compositions. For the Co-Fe-based $(\text{Co}_x\text{Fe}_{1-x})_{75}\text{Si}_{15}\text{B}_{10}$ system the magnetostriction constant, λ_s , changes with x from -5×10^{-6} at $x = 1$, to $\lambda_s \approx 35 \times 10^{-6}$ at $x \approx 0.2$, achieving vanishing value at Co/Fe ratio about 70/5 [11].

The magnetic field dependence of the impedance of magnetic conductor is mainly determined by the type of magnetic anisotropy [2–6, 12–14]. The magnetic anisotropy which can be tailored by thermal treatment and the fabrication process [9, 10].

In this paper, we studied the GMI effect (GMI ratio, $\Delta Z/Z$) and hysteretic magnetic properties in thin amorphous glass-coated microwires with vanishing magnetostriction constant and correlation of the GMI effect with magnetic anisotropy and tailoring of the magnetic field dependence of the GMI effect.

2. EXPERIMENTAL

We studied Co-rich microwires with different diameters of metallic nucleus, d , total diameters, D , and consequently different ρ -ratios ($\rho = d/D$) fabricated by the Taylor-Ulitovsky method [6, 7].

The strength of internal stresses is determined by ratio ρ [6, 15]. Therefore, controllable change of the ρ -ratio allowed us to control residual stresses.

The magnetoelastic energy, K_{me} , is given by

$$K_{me} \approx 3/2\lambda_s\sigma, \quad (1)$$

where $\sigma = \sigma_i + \sigma_a$ — total stress, σ_i — are the internal stresses, σ_a — applied stresses and λ_s — magnetostriction constant [6].

In this way we studied the effect of magnetoelastic contribution on soft magnetic properties and GMI effect of microwires controlling the magnetostriction constant, applied and/or residual stresses.

We have measured dependences of the diagonal Z_{zz} impedance and the GMI ratio, $\Delta Z/Z$, on external axial magnetic field H , using a specially designed microstrip cell as described elsewhere [6]. Hysteresis loops have been measured by the induction method, as described elsewhere [6].

3. RESULTS AND DISCUSSION

Magnetic field, H , dependence of real part, Z_1 of the longitudinal wire impedance Z_{zz} ($Z_{zz} = Z_1 + iZ_2$), measured up to 4 GHz in $\text{Co}_{66}\text{Cr}_{3.5}\text{Fe}_{3.5}\text{B}_{16}\text{Si}_{11}$ microwire is shown in Fig. 1. Double maximum dependence and shift of the field of maximum to higher magnetic fields with increasing the frequency, f , should be underlined. We observed considerable GMI effect at GHz-range frequencies. On the other hand, for the observation of the GMI effect at GHz frequencies high enough magnetic field is needed. Frequency dependence of the maximum GMI ratio, $\Delta Z/Z_m$, measured in $\text{Co}_{66.87}\text{Fe}_{3.66}\text{C}_{0.98}\text{Si}_{11.47}\text{B}_{13.36}\text{Mo}_{1.52}$ microwires with different metallic nucleus diameters are shown in Fig. 2.

The frequency dependence of maximum GMI ratio, $\Delta Z/Z_m(f)$, measured in microwires of the same composition and different diameters presents an optimum frequency (at which $\Delta Z/Z_m$ versus f exhibits the maximum) at different frequencies. Thus, for metallic nucleus diameters ranging between 8.5 and 9.0 μm the optimal frequency is about 100 MHz, while for microwires with metallic nucleus diameters between 9 and 11.7 μm the optimal frequency is about 200 MHz (see Fig. 2).

As mentioned above, the internal stresses, σ_i , arising during simultaneous rapid quenching of metallic nucleus surrounding by the glass coating are the source of additional magnetelastic anisotropy. The strength of such internal stresses can be controlled by the ρ -ratio: strength of internal stresses increases decreasing ρ -ratio (i.e., increases with increasing of the glass volume) [15].

Consequently, the parameter ρ must be considered as one of the factors that affect both soft magnetic properties and GMI.

Figure 3 shows the influence of the ρ -ratio on hysteresis loops of $\text{Co}_{67.1}\text{Fe}_{3.8}\text{Ni}_{1.4}\text{Si}_{14.5}\text{B}_{11.5}$ microwires with the same composition of the metallic nucleus, but different ρ -ratio.

As can be appreciated, all studied samples exhibited excellent magnetically soft properties with

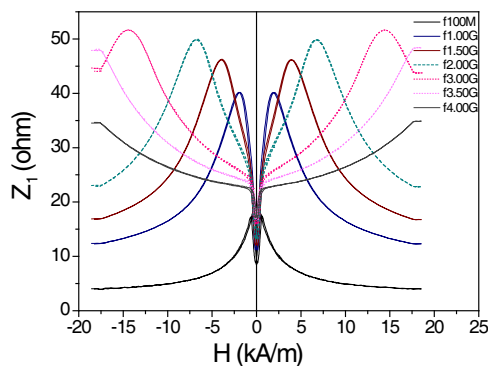


Figure 1: $Z_1(H)$ dependence of $\text{Co}_{66}\text{Cr}_{3.5}\text{Fe}_{3.5}\text{B}_{16}\text{Si}_{11}$ microwire measured at different frequencies.

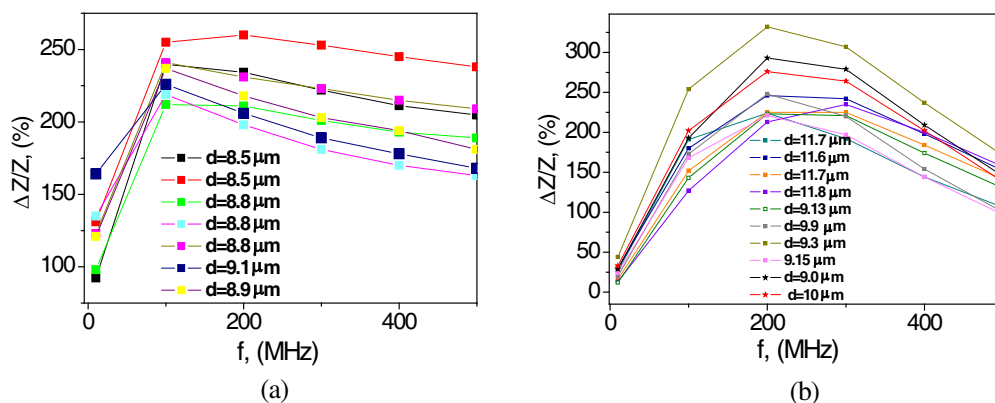


Figure 2: Frequency dependence of $\Delta Z/Z_m$, measured $\text{Co}_{66.87}\text{Fe}_{3.66}\text{C}_{0.98}\text{Si}_{11.47}\text{B}_{13.36}\text{Mo}_{1.52}$ microwires with different metallic nucleus diameters.

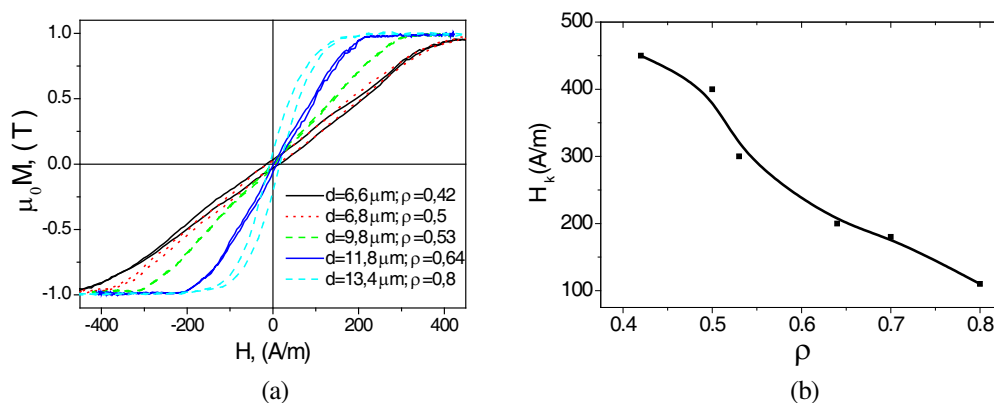


Figure 3: Hysteresis loops of $\text{Co}_{67.1}\text{Fe}_{3.8}\text{Ni}_{1.4}\text{Si}_{14.5}\text{B}_{11.5}\text{Mo}_{1.7}$ microwires with different geometry (a) and dependence of H_k on ρ -ratio (b).

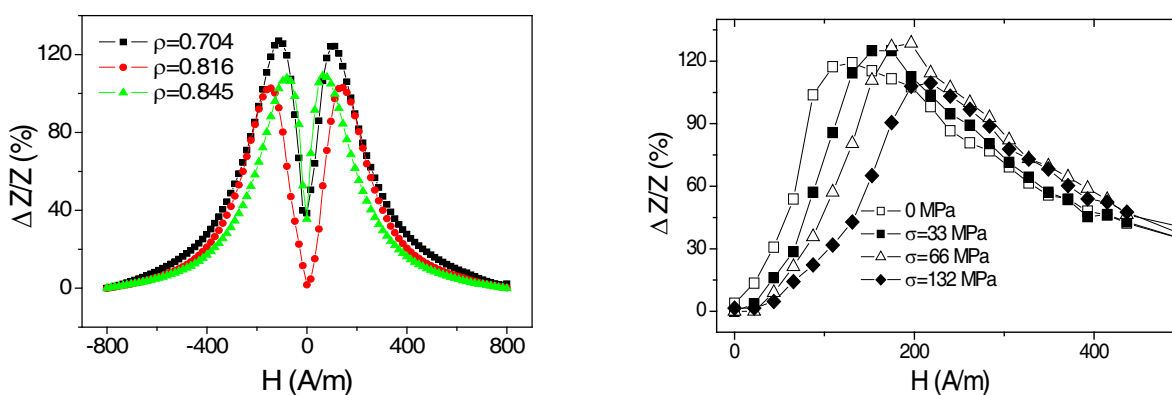


Figure 4: Effect of ρ -ratio on GMI effect in $\text{Co}_{67.05}\text{Fe}_{3.85}\text{Ni}_{1.4}\text{B}_{11.33}\text{Si}_{14.47}\text{Mo}_{1.69}$ microwire samples with different ρ -ratios.

Figure 5: $\Delta Z/Z(H)$ dependences of $\text{Co}_{68.5}\text{Mn}_{6.5}\text{Si}_{10}\text{B}_{15}$ amorphous microwires measured at different σ_a .

low coercivities (between 4 and 10 A/m). Magnetic anisotropy field, H_k , is found to be determined by the ρ -ratio, decreasing with ρ (Fig. 3(b)) previously reported [6]. Consequently, one can expect that the ρ -ratio must affect the GMI effect of studied samples.

Figure 4 presents results on magnetic field dependences of $\Delta Z/Z$ measured in $\text{Co}_{67.05}\text{Fe}_{3.85}\text{Ni}_{1.4}\text{B}_{11.33}\text{Si}_{14.47}\text{Mo}_{1.69}$ microwire samples with different ρ -ratios. Indeed both maximum values of the GMI ratio, $\Delta Z/Z_m$, and the magnetic anisotropy field present considerable dependence on samples geometry.

Considering that the magnetoelastic energy, K_{me} , is determined by both internal, σ_i , and applied stresses, σ_a , we measured the GMI effect under tensile stresses in various Co-rich microwires. Fig. 5 presents tensile stress dependence measured in $\text{Co}_{68.5}\text{Mn}_{6.5}\text{Si}_{10}\text{B}_{15}$ microwires. We observed, that $\Delta Z/Z$ and H_m are quite sensitive to the application of external tensile stresses, σ_a : here the magnetic field, H_m corresponding to the maximum of $(\Delta Z/Z)$ shows a roughly linear increase with σ (Fig. 5).

As mentioned above, the value of the dc axial field that corresponds to the maximum GMI ratio, H_m , should be attributed to the static circular anisotropy field, H_k .

In fact the tendency on the change of H_m under application of tensile stresses (Fig. 5) and the change of H_m and H_k with decreasing the ρ -ratio (Figs. 3 and 4) is the same, that confirms the effect of magnetoelastic anisotropy on hysteresis loops and GMI effect.

Summarizing, GMI magnetic field dependence can be tailored either controlling magnetoelastic anisotropy of as-prepared microwires or by heat treatment. Composite character of such microwires results in the appearance of an additional magnetoelastic anisotropy. Heat treatment is an efficient method of tailoring of the magnetic properties and the GMI effect of such microwires. Selection of proper chemical composition, geometry and adequate conditions of annealing allows achieving of high GMI effect.

4. CONCLUSIONS

In thin amorphous wires, produced by the Taylor-Ulitovsky technique, magnetic softness and magnetic field dependence of GMI effect (both longitudinal and off-diagonal) and GMI hysteresis are determined the magnetoelastic anisotropy. This magnetoelastic anisotropy can be manipulated by the sample geometry and adequate annealing. By varying the alloys composition and applying post fabrication processing it is possible to control the magnetic field dependence of the GMI effect and in this way to tailor magnetic field sensitivity of GMI effect.

REFERENCES

1. Jiles, D. C., "Recent advances and future directions in magnetic materials," *Acta Materialia*, Vol. 51, 5907–5939, 2003.
2. Mohri, K., F. B. Humphrey, K. Kawashima, K. Kimura, and M. Muzutani, *IEEE Trans. Magn.*, Vol. 26, 1789–1793, 1990.
3. Zhukov, A. P., "The remagnetization process of bistable amorphous alloys," *Materials and Design*, Vol. 14, 299–305, 1993.
4. Zhukova, V., A. Zhukov, V. Kraposhin, A. Prokoshin, and J. Gonzalez, *Sensors and Actuators A*, Vol. 106, 225–229, 2003.
5. Ciureanu, P., G. Rudkowska, L. Clime, A. Sklyuyev, and A. Yelon, "Anisotropy optimization of giant magnetoimpedance sensors," *J. Optoelectronics and Advanced Materials*, Vol. 6, 905–910, 2004.
6. Zhukova, V., M. Ipatov, and A. Zhukov, "Thin magnetically soft wires for magnetic microsensors," *Sensors*, Vol. 9, 9216–9240, 2009.
7. Vazquez, M., H. Chiriac, A. Zhukov, L. Panina, and T. Uchiyama, "On the state-of-the-art in magnetic microwires and expected trends for scientific and technological studies," *Phys. Status Solidi A*, Vol. 208, 493–501, 2011.
8. Honkura, Y., "Development of amorphous wire type MI sensors for automobile use," *J. Magn. Mater.*, Vol. 249, 375–381, 2002.
9. Panina, L. V. and K. Mohri, "Magneto-impedance effect in amorphous wires," *Appl. Phys. Lett.*, Vol. 65, 1189–1191, 1994.
10. Beach, R. and A. Berkowitz, "Giant magnetic field dependent impedance of amorphous Fe-CoSiB wire," *Appl. Phys. Lett.*, Vol. 64, 3652–3654, 1994.
11. Konno, Y. and K. Mohri, "Magnetostriction measurements for amorphous wires," *IEEE Trans. Magn.*, Vol. 25, No. 5, 3623–3625, 1989.
12. Usov, N. A., A. S. Antonov, and A. N. Lagar'kov, "Theory of giant magneto-impedance effect in amorphous wires with different types of magnetic anisotropy," *J. Magn. Magn. Mat.*, Vol. 185, 159–173, 1998.
13. Sandacci, S. I., D. P. Makhnovskiy, L. V. Panina, K. Mohri, and Y. Honkura, "Off-diagonal impedance in amorphous wires and its application to linear magnetic sensors," *IEEE Trans. Magn.*, Vol. 35, 3505–3510, 2004.
14. Makhnovskiy, D. P., L. V. Panina, and D. J. Mapps, "Field-dependent surface impedance tensor in amorphous wires with two types of magnetic anisotropy: Helical and circumferential," *Phys. Rev. B*, Vol. 63, 1444241, 2001.
15. Chiriac, H., T. A. Ovari, and G. Pop, "Internal stress distribution in glass-covered amorphous magnetic wires," *Phys. Rev. B*, Vol. 42, 10105–10113, 1995.

EM Wave Scattering by Objects Moving on Bowditch-Lissajous Trajectories

Dan Censor

Department of Electrical and Computer Engineering
Ben-Gurion University of the Negev, Beer-Sheva 84105, Israel

Abstract— A method for analyzing scattering of electromagnetic waves by objects performing complex periodic and quasi-periodic motion on Bowditch-Lissajous trajectories is presented. The method is based on the previously introduced Quasi Lorentz Transformation, facilitating the approximate analysis of scattering in the presence of varying velocity. In the present class of problems the method is specialized to time-dependent motion. A special case of scattering by cylinders is analyzed. The resulting spectrum is shown to be discrete, with sidebands determined by the frequencies of initial carrier incident wave and the mechanical motion.

1. INTRODUCTION

Scattering of electromagnetic waves by objects performing complex motion is of interest both theoretically and for applied scientific and engineering purposes. Monitoring motion by means of wave scattering facilitates remote sensing of properties of objects and constituent media.

This class of problems includes quasi-periodic motion along Bowditch-Lissajous trajectories. Salient examples are orbiting devices abounding in machinery and aviation. For comprehensive mathematical discussions and relevant references to Lissajous' original work [1], see e.g., [2, 3]. Presently motion along the principal Cartesian coordinates is investigated. Investigations of scattering by nonuniformly moving objects are found in the literature, see Van Bladel [4] for a comprehensive review of early and contemporary work.

Consider a 3D Cartesian family of parametric curves defining the velocity of a point periodically moving along the axes

$$\mathbf{v}(t) = \hat{\mathbf{x}}v_{0x} \cos \Phi_x + \hat{\mathbf{y}}v_{0y} \cos \Phi_y + \hat{\mathbf{z}}v_{0z} \cos \Phi_z, \quad \Phi_i = \Omega_i t + \psi_i, \quad i = x, y, z \quad (1)$$

where $0 \leq \varphi_i < 2\pi$. The corresponding spatial location is derived by integrating $\mathbf{v} = d_t \boldsymbol{\rho}(t)$. Ignoring constants of integration yields

$$\boldsymbol{\rho}(t) = \hat{\mathbf{x}}A_x \sin \Phi_x + \hat{\mathbf{x}}A_y \sin \Phi_y + \hat{\mathbf{x}}A_z \sin \Phi_z, \quad v_{0i} = \Omega_i A_i \quad (2)$$

In our special example both velocity and location are boxed in rectangular-cuboid regions in their respective Cartesian spaces. For rational quotients Ω_i , trajectories are closed, otherwise quasi-periodic trajectories are encountered, eventually scanning all points within the confining cuboid. Assuming time-harmonic incident plane waves, we investigate the scattered wave from objects moving along such trajectories.

The electromagnetic model used below is the Quasi Lorentz Transformation (QLT), Presently the QLT for time-dependent velocity is defined in terms of differentials, relating spatiotemporal coordinates in two relatively moving frames of reference (e.g., see [5, 6])

$$d\mathbf{r}' = d\mathbf{r} - \mathbf{v}(t)dt \quad (3)$$

$$dt' = dt - c^{-2}\mathbf{v}(t) \cdot d\mathbf{r} \quad (4)$$

valid to the First Order in v/c (FO) and therefore prescribing in (2) $\Omega_i A_i$ much smaller than c , the speed of light in free space.

Ignoring higher order terms, the Inverse Transformations (IT) of (3), (4), are approximated to FO as

$$d\mathbf{r} = d\mathbf{r}' + \mathbf{v}(t')dt' \quad (3^*)$$

$$dt = dt' + c^{-2}\mathbf{v}(t') \cdot d\mathbf{r}' \quad (4^*)$$

Henceforth the asterisk notation for IT will be understood even without explicitly writing out the expressions. Formally, all we have to do is exchange primed and unprimed quantities and replace \mathbf{v} by $-\mathbf{v}$. Note that $\mathbf{v}(t) = \mathbf{v}(t')$ are already FO expressions

For constant velocity \mathbf{v} , integration of (3), (4) with zero constants of integration leads to

$$\mathbf{r}' = \mathbf{r} - \mathbf{v}t \quad (5)$$

$$t' = t - c^{-2}\mathbf{v} \cdot \mathbf{r} \quad (6)$$

recognized as the FO velocity approximation of the exact SR (Special Relativity) Lorentz Transformation (LT) [7]. The corresponding IT (5*), (6*), follow. It is noted that both (3), (4), and (5), (6), lead to the same FO SR law for addition of velocities, which motivated the introduction of the QLT for varying velocities in the first place.

Substituting (5), (6), in the (purely mathematical) chain rule of calculus

$$\partial_{\mathbf{r}} = (\partial_{\mathbf{r}'}\mathbf{r}') \cdot \partial_{\mathbf{r}'} + (\partial_{t'}t')\partial_{t'} \quad (7)$$

$$\partial_t = (\partial_{t'}t')\partial_{t'} + (\partial_{t'}\mathbf{r}') \cdot \partial_{\mathbf{r}'} \quad (8)$$

yields for the differential operators related to (5), (6)

$$\partial_{\mathbf{r}} = \partial_{\mathbf{r}'} - c^{-2}\mathbf{v}\partial_{t'} \quad (9)$$

$$\partial_t = \partial_{t'} - \mathbf{v} \cdot \partial_{\mathbf{r}'} \quad (10)$$

respectively, where $\partial_{\mathbf{r}}$ symbolizes the Nabla operator, and applied to a vector, creates a dyadic. Note that (10*) coincides with the well known “material” or “moving” derivative used in continuum mechanics. Furthermore, taking $c \rightarrow \infty$ renders (9), (10), as a Galilean transformation with $\partial_{\mathbf{r}'} = \partial_{\mathbf{r}}$.

Integrating the differential relations (3), (4) yields the global relations

$$\mathbf{r}' = \mathbf{r} - \int^t \mathbf{v}(\bar{t})d\bar{t} \quad (11)$$

$$t' = t - c^{-2}\mathbf{v}(t) \cdot \mathbf{r} = t - c^{-2}|\mathbf{v}(t)|\xi \quad (12)$$

where \bar{t} denotes the dummy integration variable and ξ is a coordinate in the direction of the velocity at a given time t . Differentiating (11), (12), with respect to t , ξ , respectively, using the Leibnitz rule of differentiating integrals yields

$$d\mathbf{r}'/dt = d\mathbf{r}/dt - \mathbf{v}(t) \quad (13)$$

$$dt'/d\xi = dt/d\xi - c^{-2}|\mathbf{v}(t)| \quad (14)$$

and multiplying (13), (14) by dt , $d\xi$, respectively retrieves (3), (4).

For constant \mathbf{v} , substituting (9), (10) into the Maxwell Equations (ME)

$$\partial_{\mathbf{r}} \times \mathbf{E} = -\partial_t \mathbf{B}, \quad \partial_{\mathbf{r}} \times \mathbf{H} = \partial_t \mathbf{D}, \quad \partial_{\mathbf{r}} \cdot \mathbf{D} = 0, \quad \partial_{\mathbf{r}} \cdot \mathbf{B} = 0 \quad (15)$$

and collecting terms yields the ME in another reference frame as

$$\partial_{\mathbf{r}'} \times \mathbf{E}' = -\partial_{t'} \mathbf{B}', \quad \partial_{\mathbf{r}'} \times \mathbf{H}' = \partial_{t'} \mathbf{D}', \quad \partial_{\mathbf{r}'} \cdot \mathbf{D}' = 0, \quad \partial_{\mathbf{r}'} \cdot \mathbf{B}' = 0 \quad (16)$$

subject to the FO Field Transformations (FT)

$$\mathbf{E}' = \mathbf{E} + \mathbf{v} \times \mathbf{B}, \quad \mathbf{B}' = \mathbf{B} - \mathbf{v} \times \mathbf{E}/c^2, \quad \mathbf{D}' = \mathbf{D} + \mathbf{v} \times \mathbf{H}/c^2, \quad \mathbf{H}' = \mathbf{H} - \mathbf{v} \times \mathbf{D} \quad (17)$$

For variable $\mathbf{v}(t)$ we substitute (11), (12), into (7), (8), to derive (cf. (9), (10))

$$\partial_{\mathbf{r}} = \partial_{\mathbf{r}'} - c^{-2}\mathbf{v}(t)\partial_{t'} \quad (18)$$

$$\partial_t = \partial_{t'} - \mathbf{v}(t) \cdot \partial_{\mathbf{r}'} \quad (19)$$

Now upon substitution of (18), (19) into the ME (15), we encounter terms like

$$\mathbf{v}(t')\partial_{t'} \times \mathbf{E} = \partial_{t'}(\mathbf{v}(t') \times \mathbf{E}) - (\partial_{t'}(\mathbf{v}(t'))) \times \mathbf{E} \quad (20)$$

Because of the additional term $\partial_{t'}(\mathbf{v}(t'))$ we cannot extend (17) to $\mathbf{v}(t)$. However, it is noted that that field time derivatives as in $\partial_{t'} \times \mathbf{E}$ involve the wave frequencies, say ω , while $\partial_{t'}(\mathbf{v}(t'))$ involves the mechanical frequencies Ω_i as in (1), (2). Provided Ω_i is much smaller than ω , the term $\partial_{t'}(\mathbf{v}(t'))$ (20) is negligible and the field transformations (17) are valid for $\mathbf{v}(t)$ as well.

2. PLANE WAVES

Plane waves are characterized by constant vector amplitudes obeying the pertinent FT, in our case (17). Space and time variations are delegated to the appropriate phase exponentials $e^{i\theta} = e^{i\theta'}$, hence the invariance of the phase follows by definition

$$\theta(\mathbf{r}, t) = \theta'(\mathbf{r}', t') \quad (21)$$

although in general the phase is not form-invariant.

The initial incident plane wave is given in the “laboratory” unprimed reference system

$$\begin{aligned} \mathbf{E} &= \hat{\mathbf{z}}E_0e^{i\theta}, & \mathbf{H} &= -\hat{\mathbf{y}}H_0e^{i\theta}, & E_0/H_0 &= (\mu_0/\varepsilon_0)^{1/2} \\ \theta &= kx - \omega t = kr \cos \varphi - \omega t, & \omega/k &= c = (\mu_0\varepsilon_0)^{-1/2} \end{aligned} \quad (22)$$

propagating in free space (vacuum) in direction $\hat{\mathbf{x}}$, with the \mathbf{E} -field polarized along the cylindrical axis $\hat{\mathbf{z}}$. The constitutive relations in free space are

$$\mathbf{D} = \varepsilon_0\mathbf{E}, \quad \mathbf{B} = \mu_0\mathbf{H}, \quad \mathbf{D}' = \varepsilon_0\mathbf{E}', \quad \mathbf{B}' = \mu_0\mathbf{H}' \quad (23)$$

By substitution of (23) in (17), the FT reduce to two equations

$$\mathbf{E}' = \mathbf{E} + \mu_0\mathbf{v}(t) \times \mathbf{H}, \quad \mathbf{H}' = \mathbf{H} - \varepsilon_0\mathbf{v}(t) \times \mathbf{E} \quad (24)$$

where \mathbf{v} is chosen in the xy -plane according to (1) with $v_{0z} = 0$. Accordingly

$$\mathbf{E}' = \hat{\mathbf{z}}(1 - \beta_{0x} \cos \Phi_x)E_0e^{i\theta}, \quad \beta_{0x} = v_{0x}/c \quad (25)$$

$$\mathbf{H}' = -\hat{\mathbf{y}}H_0e^{i\theta}(1 - \beta_{0x} \cos \Phi_x) - \hat{\mathbf{x}}H_0e^{i\theta}\beta_{0y} \cos \Phi_y, \quad \beta_{0y} = v_{0y}/c \quad (26)$$

For arbitrary direction of propagation α (22) is replaced by

$$\begin{aligned} \mathbf{E} &= \hat{\mathbf{z}}E_0e^{i\theta}, & \mathbf{H} &= -\hat{\mathbf{y}} \cos \alpha H_0e^{i\theta} + \hat{\mathbf{x}} \sin \alpha H_0e^{i\theta} \\ \theta &= \mathbf{k} \cdot \mathbf{r} - \omega t = k_x x + k_y y - \omega t, & k_x &= k \cos \alpha, \quad k_y = k \sin \alpha \end{aligned} \quad (27)$$

According to (24), replace (25), (26), by

$$\mathbf{E}' = \hat{\mathbf{z}}E_0e^{i\theta}(1 - \beta_{0x} \cos \alpha \cos \Phi_x - \beta_{0y} \sin \alpha \cos \Phi_y) \quad (28)$$

$$\mathbf{H}' = -\hat{\mathbf{y}}H_0e^{i\theta}(\cos \alpha - \beta_{0x} \cos \Phi_x) + \hat{\mathbf{x}}H_0e^{i\theta}(\sin \alpha - \beta_{0y} \cos \Phi_y) \quad (29)$$

The phase for arbitrary direction of propagation is found from (21), (27), (11*), (12*)

$$\begin{aligned} \theta' &= \mathbf{k} \cdot \mathbf{r}' + \kappa_x \sin \Phi_x + \kappa_y \sin \Phi_y - \omega t' - (\hat{\mathbf{x}}C_x \cos \Phi_x + \hat{\mathbf{y}}C_y \cos \Phi_y) \cdot \mathbf{r}' \\ \kappa_i &= k_i v_{0i} / \Omega_i = A_i k_i, \quad C_i = \omega c^{-2} v_{0i} = k \beta_{0i}, \quad i = x, y \end{aligned} \quad (30)$$

where κ_i is of the order A_i/λ , the mechanical amplitude normalized to the wavelength, which is finite but not necessarily small, and C_i is FO in the velocity it follows that for distances satisfying r' much smaller than A_i/β_{0i} , (30) can be approximated by

$$\theta' = \mathbf{k} \cdot \mathbf{r}' + \kappa_x \sin \Phi_x + \kappa_y \sin \Phi_y - \omega t', \quad r' \ll A_i/\beta_{0i} \quad (31)$$

3. SCATTERING BY CIRCULAR CYLINDERS

For the incident wave (22) we have in (30) $\kappa_y = 0$. For simplicity we also assume presently $\psi_i = 0$. Furthermore, we assume the approximation (31) to hold, hence (25), (31) reduce to

$$\mathbf{E}' = \hat{\mathbf{z}}PE_0e^{i\theta'}, \quad P = 1 - \beta_{0x} \cos \Omega_x t', \quad \theta' = \mathbf{k} \cdot \mathbf{r}' + \kappa_x \sin \Omega_x t' - \omega t' \quad (32)$$

Recasting (32) in terms of a Bessel-Fourier series (e.g., see [8]) yields

$$\begin{aligned} \mathbf{E}' &= \hat{\mathbf{z}}PE_0e^{i\theta'} = \hat{\mathbf{z}}PE_0e^{i\mathbf{k} \cdot \mathbf{r}' - i\omega t'} \sum_n J_n e^{in\Omega_x t'} = \hat{\mathbf{z}}PE_0 \sum_n J_n e^{i\mathbf{k} \cdot \mathbf{r}' - i\omega'_n t'} \\ \omega'_n &= \omega - n\Omega_x, \quad \sum_n = \sum_{n=-\infty}^{\infty}, \quad J_n = J_n(\kappa_x) \end{aligned} \quad (33)$$

Furthermore, by recasting $P = 1 - \beta_{0x}(e^{i\Omega_x t'} + e^{-i\Omega_x t'})/2$ and rearranging the series, we obtain

$$\mathbf{E}' = \hat{\mathbf{z}}E_0 \Sigma_n e^{i\mathbf{k}\cdot\mathbf{r}' - i\omega'_n t'} \bar{J}_n, \quad \bar{J}_n = (J_n - \beta_{0x}(J_{n-1} + J_{n+1})/2) = (1 - \beta_{0x}n/\kappa_x)J_n \quad (34)$$

In (33), (34), we obtain a discrete spectrum of frequencies ω'_n , with sidebands separated by the mechanical frequency Ω_x . The reason for the absence of Ω_y is due to the specific choice of the direction of the incident wave (22). For scattering by a circular cylinder of radius a we now encounter the classical canonical problem for each discrete spectral component ω'_n . Without delving into specific scattering problems (e.g., see [9]), it is assumed that the scattered wave must satisfy the boundary conditions, and the wave equation, for each individual excitation frequency, and is therefore represented in the exterior domain $r' \geq a$ as

$$\begin{aligned} \mathbf{E}'_s &= \hat{\mathbf{z}}E_0 \Sigma_{nm} a_{m,n} K_{m,n} e^{-i\omega'_n t'}, \quad \Sigma_{nm} = \Sigma_n \Sigma_m, \quad K_{m,n} = \bar{J}_n i^m H_{m,n} e^{im\varphi'} \\ H_{m,n} &= H_m(k'_n r'), \quad k'_n = \omega'_n/c \end{aligned} \quad (35)$$

where $H_m = H_m^{(1)}$ are the first kind Hankel functions, and $a_{m,n}$ denote the scattering coefficients for each circular mode and frequency m , n , respectively.

Using the Sommerfeld integral representation (e.g., see [8]) for the cylindrical functions, (35) is recast as a superposition of plane waves

$$\begin{aligned} \mathbf{E}'_s &= \hat{\mathbf{z}}E_0 \Sigma_n \bar{J}_n \frac{1}{\pi} \int_{\varphi' - (\pi/2) + i\infty}^{\varphi' + (\pi/2) - i\infty} e^{i\theta'_n g'_n(\tau')} d\tau' \sim \hat{\mathbf{z}}E_0 \Sigma_n (2/i\pi k'_n r')^{1/2} \bar{J}_n e^{ik'_n r' - i\omega'_n t'} g'_n(\varphi') \\ \theta'_n &= \mathbf{k}'_n \cdot \mathbf{r}' - \omega'_n t' = k'_n r' \cos(\varphi' - \tau') - \omega'_n t', \quad g'_n(\varphi') = \Sigma_m a_{m,n} e^{im\varphi'} \end{aligned} \quad (36)$$

The far field in (36) asymptotically becomes an outgoing cylindrical wave governed for each frequency by the scattering amplitude $g'_n(\varphi')$.

In the integrand (36) we have plane waves propagating in complex directions τ' , with appropriate amplitudes $g'_n(\tau')$. Substituting (24*) in (36) leads to (28*), (30*) for each plane wave in (36), becoming the scattered wave *measured* in the initially (unprimed) reference frame, but still expressed in terms of the primed system of reference *coordinates*

$$\begin{aligned} \mathbf{E}_s &= \hat{\mathbf{z}}E_0 \Sigma_n \bar{J}_n \frac{1}{\pi} \int_{\varphi' - (\pi/2) + i\infty}^{\varphi' + (\pi/2) - i\infty} e^{i\theta'_n g_n(\tau')} d\tau', \quad g'_n(\tau') = \Sigma_m a_{m,n} e^{im\tau'} \\ g_n(\tau') &= g'_n(\tau') (1 + \beta_{0x} \cos \tau' \cos \Omega_x t' + \beta_{0y} \sin \tau' \cos \Omega_y t') \end{aligned} \quad (37)$$

It is noted that Ω_y featuring in (37) results from (24*), although it does not feature in (32), due to the special direction $\alpha = 0$ presently chosen for the incident wave.

Expressing $\cos \tau'$, $\sin \tau'$, in terms of exponentials and rearranging the series, we find

$$\begin{aligned} \mathbf{E}_s &= \hat{\mathbf{z}}E_0 \Sigma_n \bar{J}_n \frac{1}{\pi} \int_{\varphi' - (\pi/2) + i\infty}^{\varphi' + (\pi/2) - i\infty} e^{i\theta'_n g_n(\tau')} d\tau', \quad g_n(\tau') = \Sigma_m A_{m,n} e^{im\tau'} \\ A_{m,n} &= a_{m,n} + \cos \Omega_x t' \beta_{0x} (a_{m-1,n} + a_{m+1,n})/2 - i \cos \Omega_y t' \beta_{0y} (a_{m-1,n} - a_{m+1,n})/2 \end{aligned} \quad (38)$$

where the new coefficients $A_{m,n}$ are still time dependent, but this has no effect on the Sommerfeld integral representation. Therefore, by inspection of (35), (36), we recast (38) as

$$\mathbf{E}_s = \hat{\mathbf{z}}E_0 \Sigma_{nm} A_{m,n} K_{m,n} e^{-i\omega'_n t'} \quad (39)$$

The time dependent $A_{m,n}$ contribute to the spectrum. Rearranging indices in (39) it is recast as

$$\begin{aligned} \mathbf{E}_s &= \hat{\mathbf{z}}E_0 \Sigma_{nm} e^{-i\omega'_n t'} \left(L_{m,n} - iK_{m,n} \left(e^{i\Omega_y t'} + e^{-i\Omega_y t'} \right) \beta_{0y} (a_{m-1,n} - a_{m+1,n})/4 \right) \\ L_{m,n} &= K_{m,n} a_{m,n} + \beta_{0x} (K_{m,n-1} a_{m-1,n-1} + K_{m,n-1} a_{m+1,n-1} + K_{m,n+1} a_{m-1,n+1} \\ &\quad + K_{m,n+1} a_{m+1,n+1})/4 \end{aligned} \quad (40)$$

A choice of an obliquely incident wave (27) instead of (22) would have resulted in more symmetrical expressions with respect to Ω_x , Ω_y , but considerably complicating the mathematical manipulations.

In order to express \mathbf{E}_s exclusively in terms of unprimed coordinates one has to substitute (11), (12) into (39), (40) using the velocity (1) relevant to the present case

$$\mathbf{r}' = \mathbf{r} - (\hat{\mathbf{x}}A_x \sin \Omega_x t + \hat{\mathbf{x}}A_y \sin \Omega_y t) \quad (41)$$

$$t' = t - c^{-2} (\hat{\mathbf{x}}v_{0x} \cos \Omega_x t + \hat{\mathbf{y}}v_{0y} \cos \Omega_y t) \cdot \mathbf{r} \quad (42)$$

At distances large compared to the motional amplitudes A_x , A_y we approximate $r' = r$, and $\varphi' = \varphi$, and for all FO terms in β we approximate $t' = t$, yielding in (40)

$$\mathbf{E}_s = \hat{\mathbf{z}}E_0 \Sigma_{nm} \left[e^{-i\omega'_n t + ik'_n x \beta_{0x} \cos \Omega_x t + ik'_n y \beta_{0y} \cos \Omega_y t} (L_{m,n} - iK_{m,n} (e^{i\Omega_y t} + e^{-i\Omega_y t})) \beta_{0y} (a_{m-1,n} - a_{m+1,n}) / 4 \right] \quad (43)$$

Once again exponentials in (43) are expressed in terms of Bessel-Fourier series [8]

$$\mathbf{E}_s = \hat{\mathbf{z}}E_0 \Sigma_{nmpq} S_{p,q,n} e^{-i\omega_{n,p,q} t} (L_{m,n} - iK_{m,n} (e^{i\Omega_y t} + e^{-i\Omega_y t})) \beta_{0y} (a_{m-1,n} - a_{m+1,n}) / 4 \quad (44)$$

$$S_{p,q,n} = i^{p+q} J_p(k'_n x \beta_{0x}) J_q(k'_n y \beta_{0y}), \quad \omega_{n,p,q} = \omega'_n - p\Omega_x - q\Omega_y$$

Next $\cos \Omega_y t$ in $A_{m,n}$ is expressed in terms of exponentials and series indices adjusted, finally becoming

$$\mathbf{E}_s = \hat{\mathbf{z}}E_0 \Sigma_{nmpq} Q_{n,m,p,q} e^{-i\omega_{n,p,q} t} \quad (45)$$

$$Q_{n,m,p,q} = S_{p,q,n} L_{m,n} - iK_{m,n} (S_{p,q-1,n} + S_{p,q+1,n}) \beta_{0y} (a_{m-1,n} - a_{m+1,n}) / 4$$

clearly showing the spectral content of the scattered wave.

Subject to the approximations stated above, (45) concludes the derivation of the scattered wave for the present case.

4. DISCUSSION AND CONCLUDING REMARKS

A general discussion of scattering of EM waves by objects moving periodically and quasi periodically on Bowditch-Lissajous trajectories is presented, and the implementation to a relatively simple problem is analyzed.

SR is restricted to LT involving constant velocities. One thus encounters the problem of employing an adequate theory. Rather than assuming Galilean physics, here an attempt is made to approximate the LT for varying time dependent velocity with the QLT which in the limiting case of constant velocity becomes a LT to the FO in the velocity.

The feasibility of implementing the model is demonstrated. It is shown that the scattered wave spectrum is discrete, involving the initial carrier frequency, and sidebands at frequencies which are harmonics of the mechanical motion frequencies.

The information provided by the scattered wave facilitates the remote sensing of the motion of vibrating and orbiting objects, as often encountered in engineering and applied science.

REFERENCES

1. Lissajous, J. A., *Mémoire Sur L'étude Optique des Mouvements Vibratoires*, Annales de Chimie et de Physique, 3rd Série, Vol. 51, 140–231, 1849.
2. Deprit, A., "The lissajous transformation, I. Basics," *Celestial Mechanics and Dynamical Astronomy*, Vol. 51, 201–225, 1991.
3. Deprit, A. and A. Elipe, "The lissajous transformation, II. Normalization," *Celestial Mechanics and Dynamical Astronomy*, Vol. 51, 227–250, 1991.
4. Van Bladel, J., *Relativity and Engineering*, Springer, 1984.
5. Censor, D., "Non-relativistic scattering: Pulsating interfaces," *Progress In Electromagnetics Research*, Vol. 54, 263–281, 2005.
6. Censor, D., "The need for a first-order quasi lorentz transformation," *Proceedings of the 2nd International Conference AMiTaNS'10, AIP Conference Proceedings*, Vol. 1301, 3–13, Sozopol, Bulgaria, Jun. 21–26, 2010.
7. Einstein, A., "Zur elektrodynamik bewegter Körper," *Ann. Phys. Lpz.*, Vol. 17, 891–921, 1905; English Translation: "On the Electrodynamics of moving bodies," *The Principle of Relativity*, Dover, 1905.
8. Stratton, J. A., *Electromagnetic Theory*, McGraw-Hill, 1941.
9. Censor, D., "The mathematical elements of relativistic free-space scattering," *Journal of Electromagnetic Waves and Applications*, Vol. 19, No. 7, 907–923, 2005.

The Model of Wave Propagation in Classical Physics

Siwei Luo

Southern Illinois University, USA

Abstract— The model of wave propagation is a way to help understand and predict the behavior of wave and the principle of wave propagation. Even though there are a lot of different models and theories aiming to explain wave propagation phenomena, still there is some room for making progress in classical physics under a specific condition, especially, in the field of the electromagnetic waves. In classical physics theory, it is assumed that a wave with a specific frequency has always the same velocity in the same medium, regardless of the velocity of wave source. And the wave has different velocities in different reference systems. Four different circumstances that the source is moving, the medium is moving, both the source and the medium are moving and the wave is in different references systems are analyzed. These results of calculation on the subjects that moving source and moving medium are consistent with conclusions of Doppler effects. In particular, the paper expresses these assumptions in the technique of simple mathematical methods and partial differential equations to make it more straightforward comprehensible and systematic method in explaining these phenomena. Based on these two assumptions, from a different perspective, the paper tries to present an explanation of Michelson-Morley experiment and Fizeau experiment by classical physics theory. Additionally, according to the result of new experiment of neutrino, the main differences between classical physics and modern physics in the field of electrodynamics theory are briefly discussed. Hopefully, it would lead to a more profound calculation and modeling about this subject.

1. INTRODUCTION

From the perspective of Michelson-Morley experiment result, the earth is somehow static relative to the medium of light. If we think about the medium might be the air, then everything would be easily understand by classical physics. This article is to emphasize the application of classical model in moving medium situation. To develop the knowledge about moving medium, roles of wave source, medium and reference systems are further discussed.

2. POSTULATES

It is assumed that a wave with a specific frequency has always the same velocity in the same medium, regardless of the velocity of the wave source. Generally speaking, the same wave has different velocities in different reference systems [1].

3. MICHELSON-MORLEY EXPERIMENT

There is a brief introduction about background the null result of Michelson-Morley experiment. It was believed that there is a special reference system for light wave in the model of aether medium. The Michelson-Morley Experiment is designed to determine the velocity of the earth relative to aether medium [2].

v_m — the velocity of medium relative to the ground reference system; v_c — the velocity of light wave in respect of its medium; l — the length between semi-silvered mirror and mirror A (the

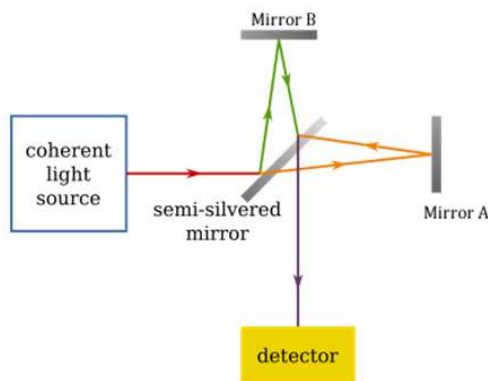


Figure 1: The equipment of Michelson-Morley Experiment [3].

same length between semi-silvered mirror and mirror B); t_{S-MA-S} — the time that a light wave propagate from semi-silvered mirror to mirror A and reflect to semi-silvered mirror; t_{S-MB-S} — the time that a light wave propagate from semi-silvered mirror to mirror B and reflect to semi-silvered mirror.

In aether dragging theory [4],

$$t_{S-MA-S} = \frac{l}{v_c - v_m} + \frac{l}{v_c + v_m} \quad (1)$$

$$t_{S-MB-S} = \frac{2l}{\sqrt{v_c^2 - v_m^2}} \quad (2)$$

$$\Delta t = t_{S-MA-S} - t_{S-MB-S} \neq 0 \quad (3)$$

Δt tells the velocity of aether relative to the ground reference system. However, the observation of Michelson-Morley experiment is not as expected, there is no movement of light interference fringe, which leads to another conclusion that

$$\Delta t = t_{S-MA-S} - t_{S-MB-S} = 0 \quad (4)$$

That is, there is a contradiction in this theory: people expect there is relative speed between the earth and the medium, however, somehow, it doesn't.

Recall the assumptions in classical physics; a wave with a specific frequency has always the same velocity in the same medium, regardless the movement of the wave source.

Aether is not the medium of light wave in Michelson-Morley experiment. In fact, the AIR is the medium of light in this experiment. Equipment of Michelson-Morley experiment was exposure to the AIR.

More importantly, the AIR is always static to the earth. Namely, the velocity of the air is always zero relative to the earth:

$$v_m = 0 \quad (5)$$

$$t_{S-MA-S} = \frac{l}{v_c - v_m} + \frac{l}{v_c + v_m} = \frac{l}{v_c} + \frac{l}{v_c} = \frac{2l}{v_c} \quad (6)$$

$$t_{S-MB-S} = \frac{2l}{v_c} \quad (7)$$

$$\Delta t = t_{S-MA-S} - t_{S-MB-S} = 0$$

And this is likely the reason no matter when and where we repeat the Michelson-Morley experiment in the atmosphere that we never observe the movement of light fringe.

4. ROLES OF WAVE SOURCE AND MEDIUM

After the analysis of null result of Michelson-Morley experiment, it is time to systematically discuss the roles of wave source and medium in wave propagation and their effects.

U — quantity; A — amplitude of a wave; v_s — the velocity of wave source relative to a reference system; φ_0 — the initial phase of oscillation; ω_0 — circular frequency of wave source oscillation;

4.1. Wave Source is in Motion and Wave Medium is Static

Wave equation:

$$U_{tt} - v_c^2 U_{xx} = 0 \quad (8)$$

To determine the boundary condition, assume the initial position of wave source is at x -axis origin point. For mathematical simplicity, assume the direction of velocity of wave source is along the positive direction of x -axis and boundary condition of wave source is

$$U = A \sin(\omega_0 t + \varphi_0) \quad (9)$$

The domain of the function is $[-v_c t, v_c t]$. We have three boundary conditions: the point of wave source and two points at the furthest points the wave propagate.

$$U(v_s t, t) = A \sin(\omega_0 t + \varphi_0) \quad (10)$$

$$U(v_c t, t) = A \sin \varphi_0 \quad (11)$$

$$U(-v_c t, t) = A \sin \varphi_0 \quad (12)$$

The solution of this wave equation U_1 and U_2 :

$$U_1 = A \sin \left(\frac{v_c}{v_c - v_s} \omega_0 t - \frac{1}{v_c - v_s} \omega_0 x + \varphi_0 \right) \quad (13)$$

Solution U_1 represents the wave that propagates to the positive direction of x -axis;

$$U_2 = A \sin \left(\frac{v_c}{v_c + v_s} \omega_0 t + \frac{1}{v_c + v_s} \omega_0 x + \varphi_0 \right) \quad (14)$$

Solution U_2 represents the wave that propagates to the negative direction of x -axis.

In golf paradox, when the ball is seen as wave source, suppose there is an observer on the direction of the ball flying, the observer will see the ball was static at the origin point first and then flying. This order would not change. Based on the result of U_1 and U_2

$$v = -\frac{\partial U_{1,2}}{\partial t} \bigg/ \frac{\partial U_{1,2}}{\partial x} = \pm v_c \neq v_c + v_s \quad (15)$$

According to the solution of wave equations U_1 and U_2 , when $v_s = 0$, frequency of wave

$$f_0 = \frac{\omega_0}{2\pi} \quad (16)$$

When $v_s \neq 0$, frequency of wave

$$f_{1,2} = \frac{v_c}{v_c \mp v_s} \frac{\omega_0}{2\pi} = \frac{v_c}{v_c \mp v_s} f_0 \quad (17)$$

It represents frequency of wave is a function of v_s . This result is consistent with our knowledge of Doppler effects in the situation that wave source is in motion and observer is static [5, 6]. The movement of the wave source has no effects on the velocity of the wave propagation, while it would affect the frequency of the wave — Doppler effects [6, 7].

5. WAVE MEDIUM IS IN MOTION AND WAVE SOURCE IS STATIC

To simplify the calculation, assume the velocity of the wave medium is to the positive direction of x -axis. On positive direction with the domain $[0, (v_m + v_c)t]$, wave equation is

$$U_{tt} - (v_m + v_c)^2 U_{xx} = 0 \quad (18)$$

On negative direction with the domain $[(v_m - v_c)t, 0]$, that is

$$U_{tt} - (v_m - v_c)^2 U_{xx} = 0 \quad (19)$$

Boundary conditions

$$U(0, t) = A \sin(\omega_0 t + \varphi_0) \quad (20)$$

$$U((v_m + v_c)t, t) = A \sin \varphi_0 \quad (21)$$

$$U((v_m - v_c)t, t) = A \sin \varphi_0 \quad (22)$$

Correspondingly, solutions U_3 and U_4 :

$$U_3 = A \sin \left(\omega_0 t - \frac{1}{v_m + v_c} \omega_0 x + \varphi_0 \right) \quad (23)$$

$$U_4 = A \sin \left(\omega_0 t - \frac{1}{v_m - v_c} \omega_0 x + \varphi_0 \right) \quad (24)$$

The Fizeau experiment [7, 8] is to measure relative speeds of light in medium. Medium in motion has dragging effects on the velocity of wave propagation. This effect can be detected by Fizeau experiment theoretically. However, in most circumstance, the light velocity is far bigger than the velocity of medium which is negligible to the light velocity. That is why it is really hard to observe the light interference fringe movement.

Still, if analysis above is correct, the Fresnel drag coefficient is 1 rather than $1 - \frac{1}{n^2}$ [9]. Then the light velocity relative to ground reference system is

$$v = \frac{c}{n} \pm v_m = v_c \pm v_m \quad (25)$$

6. BOTH WAVE SOURCE AND WAVE MEDIUM ARE IN MOTION

Same way, assume the velocity of both wave source and wave medium are to the positive direction of x -axis. On positive direction with the domain $[v_s t, (v_m + v_c)t]$, wave equation is

$$U_{tt} - (v_m + v_c)^2 U_{xx} = 0$$

On negative direction with the domain $[(v_m + v_c)t, v_s t]$,

$$U_{tt} - (v_m - v_c)^2 U_{xx} = 0$$

Boundary conditions

$$\begin{aligned} U(v_s t, t) &= A \sin(\omega_0 t + \varphi_0) \\ U((v_m + v_c)t, t) &= A \sin \varphi_0 \\ U((v_m - v_c)t, t) &= A \sin \varphi_0 \end{aligned}$$

Solutions U_5 and U_6 :

$$U_5 = A \sin \left(\frac{v_m + v_c}{v_m + v_c - v_s} \omega_0 t - \frac{1}{v_m + v_c - v_s} \omega_0 x + \varphi_0 \right) \quad (26)$$

$$U_6 = A \sin \left(\frac{v_m - v_c}{v_m - v_c - v_s} \omega_0 t - \frac{1}{v_m - v_c - v_s} \omega_0 x + \varphi_0 \right) \quad (27)$$

7. DIFFERENT INERTIAL REFERENCE SYSTEMS

In classical physics theory, wave propagation should satisfy the Galileo transformation.

Suppose there are two inertial reference system K and K' with coordinates (x, y, z, t) and (x', y', z', t') . According to inertial reference system K , the relative speed of K' is v_r and its direction is to the positive x -axis of inertial system K [9].

Galileo transformation [10]

$$\begin{cases} x' = x - v_r t \\ y' = y \\ z' = z \\ t' = t \end{cases} \quad (28)$$

Electromagnetism wave equations under Galileo transformation

In the inertial reference system K , if both reference and medium is static and relative speed of electromagnetism wave is v_c , then equations are

$$\nabla^2 E - \frac{1}{v_c^2} \frac{\partial^2 E}{\partial t^2} = 0 \quad (29)$$

In the inertial reference system K'

$$\nabla^2 E - \frac{1}{(v_c \pm v_r)^2} \frac{\partial^2 E}{\partial t^2} = 0 \quad (30)$$

Furthermore, if it is in vacuum in static reference system K , the electromagnetism wave equations are

$$\nabla^2 E - \frac{1}{c^2} \frac{\partial^2 E}{\partial t^2} = 0 \quad (31)$$

The Maxwell equations are not invariant in Galileo transformation. It claims that electromagnetism waves propagate with different velocities in respect to different reference systems.

8. TEST EXPERIMENT AND PREDICTION

There are two boxes A and B with the same shape and the same volume but A is full of medium and B is absolutely vacuum. Two boxes have the same velocity. There is a light source in middle of each box. At the same time light sources are turned on and light waves propagate in two directions left and right.

Box A:

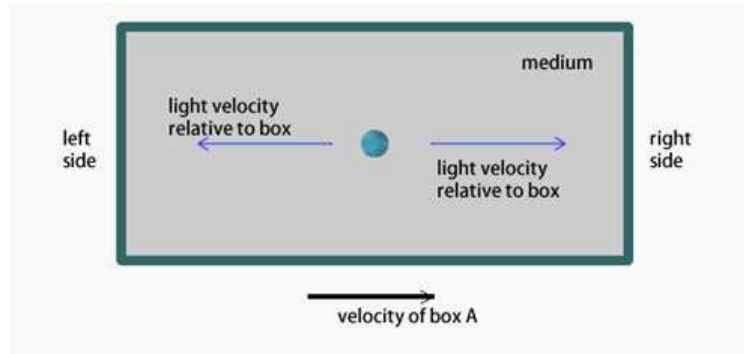


Figure 2: A light wave propagates in Box A.

t_1 — the time that the light reaches the left side of the box; t_2 — the time that the light reaches the right side of the box; l' — the length of Box A (the same length of Box B); c — the velocity that light waves propagate in vacuum; v_{box} — the velocity of Box A (the same velocity of Box B), the direction is to right;

$$t_1 = t_2 = \frac{l'}{2v_c}$$

$$\Delta t = t_2 - t_1 = 0$$

In Box A, we cannot determine the velocity of box based on Δt .

Box B:

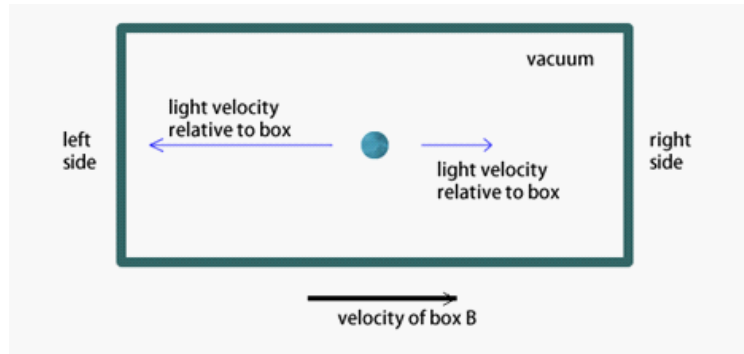


Figure 3: A light wave propagates in Box B.

$$t_1 = \frac{l'}{2(c + v_{box})}$$

$$t_2 = \frac{l'}{2(c - v_{box})}$$

$$\Delta t = t_2 - t_1 = \frac{l'}{2(c - v_{box})} - \frac{l'}{2(c + v_{box})} = \frac{v_{box}l'}{c^2 - v_{box}^2}$$

$$v_{box} = \frac{-l' \pm \sqrt{l'^2 + 4\Delta t^2 c^2}}{2\Delta t}$$

Based on this logic, v_{box} is a function of Δt , so that it can be used to determine the velocity of box B from Δt .

9. GALILEO RELATIVITY

Furthermore, Box B can be seen as an inertial reference system. It could be used to determine the difference between two inertial reference systems with different velocities.

In another words, if two inertial reference systems have different velocities, then these two inertial reference systems should be different from each other because of their different velocities. More importantly, their velocity should be detectable by the method above.

10. CONCLUSIONS

In classical physics theory, there are two conclusions as below:

1. A wave with a specific frequency has always the same velocity in respect to the same medium, regardless of the movement of the wave source, and has different velocities in respect to different reference system.
2. Different inertial reference systems with different velocity have different characteristics.

REFERENCES

1. Luo, S., “The principle of electromagnetic wave transmission in classical physics theory,” *Chinese Journal of Spectroscopy Laboratory*, Vol. 28, No. 5, 2521, Sep. 2011.
2. Michelson, A. A., *Am. J. Sci.*, 120, Aug. 22, 1881.
3. http://en.wikipedia.org/wiki/Michelson-Morley_experiment.
4. Zu, D., *Electrodynamics*, 252–254, Tsinghua University Press, Beijing, Sep. 2006, (reprint 2007).
5. Qi, A. and C. Du, *General Physics: Mechanics*, 2nd Edition, 366–368, Higher Education Press, 2005.
6. Tilley, D. E., *Contemporary College Physics*, Benjamin/Cummings Pub. Co., 469–470, 1979.
7. Frecks, J., “Fizeau’s research program on ether drag: A long quest for a publishable experiment,” *Jan. Physics in Perspective*, Vol. 7, No. 1, 35–65, Mar. 2005.
8. Su, C.-C., “Reinterpretation of Fizeau’s experiment with moving medium in accord with the sagnac effect due to Earth’s rotation,” *Journal of Electromagnetic Waves and Application*, Vol. 19, No. 4, 559–567, 2005.
9. Yin, B., “The new explanation of Fizeau experiment,” *Invention and Innovation*, Vol. 3, 28, 2005.
10. Jackson, J. D., *Classical Electrodynamics*, 3rd Edition, 515, Wiley Edition, New York, 1999, (reprint 2011).
11. Lisa, G., “Neutrino point to a new reality,” *New Scientist*, Vol. 212, No. 2832, 6–9, Oct. 1, 2011.

Prediction of a New Superconductivity-like Effect in Galilean Reference Systems (Part I)

Namık Yener

Technology Faculty, Kocaeli University, Izmit, Kocaeli 41380, Turkey

Abstract— Prediction of a hitherto unknown superconductivity-like effect is made which is independent of temperature, but rather requires Galilean reference systems moving at the speed of light in vacuum. As the medium (I) to which the laboratory frame is attached a Lorentz medium is selected whereas for medium (II) to which the rest frame is attached, a perfectly conducting medium is selected. The interface is an infinite plane perpendicular to the uniform rectilinear motion involved. The fact that the Lorentz medium appears as a metal when observed from the rest frame, is unearthed in a previously reported work by the same author. Next the limit condition which in effect requires attainment of speed of light in vacuum by the uniform rectilinear motions of the Galilean reference systems is considered, and the effective permittivity function of medium (I) observed from the rest frame is found to have a character similar to that of a superconductor. It should be stressed that the fundamental premise of the work is Lorentzian relativistic transformation and not Galilean relativistic transformation under which the permittivity function could have been invariant. This work is presented in a series of two papers. In Part (I) the models for medium (I) observed from the laboratory frame and the rest frame are presented. In Part (II) the prediction of the new superconductivity-like effect is made and equations with the same structure as London equations in a superconductor are presented. The second part also contains a discussion section on the verification of the ideas developed from the point of view of Lorentz transforms.

1. INTRODUCTION

The purpose of this work is to show that a medium that behaves as a causally dispersive dielectric medium with absorption as described by the Lorentz medium when observed from the laboratory frame behaves as a metal represented by the Drude model when observed from the rest frame and furthermore that this quality of behavior as a metal can be converted to a superconductivity-like state if the relevant Galilean reference systems attain relative speeds that approach the speed of light in vacuum [1].

The derivation in this paper is based on the ‘modified Lorentz transformation’ which incorporates two different speeds of light in vacuum for the inertial frames and for which the reader is referred to [2]. Nevertheless even if the same speeds of light in vacuum are assumed for the two Galilean frames one still will obtain similar fundamental results, if not the same. However because as shown in [3] the Special Relativity Theory falls short of accounting for the loss in medium (I), it was seen necessary to use the *modified* Lorentz transformation in this paper. One constraint that follows from the modified or non-modified classical Lorentz transform is that the frequency observed from the rest frame is pure imaginary. This constraint will be treated in a future publication.

The result of this paper is an extension of the results of [3]. The metallic behavior observed from the rest frame was implicitly obtained in this reference. It is now revealed that this metallic behavior will be a superconductivity-like state when the relative speed of the frames approaches the speed of light in vacuum. We use the term superconductivity-like effect just because of the similarity of the appearance of one medium to which is attached a Galilean reference system, to a superconductor so far as the permittivity function is considered. Otherwise the physical requirement by which this permittivity function takes effect has nothing to do with the corresponding requirements of a proper superconductivity state.

2. THE MODEL FOR MEDIUM (I) AS OBSERVED FROM K

We consider the absorption of radiation by bound charges. To this end we refer to [4]. In particular we investigate the interaction between an incident electric field and an electron bound to a nucleus.

The equation of motion for the electron will be:

$$\frac{d^2x}{dt^2} + 2\gamma\frac{dx}{dt} + \omega_0^2x = -\frac{e}{m}E_{loc}. \quad (1)$$

Here γ is the absorption decay rate, ω_0 is the resonant frequency of the motion of the electron, e is its charge, m is its mass, and E_{loc} is the incident electric field.

The Fourier transform of the two sides of the Equation (1) will be:

$$-\omega^2 X(\omega) - 2i\gamma\omega X(\omega) + \omega_0^2 X(\omega) = -\frac{e}{m} E(\omega). \quad (2)$$

Hence for the displacement of the electron we obtain:

$$X(\omega) = \frac{eE(\omega)/m}{\omega^2 - \omega_0^2 + 2i\gamma\omega}. \quad (3)$$

The dipole moment due to charge displacement $X(\omega)$ will be $\vec{p}(\omega) = -e\vec{X}(\omega)$.

The discussion so far has been in the microscopic level. The macroscopic behavior is determined by the induced polarization \vec{P} which represents the contribution of all dipole moments in a given volume. If there are N_j Lorentz oscillators as per (1) per unit volume, characterized by resonance frequencies ω_j and damping constants γ_j , then the macroscopic polarization of the medium is given by the summation over all types as:

$$P = \sum_j N_j \langle p_j \rangle = \langle E_{loc} \rangle \sum_j N_j \alpha_j(\omega) \quad (4)$$

where the angle brackets $\langle \rangle$ indicate a spatial average over atomic sites. Here

$$\alpha_j(\omega) = -\frac{e^2/m}{\omega^2 - \omega_j^2 + 2i\gamma_j\omega} \quad (5)$$

is the atomic polarizability of the Lorentz oscillator that is characterized by ω_j , γ_j and the number density N_j . Furthermore

$$N = \sum_j N_j \quad (6)$$

is the total number of electrons per unit volume interacting with the applied incident field.

The electric susceptibility $\chi_e(\omega)$ of the linear isotropic dielectric medium is defined by

$$\vec{P}(\omega) = \varepsilon_0 \chi_e(\omega) \vec{E}(\omega) \quad (7)$$

where $\vec{E}(\omega)$ is the macroscopic electric field vector. Under the approximation that $\langle E_{loc} \rangle = E$, which is valid if the N_j are not too large, the electric susceptibility of the medium is found to be

$$\chi_e(\omega) = \sum_j \alpha_j = -\sum_j \frac{N_j e^2 / (m\varepsilon_0)}{\omega^2 - \omega_j^2 + 2i\gamma_j\omega}. \quad (8)$$

From this equation the complex dielectric permittivity function $\varepsilon_r(\omega)$ of the medium is given as:

$$\varepsilon_r(\omega) = 1 + \chi_e(\omega) = 1 - \sum_j \frac{b_j^2}{\omega^2 - \omega_j^2 + 2i\gamma_j\omega} \quad (9)$$

where $b_j^2 = \frac{N_j e^2}{m\varepsilon_0}$ is the square of the plasma frequency with number density N_j .

For simplicity we confine ourselves to the study of the single-mode case and we consider:

$$n^2 = \varepsilon_r(\omega) \cdot 1 = 1 - \frac{b^2}{\omega^2 - \omega_0^2 + 2i\gamma\omega} \quad (10)$$

The symbols b , ω_0 , γ stand for the plasma frequency, resonant frequency and the damping constant. Here the relative magnetic permeability has been considered equal to 1 and n denotes the refractive index.

3. THE MODEL FOR MEDIUM (I) AS OBSERVED FROM K'

Transformation of the dispersion relation corresponding to this refractive index from the frame K to the frame K' was given by the relation

$$(k'_1)^2 = \left(\frac{\omega'}{c'}\right)^2 \left(1 - b^2 \left[\frac{\alpha c/c'}{(\alpha c/c')\omega' + i\gamma}\right] \frac{1}{\omega'} \frac{c'^2}{c^2}\right) \quad (11)$$

for the electromagnetic system considered in [3]. To repeat, that system consisted of a medium (I) which is a linear, homogeneous, temporally dispersive Lorentz medium occupying the space $x > -\infty$ and to which is attached the Galilean reference frame K , and a medium (II) which is filling the half space $x > 0$ initially and to which is attached the Galilean reference frame K' . The interface of the media is an infinite plane perpendicular to the direction of motion of K' with respect to K which is the Ox direction. In this work, however to simplify the moving boundary condition in K' , we take the second medium as a perfectly conducting medium again filling the half space $x > 0$ initially and to which is attached the Galilean reference frame K' . The interface of the media is again an infinite plane perpendicular to the direction of motion of K' with respect to K which is the Ox direction.

Note that we are considering here the Lorentzian relativistic transformation of a dispersion relation in K to K' . This is a step that exists in the literature [5].

For completeness we shall re-derive (11). First we consider the transformation of wave number and frequency under the ‘modified Lorentz transformation’ [2].

$$k_i = \alpha k'_1 - \alpha \frac{r}{c'} \omega' \quad (12a)$$

$$k_r = \alpha k'_1 + \alpha \frac{r}{c'} \omega' \quad (12b)$$

$$\omega_i = -\alpha r c k'_1 + \alpha \frac{c}{c'} \omega' \quad (13a)$$

$$\omega_r = \alpha r c k'_1 + \alpha \frac{c}{c'} \omega' \quad (13b)$$

Here c and c' are speeds of light in vacuum for K and K' , $r = -v/c$ where v is the speed of K' with respect to K and $\alpha = 1/\sqrt{1-r^2}$. In this work, we use the subscript i for the incident and r for the reflected waves. Also primed and unprimed quantities relate to frames K' and K throughout the paper.

The dispersion equation for medium (I) when observed from K for the incident wave can be written as

$$k_i^2 = \frac{\omega_i^2}{c^2} \left(1 - \frac{b^2}{\omega_i^2 - \omega_0^2 + 2i\gamma\omega_i}\right), \quad (14a)$$

and for the reflected wave as

$$k_r^2 = \frac{\omega_r^2}{c^2} \left(1 - \frac{b^2}{\omega_r^2 - \omega_0^2 + 2i\gamma\omega_r}\right), \quad (14b)$$

if one notes Equation (10) above.

It is easy to obtain

$$k_i^2 - k_r^2 = \frac{\omega_i^2 - \omega_r^2}{c^2} - \frac{b^2}{c^2} \left(\frac{\omega_i^2}{\omega_i^2 - \omega_0^2 + 2i\gamma\omega_i} - \frac{\omega_r^2}{\omega_r^2 - \omega_0^2 + 2i\gamma\omega_r}\right), \quad (15a)$$

$$k_i^2 + k_r^2 = \frac{\omega_i^2 + \omega_r^2}{c^2} - \frac{b^2}{c^2} \left(\frac{\omega_i^2}{\omega_i^2 - \omega_0^2 + 2i\gamma\omega_i} + \frac{\omega_r^2}{\omega_r^2 - \omega_0^2 + 2i\gamma\omega_r}\right). \quad (15b)$$

Noting (12) and (13), from (15a) one obtains

$$\omega_i^2 (\omega_r^2 - \omega_0^2 + 2i\gamma\omega_r) = \omega_r^2 (\omega_i^2 - \omega_0^2 + 2i\gamma\omega_i). \quad (16)$$

To see this note that

$$k_i^2 - k_r^2 = -4\alpha^2 k'_1 \frac{r}{c'} \omega' = \frac{1}{c^2} (\omega_i^2 - \omega_r^2). \quad (17)$$

This identity causes the second term on the right hand side (15a) to be equal to zero.

Noting (12) and (13), from (15b) one obtains

$$(k'_1)^2 - \left(\frac{\omega'}{c'}\right)^2 = -\frac{b^2}{c^2} \left(\frac{\omega_i^2}{\omega_i^2 - \omega_0^2 + i2\gamma\omega_i}\right). \quad (18)$$

To see this note that

$$k_i^2 + k_r^2 = 2(\alpha k'_1)^2 + 2\left(\alpha \frac{r}{c} \omega'\right)^2, \quad (19a)$$

and that

$$\frac{1}{c^2}(\omega_i^2 + \omega_r^2) = 2(\alpha r k'_1)^2 + 2\left(\alpha \frac{\omega'}{c'}\right)^2. \quad (19b)$$

From (13) we see that

$$\omega_i + \omega_r = 2\alpha \frac{c}{c'} \omega', \quad (20)$$

and

$$\omega_i \omega_r = \left(\alpha \frac{c}{c'} \omega'\right)^2 - (\alpha r c k'_1)^2. \quad (21)$$

From (16) we also obtain

$$\omega_0^2(\omega_i + \omega_r) = i2\omega_i \omega_r \gamma. \quad (22)$$

ω_0 , b , and γ are measured in the laboratory frame.

Using (21) in (22) we find $2\omega_0^2 \alpha \frac{c}{c'} \omega' = i2\omega_i \omega_r \gamma$ or $\omega_i \omega_r = \omega_0^2 \alpha \frac{c}{ic' \gamma} \omega' = \omega_0^2 \frac{\bar{b}}{i\gamma}$ where $\bar{b} = \alpha \frac{c}{c'} \omega'$. Now with some algebra we can write (18) as (23a):

$$(k'_1)^2 - \left(\frac{\omega'}{c'}\right)^2 = -\frac{b^2}{c^2} \frac{\bar{b}}{\bar{b} + i\gamma}. \quad (23a)$$

On the other hand, using (13) the equality $2\omega_0^2 \alpha \frac{c}{c'} \omega' = i2\omega_i \omega_r \gamma$ can be written as follows:

$$\omega_0^2 \alpha \frac{c}{ic' \gamma} \omega' = \left(\alpha \frac{c}{c'} \omega'\right)^2 - (k'_1 r c)^2, \quad (23b)$$

or as

$$\omega_0^2 \alpha \frac{1}{ic' \gamma} \omega' = \left(\frac{\omega'}{c'}\right)^2 - \alpha^2 r^2 \left[(k'_1)^2 - \left(\frac{\omega'}{c'}\right)^2 \right].$$

Using (18) we get

$$\omega_0^2 \alpha \frac{c}{ic' \gamma} \omega' = \left(\frac{\omega'}{c'}\right)^2 + \alpha^2 r^2 \frac{b^2}{c^2} \frac{\bar{b}}{\bar{b} + i\gamma}. \quad (23c)$$

Noting that $\bar{b} = \alpha \frac{c}{c'} \omega'$ we finally obtain after multiplying (23c) by $\bar{b} + i\gamma$,

$$\omega_0^2 \frac{\alpha^2}{c'^2} \omega'^2 \frac{1}{i\gamma} + \omega_0^2 \frac{\alpha}{cc'} \omega' = \alpha c \left(\frac{\omega'}{c'}\right)^3 + i\gamma \left(\frac{\omega'}{c'}\right)^2 + \alpha^3 r^2 \frac{b^2}{cc'} \omega',$$

or we can get after dividing by c

$$\omega_0^2 \frac{\alpha}{c^2 c'} \omega' = \alpha \left(\frac{\omega'}{c'}\right)^3 + \left(\frac{\omega'}{c'}\right)^2 \left(\frac{i\gamma}{c} + \omega_0^2 \frac{i\alpha^2}{c\gamma}\right) + \alpha^3 r^2 \frac{b^2}{c^2 c'} \omega'.$$

This expression can be cast into the form:

$$\alpha \left(\frac{\omega'}{c'}\right)^3 + \left(\frac{\omega'}{c'}\right)^2 \left(\frac{i\gamma}{c} + \omega_0^2 \frac{i\alpha^2}{c\gamma}\right) + \alpha^3 r^2 \frac{b^2}{c^2} \frac{\omega'}{c'} - \omega_0^2 \frac{\alpha}{c^2} \frac{\omega'}{c'} = 0. \quad (23d)$$

REFERENCES

1. Yener, N., “Prediction of a new superconductivity-like effect in Galilean reference systems (Part II),” *PIERS Proceedings*, Moscow, Russia, Aug. 19–23, 2012.
2. Yener, N., “On the non-constancy of speeds of light in vacuum for different Galilean reference systems,” *Journal of Electromagnetic Waves and Applications*, Vol. 21, No. 15, 2241–225, Jan. 2007.
3. Yener, N., “Non-constancy of speed of light in vacuum for different galilean reference systems in case of an impulsive plane wave,” *PIERS Proceedings*, 1638–1643, Xi’an, China, Mar. 22–26, 2010.
4. Oughstun, K. E., “Velocity of energy transport for a time harmonic field in a multiple resonance medium,” *J. of Optic. Soc. America*, Vol. 5, No. 11, 2398-1–2398-5, 1988.
5. Ko, H. C., “On the relativistic invariance of the complex phase of plane waves,” *Radio Science*, Vol. 12, No. 1, 151–155, 1977.

Satellite Monitoring for Energy Transfer Process of Tsunamigenic Earthquake

Shigehisa Nakamura
Kyoto University, Japan

Abstract—This is a note to crustal plate creeping process for a trigger of great destructive earthquake accompanied by tsunamis. For the author's convenience, a simple model is introduced to this problem in order to have his dynamical understanding at an informed attention of the sliding shift of the eastern boundary of the Eurasian plate. This process was observed at the seismic event on 11 March 2011 though it is necessary to consider on the possible energetic process of this earthquake tsunamis. This process could be seen when it is a process found in the plates in a global scale. A possibility might be expected for satellite monitoring of disturbance in positioning of the settled station on the plate in order to track this process effectively.

1. INTRODUCTION

This is a note to crustal plate creeping process for a trigger of great destructive earthquake tsunamis. A model is introduced for the author's interest to this problem in order to have his dynamical understanding at an informed attention about the hazards on and around the coastal zone in a northwestern part of the Pacific Ocean on 11 March 2011. The author has had to see what factor helps us to realize the physical process of tsunamis generated at the seismic event on that day. The sliding shift of the eastern boundary in a global scale could be helpful for realizing the observed sliding shift which might be the trigger of the great tsunamis hitting the coastal zones facing the Pacific Ocean and the islands in the northern Pacific Ocean. This process could be seen when it is taken as a plasto-elastic process of the plates in a global scale.

2. REVIEW NOTE

It is favorable to find any effective one of the related factors, parameters and conditions for expressing the phenomenological understanding in a scope of physical science in a simple form. If any observable factor is found, it is most valuable finding though it is hard in most cases to find what is in need for all of the geophysical processes in practice. For the author's convenience, it is noticed about one of the typical earthquake tsunamis known in the world. First, the author introduces what had been informed about the interested tsunami hazards.

It was strange for the author in the western part of the main island of Japan to hear a warning siren with an announcement about the tsunami threat without any signal of a seismic precursor or of an earthquake feeling to the human body on the street at that time. After some time elapse, the author had a simple noticing to be ready to evacuate out of the coastal zone everybody. At a sudden change of the event, there had not any quick response to what was noticed for those in the coastal zone. In brief, a confused phase was appeared to generate a kind of a random movement of an ensemble of the peoples in the coastal zone. Any effect of the formal training for the accidental event was disappeared. Some of the local governmental functions were destroyed or lost. It was necessary to spend for several days to see what was happened and what should be done for their recovery. The so-called scientific experts had wondered how to digest for those keeping to stay in the coastal zone.

3. KEY TO SLIDE SHIFT OF PLATE

Following to the descriptive note seen as above, the author considers to construct a simple model which might help to see the event.

A target here is what was effective to illustrate the physical process for realizing the event. The hazardous event of the great tsunami generated by an earthquake undersea simulated with significant ambiguity even after the scientists on the basis of the model for tsunami generated a specified by several seismic parameters in fail.

Then, it should be introduced another model developed. Then, it might be seen the key was a global process of the magma under the crusts covering the earth surface after reminding the volcanic event of Iceland in 2010 on a mid-Atlantic ridge here the main crusts are generated to spread to form the fresh crust undersea, then, a balance of the forcing power to the two crusts, the Eurasian

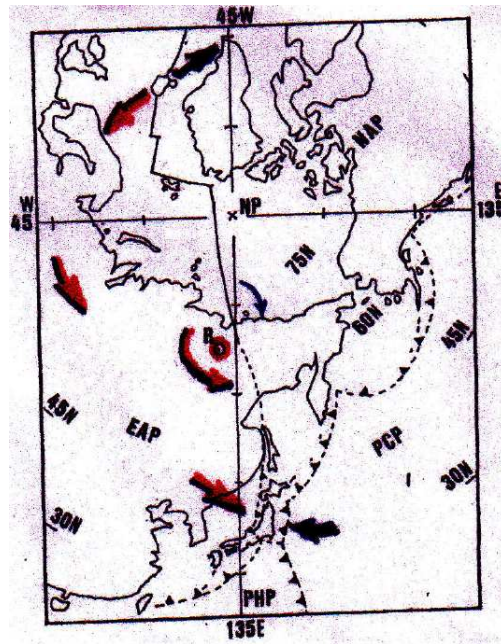


Figure 1: The plates around the Northwestern Pacific. 1) The notation NP for the geographic north pole. 2) The notations EAP, NAP, PCP and PHP for the Eurasian, North American, Pacific and Philippines plate. 3) The notation at “R” is the center of relative motions of EAP and NAP.

plate (EAP) and the North Pacific plate (PCP) must have been contributive with a condition to be driven by the motion of the magma just under the crusts. Exactly speaking, the east part of the Japanese main land had been taken by the seismologists as a part of the North American Plate (NAP) between the Eurasian plate (EAP) and the Pacific plate (PCP) as illustrated well in Figure 1.

It is now to promote scientific research on earthquake tsunamis on the basis of a more advanced understanding of the interested process without any other prejudice. For this purpose, the seismologists should learn the interested process much more referring not to the indices specifying the process but the observable factors effective to the process in order to find a key to see mechanism of earthquakes and tsunamis.

4. ROTATIONAL PLATES

It should be given here a remark to the two plates produced by the magmatic activity spreading on a couple of magma conveyers to east and west respectively because the mid-Atlantic ridge has a meridional extent as seen in Figure 1 geologically, though it is boldly taken that the other boundary of the two plates, EAP and PCP meets off the Japanese Islands so that PCP moves down to subside under EAP to be the sources of the earthquakes generated in deep (in the range of 40 to 100 km deep from the earth surface) for these one hundred years by the scientists in these seventy years. It was new geophysical finding though it should be updated on the bases of the new data in geology and geophysics.

The movement of the EAP can be tracked when the specific stations located on the surface of the plate by using the satellite monitoring techniques for positioning. It must be more effective to utilize the existing GPS (Geographical Positioning System), for example.

The author tends now an application of satellite monitoring of the interested plates is valuable for promoting the related scientific researches indeed.

5. ACTIVITY OF MID-ATLANTIC RIDGE

As for the activity of the mid-Atlantic ridge, it can be the most latest event which was the volcanic eruption in the Iceland on 14 April 2010. This event strongly affected to traffics and related services in Europe. This volcanic effect is appeared as scatter of the volcanic ash scattering over the main and local air ports to interrupt the flight navigation schedule and to threat of the social activity decaying.

As for energetics of this volcanic event, there must be several reports in the area of the western Europe, especially in EU.

This volcanic event was one of the most significant eruptions though the energy release of the activated magma must be simply seen through a vent where the surface of the magma was easily observed by eye-watch in a week after the first eruption. Nevertheless, no remark has been given whether the energy of the activated magma was completely released or not. There might be some residual energy remained to be spent for horizontal stresses of the interested plates.

6. ZONE OF INTERPLATE SHORTENING

It is already known that a zone of interplate shortening is exist as that along the extended zone of the mid-Atlantic ridge after landing on the coastal zone just neighbor the point “R” in Figure 1. This extended zone get to separate the main land of Japan to two parts, i.e., east and west parts [1]. The point “R” is understood as the center of relative motions of EAP and NAP. There might be some elasto-plastic processes must be happened at the seismic event of a tsunamigenic earthquake so that the author has note that it is in need to find what is the fact in the interested process.

7. THRUST AS COUPLING EFFECT TO PLATES

Looking at what illustrating in Figure 1, a point R located in the northern part of Siberia is the center of relative motions of EAP and PCP in seismology and plate tectonics with an undersanding of that the zone of interplate shortening is inside of EAP.

This zone of interpolate shortening helped us to realize that the tsunamis generated by the several earthquakes off the coastal zone should effectively hit to destructive forces in the coastal zones. At every one of those earthquakes in the Japan Sea, seismic fault was considered to be formed in a form of a thrust as coupling effect to the interested two plates. This means that the zone of interpolate shortening acts as a boundary separating EAP and a tip of the North American plate (NAP) and is taking part of important play at the seismic event of a fault formation to make a tsunamigenic earthquake.

8. PLATE SUBDUCTION AND THRUST

Scientists had constructed a numerical model for reproducing the processes at the past tsunamigenic earthquakes after getting their believe of their model to be well constructed to reproduce the seismic processes on the land with introducing several parameters which could be use to specify each one of the seismic events.

The model for a tsunamigenic earthquake had been accepted as one of the scientific success in geophysical processes though there had been left some ambiguity in parametric definition of a seismic source model.

The recorded dislocations were confirmed to show about 1 to 2 m to ESE on the coastal zone (National Geographic Institute) to eastward and it was dislocated as much as 31 m ESE at the offshore stations settled on the sea floor (in the range of 1000 m to 4000 m deep) off the coast facing the Northwestern Pacific by the Tohoku University and it was dislocated as much as 24 m to ESE (Hydrographic Office of Maritime Safety Agency).

The author tends to take these dislocation observed data as a effect of a residual energy of 2010 Iceland volcanic eruption to the zone of interpolate shortening and to the front of EAP where the subduction of PCP is seen. Fukushima is about 100 km south of the stations. In addition, it is easy to transfer the residual energy from Iceland to the interpolate shortening and the front of EAP and PCP through EAP referring to point “R”.

9. TSUNAMI MODEL

The existing tsunami model is consisted by a multiple nesting net system for obtaining an target process of a modeled tsunami by use of numerical computational procedure.

The author has to point out that an ambiguity of the numerical solution is simply referred to the seismic parameters originally introduced for specify each one of the past typical events related to the earthquake but to the tsunamis.

There is yet left a problem of energy transfer from the seismic source (phase of “solid”) to the ocean water (phase of “liquid”) for generating the tsunamis at an earthquake in a model.

As the seismic parameters in a form of artificial numerals, the seismic parameters can specify each one of the seismic sources as a set of numeral parameters which can demonstrate the seismic processes at the occurrence of the interested earthquake.

In the existing tsunami model, it is essentially in need though never been take care of what mechanism is at energy transfer from the seismic source to the tsunamis. This is one of the significant factors for the ambiguity of the numerical solution of the tsunami model. This mechanism is the key to see the tsunami model in a scope of science.

10. GLOBAL SCALING

With a brief notice noted above, the author has to introduce a model for realizing the great tsunamigenic earthquake, for example, the case of the 2011 East-Japan earthquake which has the epicenter off the coast facing the northwestern Pacific. The epicenter is between the coast and the Japan trench.

Referring to the past example, a seismic evaluation was given by the model though it was forced to revise repeatedly to get the final evaluation of the seismic magnitude as the level nine in scale. The details must be referred to the final report or the scientific papers which might be appear officially later.

Now, the author tends to consider about the effect of the 2010 Iceland volcanic eruption, i.e., the eruption of the volcano “Eyjafjajökull”. It was one of the great eruption so that its volcanic ashes caused to an interruption in the flight and transportation services and public activities in the area covering the European Union.

Geodetic positioning should be referred to satellite monitoring on the interested plate surfaces.

11. CONCLUSIONS

The author introduced a note to crustal plate creeping process for a trigger of great destructive earthquake tsunamis. This note aimed to find a key to have an advanced research as the next step in future. A model is introduced and several notice for the model under some assumption with a set of the seismic parameters which specifies the earthquake. A notice is given for an ambiguity in the solution of the numerical model with the seismic parameters without any confirmed reference about energy transfer mechanism from a solid plate in which a forcing disturbance may be a cause to form a fault for an earthquake. In case of subsurface earthquake, tsunamis may be generate after energy transfer from the solid crust to the sea water layer on the plate as a part of the sea floor. Special reference was for the case of 2011 East-Japan earthquake. Additional notice is given as one of the ambiguities in the model is in the seismic parameters. It should be clarify what is observable factor for realizing transfer mechanism from the seismic source to the ocean water layer at generating tsunamis. In order to have an advanced research as the next step, it should be introduced to actively utilize the data of disturbance at positioning the settled station for interested station referring to satellite monitoring.

REFERENCES

1. Nakamura, S. “Annual mean sea level variations in the Northern Pacific seismic zone,” *Marine Geodesy*, Vol. 17, 213-218, 1994.

Monitoring for Geomagnetic Reversal of the Planet Earth

Shigehisa Nakamura
Kyoto University, Japan

Abstract—This is a note to geomagnetic polar wandering in relation to the geomagnetic reversals found on the earth surface granite stratification. This stratification is possibly realized by an application of magneto-hydrodynamics to the earth's geomagnetic main field. A model is introduced for finding advanced researches in the field of planetary and space sciences. This result suggests a spacecraft monitoring of the planets in the solar system.

1. INTRODUCTION

This is a note to geomagnetic polar wandering in relation to the geomagnetic reversals found on the stratified basalt rock layers on the earth surface. Measurement of the magnetized sample pieces of the basalt rock layers, that have led to show magnetic polar reversal in a time scale of geology. This fact can be realized by modeling of the earth's magnetic main field on the basis of magnetohydrodynamics (MFD). This can be taken as a key for promoting advanced research in the fields of planetary and space sciences. This result suggests a spacecraft monitoring of the planets in the solar system in need.

2. REMANENT ROCK MAGNETISM

During the early age of rock magnetism, Motonori Matuyama (1884–1958) had measured magnetic property of the rock to notice that the magnetic reversal had been repeated [1]. This result was reported at the Imperial Academy by Professor Torahiko Terada of Tokyo University at that time.

Cox et al. [2] reported the reversals of the earth's magnetic field which might to be possible factor in order to illustrate the 9 times repeated reversal. By that time, there had been noticed on the reversal as an index of the stratified rock layers as a tool for seeing geological classification though the nine reversals were found in a time period of about 3.6×10^{10} years BP (before present).

Gilbert [3] confirmed that Matuyama [1] was the first scientist who clearly noticed about geological chronology of remanent rock magnetism after Gilbert assured Matuyama's instrumentation technique.

3. POLAR WONDERING

In the field of palaeomagnetism, Runcorn [4] estimated that the geomagnetic north pole was at the location of just neighbour of the present magnetic north pole for the recent 2×10^7 years though it was at the location of Novosibirskaya Ostrova (or New Siberian Island) in the Arctic Sea in the first half of the tertiary in the geological age.

Nagata [5] had given an illustration about the track of the geomagnetic polar wandering by a monotonous track line from the tropical zone (or the equatorial zone) to the geographic north polar zone on the earth surface of a geographical co-ordinate system for the time periods from the Cambrian age (ca 4×10^8 years BP) to present though it was restricted to the available data of remanent rock magnetism for the northern hemisphere in Nagata's interested research work. Nevertheless, Nagata could not to analyze any sample piece of the remanent magnetized rocks in the southern hemisphere though the author has understanding about what was one of his projects in his mind. Nagata simply could give to Japan to start the Antarctic Project as a part of the International Antarctic Project just after 1945.

In relation to Nagata's illustration noted above, there had been appeared several publications, for example, Irving [6] had published to note on his scope of palaeomagnetism in 1964 and Rikitake [7] had published his text on Geo-electromagnetism for an overview in 1972 in which some notice about polar wandering in his insight.

The author tends to take it suggesting to that the polar wandering might had a meridional circular track on the earth surface in his bold assumption referring to a geographic co-ordinate system. Then, what above mentioned is consistent to for example a kind of Mammoth species existence to be found in the subarctic zone or the arctic zone in the last one thousand years.

As the other references, the author may introduce those of several scientists. For example, Munk and McDonald [8] have published their notices on the rotation of the earth in 1960. After that,

Lambeck [9] has published his text book on the variable rotation with some special references on its geophysical causes and consequences in 1980 though his scientific insight on polar wandering was appeared at the last part of his text in a form of his short comment.

4. SOLAR ELEVEN YEARS CYCLE

As for the solar 11 years cycle, it is well known as an index of the solar activity, though it is not yet well understood what is the internal structure of the Sun.

Stix [10] has introduced his mean-field electrodynamics in order to have a solution by applying any of available mathematical technique.

In a case of referring to Stix's model, it can be boldly expressed when the earth surface crust layer is a solid spherical shell in which the processes of dynamics and electromagnetics could be described referring to a spherical co-ordinate $0-r \theta \phi$ by a set of the surface spherical functions. Then, any one of the interested processes could be illustrated on the geographical reference. As for the inside of the spherical shell, the materials contained in the shell are in a state of a high pressure and a high temperature so that the state of the materials could be a phase of fluidized state.

For a convenience, an assumption of no mutual interaction between the materials and the shell, then, it can be considered that any dynamic and electromagnetic processes of the materials inside the spherical shell can be described in a mathematical form. The formulation should be solved with several assumptions and under several conditions. In practice, any one of the solutions could not be expressed in any simple mathematical form. So that, it is necessary to apply various kinds of mathematical techniques for obtain the solution in need. In case of a linear problem, it is easy. Nevertheless, it is necessary to use some kind of the transcendental functions even in a case for obtaining an approximated solution. In a case including mathematical singularity, the other mathematical concept should be introduced.

Stix introduced a pseudo-tensors after some mathematical manipulation in to specify using a Cartesian co-ordinates $0-xyz$ in order to relate the factors to an axial or a spherical co-ordinate system $0-r \theta \phi$. Then, the vector in the vector can be expressed by a polar vector. First-order approximation is considered to solve the equation in a mathematical tools. For a kinematic $\alpha \Omega$ -Dynamo model, a numerical solution was obtained. It is assumed some assumption under specific boundary condition, then, the interested oscillatory kinematic $\alpha \Omega$ -model had a solution for a meridional cross section to show contours of parametric troidal field strength and poloidal lines of force. An adjustment was for the 11 years cycle in Stix's case. The other nominal parameter could be taken to fit the model's solution for the magnetic reversal processes on the planet earth in a geological time scale because the problem in this case is considered as a linear problem in order to find a bold pattern of the electromagnetic main field inside the assumed shell as the earth surface layer. To details, it is necessary to have an advanced research for this problem.

5. GEOLOGICAL TIME SCALE

It is more convenient when a theory in a numerical model is possible to apply in an extensive application to the problem on any of the dynamical process in a geological time scale.

In fact, the geological observations tell us that cycle interval is not regular so that there must be some bold assumptions for applying a primitive theoretical model or an advanced mathematical technique.

Nevertheless, it might be an idea for some specific trend which help us to realize what a possible process is seen in a geological time scale on the earth.

Now, assume the spherical shell is as the earth surface layer of a rock-content, for our convenience. The atmospheric layer covers the earth's spherical crust to separate the materials inside the spherical shell. Inside of the earth's shell, the materials are in motion as if those were a homogeneous fluid under a state of high temperature and high pressure which is determined the earth's spherical shell that is acting an imperfect thermal isolator of a exactly solid spherical shell.

It is assumed that there is no interaction between the shell and the materials inside of the spherical shell, for convenience.

Assumptions above are repeatedly written as that the rotating spherical shell for geographical reference is act as an elastic container of the material in motion inside which could described referring to another spherical co-ordinate system with a common origin. There might be introduced a model of the materials motion inside the spherical shell with an assumption of no interaction between the spherical shell and the materials in motion inside. There is a possible key to relate polar wandering as a quarter part of one polar reversal cycle.

6. SUMMARY AND CONCLUSIONS

The author noted here that it can be boldly possible to see the polar reversal cycle is reduced on the basis of the data in relation to the polar wandering from the tropical or equatorial zone to the polar zone. It is consistent to the geomagnetic reversal cycle when the polar wandering process can be for one quarter part of the earth's meridional path length. Here, that is to say, Matuyama's geological time scale (3.6×10^9 years) with some assumptions and under some conditions is taken to be supported well by the contribution in Nagata's remanent rock magnetism in the geomagnetic polar wandering from the geographical equatorial zone to the polar zone in the northern hemisphere for the time period of 4×10^8 years. With the above, the author takes it effective now to consider a project for spacecraft monitoring of the environment of the planets as well as the planet earth for advanced research in order to understanding of the planets and for a reveal of the space in a scope of science.

REFERENCES

1. Matuyama, M., "On the direction of magnetization of basalt in Japan," *Proceedings of the Imperial Academy*, Vol. 5, No. 5, 203–205, Tokyo, 1926.
2. Cox, A., R. R. Doell, and G. B. Darlymple, "Reversals of the earth's magnetic field," *Science*, Vol. 144, 1537–1543, 1964.
3. Gilbert, W., *De Magnete, Magnetistique Corporibus, et de Magnete Tellure*, 1st Edition, 1900; 368, Physiologia Nova, New York, 1958.
4. Runcorn, S. K., "Palaeomagnetic comparison between Europe and North America," *Philosophical Transaction of Royal Society*, Series A, Vol. 258, 1–12, London, 1965.
5. Nagata, T., *Rock magnetism*, 350, Maruzen, Tokyo, 1961.
6. Irving, E., *Palaeomagnetism*, 399, Willey, New York, 1964.
7. Rikitake, T., *Geo-electromagnetism*, 472, Iwanami, Tokyo, 1972.
8. Munk, W. H. and G. J. F. McDonald, *The Rotation of the Earth*, 323, Cambridge University Press, 1960.
9. Lambeck, K., *The Earth's Variable Rotation*, 1st Edition, 1941; 449, Cambridge University Press, Cambridge, U.K., 1980.
10. Stix, M., *The Sun*, 390, Springer-Verlag, 1989.

Monitoring for Inclination Stability of the Planet Magnetic Axis Normal to the Solar Equatorial Plane

Shigehisa Nakamura
Kyoto University, Japan

Abstract—This is an introduction of a monitoring for inclination stability of the planet magnetic rotation axis normal to the solar equatorial plane. It should be analyzed various kinds of the data available. The author has had a concept model for this problem.

That is, the planet rotation axis is a radial line on the solar equatorial plane for the neutral stability and is a normal line to the solar equatorial plane for the final stability. Then, it is necessary to have a monitoring for instability of the planet rotation axis in the solar axis in order to give a proof for what the author's interested stability is acceptable in the actually process in a scope of dynamics with the given electromagnetic condition.

1. INTRODUCTION

The author introduces a notice to the inclination of the planets in the solar system. First, a brief review is noted several related items. Various kinds of the data should be analyzed and referred. A concept model for this problem could be solved in a form of mathematical solution after a formulation for the equation of motion following a scope of classic dynamics with an assumption of that each one of the planets in the solar system coincides to the magnetic axis of the dipole formed to corresponding to the interesting planet rotation axis referring to the solar equatorial plane.

On the basis of magneto-hydrodynamics of the planets, it can be seen that a certain phase of an understanding. Referring to the faint understanding, it could be illustrated a cyclic polar overturning, for example, the 11-year cycle of the solar activity which could be illustrated by a internal structure of the material motions that is obtained by a formulated linear equation in a scope of the magneto-hydrodynamics.

Nevertheless, the observed results suggest that another nonlinear equation should be introduced at considering to have a proper prediction for the following process of the related variations superposed to the main magnetic field of any one of the interested planet in the solar system.

An expected solution must be to help to introduce a solution that what relation should be satisfied for the planet rotation axis in the solar system.

A possibility must be a key to have an application of the solution noted above to the other planet systems if any terms of the planets are relatively common to the planets in the solar system.

2. REVIEW NOTE

At present, we are in the age of the space science when many of the space crafts have been is launched for monitoring, surveying, and observing the planets in the solar system. The exoplanets of about three hundreds are in the strongly focused interest to the scientists in space science and astronomy. In the early age, the astronomers had observer the planets by using a specific optical telescope designed for astronomical purpose. For example, Gallileo had his astronomical understanding on the basis of his planet observations by using an optical telescope made by his own skill.

After the age of the artificial satellite monitoring of the earth surface, the scientists have had their advanced tool which has a processing function of electromagnetic waves, for example, advanced sensors mounted on the spacecrafts as the carrier (the rockets) launched above the tropopause beyond the ionospheres covering the upper atmosphere on the earth.

An international space station is under construction by the scientists after assistance of the technological scientists. This should be possible to promote for completing a d functioning by services of the space shuttle. This international space station might help to survey the environment of the space around the earth in the solar system.

Recent contributions of the spacecraft monitoring have been appeared in the publications on the planets and their astronomical satellites. Several expeditions are for detection for the asteroids by launching the more minor space shuttles. In 2010, one of the shuttle named as Hayabusa was recovered on the southern hemisphere of the earth after its space navigation for several years beyond the originally scheduled time period after landing on one of the asteroids (Itokawa as the asteroid 25143).

Comets have been traced by the optical techniques at the observatory located specific sites on the earth surface. One of the optical telescopes in the space is under operation for astronomical observation on a synchronized orbit relative to the earth. It is known by name of “Hubble” in memory of the astronomical scientists.

Now, the author has to focus his eyes to monitoring of the planets in the solar system. It is important to introduce his model in order to have a dynamical understanding about the inclination of the planet rotation axes in the solar system.

For this purpose, an advanced technique or tool should be developed for mounting on the spacecraft in order to monitor any exposure site of the stratified rocks of specific remanent magnetics on the planets in the solar system. This might give us an extensive chronology of the reversal magnetic cycle to find what relation could be seen referring to what had found by Matsuyama during the period of 1926 to 1929.

3. MONITORING MAGNETIC FIELD PATTERN ON THE EARTH

As for the magnetic field around the earth, the author had introduced after his digests of references [1] and [2], Birkeland had learned Maxwell’s electromagnetics under Henri Poincare in Paris, and had learned electromagnetic waves under Hertz, and, he had his expeditions for finding an electron flow from the sun in relation to magnetic variations. The magnetopause and magnetosphere of the earth under the influence of the solar wind was theoretically clarified to give an illustration to relate where a couple of the possible aurora ovals can be formed. It is seen that the aurora boreales and aurora australis are induced by the variations on the solar surface though no detail is noted in this work.

As for geological pattern found in the rocks which consist the stratification to form the earth surface solid layer, it had been noticed that a series of remanent rock layers shows a repeated periodical reversal in the geomagnetic field. Motonori Matsuyama had ever noticed it for about several million years after his survey for noticing a series of cyclic reversal of remanent magnetization in the stratified geological layers as found this fact by 1929. Torahiko Terada had evaluated what noticed by Matsuyama, and Terada had encouraged for Matsuyama to publish his contribution of the Science Academy in 1929.

As for the solar activity, it is well known the 11-year cycle though there is simply a model referred to the solution for a linearized equation with a nominal parameter.

Berchem and Russel [3] studied on the thickness of the magnetopause current layer around the earth in 1982. As Stix linear model might be possible to apply for the other processes in a different time scale, Matsuyama’s geomagnetic reversal found in geological stratification possibly could be illustrated well referring to the model for the 11 year solar cycle if no solar burst or no solar storm could be taken into consideration.

Miura and Pritchett [4] presented their work on local stability analysis of the MHD Kelvin-Helmholtz instability in and around a plasma sheath after a spacecraft monitoring of the magnetic factors of the planet earth.

Nevertheless, no consideration has been given for the inclination of the planets in the solar system by this time. It had been taken that the rotation axis of the planets has been generally coinciding to the axis of the dipole magnetic model to any one of the planets in the solar system. The data in the project of MESSENGER was obtained by NASA, the, the scientists reported their findings, i.e., by Anderson, Slavin, Boardsen and their colleagues during 2007 to 2010.

4. PATTERN OF MAGNETIC FIELD OF PLANET IN THE SOLAR SYSTEM

Chapman [2] had introduced his theoretical model at realizing first the environment of the earth’s geomagnetic field in relation to the solar magnetic field. Chapman has shown the spacial shape of magnetopause where the interface of magnetic balance. This made it possible to understand a couple of aurora belts under the assumption of the rotation axis to be coincided to the axis of the geomagnetic field as an equivalent dipole. Chapman model has been accepted in a revised form at present, for example, as is seen in A of Figure 1. This illustration shows a vertical cross-section relative to the solar equatorial plane. This cross-section is taken to be parallel on the radial line. The north and south poles are denoted by the marks N and S respectively. As for the tail part of the magnetopause, it has been a scientific adjustment for the consideration of plasma physics around the zone of the solar effect to the geomagnetic field. In a case of the dipole reversal, the marks N and S in A of Figure 1 are reversed and the cross-section is upside down.

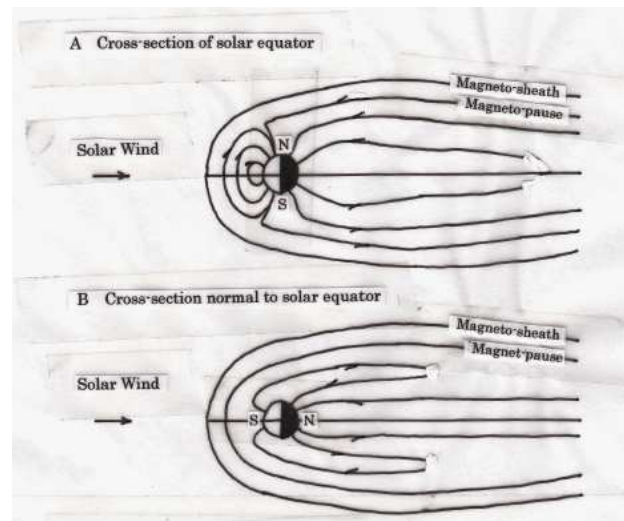


Figure 1: Magnetic field pattern of the planet in the solar system under a quiet-day solar wind effect.

Chapman model was simply for the geomagnetic field under the solar effect on a period of a solar quiet day (corresponding to the daily magnetic variation on a solar quiet day). So that, Chapman model could be called as a “Sq” model following the notation “Sq” used in the field of geomagnetism.

Chapman’s model could be applied for a case that the polar axis is parallel to the radial line on the solar equatorial plane when a planet as is same to the earth but the polar axis crosses to the earth pole. In this case, the two axes crosses to be rectangular crossing. Then, this case can be the case of inclination angle is 90 degree for 360 degree of a circle (or, $\theta = \pi/2$) after a definition of the term “inclination” is expressed by “ θ ”. In this case, the magnetopause of the planet could be shown as found in B of Figure 1. As the magnetic pole is always on the solar equatorial plane, the vertical section must be axi-symmetric about the magnetic pole of the planet. Then, the magnetopause is also found in a form of axi-symmetric pattern of the magnetosheath covering the magnetopause of the earth in shape in the magnetic environment between the planet and the sun.

Now, it is necessary to consider about what inclination is for each one of the planets in the solar system referring to the astronomical data. The data shows that the value of θ expressed in degree for each of the planets in the solar system is, as is following, the nominal for Mercury is nearly equal to zero, for Venus is 177.4, for Earth is 23.44, for Mars is 25.19, for Jupiter is 3.1, for Saturn is 26.7, for Uranus is 97.9, for Neptune is 27.3, respectively. These values of the planet rotation axis inclination in the solar system, tell us that there should be some adjustment of the magnetic pattern shown in A of Figure 1, after consideration of the inclination θ for each of the planets.

The scientists have been worked to see about environment of the planets and space around the earth. Astronomers have used to survey by using various kinds of optical tools, and the space scientists have developed to use spacecraft monitoring.

The author has noted as above on the problem for the magnetic environment between the sun and the earth with some additional remarks for the cases of the planets in the solar system.

Following to what noted above, it should be considered to obtain a key for the next step at promoting the research concerning to the earth, the planets in the solar system, the planets in the exo-sphere. In fact, the spacecrafts have launched for surveying the planets in the solar system. Now, it should be take care of the planet rotation axis inclination effect even in the cases of the planets in the exo-sphere.

5. SPACECRAFT MONITORING FOR MAGNETIC FIELD OF PLANET

After the spacecraft launched following several projects for the space and planets, the scientists have been analyzed the monitored data and sampled species in order to promote a more advanced research for obtaining a new finding.

Every one of the concerned scientific works must be a contribution of new findings, though it should be understood well in the skilled insights for scientific understanding.

For about the case for the planet Mercury, no evidence of K-H waves (Kelvin-Hermholtz waves)

was detected during the second MESSENGER flyby on 6 October 2008, during this second flyby, when the magnetic tension arising from the large tailward magnetic field component (~ 30 nT) observed on both sides of the magnetopause acted to suppress the K-H instability. Adding to the above, during MESSENGER's third flyby on 29 September 2009, multiple magnetopause crossings were observed by the MESSENGER magnetometer along the (inbound) dusk-side leg of trajectory, and, Slavin suggested that the multiple crossings could be due to the K-H instability. Then, Boardsen et al. presented an analysis of these boundary encounters, and they compared the results with the predictions of theory. Their findings indicated that the MESSENGER might have observed highly steepened, possibly turbulent, K-H boundary waves during its third flyby crossing of the dusk-side boundary of Mercury's magnetosphere.

6. CONCLUSIONS

This work concerns to problems on monitoring of spacecraft monitoring of the planets in the solar system. A linear model for the 11-year solar cycle model might be applied for the magnetic reversal in the geological stratification. As for inclination of the planet rotation axis, neutral and final stabilities are introduced in a concept model for the inclination angle between the planet rotation axis and the normal line to the solar equatorial plane. The spacecraft monitoring of the planets in the solar system has giving new findings in relation to the chronology of the earth. A bit part of the data along the spacecraft orbital path seems to suggesting Kelvin-Helmholtz instability around the magnetopause of the planet Mercury. To details, it should be promoted more advanced research in next step.

This work could be helpful for realizing the spacecraft monitoring of the planets as an extensive work of the satellite monitoring of the earth surface to find various dynamical and physical processes.

REFERENCES

1. Chapman, S. and J. Bartels, *Geomagnetism*, 1049, Oxford University Press, London, 1940.
2. Chapman, S., *Solar Prasma, Geomagnetism, and Aurora*, 141, Gordon and Breach, N.Y., 1964.
3. Berchem, J. and C. T. Russel, "The thickness of the magnetopause current layer," *Journal of Geophysical Research*, Vol. 87, 2108–2114, 1982.
4. Miura, A. and P. L. Pritchett, "Nonlocal stability analysis of the MHD Kelvin-Helmholtz instability in a compressible plasma," *Journal of Geophysical Research*, Vol. 87, 7431–7444, 1982, doi: 10.1029/JA087iA09p07431.

Superresolution: Data Mining

B. A. Lagovsky

Moscow State Institute of Radio Engineering and Automation (Technical University), Russia

Abstract— Algebraic methods allow to obtain new a priori unknown data about the image signal sources. Their use in the iterative process leads to increasing stability of inverse problems. A classification of signal sources, the assessment of their location, their characteristic features are revealed. Received additional information allows to use more efficient algorithms and to increase achieved superresolution.

1. INTRODUCTION

It is well known that the quality of the solutions of inverse problems depends on a priori information about the solution. To increase the solution stability of image reconstruction with significant superresolution is critical to have as much as possible prior information about the solution, i.e., about the signal source [1].

Our investigations have shown that information about the solution may be not only a priori.

In this paper, we used algebraic methods of solutions. They consist in the representation the approximate numerical solution in the form of an expansion in a finite function system with unknown expansion coefficients. Thus, the parametrization of inverse problems is carried out. Next, the solution is reduced to solving systems of linear algebraic equations.

Analysis of the preliminary approximate solution obtained in each step of the iterative process, allows to obtain new data about the source. Their use improves the stability of the solutions on each step of the iterative process.

A similar investigation of the received signals related to the area of data mining. Data mining is an interdisciplinary area, emergent and evolving based on pattern recognition, statistics, methods of artificial intelligence, database theory, etc.. In different systems, data mining provides many methods and algorithms — [2–4] for example. Using information obtained during the preliminary approximate solution is not typical for the most described in the literature methods of obtaining superresolution.

2. PROBLEM STATEMENT

The relationship between unknown function in the form of the angular distribution of the amplitude of the emitted signal $I(\alpha)$ and investigated signal $U(\alpha)$ in the inverse problem under investigation is expressed as a Fredholm integral equation of convolution type:

$$U(\alpha) = \int_{\Omega} f(\alpha - \phi)I(\phi)d\phi, \quad (1)$$

where Ω — the space angle in which the source is located, $f(\alpha)$ — directional pattern.

The problem is to find new, a priori unknown, the “hidden” characteristics of signal sources based on the analysis of (1) and $f(\alpha)$. It will allow finally to increase the number functions N in the representation of the approximate solutions

$$I(\alpha) = \sum_{m=1}^N b_m g_m(\alpha), \quad (2)$$

without reducing its stability, i.e., to increase the resolution.

3. MAIN RESULTS

The concept of patterns is usually taken as the basis of data mining techniques. Patterns help to solve problems of classification, pattern recognition and extraction “hidden” data from the analyzed signal. The presented method of signal analysis in order to obtain information about the signal source is based on approximate solutions of integral Equation (1) using high-speed image reconstruction algorithms. High speed algorithms based on algebraic methods making possible to obtain approximate solutions of (1) $I(\alpha)$ with a slight superresolution.

On this basis, further classification of the signal source, the evaluation of source localization and identification of its characteristics is carried out. The boundaries of the zone location of the source and its individual fragments are specified.

The analysis of preliminary approximate solutions makes it possible to reveal the “hidden” features of the source and then apply more efficient specialized algorithms to further improve the angular resolution. Specialized algorithms that are optimized for certain types of sources, adequately use received as a result of signal analysis information. It is realized as follows:

- chosen to construct a solution sequence of orthogonal functions;
- the choice of location, size and shape of the investigated region of localization of the signal source;
- additional conditions in the form of equations and inequalities between the coefficients of sequences of functions.

The choice of the orthogonal functions to represent the solutions is especially important. The dimension of the matrix systems of linear algebraic equations is limited due to the exponential growth of the instability of the solutions with increasing number of equations. This allows you to use only a small number of functions in (2) for any function system. Therefore, for each of the problem the best system functions is one in which the superposition of the first few functions represents the true source $I(\alpha)$ the best way.

During the iterations when solving the problem the information about the characteristics of the solution sequentially accumulates at each step. The obtained new information is used as an a priori data in the next step with an increasing resolution.

The described technique can significantly improve the stability of the solutions and, thus, increase the effective angular resolution.

Obtained additional information can be used not only to build the solution with increasing resolution, but also to identify the objects.

4. SIMULATION RESULTS

4.1. Using Data about the Type of Signal Source

As an example of using the new obtained information about the source the solution of inverse problem based on the Haar wavelets is shown in Fig. 1.

The obtained initial approximation to the solution showed that the source consists of two different sources with small angular dimensions. Haar wavelets were selected as the orthogonal function system on the basis of this information. They provide a high degree of localization of the sources.

During the construction of solutions at each subsequent step, only the wavelets used, that corresponded to the preliminary found solution.

Figure 1: 1 — the true source; 2 — source restored using the Haar wavelet; 3 — source restored without using the new found information about the decision, $\theta_{0.5}$ — the beamwidth of antenna.

As follows from the obtained solution the quality of the solutions when using new information about the source considerably improved.

4.2. Using Data on the Boundaries of the Zone of the Sources

Additional information of another kind — in the form of refined zone of the sources — can also be obtained in the solution process and used [5, 6].

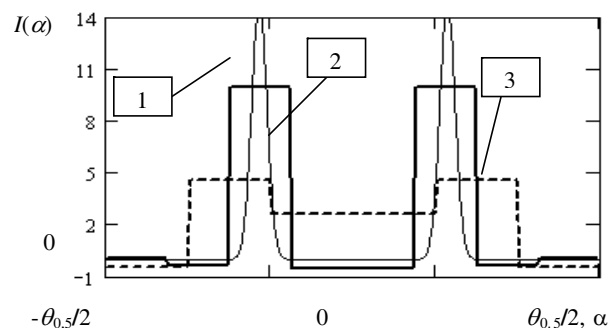


Figure 1: Restoration of the signal source by Haar wavelet using a priori information.

An example of this approach is shown in Fig. 2, where 1 — the true source of radiation. A priori, it was known that the objects with small angular dimensions can be placed in the investigated sector.

First, by representing the source of radiation in the form of an expansion to a four step functions an approximate solution was found. It is shown as a dotted line 3, with the achieved resolution $\theta_{0.5}/4$. Resulting approximate solution allowed to receive a new, “hidden” information about the location of the source and thus narrow the analyzed sector to biconnected domain ψ : $\psi \in [-\theta_{0.5}/2; -\theta_{0.5}/4] \cup [-\theta_{0.5}/2; -\theta_{0.5}/4]$.

New information was used as a priori to obtain solutions in the form of an expansion of the system of step functions in the new biconnected domain ψ .

The solution obtained in the form of an expansion of a four step functions but in a new area ψ is shown in Fig. 2 as 2. The angular resolution reached $0.2\theta_{0.5}$, the sources are localized to within $1/16\theta_{0.5}$.

Without the use of the new found information about the location of the source it would be necessary to solve the system of equations 16×16 dimension to obtain the same resolution.

As has been shown, the stability of the problem falls on the order of doubling the required resolution. So solution based on of the proposed approach has increased the stability in 100 times. Moreover, in this case the rounding errors do not allow to obtain the solution of equations with the dimension 16×16 .

Thus, consistently solving several systems of equations with the dimension 3×3 or 4×4 , it is possible to obtain new information about the location and other characteristics of the source. The use of them reduces the dimension of the system and thus significantly improves the stability of the solutions.

In turn, increasing the stability of the solutions can increase the level of superresolution achieved.

4.3. Correlation and Spectral Analysis Techniques

The method is based on an analysis of cross-correlation function of the signal and the measurement system output response to a standard object (pattern). A variation of the method is the representation of the intensity distribution of the signal source as a superposition of several standard distributions (patterns).

For the effective application of this method a database of solutions for specific consideration of the information system creates. The database is created based on patterns in the form of the simplest and most common types of sources. In addition to the database highly specialized data processing algorithms developed. Each of the algorithms used for image reconstruction with even higher resolution, but only for the signal sources strictly specific types.

The solution for each specific problem begins with the classification based on the created database. Revealed features that characterize the group that object under study belongs to. Further, on the basis of this classification is selected highly specialized algorithm. Each of these algorithms can carry out further detailed image reconstruction and to ensure the highest possible effective resolution.

Correlation and spectral analysis techniques can be used to reduce the dimension of systems of equations. To do so, the selection of several functions of the function system that represent the best solution should be performed.

The selection was carried out in several ways:

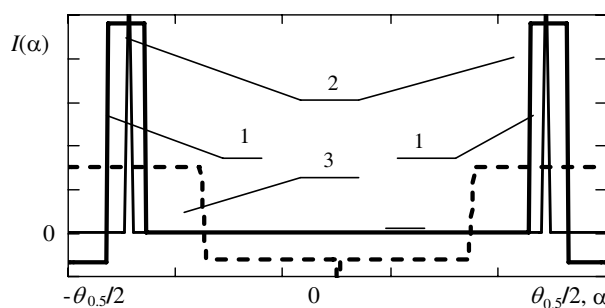


Figure 2: The solution with the new “hidden” information about the location of sources.

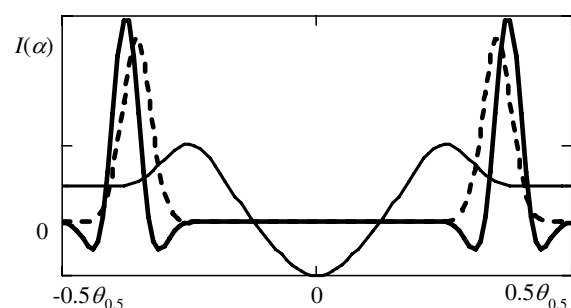


Figure 3: Restoring images using MHAT wavelets based on the analysis of their spectra.

A. Based on the analysis the signal spectrum $U(\alpha)$ and spectrum functions

$$\chi_m(\alpha) = \int_{\Omega} f(\alpha - \phi)g_m(\phi)d\phi \quad (3)$$

B. On the basis of mutual correlation functions of signals and functions $\chi_m(\alpha)$.

Figure 3 shows the results of the objects restoration with the highest resolution achieved by using MHAT-wavelets. The dashed curve — initial intensity distribution, a thin solid curve — the reconstructed image without the selection of wavelets, the solid bold curve — the image using the six selected in the analysis of $\chi_m(\alpha)$ wavelets.

When looking for the latest solution the spectral composition of the received signal was investigated. Comparison of the spectra $U(\alpha)$ and $\chi_m(\alpha)$ on the basis of MHAT-wavelets allowed to choose wavelets representing solution the best way. The resulting solution allowed to resolve two small objects, and almost exactly reproduce the angular location of the sources.

The resulting solutions have increased the effective resolution in 3–5 times and localizes small sources with an accuracy $\theta_{0.5}/4$ – $\theta_{0.5}/8$.

5. CONCLUSIONS

Methods of data mining allow to detect previously unknown regularities that connect the data analyzed and the solution. A priori unknown, “hidden” characteristics of the signal sources identified. Algebraic methods allow to use the “hidden” information about the solution. The obtained new information about the source of signal is used as a priori in the next step of finding a solution. Using this approximation to the solution improves the stability and quality of image reconstruction of objects.

The achieved angular resolution exceeded the Rayleigh criterion in 4–10 times.

REFERENCES

1. Bertero, M. and P. Boccacci, *Introduction to Inverse Problems in Imaging*, IOP Publishing, Bristol, 1998.
2. Milenova, B. and M. Campos, “Clustering large databases with numeric and nominal values using orthogonal projections,” *Oracle Data Mining Technologies*, 2002.
3. Witten, H. and E. Frank, *Data Mining: Practical Machine Learning Tools and Techniques*, 2nd Edition, Morgan Kaufmann, 2005.
4. Zhu, X. and I. Davidson, *Knowledge Discovery and Data Mining: Challenges and Realities*, Hershey, New York, 2007.
5. Lagovsky, B. A., “High performance angular resolution algorithm for radar systems,” *PIERS Proceedings*, 1637–1641, Moscow, Russia, Aug. 18–21, 2009.
6. Lagovsky, B. A., “Algorithm for the determination of targets coordinates in structure of the multiple targets with the increased effective resolution,” *PIERS Proceedings*, 1642–1645, Moscow, Russia, Aug. 18–21, 2009.

Focusing GPR Images Collected from Archaeological Investigations along the “Basilian Monks’ Path of Faith” (Aspromonte National Park — Southern Calabria, Italy): Analysis of the Performances of Different Strategies

G. Angiulli¹, V. Barrile², D. De Carlo¹, T. Isernia¹, and A. Sgró¹

¹DIMET, University of Mediterranea
via Graziella, Loc. Feo di Vito, Reggio Calabria 89100, Italy

²MECMAT, University of Mediterranea
via Graziella, Loc. Feo di Vito, Reggio Calabria 89100, Italy

Abstract— The “Basilian monks’ Path of Faith” is a religious route in the Aspromonte National Park. Along it is located the ancient town of Africo Vecchio. Here some archaeological investigations have been carried out with the aid of the Ground Penetrating Radar. In this paper, results of the performances of four different approaches to the focusing problem are reported and discussed.

1. INTRODUCTION

From the fifth to the twelfth century A.D., the Basilian monks gave a considerable impulse to development of the monasticism in the Southern Italy [1]. In that period were built many churches and monasteries, which are a cultural heritage of great artistic and historical value. The “Basilian monks’ Path of Faith” is a religious route in the Aspromonte National Park which extends itself from the town of Bova Superiore to the “Polsi’s Sanctuary”. Along this path is also located the abandoned town of Africo Vecchio (see Fig. 1) and here some GPR surveys have been carried out on the floors of two ancient churches. The aim of these investigations was to validate some hypothesis about the existence of buried structures and crypts [2]. To remedy the effect of the hyperbolic dispersion on the raw data, different focusing algorithms have been proposed in the scientific literature [3, 4]. In this paper, we analyze the performances of four focusing techniques: a) *Diffraction summation*, b) *Kirchhoff migration*, c) *F-K migration*, and d) *SAR migration* on the data collected by our surveys.

2. SUMMARY ON THE FOCUSING METHODS

In what follows we give a brief account about the focusing techniques exploited in this work.

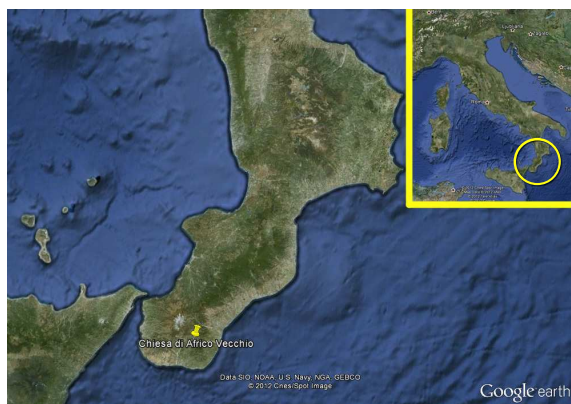


Figure 1: Location of the town of Africo Vecchio — (Calabria, Southern Italy).

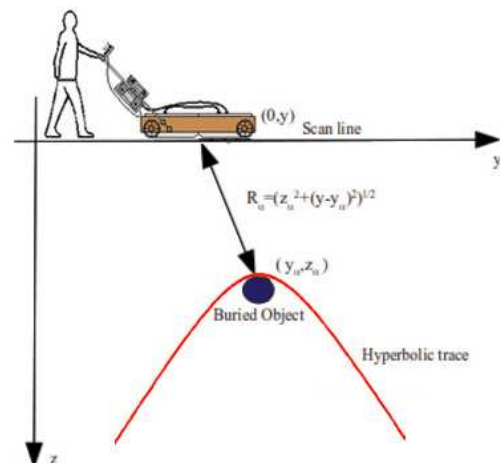


Figure 2: Pictorial representation of the hyperbolic dispersion effect.

2.1. Diffraction Summation

When a monostatic GPR is moving on a scan line along the y -axis, the presence of a buried object, situated at the point (y_α, z_α) , give rise to an hyperbolic trace inside the B-scan described by

$$R_\alpha = \sqrt{z_\alpha^2 + (y_\alpha - y_\beta)^2} \quad (1)$$

where R_α is the distance between the measuring position and the scatterer (see Fig. 2). Diffraction summation is the more simple approach to focus this trace back to the target [3, 4]. It operates as follows: if Ψ is the scalar field representative of the data collected along the scan line y , the focused scalar field Ψ_f at (y_α, z_α) can be obtained as the result of a summation of the values of Ψ along the points lying on the hyperbolic diffraction curve defined by (1)

$$\Psi_f(y_\alpha, z_\alpha) = \sum_{\beta} \Psi \left(y_\beta, t = \frac{R_\alpha}{v_e} \right) \quad (2)$$

where $v_e = \frac{v_f}{2}$ is the velocity of the waves in the medium obtained from the *exploding source* model [4].

2.2. Kirchhoff Migration

The Kirchhoff migration method is very similar to the Diffraction summation. The focused scalar field Ψ_f at (y_α, z_α) can be written as [3, 4]

$$\Psi_f(y_\alpha, z_\alpha) = \frac{1}{2\pi v_e} \sum_{\beta} \frac{\partial}{\partial t} \Psi \left(y_\beta, \frac{R_\alpha}{v_e} \right) \frac{\cos(\theta)}{R_\alpha} \quad (3)$$

where the term $\cos(\theta)$, called *obliquity* [4], takes into account of the fact that the normal to the wave front is not parallel to the normal of the measuring scan line, and the term $\frac{1}{R_\alpha}$, called *spreading factor* [4], of the spreading losses of the waves in the soil.

2.3. F-K Migration

The F-K migration can be considered a variant of the Phase Shift method, that is valid only for a homogeneous medium. It can be demonstrated that the focused field Ψ_f can be expressed via the inverse Fourier transform as

$$\Psi_f(y, z) = \iint \tilde{\Psi}(k_y, \omega) e^{j(k_z(\omega)z + k_y y)} dk_y d\omega \quad (4)$$

where k_y and k_z are the spatial wavenumbers, ω is the angular frequency and $\tilde{\Psi}(k_y, \omega)$ is the Fourier transform of $\Psi(y, t)$. Taking into account that the wavenumber k_z is given by

$$k_z = \sqrt{\left(\frac{\omega}{v_e}\right)^2 - k_y^2} \quad (5)$$

the Equation (4) becomes

$$\Psi_f(y, z) = v_e^2 \iint \frac{k_z}{\omega} \tilde{\Psi}(k_y, \omega) e^{j(k_y y + k_z z)} dk_y dk_z \quad (6)$$

The above relation is computationally attractive: the focused data $\Psi_f(y, z)$ can be obtained in simply way as the inverse Fourier transform of the product between the term $\frac{k_z}{\omega}$ and the Fourier transform $\tilde{\Psi}$ of the raw data Ψ [3, 4].

2.4. SAR Migration

The SAR migration technique can be derived starting to consider a scenario in which are buried N scatterers located at the coordinate (y_α, z_α) (for $\alpha \in \{1, \dots, N\}$), each having reflectivity ρ_α [3, 4]. $\Psi(y, t)$ can be expressed as

$$\Psi(y, t) = \sum_{\alpha} \rho_\alpha \exp \left(-j \frac{\omega}{v_e} \sqrt{z_\alpha^2 + (y_\alpha - y)^2} \right) \quad (7)$$

If the Fourier Transform of the Equation (7) is taken, and the phase stationary method is applied, we obtain

$$\tilde{\Psi}(k_y, k_z) = P(\omega) \sum_{\alpha} \rho_{\alpha} \exp(-jz_{\alpha}k_z + jy_{\alpha}k_y) \quad (8)$$

where $P(\omega)$ is the Fourier Transform of the GPR pulse, and k_z is given by relation (5) [4]. Now, if the focused GPR image $\Psi_f(y, z)$ is assumed as

$$\Psi_f = \sum_{\alpha} \rho_{\alpha} \delta(y - y_{\alpha}, z - z_{\alpha}) \quad (9)$$

follows that [4]

$$\Psi_f(y, z) = \iint \frac{\tilde{\Psi}(k_y, \omega(k_z))}{P(\omega(k_z))} \exp(-jk_y y + jk_z z) dk_y dk_z \quad (10)$$

The efficient evaluation of (10) by means of the Fast Fourier transform requires evenly spaced points in the (k_y, k_z) domain involving an interpolation problem [3, 4].

3. ARCHAEOLOGICAL SITES, MEASUREMENT EQUIPMENT, DATA ACQUISITION AND PROCESSING

The town of Africo Vecchio is situated in the heart of Aspromonte National Park at about 700 m above the sea level. It was founded by the inhabitants of Delia, a Locrian's colony, in the ninth century A. D.. Africo Vecchio was a Bova's dependence, and until the fall of feudalism it has been owned by the Archbishop of Reggio Calabria (The town was delivered to him in 1195 by Henry VI during the conquest of Sicily). It was abandoned after the "big flood" in 1951 [1]. Here some GPR surveys have been carried out in the ancient churches of San Salvatore and San Leo [2].

In our investigations we used a GPR IDS RIS-K2 system manufactured by Ingegneria Dei Sistemi S.p.A., equipped with a 200 MHz antenna. The profiles were acquired in continuous modality setting a time window of 250 ns and a time sampling of 0.5 ns. The data were stored in the ".dt" format. All the measure operations were realized by a couple of operators and the data were processed off-line exploiting the following processing sequence: i) *first-arrival time alignment*, ii) *dewow*, iii) *background removal*, iv) *time gain* [3–7]. The above sequence has been implemented in the MATLAB environment, and executed on a computer having 4 GB of main memory and mounting a 64 bit ADM Athlon Dual Core processor.

4. GPR SURVEY: RESULTS AND DISCUSSION

The investigation in San Nicola's church was taken place in front of the sacrarium on an area of 152 m² having rectangular size. We acquired 25 profiles 8 m long and 0.76 m apart in the x direction, and 16 profiles 25 m long and 0.5 m apart in the y direction (see Fig. 4). Fig. 5 shows the raw data related to the profile TAB10016_X. As it can be seen a deep and large attenuated zone extending from the time of about 40 ns to the bottom of the image. A diffraction hyperbola is clearly visible on the right of the radargram. From its shape a velocity v_e in the soil of 6.7 cm ns⁻¹ was estimated. Figs. 6, 7, and 8 show the images focused exploiting i) Hyperbolic Summation, ii) Kirchhoff migration, and iii) F-K migration, respectively (the result obtained with SAR method is not shown here, because it is very similar to that provided by F-K method). We can conclude



Figure 3: A view of San Nicola's church.

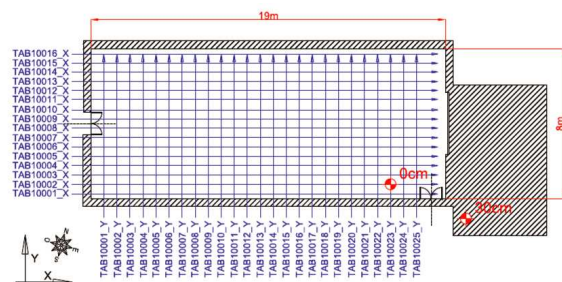


Figure 4: Planimetry with profiles locations.

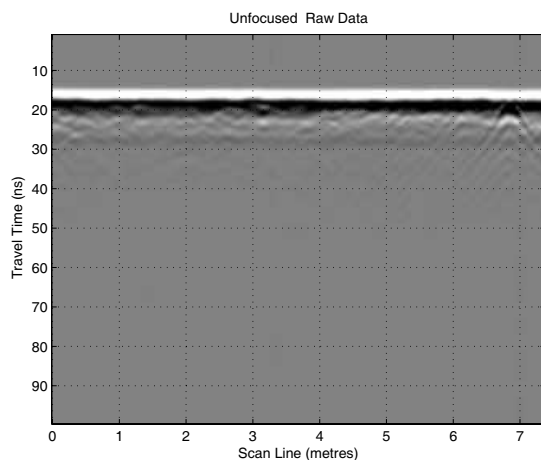


Figure 5: Raw image (TAB10024-Y B).

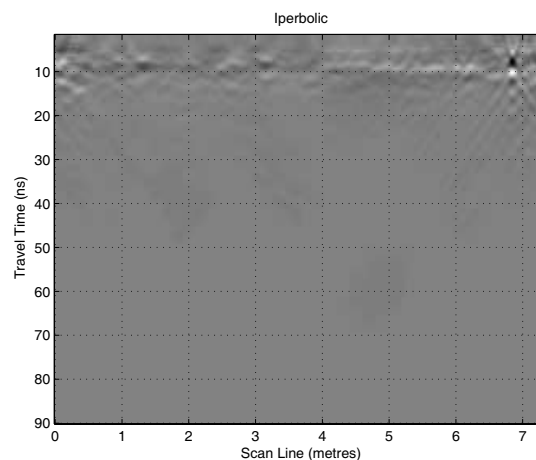


Figure 6: Image focused by diffraction summation.

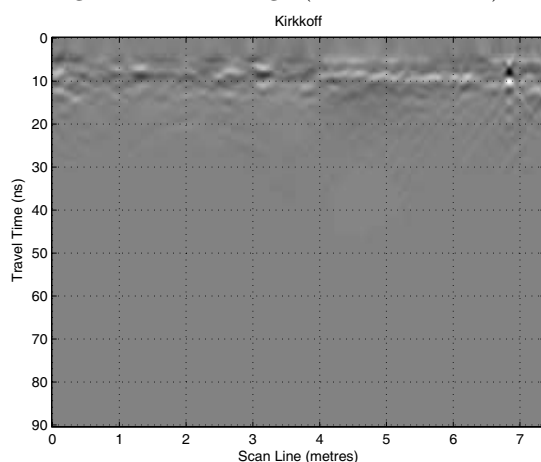


Figure 7: Image focused by Kirkhoff migration.

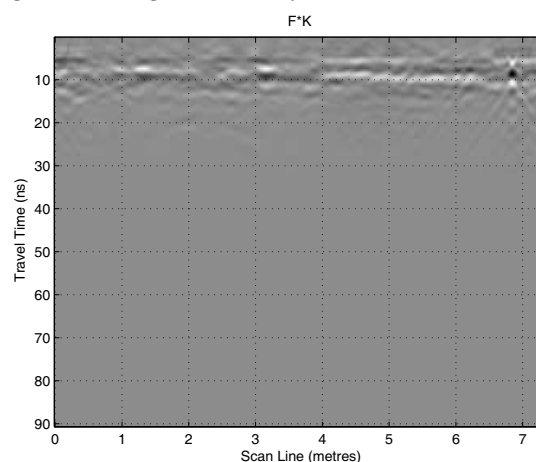


Figure 8: Image focused by F-K migration.



Figure 9: A view of San Leo's church.

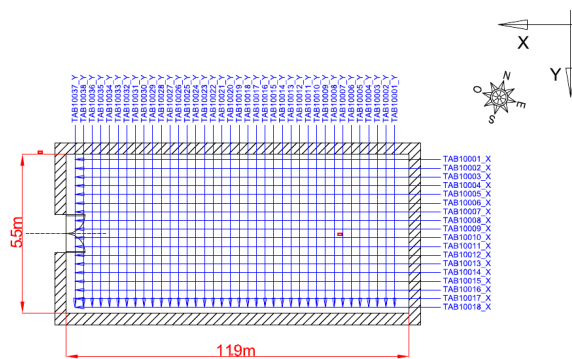


Figure 10: Planimetry with profiles locations.

from these results that the F-K migration technique focuses the hyperbola trace slightly better than the other methods (the focused anomaly is probably a cavity). In Table 1 the execution times are reported. The low computational time of the F-K migration is apparent. The survey in San Leo's church was taken place in front of the communion table on an area of about 66 m^2 having rectangular size. We acquired 37 profiles 11.5m long and 0.31 m apart in the x direction, and 18 profiles 5.5m long and 0.3m apart in the y direction, as shown in Fig. 10. Fig. 11 shows the raw data related to the profile TAB10016_X. In this radargram can be observed a large and deep attenuated zone which starts from the time of about 30 ns until its bottom. Several diffraction hyperbolas are visible at time of about 10 ns, and a velocity of 6.7 cm ns^{-1} was estimated. Also in this case the F-K migration gives better results than the other focusing methods (see Fig. 12).

Table 1: The execution times of the focusing algorithms exploited in this study.

Method	TAB10024_Y	TAB10016_X
Diffraction Summation	7.94 sec.	13.2 sec.
Kirchhoff Migration	38.2 sec.	89.8 sec.
F-K migration	1.61 sec.	2.67 sec.
SAR focusing	1.72 sec.	2.92 sec.

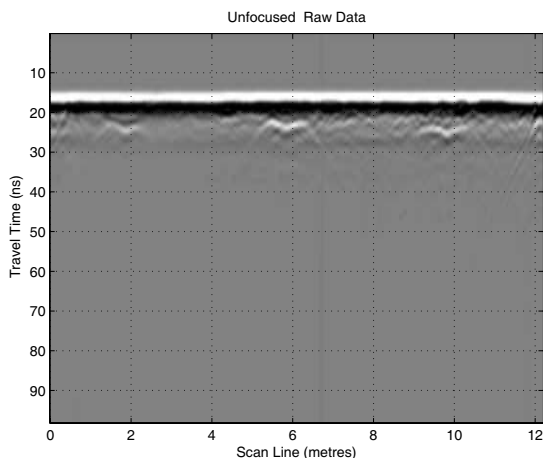


Figure 11: Raw image (TAB10016_X B-scan).

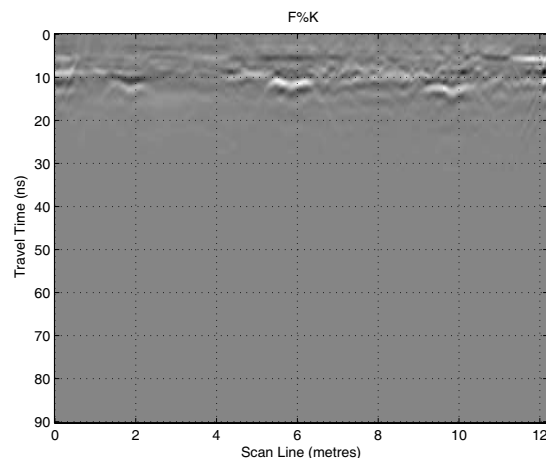


Figure 12: Image focused by F-K migration.

5. CONCLUSION

In this paper, we have reported results about the performances of different focusing strategies to process GRP images collected in two churches located in the territory of the abandoned town of Africo Vecchio. Before to focus the collected data, these have been processed following a standard approach. The obtained results point out the superiority of the F-K algorithm on the other techniques exploited in this work.

ACKNOWLEDGMENT

This work has been carried out in the framework of the regional project TECNE (at the roots of Territorial identity: innovative interdisciplinary methods for the identification, development, dissemination of artistic and cultural heritage) financed by Region Calabria and held jointly by the Academy of Fine Arts of Reggio Calabria and the University Mediterranea.

REFERENCES

1. D'Agostino, E., *Da Locri a Gerace. Storia di una diocesi della Calabria bizantina dalle origini al 1480*, Rubbettino Editore, 2005.
2. Minuto, D., *Catalogo dei monasteri e dei luoghi di culto tra Reggio e Locri*, Edizioni di Storia e Letteratura, Roma, 1977.
3. Daniels, J. D., Editor, *Ground Penetrating Radar*, 2nd Edition, The Institution of Electrical Engineers, London, 2004.
4. Turk, A. S., K. A. Hocaoglu, and A. A. Vertiy, Editors, *Subsurface Sensing*, Wiley Series in Microwave and Optical Engineering, Wiley-Blackwell, 2011.
5. Leucci, G., "Ground-penetrating radar survey to map the location of buried structures under two churches," *Archaeological Prospection*, Vol. 9, 217–228, 2002.
6. Orlando, L., "Georadar data collection, anomaly shape and archaeological interpretation — A case study from central Italy," *Archaeological Prospection*, Vol. 14, 213–335, 2007.
7. Masini, N., R. Persico, and E. Rizzo, "Some examples of GPR prospecting for monitoring of the monumental heritage," *Journal of Geophysics and Engineering*, Vol. 7, 190–199, 2010.

Nested BiCGSTAB to Solve Complex Linear Systems Arising from Discretization of EFIE

G. Angiulli¹, S. Calcagno², D. De Carlo¹, and A. Sgró¹

¹DIMET, University Mediterranea, via Graziella n.1, Reggio Calabria 89100, Italy

²MECMAT, University Mediterranea via Graziella n.1, Reggio Calabria 89100, Italy

Abstract— Although in the last years the BiCGStab has been employed with success to handle large linear systems arising from the RWG MoM discretization of electromagnetic scattering problems formulated by EFIE, its nested version, the N-BiCGstab, has received little attention. In this work, an analysis of its performances is presented. It demonstrates that N-BiCGStab is, at least in the examined cases, faster and more robust than the standard BiCGStab coupled with diagonal or ILU preconditioning.

1. INTRODUCTION

In Computational Electromagnetics (CEM) a number of alternative integral formulations are available to model the electromagnetic scattering and radiation phenomena. Among these, the standard form of the electric field integral equation (EFIE) still remains extensively exploited, even in spite of some well-known limitations (see [1] and references within). When a real life EM problem is tackled, the discretization of the EFIE provides a very large, dense and indefinite linear system of equations, that can be solved in an efficient way only by using a Krylov subspace method (KSM) in conjunction with a suitable preconditioning technique (PT) [2]. During the years, many efforts have been done by researchers to define the best choice among the different couples (KSM, PT) available in literature. Nowadays, a good compromise seems reached by the use of the Generalized Minimal Residual method (GMRES), in combination with ILU preconditioning (see [2] and references within). Although the GMRES is optimal, in the sense that it leads to a minimal residual solution over the associate Krylov subspace, such a goal is achieved against a demand in memory space that grows linearly with the number of iterations and that could become rapidly prohibitive in term of memory requirements (see [2] and references within). Even if this limitation can be circumvented when GMRES is employed in its restarted version, the GMRES(m), it is a very difficult task to assign a priori value to the restart parameter m such that both convergence and memory requirements are both optimized. Hence, especially when large and dense non-Hermitian linear systems are tackled on small workstation a technique involving a fixed amount of memory per iteration should be employed, if out-of-memory errors must to be avoided. This is the case of the Bi-Conjugate Stabilized (BiCGStab) method. In spite of being less popular than the GMRES, BiCGStab has been already exploited with success in CEM literature to treat large EM problems. However, as underlined in [3], the performances of the BiCGStab can be improved providing that the preconditioning step is treated by another KSM so realizing the Nested BiCGStab (N-BiCGStab) method. Although N-BiCGStab has been extensively employed in many others engineering fields (see for example [4] and references within), at the best of our knowledge little attention has been devoted to it in CEM. On the basis of these considerations, in this work we analyse the performances of N-BiCGStab method for solving the discretized EFIE in the case of plane wave scattering by a conducting sphere.

2. BASICS ON THE EFIE

The Electrical Field Integral Equation (EFIE) can be formulated in terms of a functional equation such as $\mathcal{L}f = g$, where \mathcal{L} is an operator between function spaces X and Y , so that $f \in X$ and $g \in Y$. In particular, \mathcal{L} is defined by

$$\Gamma \rightarrow \mathbb{C}^3 : \mathbf{J}(\mathbf{r}') \mapsto \hat{\mathbf{t}} \cdot \int_{\Gamma} \mathbf{G}(\mathbf{r}, \mathbf{r}') \cdot \mathbf{J}(\mathbf{r}') d\Gamma(\mathbf{r}') \quad (1)$$

where $\hat{\mathbf{t}}$ is the tangential unit vector on Γ , the surface of the scatterer; X and Y can be taken to be spaces of smooth Hölderian functions $\mathbb{R}^3 \rightarrow \mathbb{C}^3$ of a suitable order, $f = \mathbf{J}(\mathbf{r}')$ is the induced surface density current flowing on the obstacle defined by mathematical surface Γ , $g = \hat{\mathbf{t}} \cdot \mathbf{E}^{inc}(\mathbf{r})$

is the tangential component of the incident field and $\mathbf{G}(\cdot, \cdot') : \Omega \times \Gamma$ is the dyadic Green's function (here $\Omega = \mathbb{R}^3 \setminus \Gamma$ for notational convenience), that can be expressed in terms of the scalar Green's function $g(\cdot, \cdot')$ as

$$\mathbf{G}(\mathbf{r}, \mathbf{r}') = jk_0\eta_0 \left[\mathbf{I} + \frac{\nabla\nabla'}{k_0^2} \right] g(\mathbf{r}, \mathbf{r}'), \quad \forall(\mathbf{r}, \mathbf{r}') \in \Omega \times \Gamma \quad (2)$$

with

$$g(\mathbf{r}, \mathbf{r}') = \frac{e^{-jk_0|\mathbf{r}-\mathbf{r}'|}}{4\pi|\mathbf{r}-\mathbf{r}'|} \quad (3)$$

(the harmonic time-dependence $e^{j\omega t}$ is assumed and suppressed throughout) where k_0 is the wave-number and η_0 is the impedance of the free space. The EFIE is commonly solved by means of the MoM in conjunction with Rao-Wilton-Glisson (RWG) edge elements [1], which ultimately involves the solution of large, dense linear systems like

$$\mathbf{Z}\mathbf{i} = \mathbf{v}, \quad \mathbf{Z} \in \mathbb{C}^{n \times n} \quad \text{and} \quad \mathbf{v}, \mathbf{i} \in \mathbb{C}^n \quad (4)$$

If direct methods (i.e., LU decomposition) can be employed when the matrix system dimension n is of intermediate size, in the case of a very large and dense linear system this approach becomes prohibitive in terms of computing time. Then, the only feasible alternative to solve Eq. (4) is to resort to a Krylov Subspace method (KSM) coupled with a suitable preconditioner \mathbf{P} .

3. THE N-BICGSTAB IN A NUTSHELL

In what follows we present the ideas and principles characterizing N-BiCGStab (for a more detailed discussion see [3] and references within). The starting point of our discussion is the standard BiCGStab algorithm. Basically BiCGStab searches for an approximate solution \mathbf{i}_n of the matrix system (4) of the form

$$\mathbf{i}_n \in \mathbf{i}_0 + \mathcal{K}_n(\mathbf{r}_0, \mathbf{Z}) \quad (5)$$

in which $\mathbf{i}_0 \in \mathbb{C}^n$ is any initial guess for the solution of Eq. (4), $\mathbf{r}_0 = \mathbf{v} - \mathbf{Z}\mathbf{i}_0$ is the residual vector, and $\mathcal{K}_n(\mathbf{r}_0, \mathbf{Z})$, defined as

$$\mathcal{K}_n(\mathbf{r}_0, \mathbf{Z}) = \text{span} \{ \mathbf{r}_0, \mathbf{Z}\mathbf{r}_0, \dots, \mathbf{Z}^{n-1}\mathbf{r}_0 \} \quad (6)$$

is the n -th Krylov subspace generated by the couple $(\mathbf{r}_0, \mathbf{Z})$. The approximate solution \mathbf{i}_n , is founded imposing the Petrov-Galerkin condition

$$\mathbf{b} - \mathbf{Z}\mathbf{i}_n \perp \mathcal{K}_n(\hat{\mathbf{r}}_0, \mathbf{Z}^H) \quad (7)$$

where $\hat{\mathbf{r}}_0 \in \mathbb{C}^n$ is an arbitrary vector satisfying the condition $\langle \hat{\mathbf{r}}_0, \mathbf{r}_0 \rangle = 1$. To compute \mathbf{i}_n , BICGStab exploits a two-sided Lanczos procedure in order to build the biorthogonal bases $\{\mathbf{v}_1, \dots, \mathbf{v}_n\}$ $\{\mathbf{w}_1, \dots, \mathbf{w}_n\}$ of the Krylov subspaces $\mathcal{K}_n(\mathbf{r}_0, \mathbf{Z})$, $\mathcal{K}_n(\hat{\mathbf{r}}_0, \mathbf{Z}^H)$ generated by the matrix operators \mathbf{Z} and \mathbf{Z}^H , respectively. More specifically, the following recurrence formulas are exploited

$$\mathbf{Z}\mathbf{V}_n = \mathbf{V}_{n+1}\mathbf{T}_n \quad (8)$$

$$\mathbf{Z}^H\mathbf{W}_n = \mathbf{W}_{n+1}\hat{\mathbf{T}}_n \quad (9)$$

where

$$\mathbf{V}_n = [\mathbf{v}_1, \dots, \mathbf{v}_n] \quad \mathbf{W}_n = [\mathbf{w}_1, \dots, \mathbf{w}_n] \quad (10)$$

$$\mathbf{T}_n = \begin{bmatrix} \alpha_1 & \beta_1 & & & & \\ \gamma_1 & & \ddots & \ddots & & \\ & & \ddots & \ddots & \beta_{n-1} & \\ & & & \gamma_{n-1} & \alpha_n & \\ & & & & \gamma_n & \end{bmatrix} \quad \hat{\mathbf{T}}_n = \begin{bmatrix} \alpha_1^* & \gamma_1^* & & & & \\ \beta_1^* & & \ddots & \ddots & & \\ & & \ddots & \ddots & \gamma_{n-1}^* & \\ & & & \beta_{n-1}^* & \alpha_n^* & \\ & & & & \beta_n^* & \end{bmatrix} \quad (11)$$

from which we have that \mathbf{i}_n can be expressed as

$$\mathbf{i}_n = \mathbf{i}_0 + \hat{\mathbf{y}}_n \quad (12)$$

where $\hat{\mathbf{y}}_n$ is given by the following relations

$$\hat{\mathbf{y}}_n = \mathbf{V}_n \mathbf{y}_n \quad (13)$$

$$\mathbf{y}_n = \min_{\mathbf{y}} \|\|\mathbf{r}_0\| \mathbf{e}_1 - \mathbf{T}_n \mathbf{y}\| \quad (14)$$

Now, if the standard BiCGStab method is coupled with a preconditioner \mathbf{P} , Eq. (12) becomes of the form

$$\mathbf{i}_n = \mathbf{i}_0 + \hat{\mathbf{p}} \quad (15)$$

where the term $\hat{\mathbf{p}}$ in (15) is the solution of

$$\mathbf{P} \hat{\mathbf{p}} = \hat{\mathbf{y}}_n \quad (16)$$

Unlike the preconditioned BiGGStab, the N-BiCGStab computes the term $\hat{\mathbf{p}}$ in (15) exploiting a variable preconditioner i.e., a preconditioner \mathbf{P} capable to change itself at each step executed by the algorithm. This effect of “variable preconditioning” is obtained in N-BiCGStab by solving (16) in approximate way by means of a secondary KSM (which is chosen by the user). A pseudocode of the F-BiCGStab method is reported in Table 1.

4. NUMERICAL RESULTS

As a test case we considered the plane wave scattering by a perfect conducting metallic sphere with radius $r = 0.5$ m at the frequency $f = 150$ MHz. A computer code implementation of the MoM RWG and of the N-BiCGStab method has been developed exploiting the MATLAB framework. Simulations have been carried out using a PC with an Intel Core™ 2 Duo processor at 1.66 GHz and 4 GB of main memory. The conducting sphere has been discretized with $n = 11850$ edges. All the results have been obtained fixing an accuracy $\epsilon = 10^{-6}$ and a maximum number of iterations $\text{maxit} = 500$ for the outer level, while fixing $\epsilon = 10^{-1}$ and $\text{maxit} = 100$ for the inner level. The initial guess vector is set equal to the null vector for both levels. Different KSMs have been considered for the inner level but only results considering the BiCGStab as inner method are shown.

Table 1: Right Preconditioned N-BiCGStab method.

<p>1: Compute $\mathbf{r}_0 = \mathbf{v} - \mathbf{Z}\mathbf{i}_0$ and choose $\hat{\mathbf{r}}_0$ s.t. $\langle \mathbf{r}_0, \hat{\mathbf{r}}_0 \rangle \neq 0$. Set $\beta = \ \mathbf{r}_0\$</p> <p>2: For $i = 1, 2, \dots$</p> <p>3: Set $\rho_{i-1} = \langle \hat{\mathbf{r}}, \mathbf{r}_i \rangle$</p> <p>4: If $\rho_{i-1} = 0$ Then Method Fails</p> <p>5: If $i = 1$ Then</p> <p>6: $\mathbf{p}_i = \mathbf{r}_i$</p> <p>7: Else</p> <p>8: $\beta_{i-1} = \frac{\rho_{i-1} \alpha_{i-1}}{\rho_{i-2} \omega_{i-1}}$</p> <p>9: $\mathbf{p}_i = \mathbf{r}_{i-1} + \beta_{i-1}(\mathbf{p}_{i-1} - \omega_{i-1} \mathbf{v}_{i-1})$</p> <p>10: EndIf</p> <p>11: Solve $\mathbf{P}\hat{\mathbf{p}} = \mathbf{p}_i$ by a secondary KSM</p> <p>12: $\mathbf{v}_i = \mathbf{Z}\hat{\mathbf{p}}$</p> <p>13: $\alpha_i = \frac{\rho_{i-1}}{\langle \hat{\mathbf{r}}, \mathbf{v}_i \rangle}$</p>	<p>14: $\mathbf{s} = \mathbf{r}_{i-1} + \alpha_i \mathbf{v}_i$</p> <p>15: If $\ \mathbf{s}\$ is small enough Then Set $\mathbf{i}_i = \mathbf{i}_{i-1} + \alpha_i \hat{\mathbf{p}}$ and Stop</p> <p>16: Solve $\mathbf{P}\hat{\mathbf{s}} = \mathbf{s}$ by a secondary KSM</p> <p>17: $\mathbf{t} = \mathbf{Z}\hat{\mathbf{s}}$</p> <p>18: $\omega_i = \frac{\langle \mathbf{t}, \mathbf{s} \rangle}{\langle \mathbf{t}, \mathbf{t} \rangle}$</p> <p>19: $\mathbf{i}_i = \mathbf{i}_{i-1} + \alpha_i \hat{\mathbf{p}} + \omega_i \hat{\mathbf{s}}$</p> <p>20: $\mathbf{r}_i = \mathbf{s} - \omega_i \mathbf{t}$</p> <p>21: Check convergence, continue if necessary for continuation it is necessary that $\omega_i \neq 0$</p> <p>22: EndIf</p> <p>23: EndFor</p>
--	---

Table 2: Settings and results of numerical experiments.

Method	Preconditioner	Convergence	Iterations	Time [sec]	Residual
BiCGStab	none	no	500	~ 467	~ $2.78 \cdot 10^{-5}$
Nested BiCGStab	\mathbf{X}	yes	10	~ 150	~ $2.96 \cdot 10^{-8}$
BiCGStab	ILU	no (out of memory)	-	-	-
BiCGStab	diag(\mathbf{Z})	yes	486	~ 697	~ $3.82 \cdot 10^{-7}$

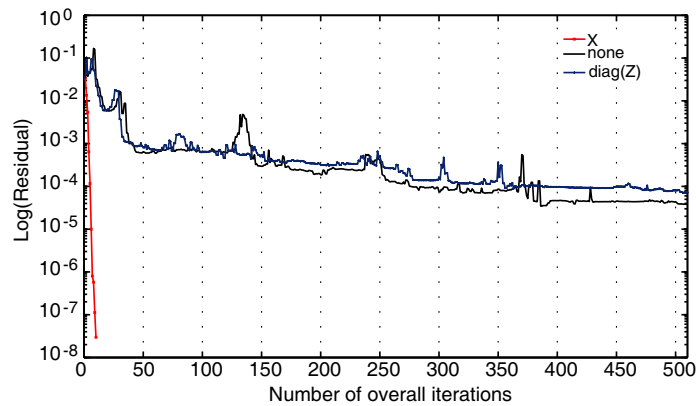


Figure 1: Euclidean norm of the residual vector. Note that in the case under consideration the ILUpreconditioned BiCGStab saturates the available memory and so cannot be compared with the other techniques.

Table 2 compares the performances of the N-BiCGStab, in which the preconditioning phase (6) is carried out exploiting the antihermitian component of \mathbf{Z} [5], with those provided by i) the standard BiCGStab algorithm and ii) some preconditioned implementations of it. Table 2 and Figure 1 make apparent how the N-BiCGStab reduces significantly both the overall number of iterations and the computational time required to reach convergence.

5. CONCLUSION

In this work, preliminary results on the performances of the N-BiCGStab for non-Hermitian linear system arising from the discretization of the EFIE is presented. At least in the examined cases, numerical results show that this technique can reduce significantly the computational burden with respect the standard BiCGStab coupled with a diagonal or ILU preconditioner.

REFERENCES

1. Angiulli, G. and S. Tringali, "Stabilizing the E -field integral equation at the internal resonances through the computation of its numerical null space," *International Journal of Applied Electromagnetics and Mechanics*, No. 32, 63–72, 2010.
2. Bunse-Gerstner, A. and I. Cañas-Gutierrez, "A preconditioned GMRES for complex dense linear systems from electromagnetic wave scattering problems," *Linear Algebra and Its Applications*, Vol. 416, 135–147, 2006.
3. Vogel, J. A., "Flexible BiCG and flexible BI-CGSTAB for nonsymmetric linear systems," *Applied Mathematics and Computation*, Vol. 188, 226–233, 2007.
4. Manguoglu, M., A. H. Sameh, T. E. Tezduyar, and S. Sathe, "A nested iterative scheme for computation of incompressible flows in long domains," *Computational Mechanics*, Vol. 43, No. 1, 73–80, 2008.
5. Angiulli, G., P. Quattrone, and S. Tringali, "An algebraic preconditioner based on properties of the skew-hermitian part of the linear systems arising from the discretization of the E -field integral equation," *International Conference on Electromagnetics in Advanced Applications, ICEAA'09*, 632–635, 2009.

Comparison of Different Metaheuristic Optimization Methods' Capability in Two Dimensional Inverse Scattering

Maysam Haghparast, S. A. Mirtaheri, and M. S. Abrishamian

Department of Electrical and Computer Engineering
K. N. Toosi University of Technology, Tehran, Iran

Abstract— Four optimization methods are considered as the solver of inverse scattering problem. Under unique condition and for two different profiles the inverse problem is solved. The reconstruction errors for permittivity and conductivity and reconstruction time are the evaluating criteria. For two scenarios this criteria are presented.

1. INTRODUCTION

The objective of an electromagnetic inverse scattering is to extract electromagnetic properties of scatterers from scattered field measurements. Generally speaking, properties could be location, shape and the profile of object [1]. The method of problem solving depends on the final aim of reconstruction. Profile reconstruction is a conventional class of inverse scattering problems and in a wide group of inverse problem is the final objective. In this group of problems, the object is discretized to cells and for each cell a value for permittivity and a value for electrical conductivity are considered as an unknown variable [2]. In order to solve this kind of problems, a group of possible answers are considered and the direct electromagnetic problem is solved for all of these answers. Then a cost function is defined as below: the difference between measured and simulated electromagnetic fields. Now the problem is to minimize the cost function. From this point of view, the inverse problem is considered as an optimization problem. There are various kinds of optimization methods and selection between them is an open problem. According to nature of inverse scattering problems usually traditional and analytical optimization methods are not proper choice. During last years, usually various metaheuristic optimization methods are proposed for inverse problems. Although all of proposed metaheuristic optimization methods are proved to be capable of optimization, their ability is varied due to nature of optimization problem. In this study we considered four of these methods: Particle swarm optimization (PSO), differential evolution (DE), ant colony optimization (ACO) and harmony search (HS).

2. INTRODUCTION OF FOUR OPTIMIZATION METHODS

Among different kind of metaheuristic optimization methods four of them are considered. In this, their ability in 2D inverse scattering problem is evaluated. Here we briefly introduce the optimization methods. For more discussion, reader may refer the references.

PSO is inspired by the movement of a group of birds and fish. This method considers a population of possible answers and updated these answers iteratively. Each particle's movement is influenced by its local best known position and is also guided toward the best known positions in the search-space, which are updated as better positions are found by other particles. This is expected to move the swarm toward the best solutions [3].

DE is a population based optimization method and classified as evolutionary method. It's similar to genetic algorithm method and uses three steps to improve the considered possible answers: mutation, selection and cross over. After a number of iteration, the answers converge to optimum answer [4].

ACO is a probabilistic method for optimization. The main version of ACO only could be applied to discrete variable problems, but a continuous version of ACO is proposed and could be applied to continuous parameter optimization. This method is classified in the group of swarm intelligence [5].

HS is a music inspired optimization method and optimization could be done through 3 steps [6].

3. TWO DIMENSIONAL INVERSE PROBLEM DESCRIPTION

In order to compare the mentioned optimization methods, a two dimensional inverse scattering problem is considered. As depicted in Figure 1, a $10 * 10$ cells square shape is considered. A transmitter and four symmetric receivers are considered.

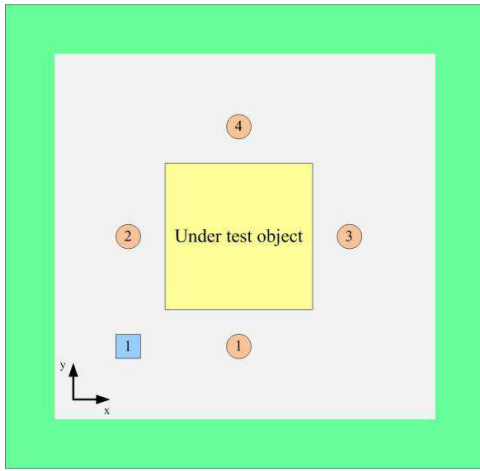


Figure 1: The arrangement of under investigation object, transmitter and receivers.

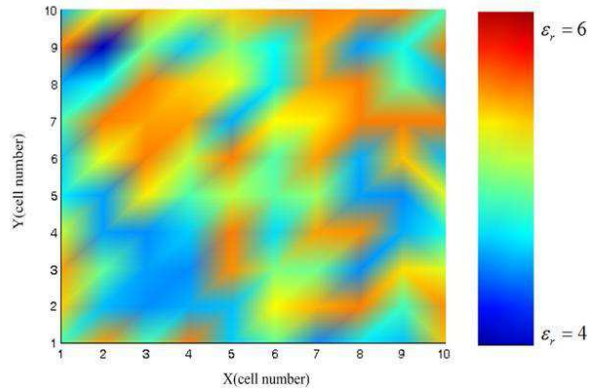


Figure 2: Graphical representation of permittivity reconstruction by ACO.

Two scenarios for profile of object are considered and for two profiles, the result of reconstruction are presented. The cost function of problem is considered as below [2]:

$$F = \frac{\sum_{i=1}^I \sum_{j=1}^J \int_0^T \left(\left\| \vec{E}_{ij}^{sim} - \vec{E}_{ij}^{meas} \right\|^2 + \eta_0^2 \left\| \vec{H}_{ij}^{sim} - \vec{H}_{ij}^{meas} \right\|^2 \right) dt}{\sum_{i=1}^I \sum_{j=1}^J \int_0^T \left(\left\| \vec{E}_{ij}^{meas} \right\|^2 + \eta_0^2 \left\| \vec{H}_{ij}^{meas} \right\|^2 \right) dt} + \lambda R(\varepsilon, \mu, \sigma) \quad (1)$$

In (1), E^{sim} and H^{sim} are the results of FDTD which are updated in each iteration and E^{meas} and H^{meas} are the value of fields obtained from measurements. $R(\varepsilon, \mu, \sigma)$ represents the regularization term. The used regularization is defined as [2]:

$$R(\varepsilon) = \lambda_1 \sum_{m=1}^M \sum_{n=1}^N |\varepsilon_{mn}| + \lambda_2 \sum_{m=1}^M \sum_{n=1}^N |\sigma_{mn}| \quad (2)$$

To quantify the reconstruction result's accuracy, the reconstruction errors of permittivity, conductivity and position are defined as below [2]:

$$error(\varepsilon) = 100 \frac{\sum_{m=1}^M \sum_{n=1}^N |\varepsilon_{mn}^{sim} - \varepsilon_{mn}^{exact}|}{\sum_{m=1}^M \sum_{n=1}^N |\varepsilon_{mn}^{exact}|} \quad (3)$$

4. SIMULATION RESULTS

To quantify the differences of optimization methods, two difference profiles are considered for object. In the first profiles the value of permittivity and conductivity is considered to be constant in all of cells ($\varepsilon_r = 5$ and $\sigma = 0.1$). The profile is reconstructed using four methods. In all of methods the initial population size is 50 and all of problems are iterated for a fixed number of cycles. The simulation results are presented in Table 1.

In the second profile the value of permittivity and conductivity is considered to vary linearly in the direction of diagonal of square. ε_r increases from 4.9 to 5.1 and 5σ increases from 0.09 to 0.11. The profile is reconstructed using 4 methods. In all of methods the initial population size is 50 and all of problems are iterated for 2000 cycles. The simulation results are presented in Table 2.

According to simulation result, it is proved that all of optimization methods are capable of solving the problem. All of methods converge to a reasonable reconstruction error. The main difference between methods is the solution time. Harmony search is significantly better than the others. The final reconstruction error of ACO is somehow better; however its time is too long.

Table 1: Reconstruction results for constant profile.

	Permittivity reconstruction error (%)	Conductivity reconstruction error (%)	Total time of reconstruction (s)
PSO	5.59	6.33	493
DE	6.11	7.67	841
ACO	4.58	4.61	954
HS	5.3	4.87	21

Table 2: Reconstruction results for linearly varied profile.

	Permittivity reconstruction error (%)	Conductivity reconstruction error (%)	Total time of reconstruction (s)
PSO	4.64	6.71	587
DE	5.63	7.36	854
ACO	4.52	5.64	998
HS	5.69	6.03	25

These results are independent of reconstructed profile and they are valid for both reconstructed profiles. The best result for permittivity reconstruction error is the result of ACO. This result is graphically depicted in Figure 2.

5. CONCLUSION

Four different optimization methods are considered. For these four methods, two profiles are reconstructed. The final results of all methods are in a satisfactory range. All of considered methods reconstructed permittivity and conductivity profiles with an acceptable error. However selecting the best method between them is not straightforward. Careful comparison between results showed that based on final reconstruction error, ACO is the best optimization method among four methods, while in the term of simulation time, HS is the best. HS showed that it is completely different from the others. Based on different criteria of comparison, the best method could be different. If someone want to define a figure of merit for optimization methods, the final reconstruction error and simulation cost could be two main parameters. Finally, based on this study, HS is the best choice. It should be mentioned that these results are for our proposed problem and cannot be considered as a general conclusion.

REFERENCES

1. Rekanos, I. T., "Shape reconstruction of a perfectly conducting scatterer using differential evolution and particle swarm optimization," *IEEE Trans. Geosciences & Remote Sensing*, Vol. 46, 1967–1974, Jul. 2008.
2. Qing, A., "Electromagnetic inverse scattering of multiple two-dimensional perfectly conducting objects y the differential evolution strategy," *IEEE Trans. Antennas and Propagation*, Vol. 51, No. 6, 1251–1262, Jun. 2003.
3. Robinson, J. and Y. Rahmat-Samii, "Particle swarm optimization in electromagnetics," *IEEE Trans. Antennas and Propagation*., Vol. 52, No. 2, 397–407, Feb. 2004.
4. Feoktistov, V., *Differential Evolution, in Search of Solutions*, Springer, 2006.
5. Socha, K., "Ant colony optimization for continuous and mixed variable domains," Ph.D. Thesis, Universite Libre de Bruxelles, 2009.
6. Geem, Z. W., *Music Inspired Harmony Search Optimization, Theory and Application*, Springer, 2009.

Localization and Electrical Parameters Estimation of a 2D Mass Using a 2 Step Method Using FDTD

Maysam Haghparast, S. A. Mirtaheri, and M. S. Abrishamian

Department of Electrical and Computer Engineering

K. N. Toosi University of Technology, Tehran, Iran

Abstract— In this study, a two-step method for estimation of location and electromagnetic profile parameters of an unknown 2D mass based on inverse scattering method is presented. FDTD is used as an EM solver and particle swarm optimization is the employed optimization method. For increasing the accuracy of solution, we present a method to select an optimum transmitter between multiple transmitters.

1. INTRODUCTION

In electromagnetic inverse scattering problems, the aim is to identify an unknown media using electromagnetic transmitted and scattered waves. To achieve this goal, the media is subjected to an electromagnetic radiation and the scattered and transmitted waves are measured in different points. The unknown constitutive parameters (ϵ , μ and σ) affect the scattered waves. The unknown scatterer is reconstructed by updating iteratively the profile of the scatterer properties. The general method for solving an inverse scattering problem is minimizing the difference between measured and estimated field data. During last decades, inverse scattering become a method with application in different branches of science and technology such as object identification, remote sensing, medical tomography, nondestructive testing, geosciences, and optics [1].

The reconstruction of electromagnetic properties of scatterers from scattered field measurements belongs to the general class of inverse scattering problems. The parameters to be determined could be any parameter which can have interaction with incident wave and then impose a variation on scattered fields. Mathematically, three main topics must be concerned in an inverse scattering problem: the non-uniqueness, the ill-posedness, and the intrinsic nonlinearity. Generally, the non-uniqueness and the ill-posedness of the inverse problems are because of the limited amount of information that can be retrieved from scattered fields. In fact, independent data achievable from the measurements of the scattered fields is inherently limited. Hence, only a finite number of parameters can be precisely reconstructed. Also, increasing the number of unknown parameters leads to more ill-posedness and subsequently more probability of the divergence of inverse algorithms [4, 6, 7]. For stabilizing the inverse problems, usually various kinds of regularizations are used. Nowadays, inverse scattering problems are considered in global optimization-based procedures. The unknown parameters of each cell of medium grid would be directly considered as the optimization parameters and several types of regularizations are used to overcome the ill-posedness. In this case, the general form of cost function for optimization routine could be written as [2]:

$$F = \frac{\sum_{i=1}^I \sum_{j=1}^J \int_0^T \left(\left\| \vec{E}_{ij}^{sim} - \vec{E}_{ij}^{meas} \right\|^2 + \eta_0^2 \left\| \vec{H}_{ij}^{sim} - \vec{H}_{ij}^{meas} \right\|^2 \right) dt}{\sum_{i=1}^I \sum_{j=1}^J \int_0^T \left(\left\| \vec{E}_{ij}^{meas} \right\|^2 + \eta_0^2 \left\| \vec{H}_{ij}^{meas} \right\|^2 \right) dt} + \lambda R(\epsilon, \mu, \sigma) \quad (1)$$

In the mentioned formula, E^{sim} and H^{sim} are the results of FDTD which are updated in each iteration and E^{meas} and H^{meas} are the value of fields obtained from measurements. $R(\epsilon, \mu, \sigma)$ represents the regularization term. The used regularization in our study is as below:

$$\lambda R(\epsilon, \sigma, \mu) = \lambda_1 \sum_{i=1}^I \sum_{j=1}^J |\epsilon_{i,j}| + \lambda_2 \sum_{i=1}^I \sum_{j=1}^J |\sigma_{i,j}| \quad (2)$$

2. PSO BRIEF DESCRIPTION

In PSO, each candidate solution \mathbf{x}_k is considered as a particle and has a velocity, \mathbf{v}_k , used to move around the solution space. In particular, the new position of the particle is given by [5]:

$$x_k(t+1) = x_k(t) + v_k(t) \quad (3)$$

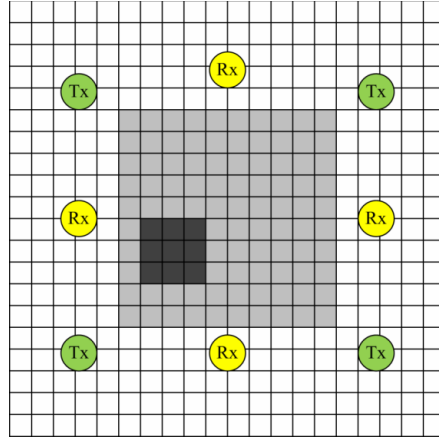


Figure 1: The structure under investigation and transmitters and receivers positions.

While the components of the velocity vector are updated according to the scheme

$$v_k = \omega v_k + c_1 q_1 (x_{kn}^b - x_{kn}) + c_2 q_2 (g_n - x_{kn}) \quad (4)$$

In (4), ω is the inertia, c_1 is the cognitive, and c_2 the social parameter, whereas q_1 and q_2 are random numbers uniformly distributed in $[0, 1]$. In addition, $\mathbf{x}^b = [x^{b1}, x^{b2}, \dots, x^b]$ is the best position ever visited by the k th particle, while $\mathbf{g} = [g_1, g_2, \dots, g_N]$ is the global best position found by the whole population. Obviously, if the new particle position derived from above relation is fitter than \mathbf{x}^b , then the latter is updated. Furthermore, \mathbf{g}_k is updated respectively. In our problem, the PSO parameters are as below [5]:

$$\omega = 1 \text{ (decrease gradually in every loop and finally reaches to 0.7)}, c_1 = c_2 = 0.68 \quad (5)$$

3. SIMULATION PROCEDURE

For solving direct problem, FDTD is used as an EM solver. PML is employed as absorbing boundary condition. A 2D FDTD with TE_z polarization is employed to solve direct problem [3]. We considered a combination of 4 symmetric transmitters and 4 symmetric receivers to solve the problem. This structure is depicted in Figure 1. We simulated our problem for a medical tomography. So the values are considered to simulate the brain characteristics at 1 GHz. In the Figure 1, the white cells represent the air, the gray cells are brain normal cells and the black cells are the malignant cells which are under investigation.

To quantify the reconstruction result's accuracy, the reconstruction errors of permittivity, conductivity and position are defined as below [8]:

$$\text{error}(\varepsilon) = 100 \sqrt{\frac{\sum_{m=1}^M |\varepsilon_m^{sim} - \varepsilon_m^e|^2}{\sum_{m=1}^M (\varepsilon_m^e)^2}} \quad (6)$$

$$\text{error}(\sigma) = 100 \sqrt{\frac{\sum_{m=1}^M |\sigma_m^{sim} - \sigma_m^e|^2}{\sum_{m=1}^M (\sigma_m^e)^2}} \quad (7)$$

$$\text{error}(\text{position}) = 100 \sqrt{\frac{|x^e - x^{sim}|^2 + |y^e - y^{sim}|^2}{|x^e|^2 + |y^e|^2}} \quad (8)$$

In the above formulas, x and y are the mass position coordinate, e indicated the exact value and sim indicated simulated values.

Table 1: Simulation results with 1 transmitter (in the left downside).

Scenario	Position reconstruction error (%)	Conductivity reconstruction error (%)	Permittivity reconstruction error (%)
1	6	5	0
2	8.8	8	3.4
3	9.2	7.9	4.8
4	6.9	7.4	0
5	7.8	7.1	0

Table 2: Simulation results with 4 transmitters and two-step solution.

Scenario	Position reconstruction error (%)	Conductivity reconstruction error (%)	Permittivity reconstruction error (%)
1	5.6	4.8	0
2	5.9	5.5	0
3	5.4	6.1	0
4	5.5	5.8	0
5	6.1	5.6	0

4. SIMULATION RESULTS

For all of our simulations, initial population size was 50 and all of them are generated randomly. The only constrain imposed to them is that they have to be in the acceptable limits. All of optimizations were repeated for 400 loops. At first step, we considered 4 different scenarios with a 3×3 cell mass, in each scenario, the location is different from others and the value of tumor constitutive parameters are randomly preset in their acceptable limits. But only one transmitter is used. Here the location of transmitter is fixed. The simulation results are mentioned in Table 1.

It should be mentioned that because of the nature of the problem, permittivity and conductivity values can have continuous value, while because of discretized area of solution, the position of the under investigation mass can have discrete values. If the optimization algorithm result becomes non integer value, it will be rounded to nearest integer value. So the final position reconstruction error will acquire discrete values. In contrary to receivers symmetric locations, using one transmitter impose an assymmetric structure to our problem. Because of unknown location of mass, different location of transmitter can result in different answers with different accuracies. A proposed way to outcome this problem is using a two-step solution. In the first step we consider 4 state with 4 transmitter and solve problem independently for a few number of steps. Then compare the result of solutions, i.e., the cost functions and select the best transmitter. In the second step, the problem is solved for example for 400 loops with the optimum transmitter.

Here, we considered 5 scenario and solved the problem with 2 step proposed algorithms. The final results are mentioned in the Table 2.

This change in the solving method will increase the amount of calculations, but it will improve the final reconstruction error meaningfully. According to Table 2, it is obvious that 2 kinds of improvement are achieved using this 2 step method:

- 1- In all of scenarios, the position reconstruction error becomes zero which shows an enhanced accuracy in the solution.
- 2- Both of conductivity and permittivity reconstruction errors are decreased.

These improvements are obtained for a cost of calculation used for pre-solution. The increase of calculation with respect to considerable achieved improvements is acceptable. It should be noted that if pre solution for 4 transmitters shows no considerable differences of accuracy, a decision making procedure for selecting optimum should be introduced. Here, in such a case, we select the transmitter randomly.

In the Figures 2 and 3, the exact and reconstructed value of permittivity and conductivity for scenario number 1 of Table 2 are plotted.

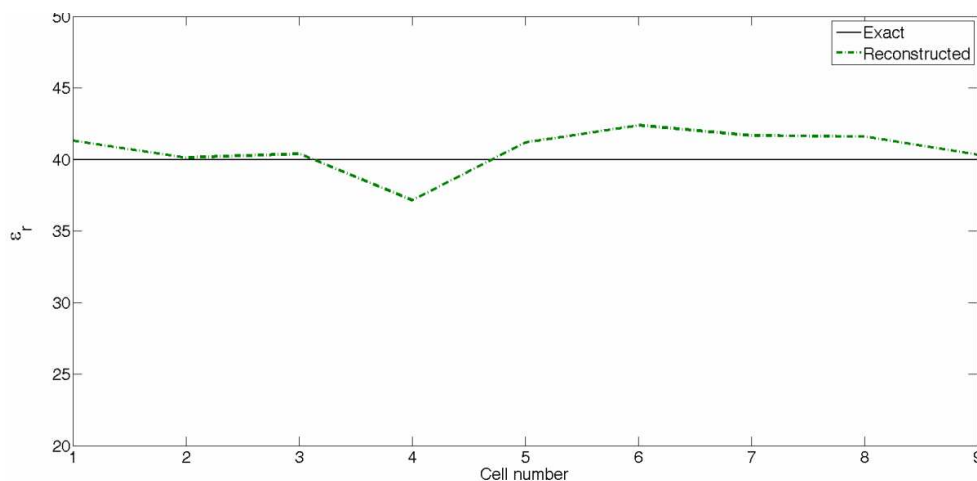


Figure 2: Exact and reconstructed value of permittivity for scenario No. 1 in the Table 2 for a 3×3 cells mass.

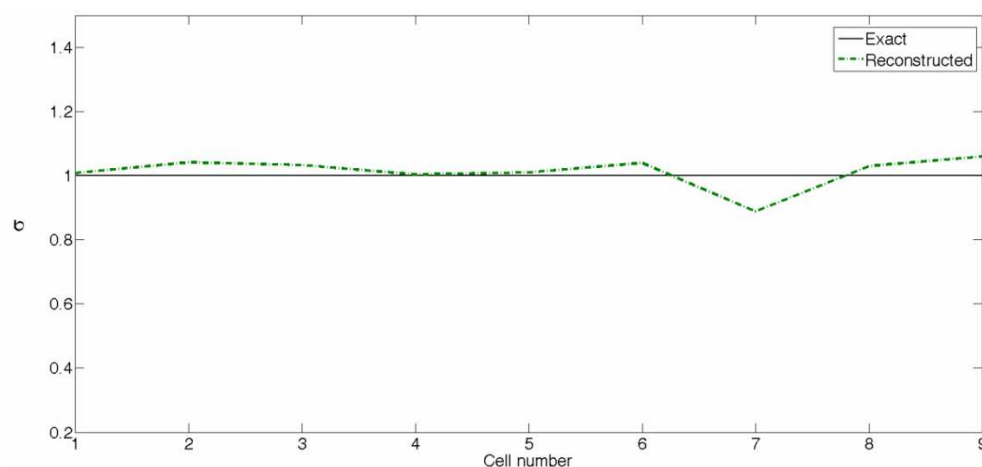


Figure 3: Exact and reconstructed value of conductivity for scenario No. 1 in the Table 2 for a 3×3 cells mass.

5. CONCLUSION

A Method for identification of an unknown mass inside of a region is presented. We proposed a method with multiple transmitters and a technique is used to find the optimum transmitter. Results for fixed and moveable transmitters are presented. Our proposed method improved the final results in comparison with the results of conventional method. We proved that this two-step method can improve the localization error very well. It is proved that this solution will increase the accuracy of final result for localization, permittivity and conductivity, in a cost of a bit more calculation which is reasonable. It reached to an error under 10% for permittivity and conductivity and a 0% error for localization.

REFERENCES

1. Rekanos, I. T., "Shape reconstruction of a perfectly conducting scatterer using differential evolution and particle swarm optimization," *IEEE Trans. Geosciences & Remote Sensing*, Vol. 46, 1967–1974, Jul. 2008.
2. Semnani, A. and M. Kamyab, "An enhanced method for inverse scattering problems using Fourier series expansion in conjunction with FDTD and PSO," *Progress In Electromagnetics Research*, Vol. 76, 45–64, 2007.
3. Taflove, A., *Computational Electrodynamics: The Finite-Difference Time-Domain Method*, 3rd Edition, 2005.
4. Qing, A., "Electromagnetic inverse scattering of multiple two-dimensional perfectly conducting

- objects by the differential evolution strategy,” *IEEE Trans. Antennas and Propagation*, Vol. 51, No. 6, 1251–1262, Jun. 2003.
5. Robinson, J. and Y. Rahmat-Samii, “Particle swarm optimization in electromagnetics,” *IEEE Trans. Antennas and Propagation*, Vol. 52, No. 2, 397–407, Feb. 2004.
 6. Chung, Y. S., C. Cheon, and S. Y. Hahn, “Reconstruction of dielectric cylinders using FDTD and topology optimization technique,” *IEEE Transactions on Magnetics*, Vol. 36, No. 4, 956–959, 2000.
 7. Rekanos, I. T. and A. Raisanen, “Microwave imaging in the time domain of buried multiple scatterers by using an FDTD- based optimization technique,” *IEEE Transactions on Magnetics*, Vol. 39, No. 3, 1381–1384, 2003.
 8. Semnani, A. and M. Kamyab, “An enhanced method for inverse scattering problems using Fourier series expansion in conjunction with FDTD and PSO,” *Progress In Electromagnetics Research*, Vol. 76, 45–64, 2007.

Reconstruction of 1-D Dielectric Scatterer with Cosine and Spline Expansions Using Differential Evolution and Particle Swarm Optimization

M. Haghparast, S. A. Mirtaheri, and M. S. Abrishamian

Department of Electrical and Computer Engineering
K. N. Toosi University of Technology, Tehran, Iran

Abstract— A reconstruction method for 1-D dielectric Scatterers using cosine and spline expansions with Differential Evolution and Particle Swarm Optimization is presented. Cubic spline and cosine expansion are compared. Two optimization methods, differential evolution (DE) and particle swarm optimization (PSO) in solving 1-D inverse scattering problems are used. In this comparison, the efficiency and calculation time of both mentioned optimization methods are examined. The comparison is carried out under the same conditions of initial population of candidate solutions and number of iterations. Numerical results show that both optimization methods are reliable tools for inverse scattering applications with both methods of expansions.

1. INTRODUCTION

The reconstruction of the electromagnetic properties of scatterers from scattered field measurements belongs to the general class of inverse scattering problems. The unknown parameters could be any factor which can interact with the incident wave and make changes in the scattered fields. Usually, the scatterer is reconstructed by updating iteratively the profile of the unknown scatterer properties. To achieve this goal, the cost function, i.e., the difference between measured and estimated field data is minimized by an optimization procedure. Inverse scattering has lots of applications in different branches of science and technology such as object detection, radar, medical tomography, nondestructive testing, geophysics, and optics [1]. From a mathematical point of view, three main topics must be concerned in an inverse scattering problem: the non-uniqueness, the ill-posedness, and the intrinsic nonlinearity. Generally, the non-uniqueness and the ill-posedness of the inverse problems are because of the limited amount of data that can be retrieved from scattered fields. In fact, the amount of independent data achievable from the measurements of the scattered fields is essentially limited. Also, increasing the number of unknown parameters leads to more ill-posedness and consequently more probability of the divergence of inverse algorithms. For stabilizing the inverse problems, usually various kinds of regularizations are used, taking into account a priori information on the parameters. Inverse scattering problems are considered in global optimization-based procedures. The unknown parameters of each cell of medium grid would be directly considered as the optimization parameters and several types of regularizations are used to overcome the ill-posedness. In this case, the general form of cost function for optimization routine could be written as [2]:

$$F = \frac{\sum_{i=1}^I \sum_{j=1}^J \int_0^T \left(\left\| \vec{E}_{ij}^{\text{sim}} - \vec{E}_{ij}^{\text{meas}} \right\|^2 + \eta_0^2 \left\| \vec{H}_{ij}^{\text{sim}} - \vec{H}_{ij}^{\text{meas}} \right\|^2 \right) dt}{\sum_{i=1}^I \sum_{j=1}^J \int_0^T \left(\left\| \vec{E}_{ij}^{\text{meas}} \right\|^2 + \eta_0^2 \left\| \vec{H}_{ij}^{\text{meas}} \right\|^2 \right) dt} + \lambda R(\varepsilon, \mu) \quad (1)$$

In the cost function, $R(\varepsilon, \mu)$ represents the regularization term and here as we use expansion method instead of direct method, we do not need this term.

In this paper, two kind of metaheuristic optimization methods are used: Differential Evolution (DE) and Particle Swarm intelligence (PSO) Following the introduction, a brief overview on DE and PSO is presented in Section 2. In Section 3, cosine expansion and spline expansion are briefly explained. In Section 4 the simulation results of reconstruction of inhomogeneous lossless scatterer is presented, while the efficiency of both expansion methods are examined. Finally, conclusions are mentioned in Section 5.

2. BRIEF DESCRIPTION FOR DE AND PSO

Let us consider that our goal is minimizing cost function $F(\mathbf{x})$ with respect to the vector of variables or parameters, $\mathbf{x} = [\mathbf{x}_1, \mathbf{x}_2, \dots, \mathbf{x}_N]$, where N is the dimension of the solution space. Evolutionary optimization algorithms are population based. In the first step, a set of candidate solutions \mathbf{x}_k , $k = 1, 2, \dots, K$, (K is the population size), is generated randomly. These solutions are updated iteratively searching the solution space for the global minimum of $F(\mathbf{x})$. In DE method, after generating the initial population, the candidate solutions are refined by applying 3 steps: mutation, crossover and selection, iteratively. During mutation, for every individual solution \mathbf{x}_k , three distinct solutions, \mathbf{x}_{r1} , \mathbf{x}_{r2} , and \mathbf{x}_{r3} , which are mutually different and different from \mathbf{x}_k , are randomly chose to create a new solution, \mathbf{y}_k , i.e., [3]:

$$\mathbf{y}_k = \mathbf{x}_{r1} + \beta(\mathbf{x}_{r2} - \mathbf{x}_{r3}) \quad (2)$$

In the mentioned relation, β is the mutation factor. Then crossover leads to generation of final offspring \mathbf{u}_k :

$$\mathbf{u}_{kn} = \begin{cases} \mathbf{y}_{kn}, & \text{if } h_n \leq H \\ \mathbf{x}_{kn}, & \text{if } h_n > H \end{cases} \quad (3)$$

$n = 1, 2, \dots, N$, h_n is a random number uniformly distributed within $[0, 1]$ and $H \in (0, 1)$ is a predefined crossover probability. It should be mentioned that \mathbf{u}_k has to inherit at least one component from \mathbf{y}_k . Finally, during selection, the offspring, \mathbf{u}_k , competes with the initial solution candidate, \mathbf{x}_k , and if it is fitter than \mathbf{x}_k , with respect to the cost function, it replaces \mathbf{x}_k in the next generation, i.e.,

$$\mathbf{x}_k = \begin{cases} \mathbf{u}_k, & \text{if } F(\mathbf{u}_k) < F(\mathbf{x}_k) \\ \mathbf{x}_k, & \text{if } F(\mathbf{u}_k) > F(\mathbf{x}_k) \end{cases} \quad (4)$$

In PSO, each candidate solution \mathbf{x}_k is considered as a particle and has a velocity, \mathbf{v}_k , used to move around the solution space. In particular, the new position of the particle is given by [4]:

$$\mathbf{x}_k(t+1) = \mathbf{x}_k(t) + \mathbf{v}_k(t) \quad (5)$$

while the components of the velocity vector are updated according to the scheme

$$\mathbf{v}_k = \omega \mathbf{v}_k + c_1 q_1 (\mathbf{x}_{kn}^b - \mathbf{x}_{kn}) + c_2 q_2 (g_n - \mathbf{x}_{kn}) \quad (6)$$

In (6), ω is the inertia, c_1 is the cognitive, and c_2 the social parameter, whereas q_1 and q_2 are random numbers uniformly distributed in $[0, 1]$. In addition, $\mathbf{x}^b = [\mathbf{x}^{b1}, \mathbf{x}^{b2}, \dots, \mathbf{x}^b]$ is the best position ever visited by the k th particle, while $\mathbf{g} = [g_1, g_2, \dots, g_N]$ is the global best position found by the whole population. Obviously, if the new particle position derived from above relation is fitter than \mathbf{x}^b , then the latter is updated. Furthermore, \mathbf{g}_k is updated respectively.

3. SHORT INTRODUCTION OF COSINE EXPANSION AND SPLINE EXPANSIONS

Instead of direct optimization of the unknowns, we expand them in terms of a set of basis functions and optimize the coefficients of this expansion in a global optimization routine like PSO and DE. In a general 1-D structure, the relative permittivity could be expressed as:

$$\varepsilon(x) = \sum_{k=0}^N d_k F_k(x) \quad (7)$$

F_k are the base functions and d_k are the coefficients which are considered as the variables and will be optimized iteratively in the optimization loop. If cosine basis functions are used for 1-D case, expansion of the permittivity profile along x direction is as below:

$$\varepsilon(x) = \sum_{k=0}^N d_k \cos(k\pi x/a) \quad (8)$$

where a is the dimension of the under investigation slab. In this case, number of optimization parameters is equal to the number of expansion terms in comparison with conventional direct methods in which this number is equal to the number of grid points. This results in a considerable reduction in the amount of computations.

In the spline expansion, basis functions are based on polynomials. Here we should consider a non-decreasing sequence of numbers (u) in the interval of interest, here $0 \leq x \leq a$, and set of functions with degree of p is generated based on functions of lower degrees with a recursive relation [5]:

$$N_{i,p}(u) = \frac{u - u_i}{u_{i+p} - u_i} N_{i,p-1}(u) + \frac{u - u_{i+p+1}}{u_{i+p+1} - u_{i+1}} N_{i+1,p-1}(u) \tag{9}$$

In *therecursive relation*, i denotes the number of interval. Here we considered cubic spline (C-Spline) functions as the basis functions.

In our simulations for both methods of expansions we considered 8 terms for each summation, i.e., $N = 7$;

Without any major effect in our analysis, here we describe the inhomogeneous media in the term of refractive index n , instead of permittivity. The relation between these two parameters is:

$$n = \sqrt{\epsilon_r} \tag{10}$$

4. SIMULATION RESULTS

We consider a case of 1-D inhomogeneous scatterer (Figure 1). The scatterer is infinite in the plane perpendicular to x -axis and it is bounded within the area $0 \leq x \leq a$. Here we considered $a = 0.01$. The refractive index of the scatterer depends on x , whereas the surrounding medium is considered to be free space. The total electric field is measured at two distinct measurement points, placed in two sides of slab, as showed in the Figure 1. The solution of the direct scattering problem is carried out by means of the FDTD applied to the discretized x -axis and excited with a Gaussian pulse. In the FDTD code, the excitation field is set at a point as shown schematically in Figure 1. The scatterer region is discretized into 20 equal line segments where within each segment the scatterer property (refractive index) is considered constant. Thus, if the scatterer’s profile is described by the vector $\mathbf{x} = [n_1, n_2, \dots, n_{20}]$. The objective of the inverse scattering procedure is to estimate \mathbf{x} by minimizing the cost function.

To quantify the reconstruction result of simulations, the reconstruction errors of refractive index is defined as:

$$\text{error}(n) = 100 \sqrt{\frac{\sum_{M=1}^M |n_m - n_m^e|^2}{\sum_{M=1}^M (n_m^e)^2}} \tag{11}$$

where n and n^e represent the estimated and the exact value of refractive index, respectively, while m denotes the cell number. For all of our simulations, initial population size was 50 and all of them are

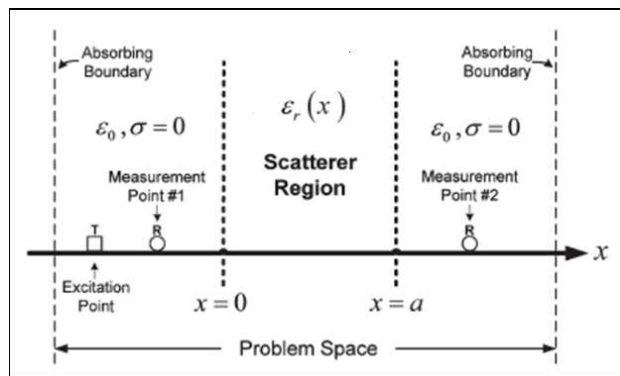


Figure 1: Structure of problem and the position of transmitter and receivers.

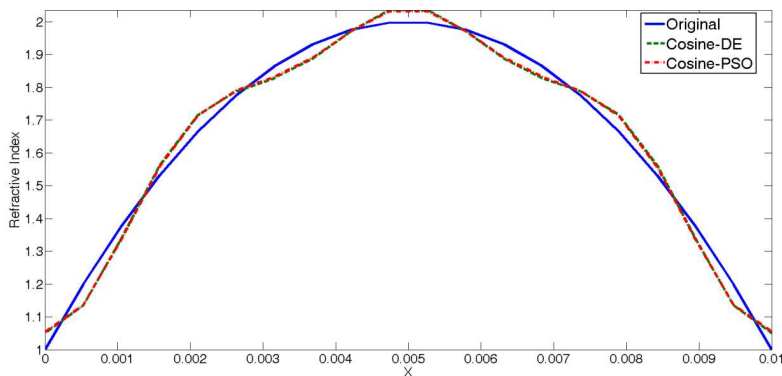


Figure 2: Exact and reconstructed refractive indexes for cosine expansion.

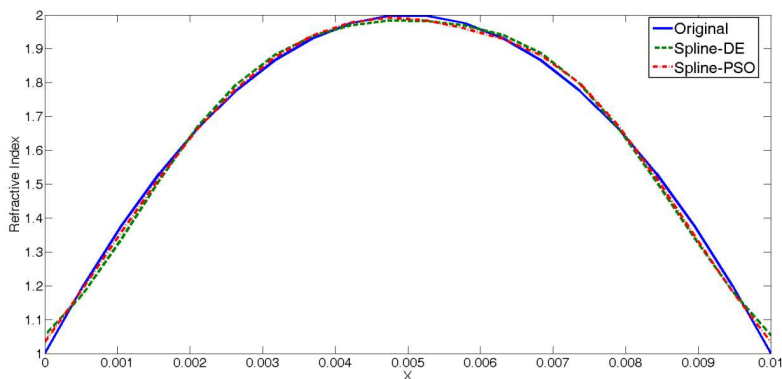


Figure 3: Exact and reconstructed refractive indexes for spline expansion.

Table 1: Reconstruction results for parabolic refractive index.

	Expansion	Optimization	Reconstruction Error (%)	Cost function (%)	Overall time (s)	Saturation cycle	Saturation time (s)
1	Cosine	PSO	2.37	3.42×10^{-6}	218	289	126
2	Cosine	DE	2.44	7.14×10^{-7}	543	241	261.7
3	Spline	PSO	1.01	9.37×10^{-5}	217	361	113.3
4	Spline	DE	1.51	2.3×10^{-4}	549	381	418.3

generated randomly. The only constrain imposed to them is that they have to be in the acceptable limit for refractive index. It should be noted that while we generate these initial solutions, cosine expansion method needs a time meaningfully more than spline method. All of optimizations were repeated for 500 loops.

Here, we considered a refractive index with parabolic variation and reconstructed it with 2 kinds of expansions and for each kind of expansions we used both DE and PSO optimization methods. For comparison we presented different parameter of each simulation in table. In this table, we mentioned cost function, reconstruction error, overall time of time simulation, the number of cycles in which the simulation saturates and the time of saturation. Here saturation means that the point in which reconstruction error became constant and will not decrease anymore.

The exact and reconstructed refractive indexes for this example are shown in Figures 2 and 3.

As shown in these figures, even though both cosine and spline expansions present good predictions for original refractive index, but spline's results are more accurate.

For all of simulations, optimization parameters were set as below:

$$\text{For DE: } H = 0.7, \beta = 0.5 \quad (12)$$

$$\text{For PSO: } \omega = 1 \text{ (decrease gradually in every loop and finally reaches to 0.7), } c_1 = c_2 = 0.5 \quad (13)$$

According to Table 1, we can reveal that for a fixed number of iterations, PSO outperforms DE significantly in the simulation time. PSO reach to steady state (saturation) point faster than DE.

Also we can say that despite of notable difference between cost function values between cosine and spline expansions, both of them result in a nearly same reconstruction error. This item can be considered a profit for spline expansion. In addition, time needed for generating initial population for spline expansion is obviously less than cosine expansion. For a fair comparison, initial population for DE and PSO are considered identical.

5. CONCLUSION

The profile reconstruction of 1-D dielectric scatterers has been investigated by applying DE and PSO optimization techniques to 2 methods of expansions. Numerical results show that both methods result in accurate reconstruction. However by comparing the simulation's results, it can be said that spline expansion can estimate the scatterer's profile more accurate than cosine expansion. In addition, the reconstruction error in both expansion methods are nearly identical while the cost functions have considerable differences and it can be considered an advantage for spline method, while having worse cost function value, result in a same reconstruction error. In the term of reconstruction error, DE and PSO result in same values. In the particular case of our investigations, PSO outperforms the DE in terms of reconstruction time. This is considered an indicative result for our example and not generally applicable.

REFERENCES

1. Rekanos, I. T., "Shape reconstruction of a perfectly conducting scatterer using differential evolution and particle swarm optimization," *IEEE Trans. on Geosciences & Remote Sensing*, Vol. 46, 1967–1974, Jul. 2008.
2. Semnani, A. and M. Kamyab, "An enhanced method for inverse scattering problems using Fourier series expansion in conjunction with FDTD and PSO," *Progress In Electromagnetics Research*, Vol. 76, 45–64, 2007.
3. Qing, A., "Electromagnetic inverse scattering of multiple two-dimensional perfectly conducting objects by the differential evolution strategy," *IEEE Trans. on Antennas and Propagation*, Vol. 51, No. 6, 1251–1262, Jun. 2003.
4. Robinson, J. and Y. Rahmat-Samii, "Particle swarm optimization in electromagnetics," *IEEE Trans. on Antennas and Propagation*, Vol. 52, No. 2, 397–407, Feb. 2004.
5. *The NURBS Book*, Springer, 2006.

Airship Radar System Modeling and Simulation

Li Zhang and Jingwen Li

School of Electronics and Information Engineering, Beihang University, Beijing, China

Abstract— A complete signal simulation system is established according to the characteristics of the airship radar in this paper. Based on the classification of different terrain and sea condition, various clutter scene models are simulated. The simulation results indicate this simulation system is essential and qualified for subsequent data processing.

1. INTRODUCTION

Airship radar is a special early warning detection system that is the application of radar equipment to airship platform. More and more attention has been paid to the airship radar in recent years [1]. Therefore, it is essential to establish the complete system simulation for further research purpose. The airship radar is mainly working on the mode of nadir looking, therefore, the ground and sea clutters are strong and complicated [2]. The characteristics of the clutter have some important effects on the airship radars with nadir look mode [3]. Thus, it is significant for subsequent data processing to add detailed ground scene and exact clutter model to implement radar signal simulation in the design.

A complete signal simulation system is established according to the characteristics of the airship radar in this paper. As the important step in the signal design, clutter signal design is specifically presented. Based on the clutter reflectivity model, amplitude distribution model and the correlation properties model, the clutter sequences in different scenes are built. The scatterer units in the irradiated area are divided with the grid-mapping format method [4] and the echo signals simulation in different clutter scenes is implemented through the coherent video signal accumulation [5]. All results are shown in MATLAB GUI. The simulation results indicate this simulation system is essential and qualified for subsequent data processing.

The rest of this paper is structured as follows: Section 2 gives the overall design scheme of the airship radar system. Section 3 introduces the design method of the ground scenes and clutter signal models. And simulation results are presented in Section 4.

2. SYSTEM DESIGN

System design includes five parts: platform design, radar design, antenna design, target design and scene design. Platform design implements the modeling of airship-to-ground geometrical relationship and the description of airship's trajectory. The influence of the Earth's curvature is considered due to the great distance between airship and the Earth. Motion errors are also considered in the platform design because of the wind and atmospheric flow effects on movement of airship [2]. In the radar design, the Pulse Doppler (PD) radar system with simple structure is selected to reduce the load of airship. To enhance the capability of detection and anti-interference, airship radar uses pulse compression technique and LFM, Baker codes and P4 codes are designed to meet the different performance requirements [3]. Transceiver antennas and bistatic antennas are designed to improve the anti-interceptive capability. The observation of major area or the whole area can be controlled. Target design accomplishes the description of the track of low-altitude moving point target. In order to make the airship radar simulation system suitable for various kinds of clutter scattering environment, scene is classified according to fluctuant state, clutter background and different ground and sea conditions. The modeling of the airship radar system is completed on the basis of the above design.

3. SCENE DESIGN

The clutter scene design, which is the simulation of the clutter scattering cross section, is the fundamental procedure of the system design. Clutter is the sum of the echo vectors of scatterers in the radar resolution units, so complex scattering cross section γ of clutter is the sum of the multiple complex scattering cross sections [5], shown in (1).

$$\gamma = \sqrt{\sigma_c} e^{j\phi_c} = \sum_{i=1}^N \sqrt{\sigma_i} e^{j\phi_i} \quad (1)$$

For the ground and sea surface clutter, σ_c equals the product of clutter backward scattering coefficient σ^0 and clutter unit area ΔA .

$$\sigma_c = \sigma^0 \Delta A \quad (2)$$

For airship radar, the theory model of clutter backward scattering is adopted to calculate the clutter backward scattering coefficient σ^0 due to the dynamic characteristics of radar platform and the bigger incidence angle of radar beam. Because the dielectric constants and geometric characteristics of the scatterers are random variables and the movement of randomly distributed scatterers can cause random fluctuation characteristics of scattering overall cross sections $|\gamma|$, which leads to the amplitude and phase change of clutter echo signal, γ is a complex random variable which has some relevant features and meet some distribution [5].

In scene design, average Radar Cross Section (RCS) and fluctuant RCS are both considered to design different landform model: desert, farmland, forest, mountain, city and different sea conditions (levels 1–5). Appropriate parameters can be chosen to exactly simulate the scattering environment of airship radar using the backward scattering coefficient model, probability distribution model and related characteristics model according to the different landform. Specifically speaking, the backward scattering coefficient model is chosen as the Morchin model of ground clutter or the Morchin model of sea clutter; probability distribution model is selected as Rayleigh distribution, Log-normal distribution, Weibull distribution or K distribution; related characteristics model is chosen as Gaussian spectrum or cubic spectrum. Furthermore, composite landform is also taken into consideration according to the weight proportion of RCS probability distribution [6] (given in Figure 1).

4. SIMULATION AND RESULT

The echo signals simulation can be achieved using the designed system. In the design of radar signal simulation, The scatterer units in the irradiated area are divided with the grid-mapping format method [6], and then the approach of coherent video signal accumulation is adopted to simulate the echo signal which contains phase information in different clutter scenes [5]. After the coherent demodulation of receiver, the expression of coherent video signal of the received signal is:

$$s_B(t) = \left[\frac{\lambda^2 G_{t0} G_{r0}}{(4\pi)^3 R^4 L} \right]^{\frac{1}{2}} F_t(t) F_r(t) u(t) \exp[j2\pi f_d(t - \tau)] \exp(j\phi) \quad (3)$$

where λ is the radar wavelength, G_{t0} and G_{r0} are the maximum gain of the transmitter and receiver, respectively, R denotes the distance of the antenna phase center to the scatter, L stands for the system loss, $F_t(t)$ and $F_r(t)$ are the transmitter and receiver gain factors, respectively, $u(t)$ presents the transmit signal envelope, f_d is the Doppler phase shift and τ the reflected object delay, ϕ represents the phase shift of the reflected object.

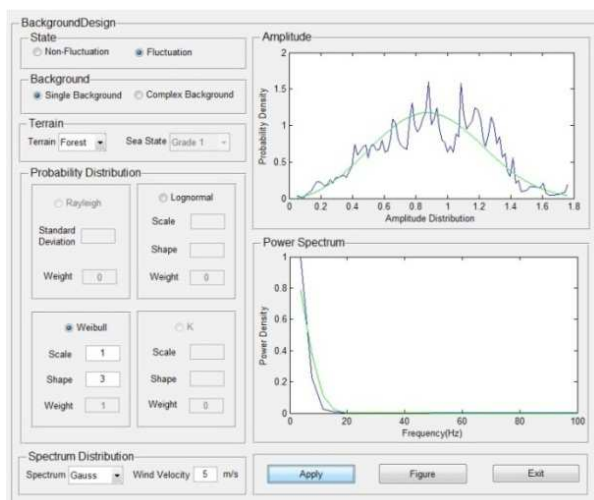


Figure 1: GUI of scene design.

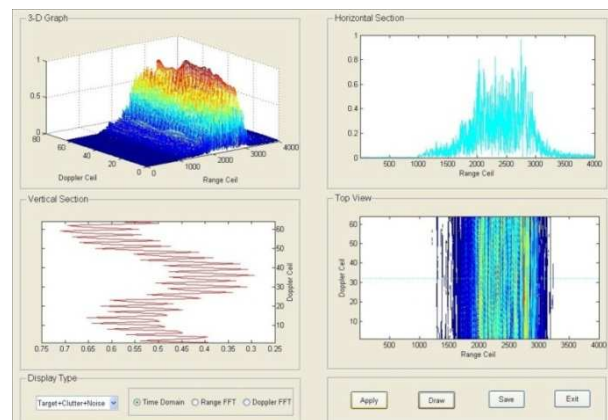


Figure 2: Airship radar echo simulation.

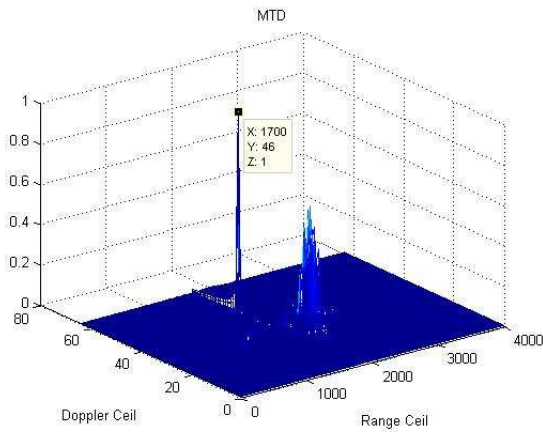


Figure 3: MTD Processing.

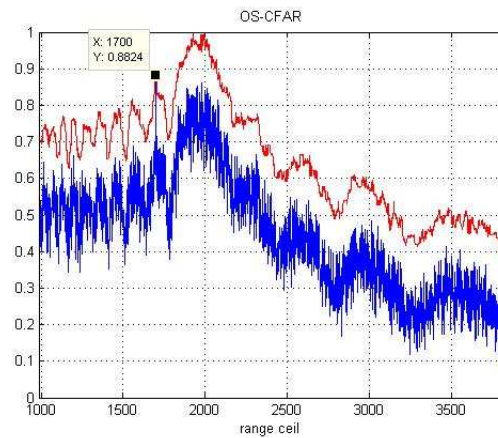


Figure 4: CFAR Processing.

Figure 2 is the simulation result of the mixture of the echo of moving point target, the noise and the fluctuant clutter echo in the farmland scene which chooses Weibull distribution and gauss spectrum. The target locates at the 1700th range cell and the 46th Doppler cell. The GUI is introduced to indicate the dynamic echo of three dimensional figure and one dimensional profiles. The effectiveness of the designed system is validated by Moving Target Detection (MTD) clutter suppression (seen in Figure 3) and Constant False Alarm Rate (CFAR) detection processing (given in Figure 4).

5. CONCLUSION

The airship radar system is comprehensively modeled, and the echo signals simulation system is designed and implemented. The clutter scene design is given in detail. The echo signals in the desired scene are simulated using the designed system. The simulation result demonstrates the effectiveness of the airship radar system is validated.

REFERENCES

1. Hochstetler, R., "Airships ahoy," *IEEE Spectrum*, Vol. 47, No. 10, 42–47, 2010.
2. Cheng, C. and P. Zhao, "Analysis of tethered aerostat borne radar system," *Radar Science and Technology*, Vol. 5, No. 6, 410–414, 2007.
3. Zhang, M. and X. Wang, *Radar System*, Publishing House of Electronics Industry, Beijing, 2008.
4. Cheng, A., "Radar echo signal modeling and simulation," Nanjing University of Science and Technology, Nanjing, China, 2004.
5. Zhang, C., "Modeling and simulation of radar clutter for radar signal simulator," Electronic Science and Engineering National University of Defense Technology, Changsha, China, 2004.
6. Li, Q. and Q. Zhang, "A clutter modeling method in the composite sea-plus-land environment," *Journal of Microwaves*, Vol. 26, No. 1, 22–25, 2010.

Absorption Dependencies of Dipolar Glass Cylindrical Waveguide Coated by SiC on Temperatures and Coated Layer Thicknesses

L. Nickelson^{1,2}, A. Bubnelis^{1,2}, and S. Asmontas¹

¹Department of Electronics, Center for Physical Sciences and Technology, Vilnius, Lithuania

²Department of Electronic System, Vilnius Gediminas Technical University, Lithuania

Abstract— We have electro-dynamically rigorously investigated the open (without metal screen) layered dipolar glass-silicon carbide (SiC) waveguides. Our electro-dynamical modeling was carried out by the partial area method with using of the Müller's method for the searching of complex propagation constants of waveguide modes. We used our developed computer code in the MATLAB language. The investigated waveguides qualify by the very large broadband widths and special mode attenuation properties in the microwave frequency range 5–100 GHz. Here we present the phase and attenuation constants of the main mode and the two higher modes of layered lossy waveguides with the external waveguide radius equal to 3 mm at three thicknesses t of coated layer SiC and the temperature T equals to 130 K or 150 K. Here are also given the waveguide broadband widths and the cutoff frequency f_{cut} of modes at different values T and thicknesses t .

1. INTRODUCTION

The intensive development of space missions leads to growing complexity of power electronic systems, extreme-temperature electronics and to an expansion of the limits of their functionality. Extreme operating conditions of novel devices can demand specific characteristics of microwave waveguide elements in a very wide temperature ranges, e.g., [1]. There is a one of the present tendencies to use the highly dispersive and dissipative composite materials in order to expand the microwave device possibilities, e.g., [2, 3]. It is important to point that the analyzed here waveguides can be controllable by temperatures T in a very wide range of value T . This temperature range could be from about cryogenics (130 K) till the very high temperatures upon 2200 K. The property of wide temperature controllability of waveguide parameters provides by the strong dependency of the dipole glass' permittivity on the very low T and of the SiC permittivity on the high T . An additional importance of the analyzed waveguides is that the external SiC layer is resistant to aggressive environments. In present work we only give dispersion characteristics at two low temperatures. We have investigated separate the dipolar glass waveguides [4] at four low T and the SiC waveguides [5] at several high T before. The dispersion characteristics of layered dipolar glass-SiC waveguide are completely different comparing with the homogeneous waveguides [5].

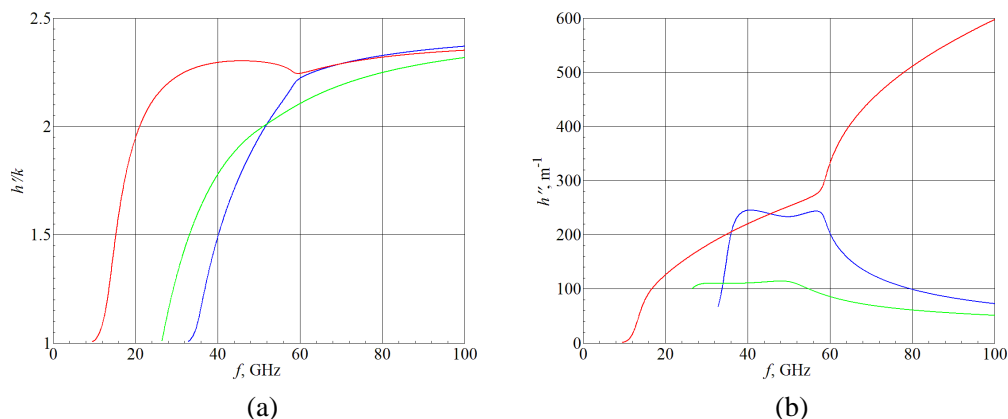


Figure 1. Dependences of (a) the phase constant and (b) the attenuation constant on the frequency when the SiC layer thickness is 2 mm at $T = 130$ K.

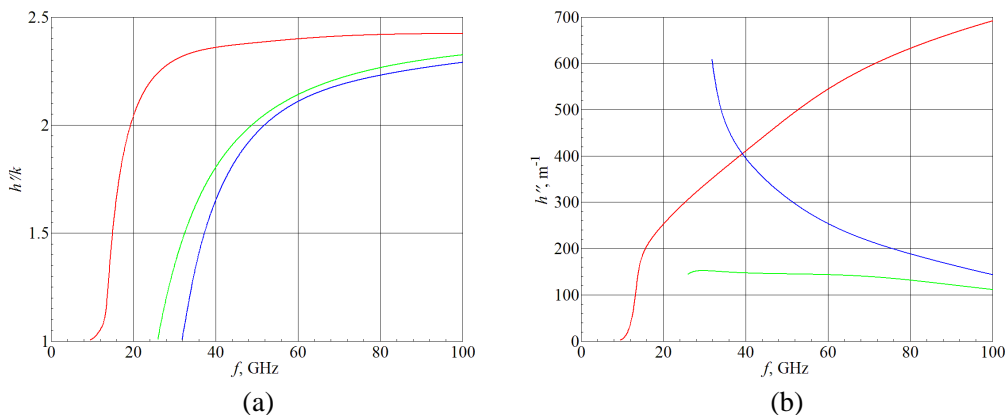


Figure 2. Dependences of (a) the phase constant and (b) the attenuation constant on the frequency when the SiC layer thickness is 1.5 mm at $T = 130$ K.

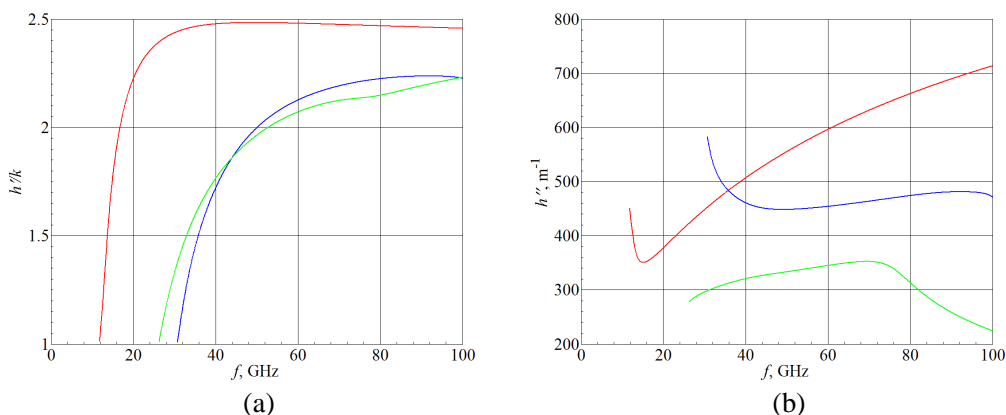


Figure 3. Dependences of (a) the phase constant and (b) the attenuation constant on the frequency when the SiC layer thickness is 1.0 mm at $T = 130$ K.

2. DISPERSION CHARACTERISTICS OF LOSSY LAYERED WAVEGUIDES AT LOW TEMPERATURES

The solution of Maxwell's equations for the open layered cylindrical waveguides made of lossy materials was carried out by the partial area method. The waveguide dispersion equation for analyzing of the full spectrum eigenmodes is given in [4]. The computer code for the dispersion characteristic calculations created in MATLAB language. We present here the dispersion characteristics of the layered dipolar glass-SiC waveguides at two low temperatures 130 K and 150 K in the frequencies f between 5 GHz and 100 GHz. We permit that the permittivity of SiC material at both low temperatures is equal to $\varepsilon = \varepsilon' - i\varepsilon'' = 6 - 0.5i$ at $f = 11$ GHz. The imaginary part of SiC permittivity is calculated according the formula $\varepsilon'' = 1/\omega\varepsilon_0\rho$, where the angular frequency $\omega = 2\pi f$, the value ρ is the material specific resistivity. The permittivity of the dipolar glass for corresponding values of frequencies and temperatures is taken from measured data. The reference on the used measured data is given in [4]. The external radius of all investigated here waveguides is 3 mm. The thicknesses of coated SiC layers can be 2 mm, 1.5 mm and 1 mm, viz. the radius of waveguide core can be 1 mm, 1.5 mm and 2 mm. In Figs. 1(a)–6(a) are presented dependences of the normalized phase constant (longitudinal propagation constant) h' to the value k on the frequency, where $h' = \pi/\lambda$, λ is the wavelength of considered main or higher modes, $k = \omega/c$ is the wave number in a vacuum, c is the speed of light in vacuum. In Figs. 1(b)–6(b) are presented dependences of mode attenuation constant h'' on frequencies. In Figs. 1–3 are shown dispersion characteristics of the waveguide at $T = 130$ K. In Figs. 4–6 presented dispersion characteristics of the waveguides at $T = 150$ K. The red curves designate the main mode, the green ones designate the first higher mode (by f_{cut}) and the blue ones designate the second modes.

The comparison of phase constants at $T = 130$ K (Figs. 1(a)–3(a)) shows that the shape of

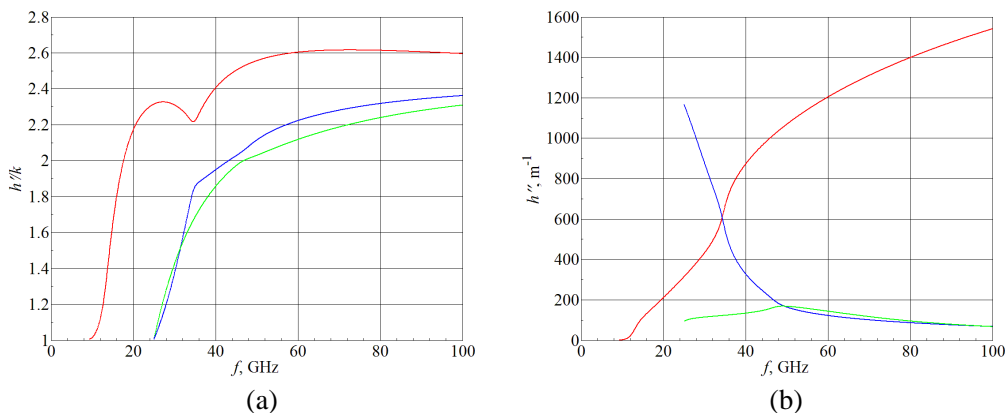


Figure 4. Dependences of (a) the phase constant and (b) the attenuation constant on the frequency when the SiC layer thickness is 2 mm at $T = 150$ K.

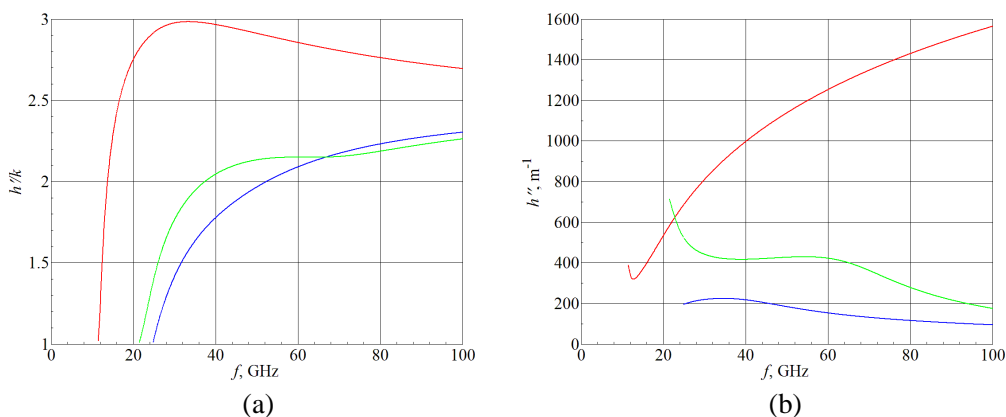


Figure 5. Dependences of (a) the phase constant and (b) the attenuation constant on the frequency when the SiC layer thickness is 1.5 mm at $T = 150$ K.

curves changes, the mode cutoff frequencies and the broadband width of waveguides are different with changing of thickness t (see also Table 1).

There is a degeneration of the main mode (red curve) and the first higher mode (green curve) in the range 64–84 GHz and also a degeneration of the first and second higher modes at $f \sim 51$ GHz when $t = 2$ mm (Fig. 1(a)). We see that in the range 51–100 GHz the second higher mode (blue curve) becomes the first one. It means that the EM field structure of the first and second high modes essentially changes in the mentioned range 51–100 GHz (Fig. 1(a)). We also see the first and second modes' transformation in the range 43–100 when $t = 1$ mm (Fig. 3(a)). The comparison of the attenuation constants at the coated SiC layer with thicknesses 2 mm, 1.5 mm, 1.0 mm and $T = 130$ K (Figs. 1(b)–3(b)) shows that the waveguide attenuations dependent on the SiC layer thickness t in a sophisticated way. A special interesting dependency of attenuation constant is for the higher mode that denoted by the green curve. The attenuation for this mode is the smallest in the range ~ 26 –100 GHz when the SiC layer thicknesses are 1.5 mm and 1.0 mm (Figs. 2(b), 3(b)). The microwave device with the changeless attenuation can be created on the base the mode which denoted by the green colour when $t = 1.5$ mm (Fig. 2(b)). A microwave attenuator can be created on the base of the main mode of waveguide with $t = 1.5$ mm. The attenuation constant of the main mode approximately linearly grows at the range $f = 20$ –100 GHz (Fig. 2(b)).

Analysis of dispersion characteristics the same three waveguides with $t = 2$ mm, 1.5 mm, 1 mm at $T = 150$ K shows that the dispersion characteristics are dramatically changing (Figs. 4–6). That means that it is possible to control the waveguide characteristics by changing of temperatures. The degeneration of the higher modes at $T = 150$ K happened at ~ 32 GHz or ~ 67 GHz when t is 2 mm or 1.5 mm, correspondingly (Figs. 4(a), 5(a)). The main mode magnitude of h'' at $T = 150$ K is larger comparing with h'' at $T = 130$ K. The lowest attenuations are for the modes denoted by the blue curves when the SiC layer thickness equals to 1.5 mm or 1.0 mm (Figs. 4(b), 5(b)). In the case

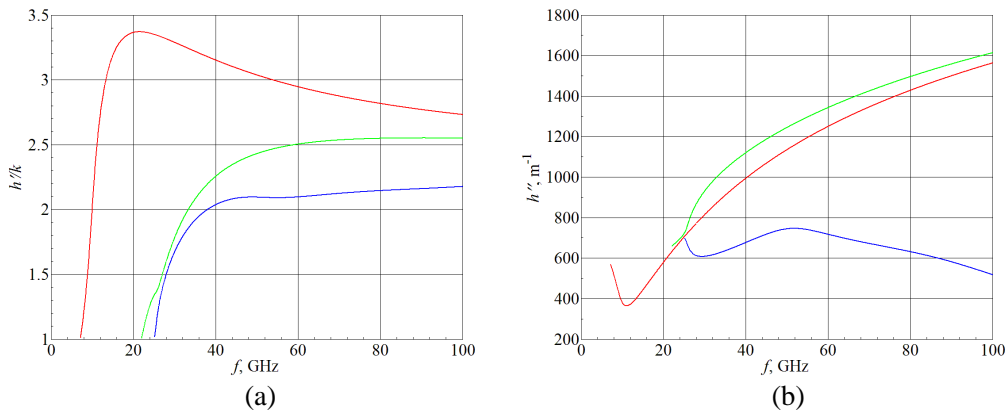


Figure 6. Dependences of (a) the phase constant and (b) the attenuation constant on the frequency when the SiC layer thickness is 1 mm at $T = 150$ K.

Table 1.

No.	t of SiC layer, mm	T , grad K	main mode f_{cut} , GHz	1st higher mode f_{cut} , GHz	2nd higher mode f_{cut} , GHz	Broadband width
1.	2.0	130	9.55	26.50	32.85	86%
2.	1.5	130	9.55	26.00	31.85	85%
3.	1.0	130	11.80	26.30	30.75	75%
4.	2.0	150	9.35	25.05	25.10	86%
5.	1.5	150	11.50	21.50	24.85	60%
6.	1.0	150	7.20	22.05	25.20	100%

the waveguide losses do not modulate the signal which propagates on the waveguide (Fig. 5(b)). This behavior of mode attenuation can be useful for creation of a microwave shifter because the waveguide losses are the almost invariable and the phase constants that denoted by blue curves changes considerably. The value f_{cut} of modes and the broadband width of waveguides with the different SiC thickness at $T = 130$ K and 150 K are presented in Table 1. We see that the value of the main mode cutoff frequency f_{cut} noticeably dependent on the temperature, e.g., f_{cut} equal to 11.8 GHz and 7.2 GHz for the waveguide with $t = 1$ mm.

3. CONCLUSIONS

1. We analyzed dispersion characteristics and the broadband width of the open layered dipolar glass-SiC cylindrical waveguides when the SiC layer thicknesses are 2 mm, 1.5 mm and 1 mm at two temperatures 130 K & 150 K in the frequency range from 5 GHz to 100 GHz.
2. We determined that all investigated dipolar glass-SiC cylindrical waveguides at temperatures 130 K & 150 K possess the great broadband width.
3. We found that the degeneration and transformation modes can be at different frequencies dependent on the SiC layer thickness and the temperature. There is a strong dependency of waveguide attenuation on the temperature.
4. We discovered that the waveguides with SiC layer thicknesses equal to 1.5 mm or 1 mm can be used for the creation of devices with low losses at $T = 130$ K (or 150 K) on the base of higher mode which denoted by the green colour (or the blue colour).

REFERENCES

1. Alberta, E. F. and W. S. Hackenberger, "Ceramic capacitors for extreme environments," Palm Springs, USA, March 2005, http://ecadigitallibrary.com/pdf/CARTS05/CARTS0543_05hi2.pdf, seen 05/28/2012.
2. Sawamura, M., T. Furuya, H. Sakai, K. Umemori, and K. Shinoe, "ERL HOM absorber development in Japan," *Proceedings of ERL09*, 63–66, Ithaca, New York, USA, June 2009.

3. Takeuchi, Y., T. Abe, T. Kageyama, H. Sakai, and F. M. Lastname, “RF dielectric properties of SiC ceramics and their application to design of HOM absorbers,” *Proceedings of Particle Accelerator Conference*, 1195–1197, Knoxville, Tennessee, May 2005.
4. Asmontas, S., L. Nickelson, A. Bubnelis, R. Martavicius, and J. Skudutis, “Hybrid mode dispersion characteristic dependencies of cylindrical dipolar glass waveguides on temperatures,” *Electronics and Electrical Engineering*, Vol. 106, No. 10, 83–86, 2010.
5. Gric, T., L. Nickelson, and S. Asmontas, “Extraordinary dependences of dispersion characteristics of lossy SiC cylindrical waveguide on the radius,” *Proceedings of MIKON 2012*, 327–330, Warsaw, Poland, May 2012.

Dispersion Characteristics of Circular Layered Zero-index Anisotropic Metamaterial — Semiconductor Waveguides

S. Asmontas¹, A. Bubnelis^{1,2}, and L. Nickelson^{1,2}

¹Department of Electronics, Center for Physical Sciences and Technology, Vilnius, Lithuania

²Department of Electronic System, Vilnius Gediminas Technical University, Lithuania

Abstract— Here we present the dispersion characteristic dependencies of main and higher eigenmodes of open (without the screen) cylindrical anisotropic metamaterial — semiconductor waveguides. The tensor components of metamaterial permittivity and permeability may accept values close or equal to zero. The values of tensor components become equal to zero at the operating frequency equal to the metamaterial electric $f_{ep} = 2.5$ GHz or (and) magnetic $f_{mp} = 2$ GHz plasma frequencies. Zero-index metamaterials as well as the semiconductor material with the low electrical resistivity are dispersive media. We present here the phase and attenuation constants of the waveguide dependant on the radius of metamaterial core in the frequency range from 0.05 GHz till 2 GHz. We present also dispersion characteristics of the waveguide with the radius of metamaterial core equal to 1 mm in the frequency range 0.05–20 GHz. There are differences between dispersion characteristics of modes which propagate in the resonance for metamaterial area till 2 GHz and of usual waveguide modes which propagate in the frequency range 2–20 GHz.

1. INTRODUCTION

In the last decade many specialist focused on the experimental and theoretical investigations of the zero-refractive index (or zero-index) metamaterials. The metamaterials attractive to researches due to their unconventional constitutive parameters and different anomalous effects too [1–3].

Here analyzed waveguides contain an anisotropic zero-index metamaterial core with the radius r and a coating n -type Si semiconductor layer with the external radius R (Fig. 1). Outside of the waveguide is a free space area.

The anisotropic metamaterial constitutive parameters were taken here of [4, 5]. Our computer program allows take into account a very large material attenuation as well as the values of non-diagonal tensor components [6, 7].

Dispersion characteristics of layered waveguides with the external radius equal to 5 mm at the left handed polarization ($\exp(im\varphi)$) of microwave will be shown here. There are unusual shape of eigenmode dispersion characteristics and anomalous sectors of the characteristics at certain frequencies. It will be shown how the value of metamaterial core radius affects on the propagating eigenmode quantity and mode cutoff frequencies f_{cut} .

2. CALCULATION RESULTS OF THE DISPERSION CHARACTERISTICS

We have electrostatically rigorously investigated the open layered cylindrical metamaterial — semiconductor waveguides. The solution of Maxwell's equations for the layered waveguide was carried out by the partial area method at the using the Müller's method for the searching of

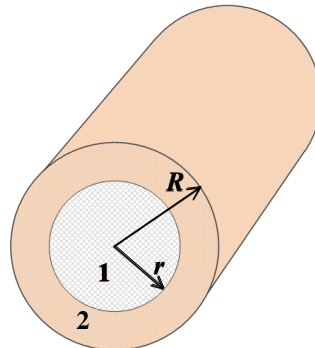


Figure 1: Model of layered metamaterial — semiconductor waveguide and designations are: area 1 is a zero-index metamaterial waveguide core and area 2 is a n -Si semiconductor layer.

complex propagation (phase and attenuation) constants of propagating modes. The computer program for the dispersion characteristic calculations has created in the MATLAB language.

In Figs. 2–4 are shown dispersion characteristics of the waveguide in the frequency range from 0.5 GHz to 2 GHz when the waveguide radius $R = 5$ mm and the metamaterial core radius r equals to 1 mm, 2 mm or 3 mm. It means that the thickness of coated semiconductor layer is 4 mm, 3 mm or 2 mm, correspondingly. We calculated the diagonal tensor component of permittivity and permeability of anisotropic metamaterial by formulae [4, 7]: $\varepsilon_{xx}^{meta} = 1 - \omega_{ep}^2/\omega$ and $\mu_{xx}^{meta} = 1 - \omega_{mp}^2/\omega$, where $\omega = 2\pi f$ is the angular frequency of EM oscillations; f is the operating frequency, metamaterial electric $f_{ep} = 2.5$ GHz and magnetic $f_{mp} = 2$ GHz plasma frequencies. We permit here that the diagonal tensor components are equal to each other. The relative permittivity of n -type Si layer is $\varepsilon_r^{n-Si} = 11.8 - i(1/\omega\varepsilon_0\rho)$ where $\rho = 0.3 \Omega\cdot\text{m}$ is the semiconductor electrical resistivity.

The metamaterial effective permittivity and permeability are negative in the frequencies below 2 GHz. The effective material parameters are close to zero in frequency range 1.5–2 GHz [7].

The phase constant characteristics in frequency range below 2 GHz have two cutoff frequencies, i.e., the low f_{cut} and the high f_{cut} . The electromagnetic waves start to propagate in low frequencies (~ 0.05 GHz) when the effective permittivity or the permeability of metamaterial are negative and finish propagating when the ones are close to zero (f is around 1.4 GHz or 1.9 GHz).

The comparison of phase constants the main (red curve) and higher modes (Figs. 2(a)–4(a)) shows that the greater radius r of metamaterial core is the more eigenmodes can propagate. We see that when $r = 1$ mm, 2 mm and 3 mm can propagate 3 modes, 5 modes and 7 modes, correspondingly. Our designations of higher modes are: the 1st mode is green curve, 2nd mode is blue, 3rd mode is yellow, and three next modes are bronze, brown and olive.

We see that the main mode and several higher modes have extremums of phase constant. In

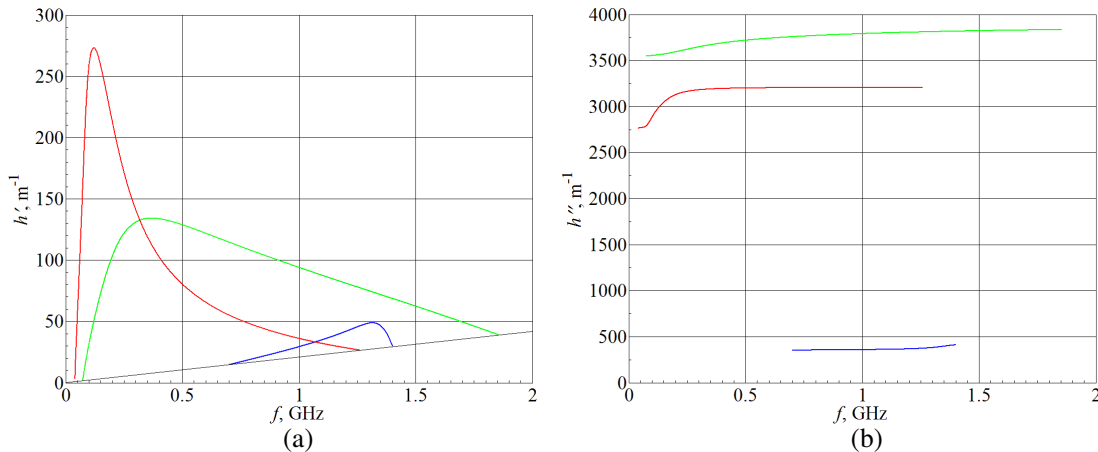


Figure 2: Dependences of the phase constant (a) and attenuation constant (b) on the frequency when the metamaterial core radius $r = 1$ mm.

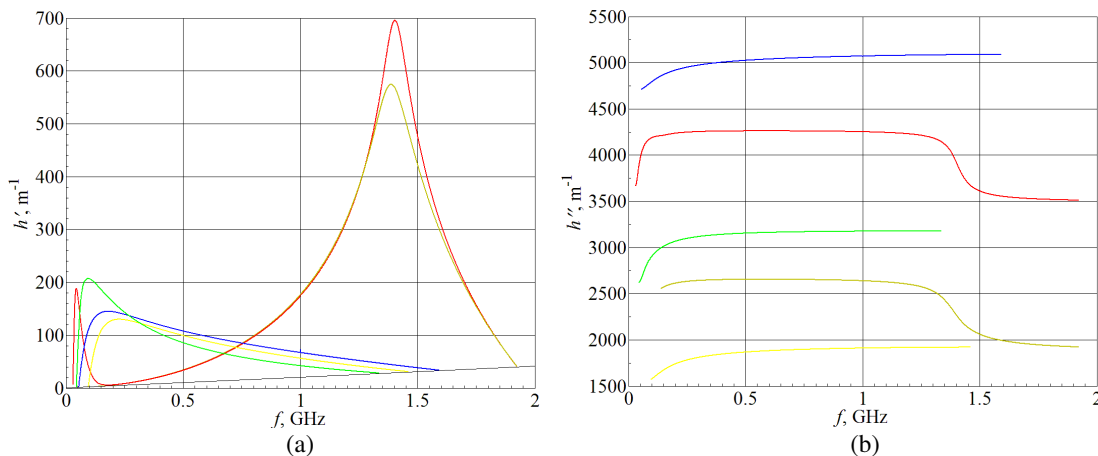


Figure 3: Dependences of the phase constant (a) and attenuation constant (b) on the frequency when the metamaterial core radius $r = 2$ mm.

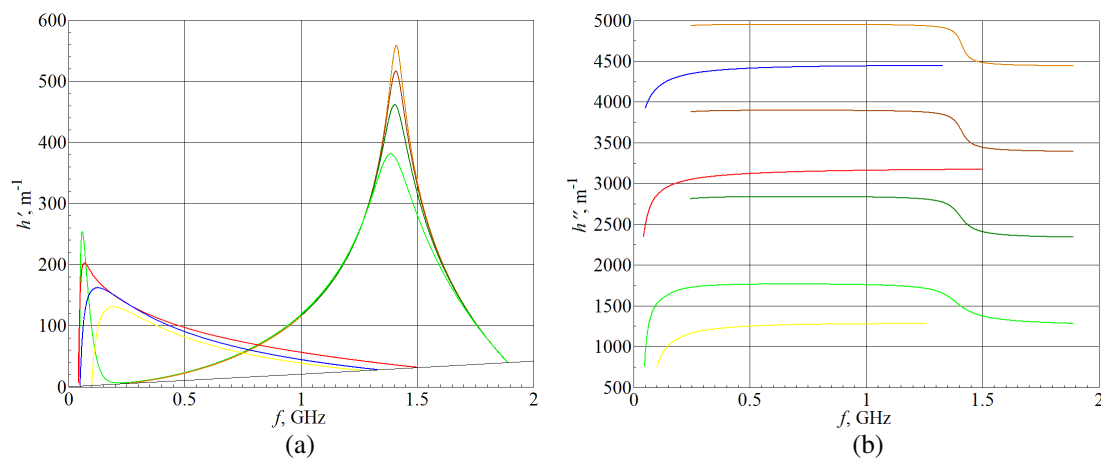


Figure 4: Dependences of the phase constant (a) and attenuation constant (b) on the frequency when the metamaterial core radius $r = 3$ mm.

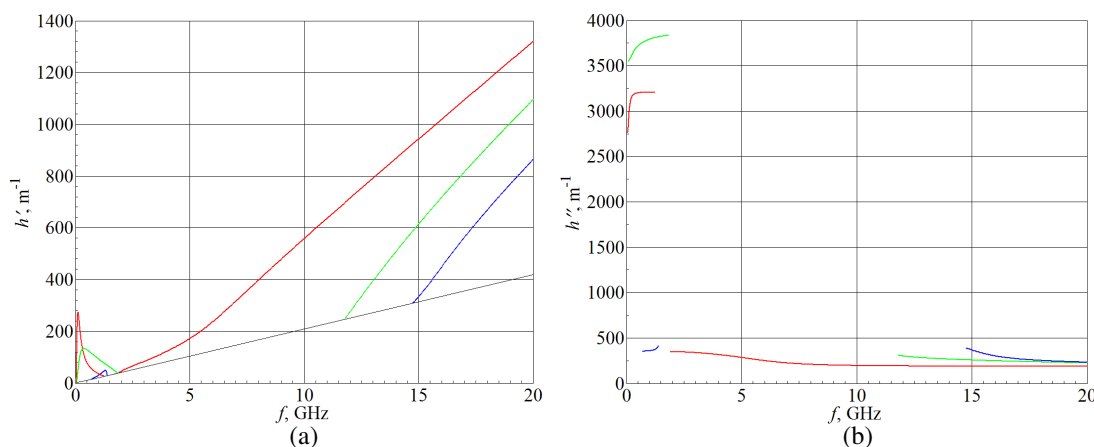


Figure 5: Dependences of the phase constant (a) and attenuation constant (b) on the frequency when the metamaterial core radius $r = 1$ mm.

the Figs. 2 and 3 we see sharp resonances of the main mode phase constant when the metamaterial core radius r is 1 mm or 2 mm. We can observe the strong sharp resonances of phase constants of second, fourth, fifth and seventh modes when the metamaterial core has radius 2 mm. We find that the radius of metamaterial core r strong influent on the attenuation constant of the main and the higher modes.

Figure 2 shows that the losses of the main (red curve) and the 1st higher modes (green curve) are large at the whole range of their propagation. The second higher mode (blue curve) only propagates in the range 0.7–1.4 GHz with a relatively small loss. The losses of the main and the first higher modes are many times larger in the comparison with the loss of second higher mode and they apparently attenuate. The attenuation of second higher mode is low and almost changeless (Fig. 2(b)). The signal propagating on the layered metamaterial — semiconductor waveguide with $r = 1$ mm in the frequency range 0.7–1.4 GHz will not be distorted.

In the Figs. 3(b), 4(b) is presented the attenuation of modes when the metamaterial core has radius equal to 2 mm or 3 mm. We see that the attenuation of the second higher mode became very large for both waveguides. The resonance area around frequency ~ 1.4 GHz is interesting because can be created attenuator on the base of higher modes (Fig. 4).

In Fig. 5 are presented metamaterial — semiconductor waveguide phase (a) and attenuation (b) characteristics in the frequency range from 0.05 GHz to 20 GHz when the external waveguide radius is 5 mm and the inner radius is 1 mm. The dispersion characteristics of the main and two higher modes in the frequency range 2–20 GHz have the usual form as for the standard dielectric waveguides [8]. We see in Fig. 5(b) that the jump losses for the main (red curve) and the high modes (green and blue curves) happened in the resonance for mrtamaterial area when frequency is less than 2 GHz. The higher modes which propagate till ~ 2 GHz vanish and any higher modes do not propagate till the certain cutoff frequencies. The first higher mode appears at $f_{cut} = 11.8$ GHz

and the second one appears $f_{cut} = 14.8$ GHz.

There are two different frequency ranges for the propagation of modes on the open cylindrical anisotropic metamaterial — semiconductor waveguides in the range 0.05–20 GHz. The waveguide losses are high due to high imaginary part of coating semiconductor layer permittivity in the low frequencies. The metamaterial permittivity and permeability tend to unity in high frequencies (in our investigations f higher than 2 GHz). Therefore, the layered metamaterial — semiconductor waveguide acts at high frequencies as a hollow-pipe semiconductor waveguide [9, 10].

3. CONCLUSIONS

1. We analyzed dispersion characteristics of the open layered cylindrical metamaterial — n -Si semiconductor waveguides when the metamaterial core radii are 1 mm, 2 mm or 3 mm and the semiconductor electrical resistivity is $0.3 \Omega \cdot \text{m}$ in the frequency range from 0.05 GHz to 20 GHz.
2. We discovered that the dispersion characteristics are very different at the low frequency range (till 2 GHz) and at the high frequency range (2–20 GHz). The first frequency range is a resonant for metamaterial area.
3. We find that curves of phase constants of analyzed waveguides contain sharp picks. The picks can be used for fast changing of the certain mode wavelength. The position of these picks on the frequency axis can be changed by the variation of metamaterial core radius.
4. The second higher mode of the layered metamaterial — n -Si waveguide with $r = 1$ mm can only propagates in the range 0.7–1.4 GHz. The attenuation of the mode is low and almost changeless. This waveguide in the frequency range 0.7–1.4 GHz do not distort a signal.

REFERENCES

1. Zhou, H., Z. Pei, S. Qu, S. Zhang, J. Wang, Q. Li, and Z. Xu, “A planar zero-index metamaterial for directive emission,” *Journal of Electromagnetic Waves and Applications*, Vol. 23, No. 7, 953–962, 2009.
2. Oraizi, H., A. Abdolali, and N. Vaseghi, “Application of double zero metamaterials as radar absorbing materials for the reduction of radar cross section,” *Progress In Electromagnetics Research*, Vol. 101, 323–337, 2010.
3. Silveirinha, M. and N. Engheta, “Design of matched zero-index metamaterials using nonmagnetic inclusions in epsilon-near-zero media,” *Physical Review B*, Vol. 75, 075119–1–10, 2007.
4. Liu, S.-H., C.-H. Liang, W. Ding, L. Chen, and W.-T. Pan, “Electromagnetic wave propagation through a slab waveguide of uniaxially anisotropic dispersive metamaterial,” *Progress In Electromagnetics Research*, Vol. 76, 467–475, 2007.
5. Smith, D. R., P. Rue, D. C. Vier, A. F. Starr, J. J Mock, and T. Perram, “Design and measurement of anisotropic metamaterials that exhibit negative refraction,” *IEICE Trans. on Electron.*, Vol. E87-C, No. 3, 359–370, 2004.
6. Nickelson, L., A. Bubnelis, A. Baskys, and R. Navickas, “The magnetoactive p -Ge rod waveguide loss analysis on the concentration of two component hole charge carriers,” *Electronics and Electrical Engineering*, Vol. 110, No. 4, 53–56, 2011.
7. Nickelson, L., S. Asmontas, T. Gric, J. Bucinskas, and A. Bubnelis, “Electrodynamical analysis of open lossy metamaterial waveguide and scattering structures,” *Metamaterial*, Dr. Xun-Ya Jiang, Ed., Chapter 2, 27–56, InTech, 2012, ISBN 978-953-51-0591-6.
8. Nickelson, L. and V. Shugurov, *Singular Integral Equations’ Methods for the Analysis of Microwave Structures*, VSP, Leiden-Boston, 2005.
9. Bubnelis A., L. Nickelson, A. Baskys, and R. Navickas, “Dispersion dependencies of circular hollow-pipe SiC waveguide on the inner radius and temperature,” *Proceedings of MIKON*, 333–336, Warsaw, Poland, May 2012.
10. Nickelson, L., A. Bubnelis, and S. Asmontas, “Phase constant peculiarities of cylindrical zero-index anisotropic metamaterial waveguide,” *Proceedings of META ’12*, 339–342, Paris, France, April 2012.

Defects Characterization in CFRP Materials Industrial e Civil Applications

D. Pellican, I. Palamara, and M. Versaci

MECMAT Department, University Mediterranea of Reggio Calabria, Italy

Abstract—The process of production of carbon fiber reinforced polymers, is very elaborate and un-free from faults and problems. Problems during the manufacturing, such as inclusion of other materials, can cause flaws in the resulting material, this way compromising its integrity. Reliable performance of a component or structure depends on its pre-service quality and inservice degradation under operating conditions. The importance of Non-Destructive Testing and Evaluation is ever increasing, above all in ensuring pre-service quality and monitoring inservice degradation, in order to avoid premature failure of the components/structures in carbon fiber reinforced polymers for industrial and civil applications. Within this framework, this work aims to propose a design of a new eddy current probe for non destructive evaluation, based on a ferrite core probe, in order to investigate the presence of defects in carbon fiber epoxy composite materials such as delaminations or inclusions [1]. Particularly, in this work we propose a Finite Element Method based approach for modelling a fast and accurate evaluation of defects in composite materials able to easily detect defects, aside from the orientation. The effect of the ferrite core is analyzed in order to focus magnetic flux density on the investigated specimen. Eddy currents generated by high speed ferrite core probe movement were investigated by using numerical simulation. Particularly, Finite Element Approach has been exploited in order to emphasize the presence of defects in a multi-layer carbon fiber epoxy structure. Proposing an high speed inspection system, that involves probe optimization, the extraction of features from FEA signals and defect characterization using signal processing techniques and Soft Computing techniques for inverse problem solution [2].

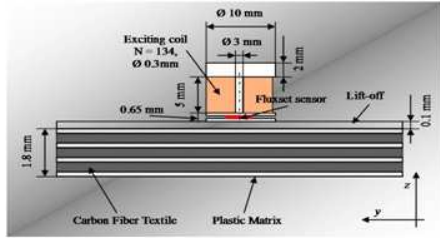
1. INTRODUCTION

Being eddy current-like very sensitive and noisy signals, a Soft Computing approach able to recognize and classify the defects, starting from the measured eddy current signals, could be very useful. The ill-posedness of the so-defined process needs a method of regularization. In this paper, a heuristic approach is proposed in order to solve the inverse problem of the characterization of the defect's size. In particular, the adopted approaches will be tested, and the robustness to noise will be evaluated. Within the framework of the civil and military industries, much attention is focused on the quality check of the manufacture process, with a special regard to the composite materials. According to the current laws, monitoring the material integrity is even carried out during its operative life, in terms of reliability as well as safety. Particularly, Carbon fiber reinforced polymers (CFRPs) are the basic product for aeronautical industry, constructing the main parts of the modern airplanes. In a production phase it often comes out defects of production with delaminations, inclusions and porosity. It arises, this way, the need of an on-line check to put into effect during the production, so to decrease eventual problems coming out later and, moreover, to avoid to the enterprise costs in surplus. Thus, Non-Destructive Testings (NDTs) and in particular ferrite core Eddy Current (EC) probes are useful for our aims, as it is possible to easily analyze even highly thick metallic as well as non-metallic materials, with a good resolution and a remarkable operative versatility [3]. This technique, based on the investigation of the magnetic flux, is used to detect and characterize possible flaws or anomalies in workpieces. This work proposes a Fuzzy Similarity approach starting from a numerical database obtained by the Finite Element Analysis (FEA). They can solve a classification problem starting from “ad hoc” features, extracted from the numerical results. For this aim, an appropriate database can be built by pre-processing the numerical measures, and the selected features must be able to assure a good class separation without incurring in the “curse of dimensionality” problem. The paper is structured as follows: Section 2 briefly describes the electrical properties of the carbon fiber; Section 3 presents the FEA approach; subsequently, results about crack detection are shown. Finally, in Section 4 our conclusions are drawn up.

2. THE EXPLOITED MODEL

2.1. Collection Data

To create a database of measures starting from a set-up of measure shown in Fig. 1 it is employed a Finite Element Method (FEM) approach that uses the $A - \Phi$ formulation [4] described by follow

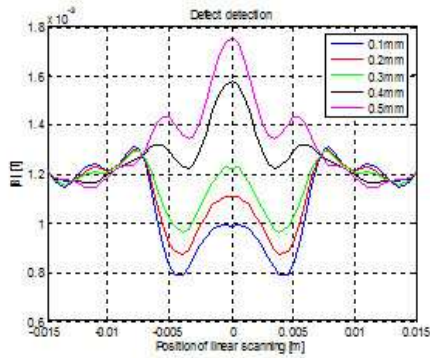


(a)

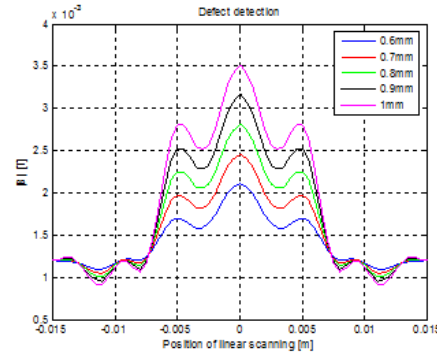
Sample	Depth [mm]	Sample	Depth [mm]
No Defect	0	#6	0.5
#1	0.1	#7	0.6
#2	0.2	#	0.7
#3	0.3	#8	0.8
#4	0.4	#9	1

(b)

Figure 1: Set-up of measure and defect kind. (a) Schematic layout of measurement set-up. (b) Table resumming examined samples of CFRP using for DataBase Composition.



(a)



(b)

Figure 2: Signal by sample inspection's different depths.

equations. The numerical model requires geometrical and physical definition of the coil, and the CFRP plate $[90^\circ, 0^\circ, 90^\circ]$ with dimensions $7[\text{cm}] \times 4[\text{cm}] \times 3[\text{mm}]$ has been modeled. The exciting current and the frequency have been chosen according to the skin-effect phenomenon. For our purpose, we have been verifying the distortion of EC's flux lines (A/m) caused by the presence of defect with different kinds of depth and the magnetic field's density (T) while the probe moves right over the surface defect.

$$-\nabla \cdot ((j\omega\sigma - \omega^2\epsilon_0\epsilon_r)\mathbf{A} - \sigma\mathbf{v} \times (\nabla \times \mathbf{A}) + (\sigma + \omega\epsilon_0\epsilon_r)\nabla V - \mathbf{J}^e) = 0 \quad (1)$$

$$(j\omega\sigma - \omega^2\epsilon_0\epsilon_r)\mathbf{A} + \nabla(\mu_0^{-1}\mu_r^{-1}\nabla \times \mathbf{A}) - \sigma\mathbf{v} \times (\nabla \times \mathbf{A}) + (\sigma + \omega\epsilon_0\epsilon_r)\nabla V = \mathbf{J}^e \quad (2)$$

where σ is the conductivity, ω is the angular pulsation, μ_0, μ_r are the void's magnetic constant and the material's permeability; ϵ_0, ϵ_r are the voids and the material's dielectric constants, respectively, \mathbf{v} is the instantaneous velocity of the object derived from the expression of the Lorentz force, and \mathbf{J}^e is the external current density, with $\mathbf{J}^e \neq 0$ on the exciting coil.

Samples (Table 1) with different kinds of defect are analyzed. The database is substantially structured in a set of signals obtained by the scanning out of specimen with presence of defect, and a set of signals obtained by scanning the specimen without defect. Typical signals are shown in Fig. 2.

2.2. Fuzzy Similarities Measures (FSM) to Evaluate Depth of Defect in CFRP

A fuzzy similarity measure is a fuzzy binary relation in $F(X)$, with X as the universe of items $S : F(X) \times F(X) \rightarrow [0, 1]$ satisfying the following properties:

- S is reflexive: $S(A, A) = [1, 1]$;
- S is symmetric: $S(A, B) = S(B, A)$;
- S is min-transitive: $S(A, C) > \min(S(A, B), S(B, C))$.

where A, B and C are fuzzy sets belonging to $F(X)$. In the literature a lot of measures [4] can be found to express the similarity between two fuzzy sets. In this work, we will use two different

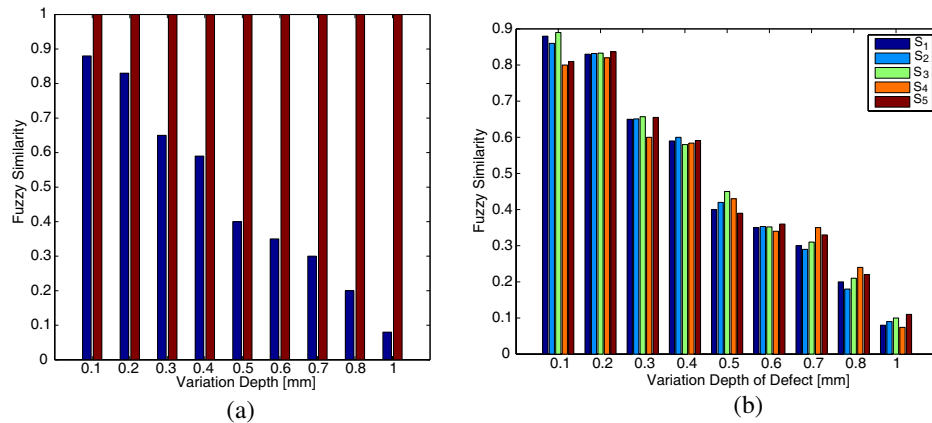


Figure 3: Some results of analysis. (a) Evaluation of S_5 Fuzzy Similarity Function for defect depth characterization. (b) Compared Fuzzy Similarity Function for different kinds of defect depth.

approaches: the first one comes out from the computation of a distance:

$$S_1 = \frac{1}{n} \sum_{i=1}^n \frac{\min(\mu_A(x_i) - \mu_B(x_i))}{\max(\mu_A(x_i) - \mu_B(x_i))} \quad (3)$$

$$S_2 = \sum_{i=1}^n \frac{1 - |(\mu_A(x_i) - \mu_B(x_i))|}{n} \quad (4)$$

$$S_3 = 1 - \sum_{i=1}^n \frac{|(\mu_A(x_i) - \mu_B(x_i))|}{(\mu_A(x_i) + \mu_B(x_i))} \quad (5)$$

$$S_4 = \frac{1}{1 + |(\mu_A(x_i) - \mu_B(x_i))|} \quad (6)$$

where n is the number of elements contained in the fuzzy sets A and B ; $\mu_A(x_i)$ and $\mu_B(x_i)$ are the membership functions of the A and B fuzzy sets respectively. In the second approach the similarity [5] is judged by looking into the common and distinctive features of the two sets, so they are not considered the single elements as points in a metrical space but as sets of features (set of logic predicates).

$$S_5 = \frac{\sum_{i=1}^n (\mu_A(x_i), \mu_B(x_i))}{\sum_{i=1}^n (\mu_A(x_i), \mu_B(x_i)) + \alpha \min(\mu_A(x_i), 1 - \mu_B(x_i)) + \beta \min(1 - \mu_A(x_i), \mu_B(x_i))} \quad (7)$$

2.3. Membership Functions

For each sample and for the one free from defect, the Gaussian membership functions are “built”. For our goal the class of data referring to sample without defect is A and the classes of data referring to samples with defect are labelled with B_j , as many of the samples.

3. RESULT

The measures of similarity Figs. 3(a), 3(b) confirm the possibility to detect the presence of defect. An analysis of the values’ range allows to make considerations also on the depth of defect. It is noticed, in fact, that the minor is the value of similarity the mayor is the defect depth in the examined sample. To test the methodology proposed as classifier, it is used an unknown sample.

4. CONCLUSION

In the present work, we propose an approach of fuzzy similarity for the detection and the classification in terms of depth of defect in CFRP sample. Starting from measures obtained by using numerical model, they’ve been implemented five different similarity measures. The results obtained confirm good performances both in terms of detection and classification. A sensor integrated with a fuzzy similarity analysis could represent a useful tool: easy to use and without any implementation of complex procedures. Any technological production would also allow an “in situ” analysis.

REFERENCES

1. Yamada, S., M. Katau, M. Iwahara, and F. P. Dawson, “Eddy current testing,” *IEEE Trans. Magn.*, Vol. 31, No. 6, 3185–3187, 1995.
2. Theodoulidis, T. P., “Model of ferrite-cored probes for eddy-current nondestructive evaluation,” *J. Appl. Phys.*, Vol. 93, 3071–3078, 2003.
3. Cacciola, M., S. Calcagno, G. Megali, F. C. Morabito, D. Pellicano, and M. Versaci, “FEA design and misdit minimization for in-depth flaw characterization in metallic plates with eddy current nondestructive testing,” *IEEE Trans. Magn.*, Vol. 45, No. 3, 1506–1509, 2009.
4. Roger, D., P. J. Leonard, and H. C. Lai, “Interfacing the general 3D A - ϕ method with a thin sheet conductor model,” *IEEE Trans. Magn.*, Vol. 28, No. 2, 1115–1117, 1992.
5. Tversky, A., “A features of similarity,” *Psychological Review*, Vol. 84, No. 4, 327–352, 1977.

Coupling Matrix Synthesis by Optimization with Cost Function Based on Daubechies D4 Wavelet Transform

J. J. Michalski, J. Gulgowski, T. Kacmajor, and Mike Piatek
TeleMobile Electronics Ltd., Poland

Abstract— This paper proposes and investigates a new cost function used in coupling matrix synthesis. In this method filter scattering characteristics are transformed with the use of Daubechies D4 transform, and then compressed. The cost function is defined as Euclidean distance between compressed D4 template reflection and transmission characteristics and the compressed D4 characteristics resulting from the optimized coupling matrix. The important feature of this method is that there is no need to represent filter characteristics in an analytical form (e.g., with the use of total least squares method). The optimization experiments show the performance of the proposed cost function in comparison to the ones already known.

1. INTRODUCTION

Optimization is a very common technique employed in microwave filter design, e.g., the coupling matrix synthesis [1, 2]. Values of coupling matrix elements are evaluated by minimization of a certain cost function. Basic examples refer to the functions involving discrete set of points of S_{11} or S_{21} characteristics. There are some other ideas known, such as the ones presented in [3, 4] — referring to zeroes and poles of reflection and transmission characteristics. This is possible because generalized eigenvalues of certain matrices related to the coupling matrix, correspond directly to zeros and poles of the admittance or reflection characteristic describing a filter. On the other hand, the zeros and poles precisely define the rational functions S_{11} and S_{12} .

Both the scattering parameters in frequency domain and sets of zeros and poles are the possible representations describing the filter, and can be used in constructing a cost function. Recently in the paper [5], a new concept of filter representation, with the application of the Daubechies D4 wavelet transform over the filter scattering characteristics has been introduced.

In this paper, we are going to propose a different attitude towards the cost function selection known so far, which is used in the optimization process of coupling matrix for a given filter scattering characteristics. We introduce the cost function based on the D4 wavelet representation of filter characteristics. The method may be applied whenever we do not have the scattering characteristics in the analytic form, but rather as a finite set of samples.

2. FORWARD AND INVERSE WAVELET TRANSFORM

In general, wavelet algorithms process data at different *scales* and *resolutions* [7]. This makes them a useful tool for data analysis and data compression. Wavelet analysis begins with a special wavelet prototype function, called *mother wavelet*. The goal of wavelet analysis is to represent the original signal or function in terms of wavelet expansion (as a linear combination of wavelet functions — i.e., mother wavelet scaled and translated in the function domain). With such representation the operations can be performed using only the corresponding wavelet coefficients. For the proper selected mother wavelet we may limit the transform result to the most important coefficients. If the wavelets are well adapted to the data, most of the important wavelet signal representations are located at the beginning of the signal, and then the signal can be truncated below a certain threshold. In consequence, the data are sparsely represented. This kind of coding makes wavelets an excellent tool for data compression. We must be aware of the fact that such truncated wavelet representation will not recreate the original signal precisely, but the recreated signal will be very similar to the original one.

For a discrete signal $S(m)$, $m = 0, 1, \dots, M - 1$ we define general Forward Discrete Wavelet Transform (FDWT) as

$$\begin{cases} w_\varphi(j_0, k) = \frac{1}{\sqrt{M}} \sum_m S(m) \varphi_{j_0, k}(m) \\ w_\psi(j, k) = \frac{1}{\sqrt{M}} \sum_m S(m) \psi_{j, k}(m) \end{cases} \quad (1)$$

and general Inverse Discrete Wavelet Transform (IDWT) as

$$S(n) = \frac{1}{\sqrt{M}} \sum_k w_\varphi(j_0, k) \varphi_{j_0, k}(n) + \sum_{j=0}^{\infty} \sum_k w_\psi(j, k) \psi_{j, k}(n) \quad j = 0, 1, \dots, R; \quad M = 2^R \quad (2)$$

where w_φ are scaling coefficients, w_ψ — wavelet coefficients, $\varphi_{j_0,k}$ — scaling functions, $\psi_{j,k}$ — wavelet functions.

In our further consideration, following the concept [5], we will use Daubechies D4 transform [7]. The D4 transform has four wavelets and scaling function coefficients. Denoted by $x[i]$ the original signal, the Daubechies D4 wavelet scaling function is defined as

$$a[i] = h_0x[2i] + h_1x[2i + 1] + h_2x[2i + 2] + h_3x[2i + 3] \quad (3)$$

and appropriate D4 wavelet function is defined as

$$c[i] = g_0x[2i] + g_1x[2i + 1] + g_2x[2i + 2] + g_3x[2i + 3] \quad (4)$$

where scaling coefficients h and wavelet coefficients g have the following values

$$h_0 = \frac{1 + \sqrt{3}}{4\sqrt{2}}, \quad h_1 = \frac{3 + \sqrt{3}}{4\sqrt{2}}, \quad h_2 = \frac{3 - \sqrt{3}}{4\sqrt{2}}, \quad h_3 = \frac{1 - \sqrt{3}}{4\sqrt{2}} \quad (5)$$

$$g_0 = h_3, \quad g_1 = -h_2, \quad g_2 = h_1, \quad g_3 = -h_0 \quad (6)$$

The index i is incremented by two at each iteration during the calculation of the coefficients.

3. COST FUNCTION DEFINITION BASED ON D4 TRANSFORM FILTER CHARACTERISTIC

Let us assume now that the designed reflection (template characteristics — optimization goals) and transmission characteristics $S_{11}(\lambda)$ and $S_{21}(\lambda)$ are known. They are sampled at a given number of L frequency points and create a vector of L complex numbers (i.e., $2L$ real numbers), which is transformed by a discrete D4 wavelet transform. Then the output of the transform is truncated to the first K coordinates. As a result, we obtain the vector D_0 of R^K , which may be treated as the goal of our approximation process [5]. Now we have the $(N + 2) \times (N + 2)$ coupling matrix M , and for this matrix we find the reflection and transmission characteristics defined by the following equations

$$S'_{11}(\lambda) = 1 + 2j[M - jR + \lambda I_N]_{11}^{-1} \quad (7a)$$

$$S'_{21}(\lambda) = -2j[M - jR + \lambda I_N]_{(N+2)1}^{-1} \quad (7b)$$

where R is the matrix with $R_{11} = R_{(N+2),(N+2)} = 1$ as the only non-zero elements, and I_N is the identity matrix with elements $I_{N+1} = I_{N(N+2),(N+2)}$ set to 0. Now we sample $S'_{11}(\lambda)$ and $S'_{21}(\lambda)$ at the same L points which we used to sample $S_{11}(\lambda)$ and $S_{21}(\lambda)$ and apply D4 discrete wavelet transform to the sampled vector. Then we truncate the output of the wavelet transform to the first K values, in order to obtain the compressed D4 filter representation denoted by D_M . Now we define the cost function as the Euclidean norm of the difference $D_M - D_0$, i.e.,

$$C = \left(\sum_{k=1}^K (D_M(k) - D_0(k))^2 \right)^{1/2} \quad (8)$$

This is a cost function proposed by us, which was used in further experiments.

4. EXPERIMENTS

To verify the proposed concept in practice, the optimization process has been employed to synthesize the coupling matrices of selected filters. The first chosen 4th order asymmetric bandstop filter was reported in [4] and the second 7th order asymmetric bandpass “cul-de-sac” filter was reported in [6]. In the optimization process we have used the Simulated Annealing algorithm. In our experiments, for each filter, we performed 100 optimization runs for three different cost functions: D4 — proposed here by us, the LM cost function based on zeros and poles used in [4], and the third cost function based on the Euclidean distance between discrete scattering characteristics denoted here by $\sum(S_0 - S)$.

Each optimization procedure started with the coupling matrix having all elements randomly distributed between -1 and 1 . In all optimization experiments we used filter characteristics represented by 128 complex frequency points, and the D4 transforms were cut (compressed) after $K = 32$ vector element.

Figure 1 presents reflection and transmission characteristics of the considered 4th order filter. The synthesized coupling matrix is presented in (9). The entries of synthesized matrix are the same as the ones in [4].

$$\begin{matrix}
 0 & 1.5500 & 0 & 0 & 0 & 1.0000 \\
 1.5500 & 0.5200 & 1.2900 & 0 & 1.2010 & 0 \\
 0 & 1.2900 & -0.0560 & 0 & 0 & 0 \\
 0 & 0 & 0 & -1.0190 & 0.4180 & 0 \\
 0 & 0.2010 & 0 & 0.4180 & -0.2080 & 1.5500 \\
 1.0000 & 0 & 0 & 0 & 1.5500 & 0
 \end{matrix} \quad (9)$$

Table 1 presents the comparison of optimization results for three considered cost functions, with regard to time and efficiency of the optimization. By optimization efficiency we define how many optimization runs converged to the global minimum.

While analysing the obtained results we can observe that the efficiency of the cost function proposed by us (8) is a little smaller when compared to the cost function LM used in [4], but the optimization time is considerably shorter. The worst results were obtained with the use of the cost function based directly on S characteristics of a filter.

Reflection and transmission characteristics for the second filter are presented in Fig. 2. The synthesized coupling matrix is presented below in (10).

$$\begin{matrix}
 0 & 1.0572 & 0 & 0 & 0 & 0 & 0 & 0 & 0 \\
 1.0572 & 0.0211 & 0.6282 & 0 & 0 & 0 & 0.6282 & 0 & 0 \\
 0 & 0.6282 & -0.0683 & 0.5798 & 0 & 0 & 0 & -0.6282 & 0 \\
 0 & 0 & 0.5798 & -0.1912 & 0 & 0 & 0 & 0 & 0 \\
 0 & 0 & 0 & 0 & -0.4856 & 0.6836 & 0 & 0 & 0 \\
 0 & 0 & 0 & 0 & 0.6836 & 0.1869 & 0.6499 & 0 & 0 \\
 0 & 0.6282 & 0 & 0 & 0 & 0.6499 & 0.1199 & 0.6282 & 0 \\
 0 & 0 & -0.6282 & 0 & 0 & 0 & 0.6282 & 0.0211 & 1.0572 \\
 0 & 0 & 0 & 0 & 0 & 0 & 0 & 1.0572 & 0
 \end{matrix} \quad (10)$$

For the filter the synthesized coupling matrix is identical to the one reported in [6].

Having analysed the results we can see that the cost function based on D4 transforms of filter characteristics (8) gives the biggest probability of optimization convergence. In the case of this filter, the cost function used in [4] gives the convergence ratio which equals zero. The reason for

Table 1: Comparison of optimization results for chosen cost functions.

	D4	LM	$\sum(S_0 - S)$
Opt. time [min]	55	126	64
Opt. efficiency [%]	10	12	4

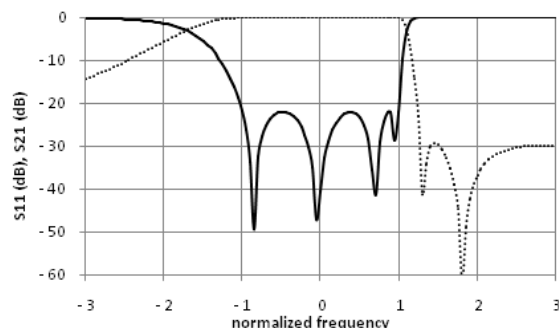


Figure 1: Response of the 4th order bandstop filter (lowpass prototype). Solid line — transmission characteristic, dotted line — reflection characteristic.

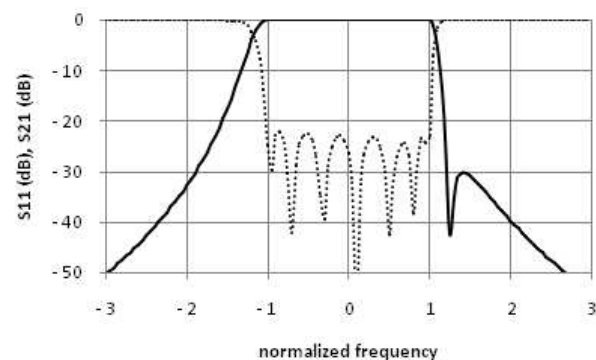


Figure 2: Response of 7th order bandpass filter (lowpass prototype). Solid line — transmission characteristic, dotted line — reflection characteristic.

Table 2: Comparison of optimization results for selected cost functions.

	D4	LM	$\sum(S_0 - S)$
Opt. time [min]	95	72	122
Opt. efficiency [%]	13	0	8

this is that, in general, zeros and poles of filter characteristics, calculated from the left side of (7) and eigenvalues, calculated from the right side of (7), form unordered sets, and in consequence, the cost function used in [4] does not guarantee a proper order while they are being compared. To solve this problem the new cost function definition used in coupling matrix optimization process, based on Hausdorff distance, was proposed in [8]. As our goal was to compare our cost functions and other selected ones, we were not concerned with absolute efficiency. Optimization results for all cost functions can be improved by introducing, for example, a different gradient optimization method.

5. CONCLUSION

In this paper, a new cost function definition was used in the optimization technique in filter coupling matrix synthesis. The Euclidean distance between compressed Daubechies D4 filter characteristics and the expected (ideal) compressed D4 characteristic has been used as the value of the proposed cost function. The performed optimization of coupling matrices of selected filters showed high efficiency of the method, in comparison to the methods used nowadays in coupling matrix optimization techniques.

ACKNOWLEDGMENT

This work was supported by Polish National Ministry for Science & Higher Education (Decision Nr. 736/N-COST/2010/0), under the project name “New optimization methods and their investigation for the application in physical microwave devices which require tuning”, performed within the COST Action RFCSET IC0803.

REFERENCES

1. Atia, W. A. and K. A. Zaki, “Synthesis of general topology multiple coupled resonator filters by optimization,” *IEEE Microwave Theory Tech. Dig.*, Vol. 2, 821–824, Jun. 7–12, 1998.
2. Amari, S., “Synthesis of cross-coupled resonator filters using an analytical gradient-based optimization technique,” *IEEE Trans. Microwave Theory Tech.*, Vol. 48, 1559–1564, Sep. 2000.
3. Lamecki, A., P. Kozakowski, and M. Mrozowski, “Fast synthesis of coupled-resonator filters,” *IEEE Microwave and Wireless Components Letters*, Vol. 14, No. 4, 174–176, Apr. 2004.
4. Lamecki, A. and M. Mrozowski, “Bandpass/bandstop coupling matrix synthesis based on rational representation of scattering parameters,” *Proceedings of Asia-Pacific Microwave Conference*, 1974–1976, 2010.
5. Michalski, J. J. and T. Kacmajor, “Filter tuning algorithm with compressed reflection characteristic by daubechies D4 wavelet transform,” *Proceedings of the 41st European Microwave Conference*, 778–781, Manchester, UK, Oct. 9–14, 2011.
6. Cameron, R. J., “Advanced coupling matrix synthesis techniques for microwave filters,” *IEEE Trans. Microwave Theory Tech.*, Vol. 51, 1–110, Jan. 2003.
7. Daubechies, I., *Ten Lectures on Wavelets*, CBMS-NSF Conference Series in Applied Mathematics, SIAM, Ed., 1992.
8. Kacmajor, T., J. Gulowski, and J. J. Michalski, “Filter tuning and coupling matrix synthesis by optimization with cost function based on zeros, poles and hausdorff distance,” *Microwave Symposium Digest (MTT)*, 2012 *IEEE MTT-S International Microwave Symposium*, Montreal, Canada, Jun. 17–22, 2012.

A Quaternion Widely Linear One-stage Prediction Algorithm

R. M. Fernández-Alcalá¹, J. Navarro-Moreno¹, J. C. Ruiz-Molina¹,
C. Jahanchahi², and D. H. Dini²

¹Department of Statistics and Operations Research, University of Jaén, Spain

²Department of Electrical and Electronic Engineering
Imperial College London, London, United Kingdom

Abstract— This paper addresses the one-stage prediction problem for three- and four-dimensional random signals, in the quaternion space. Specifically, a quaternion widely linear processing is employed for designing a recursive algorithm for the one-stage prediction of a special class of quaternion signals, called wide-sense stationary. The achievement of the proposed solution is analyzed by means of a simulation example where the three-dimensional position of an aircraft is predicted one-stage ahead.

1. INTRODUCTION

Recent advances in communication and signal processing have awoken the interest in multidimensional signals. Although these signals could be treated from a real or complex vectorial approach, the latest studies have shown the enhancement of using quaternions instead of vectorial signals [1].

Basically, quaternions can be considered as a noncommutative expansion of complex numbers which are given by a scalar real part and a vectorial part formed by three imaginary variables. Hence, they are suitable for modeling three and four-dimensional signals, collecting in a natural way the correlation between their components.

Analogously to the complex case, a widely linear processing is the appropriate approach to take advantage of all the available second-order statistical information [2]. Quaternion widely linear processing (QWL) is characterized by considering a four-dimensional vector whose elements are chosen among the signal, its conjugate, and the three perpendicular quaternion involutions, taking into account a possible impropriety in the quaternion signals involved.

It is only recently that the quaternion widely linear model [2, 3] has been developed. This has led to the development of numerous widely linear algorithms, among others, the quaternion widely linear least mean square [4] and the widely linear recursive least squares [5], both benefiting from the full second order statistics and therefore offering better performance for noncircular signals (circular signals have rotation invariant distributions).

In this paper, a quaternion widely linear processing is employed in the design of a one-stage prediction algorithm for a special class of quaternion random signals characterized by having an autocorrelation function of the augmented quaternion vector that is only dependent on the difference of time instants. This type of signal will be called wide-sense stationary (WSS). In our methodology, the multivariate Durbin-Levinson algorithm [6], proper of stationary time series analysis, is adapted for the one-stage prediction of a WSS quaternion signal.

The paper is structured as follows. In the next section, Section 2, a brief summary of the necessary properties of the quaternion algebra is given. Next, Section 3 is devoted to solving the one-stage prediction problem. Moreover, the achievement of the proposed solution is analyzed in Section 4 by means of a simulation example where the three-dimensional velocity of an aircraft is predicted from the information supplied by its three-dimensional position.

2. QUATERNION ALGEBRA

In the following, and without losing generality, all signals are supposed to be zero-mean. The superscripts ‘*’, ‘T’ and ‘H’ represent the quaternion conjugate, transpose and quaternion conjugate transpose operators, respectively.

Define a quaternion random signal by

$$q_t = a_t + ib_t + jc_t + kd_t$$

where $a_t, b_t, c_t, d_t \in \mathbb{R}$ are random variables and

$$i^2 = j^2 = k^2 = ijk = -1$$

which implies that $ij = k = -ji$, $ki = j = -ik$, and $jk = i = -kj$. Note that, the quaternion product is noncommutative.

Let $\mathbf{x} = [x_1, \dots, x_{n_1}]^T$ and $\mathbf{y} = [y_1, \dots, y_{n_2}]^T$ be two n_1 and n_2 -dimensional quaternion random vectors, where x_i and y_j are quaternion random signals. Define the inner product $\langle \mathbf{x}, \mathbf{y} \rangle_{\mathcal{Q}} = E[\mathbf{xy}^H]$ with

$$\mathbf{xy}^H = \begin{bmatrix} x_1 y_1^* & x_1 y_2^* & \dots & x_1 y_{n_2}^* \\ \vdots & \vdots & \vdots & \vdots \\ x_{n_1} y_1^* & x_{n_1} y_2^* & \dots & x_{n_1} y_{n_2}^* \end{bmatrix}$$

where $x_i y_j^*$ represents the quaternion product between the quaternions x_i and y_j^* (see [2] for more details).

Denote by $\overline{\text{sp}}\{\mathbf{q}_1, \dots, \mathbf{q}_n\}$ the closed span of $\{\mathbf{q}_1, \dots, \mathbf{q}_n\}$.

From [2] we know that a complete description of the second order statistics of the quaternion q_t in the quaternion domain \mathbb{H} can be given by the augmented quaternion vector $\mathbf{q}_t = [q_t, q_t^*, q_t^i, q_t^j]^T$, where q_t^* , q_t^i and q_t^j are defined by

$$\begin{aligned} q_t^* &= a_t - ib_t - jc_t - kd_t \\ q_t^i &= a_t + ib_t - jc_t - kd_t \\ q_t^j &= a_t - ib_t + jc_t - kd_t \end{aligned}$$

Note that this choice is not unique and that any other combination of four elements of $\{q_t, q_t^*, q_t^i, q_t^j, q_t^k\}$, with $q_t^k = a_t - ib_t - jc_t + kd_t$, or their conjugates can be used with the same effect.

Moreover, [2] introduces the concept of WSS in the quaternion domain in the following way. Denote the autocorrelation function of \mathbf{q}_t as $\mathbf{\Gamma}_{\mathbf{q}}(t, s) = \langle \mathbf{q}_t, \mathbf{q}_s \rangle_{\mathcal{Q}}$. A quaternion random signal q_t is said to be WSS if and only if the autocorrelation function is a function of only the lag τ , that is

$$\mathbf{\Gamma}_{\mathbf{q}}(\tau) = \langle \mathbf{q}_{t+\tau}, \mathbf{q}_t \rangle_{\mathcal{Q}} \quad (1)$$

On the other hand, for a quaternion random signal, there exist two main kinds of properness [7]: \mathcal{Q} -properness (or \mathbb{H} -circularity) and \mathcal{C}^{η} -properness (or \mathcal{C}^{η} -circularity). A quaternion random vector q_t is \mathcal{Q} -proper if and only if the three complementary functions $C_{q, q^i}(t, s) = E[q_t q_s^i]$, $C_{q, q^j}(t, s) = E[q_t q_s^j]$ and $C_{q, q^k}(t, s) = E[q_t q_s^k]$ vanish. Moreover, a quaternion random vector q_t is \mathcal{C}^{η} -proper, for any pure imaginary unit $\eta \in \{i, j, k\}$ if and only if all the complementary functions vanish except $\mathbf{C}_{q, q^{\eta}}(t, s) = E[q_t q_s^{\eta}]$. Note that, \mathcal{Q} -properness implies \mathcal{C}^{η} -properness.

3. ONE-STAGE PREDICTION ALGORITHM

Our purpose in this section is to provide an efficient algorithm for the one-stage prediction of a WSS quaternion signal based on its past information history.

Concretely, we consider a quaternion signal q_t which is WSS in the sense defined above. By following a QWL processing, we want to predict the signal q_{n+1} on the basis of the quaternion observations $\mathbf{q}_1, \dots, \mathbf{q}_n$. This predictor, named QWL one-stage predictor, will be denoted by $\hat{q}^{WL}(n+1/n)$.

This problem is equivalent to obtain the projection of the augmented quaternion vector \mathbf{q}_{n+1} onto the space $\overline{\text{sp}}\{\mathbf{q}_1, \dots, \mathbf{q}_n\}$. Thus, denoting this projection of the form

$$\hat{\mathbf{q}}(n+1/n) = \sum_{j=1}^n \Theta_{n,j} \mathbf{q}_{n+1-j} \quad (2)$$

the QWL one-stage predictor $\hat{q}^{WL}(n+1/n)$ is trivially

$$\hat{q}^{WL}(n+1/n) = \sum_{j=1}^n \theta_{n,j} \mathbf{q}_{n+1-j}$$

with $\theta_{n,j} = [1, 0, 0, 0] \Theta_{n,j}$ and whose associated mean-square error, named QWLMSE, is $\varepsilon_{n,1} = [1, 0, 0, 0] \Sigma_{n,1} [1, 0, 0, 0]^T$ where

$$\Sigma_{n,1} = \langle \mathbf{q}_{n+1} - \hat{\mathbf{q}}(n+1/n), \mathbf{q}_{n+1} - \hat{\mathbf{q}}(n+1/n) \rangle_{\mathcal{Q}}$$

A priori, the computation of (2) can seem more difficult than the direct computation of $\hat{q}^{WL}(n+1/n)$. However, WSS quaternion properties are going to allow us the efficient computation of the terms $\Theta_{n,j}$ and $\Sigma_{n,1}$. Then, using the Hilbert space theory and property (1), a method similar to the Durbin-Levinson algorithm is proposed for the efficient computation of these terms.

This algorithm requires the simultaneous solution of two sets of equations, one arising from the computation of the predictor (2) and the other from the computation of the estimator

$$\hat{\mathbf{q}}(1/2 \dots n) = \sum_{j=2}^n \tilde{\Theta}_{n-1,j-1} \mathbf{q}_j$$

where $\hat{\mathbf{q}}(1/2 \dots n)$ denotes the estimator \mathbf{q}_1 based on the observations $\mathbf{q}_2, \dots, \mathbf{q}_n$, and whose associated mean-square error is given by

$$\tilde{\Sigma}_{n-1,1} = \langle \mathbf{q}_1 - \hat{\mathbf{q}}(1/2 \dots n), \mathbf{q}_1 - \hat{\mathbf{q}}(1/2 \dots n) \rangle_{\mathcal{Q}}$$

Next, the multivariate Durbin-Levinson algorithm [6] for quaternion signals is provided.

Algorithm 1.

$$\begin{aligned} \Theta_{n,n} &= \Delta_{n-1} \tilde{\Sigma}_{n-1,1}^{-1} \\ \tilde{\Theta}_{n,n} &= \Delta_{n-1}^H \Sigma_{n-1,1}^{-1} \\ \Theta_{n,j} &= \Theta_{n-1,j} - \Theta_{n,n} \tilde{\Theta}_{n-1,n-j}, \quad j = 1, \dots, n-1 \\ \tilde{\Theta}_{n,j} &= \tilde{\Theta}_{n-1,j} - \tilde{\Theta}_{n,n} \Theta_{n-1,n-j}, \quad j = 1, \dots, n-1 \end{aligned} \quad (3)$$

where

$$\begin{aligned} \Sigma_{n,1} &= \Sigma_{n-1,1} - \Theta_{n,n} \Delta_{n-1}^H \\ \tilde{\Sigma}_{n,1} &= \tilde{\Sigma}_{n-1,1} - \tilde{\Theta}_{n,n} \Delta_{n-1} \\ \Delta_n &= \Gamma_{\mathbf{q}}(n+1) - \sum_{j=1}^n \Theta_{n,j} \Gamma_{\mathbf{q}}(n+1-j) \end{aligned} \quad (4)$$

with $\Sigma_{0,1} = \tilde{\Sigma}_{0,1} = \Gamma_{\mathbf{q}}(0)$ and $\Delta_0 = \Gamma_{\mathbf{q}}(1)$.

4. NUMERICAL EXAMPLE

In this section, the performance of our solutions is checked by means of a numerical example where we have simulated in MATLAB the moving of an aircraft in a closed form orbit similar to the trajectory represented in Fig. 1. Note that in its most simple form this is a circular orbit, but more complex trajectories have been also simulated, with the trajectory taking the shape of a closed form helix.

The goal of the experiment has been to predict one-stage ahead the three-dimensional position of a target moving. Then, taking the three dimensional position as components of a pure quaternion q_n , we aim to predict the signal q_{n+1} , on the basis of its own past information q_1, \dots, q_n .

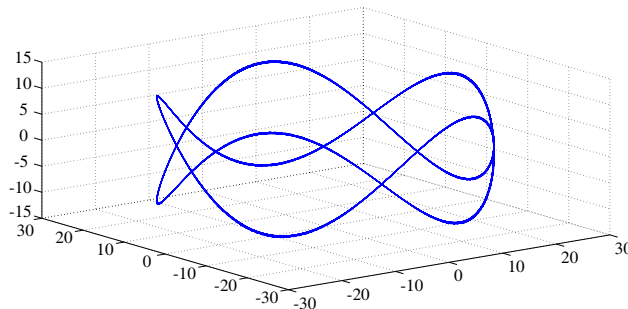


Figure 1: Orbit described for the moving of an aircraft.

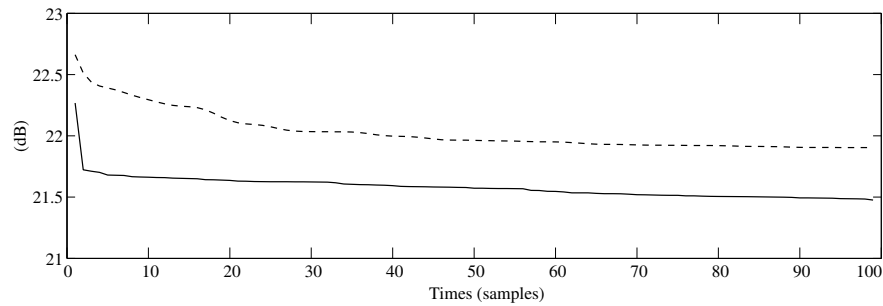


Figure 2: QWLMSE (solid line) and SLMSE (dotted line) (dB) for the one-stage predictor of the position of the aircraft.

Then, we first compare the proposed QWL one-stage predictor with the one obtained from a conventional or strictly linear (SL) processing, which only considers the information supplied by the quaternion signal. With this aim, Fig. 2 depicts the associated errors, QWLMSE and SLMSE. As it could be expected, QWL one-stage predictions show a better behavior than the one provided by the SL one-stage predictions.

5. CONCLUSION

An efficient QWL one-stage prediction algorithm is provided for the class of quaternion signals which are WSS.

In our procedure, we extend the multivariate Durbin-Levinson algorithm to the quaternion domain. This extension allows the recursive computation of the QWL one-stage predictor for a quaternion signal, using correlation information.

REFERENCES

1. Mandic, D. P. and V. S. L. Goh, *Complex Valued Nonlinear Adaptive Filters. Noncircularity, Widely Linear and Neural Models*, Wiley, New York, 2009.
2. Cheong Took, C. and D. P. Mandic, "Augmented second-order statistics of quaternion random signals," *Signal Processing*, Vol. 91, No. 2, 214–224, 2011.
3. Via, J., D. Ramirez, and I. Santamaria, "Properness and widely linear processing of quaternion random vectors," *IEEE Transactions on Information Theory*, Vol. 56, No. 7, 3502–3515, 2010.
4. Cheong Took, C. and D. P. Mandic, "A quaternion widely linear adaptive filter," *IEEE Transactions on Signal Processing*, Vol. 58, No. 8, 4427–4431, 2010.
5. Jahanchahi, C., C. Cheong Took, and D. P. Mandic, "The widely linear quaternion recursive least squares filter," *2nd International Workshop on Cognitive Information Processing (CIP)*, No. 6, 87–92, 2010.
6. Brockwell, P. J. and R. A. Davis, *Time Series: Theory and Methods*, 2nd Edition, Springer-Verlag, New York, 1991.
7. Ujang, B. C., C. Cheong Took, and D. P. Mandic, "Quaternion-valued nonlinear adaptive filtering," *IEEE Trans. Neural Networks*, Vol. 22, No. 8, 1193–1206, 2011.
8. Navarro-Moreno, J., "ARMA prediction of widely linear systems by using the innovations algorithm," *IEEE Transactions on Signal Processing*, Vol. 7, 3061–3068, 2008.
9. Picinbono, J. and P. Bondon, "Second-order statistics of complex signals," *IEEE Transactions on Signal Processing*, Vol. 45, No. 2, 411–420, 1997.

Magnetoelectric Magnetic Field Sensors

I. N. Soloviev, M. I. Bichurin, and R. V. Petrov

Novgorod State University, Russia

Abstract— The magnetoelectric magnetic field sensors based on magnetoelectric materials to work in DC and AC circuits and to detect alternating electromagnetic field and constant magnetic field were investigated. The PZT-Metglas, PZT-Terfenol-D, and PZT-Ni ME sensors characteristics were measured and compared.

1. INTRODUCTION

The magnetoelectric (ME) magnetic field sensors based on ME materials design to work in DC and AC circuits and to detect alternating electromagnetic field and constant magnetic field [1]. The devices have a very diverse range of applications, including medical technology such as magnetoencephalography, magnetocardiography or measuring body processes magnetic fields, military technology in locating objects such as submarines, sunken ships. They also have applications in heart beat monitors, weapon systems positioning, weather prediction, steel pylons, archaeology, hazards warning systems, plate tectonics and radio wave propagation and planetary exploration. The main aim of the article is study of the ME sensors characteristics to determine the feasibility of developing the ME magnetometers.

2. THE SENSOR DESIGN

The sensor is a layered structure (Fig. 1) consists of a thin piezoceramic plate of PZT ($0.9[\text{Pb}(\text{Zr}_{0.52}\text{Ti}_{0.48})\text{O}_3] - 0.1[\text{Pb}(\text{Zn}_{1/3}\text{Nb}_{2/3})\text{O}_3 + 3\text{mol}\%\text{MnO}_2]$) placed between two magnetostrictive layers of Metglas (FeBSiC) that perform a function of electrodes. It can be used any other magnetostrictive material like Ni or Terfenol-D instead Metglas. Piezoelectric ceramic compositions $0.9[\text{Pb}(\text{Zr}_{0.52}\text{Ti}_{0.48})\text{O}_3] - 0.1[\text{Pb}(\text{Zn}_{1/3}\text{Nb}_{2/3})\text{O}_3 + 3\text{mol}\%\text{MnO}_2]$ were synthesized using a conventional mixed oxides ceramic processing route followed by fabrication of sintered plates using a tape casting approach involving formation of slurry, tape-casting, binder burn-off and sintering. The final dimensions of the sintered plates were $20 \times 5 \times 0.75 \text{ mm}^3$. The PZT layer was poled in an electric field in the thickness direction.

The samples were fabricated by using glue. A thin foil of Metglas (FeBSiC) of dimensions $20 \times 5 \times 0.02 \text{ mm}^3$ was glued on each side of the piezoceramic plate in order to fabricate the ME layered structure as shown in Fig. 1. Glues were chosen according to manufacturability and reliability. The optimum one is a two-component epoxy quick drying glue. It's desirable that the glue layer thickness was as thin as possible and not bigger than a few microns.

3. THE EXPERIMENTAL SET UP

Figure 2 shows the experimental set up for measuring the ME response of the samples. A typical measurement system for the ME effect consists of a DC electromagnet with the Helmholtz coils. The electromagnet creates a bias magnetic field of 500 Oe. A Helmholtz coil was designed in order to apply magnetic field of 10 Oe to the magnetostrictive layers. The voltage and current flowing through the coil were adjusted in order to generate uniform AC magnetic field.

The structures to be measured are then placed between the Helmholtz coils. The electromagnet is driven by a constant-current source, and the Helmholtz coils are driven by a generator with a frequency bandwidth of $20 < f < 2 \cdot 10^5 \text{ Hz}$. To measure the induced voltage, the electrodes of a

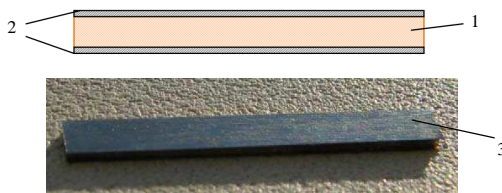


Figure 1: The magnetoelectric magnetic field sensor.

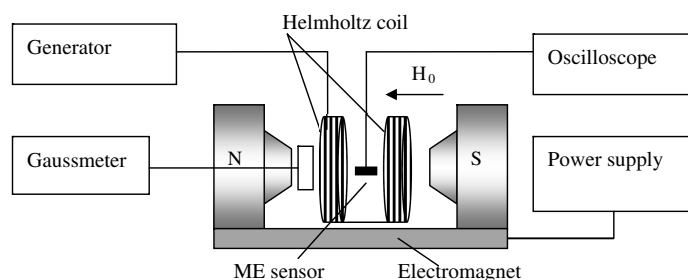


Figure 2: The experimental set up.

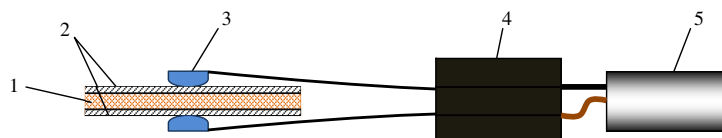


Figure 3: The contact device for measurements: 1 + 2 — the ME sample, 3 — relay contacts, 4 — the contact holder, 5 — a coaxial cable.

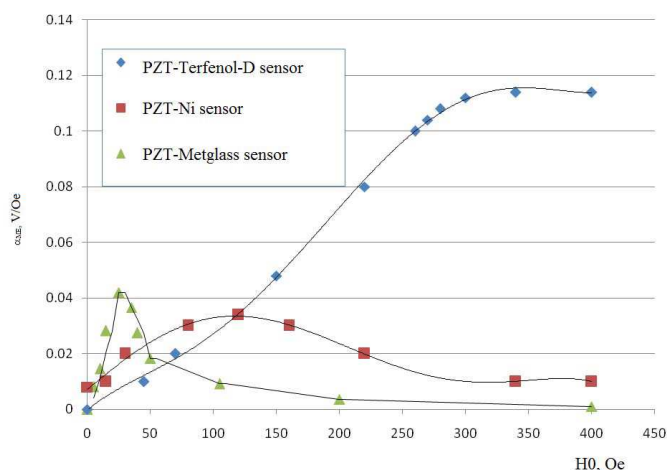


Figure 4: Comparison of the different types sensors ME response.

sample are then electrically connected to an operational amplifier, which subsequently feeds into an oscilloscope. The ME coefficient was measured by subjecting the sample to a dc magnetic bias H from the electromagnet and an ac magnetic field δH driven by the Helmholtz coils while measuring the ac induced electrical field by using the oscilloscope. The ME voltage coefficient is the ratio of the electric field induced across the piezoelectric component to the magnetic field applied to magnetostrictive one: i.e., $\alpha_E = \frac{p}{m} E/H$.

The contact device shown in Fig. 3 was used for convenience implementation and qualitative measurements.

4. EXPERIMENTAL RESULTS

The three types of ME structures used in the ME sensors was fabricated. The structures have different material for the magnetostrictive layer and its thickness. The PZT layer is the same for all the structures. Metglas, Nickel (Ni) and Terfenol-D were used as magnetostrictive layer material. The first sample consists of two Metglas layers of 0.02 mm thickness. The second one has two 4 mm thickness magnetostrictive layers of Terfenol-D. At last the third one has two Ni layers of 1 mm thickness. The ME voltage coefficients field dependences of the samples were measured and compared in Fig. 4.

The Metglas sample has the best response under the lowest value of the bias field. The ME voltage coefficient is 0.046 V/Oe, and the appropriate bias field is 25 Oe. The second sample displays lower the ME voltage coefficient at the low field but the highest one at the fields over 150 Oe. The

pick of the ME voltage coefficient is 0.11 V/Oe under the bias field of 300 Oe. The third sample has medium results of ME response. The lowest value of the bias field and possibly higher ME voltage coefficient are more important for the applications. Thus the first sample was chosen for further measurements.

Figure 5 shows the ME voltage coefficient frequency dependence of the first one in a wide range of frequencies from 20 Hz to 200 kHz.

The curve shown in Fig. 5 is nonlinear. One can see slight increase of value from 20 Hz to 150 Hz and the local maximum of 0.46 V/Cm · Oe at 150 Hz–400 Hz frequency range. Next nonlinear decrease of the ME voltage coefficient to 0.04 V/Cm · Oe at 16 kHz was observed. A resonant enhancement at about 29.5 kHz was determined. The resonant ME voltage coefficient is an order of magnitude higher than the low frequency value.

5. ME MAGNETOMETER

The ME magnetometer based on studied ME sensors was designed and fabricated. The block diagram and design of the magnetometer shown in Figs. 6 and 7, respectively.

Technical characteristics are as follows: the detected signal frequency is 1...500 Hz, the minimum value of the signal is 3 Oe, the ME sensor sensitivity is 20 mV/Oe. When the electromagnetic field over 3 Oe is detected the LED will light up green. The indicator can have potential applications such as detection magnetic and electromagnetic fields, measurement of leakage currents on printed circuit boards, security systems, and much more.

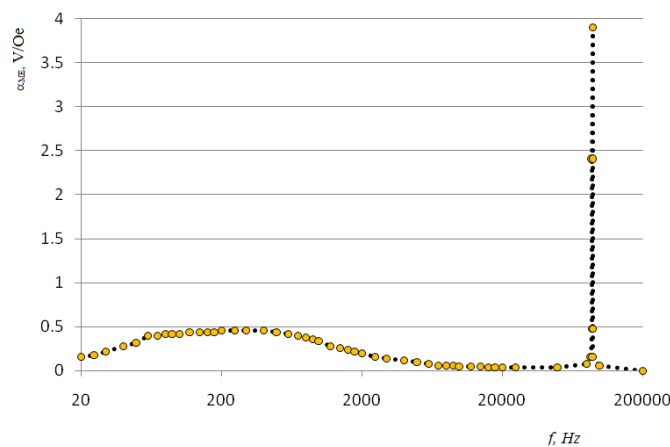


Figure 5: The ME voltage coefficient frequency dependence of the Metglas-PZT sample.

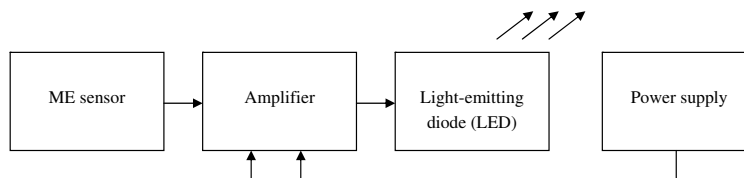


Figure 6: The block diagram of the ME magnetometer.



Figure 7: Design of ME magnetometer.

6. CONCLUSIONS

The data show well ME PZT-Metglas sensors characteristics which can be the basis for developing various devices. The sensors sensitivity reaches $0.46 \text{ V/Cm} \cdot \text{Oe}$ under the bias field value of about 25 Oe. The other materials with higher characteristics can be used in ME sensors. For increasing the sensor sensitivity one needs to use the large magnetostrictive and high strain-sensitive piezoelectric ME composite materials. The further improvement of the sensors is using push-pull schemes and the new piezoelectric type named by piezofiber [2]. All of this allows us to predict an increase in the ME coefficient an order of magnitude. Wide applications of the ME magnetometers are biomagnetic measurements like magnetoencephalography and magnetocardiography, motion detection, engine control, control of linear and angular accelerations and others.

ACKNOWLEDGMENT

The work at Novgorod State University was supported by the Federal Target Program “Scientific and scientific-pedagogical personnel of innovative Russia in 2009–2013” from the Ministry of Education and Science of the Russian Federation.

REFERENCES

1. Bichurin, M. I., V. M. Petrov, R. V. Petrov, Y. V. Kiliba, F. I. Bukashev, Y. V. Smirnov, and D. N. Eliseev, “Magnetolectric sensor of magnetic field,” *Proceedings of the Fourth Conference on Magnetolectric Internation Phenomena in Crystals (MEIPIC-4)*, Vol. 280, 199, Ferroelectrics, 2002.
2. Wang, Y., D. Gray, D. Berry, J. Gao, M. Li, J. Li, and D. Viehland, “An extremely low equivalent magnetic noise magnetolectric sensor,” *Adv. Mater.*, Vol. 23, 4111–4114, 2011.

Electromagnetic Sensing of Partial Discharge in Air-insulated Medium Voltage Switchgear

B. Zheng and A. Bojovski

School of Electrical and Computer Engineering, RMIT University, Melbourne, VIC 3001, Australia

Abstract— The importance of detecting accurately the partial discharge in high voltage power industry becomes obvious as the infrastructure ages. In this work electromagnetic sensing for detecting the electromagnetic radiation, associated with partial discharge, in an air-insulated medium voltage switchgear (Type D24-121114 of Driescher) is used. The study relies on Finite Element Method as implemented in High Frequency Structure Simulator. The partial discharge is approximated by Gaussian source. Coaxial patch antenna is employed for electromagnetic sensing. This transducer is optimized to have highest efficiency in the frequency band of interest, for partial discharge detection, of 800 MHz to 900 MHz. The antenna is placed in the switchgear system and its ability to sense partial discharge in the air-insulated switchgear is addressed. The optimized location in the switchgear system of the antenna for an efficient sensing is presented. The current density induced in the electromagnetic sensors by the radiation emitted from the partial discharges is used as an indicator of efficient radiative coupling. As repetitive partial discharge leads to the failure of the air-insulated switchgear, this method provides a sensitive method for pre-fault detection.

1. INTRODUCTION

With the increasing expectation of power system stakeholders on higher equipment reliability, greater safety and lower cost, fault diagnosis of electrical equipment (e.g., switchgear) becomes a vital task. As one of most important reasons for high voltage system failure, partial discharge (PD) phenomenon can be detected accurately by electromagnetic (EM) radiation detection technique. Among the techniques, ultra high frequency (UHF) method was initially applied for PD diagnostics in Gas Insulated Substations twenty years ago [1]. In that work the efficiency, sensitivity and applicability of UHF method are determined. Since then, the UHF method has been extensively applied in gas insulated equipment worldwide with excellent results on-line or before commissioning. This method overcame some of the well-known disadvantages of classical PD measurements [2, 3]. As a highly sensitive means of detection, UHF method is used to detect reliably PD signals in the UHF band (300 MHz–3 GHz) because the noise level decreases at higher frequencies.

Recently PD in aged switchgear systems is a cause of concern. The EM radiation emitted by PD is contained within the switchgear enclosure and can be detected by internal sensors purpose-fitted to the enclosure or by external coupling device placed at appropriate apertures in the chamber. PD identification and diagnosis in gas-insulated switchgear (GIS) using UHF sensors generated huge interest and is actively studied worldwide [4–10], but UHF sensing of PD in air-insulated switchgear (AIS) is rarely referred.

One of the sensors used for PD detection is patch antenna. Patch antenna features narrow operating bandwidths, satisfactory radiation properties, compact structures, light weight, inexpensive, easiness of manufacturing. The patch antenna, also called as microstrip antenna, is used popularly in the field of communication, such as mobile phones and personal computers. The investigation of interaction between EM wave induced by PD and patch antenna can be analyzed based on a simple transmission-line model [11]. It has been shown that PD on a twisted pair specimen of a motor winding can be detected effectively by a patch antenna [12].

Stemming from above consideration, coaxial patch antenna is proposed and investigated based on our pre-established AIS system to achieve EM sensing of PD. The coaxial patch antenna is potentially capable of detecting accurately PD in the actual AIS system.

2. METHOD

The proposed coaxial patch antenna consists of a cupreous patch on a grounded substrate, which is illustrated in Figure 1. The FR4 dielectric used as substrate has a thickness $T = 48$ mm, a relative permittivity of 4.4 and loss tangent of 0.02. In the optimum design the radius of the circular patch (Figure 1) is $R = 6.8$ mm. The size of the dielectric substrate and the ground is $40 \text{ mm} \times 40 \text{ mm}$ in the xy plane. The coaxial line feed has inner and outer radii of $r_i = 0.65$ mm and $r_o = 1.1$ mm and is filled with teflon of relative permittivity 2.1.

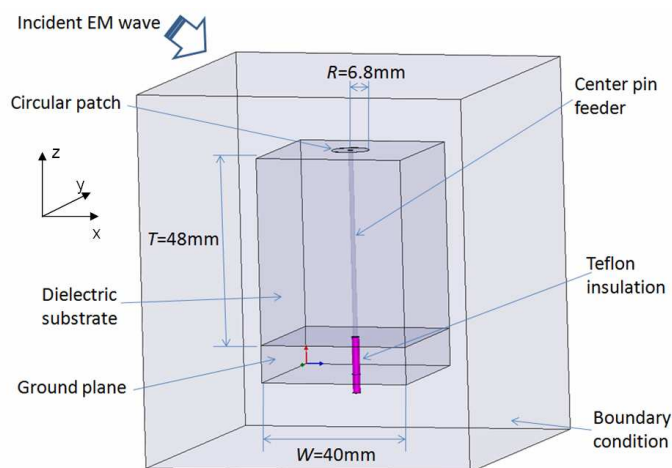


Figure 1: Schematic configuration of the proposed circular coaxial patch antenna.

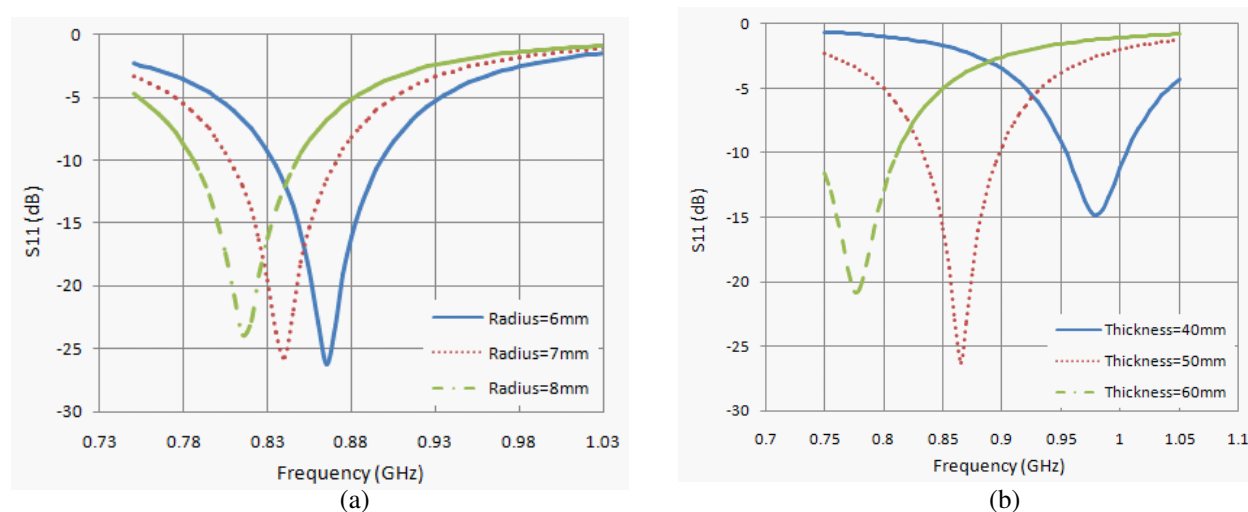


Figure 2: Experimental S_{11} results of various R , T dimensions of the patch antenna.

Finite Element Method (FEM) implemented in Ansoft High Frequency Structure Simulator (HFSS) 13 [13] is utilized in this work to design, optimize the patch and to simulate it in the medium voltage switchgear system (Type D 24 — 121114 of DRIESCHER — Compact Switchgears 24 kV). The PD source is simulated numerically in the AIS by a Gaussian pulse [14] with the centre frequency of 750 MHz and a width of 200 MHz. The radius (ω_0) of the Gaussian beam waist is 10 mm which corresponds with the size of the surface PD. The intensity of the Gaussian source is of 1 V/m and it is set to propagate in the x direction. This is related with discharge distribution. The proposed coaxial patch antenna is designed to operate around the 800 MHz to 900 MHz frequency band. This was chosen as all the PD activities such as cavity discharge, corona, dry-band arcing emit in this frequency band [15, 16].

3. RESULTS

In the optimizing process, there are mainly three important design parameters that affect the coaxial patch antenna performance. They are the radius of the patch R , the thickness of the dielectric substrate T , the x and y dimensions of the patch (Figure 1). In Figure 2, three design variables are parameterized. This led to the optimum structure with the 800 to 900 MHz frequency band. From Figure 2(a) it can be noted that with the increase of R , the resonance frequency will decrease accordingly. The effect on the return loss (S_{11}) curves of the T is also indicated in Figure 2(b). They not only affect the resonance frequency, but also vary significantly the dB level.

Figure 3 shows the simulated return loss for the optimized structure of the patch antenna. The resonance frequency is at 850 MHz. The E -plane radiation pattern for the optimum structure of the patch antenna is shown in Figure 4. The fractional bandwidth (FBW) of the coaxial patch

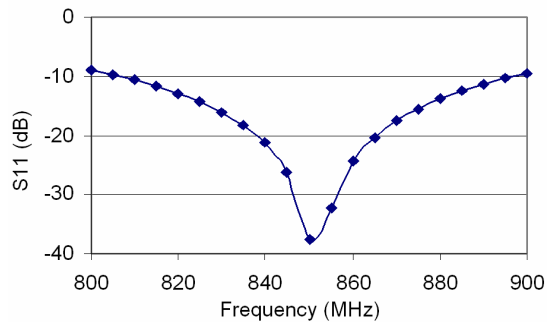


Figure 3: Simulated return loss curves (S_{11}) of the proposed coaxial patch antenna.

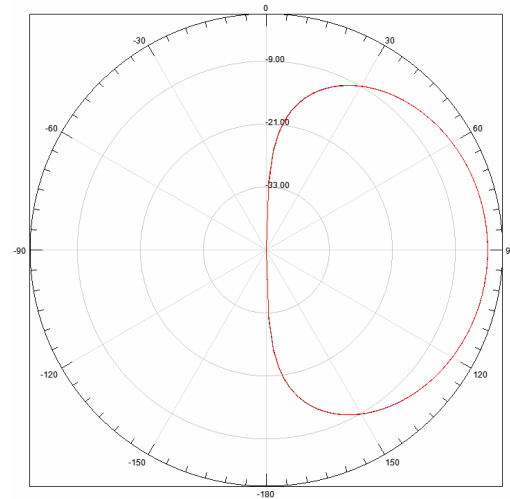


Figure 4: Simulated radiation patterns at 850 MHz of the proposed coaxial patch antenna (E plane).

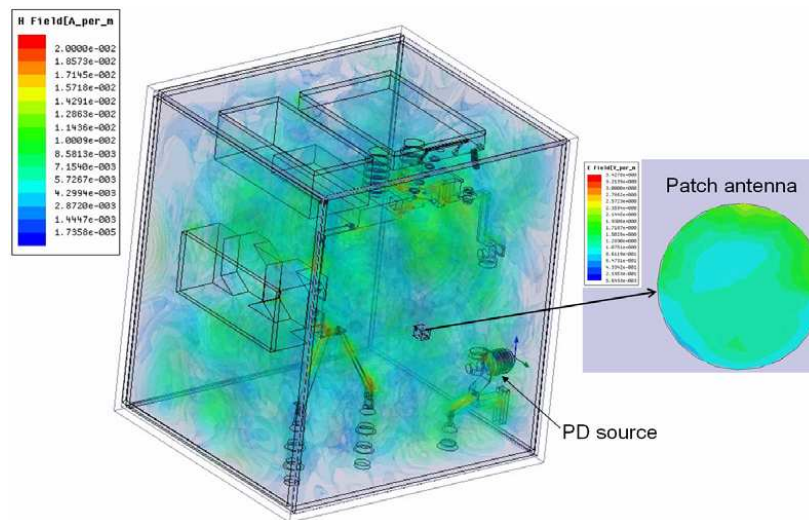


Figure 5: Optimized location of coaxial patch antenna in the AIS system.

antenna at -10 dB return loss can be calculated using the following equation:

$$\text{FBW} = \frac{f_2 - f_1}{f_c} = \frac{899 \text{ MHz} - 806 \text{ MHz}}{850 \text{ MHz}} \times 100\% \approx 10.94\% \quad (1)$$

The location of the PD sensors has a significant effect on the sensitivity of the UHF method. The optimized location of the designed sensor in the switchgear enclosure is showed below. The propagation of radiation from the PD creates spectral distributions of different intensity in the switchgear represented in Figure 5 by magnetic field lines. The electric field induce in the patch antenna is shown in the same figure. Its maximum intensity is of 3.42 V/m . Considering that in this study the PD source has an intensity of 1 V/m an accurate detection is possible.

4. CONCLUSIONS

The simulation results of a circular coaxial patch antenna covering 806 MHz to 899 MHz frequency band have been presented. It has been shown that the performance of the antenna in terms of its frequency domain characteristics is mostly dependent on the radius of the patch, the thickness of the substrate and the dimensions of the x and y dimensions. The optimized location of antenna in the particular AIS system for an efficient sensing is presented. This indicates that the optimum location for fault detection can be predicted computationally for a given switchgear system.

ACKNOWLEDGMENT

The authors acknowledge Dr. Hubert Schlapp (SebaKMT, Germany) for providing the initial interest to this topic and for fairly representative documents. The authors would like to express gratitude to Mr. Thomas Benke and Mr. Kyrie Hadjiloizou for providing technical support.

REFERENCES

1. Bargigia, A., W. Koltunowicz, and A. Pignini, "Detection of partial discharges in gas insulated substations," *IEEE Transactions on Power Delivery*, Vol. 7, 1239–1249, 1992.
2. Bell, R., C. Charlson, S. P. Halliday, T. Irwin, J. Lopez-Roldan, and J. Nixon, "High-voltage onsite commissioning tests for gas-insulated substations using UHF partial discharge detection," *IEEE Transactions on Power Delivery*, Vol. 18, 1187–1191, 2003.
3. Raja, K., F. Devaux, and S. Lelaidier, "Recognition of discharge sources using UHF PD signatures," *IEEE Electrical Insulation Magazine*, Vol. 18, 8–14, 2002.
4. Judd, M. D., O. Farish, and B. F. Hampton, "The excitation of UHF signals by partial discharges in GIS," *IEEE Transactions on Dielectrics and Electrical Insulation*, Vol. 3, 213–228, 1996.
5. Meijer, S., E. Gulski, and J. J. Smit, "Pattern analysis of partial discharges in SF6 GIS," *IEEE Transactions on Dielectrics and Electrical Insulation*, Vol. 5, 830–842, 1998.
6. Kurrer, R. and K. Feser, "The application of ultra-high-frequency partial discharge measurements to gas-insulated substations," *IEEE Transactions on Power Delivery*, Vol. 13, 777–782, 1998.
7. Hoshino, T., K. Nojima, and M. Hanai, "Real-time PD identification in diagnosis of GIS using symmetric and asymmetric UHF sensors," *IEEE Transactions on Power Delivery*, Vol. 19, 1072–1077, 2004.
8. Tenbohlen, S., D. Denissov, S. Hoek, and S. M. Markalous, "Partial discharge measurement in the ultra high frequency (UHF) range," *IEEE Transactions on Dielectrics and Electrical Insulation*, Vol. 15, 1544–1552, 2008.
9. Okabe, S., T. Yamagiwa, and H. Okubo, "Detection of harmful metallic particles inside gas insulated switchgear using UHF sensor," *IEEE Transactions on Dielectrics and Electrical Insulation*, Vol. 15, 701–709, 2008.
10. Koo, J. Y., S. Y. Jung, C. H. Ryu, S. W. Lee, and B. W. Lee, "Identification of insulation defects in gas-insulated switchgear by chaotic analysis of partial discharge," *IET Science, Measurement & Technology*, Vol. 4, 115–124, 2010.
11. Shibuya, Y., S. Matsumoto, M. Tanaka, H. Muto, and Y. Kaneda, "Electromagnetic waves from partial discharges and their detection using patch antenna," *IEEE Transactions on Dielectrics and Electrical Insulation*, Vol. 17, 862–871, 2010.
12. Shibuya, Y., S. Matsumoto, T. Konno, and K. Umezu, "Electromagnetic waves from partial discharges in windings and their detection by patch antenna," *IEEE Transactions on Dielectrics and Electrical Insulation*, Vol. 18, 2013–2023, 2011.
13. Ansoft HFSS 12.1.2, online resource, 2010.
14. Bojovschi, A., A. K. L. Wong, and W. S. T. Rowe, "Impact of electromagnetic radiation on cascaded failure in high voltage insulators," *Applied Physics Letters*, Vol. 98, 051504-1–3, 2011.
15. Fernando, S. C., A. K. L. Wong, and W. S. T. Rowe, "Detection of corona and dry-band arc discharges on nano-composite epoxy insulators using RF sensing," *Progress In Electromagnetics Research*, Vol. 125, 237–254, 2012.
16. Bojovschi, A., W. S. T. Rowe, and A. K. L. Wong, "Electromagnetic field intensity generated by partial discharge in high voltage insulating materials," *Progress In Electromagnetics Research*, Vol. 104, 167–182, 2010.

Transformations of Field Equations in Octonion Spaces

Zi-Hua Weng

School of Physics and Mechanical & Electrical Engineering
Xiamen University, Xiamen 361005, China

Abstract— J. C. Maxwell was the first to mix two methods, the vector and the quaternion, to describe the electromagnetic theory. It inspires the scholars to adopt the octonion to describe the gravitational equations and the electromagnetic equations. The octonion can be separated into two parts, the quaternion and the S -quaternion. And the quaternion is suitable for describing gravitational features, meanwhile the S -quaternion is fit for depicting electromagnetic properties. In order to contrast the octonion field equations to the classical field equations, the electromagnetic equations described by the S -quaternion should be transferred equivalently into that in the 3-dimensional vector space, while the gravitational equations depicted by the quaternion should be transformed equally into that in the 3-dimensional vector space. After transferring the octonion field equations, the study reveals that the electromagnetic equations described by the S -quaternion are the same as the Maxwell equations in the classical electromagnetic theory, except for a few discrepancies. And one of the gravitational equations depicted by the quaternion is identical to the Newton's law of gravitation in the classical gravitational theory.

1. INTRODUCTION

J. C. Maxwell [1] was the first to mix two methods, the vector and the quaternion, to describe the feature of electromagnetic fields. The quaternion was invented by W. R. Hamilton. Meanwhile the octonion [2, 3], as the ordered pair of quaternions, was created by J. T. Graves and A. Cayley independently. Subsequently the quaternion was divided into the scalar part and vectorial part. The latter was evolved into the conventional 3-dimensional vector.

The electromagnetic theory described by the vector is quite brilliant, while it is not successful to adopt the quaternion to depict the electromagnetic features. By contrast, the electromagnetic theory described by the octonion achieves some developments to a certain extent [4, 5].

One octonion can be separated into two components, the quaternion and the S -quaternion. It is found that the quaternion is suitable for describing the gravitational features, while the S -quaternion is fit for depicting the property of electromagnetic field. Nowadays there are abundant in identical inferences between the electromagnetic features described by the S -quaternion and that by the vector. While there are similar conclusions between the gravitational properties depicted with the quaternion and that with the vector.

In order to deduce the above conclusions, it is necessary to transfer equivalently the electromagnetic equations in the S -quaternion space into that in the quaternion space. Further it is requisite to transfer the latter into that in the 3-dimensional vector space, to achieve the contrasting to the Maxwell equations in the classical electromagnetic theory. Similarly the gravitational equations will be transformed into that in the vector space.

The analysis reveals that the electromagnetic equations described by the S -quaternion can transfer equivalently into that in the 3-dimensional vector space. And the electromagnetic equations are the same as the Maxwell equations, except for a little dissimilarity. Meanwhile one of the quaternion gravitational equations is identical to the Newton's law of gravitation.

2. OCTONION FIELD EQUATIONS

Applying the algebra of octonions to describe simultaneously the electromagnetic field and the gravitational field will relate to the constitution of octonion space. According to the view points of R. Descartes, M. Faraday, and A. Einstein etc. [6], the field is an irreducible element of physical description up to now, while the space-time is only the extension of the field and does not claim existence on its own. Furthermore each different field can extend out its distinct space-time. Therefore the space-time extended from the electromagnetic field is different to the one from the gravitational field. And they are quite similar but independent to each other.

According to the view points of W. R. Hamilton and J. C. Maxwell etc, the space-time can be chosen as the quaternion space. This means that the two space-times, which extended respectively from the electromagnetic field and the gravitational field, both can be considered as the quaternion space, and are orthogonal to each other so that they can combine together to become an octonion

space [7]. As a result the octonion space can be used to describe the physical property of the electromagnetic field and of the gravitational field simultaneously.

In the octonion space which consists of two orthogonal quaternion spaces, the physical quantity of the electromagnetic field should be multiplied by one coefficient to maintain the dimensional homogeneity with that of the gravitational field, when these two different kinds of physical quantities coexist on same one formula. The coefficient value can be determined by comparing with the classical electromagnetic theory and the classical gravitational theory.

In the quaternion space for gravitational field, the basis vector is $\mathbb{E}_g = (\mathbf{i}_0, \mathbf{i}_1, \mathbf{i}_2, \mathbf{i}_3)$, the coordinate is r_i , the radius vector is $\mathbb{R}_g = \sum(r_i \mathbf{i}_i)$, the velocity is $\mathbb{V}_g = \sum(v_i \mathbf{i}_i)$. In the quaternion space for electromagnetic field (the S -quaternion space, for short), the basis vector is $\mathbb{E}_e = (\mathbf{I}_0, \mathbf{I}_1, \mathbf{I}_2, \mathbf{I}_3)$, the coordinate is R_i , the radius vector is $\mathbb{R}_e = \sum(R_i \mathbf{I}_i)$, the velocity is $\mathbb{V}_e = \sum(V_i \mathbf{I}_i)$. Herein $\mathbb{E}_e = \mathbb{E}_g \circ \mathbf{I}_0$. The symbol \circ denotes the octonion multiplication. $r_0 = v_0 t$, v_0 is the speed of light, t is the time. $\mathbf{i}_0 = 1$, $i = 0, 1, 2, 3$.

In the octonion space, the basis vector is $\mathbb{E} = (\mathbf{i}_0, \mathbf{i}_1, \mathbf{i}_2, \mathbf{i}_3, \mathbf{I}_0, \mathbf{I}_1, \mathbf{I}_2, \mathbf{I}_3)$, the radius vector is $\mathbb{R} = \sum(r_i \mathbf{i}_i + k_{eg} R_i \mathbf{I}_i)$, and the velocity is $\mathbb{V} = \sum(v_i \mathbf{i}_i + k_{eg} V_i \mathbf{I}_i)$. The octonion field potential is $\mathbb{A} = \sum(a_i \mathbf{i}_i + k_{eg} A_i \mathbf{I}_i)$ consists of the gravitational field potential, $\mathbb{A}_g = \sum(a_i \mathbf{i}_i)$, and the electromagnetic field potential, $\mathbb{A}_e = \sum(A_i \mathbf{I}_i)$. Herein k_{eg} is the undetermined coefficient for the dimensional homogeneity.

The octonion field strength \mathbb{B} and the octonion field source \mathbb{S} may be obtained by repeatedly application of the quaternion operator \diamond on the octonion field potential \mathbb{A} . The octonion field strength, $\mathbb{B} = \sum(b_i \mathbf{i}_i + k_{eg} B_i \mathbf{I}_i)$, is defined as,

$$\mathbb{B} = \diamond \circ \mathbb{A}, \quad (1)$$

where the gravitational field strength is $\mathbb{B}_g = \diamond \circ \mathbb{A}_g = \sum(b_i \mathbf{i}_i)$, the electromagnetic field strength is $\mathbb{B}_e = \diamond \circ \mathbb{A}_e = \sum(B_i \mathbf{I}_i)$. The gauge equations are chosen as $b_0 = 0$ and $B_0 = 0$. The quaternion operator is $\diamond = \sum(\mathbf{i}_i \partial_i)$, with $\nabla = \sum(\mathbf{i}_j \partial_j)$, and $\partial_i = \partial / \partial r_i$, $j = 1, 2, 3$.

The octonion field source \mathbb{S} is defined as

$$\mu \mathbb{S} = -(\diamond + \mathbb{B}/v_0)^* \circ \mathbb{B}, \quad (2)$$

and

$$\mu \mathbb{S} = (\mu_g \mathbb{S}_g + k_{eg} \mu_e \mathbb{S}_e) - \mathbb{B}^* \circ \mathbb{B}/v_0, \quad (3)$$

where μ is a coefficient, μ_g and μ_e are the constant of gravitational field and of electromagnetic field respectively. The \mathbb{S}_g and \mathbb{S}_e are the gravitational field source and the electromagnetic field source respectively. The symbol $*$ denotes the octonion conjugate.

Separating the above equation according to the basis vector ($\mathbb{E}_g, \mathbb{E}_e$) and the undetermined coefficient k_{eg} , yields the source equation of the gravitational field and of the electromagnetic field respectively as follows,

$$\mu_g \mathbb{S}_g = -\diamond^* \circ \mathbb{B}_g, \quad (4)$$

$$\mu_e \mathbb{S}_e = -\diamond^* \circ \mathbb{B}_e. \quad (5)$$

Expanding the above two equations will deduce respectively the Newton's law of gravitation in the classical gravitational theory and the Maxwell equations in the classical electromagnetic theory. And the scalar term, $\mathbb{B}^* \circ \mathbb{B}/\mu_g$, in Eq. (3) can be disassembled further as,

$$\mathbb{B}^* \circ \mathbb{B}/\mu_g = \mathbb{B}_g^* \circ \mathbb{B}_g/\mu_g + \mathbb{B}_e^* \circ \mathbb{B}_e/\mu_e, \quad (6)$$

where $k_{eg}^2 = \mu_g/\mu_e$, by comparing with the classical electromagnetic theory. The $\mathbb{B}_e^* \circ \mathbb{B}_e/(2\mu_e)$ is the field energy density of electromagnetic fields, while the $\mathbb{B}_g^* \circ \mathbb{B}_g/(2\mu_g)$ is considered as the field energy density of gravitational fields.

3. GRAVITATIONAL FIELD

3.1. Gravitational Equations

In the quaternion space for the gravitational field, the field strength is $\mathbb{B}_g = b_0 + \mathbf{k}$, and the field source is $\mathbb{S}_g = s_0 + \mathbf{s}$. Eq. (1) and the gauge equation $b_0 = 0$ state that the \mathbf{k} involves the two components, \mathbf{g} and \mathbf{b} , that is,

$$\mathbf{g}/v_0 = \partial_0 \mathbf{a} + \nabla a_0, \quad \mathbf{b} = \nabla \times \mathbf{a}, \quad (7)$$

where $\mathbf{a} = \sum(a_j \mathbf{i}_j)$, $\mathbf{k} = \sum(k_j \mathbf{i}_j) = \mathbf{g}/v_0 + \mathbf{b}$, $\mathbf{b} = \sum(b_j \mathbf{i}_j)$, $\mathbf{g} = \sum(g_j \mathbf{i}_j)$.

Separating Eq. (4) according to the scalar part and the vectorial part, obtains the scalar equation and the vectorial equation as follows,

$$-\mu_g s_0 = \nabla^* \cdot \mathbf{k}, \quad (8)$$

$$-\mu_g \mathbf{s} = \nabla^* \times \mathbf{k} + \partial_0 \mathbf{k}, \quad (9)$$

where $\mathbb{S}_g = m \mathbb{V}_g$, for one single mass particle, by comparing with the classical gravitational theory. $\mathbb{V}_g = v_0 + \mathbf{v}$, $s_0 = m v_0$, $\mathbf{s} = m \mathbf{v}$, $\mathbf{v} = \sum(v_j \mathbf{i}_j)$, m is the mass density.

The above will yield the gravitational equations,

$$\nabla \cdot \mathbf{b} = 0, \quad (10)$$

$$\nabla^* \times \mathbf{g}/v_0 + \partial_0 \mathbf{b} = 0, \quad (11)$$

$$-\mu_g m v_0 = \nabla^* \cdot \mathbf{g}/v_0, \quad (12)$$

$$-\mu_g m \mathbf{v} = \nabla^* \times \mathbf{b} + \partial_0 \mathbf{g}/v_0. \quad (13)$$

The above analysis states that Eqs. (10) ~ (13) constitute the gravitation equations in the quaternion space. Comparing with the classical gravitational theory, it finds that Eq. (12) will be totally identical to the Newton's law of gravitation depicted by the vector terminology. In case $\mathbf{a} = 0$ and $\partial_0 \mathbf{g} = 0$, the above will be reduced to the Newton's law of gravitation.

3.2. Transformations of Gravitational Equations

By means of the proper transformation, the gravitational equations in the quaternion space \mathbb{E}_g can be transferred equivalently into that in the 3-dimensional vector space. In the first step of transformation, the transferring will only aim at the gravitational strength, while all the other physical quantities keep unchanged. The gravitational strength transfers from the \mathbb{B}_g to the \mathbb{B}_g'' , that is, $\mathbb{B}_g'' = -\mathbb{B}_g$. Meanwhile the gravitational potential \mathbb{A}_g , the field source \mathbb{S}_g , and the velocity \mathbb{V}_g etc. all remain the same.

In the second step of transferring, it is only necessary to substitute the quaternion basis vector \mathbf{i}_j by the basis vector \mathbf{j}_j of the 3-dimensional vector space, while the basis vector \mathbf{i}_j in the physical quantity should be replaced subsequently. Contrasting the multiplication tables of the quaternion and of the 3-dimensional vector, it is realized that the $\mathbf{i}_j \circ \mathbf{i}_j$ and the $\mathbf{i}_j \times \mathbf{i}_k$ should be replaced by the $(-\mathbf{j}_j \cdot \mathbf{j}_j)$ and the $\mathbf{j}_j \times \mathbf{j}_k$ respectively, in the case of substituting the basis vector \mathbf{i}_j by the \mathbf{j}_j . Meanwhile the operator $\nabla = \sum(\mathbf{i}_j \partial_j)$ is replaced by the $\nabla = \sum(\mathbf{j}_j \partial_j)$. Expanding the above to form the scalar type of equations and contrasting those equations one by one, it is found that the $\nabla \cdot \mathbf{g}''$ and the $\nabla \times \mathbf{g}''$ will be substituted by the $(-\nabla \cdot \mathbf{g}''')$ and the $\nabla \times \mathbf{g}'''$ respectively. Herein $\mathbf{g}'' = -\sum(g_j \mathbf{i}_j)$, $\mathbf{g}''' = -\sum(g_j \mathbf{j}_j)$. $\mathbf{b}'' = -\sum(b_j \mathbf{i}_j)$, $\mathbf{b}''' = -\sum(b_j \mathbf{j}_j)$. $k = 1, 2, 3$.

For one single mass particle, the gravitational equations in the quaternion space can be transferred to that in the conventional 3-dimensional space,

$$\nabla \cdot \mathbf{b}''' = 0, \quad (14)$$

$$\nabla \times \mathbf{g}'''/v_0 + \partial_0 \mathbf{b}''' = 0, \quad (15)$$

$$\mu_g m v_0''' = \nabla \cdot \mathbf{g}'''/v_0, \quad (16)$$

$$\mu_g m \mathbf{v}''' = \nabla \times \mathbf{b}''' + \partial_0 \mathbf{g}'''/v_0, \quad (17)$$

where $\mathbf{v}''' = \sum(v_j \mathbf{j}_j)$, $v_0''' = v_0$, $\mathbf{s}''' = m \mathbf{v}'''$, $s_0''' = m v_0'''$.

The above analysis reveals that the quaternion is suitable for describing the gravitational equations, just like the 3-dimensional vector is fit for depicting the Newton's law of gravitation. And the gravitational equations described by the quaternion can transfer equivalently into that in the 3-dimensional vector space. And Eq. (16) in the above gravitational equations is the same as the Newton's law of gravitation, when $\mathbf{a} = 0$ and $\partial_0 \mathbf{g} = 0$.

Subsequently the process of transformations for the gravitation equations can be analogized to that for the electromagnetic equations.

4. ELECTROMAGNETIC FIELDS

4.1. Electromagnetic Equations

In the S -quaternion space for the electromagnetic field, the field strength is $\mathbb{B}_e = \mathbf{B}_0 + \mathbf{K}$, and the field source is $\mathbb{S}_e = \mathbf{S}_0 + \mathbf{S}$. Eq. (1) and the gauge equation $B_0 = 0$ claim that the \mathbf{K} involves the

Table 1: Field equations of electromagnetic fields and gravitational fields in the octonion space.

Field	Gravitational Field	Electromagnetic Field
Subspace	\mathbb{E}_g	\mathbb{E}_e
Field Potential	\mathbb{A}_g	\mathbb{A}_e
Field Strength	$\mathbb{B}_g = \diamond \circ \mathbb{A}_g$	$\mathbb{B}_e = \diamond \circ \mathbb{A}_e$
Field Source	$\mathbb{S}_g = m\nabla_g$	$\mathbb{S}_e = q\nabla_e$
Field Equation	$\mu_g \mathbb{S}_g = -\diamond^* \circ \mathbb{B}_g$	$\mu_e \mathbb{S}_e = -\diamond^* \circ \mathbb{B}_e$
Field Energy	$\mathbb{B}_g^* \circ \mathbb{B}_g / (2\mu_g)$	$\mathbb{B}_e^* \circ \mathbb{B}_e / (2\mu_e)$

two components, \mathbf{E} and \mathbf{B} , that is,

$$\mathbf{E}/v_0 = \partial_0 \mathbf{A} + \nabla \circ \mathbf{A}_0, \quad \mathbf{B} = \nabla \times \mathbf{A}, \quad (18)$$

where $\mathbf{A} = \sum(A_j \mathbf{I}_j)$, $\mathbf{A}_0 = A_0 \mathbf{I}_0$, $\mathbf{K} = \sum(K_j \mathbf{I}_j) = \mathbf{E}/v_0 + \mathbf{B}$, $\mathbf{B} = \sum(B_j \mathbf{I}_j)$, $\mathbf{E} = \sum(E_j \mathbf{I}_j)$, $\mathbf{B}_0 = B_0 \mathbf{I}_0$.

Separating Eq. (5) according to the scalar part and the vectorial part, achieves the scalar equation and the vectorial equation as follows,

$$-\mu_e \mathbf{S}_0 = \nabla^* \cdot \mathbf{K}, \quad (19)$$

$$-\mu_e \mathbf{S} = \nabla^* \times \mathbf{K} + \partial_0 \mathbf{K}, \quad (20)$$

where $\mathbb{S}_e = q\nabla_e$, for one single charged particle, by comparing with the classical electromagnetic theory, q is the electric charge density, $\nabla_e = \mathbf{V}_0 + \mathbf{V}$, $\mathbf{S}_0 = q\mathbf{V}_0$, $\mathbf{S} = q\mathbf{V}$, $\mathbf{V} = (V_j \mathbf{I}_j)$, $\mathbf{V}_0 = V_0 \mathbf{I}_0$.

The above will yield the electromagnetic equations in the S -quaternion space,

$$\nabla \cdot \mathbf{B} = 0, \quad (21)$$

$$\nabla^* \times \mathbf{E}/v_0 + \partial_0 \mathbf{B} = 0, \quad (22)$$

$$-\mu_e q \mathbf{V}_0 = \nabla^* \cdot \mathbf{E}/v_0, \quad (23)$$

$$-\mu_e q \mathbf{V} = \nabla^* \times \mathbf{B} + \partial_0 \mathbf{E}/v_0. \quad (24)$$

Comparing with the classical electromagnetic theory, it claims that the field potential, the field strength, and the field equations described by the S -quaternion are respectively identical to that by the vector terminology, except for a few discrepancies, such as the gauge equation, the direction of displacement current, and the velocity of charged particle etc..

4.2. Transformation of Electromagnetic Equations

In the first step of transferring, the electromagnetic equations in the S -quaternion space \mathbb{E}_e can be transferred equivalently into that in the quaternion space \mathbb{E}_g , by means of the proper transformation. In the quaternion space \mathbb{E}_g , the electromagnetic potential is transferred as, $\mathbb{A}'_e = \mathbb{A}_e \circ \mathbf{I}_0^* = \mathbf{A}'_0 + \mathbf{A}'$, with $\mathbf{A}'_0 = A_0 \mathbf{i}_0 = A'_0$, and $\mathbf{A}' = \sum(A_j \mathbf{i}_j)$. Similarly the electromagnetic strength can be transferred as, $\mathbb{B}'_e = \mathbb{B}_e \circ \mathbf{I}_0^* = \mathbf{B}'_0 + \mathbf{K}'$. And the gauge equation is, $\mathbf{B}'_0 = B_0 \mathbf{i}_0 = B'_0 = 0$.

In the second step of transferring, the transferring will only aim at the electromagnetic strength, while all the other physical quantities keep unchanged. The electromagnetic strength transfers from the \mathbb{B}'_e to the \mathbb{B}''_e , that is, $\mathbb{B}''_e = -\mathbb{B}'_e$. Meanwhile the electromagnetic potential \mathbb{A}'_e , the field source \mathbb{S}'_e , and the velocity \mathbb{V}'_e etc. will remain the same.

In the third step of transferring, it is only necessary to substitute the quaternion basis vector \mathbf{i}_j by the basis vector \mathbf{j}_j of the 3-dimensional vector space, while the basis vector \mathbf{i}_j in the physical quantity should be replaced accordingly. Later it is found that the $\mathbf{i}_j \circ \mathbf{i}_j$ and the $\mathbf{i}_j \times \mathbf{i}_k$ should be replaced by the $(-\mathbf{j}_j \cdot \mathbf{j}_j)$ and the $\mathbf{j}_j \times \mathbf{j}_k$ respectively, in the case of substituting the basis vector \mathbf{i}_j by the \mathbf{j}_j . Meanwhile the operator ∇ is replaced by the ∇ . Expanding the above to form the scalar type of equations and contrasting those equations one by one, it is found that the $\nabla \cdot \mathbf{E}''$ and the $\nabla \times \mathbf{E}''$ will be substituted by the $(-\nabla \cdot \mathbf{E}''')$ and the $\nabla \times \mathbf{E}'''$ respectively. Herein $\mathbf{E}'' = -\sum(E_j \mathbf{i}_j)$, $\mathbf{E}''' = -\sum(E_j \mathbf{j}_j)$, $\mathbf{B}'' = -\sum(B_j \mathbf{i}_j)$, $\mathbf{B}''' = -\sum(B_j \mathbf{j}_j)$.

For one single charged particle, the electromagnetic equations in the S -quaternion space can be

transferred to that in the conventional 3-dimensional space,

$$\nabla \cdot \mathbf{B}''' = 0, \quad (25)$$

$$\nabla \times \mathbf{E}'''/v_0 + \partial_0 \mathbf{B}''' = 0, \quad (26)$$

$$\mu_e q V_0''' = \nabla \cdot \mathbf{E}'''/v_0, \quad (27)$$

$$\mu_e q \mathbf{V}''' = \nabla \times \mathbf{B}''' + \partial_0 \mathbf{E}'''/v_0, \quad (28)$$

where $\mathbf{V}''' = \sum(V_j \mathbf{j}_j)$, $V_0''' = V_0$, $\mathbf{S}''' = q\mathbf{V}'''$, $S_0''' = qV_0'''$.

The above analysis reveals that the S -quaternion is suitable for describing the electromagnetic equations, just like the 3-dimensional vector is fit for depicting Maxwell equations in the classical electromagnetic theory. Further the electromagnetic equations described by the S -quaternion can transfer equivalently into that in the 3-dimensional vector space. And the electromagnetic equations are the same as the Maxwell equations, except for the direction of displacement current etc..

5. CONCLUSIONS

The octonion can be decomposed into two components, the quaternion and the S -quaternion. The quaternion is suitable for describing the gravitational field, while the S -quaternion is fit for depicting the electromagnetic field.

The electromagnetic equations in the S -quaternion space can be transferred into that in the vector space. In the 3-dimensional vector space, comparing the transferred electromagnetic equations with the Maxwell equations reveals that these two equations are the same, except for the orientation of the displacement current. However the inspection of this orientation has not been fulfilled yet in the electromagnetic theory until to now.

The gravitational equations in the quaternion space can be transformed into that in the vector space. In the 3-dimensional vector space, contrasting the transferred gravitational equations to the Newton's law of gravitation shows that one of the transferred gravitational equations is identical with the Newton's law of gravitation.

The study can clearly indicate that the octonion field equations can be transferred equivalently from the octonion space into that in the vector space. In the 3-dimensional vector space, the transferred field equations can be contrasted with the classical field equations. It states that the octonion field equations are the same as the classical field equations, except for a few discrepancies. For the future study, the research will concentrate on the discrepancies, such as the orientation of displacement currents.

ACKNOWLEDGMENT

This project was supported partially by the National Natural Science Foundation of China under grant number 60677039.

REFERENCES

1. Maxwell, J. C., *A Treatise on Electricity and Magnetism*, Dover Publications Inc., New York, 1954.
2. Wills-Toro, L. A., "Symmetry transformations with noncommutative and nonassociative parameters," *International Journal of Theoretical Physics*, Vol. 36, No. 12, 2963–2997, 1997.
3. Chanyal, B. C., P. S. Bisht, and O. P. S. Negi, "Generalized octonion electrodynamics," *International Journal of Theoretical Physics*, Vol. 49, No. 6, 1333–1343, 2010.
4. Gogberashvili, M., "Octonionic electrodynamics," *Journal of Physics A*, Vol. 39, No. 22, 7099–7104, 2006.
5. Zenczykowski, P., "Nonrelativistic phase-space and octonions," *International Journal of Theoretical Physics*, Vol. 29, No. 8, 835–852, 1990.
6. Einstein, A., *Relativity: The Special and the General Theory (A Popular Exposition)*, 15th Edition, Translated by Robert W. Lawson, Crown Publishers, New York, 1961.
7. Weng, Z.-H., "Displacement current and experimental inspection in the octonion space," *Scientific Journal of Physical Science*, Vol. 2, No. 1, 1–13, 2012 (in Chinese).

Electromagnetic and Gravitational Fields in the Curved Octonion Spaces

Zi-Hua Weng

School of Physics and Mechanical & Electrical Engineering
Xiamen University, Xiamen 361005, China

Abstract— J. C. Maxwell was the first to adopt the quaternion and the vector to describe the electromagnetic theory. It inspired the scholars to use the quaternion and the octonion to depict the electromagnetic and gravitational theories. On the other hand, A. Einstein adopted the tensor and the curved space to picture the property of gravitational field. It encouraged the scholars to depict the features of electromagnetic fields and gravitational fields by means of the curved quaternion space and the curved octonion space. The orthogonality of two quaternions can be defined via the scalar product of quaternions. The parallel transport and the covariant derivation can be defined in the curved quaternion space, and they can be applied to describe the property of gravitational fields in the curved quaternion space. Similarly the orthogonality of two octonions can be defined by the scalar product of octonions. And the parallel transport and the covariant derivative can be defined in the curved octonion space, and then they can be applied to describe the property of electromagnetic fields and gravitational fields in the curved octonion space simultaneously. The results reveal that the connection coefficient and the curvature of the curved octonion space can impact directly the field strength and the field source etc in electromagnetic fields and gravitational fields.

1. INTRODUCTION

J. C. Maxwell was the first to describe the electromagnetic field with the quaternion and the vector. In the recent years, the quaternion has been applied to depict the gravitational fields [1]. After the vector evolved into the tensor, the latter was used by A. Einstein to represent the gravitational field in the curved space [2]. Subsequently the quaternion [3] and the octonion are applied to depict the gravitational fields and of electromagnetic fields [4] in the curved spaces.

In the transformation of quaternion coordinates, the scalar part of the quaternion power product will remain unchanged. And that the scalar part can be written as the space-time interval. Therefore the scalar part of the quaternion power product can substitute the norm for the arc length, to describe the gravitational field equations. In the curved quaternion space, the quaternion parallel transport and the quaternion covariant derivative, which defined from the quaternion orthogonal property, can be used to describe the feature of gravitational fields.

Similarly in the transformation of octonion coordinates, the scalar part of the octonion power product will keep the same [5]. And the scalar part can be written as the space-time interval. So the scalar part of the octonion power product can substitute the norm for the arc length, to describe the electromagnetic equations and the gravitational equations. In the curved octonion space, the octonion parallel transport and the octonion covariant derivative, which defined from the octonion orthogonal property, can be used to describe the electromagnetic fields and gravitational fields.

The results reveal that the connection coefficients and the curvature of the curved octonion space have an influence on the field strength and the field source of electromagnetic fields and gravitational fields to a certain extent. Contrarily the measurement of the field strength and the field source of electromagnetic fields and gravitational fields will appraise the departure degree of the curved octonion space from the flat octonion space.

2. CURVED QUATERNION SPACE

2.1. Quaternion Space-time Interval

In the flat quaternion space, the quaternion is $\mathbb{X}(x^0, x^1, x^2, x^3)$, and the basis vector is \mathbf{i}_i . According to the definition of quaternion product, the norm S is written as the $S^2 = \mathbb{X} \circ \mathbb{X}^* = (x^0)^2 + (x^1)^2 + (x^2)^2 + (x^3)^2$. Obviously in the curved quaternion space, the method considered the S as the arc length cannot meet the requirement of the space-time interval in the physics theory.

However, for the power product, $\mathbb{Y}^2 = \mathbb{X} \circ \mathbb{X}$, of the quaternion $\mathbb{X}(x^0, x^1, x^2, x^3)$, its scalar part R^2 will meet the requirement of the space-time interval. The scalar part can be written as, $R^2 = \mathbb{X} \odot \mathbb{X} = (x^0)^2 - (x^1)^2 - (x^2)^2 - (x^3)^2$. Therefore in the curved quaternion space, the method considered the R as the arc length meets the requirement of the space-time interval.

In the curved quaternion space, the quaternion is $\mathbb{R}_g(u^0, u^1, u^2, u^3)$, and the tangent frame quaternion is \mathbf{e}_i . The quaternion space-time interval is defined as

$$dR^2 = d\mathbb{R}_g \odot d\mathbb{R}_g = g_{ij} du^i du^j, \quad (1)$$

where the metric coefficient $g_{ij} = \mathbf{e}_i \odot \mathbf{e}_j$. The tangent frame quaternion $\mathbf{e}_j = \partial\mathbb{R}_g/\partial u^j$. \mathbf{e}_0 is chosen as the scalar. \odot denotes the scalar product of quaternions. $x^0 = ct$, c is the speed of light, and t is the time. $i, j, k, m = 0, 1, 2, 3$.

2.2. Quaternion Parallel Transport

In the curved quaternion space, neither the conventional parallel transport (Euclidean space) nor the Levi-Civita parallel transport (Riemann space) is suitable. Because both of them adopt the inner product of vectors and choose the norm as the arc length, while the physics theory considers the space-time interval as the arc length and applies the inner product of quaternions. It is necessary to introduce one new parallel transport for the curved quaternion space. And it is similar to the Levi-Civita parallel transport and meets the requirement of the space-time interval.

In the quaternion space, for the quaternion $\mathbb{A}(a^0, a^1, a^2, a^3)$ and $\mathbb{B}(b^0, b^1, b^2, b^3)$, the quaternion product $\mathbb{A} \circ \mathbb{B}$ includes the scalar part $\mathbb{A} \odot \mathbb{B}$ and the vector part $\mathbb{A} \otimes \mathbb{B}$. In case $\mathbb{A} \odot \mathbb{B} = 0$, \mathbb{A} and \mathbb{B} are orthogonal. This definition is called the quaternion orthogonality. By analogy with the deduction process of the Levi-Civita parallel transport in the Riemann space, the quaternion parallel transport in the curved quaternion space can be defined via the definition of the quaternion orthogonality. Especially the \mathbb{A} is called the isotropic quaternion when $\mathbb{A} \odot \mathbb{A} = 0$.

In the curved quaternion space, the quaternion quantity \mathbb{A}_1 in the tangent space \mathbb{T}_1 of one point \mathbb{M}_1 on the quaternion manifold can be decomposed in the tangent space \mathbb{T}_2 of the point \mathbb{M}_2 near the \mathbb{M}_1 . According to the definition of the quaternion orthogonality, the quaternion quantity \mathbb{A}_1 can be decomposed as the projection part \mathbb{A}_2 in the tangent space \mathbb{T}_2 , and the orthogonal part \mathbb{N}_2 to be orthogonal to the tangent space \mathbb{T}_2 . The quaternion quantity \mathbb{A}_2 is called to be parallel transported from the quaternion quantity \mathbb{A}_1 . And the parallel transport is called the quaternion parallel transport. Obviously when the scalar parts of the quaternion quantity \mathbb{A}_1 and \mathbb{A}_2 are equal to zeros, the quaternion quantity \mathbb{A}_1 and \mathbb{A}_2 will be degenerated to the vectors, meanwhile the quaternion orthogonality and the quaternion parallel transport will be degenerated to the vector orthogonality and the Levi-Civita parallel transport respectively.

2.3. Quaternion Covariant Derivation

In the Riemann space, if the conventional parallel transport and the basis vector are substituted by the Levi-Civita parallel transport and the tangent frame vector respectively, the method that the partial derivation is defined by the limit can be extended directly into the covariant derivation for the Riemann space.

Similarly the method that the covariant derivation is defined from the limit in the Riemann space can be extended directly to the covariant derivation for the curved quaternion space, when the Levi-Civita parallel transport and the tangent frame vector are substituted by the quaternion parallel transport and the tangent frame quaternion respectively, meanwhile the vector orthogonality is substituted by the quaternion orthogonality.

In the curved quaternion space, for 1 rank contravariant tensor $Y^i(\mathbb{P})$ of one point \mathbb{P} , the component of the quaternion covariant derivation with respect to the coordinate u^k is,

$$\nabla_k Y^i = \partial Y^i / \partial u^k + \Gamma_{jk}^i Y^j, \quad (2)$$

where Γ_{jk}^i is the connection coefficient. The connection coefficient can be expressed by the metric tensor, $\Gamma_{jk}^i = (1/2)g^{mi}(\partial g_{jm}/\partial u^k + \partial g_{mk}/\partial u^j - \partial g_{kj}/\partial u^m)$, with $g^{mi} = (g_{mi})^{-1}$.

3. GRAVITATIONAL FIELD EQUATIONS

In the curved quaternion space, the gravitational potential $\mathbb{A}_g(a^0, a^1, a^2, a^3)$ is defined as,

$$\mathbb{A}_g = \diamond \circ \mathbb{X}_g = \diamond \odot \mathbb{X}_g + \diamond \otimes \mathbb{X}_g, \quad (3)$$

where $\diamond A^i = \mathbf{e}^k \nabla_k A^i$, with $\mathbf{e}^j = g^{ij} \mathbf{e}_j$. The quaternion quantity $\mathbb{X}_g = x^j \mathbf{e}_j$. $\diamond \odot \mathbb{X}_g = a^0 \mathbf{e}_0 = a$ is the scalar part of the \mathbb{A}_g ; $\diamond \otimes \mathbb{X}_g = a^p \mathbf{e}_p = \mathbf{a}$ is the vector part of the \mathbb{A}_g . $p, q = 1, 2, 3$.

The gravitational strength $\mathbb{B}_g(k^0, k^1, k^2, k^3)$ is defined as,

$$\mathbb{B}_g = \diamond \circ \mathbb{A}_g = \diamond \odot \mathbb{A}_g + \diamond \otimes \mathbb{A}_g, \tag{4}$$

where $\diamond \odot \mathbb{A}_g = k^0 \mathbf{e}_0$ is the scalar part of the \mathbb{B}_g , and $\diamond \otimes \mathbb{A}_g = k^p \mathbf{e}_p$ is the vector part of the \mathbb{B}_g . The vector part of the gravitational strength can be decomposed as, $k^p \mathbf{e}_p = \mathbf{g}/v_0 + \mathbf{b}$. The component, $\mathbf{g}/v_0 = \nabla_0 \mathbf{a} + \nabla a$, is connected with the acceleration, while the component, $\mathbf{b} = \nabla \times \mathbf{a}$, is related with the angular velocity. The gauge equation is chosen as, $k^0 = 0, \nabla a = (\mathbf{e}^q \nabla_q) \circ (a^0 \mathbf{e}_0), \nabla \times \mathbf{a} = (\mathbf{e}_q \nabla_q) \otimes (a^p \mathbf{e}_p), \nabla_0 \mathbf{a} = \nabla_0 (a^p \mathbf{e}_p) = (\nabla_0 a^p) \mathbf{e}_p$.

The gravitational source $\mathbb{S}_g(s^0, s^1, s^2, s^3)$ is defined as,

$$-\mu \mathbb{S} = -(\mu_g \mathbb{S}_g - \mathbb{B}_g^* \circ \mathbb{B}_g / v_0) = (\diamond + \mathbb{B}_g / v_0)^* \circ \mathbb{B}_g,$$

or

$$-\mu_g \mathbb{S}_g = \diamond^* \circ \mathbb{B}_g = \diamond^* \odot \mathbb{B}_g + \diamond^* \otimes \mathbb{B}_g, \tag{5}$$

where $-\diamond^* \odot \mathbb{B}_g / \mu_g = s^0 \mathbf{e}_0$ is the scalar part of the \mathbb{S}_g , while $-\diamond^* \otimes \mathbb{B}_g / \mu_g = s^p \mathbf{e}_p$ is the vector part of the \mathbb{S}_g . μ and μ_g are the coefficients.

Combined with the definition of the gravitational strength, the decomposition of the above will yield the component equations of gravitational fields in the curved quaternion space. And it deals with the curvature and the torsion etc of the curved spaces. In the curved quaternion space, the quaternion physics quantity $\diamond Y^i$ involves in the connection coefficient Γ_{jk}^i , while the quaternion physics quantity $\diamond^* \circ (\diamond Y^i), \diamond \circ (\diamond^* Y^i),$ and $(\diamond \circ \diamond) Y^i$ relate to the curvature R_{jkm}^i etc..

The definition of the gravitational strength is written as, $\mathbb{B}_g = \diamond \circ (\diamond \circ \mathbb{X}_g) = (\diamond \circ \diamond) \circ \mathbb{X}_g$, and is decomposed into, $k^0 \mathbf{e}_0 = (\diamond \circ \diamond) \circ x^0 \mathbf{e}_0$ and $k^p \mathbf{e}_p = (\diamond \circ \diamond) \circ x^q \mathbf{e}_q$. Meanwhile the definition of the gravitational source is rewritten as, $-\mu_g \mathbb{S}_g = \diamond^* \circ (\diamond \circ \mathbb{A}_g) = (\diamond^* \circ \diamond) \circ \mathbb{A}_g = \diamond^2 \circ \mathbb{A}_g$, and is separated into, $-\mu_g s^0 \mathbf{e}_0 = \diamond^2 \circ a^0 \mathbf{e}_0$ and $-\mu_g s^p \mathbf{e}_p = \diamond^2 \circ a^q \mathbf{e}_q$. The above are the d'Alembert equation of gravitational fields in the curved quaternion space.

4. CURVED OCTONION SPACE

4.1. Octonion Space-time Interval

In the flat quaternion space, the quaternion is $\mathbb{X}_g(x^i)$, and the basis vector is \mathbf{i}_i . Meanwhile in the flat S -quaternion space, the S -quaternion is $\mathbb{X}_e(X^j)$, and the basis vector is \mathbf{I}_j . The $\mathbb{X}_g(x^i)$ and $\mathbb{X}_e(X^j)$ can be combined together to become the octonion \mathbb{X} in the flat octonion space,

$$\mathbb{X} = \mathbb{X}_g + k_{eg} \mathbb{X}_e = x^s \mathbf{i}_s, \tag{6}$$

where $x^{j+4} = k_{eg} X^j$, and $\mathbf{i}_{j+4} = \mathbf{I}_j$. $r, s, t, u = 0, 1, 2, 3, 4, 5, 6, 7$.

According to the definition of the octonion multiplication, the octonion norm is written as, $S^2 = \mathbb{X} \circ \mathbb{X}^* = \Sigma(x^s)^2$. But in the curved octonion space, the method considered the S as the arc length cannot meet the requirement of the space-time interval in the physics theory.

Similarly the scalar part R^2 of the power product, $\mathbb{Y}^2 = \mathbb{X} \circ \mathbb{X}$, of the octonion $\mathbb{X}(x^s)$ will meet the requirement of the space-time interval. The scalar part can be written as, $R^2 = \mathbb{X} \odot \mathbb{X} = (x^0)^2 - \Sigma(x^f)^2$. Therefore in the curved octonion space, the method considered the R as the arc length meets the requirement of the space-time interval, $f = 1, 2, 3, 4, 5, 6, 7$.

In the curved octonion space, the octonion is $\mathbb{R}(u^i, U^j) = \mathbb{R}_g(u^i) + k_{eg} \mathbb{R}_e(U^j)$. In the quaternion space for the gravitational field, the quaternion is $\mathbb{R}_g(u^i)$, and the tangent frame quaternion is \mathbf{e}_i . In the S -quaternion space for the electromagnetic field, the S -quaternion is $\mathbb{R}_e(U^j)$, and the tangent frame S -quaternion is \mathbf{E}_j . By means of the transformation $u^{j+4} = k_{eg} U^j$ and $\mathbf{e}_{j+4} = \mathbf{E}_j$, the octonion \mathbb{R} is written as, $\mathbb{R} = u^s \mathbf{e}_s$.

The octonion space-time interval is defined as

$$dR^2 = d\mathbb{R} \odot d\mathbb{R} = g_{rs} du^r du^s, \tag{7}$$

where the metric coefficient $g_{rs} = \mathbf{e}_r \odot \mathbf{e}_s$. The tangent frame octonion $\mathbf{e}_r = \partial \mathbb{R} / \partial u^r$. \mathbf{e}_0 is chosen as the scalar, and $\mathbf{E}_0 = \mathbf{e}_0 \circ (k \mathbf{I})$, with $\mathbf{I} \circ \mathbf{I}^* = 1$. k is the scalar. \odot denotes the scalar product of octonions. $x^0 = ct$, c is the speed of light, and t is the time.

4.2. Octonion Parallel Transport

In the curved octonion space, the conventional parallel transport (Euclidean space), the Levi-Civita parallel transport (Riemann space), and the quaternion parallel transport (curved quaternion space) are not suitable. Therefore it is necessary to introduce one new concept of parallel transport for the curved octonion space. The new parallel transport is similar to the quaternion parallel transport and meets the requirement of the space-time interval.

In the octonion space, for the octonion $\mathbb{A}(a^r)$ and $\mathbb{B}(b^s)$, the octonion product $\mathbb{A} \circ \mathbb{B}$ includes the scalar part $\mathbb{A} \odot \mathbb{B}$ and the vector part $\mathbb{A} \otimes \mathbb{B}$. In case $\mathbb{A} \odot \mathbb{B} = 0$, \mathbb{A} and \mathbb{B} are orthogonal. This definition is called the octonion orthogonality. By analogy with the deduction process of the quaternion parallel transport in the curved quaternion space, the octonion parallel transport in the curved octonion space can be defined via the definition of the octonion orthogonality. Especially the \mathbb{A} is called the isotropic octonion when $\mathbb{A} \odot \mathbb{A} = 0$.

In the curved octonion space, the octonion quantity \mathbb{A}_1 in the tangent space \mathbb{T}_1 of one point \mathbb{M}_1 on the octonion manifold can be decomposed in the tangent space \mathbb{T}_2 of the point \mathbb{M}_2 near the \mathbb{M}_1 . According to the definition of the octonion orthogonality, the octonion quantity \mathbb{A}_1 can be decomposed as the projection part \mathbb{A}_2 in the tangent space \mathbb{T}_2 , and the orthogonal part \mathbb{N}_2 to be orthogonal to the tangent space \mathbb{T}_2 . The octonion quantity \mathbb{A}_2 is called to be parallel transported from the octonion quantity \mathbb{A}_1 . And the parallel transport is called the octonion parallel transport. Obviously when the scalar parts of the octonion quantity \mathbb{A}_1 and \mathbb{A}_2 are equal to zeros, the octonion quantity \mathbb{A}_1 and \mathbb{A}_2 will be degenerated to the vectors, while the octonion orthogonality and the octonion parallel transport will be degenerated to the vector orthogonality and the Levi-Civita parallel transport respectively. When the octonion quantity is degenerated to the quaternion quantity, and the octonion orthogonality and the octonion parallel transport will be degenerated to the quaternion orthogonality and the quaternion parallel transport.

4.3. Octonion Covariant Derivation

In the curved quaternion space, the method that the covariant derivation is defined from the limit in the Riemann space can be extended directly to the covariant derivation for the curved quaternion space, in the case of the Levi-Civita parallel transport and the tangent frame vector are substituted by the quaternion parallel transport and the tangent frame quaternion respectively, as well as the vector orthogonality is substituted by the quaternion orthogonality.

Similarly in curved octonion space, the method that the covariant derivation is defined from the limit in the curved quaternion space can be extended directly to the covariant derivation for the curved octonion space, when the quaternion parallel transport and the tangent frame quaternion are substituted by the octonion parallel transport and the tangent frame octonion respectively, meanwhile the quaternion orthogonality is substituted by the octonion orthogonality.

In the curved octonion space, for 1 rank contravariant tensor $Y^s(\mathbb{P})$ of one point \mathbb{P} , the component of the octonion covariant derivation with respect to the coordinate u^t is,

$$\nabla_t Y^s = \partial Y^s / \partial u^t + \Gamma_{rt}^s Y^r, \quad (8)$$

where Γ_{rt}^s is the connection coefficient. The connection coefficient can be expressed by the metric tensor, $\Gamma_{rt}^s = (1/2)g^{us}(\partial g_{ru} / \partial u^t + \partial g_{ut} / \partial u^r - \partial g_{tr} / \partial u^u)$, with $g^{us} = (g_{us})^{-1}$.

5. ELECTROMAGNETIC FIELD EQUATIONS

In the curved octonion space, the octonion field potential, $\mathbb{A} = \mathbb{A}_g + k_{eg}\mathbb{A}_e$, is defined as

$$\mathbb{A} = \diamond \circ \mathbb{X} = \diamond \odot \mathbb{X} + \diamond \otimes \mathbb{X}, \quad (9)$$

where $\mathbb{A}_e(A^0, A^1, A^2, A^3)$ is the electromagnetic potential. $\diamond A^p = \mathbf{e}^k \nabla_k A^p$, $\mathbb{X} = \mathbb{X}_g + k_{eg}\mathbb{X}_e$ is the octonion quantity. $\mathbb{X}_e = X^j \mathbf{E}_j$ is the S -quaternion quantity. $\diamond \odot \mathbb{X}_e = A^0 \mathbf{E}_0 = \mathbf{A}_Q$ is the ‘scalar’ part of the \mathbb{A}_e ; $\diamond \otimes \mathbb{X}_e = A^p \mathbf{E}_p = \mathbf{A}$ is the ‘vector’ part of the \mathbb{A}_e .

The octonion field strength, $\mathbb{B} = \mathbb{B}_g + k_{eg}\mathbb{B}_e$, is defined as,

$$\mathbb{B} = \diamond \circ \mathbb{A} = \diamond \odot \mathbb{A} + \diamond \otimes \mathbb{A}, \quad (10)$$

where $\mathbb{B}_e(K^0, K^1, K^2, K^3)$ is the electromagnetic strength. $\diamond \odot \mathbb{A}_e = K^0 \mathbf{E}_0$ is the ‘scalar’ part of the \mathbb{B}_e , while $\diamond \otimes \mathbb{A}_e = K^p \mathbf{E}_p$ is ‘vector’ part of the \mathbb{B}_e . The gauge equation is chosen as, $K^0 = 0$. The ‘vector’ part of the electromagnetic strength can be decomposed as, $K^p \mathbf{E}_p = \mathbf{E}/v_0 + \mathbf{B}$.

$\mathbf{E}/v_0 = \nabla_0 \mathbf{A} + \nabla \circ \mathbf{A}_Q$ is the electric field intensity, while $\mathbf{B} = \nabla \times \mathbf{A}$ is the magnetic flux density. $\nabla \circ \mathbf{A}_Q = (\mathbf{e}_p \nabla_p) \circ (A^0 \mathbf{E}_0)$, $\nabla \times \mathbf{A} = (\mathbf{e}_q \nabla_q) \otimes (A^p \mathbf{E}_p)$, $\nabla_0 \mathbf{A} = \nabla_0 (A^p \mathbf{E}_p) = (\nabla_0 A^p) \mathbf{E}_p$.

The octonion field source, $\mu \mathbb{S} = \mu_g \mathbb{S}_g + k_{eg} \mu_e \mathbb{S}_e$, is defined as,

$$-\mu \mathbb{S} = -(\mu_g \mathbb{S}_g + k_{eg} \mu_e \mathbb{S}_e - \mathbb{B}^* \circ \mathbb{B}/v_0) = (\diamond + \mathbb{B}/v_0)^* \circ \mathbb{B},$$

or

$$-\mu_g \mathbb{S}_g = \diamond^* \circ \mathbb{B}_g = \diamond^* \odot \mathbb{B}_g + \diamond^* \otimes \mathbb{B}_g, \quad (11)$$

$$-\mu_e \mathbb{S}_e = \diamond^* \circ \mathbb{B}_e = \diamond^* \odot \mathbb{B}_e + \diamond^* \otimes \mathbb{B}_e, \quad (12)$$

where $\mathbb{S}_e(S^0, S^1, S^2, S^3)$ is the electromagnetic source. $-\diamond^* \odot \mathbb{B}_e/\mu_e = S^0 \mathbf{E}_0$ is the ‘scalar’ part of the \mathbb{S}_e , while $-\diamond^* \otimes \mathbb{B}_e/\mu_e = S^p \mathbf{E}_p$ is the ‘vector’ part of the \mathbb{S}_e . μ and μ_e are the coefficients.

Combined with the definition of the electromagnetic strength, the decomposition of the above will yield the component equations of electromagnetic fields in the curved S -quaternion space. And it deals with the curvature and the torsion etc of the curved spaces. In the curved octonion space, the octonion physics quantity $\diamond Y^s$ involves in the connection coefficient Γ_{rt}^s , and the octonion physics quantity $\diamond^* \circ (\diamond Y^s)$, $\diamond \circ (\diamond^* Y^s)$, and $(\diamond \circ \diamond) Y^s$ relate to the curvature R_{rtu}^s etc..

Moreover the definition of the electromagnetic strength can be written as, $\mathbb{B}_e = \diamond \circ (\diamond \circ \mathbb{X}_e) = (\diamond \circ \diamond) \circ \mathbb{X}_e$, and can be decomposed into, $K^0 \mathbf{E}_0 = (\diamond \circ \diamond) \circ X^0 \mathbf{E}_0$ and $K^p \mathbf{E}_p = (\diamond \circ \diamond) \circ X^q \mathbf{E}_q$. The definition of the electromagnetic source can be written as, $-\mu_e \mathbb{S}_e = \diamond \circ (\diamond^* \circ \mathbb{A}_e) = (\diamond \circ \diamond^*) \circ \mathbb{A}_e = \diamond^2 \circ \mathbb{A}_e$, and can be separated into, $-\mu_e S^0 \mathbf{E}_0 = \diamond^2 \circ A^0 \mathbf{E}_0$ and $-\mu_e S^p \mathbf{E}_p = \diamond^2 \circ A^q \mathbf{E}_q$. The above are the d’Alembert equations of the electromagnetic field in the curved octonion space.

6. CONCLUSIONS

In the curved quaternion space, the paper introduces the definitions of the quaternion orthogonality and the quaternion parallel transport, and then obtains the quaternion covariant derivation to describe the gravitational field equations. In the curved quaternion space for the gravitational field, the connection coefficient can impact the gravitational potential and the gravitational strength etc., while the curvature has an influence on the gravitational strength and the gravitational source etc..

In the curved octonion space, the paper introduces the definitions of the octonion orthogonality and the octonion parallel transport, and then achieves the octonion covariant derivation to depict the electromagnetic field equations. In the curved S -quaternion space for the electromagnetic field, the connection coefficient can affect the electromagnetic potential and the electromagnetic strength etc, while the curvature may exert the influences on the electromagnetic strength and the electromagnetic source etc..

It should be noted that the investigation for the curved octonion space has examined only some simple cases. Despite its preliminary character, this study can clearly indicate that the gravitational field and the electromagnetic field may exert the influences on the curved octonion space. Meanwhile the connection coefficient and the curvature of the curved octonion space will impact the measurement of the field strength and the field source of two fields. For the future studies, the research will concentrate on only the influences of the curved space on the gravitational field equations and the electromagnetic field equations.

ACKNOWLEDGMENT

This project was supported partially by the National Natural Science Foundation of China under grant number 60677039.

REFERENCES

1. Beckwith, A., “Octonionic gravity formation, its connections to micro physics,” *Open Journal of Microphysics*, Vol. 1, No. 1, 13–18, 2011.
2. Bishop, R. L., “There is more than one way to frame a curve,” *The American Mathematical Monthly*, Vol. 82, No. 3, 246–251, 1975.
3. Hanson, A. J. and H. Ma, “Quaternion frame approach to streamline visualization,” *IEEE Transactions on Visualization and Computer Graphics*, Vol. 1, No. 2, 164–174, 1995.
4. Tsagas, C. G., “Electromagnetic fields in curved spacetimes,” *Classical and Quantum Gravity*, Vol. 22, No. 2, 393–407, 2005.
5. Weng, Z.-H., “Electromagnetic field equations described with the octonions,” *Modern Physics*, Vol. 1, No. 1, 17–22, 2011 (in Chinese).

On-body Textile Monopole Antenna Characterisation for Body-centric Wireless Communications

H. A. Rahim¹, F. Malek¹, I. Adam¹, S. Ahmad¹, N. B. Hashim¹, and P. S. Hall²

¹Embedded Computing Research Cluster (ECRC)
School of Computer and Communication Engineering
Universiti Malaysia Perlis, Perlis, Malaysia

²School of Electronics, Electrical and Computer Engineering
The University of Birmingham, Edgbaston, Birmingham B 15 2TT, United Kingdom

Abstract— In this paper, the on-body performance of a light-weight and simple structure textile monopole antenna was investigated by determining reflection coefficient and bandwidth characteristics at 2.45 GHz. ShieldIt Super with conductivity of 1.96×10^5 S/m, is used as a conductive textile. The investigation of textile monopole antenna is carried out in the vicinity of human body, simulated by using HUGO model in CST Microwave Studio software, defined at a $8 \times 8 \times 8$ mm³ voxel resolution. The distance of the antenna placed on human shoulder was varying between 0 and 15 mm. The investigation was aimed to study the changes in textile antenna's characteristics in terms of frequency detuning, bandwidth and reflection coefficient characteristics when the antenna was placed on the human body. The result showed that the reflection coefficient values were improved by 70.8% with a gradual enhancement of downward frequency shift as the textile monopole was varying between 0 and 15 mm. The result also demonstrated that an improvement up to a maximum of 72.8% in bandwidth was obtained when the textile monopole was positioned in the range of 2 to 15 mm away from the human shoulder.

1. INTRODUCTION

Recently, body-centric wireless communications (BCWC) has become an important area of research that is very potential to be applied in the area of home/health care, medical, military, sports, multimedia and other areas [1–6]. Meanwhile, the emergence of wearable intelligent textile systems is predicted to be the main driver for the future wireless technologies to be integrated into human's clothing. Wearable antenna is an element of clothes that is mainly used to assist people in telecommunication field such as tracking, navigation, remote computing and public safety [7]. The aim of BCWC is to provide with constant availability, reconfigurability and unobtrusiveness that suits with the need of the future wearable system [8]. Hence, a small, lightweight, robust, unobtrusive to the user and conformal to the body surface is needed for the applications of BCWC [6] where textile antenna is seen to suit these requirements. The objective of this paper is to investigate the effect of frequency detuning, bandwidth and reflection coefficient due to the presence of human lossy tissues by varying the distance of wearable textile antenna from the human body. The changes in these characteristics are then compared to the antenna placement in free space.

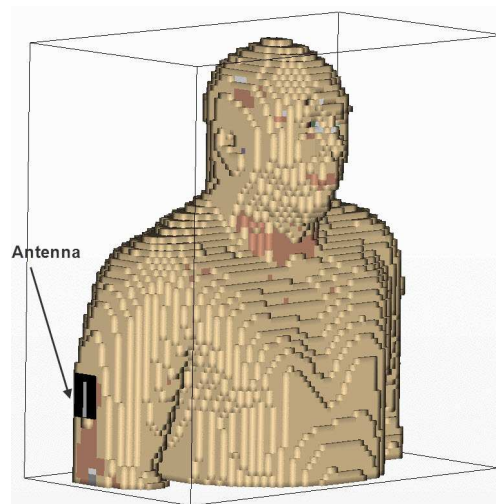


Figure 1: Textile monopole antenna placement on human shoulder.

2. PLACEMENT OF WEARABLE TEXTILE MONOPOLE ANTENNA

The monopole antenna is made out of ShieldIt Super conductive fabric, manufactured by LessEM Inc, USA. ShieldIt Super is a rip-stop fabric with a thickness, t , of 0.17 mm and a surface resistance, R_s , of less than $0.05 \Omega/\text{sq}$. This fabric is made from woven polyester, coated with copper and nickel. The design of monopole antenna is presented in [9]. Both top radiator and ground plane of textile monopole are separated by a felt fabric with a relative permittivity, ϵ_r of 1.22 [10]. The textile monopole was mounted on human shoulder as this location suits body-centric wireless applications and can minimize the effect of antenna bending. The antenna is simulated in proximity of a HUGO voxel model in CST Microwave Studio software with truncation in order to reduce computational time. 8 mm resolution is applied to the model with the electrical properties of human tissues defined at 2.45 GHz for all organs and tissues used [11]. Figure 1 illustrates the selected body part

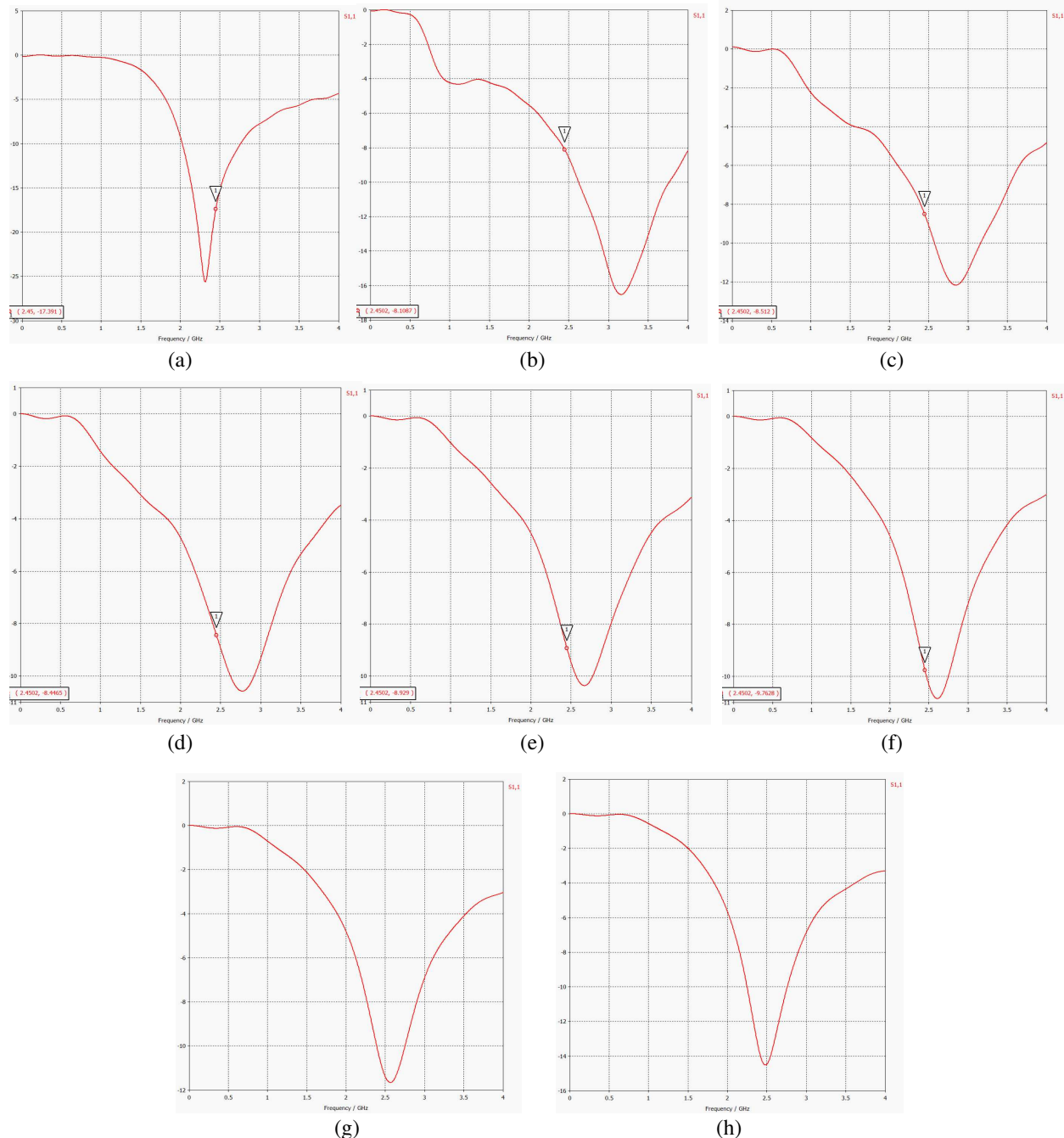


Figure 2: Simulated reflection coefficient at location of: (a) free space, (b) 0 mm, (c) 2 mm, (d) 4 mm, (e) 6 mm, (f) 8 mm, (g) 10 mm and (h) 15 mm away from human shoulder.

for HUGO voxel model simulation and placement of the textile monopole utilized in this simulation.

3. RESULTS AND DISCUSSION

The prototype was analysed in the vicinity of human body, particularly on the shoulder. This investigation is crucial as the wearable textile was aimed to be mounted on the user. Thus, the wearable textile monopole was placed at various distances from the human body and the on-body performance was compared to the antenna's free space performance. The simulated reflection coefficient at various distances away from the shoulder and free space are illustrated in Figures 2(a)–(h). It is seen that the textile monopole resonated at higher f_c when the antenna was placed on the human shoulder and gradually decreased as distance was varied from 2 mm to 15 mm. The worst frequency detuning occurred when the antenna was mounted directly on the body with spacing of 2 mm by 19.8%, indicating larger amount of f_c shift in comparison to free space. Furthermore, the least frequency detuning of 4.6% was observed at a distance of 15 mm away from the human body. This is mainly due to the absence of full ground plane that supposes to act as a shield, protecting the human body from the radiating power of the antenna. Because of the partial ground plane, the textile monopole experience the worst frequency detuning as more power is absorbed by the human lossy tissues. From the obtained results, it is observed that frequency detuning reduced significantly about 65% as the distance was increased between the antenna and the human body.

The degradation of textile monopole bandwidth also was observed as the antenna was positioned at various distances from the human shoulder. The worst bandwidth degradation occurred at a distance of 6 mm from the human shoulder about 200 MHz, 71.9% in comparison to free space. Meanwhile, the least degradation of about 500 MHz, 30.9% in comparison to free space, was seen at the furthest distance, 15 mm away from the human shoulder. As the spacing between the textile monopole and the human shoulder increased, bandwidth of the textile monopole improved significantly by a maximum of 70.8%. Due to a small size of ground plane, the bandwidth of textile monopole with close proximity of human body was greatly affected. The summary of results is tabulated in Table 1.

Table 1: Summary of the wearable textile and conventional monopole antennas in free space and on-body.

Position of Wearable Textile Monopole (mm)	f_l (GHz)	f_h (GHz)	BW (MHz)	$f_{c,calc}$ (GHz)
Free space	2.025	2.762	737.3	2.394
Direct on-body	0	0	0	0
2	2.574	3.162	587.7	2.868
4	2.624	2.919	295.0	2.771
6	2.565	2.772	207.0	2.668
8	2.470	2.752	278.9	2.610
10	2.392	2.752	360.3	2.572
15	2.250	2.760	509.8	2.505

Legend: f_l — lower 10 dB limit, f_h — higher 10 dB limit, BW — bandwidth, $f_{c,calc}$ — calculated centre frequency

Table 2: Simulated return loss and gain summary of the wearable textile and conventional monopole antennas reflection coefficient.

Location	Distance (mm)	Simulated Min S_{11} (dB)
Free Space	-	-17.39
On-body	0	-8.11
	2	-8.51
	4	-8.45
	6	-8.93
	8	-9.76
	10	-10.57
	15	-13.85

Table 2 summarizes the comparison between simulated textile in free space and on-body performance. From Table 2, it exhibited that the reflection coefficient for 0 mm (on body) to 8 mm from human shoulder was obtained less than -10 dB at desired frequency of 2.45 GHz. However, a significant reflection coefficient enhancement was yielded, up to a maximum of 72.8%, when the antenna was placed in the range of 2 to 15 mm from the human shoulder.

4. CONCLUSIONS

This paper presents the investigation of on-body performance of a wearable textile monopole antenna when the antenna was mounted at various distances from the human shoulder. It was found that the performance of textile monopole was greatly degraded by the presence of the human body due to the lossy human body tissues. However, as the placement of the antenna increased from the human body, the frequency detuning, bandwidth and reflection coefficient values improved significantly. The wearable textile monopole antenna should be placed more than 10 mm away from the human body to suit for body-centric wireless applications due to the antenna's small fabric ground plane.

ACKNOWLEDGMENT

This work is partially supported by the Short Term Grant (STG) scheme Universiti Malaysia Perlis, under grant 9001-00436 and Knowledge Transfer Programme Grant, grant No.: 9011-00003, under Ministry of Higher Education (MOHE). The authors would like to express their highest gratitude to Universiti Malaysia Perlis and MOHE.

REFERENCES

1. Alomainy, A., et al., "Statistical analysis and performance evaluation for on body radio propagation with microstrip patch antenna," *IEEE Trans. on Antennas and Propagation*, Vol. 55, No. 1, 245–248, 2007.
2. Reusens, E., et al., "Characterization of on-body communication channels and energy efficient topology design for wireless body area networks," *IEEE Trans. on Information Technology in Biomedicine*, Vol. 13, No. 6, 933–945, 2009.
3. Lim, H. B., D. Baumann, and E.-P. Li, "A human body model for efficient numerical characterization of UWB signal propagation in wireless body area networks," *IEEE Trans. on Biomedical Engineering*, Vol. 55, No. 3, 689–697, 2011.
4. Chen, X., X. Lu, D. Jin, L. Su, and L. Zeng, "Channel modeling of UWB-based wireless body area networks," *Proceedings of 2011 IEEE International Conference on Communications, ICC*, 1–5, Dresden, Germany, Jun. 2011.
5. Wang, Q., T. Tayamachi, I. Kimura, and J. Wang, "An on-body channel model for UWB body area communications for various postures," *IEEE Trans. on Antennas and Propagation*, Vol. 57, No. 4, 991–998, 2009.
6. Conway, G. A. and W. G. Scanlon, "Antennas for over-body-surface communication at 2.45 GHz," *IEEE Trans. on Antennas and Propagation*, Vol. 57, No. 4, 844–855, 2009.
7. Wnuk, M. T., M. Bugaj, R. Przesmycki, L. Nowosielski, and K. Piwowarczyk, "Wearable antenna constructed in microstrip technology," *PIERS Proceedings*, 67–71, Kuala Lumpur, Malaysia, Mar. 27–30, 2012.
8. Alomainy, A., Y. Hao, C. G. Parini, and P. S. Hall, "Comparison between two different antennas for UWB on-body propagation measurements," *IEEE Antennas and Wireless Propagation Lett.*, Vol. 4, 31–34, 2005.
9. Rahim, H. A., F. Malek, I. Adam, S. Ahmad, N. B. Hashim, and P. S. Hall, "Design and simulation of a wearable textile monopole antenna for body-centric wireless communications," unpublished.
10. Mantash, M., A. C. Tarot, S. Collardey, and K. Mahdjoubi, "Wearable monopole zip antenna," *Electronics Lett.*, Vol. 47, No. 23, 1–2, 2011.
11. Voelter, S., *Anatomical Human Dataset*, Apr. 20, 2012, <http://www.vr-laboratory.com/>.

Design and Simulation of a Wearable Textile Monopole Antenna for Body Centric Wireless Communications

H. A. Rahim¹, F. Malek¹, I. Adam¹, S. Ahmad¹, N. B. Hashim¹, and P. S. Hall²

¹Embedded Computing Research Cluster (ECRC)
School of Computer and Communication Engineering
Universiti Malaysia Perlis, Perlis, Malaysia

²School of Electronics, Electrical and Computer Engineering
University of Birmingham, Edgbaston, Birmingham B 15 2TT, United Kingdom

Abstract— This paper presents a light-weight and simple structure of monopole antenna using conductive textile. Pure Copper Polyester Tafetta Fabric (PCPTF) is used as a conductive textile, in comparison with conventional microstrip monopole antenna. The prototype is designed with $40\text{ mm} \times 60\text{ mm}$ total dimension and spaced by a 2 mm thick felt fabric for Body-Centric Wireless Communications (BCWC) operating in the 2.45 GHz Industrial, Scientific and Medical (ISM) band. A parametric study has been carried out in order to investigate the antenna basic characteristics, thereby enhancing the antenna performance. The result showed that a slight downward frequency shift of wearable textile monopole was observed against the conventional monopole antenna. The wearable textile antenna is seen to produce about 4 dB higher in reflection coefficient than the conventional monopole antenna. Besides, a satisfactory gain characteristic was obtained by wearable textile monopole comparable to the conventional monopole antenna.

1. INTRODUCTION

On-body antenna is very important element to be used for various future IEEE802.15 wireless standard applications [1]. Textile antenna is suitable for on-body radio communication as it is flexible and comfortable to be integrated into clothing [2]. The textile monopole antenna is chosen because this type of antenna is polarized normally to the body surface and therefore it preserves a strong ray diffracted around the body [3]. This present work describes design and analysis of a textile monopole antenna basic characteristic. The performance of the textile monopole antenna is compared to a conventional monopole microstrip antenna that operates in the 2.45 GHz ISM band. The conducting ground plane and radiating element of the textile monopole antenna comprise of PCPTF, a light-weight and flexible conductive fabric. As for a substrate, felt fabric is utilized.

2. ANTENNA DESIGN

Two antenna prototypes are investigated in this work; conventional monopole antenna using microstrip and textile monopole antenna. The geometry of monopole antenna is illustrated in Fig. 1. The proposed antenna uses PCPTF as a conductive textile, a thick plain woven polyester textile with 0.08 mm thickness and surface resistivity less than $0.05\ \Omega/\text{sq}$. The felt fabric is used as a substrate with a relative dielectric permittivity $\epsilon_r = 1.22$, thickness, of, 2 mm and loss tangent, $\text{tg}\delta$ of 0.016 [4]. The conductivity of fabric material has to be determined based on thickness and

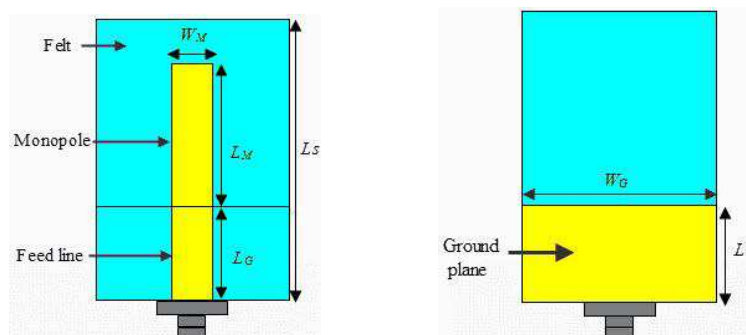


Figure 1: A textile monopole antenna geometry.

Table 1: Dimension of wearable textile monopole antenna.

Parameter	Dimension, mm
W_M	8.5
L_M	30.6
W_G	40.0
L_G	20.0
L_S	60.0

Table 2: Summary of the wearable textile and conventional monopole antennas in free space.

Structure	f_l (GHz)	f_h (GHz)	BW (MHz)	f_c calc (GHz)
Textile monopole	2.097	2.747	650.0	2.422
Conventional monopole	2.264	2.587	323.0	2.426

Legend: f_l — lower 10 dB limit, f_h — higher 10 dB limit, BW — bandwidth, f_c calc — calculated centre frequency.

surface resistance, given as follows [5],

$$\sigma = \frac{1}{R_s \times t} \quad (1)$$

where R_s is surface resistance of the material, t is thickness of the material and σ is conductivity of the material. The width, W_M and length, L_M are the dimension for radiating element. L_M is the length of the monopole which is measured from a point perpendicular to the end of the ground plane. L_S is the length of the substrate. The length of monopole antenna is $\lambda/4$ that resonates frequency at 2.45 GHz. The ground plane is dimensioned using its width, W_G and length, L_G . The structure is fed by 50 Ω SMA connector. The conventional microstrip antenna is designed on a FR-4 substrate with 1.6 mm thickness, h , copper thickness, t , of 0.035 mm and substrate permittivity, $\epsilon_r = 4.7$. The conventional microstrip is taken as reference. The dimension of proposed textile antenna's patch length, L_M , is calculated using a simple formula [6],

$$L_M = \frac{c}{4f} \quad (2)$$

where $c =$ velocity of light (3×10^8) m/s and $f = 2.45$ GHz. The antenna dimension is summarized in Table 1.

3. RESULTS AND ANALYSIS

Table 2 summarizes the comparison between simulated textile and conventional monopole antennas reflection coefficients. The antennas are designed for operation at the center frequency, f_c , of 2.45 GHz, however, a slight downward frequency shift is observed. The textile antenna showed a shifting at 1.1%, compared to the conventional monopole that produced the shifting at 0.98%. This can conclude that the textile monopole is comparable to the conventional monopole. The textile monopole produced a satisfactory result for reflection coefficient and gain. The textile antenna is seen to produce about 4 dB higher in reflection coefficient than conventional monopole antenna. Fig. 2 illustrated the simulated return loss for textile monopole and conventional monopole antennas. It was also found that the bandwidth yielded by textile monopole in free space was twice as the bandwidth of conventional monopole antenna, indicating that a broader bandwidth was achieved by the textile monopole at frequency of 2.45 GHz. However, the textile produced about 0.33 dB lower in gain, when compared to the conventional monopole antenna. It can be summarized that the textile antenna works like a conventional monopole. The reflection coefficient and gain values are summarized in Table 3. The radiation patterns for textile and conventional monopole prototypes are illustrated in Fig. 6, indicating an omni-directional coverage in the azimuth plane.

The length L_G was varied between 10 and 30 mm while other parameters were kept constant. It was observed by simulation that the reflection coefficient could be improved by several dB when

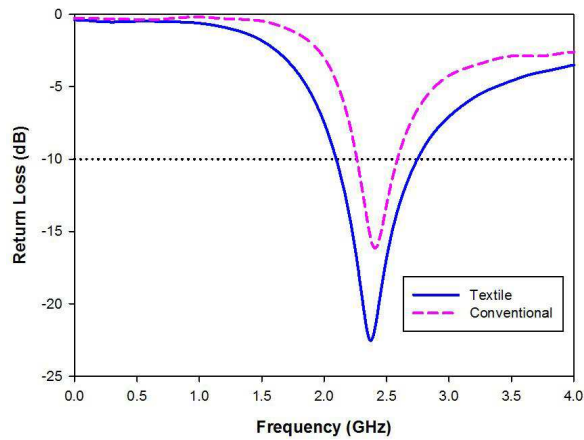


Figure 2: Simulated return loss for textile monopole and conventional monopole antennas.

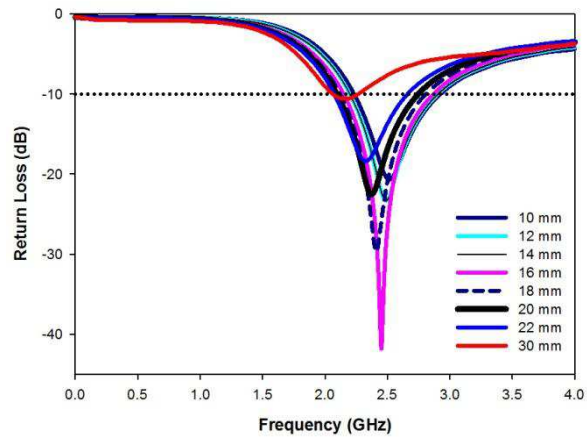


Figure 3: Simulated return loss with the variation of ground plane length, L_G .

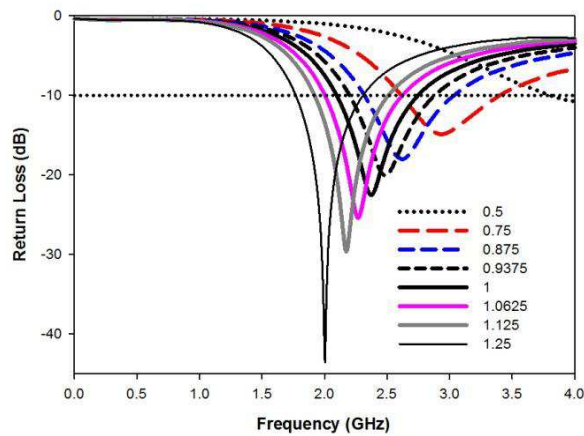


Figure 4: Simulated return loss with the variation of radiating element length, L_M .

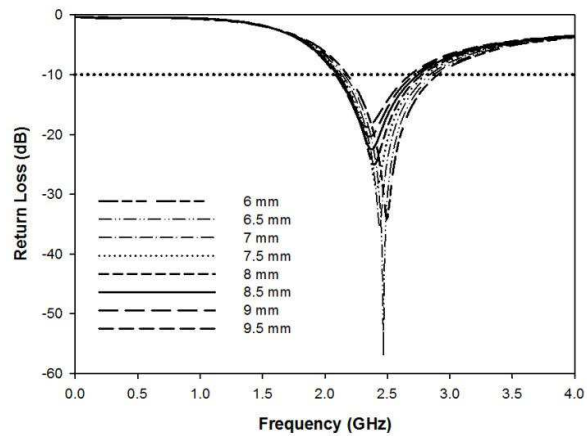


Figure 5: Simulated return loss with the variation of radiating element width, W_M .

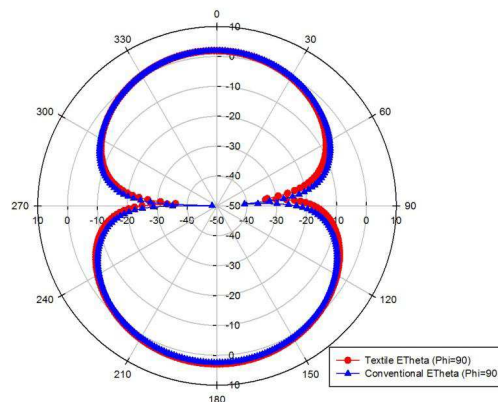


Figure 6: Radiation pattern of textile and conventional monopole antennas at 2.45 GHz.

the length of ground plane was increased from 10 to 16 mm. The reflection coefficient degraded as the length of ground plane was increased from 18 mm to 30 mm. Besides that, it was also observed that resonant frequency was shifted down with increasing length of the ground plane. However, 20 mm were taken as optimum as it covered the desired 2.45 GHz ISM band (reflection coefficient less than -10 dB) and matched with the input impedance. Simulation result is shown in Fig. 3.

Table 3: Simulated return loss and gain summary of the wearable textile and conventional monopole antennas reflection coefficient.

Parameter	Simulated	
	<i>Textile Monopole</i>	<i>Conventional Monopole</i>
Min S_{11} (dB)	-19.40	-15.29
Gain (dB)	3.258	3.584

Variation of L_M is seen to be critical in affecting the resonance of textile monopole as the increase in L_M is found to move the resonance down the frequency scale. The L_M was varied between $0.5\lambda_f$ and $1.25\lambda_f$. The increase in L_M was seen to shift the 10 dB-bandwidth towards lower frequencies. When L_M is λ_f , the textile monopole covered the 2.45 GHz ISM band. The L_M variations are shown in Fig. 4. The width of radiating element, W_M , has some influence on the resonance frequency, as seen in Fig. 5. The increase of 0.5 mm from 6 to 9.5 mm resulted the resonance shifting slightly downwards. The value of 8.5 mm for W_M was confirmed as optimum.

4. CONCLUSIONS

A light-weight and simple monopole antenna prototype using conductive textile material suited for BCWC applications is presented and discussed in this paper. The result demonstrated the wearable textile monopole produced higher reflection coefficient value, with a reasonable gain compared to the conventional monopole antenna. Besides, variations on the length and width of top radiator affect the resonance frequency of the textile monopole, while the variations on the length of ground plane affects significantly reflection coefficient of the textile monopole. The simulated results exhibited that the textile monopole is able to operate like a conventional monopole antenna in free space.

ACKNOWLEDGMENT

This work is partially supported by the Short Term Grant (STG) scheme Universiti Malaysia Perlis, under grant 9001-00436 and Knowledge Transfer Programme Grant, grant No. 9011-00003, under Ministry of Higher Education (MOHE). The authors would like to express their highest gratitude to Universiti Malaysia Perlis and MOHE.

REFERENCES

1. Soh, P. J., G. A. E. Vandenbosch, S. L. Ooi, and M. R. N. Husna, "Wearable dual-band Sierpinski fractal PIFA using conductive fabric," *Electronics Lett.*, Vol. 47, No. 6, 2011.
2. Locher, I., M. Klemm, T. Kirstein, and G. Troster, "Design and characterization of purely textile patch antennas," *IEEE Trans. on Advanced Packaging*, Vol. 29, No. 4, 777–788, 2006.
3. Nechayev, Y. I., P. S. Hall, I. Khan, and C. C. Constantinou, "Wireless channels and antennas for body-area networks," *Proceedings of 2010 Seventh International Conference on Wireless On-demand Network Systems and Services (WONS)*, 137–144, Kranjska Gora, Germany, February 2010.
4. Mantash, M., A. C. Tarot, S. Collardey, and K. Mahdjoubi, "Wearable monopole zip antenna," *Electronics Lett.*, Vol. 47, No. 23, 1–2, 2011.
5. Data available at www.cst.com.
6. Balanis, C. A., *Antenna Theory Analysis and Design*, Wiley-Interscience, New Jersey, 2005.

An Interpretation of a Classical Diffraction Problem of Electromagnetism with a Fractional Derivative

P. Vaudon

Xlim, Mixt Research Unit CNRS, University No. 6172
123 rue Albert Thomas, Limoges 87000, France

Abstract—We propose to show that the formalism using fractional derivatives is adequate to derive some calculations of diffracted fields. First, we analyze the derivative of the e^{jx} function to the fractional order $-1/2$, then we show that the FRESNEL integral may be expressed in terms of this fractional derivative: this allows to give an original formulation of the edge diffracted field. We conclude with a non-integer equation, from which the diffracted field is solution.

1. THE DERIVATIVE OF ORDER $-1/2$ OF THE FUNCTION e^{jx}

A very important set of propagation phenomena is described with the help of sinusoidal functions, or, in the associated formalism, with complex exponential functions as $\exp(jx)$.

We propose to show that the derivative of order $-1/2$ of this function may be expressed with a complex FRESNEL function. This last one plays a fundamental role in many optical problems, and also in many microwave problems of diffraction. This will lead us to express, in the next section, the edge diffracted field as a function of a non integer derivative.

Starting with the definition given by LIOUVILLE [2]:

$${}_a D_x^{-\alpha} f(x) = \frac{1}{\Gamma(\alpha)} \int_a^x f(t)(x-t)^{\alpha-1} dt \quad (1)$$

We obtain, after a variable change, for the function $\exp(jx)$:

$$D_x^{-\frac{1}{2}}(e^{jx}) = \frac{e^{jx}}{\sqrt{\pi}} \int_0^{\sqrt{x}} \frac{e^{-j\tau^2}}{\tau} \cdot 2\tau d\tau = \frac{2e^{jx}}{\sqrt{\pi}} \int_0^{\sqrt{x}} e^{-j\tau^2} d\tau \quad (2)$$

Equation (2) shows very clearly the link between the derivative of order $-1/2$ of the function $\exp(jx)$ and the complex FRESNEL function as it is described for example by CLEMMOW in reference [1] (Eq. 3.41).

2. AN EXPRESSION OF THE EDGE DIFFRACTED FIELD WITH A FRACTIONAL DERIVATIVE

We propose to show, in this section, that the total field surrounding a perfectly conducting edge upon which falls a plane wave may be expressed in a simple manner, by using the notion of fractional derivative.

The Figure 1 indicates the parameters which take place in such a situation. ϕ_0 represents the incidence angle of the plane wave which is supposed to be in magnetic polarization.

The point P is the observation point for the total field. It is located at a distance ρ from the edge and its direction makes an angle ϕ with the plane screen. The analytical solution of this problem

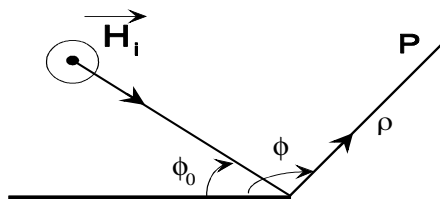


Figure 1: Representation of a plane wave falling on a half screen.

has been given by SOMMERFELD and may be presented under the following formula:

$$H_{TOTAL} = Y \left[\cos \frac{\phi - \phi_0}{2} \right] \cdot e^{jk\rho \cos(\phi - \phi_0)} - \operatorname{sgn} \left(\cos \frac{\phi - \phi_0}{2} \right) K_- \left\{ \sqrt{2k\rho \cos^2 \frac{\phi - \phi_0}{2}} \right\} e^{-jk\rho} \\ + Y \left[\cos \frac{\phi + \phi_0}{2} \right] \cdot e^{jk\rho \cos(\phi + \phi_0)} - \operatorname{sgn} \left(\cos \frac{\phi + \phi_0}{2} \right) K_- \left\{ \sqrt{2k\rho \cos^2 \frac{\phi + \phi_0}{2}} \right\} e^{-jk\rho} \quad (3)$$

where Y represents the HEAVYSIDE step and $K_-(x)$ a particular form of the FRESNEL integral:

$$K_-(x) = \frac{\sqrt{j}}{\sqrt{\pi}} \cdot e^{jx^2} \int_x^\infty e^{-j\tau^2} d\tau \quad (4)$$

If we want to establish the link between the relation (3) and the fractional derivative of the function $\exp(jx)$, we must first express the $K_-(x)$ function with this derivative:

From Equation (2), we obtain:

$$D_x^{-1/2}(e^{jx}) = \frac{1}{\sqrt{j}} \{e^{jx} - 2K_-(\sqrt{x})\} \quad (5)$$

By using a classical property of any derivative, and by recalling that x is a positive real, the relation (5) becomes:

$$D_{jx}^{-1/2}(e^{jx}) = e^{jx} - 2K_-(\sqrt{x}) \quad (6)$$

or, as an equivalent relation:

$$K_-(\sqrt{x}) = \frac{1}{2} \{e^{jx} - D_{jx}^{-1/2}(e^{jx})\} \quad (7)$$

We only need to introduce this result in the expression of the total field (3) to obtain after reduction:

$$H_{TOTAL} = \frac{e^{-jk\rho}}{2} \left\{ e^{jx} + \operatorname{sgn} \left(\cos \frac{\phi - \phi_0}{2} \right) \cdot D_{jx}^{1/2}(e^{jx}) \right\}_{x = 2k\rho \cos^2 \frac{\phi - \phi_0}{2}} \\ + \frac{e^{-jk\rho}}{2} \left\{ e^{jx} + \operatorname{sgn} \left(\cos \frac{\phi + \phi_0}{2} \right) \cdot D_{jx}^{-1/2}(e^{jx}) \right\}_{x = 2k\rho \cos^2 \frac{\phi + \phi_0}{2}} \quad (8)$$

The value of x which appears in this relation is the classical one which is used in the uniform asymptotic theory. It is sometimes called the detour parameter because of its physical significance.

By observing that:

$$2k\rho \cos^2 \left(\frac{\phi - \phi_0}{2} \right) = k\rho + k\rho \cos(\phi - \phi_0) \quad (9)$$

We can remark that the detour parameter is equal to the phase of the incident wave at the observation point ($k\rho \cos(\phi - \phi_0)$) added with the detour phase due to the propagation from the edge towards the point P, that is to say $k\rho$. More details may be found in [3].

It is now possible to retrieve some characteristics features of the diffracted field. Particularly, on the shadow and light boundaries ($x = 0$), the fractional derivative is equal to zero, which gives the corresponding term equal to $\frac{e^{-jk\rho}}{2}$, that is to say the half of the incident or reflected field, as an expected result.

We have made a numerical verification of the relation (8). We have substituted the operator $D_{jx}^{-\frac{1}{2}}(e^{jx})$ with the operator $\sqrt{j}D_x^{-\frac{1}{2}}(\cos(x) + j \sin(x))$ to allow a computation on real variables.

A particular care must be brought to the numerical analysis, in order to treat correctly the divergence of the function $(x - t)^{-1/2}$ which appears as t tends to x . In a general case, we have to compute the following integral:

$$\int_0^x \frac{f(t)}{\sqrt{x - t}} dt \quad (10)$$

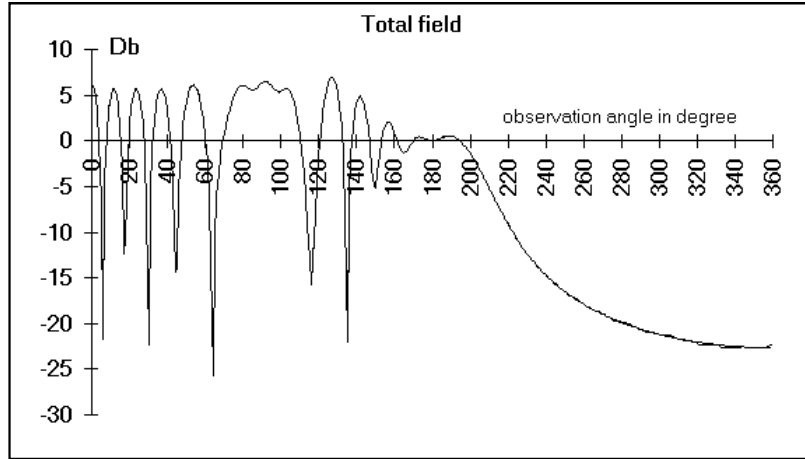


Figure 2: Representation of the total field surrounding an edge at a fixed distance versus the direction of the observation point. Incidence angle: 30° — Magnetic polarization — Distance of the observation point: 5λ . - - - -: Computed with the FRESNEL integral (Eq. (3)). ———: Computed with the fractional derivative (Eq. (8)).

On a numerical point of view, the difficulty occurs when t approaches to x . If we call s the numerical step of integration, the part of (10) which cannot be evaluated by a numerical method is:

$$\int_{x-s}^x \frac{f(t)}{\sqrt{x-t}} dt \quad (11)$$

Assuming that $f(t)$ is slowly varying in the small interval between $x-s$ and x , (which is the case in this paper), we put $f(t)$ as a constant equal to $f(x-s/2)$ and we obtain:

$$\int_{x-s}^x \frac{f(t)}{\sqrt{x-t}} dt \approx 2\sqrt{s} \cdot f\left(x - \frac{s}{2}\right) \quad (12)$$

The results presented on figure 2 show a perfect agreement with those obtained with an exact solution computed with the complex FRESNEL integral.

3. INTRODUCTION OF A NON-INTEGER DIFFERENTIAL EQUATION

The total field as given by Equation (8) may be clearly divided in two parts: the first part expressed with the factor $\cos((\phi - \phi_0)/2)$ is associated to the incident field, whereas the second part, associated with the factor $\cos((\phi + \phi_0)/2)$ is linked to the reflected field.

In the two cases, the function of x which answers to the problem may be written in the following manner

$$y(x) = \frac{1}{2} \left\{ e^{jx} \pm D_{jx}^{-\frac{1}{2}}(e^{jx}) \right\} \quad (13)$$

In the relation (13), the sign $+$ and $-$ is linked to the relative position of the observation point. If this point is in the lighted area, the sign $+$ is valid; if this point is in the shadow area, we must use the sign $-$.

By applying a derivation of order $-1/2$ to each member of the equality, we obtain:

$$D_{jx}^{-\frac{1}{2}}(y(x)) = \frac{1}{2} \left(D_{jx}^{-\frac{1}{2}}(e^{jx}) \pm D_{jx}^{-\frac{1}{2}} D_{jx}^{-\frac{1}{2}}(e^{jx}) \right) \quad (14)$$

The right term, in which we found two successive derivations, may be condensed by using the addition rule of the fractional operator [4]:

$$D_{jx}^{-\frac{1}{2}} \cdot D_{jx}^{-\frac{1}{2}}(e^{jx}) = D_{jx}^{-1}(e^{jx}) = e^{jx} - 1 \quad (15)$$

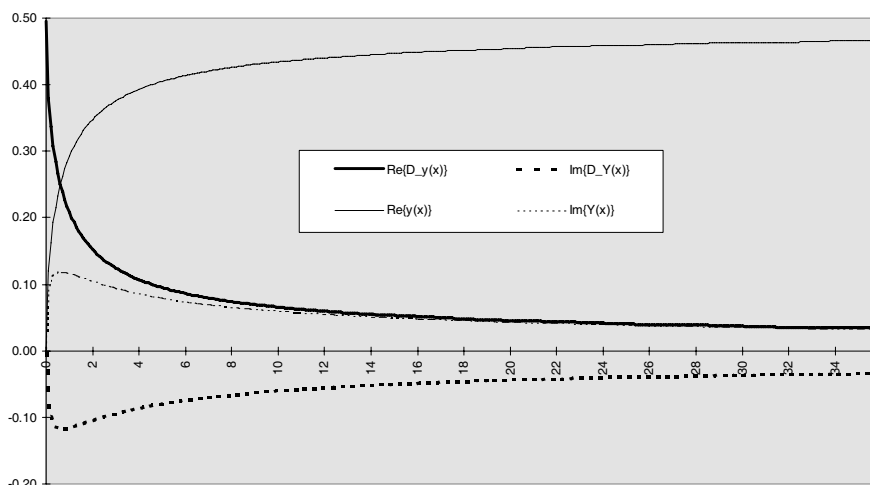


Figure 3: Numerical verification of the relation $D_{jx}^{-\frac{1}{2}}(y(x)) = -y(x) + \frac{1}{2}$ (shadow area).

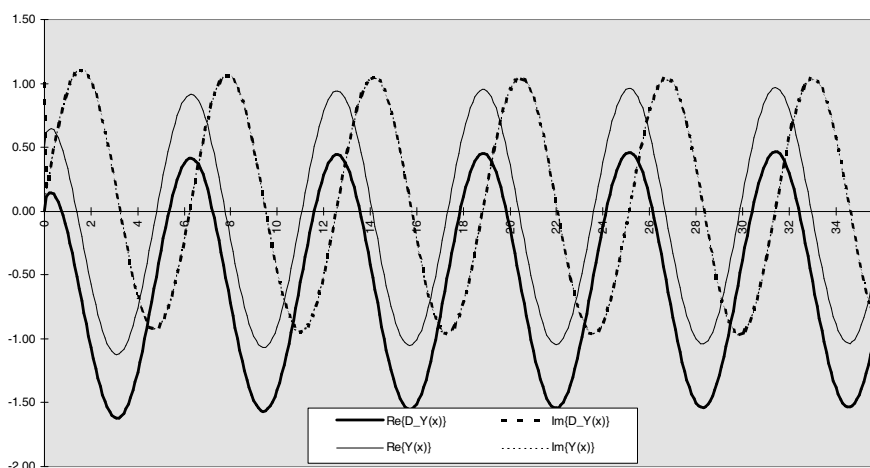


Figure 4: Numerical verification of the relation $D_{jx}^{-\frac{1}{2}}(y(x)) = y(x) - \frac{1}{2}$ (lighted area).

Thus, we found, for Equation (14):

$$D_{jx}^{-\frac{1}{2}}(y(x)) = \frac{1}{2} \left\{ D_{jx}^{-\frac{1}{2}}(e^{jx}) \pm (e^{jx} - 1) \right\} \quad (16)$$

A comparison with Equation (13) shows that the function which describes the total field $y(x)$, verifies a very simple differential equation:

$$D_{jx}^{-\frac{1}{2}}(y(x)) = \pm y(x) \mp \frac{1}{2} \quad (17)$$

where the signs $+$ and $-$ have the same interpretation as in the relation (13). We have made a numerical verification of this last relation which is reported on the Figures 3 and 4. As an expected result, the curves are smoothly varying in the shadow area (Figure 3), showing that the diffracted field decreases smoothly; and are oscillating in the lighted area (Figure 4), showing the interferences between the incident and the reflected field. Such a behavior is also in agreement with a study on generalized fractional differential systems presented in reference [5].

4. CONCLUSION

We have tried to show that a well known problem of diffraction may be presented by using the notion of fractional derivative. This new formulation appears as a function of two very useful tools in electromagnetic diffraction problems: the complex FRESNEL integral, and the Detour

parameter. We have proved that the function which describes the total field is solution of a very simple differential equation to the order $-1/2$.

Furthermore, we know that the FRESNEL integral plays a fundamental role in all asymptotic formulations of the diffracted field by a wedge [6]. We think that this formalism may be useful to present and to highlight the asymptotic theories of diffraction under a new point of view.

REFERENCES

1. Clemmow, P. C., *The Plane Wave Spectrum Representation of Electromagnetic Fields*, Pergamon Press, 1966.
2. Liouville, J., “Mémoire sur l’intégration des équations différentielles à indices fractionnaires,” *J. Ecole Polytech.*, Vol. 13, No. 25, 58–84, 1873.
3. Lee, S. W. and G. A. Deschamps, “A uniform asymptotic theory of electromagnetic diffraction by a curved edge,” *IEE Transactions on Antenna and Propagation*, Vol. 24, No. 1, 1976.
4. Miller, K. S. and B. Ross, *An Introduction to the Fractional Calculus and Fractional Differential Equations*, John Wiley & Sons, 1993.
5. Matignon, D., “Stability properties for generalized fractional differential systems,” *ESAIM Proceedings*, No. 5, 145–148, 1998.
6. Vaudon, P., B. Jecko, and A. Reineix, “Asymptotic formulations for the wedge diffracted field,” *Microwave and Optical Technology Letters*, Vol. 5, No. 12, 649–653, 1992.

Gradient Index Metamaterial with Arbitrary Loss Factors in RHM and LHM Media: The Case of Constant Impedance throughout the Structure

M. Dalarsson¹, M. Norgren¹, T. Asenov², and N. Dončov²

¹Division of Electromagnetic Engineering, School of Electrical Engineering
Royal Institute of Technology, Stockholm SE-100 44, Sweden

²Faculty of Electronic Engineering, University of Niš, Niš 18000, Serbia

Abstract— The transmission and reflection properties of lossy structures involving left-handed materials with graded permittivity and permeability have been investigated. We present an exact analytical solution to Helmholtz' equation for a lossy case with the graded both real and imaginary parts of permittivity and permeability profile changing according to a hyperbolic tangent function along the direction of propagation. This allows for different loss factors in the two media. The expressions and graphical results for the field intensity along the graded structure are presented. The analytical solution is validated by a dispersive numerical model of lossy metamaterials that uses a transmission line matrix method based on Z-transforms, where a close agreement between the analytic and numerical results is obtained.

1. INTRODUCTION

Electromagnetic metamaterials (MM) in electromagnetics and (nano) plasmonics are defined as artificial composites with electromagnetic properties not readily found in nature. A special class of MMs are the negative refractive index metamaterials (NRM or NIM), also known as the left-handed materials (LHM). They were theoretically described by Veselago in 1967 [1], but about three decades passed before their practical implementations were proposed by Pendry [2, 3].

LHM are typically produced using subwavelength “particles” or “atoms” with negative effective relative permittivity and permeability as their structural units. The first proposed LHM particles were split-ring resonators and nanowires, their composites simultaneously furnishing negative permeability and permittivity [3]. Split-ring resonators and wire media are still widely used in the microwave domain and are now well understood, but many other particles such as complementary split-ring resonators [4], cut-wire pairs and plate pairs [5] and double fishnets [6–8] have been investigated. The first experimental confirmation of a left-handed material was published in 2001 [9]. Until today, experimental fishnet-type LHM for the visible range have been fabricated and described [10].

The novel and often counter-intuitive properties of the LHM, which include negative index of refraction (and, hence, negative phase velocity), inverse Doppler effect, radiation tension instead of pressure, etc. [11, 12] resulted in numerous proposed applications. These applications include superlenses and hyperlenses that enable imaging far below the diffraction limit [13, 14], resonant cavities and waveguides with geometrical dimensions even orders of magnitude smaller than the operating wavelength [15], as well as invisibility cloaks and transformation optics [16].

A majority of cases consider structures with constant refractive index within the MM structure and abrupt interfaces with the surrounding positive index material (“right-handed” media, RHM). There is however a practical interest for metamaterials with spatially varying refractive index and with gradual transition from the RHM to LHM and vice versa, since many real-world applications would benefit from such structures. Graded refractive index is interesting for transformation optics and hyperlenses [17], and a class of the invisibility cloaks using spherically graded MM has been described [18]. Various other proposed applications of graded metamaterials include beam shaping and directing, enhancement of nonlinear effects [19], superlenses [20], etc..

As far as the authors are informed, the first paper dedicated to gradient refractive index LHM was published in 2005 [21]. Analytical approaches to graded index metamaterial structures are of special interest, since they ensure fast, simple and direct routes to the determination of the field distribution and the calculation of the scattering parameters within such materials. Some publications include [22–28].

In the present paper, we present an exact analytical solution of Helmholtz' equation for the propagation of electromagnetic waves through a lossy graded metamaterial structure, where both

the permittivity and the permeability vary according to a hyperbolic tangent function. We offer the most general case of lossy wave propagation with constant impedance throughout the entire structure, where loss factors can be chosen arbitrarily in both RHM and LHM media. This provides the opportunity to model the significantly higher losses in LHM materials compared to those in the RHM materials.

In addition to that, a numerical model, developed in [29] by using the Transmission Line Matrix (TLM) method based on Z -transforms [30] and capable to take into account the dispersive properties of metamaterials in the time-domain, is presented here and compared with the analytically obtained solutions.

2. PROBLEM FORMULATION

We assume the time-harmonic waves with an $\exp(-i\omega t)$ dependency in isotropic materials, where the effective medium approximation is valid. The geometry of the problem is illustrated in Fig. 1. The electric field is directed along the y -axis, $\vec{E}(\vec{r}) = E(x)\vec{e}_y$, whereas the magnetic field is directed along the z -axis, $\vec{H}(\vec{r}) = H(x)\vec{e}_z$. The propagation direction of the wave is along the x -axis. Since the fields depend only on the x -coordinate, the one-dimensional Helmholtz' equations have the form [24]

$$\frac{d^2 E}{dx^2} - \frac{1}{\mu} \frac{d\mu}{dx} \frac{dE}{dx} + \omega^2 \mu \epsilon E(x) = 0, \quad \frac{d^2 H}{dx^2} - \frac{1}{\epsilon} \frac{d\epsilon}{dx} \frac{dH}{dx} + \omega^2 \mu \epsilon H(x) = 0, \quad (1)$$

where $\epsilon = \epsilon(\omega, x)$ and $\mu = \mu(\omega, x)$ are the frequency-dependent and stratified dielectric permittivity and magnetic permeability, respectively.

3. SOLUTIONS OF THE FIELD EQUATIONS

We assume an inhomogeneous medium for which the effective permittivity and permeability vary according to following hyperbolic tangent functions

$$\mu(\omega, x) = -\mu_0 \mu_R \tanh(\rho x) - i\mu_0 \left[\frac{\mu_{I1} + \mu_{I2}}{2} - \frac{\mu_{I1} - \mu_{I2}}{2} \tanh(\rho x) \right], \quad (2)$$

$$\epsilon(\omega, x) = -\epsilon_0 \epsilon_R(\omega) \tanh(\rho x) - i\epsilon_0 \left[\frac{\epsilon_{I1} + \epsilon_{I2}}{2} - \frac{\epsilon_{I1} - \epsilon_{I2}}{2} \tanh(\rho x) \right], \quad (3)$$

where ρ is a parameter describing the steepness of the transition from the RHM material at $x < 0$ to the LHM material at $x > 0$. For passive materials, we require $\epsilon_{I1}, \epsilon_{I2} > 0$ and $\mu_{I1}, \mu_{I2} > 0$. A constant wave impedance throughout the structure, requires that the real and imaginary parts of the effective permittivity and permeability satisfy the condition

$$\beta(\omega) = \frac{\mu_{I1} + \mu_{I2}}{2\mu_R - i(\mu_{I1} - \mu_{I2})} = \frac{\epsilon_{I1} + \epsilon_{I2}}{2\epsilon_R - i(\epsilon_{I1} - \epsilon_{I2})}. \quad (4)$$

When the condition (4) is satisfied, we have

$$\mu(\omega, x) = -\mu_0 \frac{\mu_{I1} + \mu_{I2}}{2\beta} (\tanh(\rho x) + i\beta), \quad \epsilon(\omega, x) = -\epsilon_0 \frac{\epsilon_{I1} + \epsilon_{I2}}{2\beta} (\tanh(\rho x) + i\beta), \quad (5)$$

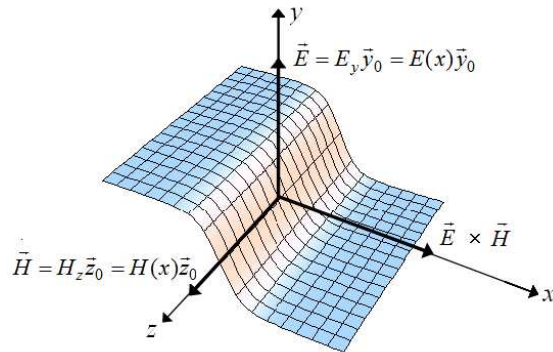


Figure 1: Propagation of a wave through a graded index structure with a hyperbolic tangent profile.

Note that the wave impedance $Z = Z_0 Z(\omega) = \sqrt{\mu(\omega, x)/\epsilon(\omega, x)}$ is constant throughout the entire structure and there is no reflection on the graded interface between the two materials. The two differential Equations (1) have the exact solutions

$$E(x) = E_0 e^{-\kappa\beta x} [2 \cosh(\rho x)]^{i\frac{\kappa}{\rho}}, \quad H(x) = H_0 e^{-\kappa\beta x} [2 \cosh(\rho x)]^{i\frac{\kappa}{\rho}}, \quad (6)$$

where E_0 and H_0 are the amplitudes of the electric and magnetic fields at the boundary $x = 0$, and

$$\kappa = k + i\alpha = \frac{\omega}{c} \sqrt{\mu_R \epsilon_R} + i \frac{\omega}{2c} \sqrt{\frac{\epsilon_R}{\mu_R}} (\mu_{I2} - \mu_{I1}), \quad (7)$$

We note that in the absence of losses, the results (6) are reduced to the results in reference [24] as a special case. The field amplitudes are related by $E_0 = Z_0 Z(\omega) H_0$. The exact solutions (6) are valid for arbitrary steepness ρ of the graded index interface and arbitrary losses. In the RHM material, we obtain for $x \rightarrow -\infty$

$$E(x, t) \sim E_0 e^{-\gamma_1 x} \cos(\omega t - kx), \quad H(x, t) \sim H_0 e^{-\gamma_1 x} \cos(\omega t - kx), \quad \gamma_1 = \frac{\omega}{c} \sqrt{\frac{\epsilon_R}{\mu_R}} \mu_{I1} \quad (8)$$

In the LHM material, we obtain for $x \rightarrow +\infty$ that

$$E(x, t) \sim E_0 e^{-\gamma_2 x} \cos[\omega t - (-k)x], \quad H(x, t) \sim H_0 e^{-\gamma_2 x} \cos[\omega t - (-k)x], \quad \gamma_2 = \frac{\omega}{c} \sqrt{\frac{\epsilon_R}{\mu_R}} \mu_{I2} \quad (9)$$

For $x \rightarrow -\infty$, it follows (8) that the wave in the RHM with the wavevector $\vec{k}_{RHM} = +k\vec{e}_x$ propagates in the $+x$ -direction. For $x \rightarrow +\infty$, it follows (9) that the wave in the LHM with wavevector $\vec{k}_{LHM} = -k\vec{e}_x$ propagates in the $-x$ -direction. The energy flux (the Poynting vector) is still in the $+x$ -direction in both media as expected.

4. DISPERSIVE TLM Z-TRANSFORM MODEL OF METAMATERIALS

A dispersive TLM Z-transform model of the MTM is described in [29], and here we present it in a more general form through a signal flow diagram. The same form was used in [30] to present the general scattering and connecting process algorithm of Z-transform-based TLM approach, shown in Fig. 2(a), in which this dispersive numerical model is implemented.

Details of the inclusion into the 3D TLM method of the Z-transform models, developed for various types of conventional time-dependent materials, as well as the expressions for vectors and matrices from Fig. 2(a) are given in [30]. Drude model for electric and magnetic susceptibilities is used. The complete description of each block in Figs. 2(b)–(c) can be found in [29].

5. GRAPHICAL PRESENTATION AND DISCUSSION OF THE RESULTS

A comparison between the exact analytical solutions for the electric field $E(x)$, given by Eq. (6) with the corresponding numerical results obtained by means of the dispersive TLM Z-transform model,

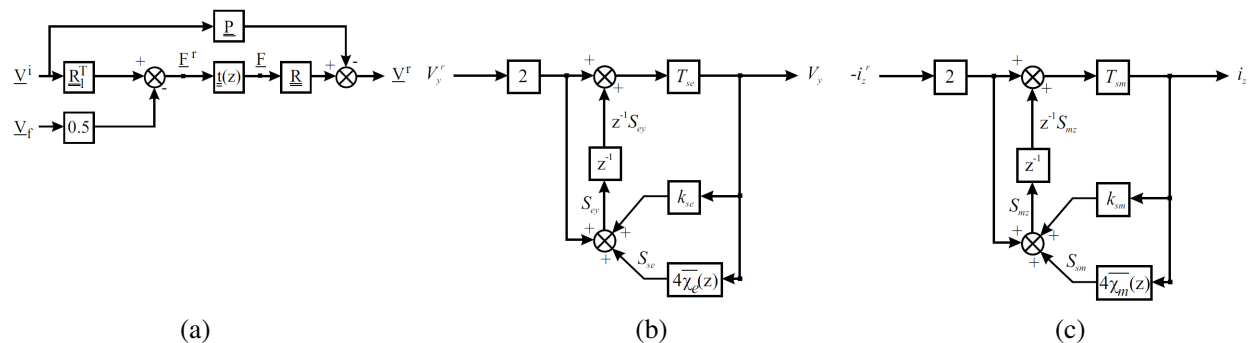


Figure 2: (a) Signal flow diagram of the general algorithm of TLM method based on Z-transform [30]. (b) Dispersive TLM Z-transform model for metamaterials — calculation of E_y in the time-domain. (c) Dispersive TLM Z-transform model for metamaterials — calculation of H_z in the time-domain.

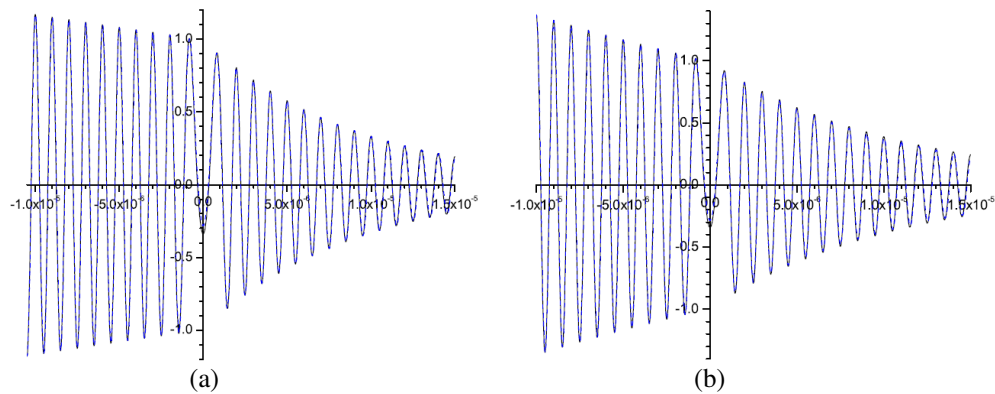


Figure 3: Numerical results (blue dash line) vs analytical results (black solid line) for electric field $E(x)$ as a function of x , with $E_0 = 1$, $k = 2\pi/(10^{-6} \text{ m})$, $\rho = 1/(10^{-6} \text{ m})$, $\kappa\beta = 2\pi/(10^{-4} \text{ m})$ as well as (a) $\alpha = 0.75\kappa\beta$ and (b) $\alpha = 0.50\kappa\beta$.

for two different values of the numerical parameters are presented in Fig. 3. From Fig. 3, we see that the numerical and analytical results show an excellent agreement with each other. Furthermore, we see that there is no reflection at the interface between RHM and LHM, as expected, since the impedance is constant throughout the entire space. However we see that the loss factors γ_1 and γ_2 in RHM and LHM respectively are different.

6. CONCLUSION

An exact analytical solution to lossy Helmholtz' equations with graded profile, changing according to a hyperbolic tangent function along the direction of propagation, is presented. The expressions and graphical results for the field intensities along the graded structure have been presented. The model allows for arbitrary temporal dispersion and arbitrary loss factors.

In addition to that, the enhanced Z-transform based TLM method which enables the direct time-domain modelling of lossy metamaterials has been presented. The accuracy and stability of the model were demonstrated for the gradient transitions of effective electromagnetic parameters for which analytical solutions were presented in this paper. The model can be easily adapted to describe Lorentz or higher-order material responses and is generally usable to arbitrary gradient metamaterial profiles.

ACKNOWLEDGMENT

The work of T.A. and N.D. was funded by the Serbian Ministry of Science and Technology within the project TR-32024.

REFERENCES

1. Veselago, V. G., *Sov. Phys. Uspekhi*, No. 10, 509–514, 1968.
2. Pendry, J. B., A. J. Holden, D. J. Robbins, and W. J. Stewart, *J. Phys. Condens. Mat.*, No. 10, 4785–4809, 1998.
3. Pendry, J. B., A. J. Holden, D. J. Robbins, and W. J. Stewart, *IEEE T. Microw. Theory*, No. 47, 2075–2084, 1999.
4. Falcone, F., T. Lopetegui, M. A. G. Laso, J. D. Baena, J. Bonache, M. Beruete, F. Martiacute, and M. Sorolla, *Phys. Rev. Lett.*, No. 93, 197401, 2004.
5. Dolling, G., C. Enkrich, M. Wegener, J. F. Zhou, C. M. Soukoulis, and S. Linden, *Opt. Lett.*, No. 30, 3198–3200, 2005.
6. Zhang, S., W. Fan, N. C. Panoiu, K. J. Malloy, R. M. Osgood, and S. R. J. Brueck, *Phys. Rev. Lett.*, No. 95, 1–4, 2005.
7. Kafesaki, M., I. Tsiapa, N. Katsarakis, T. Koschny, C. M. Soukoulis, and E. N. Economou, *Phys. Rev. B*, No. 75, 235114, 2007.
8. Valentine, J., S. Zhang, T. Zentgraf, E. Ulin-Avila, D. A. Genov, G. Bartal, and X. Zhang, *Nature*, No. 455, 376–379, 2008.
9. Shelby, R. A., D. R. Smith, and S. Schultz, *Science*, No. 292, 77–79, 2001.

10. Xiao, S., U. K. Chettiar, A. V. Kildishev, V. P. Drachev, and V. M. Shalaev, *Opt. Lett.*, No. 34, 3478–3480, 2009.
11. Cai, W. and V. Shalaev, *Optical Metamaterials: Fundamentals and Applications*, Springer, Dordrecht, 2009.
12. Ramakrishna, S. A. and T. M. Grzegorzczuk, *Physics and Applications of Negative Refractive Index Materials*, SPIE Press Bellingham, WA & CRC Press, Taylor & Francis Group, Boca Raton, FL, 2009.
13. Pendry, J. B., *Phys. Rev. Lett.*, No. 85, 3966–3969, 2000.
14. Fang, N., H. Lee, C. Sun, and X. Zhang, *Science*, No. 308, 534–537, 2005.
15. Engheta, N., *IEEE Anten. Wirel. Propag. Lett.*, No. 1, 10–13, 2002.
16. Pendry, J. B., D. Schurig, and D. R. Smith, *Science*, No. 312, 1780–1782, 2006.
17. Jacob, Z., L. V. Alekseyev, and E. Narimanov, *Opt. Express*, No. 14, 8247–8256, 2006.
18. Cai, W., U. K. Chettiar, A. V. Kildishev, and V. M. Shalaev, *Nat. Photonics*, No. 1, 224–227, 2007.
19. Fung, T. H., L. L. Leung, J. J. Xiao, and K. W. Yu, *Opt. Commun.*, No. 282, 1028–1031, 2009.
20. Ramakrishna, S. A. and J. B. Pendry, *Phys. Rev. B*, No. 69, 115115, 2004.
21. Smith, D. R., J. J. Mock, A. F. Starr, and D. Schurig, *Phys. Rev. E*, No. 71, 036609, 2005.
22. Pinchuk, A. O. and G. C. Schatz, *J. Opt. Soc. Am. A*, No. 24, A39–A44, 2007.
23. Litchinitser, N. M., A. I. Maimistov, I. R. Gabitov, R. Z. Sagdeev, and V. M. Shalaev, *Opt. Lett.*, No. 33, 2350–2352, 2008.
24. Dalarsson, M. and P. Tassin, *Opt. Express*, No. 17, 6747–6752, 2009.
25. Dalarsson, M., Z. Jakšić, and P. Tassin, *J. Optoelect. Biomed. Mat.*, No. 1, 345–352, 2009.
26. Dalarsson, M., Z. Jakšić, and P. Tassin, *Microwave Rev.*, No. 15, 1–5, 2009.
27. Dalarsson, M., M. Norgren, and Z. Jakšić, *J. Nanophoton.*, No. 5, 051804, 2011.
28. Dalarsson, M., M. Norgren, and Z. Jakšić, *Microwave Rev.*, No. 17, 1–6, 2011.
29. Dončov, N., B. Milovanović, T. Asenov, and J. Paul, *Microwave Rev.*, No. 16, 2–7, 2010.
30. Paul, J., C. Christopoulos, and D. W. P. Thomas, *IEEE Trans. Antennas and Propag.*, No. 47, 1528–1542, 1999.

A Dual Band Planar Metamaterial Based on Hybrid Structures in Terahertz Regime

S. Hussain^{1,2}, J. Y. Lee^{1,2}, and J. H. Jang^{1,2}

¹School of Information and Communications

Gwangju Institute of Science and Technology, Gwangju 500-712, South Korea

²WCU Department of Nano-Bio Materials and Electronics

Gwangju Institute of Science and Technology, Gwangju 500-712, South Korea

Abstract— The design of a planar dual-band metamaterial, based on the magnetically resonant ring and electrically resonant plus shaped strip structures, in terahertz frequencies is presented. The advantages of the metamaterial are (a) dual band behaviour that comes from the individual resonance of each structure (b) structural symmetry of the ring shape brings about polarization independency for the first resonance and plus shaped structure, responsible for the second resonance, is insensitive to x - y polarization. We have also shown that by using an ultra-thin substrate, a wide band response may be obtained. Our planar metamaterial is easy to fabricate, insensitive to the minute fabrication misalignments and furnishes a simple way to realize a metamaterial that may be used in terahertz filter applications.

1. INTRODUCTION

Artificial media or metamaterials have been a topic of great discussion among researchers since Veselgo, in 1968, proposed such materials which may have negative values of electric permittivity ϵ and magnetic permeability μ . He also explained the behaviour of electromagnetic waves in such materials with the help of Maxwell's equations [1]. It was until 1999 that these metamaterials were not noticed inadvertently because of the unavailability of such materials in nature when Smith, at University of California at San Diego, showed that such artificial media may be realized with a simple wire-ring medium [2, 3]. The ring structure contributes to the negative μ and the wire structure contributes to negative ϵ values. The possibility of fabricating such materials leads to a new area in the field of electromagnetics and opened the gateway to numerous potential applications like perfect lens [4], invisible cloak [5], electronic band gap structures (EBG) [6], filters [7], absorbers [8] and many more.

The frequency band which has recently grabbed the attention is terahertz (THz) frequency band because of the scarcity of most of the electronic devices operating in this band. Terahertz frequency band, where an electronic transistor encounters technical limitations like low mobility, high resistivity, etc. and the lower end optical devices are unable to operate, needs to be filled in to get the possible advantages of these frequencies. THz radiations are non-destructive and highly penetrating into non conducting materials. Electromagnetic metamaterials seem to be promising in THz regime, where the unit cell dimensions are usually in micrometres, which may be employed to construct such devices. Filters, absorbers, modulators operating in terahertz band based on electromagnetic metamaterials have been reported recently [9–12].

In this paper, we have focussed on the basic structures to realize a planar dual-band metamaterial that operates in two frequency bands. The renowned ring structure resonates at the lower frequency whereas the plus shaped structure lying within the ring resonates at the higher frequency. The merits of the proposed design are polarization independence and ultra-low loss which may be achieved by fabricating the proposed structure on the thin membrane [13]. The proposed structure may be used in the filters or absorber applications in terahertz spectrum.

2. DESIGN AND SIMULATION

The proposed structure is shown in Figure 1(a). The design of the proposed structure is very simple and follows the Eq. (1).

$$L = \frac{\lambda_0}{2\sqrt{\epsilon_{eff}}} \quad (1)$$

The final dimensions were optimized using the numerical simulator engine. The optimized values for l , r and w were $36 \mu\text{m}$, $24 \mu\text{m}$ and $3 \mu\text{m}$ respectively. Unit cell dimensions were optimized to $62 \mu\text{m}$ on each side. Thickness of the metallic strips was taken to be 300 nm . The ring structure

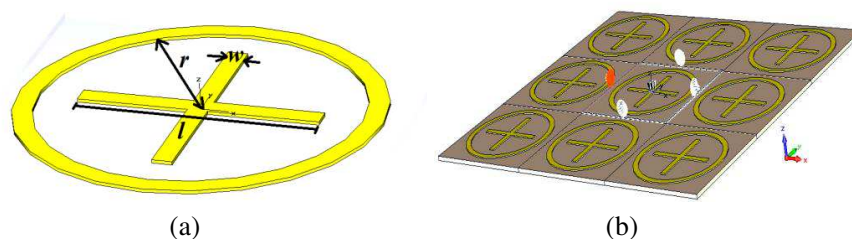


Figure 1: (a) Unit cell of the proposed metamaterial. (b) Metamaterial surface is shown on an ultra-thin GaAs substrate of thickness $2\ \mu\text{m}$.

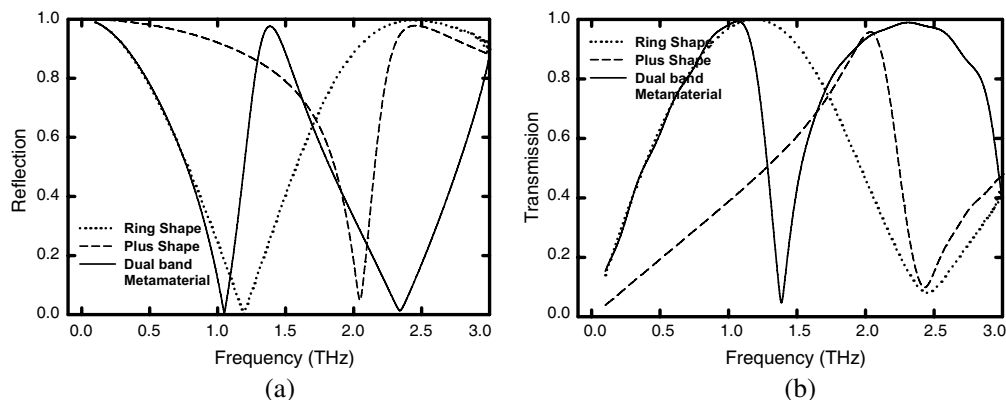


Figure 2: (a) Transmission characteristic of the individual ring shaped structure, plus shaped structure and their combination is shown for the substrate thickness of $2\ \mu\text{m}$. (b) Reflection characteristic of the dual band metamaterial fabricated on the substrate thickness of $2\ \mu\text{m}$.

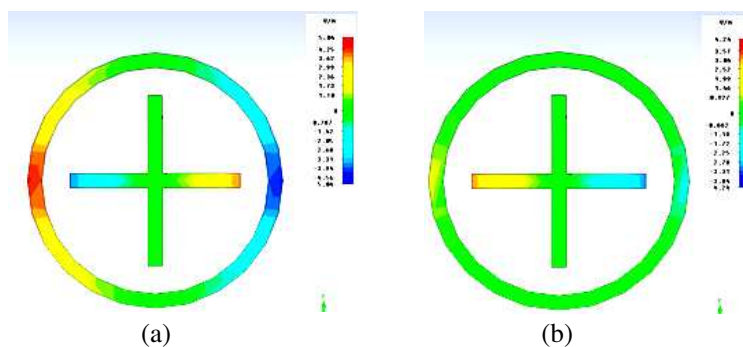


Figure 3: (a) Electric field distribution at the first resonance frequency of 1.05 THz. (b) Electric field distribution at the second resonance frequency of 2.43 THz.

may also be considered as a sub-wavelength structure and its circumference was also determined by Eq. (1). Numerical simulation for the dual-band metamaterial was performed using a commercial simulation engine CST Microwave Studio that solves the given 3D electromagnetic problem using Finite Difference Time Domain Method (FDTD). Time based computational method was preferred since we could limit the time window, i.e., ignore the effect of late arrival pulses in the computed results.

Simulation model included the unit cell fabricated on lossy GaAs substrate (ϵ_R : 12.94 and $\tan \delta$: 0.006). Periodic boundary condition was applied on the sides to realize a practical situation where there are hundreds of unit cell on a $2\ \text{mm} \times 2\ \text{mm}$ sample. The metamaterial unit cell was excited using a plane wave source on one side with electric field amplitude of $1\ \text{V/m}$ and the transmitted electric field amplitude was measured on the other side of the metamaterial.

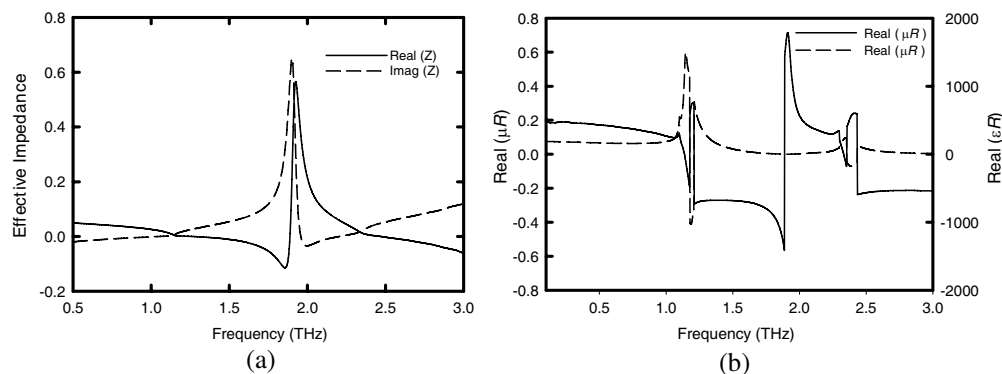


Figure 4: (a) Real and imaginary part of the effective impedance. (b) Real parts of ϵ and μ .

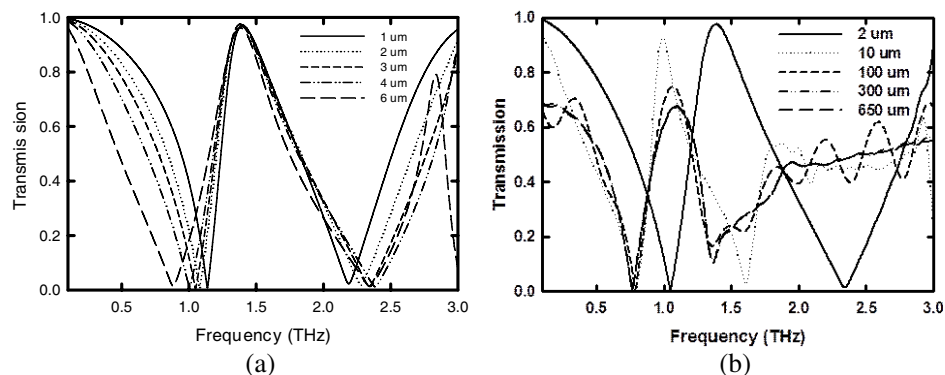


Figure 5: (a) Variation of metallic strip width is shown for the substrate thickness of $2 \mu\text{m}$ and keeping r fixed to $24 \mu\text{m}$. (b) Variation of the substrate thickness is shown.

3. RESULTS AND DISCUSSION

Transmission characteristic of the proposed metamaterial is shown in Figure 2(a) where the individual response of the ring shape and plus shape is also plotted. In Figure 2(b), reflections were computed and plotted. We observe that the proposed metamaterial may be used as a notch filter in reflected mode. While in Figure 3, electric field distribution on the metamaterial structure is shown when excited with x -polarized incident plane wave. This clearly depicts the response of individual structure at lower resonance frequency (i.e., 1.05 THz) and higher resonance frequency (i.e., 2.43 THz). The ring structure resonates at the lower frequency while the plus structure resonates at the higher one.

Since, transmitted and reflected amplitudes are measured along with the phase. So, we can compute the effective impedance, electric permittivity ϵ and magnetic permeability μ values the parameter extraction method explained in [14]. The real and imaginary parts of effective impedance are plotted in Figure 4(a) and the real values of ϵ and μ are presented in Figure 4(b).

Finally, we applied variations to the metallic strip widths and to the thickness of substrate. The effect of these variations on the transmission characteristic is presented in Figure 5(a) and Figure 5(b) respectively. For the strip width variation, we see a red shifted primary resonance which is due to the increased capacitive coupling of the ring structure with the plus structure. For the substrate thickness variation, we see red shift in both resonance frequencies, as explained in [15, 16]. The decreased amplitudes for the thicker substrates come from the loss offered by the respective substrate. Here, we observe that for an ultra-thin substrate of $2 \mu\text{m}$ thickness, we can obtain a low insertion loss and wide band response.

4. CONCLUSIONS

The design of a dual band planar metamaterial based on ring and plus shaped structure has been demonstrated. The resonant frequencies can be determined independently by adjusting the dimensions of the individual resonant structure. The calculated values for dielectric permittivity ϵ

and magnetic permeability μ , from simulated S -parameters, exhibit at least two frequency bands where negative index of refraction has been obtained. Variations of strip widths and substrate thickness are applied and their effects on the transmission characteristic are recorded. An ultra-low loss and wide band response may be obtained by fabricating the dual-band metamaterial on an ultra-thin substrate.

ACKNOWLEDGMENT

This work was supported by the National Research Foundation of Korea through the Grant (No. 20-110017603) and the World Class University (WCU) program at GIST through a Grant provided by the Ministry of Education, Science and Technology (MEST) of Korea (No. R3110026).

REFERENCES

1. Veselago, V. G., "The electrodynamics of substances with simultaneously negative values of ϵ and μ ," *Soviet Physics Uspekhi*, Vol. 10, 509–514, 1968.
2. Smith, D. R., et al., "Composite medium with simultaneously negative permeability and permittivity," *Physics Review Letters*, Vol. 84, 4184–4187, 2000.
3. Shelby, R. A., D. R. Smith, and S. Schultz, "Experimental verification of a negative index of refraction," *Science*, Vol. 292, 77, 2001.
4. Pendry, J. B., "Negative refraction makes a perfect lens," *Physical Review Letters*, Vol. 85, 3966–3969, 2000.
5. Schurig, D., et al., "Metamaterial electromagnetic cloak at microwave frequencies," *Science*, Vol. 314, No. 5801, 977–980, 2006.
6. Caminita, F., et al., "Reduction of patch antenna coupling by using a compact EBG formed by shorted strips with interlocked branch-stubs," *IEEE Antennas and Wireless Propagation Letters*, Vol. 8, 2009.
7. Biber, S., et al., "Frequency selective surface for harmonic suppression in THz-multipliers," *Antennas and Propagation Society International Symposium*, Vol. 4b, 2638, 2005.
8. Landy, N. I., et al., "Perfect metamaterial absorber," *Physical Review Letters*, Vol. 100, 207402, 2008.
9. Chen, H. T., et al., "Active terahertz metamaterial devices," *Nature Photonics*, Vol. 444, 597–600, 2006.
10. Chen, H. T., et al., "A metamaterial solid-state Terahertz phase modulator," *Nature Photonics*, Vol. 3, 148–151, 2009.
11. Seo, M., et al., "Active terahertz nanoantennas based on VO₂ phase transition," *Nano Letters*, Vol. 10, No. 6, 2064–2068, 2010.
12. Kyoung, J. S., et al., "Active Terahertz metamaterials: Nano-slot antennas on VO₂ thin films," *Physics Status Solidi C*, 1–4, 2011.
13. Hussain, S., D. Kim, and J. H. Jang, "A Terahertz meta surface filter employing sub-wavelength metallic apertures on a thin substrate," *PIERS Proceedings*, 1744–1747, Kuala Lumpur, Malaysia, Mar. 27–30, 2012.
14. Smith, D. R., et al., "Electromagnetic parameter retrieval from inhomogeneous metamaterials," *Physical Review E*, Vol. 71, 036617, 2005.
15. Kang, J. H., et al., "Substrate effect on aperture resonances in a thin metal film," *Optics Express*, Vol. 17, No. 18, 15652–15658, 2009.
16. Park, H. R., et al., "Resonance behavior of single ultrathin slot antennas on finite dielectric substrates in Terahertz regime," *Applied Physics Letters*, Vol. 96, No. 21, 211109–211109–3, 2010.

Effect of Random Variations of Both the Composition and Thickness on Photonic Band Gap of One-dimensional Plasma Photonic Crystal

V. V. Rumyantsev and S. A. Fedorov

Donetsk Institute for Physics and Engineering, National Academy of Sciences, Ukraine

Abstract— Propagation of an electromagnetic excitation in a Si/liquid crystal composite materials — nonideal 1D photonic crystal that constitutes a topologically ordered set of layers with a random number of admixture plasma layers is numerically simulated within the virtual crystal approximation. Peculiarities of the dependence of photonic band gap width on admixture plasma layers concentration have been studied. The results are the evidence of substantial photon mode spectrum reconstruction caused by presence of defect layers which differ from the basic ones in both the composition and thickness.

1. INTRODUCTION

Propagation of electromagnetic waves in layered crystalline ambiences is currently drawing a close attention. Ref. [1] gives the account of the related research carried out for photonic crystals based on silicon and liquid crystal (LC), Ref. [2] — for composite materials containing the plasma layers. The interest towards these objects is on one hand due to their significance for electronics, and on the other hand due to the advance of technology allowing growth of ultrathin films and periodic structures with controlled characteristics.

There are numerous theoretical and experimental studies exciton-like excitations in ideal dielectric superlattices. A general theory of optical waves in anisotropic crystals, including those, formed of macroscopic layers, is discussed in Ref. [3]. The further development of the theory of layered structures requires considering more complex models like superlattices with randomly included admixture layers. A better understanding of how the optical properties of such systems depend on concentration of admixture layers gives basis for modeling and constructing the layered materials with prescribed characteristics.

The method applied for calculating polariton excitation spectra is rather similar to the ones, used in cases of other quasiparticle excitations, like electronic, phononic etc. In the present work we employ the virtual crystal approximation (VCA) [4], based on configurational averaging, for description of polariton excitations in a *macroscopically* inhomogeneous medium. It is a well-known method; however its use up to now [5] has been limited to *microscopic* calculating the quasiparticles excitations spectra in disordered systems. Mathematical posing of the problem is similar in these two cases. Within VCA the configurationally dependent parameters of the Hamiltonian are replaced with their configurationally averaged values. Description of transformation of a polariton spectrum in a sufficiently simple superlattice, using this approximation, is the first step towards the study of imperfect systems. However investigation of properties of polariton spectra and the related physical quantities (density of elementary excitation states, characteristics of the normal electromagnetic waves etc.) in less simple systems requires application of more complex method (such are the method of the coherent potential or the averaged T-matrix method).

In the paper a superlattice is modeled as a set of macroscopically homogeneous layers with randomly included extrinsic (with respect to the ideal superlattice) layers of variable composition and thickness. Corresponding configuration-dependent material tensors in our model of an imperfect superlattice are represented in terms of random quantities. After configuration-averaging the translational symmetry of a considered system is “restored” that allows us obtain the system of equations which define normal modes of electromagnetic waves, propagating in one-dimensional “periodic” medium.

Investigation of disorder effects in an imperfect superlattice allowing modeling the properties of photonic crystal containing the plasma layers is still of a great interest [2]. Development of the theory of photonic structures requires consideration of model systems such as photonic superlattice with plasma layers. Within the VCA we study a model of 1D-superlattice as a macroscopically homogeneous layered system, which is a topologically ordered ensemble of Si (layers of variable thickness) and LC sublattice with randomly included admixture plasma layers.

2. THEORETICAL FUNDAMENTALS

Dielectric $\hat{\varepsilon}(\vec{r})$ and magnetic $\hat{\mu}(\vec{r})$ permeability, which determine optical characteristics of a periodic medium, must satisfy the periodic boundary conditions: $\hat{\varepsilon}(x, y, z) = \hat{\varepsilon}(x, y, z + d)$, $\hat{\mu}(x, y, z) = \hat{\mu}(x, y, z + d)$, where $d = \sum_{j=1}^{\sigma} a_j$ is the period of the superlattice, σ is the number of layers per elementary cell, a_j are the thicknesses of the layers which form a one-dimensional chain of elements oriented along the z -axis. The material tensors $\hat{\varepsilon}$ and $\hat{\mu}$ of a crystalline superlattice with an arbitrary number of layers σ have the following form in the coordinate representation:

$$\begin{pmatrix} \hat{\varepsilon}(z) \\ \hat{\mu}(z) \end{pmatrix} = \sum_{n, \alpha} \begin{pmatrix} \hat{\varepsilon}_{n\alpha} \\ \hat{\mu}_{n\alpha} \end{pmatrix} \left\{ \theta \left[z - (n-1)d - \left(\sum_{j=1}^{\alpha} a_{nj} - a_{n\alpha} \right) \right] - \theta \left[z - (n-1)d - \sum_{j=1}^{\alpha} a_{nj} \right] \right\}. \quad (1)$$

In Eq. (1), $\theta(z)$ is the Heaviside function, $n = \pm 1, \pm 2, \dots$ is the number of a one-dimensional crystal cell, index $\alpha = 1, 2, \dots, \sigma$ designates the elements of the cell. Within our model, the configurationally dependent tensors $\hat{\varepsilon}_{n\alpha}$, $\hat{\mu}_{n\alpha}$ are expressed through the random quantities $\eta_{n\alpha}^{\nu}$ ($\eta_{n\alpha}^{\nu} = 1$ if the $\nu(\alpha)$ -th sort of layer is in the $(n\alpha)$ -th site of the crystalline chain, $\eta_{n\alpha}^{\nu} = 0$ otherwise):

$$\begin{pmatrix} \hat{\varepsilon}_{n\alpha} \\ \hat{\mu}_{n\alpha} \end{pmatrix} = \sum_{\nu(\alpha)} \begin{pmatrix} \hat{\varepsilon}_{\alpha}^{\nu(\alpha)} \\ \hat{\mu}_{\alpha}^{\nu(\alpha)} \end{pmatrix} \eta_{n\alpha}^{\nu(\alpha)} \quad (2)$$

Calculation of a polariton spectrum for the imperfect superlattice is realized within the VCA (similarly to the solid quasi-particle approach) through the following replacement: $\hat{\varepsilon} \rightarrow \langle \hat{\varepsilon} \rangle$, $\hat{\mu} \rightarrow \langle \hat{\mu} \rangle$ (in the case of the variable layer thickness replacement is $d \rightarrow \langle d \rangle$ and $a_{n\alpha} \rightarrow \langle a_{\alpha} \rangle$). Angular parentheses designate the procedure of configuration averaging. In addition, from Eq. (2) we have:

$$\begin{pmatrix} \langle \hat{\varepsilon}_{n\alpha} \rangle \\ \langle \hat{\mu}_{n\alpha} \rangle \end{pmatrix} = \sum_{\alpha, \nu(\alpha)} \begin{pmatrix} \hat{\varepsilon}_{\alpha}^{\nu(\alpha)} \\ \hat{\mu}_{\alpha}^{\nu(\alpha)} \end{pmatrix} C_{\alpha}^{\nu(\alpha)}, \quad \langle a_{n\alpha} \rangle = \sum_{\nu(\alpha)=1}^{r(\alpha)} a_{\alpha}^{\nu(\alpha)} C_{\alpha}^{\nu(\alpha)} \quad (3)$$

where $C_{\alpha}^{\nu(\alpha)}$ is the concentration of the $\nu(\alpha)$ -th sort of admixture layer in the α -th sublattice. There is a normalization condition $\sum_{\nu(\alpha)} C_{\alpha}^{\nu(\alpha)} = 1$. It follows from Eq. (1) that the Fourier-amplitudes $\hat{\varepsilon}_l$, $\hat{\mu}_l$ and the averaged dielectric $\langle \hat{\varepsilon}_{n\alpha} \rangle$ and magnetic $\langle \hat{\mu}_{n\alpha} \rangle$ permeability of layers (3) are related as

$$\begin{pmatrix} \hat{\varepsilon}_l \\ \hat{\mu}_l \end{pmatrix} = -\frac{i}{2\pi l} \sum_{\alpha} \begin{pmatrix} \langle \hat{\varepsilon}_{n\alpha} \rangle \\ \langle \hat{\mu}_{n\alpha} \rangle \end{pmatrix} \left\{ \exp \left(i \frac{2\pi}{d} l \sum_{j=1}^{\alpha} a_j \right) - \exp \left[i \frac{2\pi}{d} l \left(\sum_{j=1}^{\alpha} a_j - a_{\alpha} \right) \right] \right\} \quad (4)$$

Since the configurationally averaging “restores” the translational symmetry of a crystalline system, in the considered case of imperfect superlattice the “acquired” translational invariance of the one-dimensional chain allows us to write Maxwell equations for harmonic dependency of the electric and magnetic field strengths $\vec{E}(\vec{r}, \omega)$, $\vec{H}(\vec{r}, \omega)$ on a time. Hence, according to the Floquet theorem, Fourier-amplitudes $\vec{f}_{K,p}^{(E,H)}$ of the electric and magnetic field strengths satisfy the following relation:

$$\left[\vec{\beta} + \left(K + p \frac{2\pi}{d} \right) \vec{e}_z \right] \times \begin{pmatrix} \vec{f}_{K,p}^{(H)} \\ \vec{f}_{K,p}^{(E)} \end{pmatrix} = \frac{\omega}{c} \begin{bmatrix} -\sum_l \hat{\varepsilon}_l \cdot \vec{f}_{K,p-l}^{(E)} \\ \sum_l \hat{\mu}_l \cdot \vec{f}_{K,p-l}^{(H)} \end{bmatrix}. \quad (5)$$

Here $\vec{\beta}$ is an arbitrary planar (in the XOY plane) wave vector, \vec{e}_z is a unit vector along the z -axis, $\vec{K} = (0, 0, K)$ is the Bloch vector. The system (5) defines normal modes of electromagnetic waves, propagating in the considered “periodic” medium. Below, for simplicity, we shall restrict our study to the case of light, propagating along the z -axis ($\vec{\beta} = 0$) in a nonmagnetic lattice ($\hat{\mu} = \hat{I}$ is a unit matrix); the liquid-crystal layers we shall treat as uniaxial ($\varepsilon_{ij} = \varepsilon_{xx} \delta_{xi} \delta_{jx} + \varepsilon_{yy} \delta_{yi} \delta_{jy} + \varepsilon_{zz} \delta_{zi} \delta_{jz}$; obviously, that for $\vec{K} \parallel z$, zz -components of the tensor $\hat{\varepsilon}$ do not appear in final formulas, and $\varepsilon_{xx} =$

$\varepsilon_{yy} \equiv \varepsilon$). Furthermore, we shall (like in Ref. [3]) assume, that K is close to the value, defined by the Bragg's condition: $|K - \frac{2\pi}{d}| \approx K$, $c^2 K^2 \approx \omega^2 \varepsilon_0$. This case corresponds to a resonance of plane waves between the components $\bar{f}_{K,p}^{(E,H)}$ at $p = 0, -1$ (these terms dominate in the system (6)). After eliminating the $\bar{f}^{(H)}$ variables, Eqs. (5) with respect to $\bar{f}^{(E)}$ take the form:

$$\begin{bmatrix} K^2 - \frac{\omega^2}{c^2} \varepsilon^{(0)} & -\frac{\omega^2 \varepsilon^{(1)}}{c^2} \\ -\frac{\omega^2 \varepsilon^{(-1)}}{c^2} & (K - \frac{2\pi}{d})^2 - \frac{\omega^2}{c^2} \varepsilon^{(0)} \end{bmatrix} \begin{pmatrix} f_{K,0}^{(E)} \\ f_{K,-1}^{(E)} \end{pmatrix} = 0, \quad (6)$$

where $\varepsilon_{l=0} \equiv \varepsilon^{(0)}$, $\varepsilon_{l=\pm 1} \equiv \varepsilon^{(\pm 1)}$. Putting the determinant of the system (6) equal to zero we obtain the dispersion relations $\omega_{\pm} = \omega(K)$. Two roots of this equation ω_{\pm} define the boundaries of the spectral band: at frequencies $\omega_-(K) < \omega < \omega_+(K)$ (band gap) the roots are complex and electromagnetic waves decay (Bragg's reflection); frequencies $\omega < \omega_-$, $\omega > \omega_+$ correspond to propagating waves.

3. RESULTS

To specify the results, consider the propagation of electromagnetic excitation in an imperfect Si/LC 1D superlattice with two elements (layers) in the cell, namely, with the first layer of silicon ($\varepsilon_1 = 11.7$) and the second layer of liquid crystal ($\varepsilon_2^{(1)} = 5.5$). Note that the permittivity profile for inhomogeneous plasma is $\varepsilon_2^{(2)}(z) = 1 - \omega_e^2(z)/\omega^2$. For considered model plasma frequency is $\omega_e \ll \omega$ (collisions in plasma are neglected) and plasma density for $a_{n\alpha}$ -th layer varies exponentially:

$$n(z) = n_{cr} \left\{ \exp \left[-p \left[z - (n-1)d - \sum_{j=1}^{\alpha} a_{nj} + a_{n\alpha} \right] / a_{n\alpha} \right] + \exp \left[-p \left(-z + a(n-1)d + \sum_{j=1}^{\alpha} a_{nj} \right) / a_{n\alpha} \right] \right\} / 2, \quad (7)$$

gradation parameter p corresponds to the volume average plasma permittivity $\langle \varepsilon_2^{(2)} \rangle = 0.9$. Below we are considered the case of admixture plasma layers only in liquid crystal sublattice. The concentration, thickness and permittivity of the basic material layer in the first and second sublattices are denoted as $C_1^{(1)}, a_1^{(1)} = a_1, \varepsilon_1^{(1)} \equiv \varepsilon_1$ and $C_2^{(1)}, a_2^{(1)}, \varepsilon_2^{(1)} \equiv \varepsilon_2$, and the corresponding parameters of impurity layers with a different composition $C_{2C}^{(2)} \equiv C_C$ and thickness $C_{1T}^{(2)} \equiv C_T$, as well as $a_2^{(2)}, \varepsilon_2^{(2)}$. Simple calculations taking into account (3)–(7), yield the dependence the lowest photonic band gap width $\Delta\omega = |\omega_+ - \omega_-|$ on plasma concentration $\Delta\omega(C_C, C_T)$ of the system studied (see Fig. 1) for different relative both composition and thickness of layers. Surface 1 refers the case of $a_1/a_2 = 0.1$ and $a_1^{(2)}/a_2 = 0.5$, surface 2 corresponds to the case of $a_1/a_2 = 0.5$ and $a_1^{(2)}/a_2 = 0.1$.

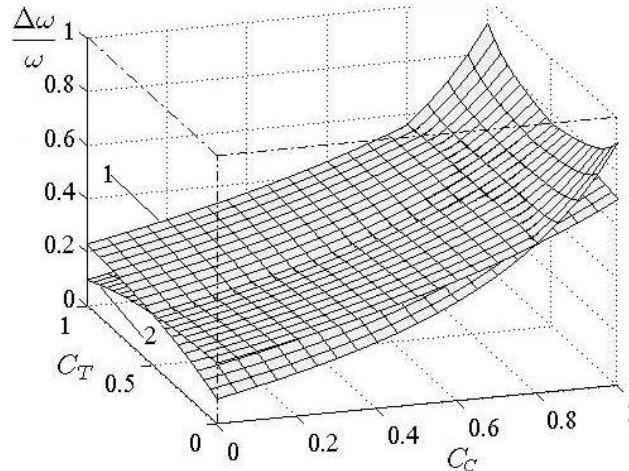


Figure 1: Concentration dependence for a nonideal Si/LC 1D superlattice which contains plasma layers in LC-sublattice.

4. CONCLUSIONS

Our results show that the optical characteristics of imperfect 1D superlattice may be significantly altered owing to transformation of their photon mode spectrum resulted a presence of admixture layers. Graphic representation $\Delta\omega(C_C, C_T)$ proves that the concentration dependence for the binary systems considered above differs for different relative composition of plasma layers. The case of nonideal multilayered systems with a larger number of sublattices and components of alien layers supposes a wide variety of specific behaviors of the photonic gap width. This circumstance extends considerably the promises of modeling composite materials with predetermined properties.

REFERENCES

1. Tolmachov, V. A., T. S. Perova, and E. V. Astrova, “Thermo-tunable defect mode in one dimensional photonic structure based on grooved silicon and liquid crystal,” *Phys. Stat. Sol. (RRL)*, Vol. 2, No. 3, 114–116, 2008.
2. Kong, X.-K., S.-B. Liu, H.-F. Zhang, and H.-L. Guan, “The effect of random variations of structure parameters on photonic band gaps of one-dimensional plasms photonic crystal,” *Optics Communications*, Vol. 284, No. 12, 2915–2918, 2011.
3. Yariv, A. and P. Yeh, *Optical Waves in Crystals*, John Willey & Sons, Inc., New York, 1987.
4. Parmenter, R. H., “Energy levels of a disordered alloy,” *Phys. Rev.*, Vol. 97, 587–698, 1955.
5. Ziman, J. M., *Models of Disorder. The Theoretical Physics of Homogeneously Disordered Systems*, John Willey & Sons, Inc., New York, 1979.

Procedure of Near Ground Propagation Model Development for Pine Tree Forest Environment

O. Kurnaz¹, M. Bitigan², and S. Helhel¹

¹Department of Electrical and Electronics Engineering, Akdeniz University, Turkey

²Department of RF Planning, Turkcell Communication Coop., Turkey

Abstract—In this study, the procedure of new model development steps has been presented starting with plane earth measurements. A propagation model experimentally derived from both free space and near ground plane earth path loss models for pine tree forest with foliage depth lower than 400 m has been proposed. It is a piecewise model taking foliage depth of 150 m as a boundary. Different from Weissberger, ITU-R and COST235 models, the proposed one takes trunk height gain k into account. Mean error has been obtained as 6.55 dB for proposed model, 31.72 dB for COST235, 17.42 dB for Weissberger and 21.03 dB for ITU-R at 900 MHz.

1. INTRODUCTION

Increased popularity of wireless technologies requires that development of a proper propagation model is essential for uninterrupted communication in both urban and unsettled areas including forests and hilly territories. Use of a proper model is not only required for personal cell phone communication but also vital for military, governmental and unmilitary personal radiotelephone communication especially in forest areas. These requirements force scientists and international organizations to investigate propagation mechanisms in forested area [1–3].

Weissberger's model [1], Cost 235 [2] and ITU Recommendation (ITU-R) models [3] are three well-known examples of empiric models applicable to foliage loss estimation. They conducted measurements mainly at UHF band, and developed empiric formulas valid between 200 MHz and 95 GHz.

Bitirgan et al. [4] proposed a propagation model derived from free space model by taking experimentally determined foliage effect into consideration. They noted that it is possible to develop propagation models for certain areas by using plane earth measurements as reference.

Kurnaz and Helhel [5] proposed a new model taking forest property into account. Their model takes trunk height gain k into account and they compared their model with Weissberger, ITU-R and COST235 models. They found that their model gives more accurate result at certain areas.

Most of the forested areas in Turkey are covered by pine trees, and there are civil and governmental based issues which require development of specific propagation models. This requirement motivated us to generate a new model for such an environment. In this study, the procedure of new model development steps has been presented starting with plane earth measurements.

2. FREE SPACE AND PLANE EARTH PATH LOSS MODELS

The free space path loss model can be used as a lower bound [5] to estimate path loss. The decrease in signal strength of an electromagnetic wave which would result from an unobstructed line of sight path through free space is called free space path loss. Free space path loss model can be obtained by the help of Friis transmission equation. The ratio of received power P_r from a radiated transmit antenna to base station transmit power P_t is given by the formula

$$\frac{P_r}{P_t} = \frac{G_t G_r \lambda^2}{(4\pi)^2 d^2 L} \quad (1)$$

where G_t is isotropic transmit antenna gain, G_r is receive antenna gain, λ is signal wavelength in meters (m), d is distance between transmit and receive antennas in meters (m) and L is system loss factor not related to propagation ($L \geq 1$). If the radio wave propagates near the earth surface rather than through free space, plane earth path loss model, which includes the effect of ground reflection, can better be adopted. After including the ground reflection effect, the plane earth path loss model is formulated as

$$\frac{P_r}{P_t} = \frac{G_t G_r h_t^2 h_r^2}{d^4 L} \quad (2)$$

where h_t and h_r are the heights of the transmit and receive antennas in meters (m), respectively. Derivation of (2) requires some assumptions [6] and it is valid when d is much larger than h_t and h_r . It is seen that the model is frequency independent at large distances.

3. DERIVATION OF NEW EMPIRIC MODEL

At first glance, it seems that it had better adopt plane earth model rather than the free space model as a starting point to derive a new model; however, comparison of measured and simulated data suggests using both models in piecewise manner. In Fig. 1, simulated results of (1) and (2), as well as measured data at 900 MHz is shown. Measurements were conducted on an uncultivated area, which is covered only by grass, where no obstruction exists on line of sight between the transmitter and receiver, the heights of which were both 2 m. Maximum distance in measurements was 145 m. Analysis of Fig. 1 suggests that free space model predicts path loss better than plane earth model. To investigate the intersection distance of both models, they have been simulated up to 500 m. Fig. 2 shows that path loss predictions of both models intersect at 150 m for 900 MHz. Therefore, a distance of 150 m has been selected as boundary in our model; the model adopted as a starting point for model derivation is free space model for distances below 150 m and plane earth model for distances above 150 m.

Path loss (PL) in a forest environment can be expressed in dB as in Eq. (3)

$$PL(\text{dB}) = -10 \log(G_t G_r) - 20 \log(\lambda) + 20 \log(4\pi d) + L_E \quad (3)$$

by using (1) and as in Eq. (4)

$$PL(\text{dB}) = -10 \log(G_t G_r) - 20 \log(h_t h_r) + 40 \log(d) + L_E \quad (4)$$

by using (2), where L_E stands for the excess loss in both cases. We may define L_E as in Eq. (5)

$$L_E = L_{veg} + L_{sys} \quad (5)$$

where L_{veg} is the loss caused by vegetation canopies and L_{sys} is the miscellaneous loss, which includes transmission line attenuation and antenna losses [6], caused by the system. Since the output power of the transmitter can be predefined in our system and the error margin of our receiver is known to be at ± 1 dB [7, 8], which is much smaller than foliage path loss, L_{sys} is ignored in our model.

The vegetation loss factor L_{veg} can be empirically calculated as in Eq. (6)

$$L_{veg} = PL_{forest} - PL_{plane} \quad (6)$$

where PL_{plane} is the reference path loss in dBm measured for plane earth scenario when no obstruction is present on line of sight and PL_{forest} is the measured path loss in dBm in the presence of foliage. In determination of L_{veg} , the data belonging to GSM1800 were used as reference and frequency effect is included in the model later on.

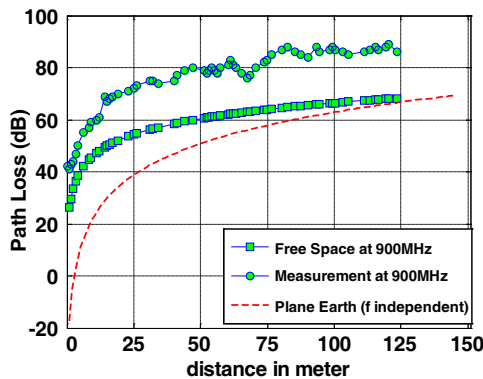


Figure 1: Simulated results of plane earth and free space models which are compared with experimental plane earth data.

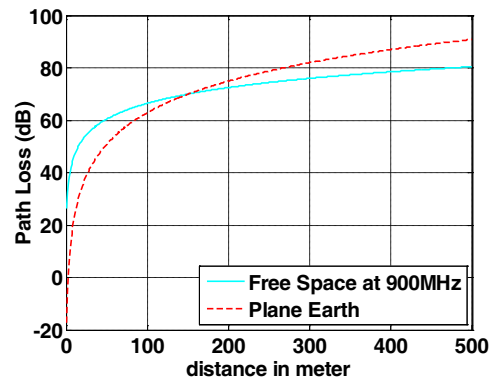


Figure 2: Simulated results of plane earth and free space models.

By using the data obtained, L_{veg} can be written as a function of foliage depth d as in Eq. (7)

$$L_{veg}(d) = \frac{c_1 d + c_2}{d + c_3} \quad (7)$$

where c_1 , c_2 and c_3 are all constant and non-unique numbers determined by fitting the obtained L_{veg} data. It is obvious that L_{veg} would not be same for different environments. This is due to the fact that attenuation caused by needle and leaves is much higher than that caused by tree trunks and branches, as shown for trees in a park environment [9]. Therefore, trunk height gain k can be proposed as in Eq. (8)

$$k = \frac{h_{ref}}{h_{ex}} \quad (8)$$

where h_{ref} is the height of *tree part without leaves* in reference environment and h_{ex} is the height of *tree part without leaves* in examined environment.

Frequency effect also needs to be included in the model. Since frequency effect has already been included in Eq. (3) in terms of wave length, a term “ $20 \log(f/1.8)$ ” has been added to the Eq. (4) where f is frequency in GHz. After all the steps, the proposed model estimating the total path loss including both propagation and foliage effect can be expressed in dB as in Eq. (9).

$$PL_P = \left\{ \begin{array}{ll} 21 - 10 \log \frac{G_t G_r}{(4\pi d)^2} - 20 \log(\lambda) + kL(d) & d \leq 150 \text{ m} \\ 21 - 10 \log \frac{G_t G_r (h_t h_r)^2}{d^4} + 20 \log \left(\frac{f}{1.8} \right) + kL(d) & d > 150 \text{ m} \end{array} \right\} \quad (9)$$

where $L(d)$ is found by Eq. (10)

$$L(d) = \frac{2584d - 38570}{d + 11900} \quad (10)$$

after fitting operation, where 21 is a constant in dB, which stands for the offset value observed in Fig. 1.

4. RESULTS AND CONCLUSIONS

Figures 3 and 4 show path loss estimations and errors of models for verification measurement conducted in a forest different from forest area where model derivation had been realized. Root mean square error E_{rms} has been obtained as 6.55 dB for proposed model, 31.72 dB for COST235, 17.42 dB for Weissberger and 21.03 dB for ITU-R at 900 MHz. Performance is quantified by using root mean square (RMS) error, defined by the formula

$$E_{rms} = \sqrt{\frac{\sum_{i=1}^n E_i^2}{n}} \quad (11)$$

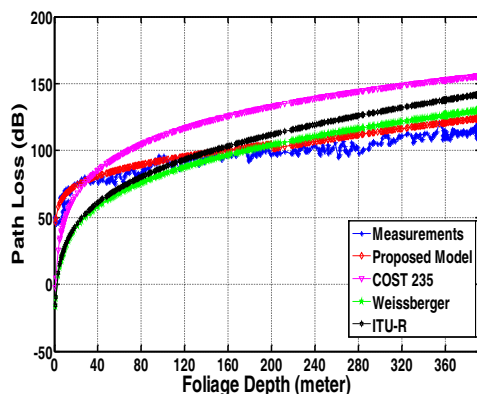


Figure 3: Path loss at 900 MHz.

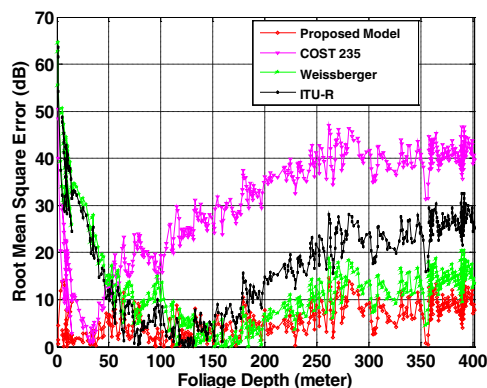


Figure 4: Root mean square error at 900 MHz.

where E_i is the difference between estimated and measurement value at i th point of measurement in dB and n is the number of measurement points.

In this study, a propagation model for pine tree forest environments experimentally derived from both free space and near ground plane earth path loss models has been presented. Model has been developed and verified in pine tree forest with foliage depth lower than 400 m in a hot climate region in Turkey. It has been compared with Weissberger's modified exponential decay model, ITU Recommendation model and COST235 model which are three well-known empiric models. The results show that best performance has been obtained from the proposed one among all models. At the same time, it has been observed that path loss estimation of COST235 is higher than that of Weissberger and ITU-R.

ACKNOWLEDGMENT

This project was supported by Akdeniz University, Scientific Research Projects Supporting Unit (BAPYB), Grant Number: 2011.02.0121.007 and 2012.05.0102.024.

REFERENCES

1. Weissberger, M. A., "An initial critical summary of models for predicting the attenuation of radio waves by trees," ESD-TR-81-101, Electromagnetic Compatibility Analysis Center, Annapolis, Maryland, 1981.
2. COST 235, "Radio propagation effects on next-generation fixed-service terrestrial telecommunication systems," Final Rep., Luxembourg, 1996.
3. CCIR, "Influences of terrain irregularities and vegetation on troposphere propagation," CCIR Rep., 235–236, Geneva, 1986.
4. Bitirgan, M., Y. E. Yoruk, S. Celik, O. Kurnaz, S. Helhel, and S. Ozen, "Generation of an empiric propagation model for forest environment at GSM900/GSM1800/CDMA2100," *2011 XXXth URSI General Assembly and Scientific Symposium*, Istanbul, Aug. 13–20, 2011.
5. Kurnaz, O. and S. Helhel, "Near ground propagation model for pine tree forest environment," *IEEE Transactions on Antennas and Propagation*, submitted for publication, Feb. 2012.
6. Rappaport, T. S., *Wireless Communications: Principles and Practice*, Chap. 4, Prentice Hall, New Jersey, 2002.
7. Helhel, S., "Comparison of 900MHz and 1800MHz indoor propagation deterioration," *IEEE Trans. Antennas and Propagation*, Vol. 54, 3921–3924, Dec. 2006.
8. Helhel, S., S. Ozen, I. B. Basyigit, O. Kurnaz, Y. E. Yoruk, M. Bitirgan, and Z. Colak, "Radiated susceptibility of medical equipments in health care units: 2G and 3G mobile phones as an interferer," *Microwave and Optical Technology Letters*, Vol. 53, 2657–2661, Nov. 2011.
9. Seker, S. and F. C. Kunter, "Multi-Components mobile propagation model of park environment," *IEEE Trans. Magnetism*, Vol. 47, 1494–1497, May 2011.

Normalized Differenzial Spectral Attenuation among Co-rotating LEO Satellites: Performance Analysis for Estimating the Tropospheric Water Vapor

F. Cuccoli¹, L. Facheris², and F. Argenti²

¹U.O. CNIT RaSS, c/o Dipartimento di Elettronica e Telecomunicazioni, Università di Firenz
Via di Santa Marta, 3, Firenze 50139, Italy

²Dipartimento di Elettronica e Telecomunicazioni, Università di Firenze
via di Santa Marta, 3, Firenze 50139, Italy

Abstract— NDSA (Normalized Differential Spectral Absorption) is as a differential attenuation measurement method for the estimation of the total content of water vapor (IWV, Integrated Water Vapor) along a tropospheric propagation path between two Low Earth Orbit (LEO) satellites. The NDSA has been deeply analyzed assuming two counter rotating satellites in Ku and K band for tangent altitudes up to 10 km. In this paper we present the main NDSA measurement characteristics of the CO-rotating configuration with one transmitting satellite and many receiving ones assuming the multi-band (K, Ku and M) approach on each radio link and plausible reference propagation conditions for tangent altitudes up to 15 km.

1. INTRODUCTION

The Normalized Differential Spectral Attenuation (NDSA) approach is based on the conversion of a spectral parameter called “Spectral Sensitivity” (SS) into the total content of water vapor along the propagation path between two LEO satellites. In [1] the potential of spectral sensitivity in providing direct estimates of Integrated Water Vapor (IWV) along LEO-LEO tropospheric propagation paths in the 15–25 GHz range is shown while in [2] the accuracy with which the spectral sensitivity parameter can be measured has been analyzed.

A basic result was that the spectral sensitivity measurement accuracy can be estimated through the theoretical approximation as long as the averaged Signal to Noise Ratio (SNR) keeps above 20 dB, while below such SNR level measurements become not reliable. Moreover, this holds as long as the integration time used for measurements keeps smaller than the decorrelation time of the scintillation phenomenon.

A complete simulation tool has been presented in [3] for the study of the NDSA measurement performance in counter rotating LEO-LEO configuration (see Figure 1(a)) at global scale for single and multiple global atmospheric profiles, assuming spherical symmetry for the atmospheric structure, realistic LEO satellites’ orbit configuration, link budget, and disturbances sources. The main results of this performance analysis is that NDSA at 17.25 GHz can be measured in case of medium scintillation up to 6 km tangent altitude with NSED (the standard deviation of the absolute error) smaller than 50% and at 20.20 GHz can be estimated both in medium scintillation conditions between 3 and 7 km with NSED smaller than 20% and also in strong scintillation conditions with NSED smaller than 60%.

Some other studies about the NDSA in counter rotating LEO-LEO configuration in K/Ku bands have been completed under the independent ESA (European Space Agency) study called AlMetLEO [4] that provided a significant insight into the SS-IWV relationships up to 12 km altitude in the limb geometry based on an extended radiosonde data analysis, into the modelization of signal fluctuations due to tropospheric turbulence and into the SS accuracy achievable under given SNR and scintillation levels.

In [5] for the first time the use of M band for NDSA measurements, always in counter rotating LEO-LEO configuration, has been introduced. Specifically, 179 and 182 GHz have been proposed as good candidates for water vapor estimates at tangent altitudes higher than 11 km, since M band measurements are very robust to receiver noise and practically insensitive to scintillation effects.

While the counter-rotating configuration provides valid SS measurements data only during the relative set/rise occultation events the co-rotating one provide them in a time continuous manner. For this reason the authors decided to investigate the NDSA capabilities also in LEO-LEO co-rotating configuration (see Figure 1(b)).

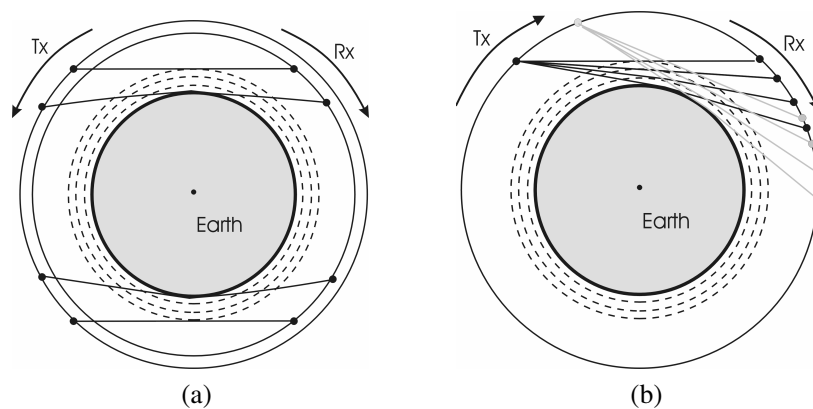


Figure 1: (a) Counter rotating and (b) co-rotating LEO-LEO configuration.

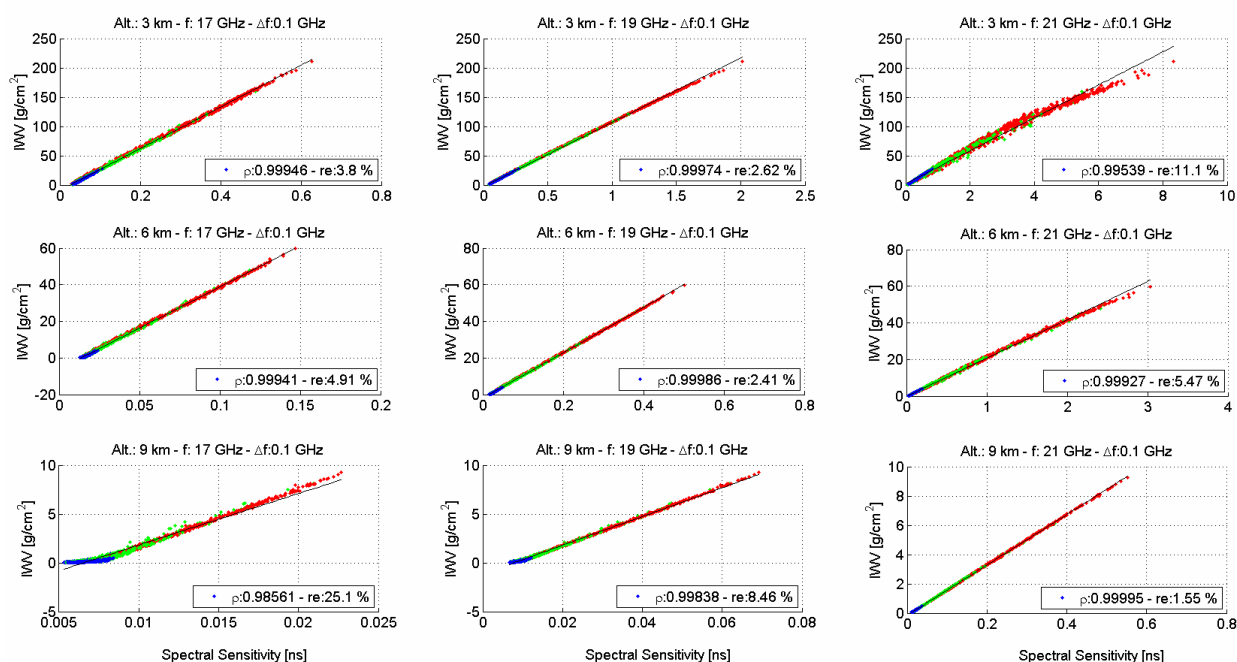


Figure 2: IWV at (top-down) 3, 6 and 9 km tangent altitude vs. SS at (left to right) 17, 19 and 21 GHz. For each plot the correlation coefficient ρ and the relative error re after a linear least squares fit are shown. Red, green and blue colors are related to the latitude range: red for $[0^\circ-30^\circ]$, green for $[30^\circ-60^\circ]$ and blue for $[60^\circ-90^\circ]$ both for the Northern and the Southern hemisphere.

In this paper we present the main NDSA measurement characteristics of the CO-rotating configuration (see Figure 1(b)) with one transmitting satellite and many receiving ones. We discuss the result of a performance analysis of the sensitivity measurements assuming the multi-band (K, Ku and M) approach on each radio link and plausible reference propagation conditions.

2. SENSITIVITY MEASUREMENTS VS INTEGRATED WATER VAPOR

In order to recall the main features of the SS-IWV relationships, Figure 1 shows the SS vs. the IWV for the 17, 19 and 21 GHz sensitivity channels at 3, 6 and 9 km tangent altitudes. The plots are computed basing on atmospheric vertical profiles at global scale related to the ECMWF (European Centre for Medium-Range Weather Forecasts) model for the 12:00 UTC on 15 October 2011 interpolated on a 5° latitude \times 5° longitude grid. The SS are computed using the simulation tool developed in [3].

Notice that the highest correlations are: at 3 km for 17 GHz, at 6 km for 19 GHz and at 9 km for 21 GHz.

Table 1: Values of the link power budget parameters. f_0 : sensitivity channel, $f_{1/2}$ frequency tones.

f_0 [GHz]	f_1 [GHz]	f_2 [GHz]	Tx Power [dBW]	Tx & Rx Antenna Gain [dB]	Rx System noise temp. [dBK]
17.00	16.90	17.10	3.0	26.9	25.3
19.00	18.90	19.10	3.0	27.8	25.8
21.00	20.90	21.10	3.0	28.5	26.3
179.00	178.80	179.20	3.0	34.8	23.8
182.00	181.80	182.20	3.0	34.9	23.8

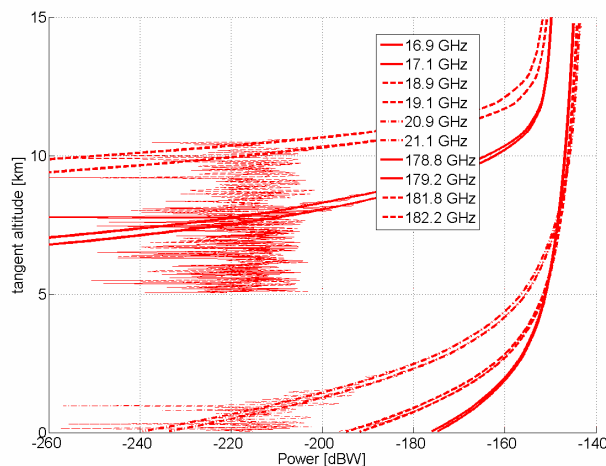


Figure 3: Received power vs. tangent altitude.

3. CO-ROTATING OBSERVATION GEOMETRY

Assuming an elliptical orbit with the semi-major axis of 6651 km, the spherical Earth with the radius of 6371 km, the eccentricity of 0.0005 and two satellites separated by an angle of 0.582398 rad (this case corresponds to the 0 km tangent altitude for circular orbit), the tangent altitude varies between 3 and 10 km and the LEO-LEO link length vary between 3777 and 3780 km corresponding, respectively, to 10 and 3 km tangent altitude. The revolution period for this kind of orbit is 5061 s that gives an average speed of about 8 km/s for the link projection point at ground. Assuming a sampling time of 1 s, the link altitude can be considered constant during the integration interval. Therefore, a sensitivity measurement each 8 km is provided and this is related to the constant tangent altitude, given by orbital position, within the 3–10 km range.

In order to sweep the troposphere between 3 and 15 km with the minimum number of two receiving satellites, the angular separation must vary between 0.005232 and 0.005242 rad (that correspond to a distance of about 34 km). In this way, when the tangent altitude of the farther receiving satellite link is 3 km, the tangent altitude of the closer one is 8 km and when the tangent altitude of the farther receiving satellite link is 10 km the tangent altitude of the closer one is 15 km.

4. PERFORMANCE OF THE SENSITIVITY MEASUREMENT IN CO-ROT GEOMETRY

Using the theoretical analysis proposed in [2] it is possible to compute the Normalized Root Mean Square Error (NRMSE) of the spectral sensitivity as function of the SNR_m (the average SNR of the two tones received on the corresponding channels), the differential attenuation ΔA (between the two tones of each channel) and two other parameters for the scintillation impairment (i.e., ρ than accounts for the frequency tone correlation and σ_χ that accounts for the scintillation power).

For the computation of SNR_m and ΔA we simulated the power at the receiver assuming the link power budget parameters listed in Table 1, the MLS Atmospheric model [1] and a spherical symmetry for the atmospheric structure. The propagation effects have been simulated using the core of the software tool developed in [3] that is based on the MPM93 propagation model [5]. Notice that the MLS model does not account for liquid and ice particles, therefore the simulated propagation scenario is related to a so called “dry atmosphere”.

Figure 3 shows the received power for each tone and Figure 4 shows ΔA and SNR_m for each

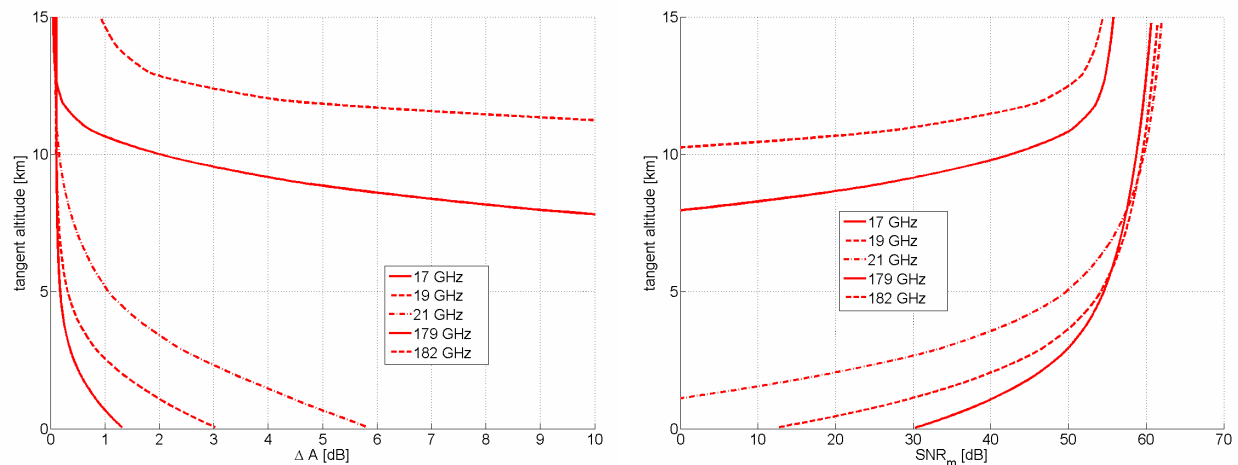


Figure 4: Differential attenuation and SNR_m vs. tangent altitude.

sensitivity channel. Notice that SNR_m is greater than 40 dB above 1 km at 17 GHz channel, above 2 km at 19 GHz, above 3 km at 21 GHz and above 10 km for the M band.

Considering ΔA greater than 1 dB and SNR_m greater than 40 dB (that are surely optimal conditions for converting the SS in IWV) the NRMSE of the spectral sensitivity computed using the theoretical analysis proposed in [2] is lower than 10% for medium scintillation cases ($\sigma_\chi = 0.3$ dB) and lower than 5% for low scintillation cases ($\sigma_\chi = 0.03$ dB).

5. CONCLUSIONS

The performance of the SS measurements in CO-RO has been evaluated in a reference atmospheric scenario. Assuming a plausible power link budget for a CO-RO orbital geometry covering the tangent altitudes between 0 and 15 km, the received power has been simulated for the frequency tones related to the 17, 19, 21, 179 and 182 GHz sensitivity channels. The NRMSE of SS has been computed for ΔA greater than 1 dB and SNR_m greater than 40 dB. In these conditions, the NRMSE is lower than 10% and 5% for hypothesis of medium and low scintillation effects, respectively. Even if the scintillation effects in CO-RO is still not fully developed it is envisaged that the CO-RO configuration should be characterized by low scintillation impairments. Further studies are in progress in order to develop a scintillation model for the CO-RO geometry following the same approach used in [3] for the COUNT-RO case.

REFERENCES

1. Cuccoli, F. and L. Facheris, "Normalized differential spectral attenuation (NDSA): A novel approach to estimate atmospheric water vapor along a LEO — LEO satellite link in the Ku/K bands," *IEEE Transactions on Geoscience and Remote Sensing*, Vol. 44, No. 6, 1493–1503, 2006.
2. Cuccoli, F., L. Facheris, and F. Argenti, "Normalized differential spectral attenuation (NDSA) measurements between two LEO satellites: Performance analysis in the Ku/K bands," *IEEE Transactions on Geoscience and Remote Sensing*, Vol. 46, 2345–2356, 2008.
3. Cuccoli, F. and L. Facheris, "NDSA measurements between two LEO satellites in Ku and K bands for the tropospheric water vapor estimate: Performance evaluation at global scale," *IEEE International Geoscience and Remote Sensing Symposium, IGARSS 2009*, Vol. 5, V-296–V-299, 2009.
4. Facheris, L., et al., "Alternative measurements techniques for LEO-LEO radio occultation (AIMeTLEO)," ESA-ESTEC Contract, No. 17831/03/NL/FF Final Report, Jul. 2004.
5. Liebe, H. J., G. A. Hufford, and M. G. Cotton, "Propagation modeling of moist air and suspended water/ice particles at frequencies below 1000 GHz," *AGARD, 52nd Specialists Meeting of the Electromagnetic Wave Propagation Panel on "Atmospheric Propagation Effects through Natural and Man-Made Obscurants for Visible to MMWave Radiation"*, Palma de Mallorca, Spain, May 1993.

Magnetic Response of Random Ensemble of Small Non-magnetic Particles in Theory of Electromagnetic Wave Multiple Scattering

M. Yu. Barabanenkov

Institute of Microelectronics Technology, Russian Academy of Sciences
Chernogolovka, Moscow Region 142432, Russia

Abstract— Magnetic response of Mie resonance-based random composites consisting of silicon and gold particles is numerically investigated in the visible and terahertz frequency ranges on the basis of general theory of wave multiple scattering in random discrete media. In particular, in the approximation of independent spherical particles it is shown that excitation of the lowest Mie modes leads to the most pronounced resonant character of the effective magnetic permeability.

1. INTRODUCTION

Increasing attention on metamaterials has been paid due to their exciting physical behaviors and potential applications. While most of such artificial material structures have been developed on base of metallic resonant structure (see, e.g., [1]), Mie resonances of dielectric particles opened a simple and more versatile route for construction of isotropic metamaterials with higher operating frequencies (see, e.g., [2, 3]). Note, usually above metallic or dielectric composites are thought as periodic structures, with Maxwell's equations averaging over crystal unit cell followed by applying some intuitively appropriate Clausius-Mossotti relations for both effective dielectric permittivity and magnetic permeability [4, 5].

In this paper, we consider frequency spectra of effective magnetic permeability and dielectric permittivity of Mie resonance-based random (not periodic) composites, calculated on the basis of general theory of wave multiple scattering in random discrete media [6], with Maxwell's equations averaging over statistical ensemble of particles.

2. BASIC EQUATIONS

The subject of our interest is a random composite consisting of statistical ensemble of non-magnetic particles with given frequency ω dependent dielectric permittivity $\hat{\varepsilon}_1 = \varepsilon_1 + i4\pi\sigma_1/\omega$ randomly placed in a homogeneous background medium with constant dielectric permittivity ε_0 and unit magnetic permeability $\mu_0 = 1$. A homogenization has been done [7] of stochastic Maxwell's equations for electromagnetic field in such random composite by averaging over statistical ensemble, with using the technique of Dyson equation [8] for wave multiple scattering theory and applying different approximations [7] for transformed mass operator \tilde{M} . On this way we derive a generalized Lorentz-Lorenz formula for effective dielectric permittivity described the ensemble averaged electromagnetic wave field propagation in random composite under consideration. This generalized Lorentz-Lorenz formula for transversal $\varepsilon_{eff}^t(k)$ and longitudinal $\varepsilon_{eff}^l(k)$ components of effective dielectric permittivity tensor with respect to a wave vector \vec{k} in the random media reads

$$\frac{\varepsilon_{eff}^{t,l}(k) - \varepsilon_0}{\varepsilon_{eff}^{t,l}(k) + 2\varepsilon_0} = -\frac{\tilde{M}^{t,l}(k)}{3k_0^2} \quad (1)$$

where $k_0 = \varepsilon_0^{1/2}\omega/c$ stands for the wavenumber in the background medium.

Equation (1) is quite general, including such known cases as Maxwell-Garnett mixing rule with Clausius-Mossotti formula in the presence of multiple scattering on small non-correlated dielectric spheres [9], the popular Bruggeman mixing rule [10] at mass operator expansion along scattering potential powers, and a few collective effects. The generalized Lorentz-Lorenz formula obtained leads to effective dielectric permittivity tensor with spatial dispersion that gives possibility to extract an effective magnetic permeability by known limit procedure [11] at weak spatial dispersion.

In the next section, we calculate an effective magnetic permeability of a random Mie medium in the first order of the particle number density on the basis of this medium effective dielectric permittivity with spatial dispersion utilizing the well-known Lindhard rule [12]

$$1 - \frac{1}{\mu_{eff}} = \left(\frac{\omega}{c}\right)^2 \frac{\varepsilon_{eff}^t(k) - \varepsilon_{eff}^l(k)}{k^2} \quad (2)$$

in the long wavelength limit $k \rightarrow 0$.

3. NUMERICAL RESULTS

In this section, we evaluate the effective magnetic permeability defined by Eq. (2) in the approximation of wave electric and magnetic dipole scattering on independent spherical particles. In such a case Eq. (2) acquires a form

$$1 - \frac{1}{\mu_{eff}} = \frac{4\pi f_1 \chi}{(1 - 4\pi f_1 \eta/3)^2} \quad (3)$$

Here f_1 stands for the particle number density; electric η and magnetic χ susceptibilities of a spherical particle are given by [13] $\eta_{Mie} = (3i/2k_0^3)a_1$ and $\chi_{Mie} = (3i/2k_0^3)b_1$ where a_1 and b_1 are the Mie scattering coefficients. Besides, magnetic susceptibility of small spherical particle obeys the well-known asymptotic behavior [11]

$$\frac{\chi_{LL}}{\Omega} = -\frac{3}{8\pi} \left(1 - \frac{3}{\kappa^2 r_0^2} + \frac{3}{\kappa r_0} \text{ctg} \kappa r_0 \right) \quad (4)$$

where spherical particle has radius r_0 and volume Ω ; $\kappa = (\hat{\epsilon} - \epsilon_0)^{1/2} \omega/c$ is specific complex wavenumber. We suppose that the wavenumber $k_1 = \epsilon_1^{1/2} \omega/c = 2\pi/\lambda_1$ inside sphere's material with positive dielectric permittivity $\epsilon_1 \geq 0$ is greater than the inverse skin layer depth $p = (\hat{\epsilon}_1''/2)^{1/2} \omega/c$, $|k_1^2 - k_0^2| - p^2 \gg 0$, and the wavelength λ_1 is smaller than sphere radius, $r_0(k_1^2 - k_0^2)^{1/2} \approx k_1 r_0 \gg 1$.

We start with interesting computational result of perfect diamagnetism of gold spheres ensemble in the frequency range from 10 up to 200 THz followed by narrow deep at the frequency $\omega = 425$ THz and spike (Fig. 1). Frequency dispersion of the gold dielectric permittivity was taken from [14]. It is seen that the effective permeability is resonant function with typical shape which may be called as “deep and spike” (DS). Unfortunately, the curve in Fig. 1 corresponds to unphysical value of volume filling factor equal to $\Omega f_1 = 0.9$. At the same time, as it is seen from Fig. 2 gold composites with particles radius varied from 0.062 up to 0.6 μm and fixed particle density demonstrate magnetic response at the frequency $\omega = 425$ THz with the magnitude of μ_{eff} crossing the zero value at filling factor of 0.62. The latter also means that the composite is dense medium. Our calculations show that if filling factor falls in the range from 0.2 up to 0.3 with constant radius equal to 0.6 μm , the value of $\Re \mu_{eff}$ will be in the range from 0.8 down to 0.7.

Figure 3 represents results of computations by Eq. (2) for random ensemble of silicon spheres in the visible part of electromagnetic wave frequencies. The frequency position of the DS area may be tuned by the particles size according to the rule that the bigger the particle size, the slightly lower is the frequency position of the DS area with simultaneous spectral shrinkage of this area itself. Note, the dependence of the μ_{eff} upon frequency is represented by a dense set of deeps and peaks when the silicon particles size is of the order of a few micrometers. A lot of Mie modes excited in sufficiently big spheres may be responsible for abovementioned set of deeps and peaks on the analogy of these modes responsibility for spikes in the transmission spectra of photonic crystals [15].

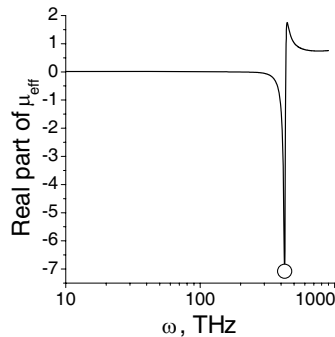


Figure 1: Calculated by Eq. (3) (using χ_{Mie} expression) dependence of $\Re \mu_{eff}$ of gold spheres ($r_0 = 0.6 \mu\text{m}$, $f_1 = 10^{12} \text{cm}^{-3}$) dispersed in air on frequency. Open circle visualizes the deep frequency of 425 THz.

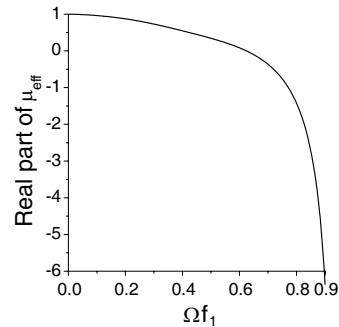


Figure 2: Calculated dependence of $\Re \mu_{eff}$ of gold spheres dispersed in air upon composite filling factor at the frequency of 425 THz. The number density of the composite is fixed at $f_1 = 10^{12} \text{cm}^{-3}$ while spheres radius is varied from 0.06 up to 0.6 μm .

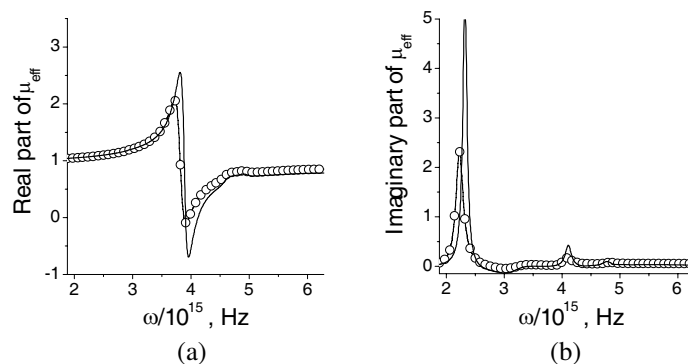


Figure 3: The dependence of the (a) real and (b) imaginary parts of effective magnetic permeability of silicon spheres ($r_0 = 0.05 \mu\text{m}$, $f_1 = 4 \times 10^{14} \text{cm}^{-3}$, $f_1\Omega = 0.21$) dispersed in air. Solid curves with open circles and solid curves without symbols are calculated by Eq. (3) in terms of the Hulst partial scattering amplitudes a_1 , b_1 and asymptotic Eq. (4), respectively.

4. CONCLUSIONS

In the approximation of independent spherical particles our calculations predict magnetic response of random composites consisting of small silicon and gold particles in the visible and terahertz frequency ranges, respectively. Physically, small size of silicon particles means that only the lowest magnetic Mie mode is excited in each particle during wave scattering (in the calculations radius of silicon spheres was smaller than $0.1 \mu\text{m}$ with the filling factor of about 0.2). Excitation of the lowest Mie modes leads to the most pronounced resonant character of the effective magnetic permeability. A contribution of high-order Mie modes into magnetic response of random media under consideration is required further investigation.

ACKNOWLEDGMENT

This work was supported in part by the Russian Academy of Sciences projects “Scientific bases of heterogeneous telecommunication and location systems”, “Fundamental bases of nanostructures and materials technology”.

REFERENCES

1. Linden, S., C. Enkrich, G. Dolling, M. W. Klein, J. Zhou, T. Koschny, C. M. Soukoulis, S. Burger, F. Schmidt, and M. Wegener, “Photonic metamaterials: Magnetism at optical frequencies,” *IEEE J. Selected Topics Quant. Electr.*, Vol. 12, No. 6, 1097–1104, 2006.
2. Zhao, Q., J. Zhou, F. Zhang, and D. Lippens, “Mie resonance-based dielectric metamaterials,” *Materials Today*, Vol. 12, No. 12, 60–69, 2009.
3. Merlin, R., “Metamaterials and Landau-Lifshitz permeability arguments: Large permittivity begets high-frequency magnetism,” *PNAS*, Vol. 106, 1693–1698, 2009.
4. Silveirinha, M. G., “Metamaterial homogenization approach with application to the characterization of microstructured composites with negative parameters,” *Phys. Rev. B*, Vol. 75, No. 1, 115104–115119, 2007.
5. Silveirinha, M. G., “Generalized Lorentz-Lorenz formulas for microstructured materials,” *Phys. Rev. B*, Vol. 76, No. 4, 245117–145126, 2007.
6. Barabanenkov, Y. N., “Asymptotic limit of the radiative transfer theory in problems of multiple wave scattering in randomly inhomogeneous media,” *Physics-Uspexhi*, Vol. 52, No. 5, 502–506, 2009.
7. Barabanenkov, Y. N., M. Y. Barabanenkov, and S. A. Nikitov, “Artificial magnetism in theory of wave multiple scattering by random discrete non-magnetic conducting media,” Sep. 24, 2010, arXiv:1009.4770v1 [cond-mat.dis-nn].
8. Frish, V., *Wave Propagation in Random Media. Multiple Scattering by N Bodies (Provisional Version)*, Institut d’Astrophysique, Paris, 1965.
9. Mallet, P., C. A. Guerin, and A. Sentenac, “Maxwell-Garnett mixing rule in the presence of multiple scattering: Derivation and accuracy,” *Phys. Rev. B*, Vol. 72, 014205–014214, 2005.
10. Bruggeman, D. A. G., “Berechnung verschiedener physikalischer konstanten von heterogenen substanzen,” *Ann. Phys.*, Vol. 24, 636–679, 1935.

11. Landau, L. D. and E. M. Lifshitz, *Electrodynamics of Continuous Media, Course of Theoretic Physics*, Vol. 8, Butterworth-Heinemann, Elsevier, Oxford, 2004.
12. Lindhard, J., “On the properties of a gas of charged particle,” *S. Dan. Mat. Fys. Medd.*, Vol. 28. No. 8, 3–57, 1954.
13. Van de Hulst, H. C., *Light Scattering by Small Particles*, John Wiley, New York, 1957.
14. El-Kady, I., M. M. Sigalas, R. Biswas, K. M. Ho, and C. M. Soukoulis, “Metallic photonic crystals at optical wavelengths,” *Phys. Rev. B*, Vol. 62, No. 23, 15299–15302, 2000.
15. Barabanenkov, Y. N. and M. Y. Barabanenkov, “Mie resonances and Bragg-like multiple scattering in opacity of two-dimensional photonic crystals,” *JOSA A*, Vol. 23, No. 3, 581–585, 2006.

Radiometric Methods of Measurement of the Total Reflectivity, the Total Transmissivity and the Coherent Transmissivity of a Weakly Absorbing Random Discrete Medium Layer in the Millimeter Wavelengths Range

V. A. Golunov and Yu. N. Barabanenkov

V. A. Kotelnikov Institute of Radioengineering and Electronics of RAS, Fryazino Branch, Russia

Abstract— Radiometric methods of measurement of the total reflectivity, the total transmissivity and the coherent transmissivity have been devised and are presented. The methods of measurements of the total reflectivity and the total transmissivity are based on changes of front and back radiation background brightness within solid angle 2π . The method of measurement of the coherent transmissivity is based on the experimental dependence of the transmissivity on angular size of thermal source irradiating the under consideration medium sample. In contrast to the classic method based on using an oscillator or a noise generator, the devised method permits to measure the coherent transmissivity with the exception of necessity to average out an ensemble of under consideration random discrete medium realizations. The experimental setup by means of which the characteristics listed above have been measured is described.

1. INTRODUCTION

Set of characteristics such as the total reflectivity, the total transmissivity and the coherent transmissivity provides sufficient information on the effects of volume scattering electromagnetic waves from random discrete medium layer. It is well-known [1] that the classic method of measurement of the coherent transmissivity is based on using an oscillator or a noise generator and requires averaging-out an ensemble of under consideration random discrete medium realizations. To measure the coherent transmissivity together with the total reflectivity and the total transmissivity of the single sample of a random discrete medium, the radiometric methods have been devised and are presented.

2. DEFINITIONS

The total reflectivity R and the total transmissivity t of a scattering layer can be written as

$$R(\vartheta, \varphi) = \sec \vartheta \int_0^{2\pi} d\varphi \int_0^{\pi/2} g(\vartheta, \varphi; \vartheta_0, \varphi_0) \cos \vartheta_0 \sin \vartheta_0 d\vartheta_0, \quad (1)$$

$$t(\vartheta, \varphi) = \sec \vartheta \int_0^{2\pi} d\varphi \int_{-\pi/2}^0 g(\vartheta, \varphi; \vartheta_0, \varphi_0) \cos \vartheta_0 \sin \vartheta_0 d\vartheta_0, \quad (2)$$

where $g(\Omega, \Omega_0)$ — bistatic indicatrix (phase function) [2], $\Omega_0 = \Omega(\vartheta_0, \varphi_0)$ and $\Omega = \Omega(\vartheta, \varphi)$ — incidence and receive directions. We write the coherent transmissivity t_c as

$$t_c = \lim_{\Delta\Omega_S \rightarrow 0} t(\Delta\Omega_S) = \lim_{\Delta\Omega_S \rightarrow 0} \int_{\Delta\Omega_S} g(\Omega, \Omega_0) d\Omega_0, \quad (3)$$

where $\Delta\Omega_S$ — solid angle of the thermal source with uniform brightness.

In Raleigh-Jean's approximation the apparent temperature T of the layer with uniform thermodynamic temperature T_c can be written as follows:

$$T = \varkappa T_c + RT_R^* + tT_t^*, \quad (4)$$

where \varkappa — the emissivity of the layer, T_R^* and T_t^* — the brightness temperatures of front and back illumination which can be determined as:

$$T_{R,t}^*(\Omega) = \frac{\int g_{R,t}(\Omega, \Omega_0) T_{R,t}(\Omega_0) \cos \vartheta_0 d\Omega_0}{\int_{2\pi} g_{R,t}(\Omega, \Omega_0) \cos \vartheta_0 d\Omega_0} \quad (5)$$

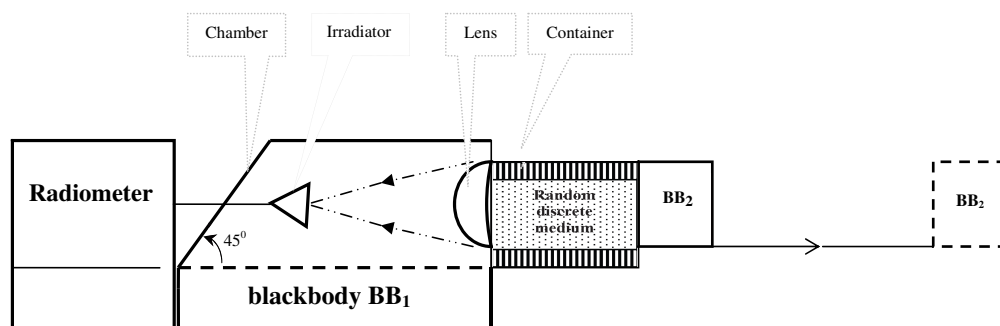
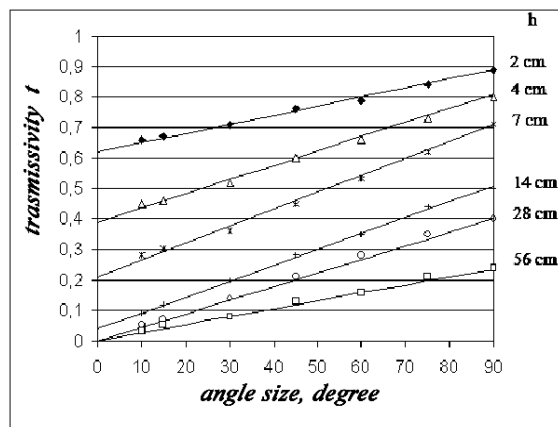


Figure 1: Principle setup of radiometric bench instrument.

Figure 2: Relationship between the transmissivity of like-snow medium layer with thickness h (mixture of granulated polythelene and styrofoam with volume density 0.09) and the angular size $\theta = \arctg(d/2L)$ of the blackbody BB_2 with round form. Wave-length $\lambda = 8$ mm.

3. METHODS OF MEASUREMENT OF THE TOTAL REFLECTIVITY AND THE TOTAL TRANSMISSIVITY

Let two measurements of the apparent temperature T_1 and T_2 of the layer have been conducted provided that $T_t^* = \text{const}$, $T_R^* = \{T_{R1}^*, T_{R2}^*\}$. Then the total reflectivity can be obtained from (4) in the form:

$$R = \frac{T_1 - T_2}{T_{R1}^* - T_{R2}^*} \quad (6)$$

In the case of $T_R^* = \text{const}$, $T_t^* = \{T_{t1}^*, T_{t2}^*\}$, one can obtain the total transmissivity expression in the form:

$$t = \frac{T_1 - T_2}{T_{t1}^* - T_{t2}^*} \quad (7)$$

Since output voltage u of microwave radiometers depends linearly on the apparent temperature, the expressions (6) and (7) can be rewritten as

$$R = \frac{u_1 - u_2}{u_{R1}^* - u_{R2}^*}, \quad t = \frac{u_1 - u_2}{u_{t1}^* - u_{t2}^*} \quad (8)$$

Thus the procedure of the radiometric measurements can be realized without absolute calibration of radiometers.

4. EXPERIMENTAL RADIOMETRIC BENCH INSTRUMENT

Principle setup of radiometric bench instrument designed for the measurements of the total reflectivity, the total transmissivity and the coherent transmissivity is shown in Fig. 1.

The experimental radiometric bench instrument consists of some of radiometers operating between 20 GHz and 94 GHz, the metallic chamber with the lens and the black body (BB_1) cooled

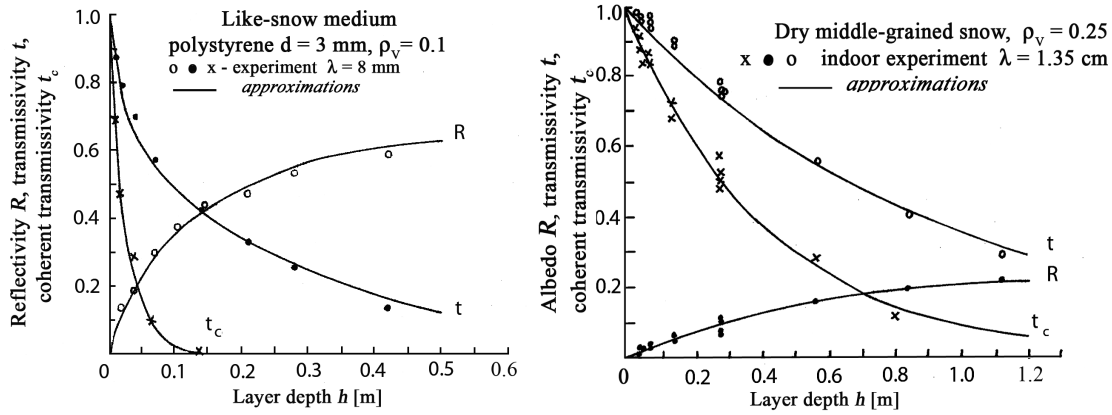


Figure 3: Experimental plots of the total reflectivity R , the total transmissivity t and the coherent transmissivity t_c versus thickness of scattering layer thickness.

down by means of liquid nitrogen. Teflon lens with diameter 0.2 m and focus length 0.4 m is placed on the front wall of the chamber. There is a hole for the radiometer guide and irradiator on the opposite wall. The irradiator is located in the lens focus.

The sample being investigated are placed into a metallic cylindrical container with diameter 0.2 m and is put closely to the lens during the measurement. It is significant the lens plays double role: on the one hand it forms a receive beam and on the other hand it is a transparent window for the sample illumination by the blackbody BB_1 . The second blackbody BB_2 cooled down by means of liquid nitrogen is used to measure the total transmissivity and the coherent transmissivity. In the latter case the blackbody BB_2 is removed from the sample along optical axis of the lens.

5. THE FEATURES OF THE MEASUREMENTS OF THE TOTAL REFLECTIVITY AND THE TOTAL TRANSMISSIVITY

All measurements concerned below were conducted indoors under $T_c = T_{R1} = T_{t1} = T_r$ (see (4)–(7)), T_r — thermodynamic temperature of the room.

When the total reflectivity being measured, the thermodynamic temperature $T(BB_1)$ of the blackbody BB_1 is varied from $T(BB_1)_1 = T_r = 290\text{--}300\text{ K}$ to $T(BB_1)_2 = 77\text{ K}$ under the thermodynamic temperature of the blackbody BB_2 , $T(BB_2) = T_r$. The brightness temperature of the special metallic scatterer (for example, sphere) was used as T_{R2}^* . It is necessary to take proper account of thermal negative profit into the chamber and to use true brightness temperature T_{R2}^* in (6). The scatterer with diameter 0.2 m enclosed within the metallic cylindrical container was put closely to the lens (i.e., in the sample absence) under $T(BB_1)_2 = 77\text{ K}$.

Thus the total reflectivity (6) was determined as follows:

$$R = \frac{T_r - T_2}{T_r^- T_{R2}^*} = \frac{u_r - u_2}{u_r - u_{R2}^*}$$

When the total transmissivity being measured, the thermodynamic temperature $T(BB_2)$ of the blackbody BB_2 is varied from $T(BB_2)_1 = T_r = 290\text{--}300\text{ K}$ to $T(BB_2)_2 = 77\text{ K}$ under the thermodynamic temperature of the blackbody BB_1 , $T(BB_1) = T_r$. At the same time $T_{t1}^* = T_r$, $T_{t2}^* = 77\text{ K}$ in (7). Thus the total transmissivity is determined as follows:

$$t = \frac{T_r - T_2}{T_r^- T_{t2}^*} = \frac{u_r - u_2}{u_r - u_{t2}^*}$$

6. THE FEATURES OF THE MEASUREMENTS OF THE COHERENT TRANSMISSIVITY

The procedure of the measurement of the coherent transmissivity consists in that distance L between the sample and blackbody BB_2 with $T(BB_2) = 77\text{ K}$ is discretely varied under $T(BB_1) = T_r$. To give proper weigh beam divergency, at every distance L radiometer output voltage u is records in two different situations: a) the sample is placed near the lens — $u(L)$; b) the sample is removed from the lens — $u_0(L)$. If the latter is the case, the distance L between the lens and blackbody BB_2 is fixed. When the blackbody BB_2 has been removed out the lens field of vision, additional level

of radiometer output voltage u_r required for measurements is records. This level is independent of distance L .

Thus the transmissivity $t(L)$ is determined as follows:

$$t(L) = \frac{u_r - u(L)}{u_r - u_0(L)}$$

It follows from experimental data handling, in the case of the samples of a weakly absorbing random discrete media, the dependence of the transmissivity on the angular size $\theta = \arctg(d/2L)$ of the blackbody BB_2 with round form and diameter d is linear:

$$t(\theta) = a + b\theta, \quad (9)$$

where a , b — constants of proportionality (see Fig. 2).

Since the coherent transmissivity is determined provided that the thermal source is point one, so it follows from (9):

$$t_c = \lim_{\theta \rightarrow 0} t(\theta) = a$$

It is well-known [3] that when a thermal distant radiation source with angular size $\theta > \lambda/d$ being used, the effect of interference under diversity technique is smoothed and at the same time the more size the stronger smoothing. In the case of using devised method of measurement of the coherent transmissivity, this property of thermal radiation sources excludes necessity to average out an ensemble of realizations of under consideration random discrete medium.

As illustrations of results of measurements by developed methods, Figs. 3 and 4 show plots of the total reflectivity, the total transmissivity and the coherent transmissivity of a like-snow medium layer and undisturbed sample of snow layer versus layer thickness.

7. CONCLUSIONS

It is shown that by using developed methods and designed radiometric bench instrument one can measure three important parameters, namely the total reflectivity, the total transmissivity and the coherent transmissivity, of only one sample of a weakly absorbing random discrete media layer under indoor conditions. Such ability are of great importance in connection with that at present time an experiment is only effective method of investigation of strongly scattering random discrete media (for example, dry snow cover in the millimeter wavelength range [4]).

REFERENCES

1. Ishimaru, A. and V. Kuga, "Attenuation constant of coherent field in dense distributions of particles," *J. Opt. Soc. Amer.*, Vol. 72, No. 10, 1317–1320, 1982.
2. Golunov, V. A., V. A. Korotkov, and E. V. Suckhonin, "Volume scattering effects under millimeter emission from atmosphere and snow cover," *Itogy Nauky i Teckniky*, Vol. 40, 68–136, Ser. Radiotekhnika, M., Vinity, 1990 (in Russian).
3. Born, M. and E. Wolf, *Principles of Optics*, Pergamon, Oxford, 1980.
4. Golunov, V. A., "Thermal emission from dry homogeneous snow cover in the millimeter wavelength range," *Zarubegnaia Radioelektronika — Uspekhy Sovremennoy Radioelektroniky*, No. 6, 35–44, 2002 (in Russian).

Analysis of the Radiated Emissions of IT Equipment

R. Przesmycki, M. Wnuk, L. Nowosielski, K. Piwowarczyk, and M. Bugaj

Faculty of Electronics, Military University of Technology
Gen. S. Kaliskiego 2 Str., Warsaw 00-908, Poland

Abstract— Telecommunications and data communications devices are integral part of complex systems, which determine the correct functioning of economy. Efficiency and reliability of the functioning of electric and electronic devices decide about the functioning and development of national economy. In the article special attention is undesirable emissions. These emissions are by products generated unintentionally during realization of basic function of the device. They are formed in electric circuits containing inductances and capacities in which there occur sudden changes of current or voltage, relatively fluctuating changes of density of electric charge carriers or in which there occurs positive back coupling.

In the article presented the disturbances of generated emissions by IT equipments, the methodology of measuring radiated emissions generated by IT devices in accordance with the EN 55022:2006 standard is presented and the results of measurements carried out on particular number of samples consisting of central processing units produced in the years 2007–2011 are demonstrated. The measurements of radiated emissions generated by IT equipments have been performed in the Electromagnetic Compatibility Laboratory at the Faculty of Electronics of the Military University of Technology in Poland.

1. INTRODUCTION

Modern societies have become dependent on a number of electrical and electronic equipment. A special role is played by devices for transmission, storage and processing of information. Therefore, computing devices have become an integral part of the complex systems conditioning the proper functioning of the economy.

The reliability and correct functioning of IT equipment determines the operation and development of many areas of a country's economy. It depends largely on the resistance to electromagnetic exposure (continuous and pulsed) and the level of the electromagnetic interference in the external environment surrounding the systems. Therefore, we should test not only the resistance of IT equipment to electromagnetic fields, but also the level of electromagnetic interferences emitted into the surrounding environment (emission testing). The level of interference in the environment depends not only on the level of interferences emitted into the environment by equipment and systems operating in the environment surrounding the facility, but also on the level of electromagnetic fields radiated by the facility itself.

The above issue should be considered not only in terms of electromagnetic compatibility, but also because of the need to ensure the security of information transmitted or processed. Currently available devices and systems allow the recovery of the processed or transmitted information from the emission of electromagnetic interference (scattered electromagnetic fields). Therefore, developed countries pay special attention to issues related to IT equipment emissivity and resistance to electromagnetic fields. Requirements for both emissivity and resistance to electromagnetic exposure, especially of IT equipment belong today to the category of basic requirements.

The article presents the results of measurements of radiated emission levels of modern IT equipment obtained through tests performed on a limited number of samples consisting of PC CPUs produced in 2007–2011. The tests were performed at the Laboratory for Electromagnetic Compatibility of the Electronics Department at the Military Technical Academy in accordance with the methodology set out in PN-EN 55022:2006.

2. A DEVICE'S EMISSIVITY RATING

Each IT device is characterized by a parameter ε which determines its emission capacity. This is a function of emission direction φ , pulsation ω , and time t [1]:

$$\varepsilon = f(\varphi, \omega, t). \quad (1)$$

Electromagnetic energy emitted by IT devices to the surrounding environment is divided into two groups. The first group are wanted emissions associated with the transmission and processing of signals carrying useful information. Wanted emissions are eliminated through a proper

and meticulous allocation of frequency bands or single frequencies. This phenomenon is called the electromagnetic spectrum management, or building resistance (where possible) of objects to electromagnetic fields.

In this paper, particular attention is paid to the second group of electromagnetic emissions, namely unwanted emissions. These emissions are by-products produced inadvertently during the implementation of the basic functions of IT equipment. They arise in electrical circuits containing inductance and capacitance, in which sudden changes of current or voltage, or fluctuating changes in the density of charge carriers occur, or in which a positive feedback or negative resistance take place.

The formation and distribution of interference energy in the frequency spectrum and temporal characteristics are dependent on the structure and electrical parameters of an object in the high-frequency field, its temporal characteristics and the impedance. Taking into account the temporal characteristics, interferences generated by any objects can be divided into continuous and short-term (pulse), whereas in terms of the frequency characteristics into narrowband and broadband.

Electromagnetic energy is released into the surrounding environment as a result of: electromagnetic radiation; conduction through power cables, signal cables, connecting the source of interference with the surrounding environment; capacitive coupling; inductive coupling.

As the interference energy penetrates the external environment on different routes, levels of interferences generated by an object (the source of interferences) is variously defined. Most frequently the level of interferences emitted by a device is determined by specifying the value of radiated power (P_z) or the intensity of electromagnetic field (E_z) or (H_z), at a specified distance from the source or the voltage (U_z), or interference current (I_z) measured in the branch line of known impedance. These values are given as a function of frequency, i.e., their spectral characteristics [1].

3. DEFINITION OF INTERFERENCE

Frequency is the basic parameter of an electromagnetic interference. Basically the EMC standards cover the range from 0 Hz to 40 GHz. Currently, however, not all frequency ranges are fully regulated. The first important range is the range in the vicinity of power frequency (50 Hz in Europe). Most of the loads connected to the mains are non-linear. This creates a serious problem, because these loads tend to generate more current at the frequency equal to a multiple mains frequency. These currents, called harmonics, are generally considered to 40 or 50 multiples of mains frequency. In other words, our first frequency ranges from 50 Hz to 2 kHz or 2.5 kHz. For 60 hertz mains — from 60 Hz to 2.4 kHz or 3 kHz. From the end of the harmonics range of 9 kHz, the frequency range is currently not regulated by any standards. The high-frequency range begins above 9 kHz. This range is often called the radio frequency range or the RF range. EMC regulations restrict the frequency range up to 400 GHz, although the measurement methods for all the above range are not yet defined. Existing standards define test methods from 9 kHz to 6 GHz. Looking at the harmonics frequencies, even above 6 GHz, the regulations do not adequately address the problems of the full RF range. The RF range is generally divided into two sub-ranges: conducted and radiated. For lower RF ranges, disturbance is considered as a signal conducted by wire, rather than by radiation. The main reason is the construction of the measuring antennas which requires larger dipoles for lower frequencies. In other words, the physical size of most devices is simply not sufficient for interference radiation. Once the exact frequency is not defined, the standards establish the conducted RF range between 150 kHz and 30 MHz. The upper frequency of 30 MHz is then the beginning of the radiated RF range. The upper limit of the radiated RF range depends on the standards, but generally it is about 6 GHz [3].

4. RADIATED EMISSION LEVELS OF IT DEVICES RANGING FROM 30 MHz TO 6000 MHz

Radiated emission levels of modern IT equipment were determined on the basis of measurements of disturbances of radiated emissions coming from PC CPUs, carried out on a specific number of pieces of equipment at a distance of 3 m from a test device. The measurement results made it possible to analyse the radiated emission levels of modern IT equipment.

The measurements were performed in the frequency range from 30 MHz to 6000 MHz using a peak detector. However, due to research methodology in line with PN-EN 55022:2006 and measuring equipment used (mostly antennas), measurements were divided into two sub-bands. The first frequency range extended from 30 MHz to 1000 MHz, the second — from 1000 MHz to 6000 MHz. In the first frequency range, 139 PCs were tested, in the second frequency range — 104 PCs. Figures 1

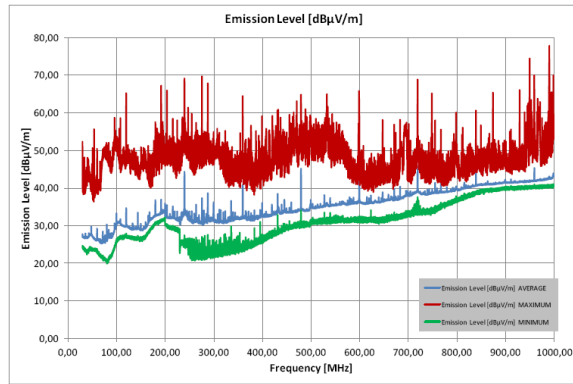


Figure 1: Maximum, minimum and average levels of radiated interferences within 3 m from any PC in the frequency range from 30 MHz to 1000 MHz.

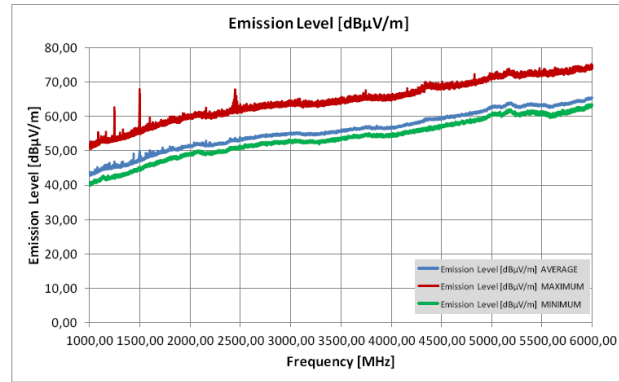


Figure 2: Maximum, minimum and average levels of radiated interferences within 3 m from any PC in the frequency range from 1000 MHz to 6000 MHz.

Table 1: Electromagnetic field strength levels of the test device from PC CPU internal components.

The device /type of interface	f [MHz]	The emission level at a distance of 3 m from the EUT [dB μ V/m]	
		MAX	AVERAGE
USB	119.00	46.48	29.86
USB	120.00	65.26	35.11
Mouse/PS2	126.00	49.66	30.04
Printer/LPT	144.00	48.33	33.42
HDD	155.00	46.58	29.09
Mouse/PS2	166.00	39.58	30.54
USB	180.00	57.50	35.96
Keyboard/USB	200.00	48.31	35.37
USB	240.00	69.17	42.21
HDD	255.00	46.57	31.92
Graphics card /VGA	350.00	46.23	32.43
Graphics card /VGA	380.00	44.93	32.41
USB	480.00	55.56	42.34
HDD	535.00	53.14	35.27
Graphics card /VGA	605.00	43.71	35.99
Graphics card /DVI	720.00	68.89	44.96
Graphics card /VGA	820.00	44.15	40.08
USB	960.00	58.89	43.18

and 2 show the maximum, minimum and average levels of the measured values of electromagnetic field strength radiated by modern information technology equipment, including all test equipment.

5. THE ANALYSIS OF THE MEASUREMENT RESULTS CONCERNING IT EQUIPMENT RADIATED EMISSION

Analysing the average values of radiated interferences, we can see that for a few frequencies, emission levels are much higher than for others. For these frequencies, components were identified using the elimination method which involves disconnecting successive interface loads of test PC CPUs. Table 1 shows the frequency of radiated emissions emanating from various components inside a PC CPU, and their levels measured in accordance with the methodology described in the standard PN-EN 55022:2006. The frequency of certain radiated interference levels were determined for selected frequencies. Then, on this basis, probability distributions of particular radiated interference values

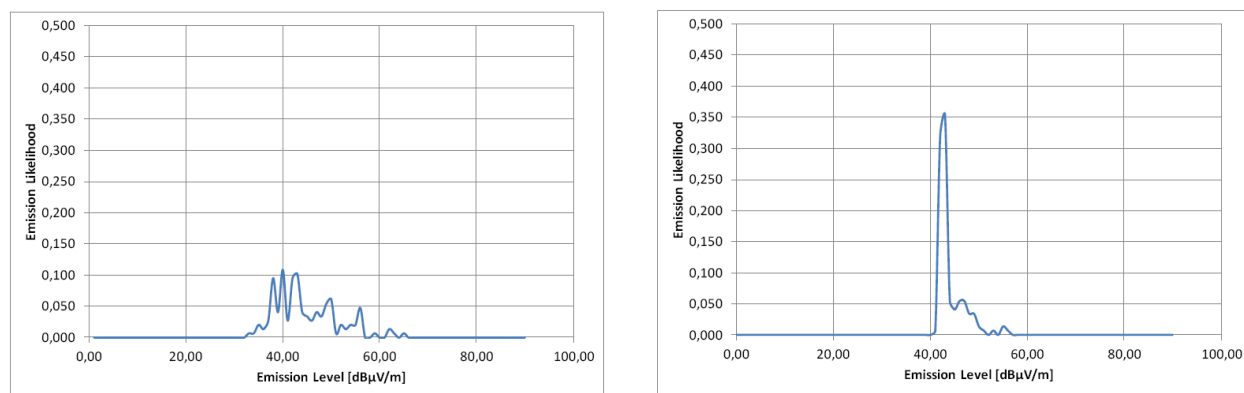


Figure 3: Emissions likelihood of individual values of radiated emission for $f = 480$ MHz and $f = 1$ GHz.

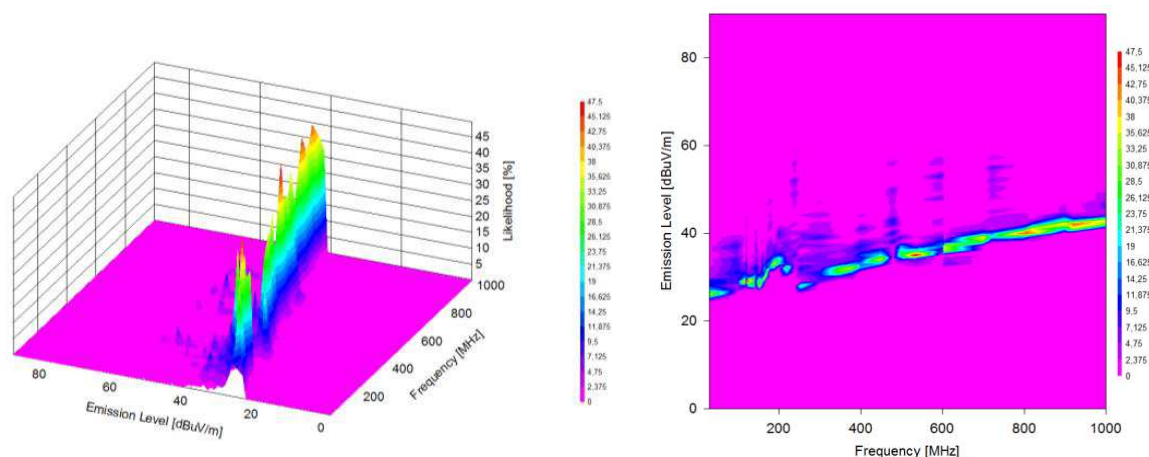


Figure 4: Three-dimensional view of the probability distributions of individual values of radiated interferences in the frequency range from 30 MHz to 1000 MHz.

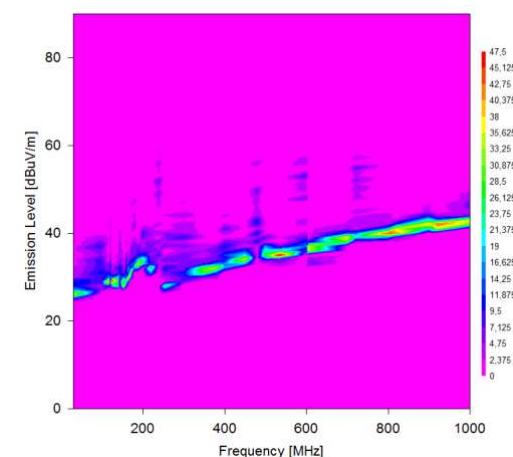


Figure 5: Graph of the probability distributions of individual values of radiated interferences in the frequency range from 30 MHz to 1000 MHz.

for a given frequency were defined (Figure 3). This allows us to learn whether it is one or more interference values that occur for a particular frequency. In the case of one dominant value in the distribution, there is no interference, while a certain level means the measurement environment background noise. In another case, we deal with the occurrence of interferences originating from individual PC CPU modules, with different values for the equipment under test. A summary of the probability distributions is shown in Figure 4 and Figure 5.

6. CONCLUSIONS

The creation of the European Union, with its unified legislation, and thus harmonized requirements relating to electromagnetic compatibility (EMC), means that all IT equipment must meet certain standards for the applicable New Approach directives. Due to the compatibility of IT equipment with the EMC Directive, this article presents the radiated emission levels of modern IT equipment obtained in the course of tests in the frequency range from 30 MHz to 6000 MHz according to PN-EN 55022:2006.

The article presents and sets the maximum levels of radiated emissions originating from modern computer equipment available on the Polish market, and thus the European Union market. Manufacturers of computer equipment aspire to decrease the levels as much as possible. During the tests a trend of declining levels of radiated interferences in the function of testing time was observed. Individual components of PC CPUs were also identified, based on spectra of radiated emissions from PC CPUs.

ACKNOWLEDGMENT

The research work financed from the financial funds assigned to the science in the year 2012 as the development work. The research work is realized in Poland.

REFERENCES

1. Więkowski, T., “Badania kompatybilności elektromagnetycznej urządzeń elektrycznych i Elektronicznych,” *Oficyna Wydawnicza Politechniki Wrocławskiej*, Wrocław, 2001.
2. PN-EN 55022:2006, “Information technology equipment. Radio disturbance characteristics. Limits and methods of measurement,” 2011.
3. Przesmycki, R., et al., “Analiza poziomów emisji promieniowanej współczesnych urządzeń informatycznych w paśmie 30 Hz–6000 MHz,” *Przegląd Telekomunikacyjny*, 384–387, Jun. 2010, ISSN 1230-3496.
4. Przesmycki, R., L. Nowosielski, M. Bugaj, and K. Piwowarczyk, “Analiza emisji promieniowanej współczesnych urządzeń informatycznych,” *Przegląd Elektrotechniczny (Electrical Review)*, Str: 4-6, Feb. 2012, ISSN 0033-2097.

Antenna Gain Measurement by Comparative Method Using an Anechoic Chamber

R. Przesmycki, M. Wnuk, L. Nowosielski, K. Piwowarczyk, and M. Bugaj

Faculty of Electronics, Military University of Technology
Gen. S. Kaliskiego 2 Str., Warsaw 00-908, Poland

Abstract— The article focuses on the implementation of the antenna gain measurements in the anechoic chamber. In the article showed a detailed description of the developed procedure of measuring gain by the comparative method. In the article also described the methodology and principles of the laboratory stand for measuring gain of antennas in the anechoic chamber. The developed method of measuring the gain of antennas provides an easy way to determine the value of this parameter and is often used in antenna measurements. It is a method that is not time consuming. However, preparing the measurement requires more attention and time. From preparing the laboratory stand by the right way depends the measurement results. The summary of this article presented the results of measurement and interpretation of results for the sample antenna in anechoic chamber.

1. INTRODUCTION

It is not easy to define the concept of an antenna in simple words. An antenna is most often defined by the function it fulfils in the radio-communication process. We say that an antenna is a device which converts electromagnetic energy conducted on closed paths into electromagnetic waves propagating in space for transmitting antennas, and vice versa for receiving antennas. An antenna is thus a sort of device that matches a waveguide to a free space. Because of its location between a transmitting or a receiving device and the space, requirements relating to antennas are imposed both by the conditions of electromagnetic wave propagation in space and by the impact of an antenna, as part of a device, on its work. An antenna is characterized by many parameters which determine its properties. In practice, the most commonly measured parameters of antennas are: the characteristics of radiation, standing wave ratio, directivity and energy gain. Antenna directivity (D) is a parameter describing the ability of a single antenna to directionally radiate electromagnetic energy in comparison to a reference antenna. It is the ratio of active power radiated per unit solid angle by a given antenna and a reference antenna in the direction of the maximum radiation of the two antennas, provided that the radiation powers are the same. Antenna gain (G) can be defined as the ratio of the density of radiation in a given direction to the density of radiation which would be obtained, if the same power brought to an antenna was radiated isotropically. This parameter does not include losses arising from impedance or polarizing mismatch (it only takes into account losses in the antenna). Directivity and gain of an antenna are combined by the following relationship:

$$G = D * \eta, \quad (1)$$

where η — antenna power efficiency.

Later in this article I focus on the implementation of the measurements of one of the above parameters — antenna power gain.

2. DETERMINING A DISTANCE BETWEEN ANTENNAS AND THEIR SUSPENSION HEIGHT

Antennas can be tested with a measurement procedure using signal sources, reference antennas and measuring receivers available in the Laboratory. The procedure is applied to test antennas: in terms of the antenna operation frequency range of 100 MHz ÷ 20 GHz, the maximum dimension of the test antenna — 2 m, the maximum antenna weight — 10 kg. The procedure can be used only when the room temperature in the Laboratory ranges from +20°C ÷ +30°C, and the relative humidity is 30% ÷ 85%.

Before measurements, it is necessary to check what type of measurement stand may be used to test the antenna. For this purpose, the critical distance of the far field must be defined. Setting the antennas at a distance greater than the critical distance of the field will provide lighting of the receiving antenna with a quasi-planar wave. An auxiliary antenna should always serve as the

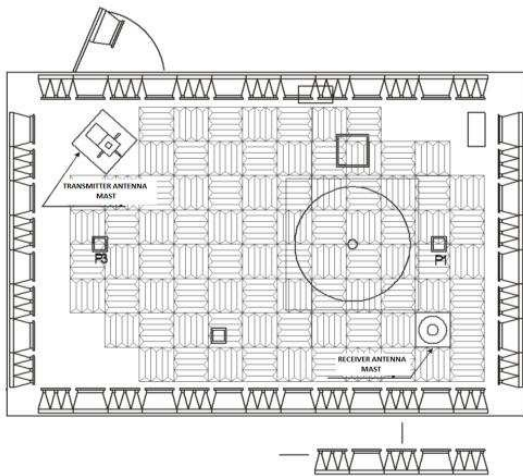


Figure 1: Layout of the measurement stand elements and the method of lining the chamber floor with absorbent material.

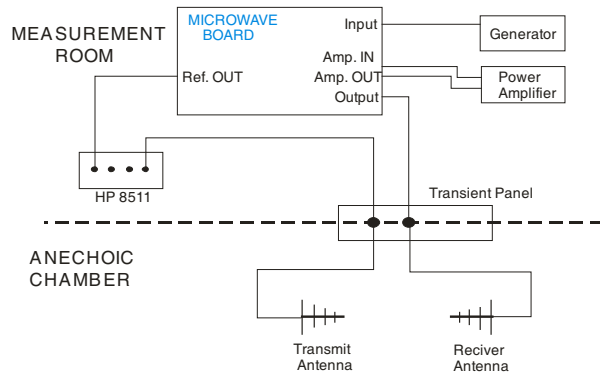


Figure 2: Diagram of high frequency connections in the position for measuring antenna gains.

transmitting antenna in the measuring system. A test antenna serves as the receiving antenna. Determination of the minimum distance between the antennas is based on Equation (2):

$$R_{\min} \geq \frac{2D^2}{\lambda}, \quad (2)$$

where: R_{\min} — the minimum distance between the transmitting and receiving antennas in [m], D — the maximum transverse dimension of the receiving antenna in [m], λ — the wavelength at which measurements are performed in [m].

The transmitting antenna should be located at a minimum height of 2 m. If tests are conducted in an anechoic chamber prepared for the measurements, it is best to place the transmitting antenna at a height of 2.5 m. This will ensure that the antenna is placed at equal distances from the absorber located on the floor and ceiling of the chamber. The receiving antenna should be placed on a mast to allow adjustment of its position in the range of 1 ÷ 4 m. The transmitting antenna should be connected to the signal source, and the auxiliary antenna — to the received signal level meter. The desired frequency of the signal source should be set and the source output power level should be controlled so as to get a high enough level of the received signal to guarantee the smallest error of measurement made by the receiver. After the mutual arrangement of the antennas, their angular position should not be changed.

3. THE MEASUREMENT STAND ARRANGEMENT

The measurement stand for testing antenna gains in an anechoic chamber requires lining the chamber with floor absorbers. If the frequencies at which the antenna will be tested cover a range below 500 MHz, it is necessary to put panels with ferrite tiles on the floor, and then to lay IP-045C absorbers on top of them. For measurements at frequencies greater than 500 MHz, it is sufficient to line the floor with IP-045C absorbers without ferrite panels. The arrangement of individual elements of the measuring path and absorbent materials is shown in Figure 1. During the preparation procedure, all the elements of the transmission and reception paths must be connected according to the diagram shown in Figure 2.

Before the measurements, the desired temperature and humidity conditions must be stabilized in the chamber and the measuring and control equipment rooms. For this purpose, the air conditioning system in the chamber and apparatus rooms, and the devices that will be used during the measurements should be started at least one hour before the measurements start. If possible, additional air circulation should be limited, i.e., the main entrance and service door of the chamber and the doors on ancillary premises should be closed.

Measuring the test antenna gain requires one or two additional auxiliary antennas. Auxiliary antennas should have a narrow main beam of radiation, low side lobe level and linear polarization. Below 200 MHz a biconical antenna or possibly symmetrical dipoles can be used as the transmitting

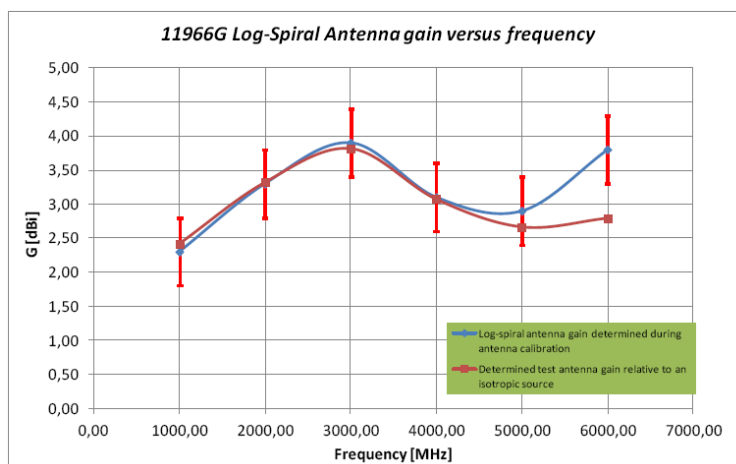


Figure 3: Gain of the tested antenna in the frequency function $G[\text{dBi}] = f(f[\text{MHz}])$.

antenna. A log-periodic antenna can be used for frequencies ranging 200 MHz–1 GHz. For measurements above 1 GHz, it is best to use horn antennas or broadband dorsal horns, but log-periodic antennas can also be applied.

4. THE MAIN GAIN MEASUREMENT PROCEDURE USING THE COMPARATIVE METHOD

When measuring gain with the comparative method, it is necessary to have detailed information on the course of the auxiliary antenna gain. This antenna is used as a reference antenna which will be referred to when defining the test antenna gain. The second auxiliary antenna is used as the transmitting antenna, and should ensure only the emission of electromagnetic waves with the desired frequency, in a relatively narrow angle sector. The comparative method involves measuring the signal received by the reference antenna and the test antenna, and determining on this basis the relative difference in the gain of both antennas. With information on the relative difference in gain of both antennas, we can determine the value of the test antenna gain. Depending on needs, such measurements can be performed at several frequencies. These frequencies are required to be in the bandwidth of the reference antenna (the gain values for these frequencies must be made readable).

The reference antenna must be installed as the first on the receiving side. The measurement procedure is implemented as follows:

- Check if the signal source and the meter have ended the process of heating and stabilizing conditions;
- At constant suspension height of the transmitting antenna, move the receiving antenna between the suspension height of 1 m above the ground to a height of 4 m, watching the value of the maximum received signal level indication;
- Record the observed value of the received signal maximum level and the corresponding suspension height of the receiving antenna in a measurement table.

Then, the test antenna should be mounted in place of the reference antenna. Because it is necessary to maintain the same distance between the antennas, we should check whether the distance from the transmitting antenna to the receiving antenna electrical centre is the same as for the measured reference antenna. If the longitudinal dimension of the test antenna changed the distance, it is necessary to correct it by moving the stand. Such a shift should be performed along the ‘transmitting antenna — test antenna’ axis.

After installing the test antenna, the direction of its maximum radiation must be also determined. The procedure of setting the antenna should be the same as with the reference antenna. Then a series of measurements of the received signal should follow for the same frequencies as in the case of the reference antenna. The measurement procedure is implemented as follows:

- At constant suspension height of the transmitting antenna, move the receiving antenna between the suspension height of 1 m above the ground to a height of 4 m, watching the value of the maximum received signal level indication.

- Record the observed value of the received signal maximum level and the corresponding suspension height of the receiving antenna in a measurement table.

The measurement results for certain frequencies should be recorded in a measurement protocol in the column labeled as P_B [dBm]. The test antenna gain G_B [dBi] should be determined from the relation (3):

$$G_B \text{ [dBi]} = G_W \text{ [dBi]} + P_B \text{ [dBm]} - P_W \text{ [dBm]}, \quad (3)$$

where: G_B [dBi] — test antenna gain determined for a particular frequency relative to the isotropic antenna, G_W [dBi] — reference antenna gain read from the calibration table for a particular frequency relative to the isotropic antenna, P_B [dBm] — measured signal power level received by the test antenna for a specific frequency, P_W [dBm] — measured signal power level received by the reference antenna for a given frequency.

5. DETERMINING A GAIN MEASUREMENT ERROR

In order to determine measurement uncertainty, we must clarify the sources of errors occurring during measurements. The main sources of errors which may occur while measuring an antenna gain are as follows:

- a finite distance between the antennas during tests and the measurement stand environment,
- auxiliary antennas used for measurements,
- other components of the measurement stand.

In the case of measuring an antenna gain, one of the errors that are most difficult to estimate result from the need for locating the transmitting and receiving antennas at a finite distance. These are systematic errors which decrease asymptotically with increasing distance between the antennas. To determine the value of this error, it is necessary to distinguish two basic sources of its formation. The first is the fact that the value of the test antenna gain varies with the change of distance between the antennas as long as the wave which impinges on the receiving antenna contains near-field components (a radial component). Unfortunately, this component exists even at a distance greater than the analyzed far-field distance described in the relation (1). Thus, the far-field condition does not eliminate the gain measurement error. For typical antennas at a measurement distance equal to the distance resulting from the far-field condition, the error caused by the near-field components is about 0.05 dB. This error underestimates the measured antenna gain value and decreases with increasing distance between the antennas. The second source of errors associated with finite measurement distance is the absence of uniform illumination of a test antenna by a transmitting antenna, i.e., the problem with getting a plane wave in the aperture of the test antenna. This problem is associated both with the dimensions of the transmitting and receiving antennas and the wavelength. Assuming the amplitude fluctuations of the wave which stimulates the receiving antenna at 0.25 dB, which corresponds to the distance between the antennas equal to the far-field distance, the error is about 0.1 dB. Thus, placing the antennas at a distance equal to the critical distance of the far-field, we get the total measurement error of about 0.15 dB. Reducing the value of this error requires an increase in the measurement distance or the use of a transmitting antenna with wide radiation characteristics which will result in smaller fluctuations in the amplitude of the field which stimulates the receiving antenna. But we must remember that the use of antennas with wide characteristics can result in an increase of signals reaching the receiving antenna due to multipath propagation which will also increase the error. Auxiliary antennas are the second source of errors arising during antenna gain measurements. Impedance and polarization mismatches are among the main errors here. Expanded uncertainty of the developed measuring stand is ± 0.5 dB.

6. THE RESULTS OF THE ANTENNA GAIN MEASUREMENT

Measuring distance R_{POM} : 4.56 m; Test antenna type: 11966G log-spiral antenna; Max. test antenna dimension D_{max} : 0.4 m; Reference antenna: DRG 118/A.

7. CONCLUSIONS

The presented method of measuring antenna power gain provides an easy way to determine the value of this parameter and is often used in antenna measurements. This method is not time consuming, and only the preparation of a measurement stand requires more time and attention.

Appropriate preparation of the measurement stand is what determines measurement results. The presented results of the log-spiral antenna tests show the correctness of the measurement method applied. Only for frequency 6 GHz the measured gain value deviates significantly from the values determined during the antenna calibration. This proves that during the measurement we should meet all the conditions of the measurement method. This method therefore has some limitations as to its application and they are mainly associated with the dimensions of a test antenna and the frequency at which the antenna power gain is determined.

ACKNOWLEDGMENT

The research work financed from the financial funds assigned to the science in the years 2011/2013 as the development work. The research work is realized in Poland. The number of work is 4708/B/T02/2011/40.

REFERENCES

1. Bem, D. J., “Anteny i rozchodzenie się fal radiowych,” *Wydawnictwa Naukowo-techniczne*, Warszawa, 1973.
2. Przesmycki, R., “Procedura badawcza PB — 05 pomiar zysku anten,” LAB-KEM WEL WAT, Warszawa, 2007.

Multilayer Microstrip Antennas Array Operating in Dual Bands

Marek Bugaj, Rafal Przesmycki, Leszek Nowosielski,
Kazimierz Piwowarczyk, and Marian Wnuk
Faculty of Electronics, Military University of Technology
Gen. S. Kaliskiego 2 Str., Warsaw 00-908, Poland

Abstract— The paper describes problems related to antenna technology. The paper shows the construction of multilayer microstrip antenna array on a dielectric substrate operating in dual band (2.4 GHz and 5.8 GHz). Microstrip antennas in antenna technology appeared relatively late, but in recent years there has been a large development of the design of these antennas and a huge interest in their capabilities. Microstrip antennas are often used in all areas of radio communications. This is due to the simplicity of their design, easiness of implementation and relatively low production costs. An important advantage of these antennas is their shape, small size, low weight and aesthetic appearance. Microstrip antennas also provide high repeatability parameters and high resistance to weather conditions.

The article presents two arrays (2×1 and 4×1) of microstrip antennas operating at frequencies of 2.4 GHz and 5.8 GHz. To the feed microstrip arrays we used parallel feed configuration. The distance from the input port to each radiating element is identical. For a uniform aperture distribution, the power is equally split at each junction. In this antenna two operating frequencies have the same polarization planes. The antenna consists of three layering and has two rectangular radiating elements on different layers.

1. INTRODUCTION

The microstrip antennas have been one of the most innovative fields of antenna techniques for the last fifteen years. In high-performance spacecraft, aircraft, missile and satellite applications, where size, weight, cost, performance, easiness of installation, and aerodynamic profile are constraints, low profile antennas may be required. Presently, there are many other government and commercial applications, such as mobile radio and wireless communications that have similar specifications. To meet these requirements, microstrip antennas can be used. These antennas are low-profile, conformable to planar and non-planar surfaces, simple and inexpensive to manufacture using modern printed circuit technology, mechanically robust when mounted on rigid surfaces, compatible with MMIC designs, and when particular patch shape and mode are selected they are very versatile in terms of resonant frequency, polarization, pattern, and impedance. In addition, by adding loads between the patch and the ground plane, such as pins and varactor diodes, adaptive elements with variable resonant frequency, impedance, polarization, and pattern can be adjusted [1]. Radiating patch may be square, rectangular, circular, elliptical, triangular, and any other configuration. In this work, rectangular microstrip antennas are the under consideration.

The methods of analysis and projection of microstrip antennas have developed simultaneously with the development of aeriels. Nowadays several methods of analyzing the antennas on dielectric surface are used, however, the most commonly used ones are the full wave model based on Green's function and the method of moments where analysis relies on solution of integral equation, concerning electric field, with regard to unknown currents flowing through elements of the antenna and its feeding system [2].

2. ANTENNA ARRAYS

The aggregate of at least two antennas is called an antenna array. Typically, antennas are usually spaced half a wavelength apart. This allows us to obtain the desired radiation characteristics of such antenna system. Antenna arrays can be fed in series or in parallel, or a combination of the power of parallel and serial.

When the array antenna is fed in series then supply lines are connected to the radiating elements as shown in Figure 1(a). If the array is fed in parallel (Figure 1(b)), the input signal is separated into individual patches (radiators). Such methods fed of antenna elements give the possibility to form amplitude and phase of individual radiating elements, which leads to changes in the shape of the radiation pattern.

If a single antenna (radiator) does not provide the desired energy gain, or if the presence of interference requires the elimination of incoming signals from a particular direction, we can combine several antennas (radiators) in a single antennas array.

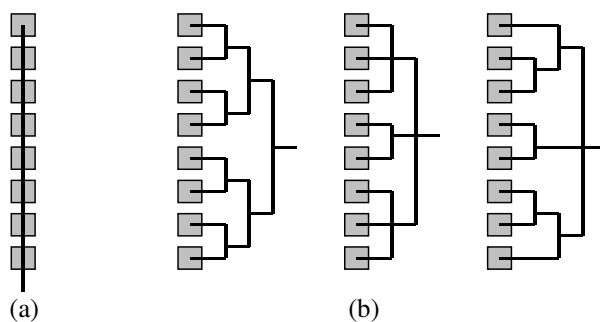


Figure 1: Methods of the power supplies of microstrip arrays: (a) in series, (b) parallels.

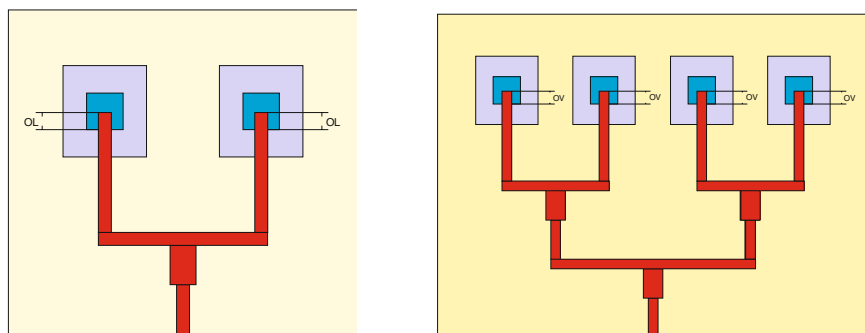


Figure 2: Constructions of the antenna array.

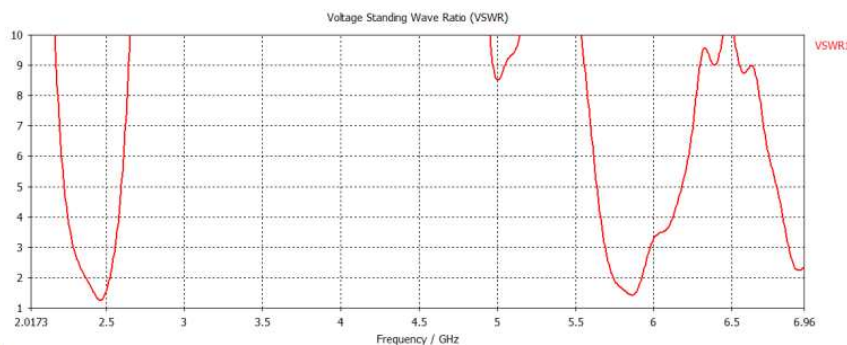


Figure 3: The VSWR course of 2 element planar microstrip array in frequency function.

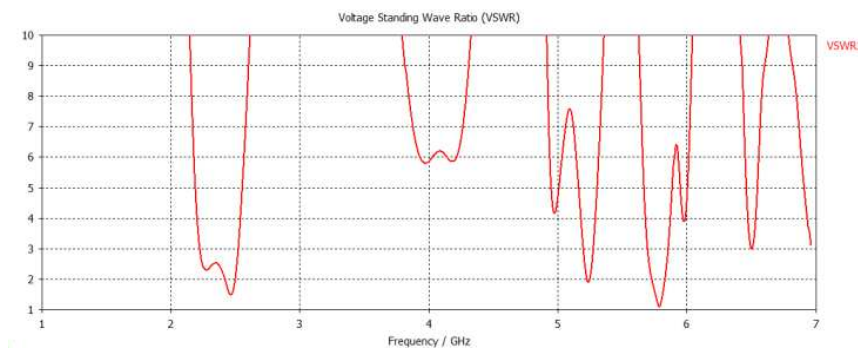


Figure 4: The VSWR course of 4 element planar microstrip array in frequency function.

3. CONSTRUCTION OF THE ANTENNA ARRAY

In the paper there have been discussed two microstrip arrays, different in number element. The first planar array consists of two radiators. Radiators are microstrip rectangular patches. The microstrip patches are fed by electromagnetic coupling. The next antenna array consists of four radiators.

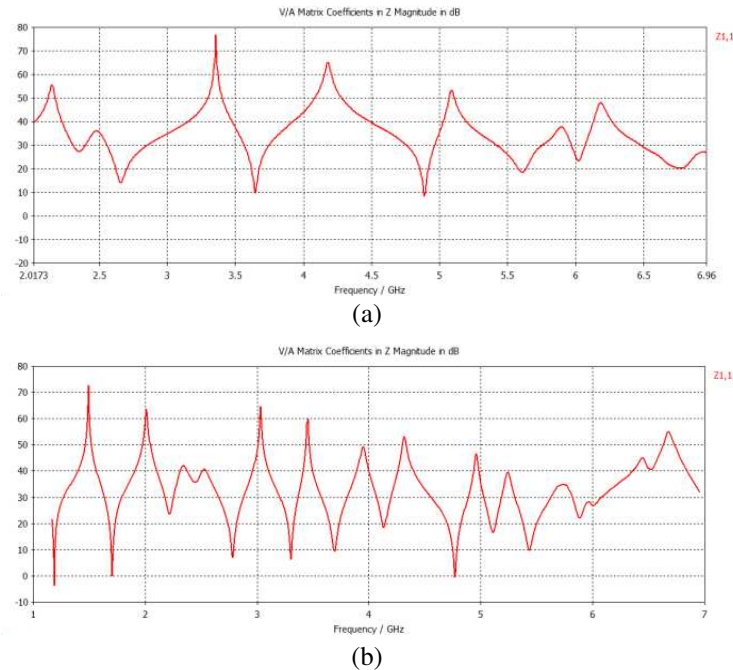


Figure 5: The impedance course of tested antennas in the frequency domain: (a) 2×1 , (b) 4×1 .

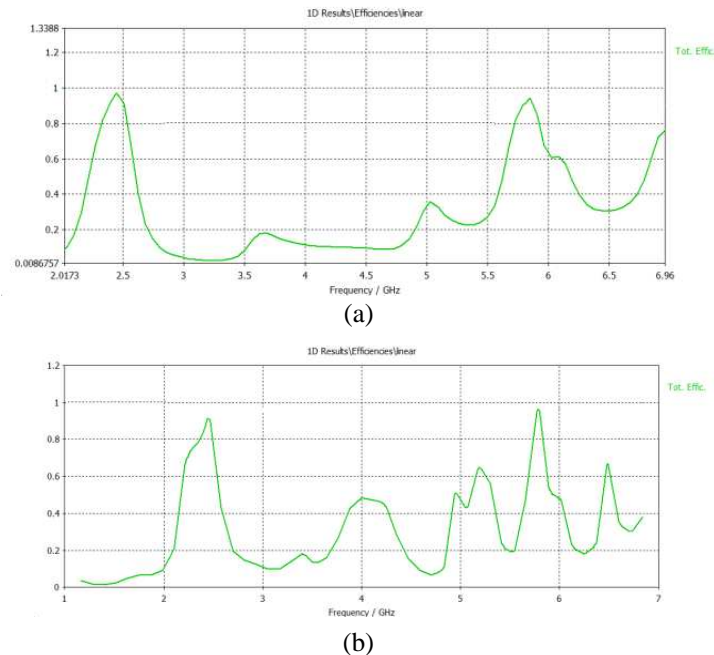


Figure 6: Efficiency of the tested antennas in frequency domain: (a) 2×1 , (b) 4×1 .

In structure of antennas there have been used dielectrics of various electrical and geometrical (thickness) parameters.

4. THE RESULTS OF COMPUTER SIMULATIONS

In the process simulation of antennas the following parameters have been determined: VSWR, gain, radiation patterns and input impedance. In Figures 3 and 4 there are shown VSWR and input impedance for an antenna built on a flat surface.

The antenna operates in the two ISM bands: 2,400–2,485 and 5,725–5,758 GHz. For this range the value of VSWR < 2 , input impedance varies in the range from 35 $[\Omega]$ to 44 $[\Omega]$.

Figure 7 shows the radiation characteristics of two antennas. The shape of the radiation characteristics is consistent with theoretical assumptions. In the plane E vector useful width of the

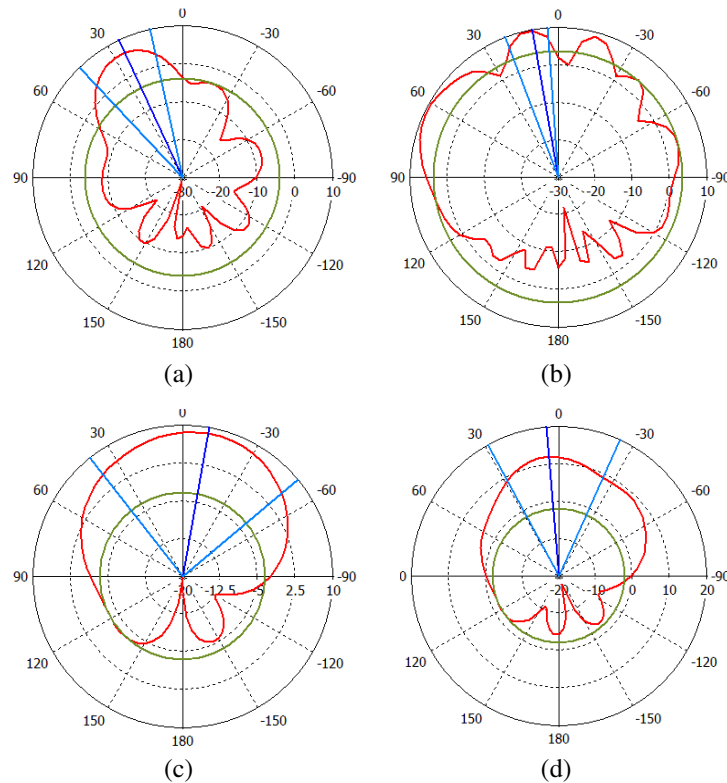


Figure 7: Radiation patterns of antenna array for: (a) 5.8 GHz — 2×1 array, (b) 5.8 GHz — 4×1 array, (c) 2.4 GHz — 2×1 array, (d) 2.4 GHz — 4×1 array.

main beam narrows with increasing the active elements in array antenna also improves the value of energy gain.

Calculated efficiency of the antenna for frequencies between 2.4 and 5.8 GHz at a level above 90%.

5. CONCLUSION

The analysis of the antenna was made by the usage of CST Microwave Studio. The presented antenna works in two frequency ranges of ISM band. This antenna can work in Wireless systems: Bluetooth 2450 MHz, HIPERLAN 5800 MHz, IEEE 802.11/WiFi 2450 MHz and 5800 MHz, IEEE 802.15.4, ZigBee and other personal area networks 2450 MHz (may use too the 915 MHz) ISM bands. The bandwidth of aerial is the result of way feed as well as the utilization to build the many-layers substrates and selection of their parameters.

ACKNOWLEDGMENT

The research work financed from the financial funds assigned to the science in the years 2011/2013 as the development work. The research work is realized in Poland. The number of work is 4708/B/T02/2011/40.

REFERENCES

1. Turker, N., F. Gunes, and T. Yildirim, "Artificial neural design of microstrip antennas," *Turk. J. Elec. Engin.*, Vol. 14, No. 3, 445–453, Tubitak, 2006.
2. Pozar, D. M., "A reciprocity method of analysis for printed slot and slot-coupled antennas," *IEEE Trans. Antennas Propaga.*, Vol. 34, No. 12, 1439–1446, Dec. 1986.

Dual Band Microstrip Antenna Working in the Frequency Bands 2.4 GHz and 5.8 GHz

Marek Bugaj, Rafal Przesmycki, Leszek Nowosielski,
Kazimierz Piwowarczyk, and Marian Wnuk

Faculty of Electronics, Military University of Technology
Gen. S. Kaliskiego 2 Str., Warsaw 00-908, Poland

Abstract— The article presents a multilayer structure of microstrip antennas operating at frequencies of 2.4 GHz and 5.8 GHz. The microstrip patches are fed by coupled microstrip line. Coplanar microstrip feeds are easy to manufacture. In this antenna two operating frequencies have the same polarization planes. The antenna consists of three layering and has two rectangular radiating elements on different layers. For such performed antenna model there were made measurements in the anechoic chamber of typical electrical parameters, such as standing wave ratio, input impedance, radiation pattern, gain. The article also analyzes the results of computer simulations and measurements.

1. INTRODUCTION

Portable electronic devices are becoming more and more common in our daily life. People use not only simple mobile phones, but also multimedia equipment which enables, e.g., regular access to Internet or establishing user's position through GPS system. This can be assumed to be a transitional stage in the direction to integrating of many electronic devices with clothes and building a system which will consist of elements enabling person's contact with the whole world and unlimited access to every information as well as monitoring person's vital functions and alarming him/her and relevant authorities about potential risks and threats.

Fast development of technology of wireless access to Internet and requirements of standards imposed on WLAN, WiMAX and other technologies of wireless networks entourage demand for equipment which is not only reliable and functional but also is characterized by small size. As antenna is an essential element of each wireless system it also has to be miniaturized as well as enable work in more than one frequency strip. Antennas which due to their characteristics are the best to meet above-mentioned requirements are microstrip antennas. This article presents multilayer microstrip antenna which operate at two frequencies: 2.4 GHz and 5.8 GHz.

2. CONSTRUCTION OF THE ANTENNA

Model of three-layer microstrip antenna fed by microstrip line through electromagnetic coupling was made on the base of technical assumptions. Antenna has two radiating patches situated on separate layers of antenna. Each of patches is responsible for work at different frequency bands. Patch situated on inner layer (layer no 2) operates at frequency of 5.8 GHz, while patch situated on upper layer (3) operates at frequency of 2.4 GHz. Figure 1 shows graphic imaging of antenna model and location of its particular elements.

Figure 1 shows antenna model with detailed description of particular layers and radiating elements. The following dielectrics were selected for construction of initial model:

- layer 1: ULTRALAM 2000 ($\epsilon_r = 2.60$; $h = 1.524$ mm),
- layer 2: ULTRALAM 2000 ($\epsilon_r = 2.40$; $h = 1.524$ mm),
- layer 3: Duroid 6202 or Duroid 6200 ($\epsilon_r = 2.94$; $h = 0.762$ mm).

Model of microstrip antenna consists of three separate layers of dielectric. To build antenna there were used dielectrics of similar electric and geometric parameters (thickness). The first layer is a 1.524 mm thick dielectric with permittivity of $\epsilon_r = 2.6$. This layer contains a screen from beneath and a feeding line from the top. The second layer is a dielectric with the same electric and geometric parameters as layer 1. This layer contains a top radiating element with dimensions of 14×14 mm. The third layer is a 0.762 mm thick dielectric with permittivity equal to $\epsilon_r = 2.94$ on which the second 35×32 mm radiating patch is situated. The patch is parallel to the first radiating patch in the second layer. External dimensions of all three layers are the same: width-68 mm, length 84 mm. Total thickness of antenna is ca 3.9 mm.

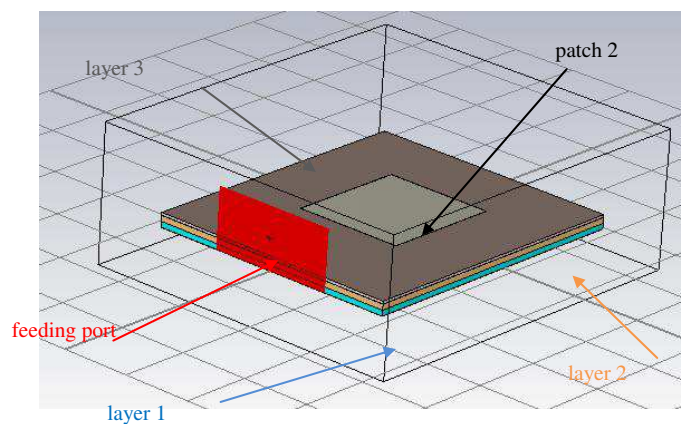


Figure 1: Model of antenna — general view.

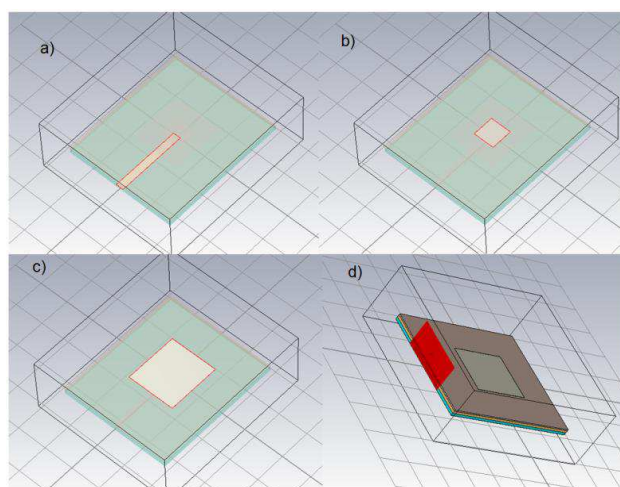


Figure 2: Location of particular elements of antenna: (a) layer 1 and feeding line, (b) layer 2 and radiating patch at 5.8 GHz, (c) layer 3 and radiating patch at 2.4 GHz, (d) general view of antenna with feeding port.

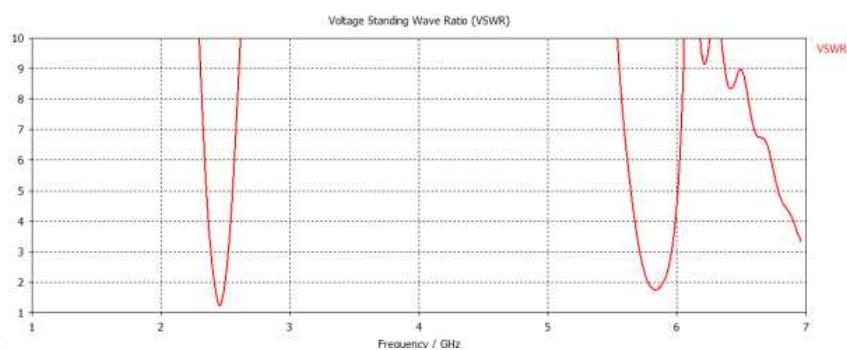


Figure 3: The VSWR course of tested antennas in the frequency domain.

3. THE RESULTS OF COMPUTER SIMULATIONS

In the process simulation of antennas there were determined the following parameters: VSWR, gain, radiation patterns and input impedance. Figures 4 and 5 show VSWR and input impedance for an antenna built on a flat surface.

The result of the efficiency simulations of the discussed microstrip antennas is shown in Figure 5.

VSWR adopts value below two for frequency band from 2.41 GHz to 2.49 GHz and from 5.77 GHz to 5.89 GHz. This is a work frequency band fully covering two sub-ranges in ISM range 2.4 and 5.8 GHz. For simulation model there was determined reflection ratio of S_{11} which course is shown

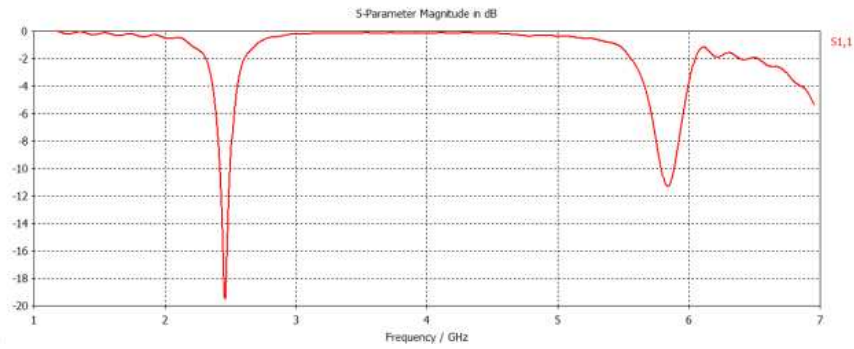


Figure 4: The S_{11} course of tested antennas in the frequency domain.

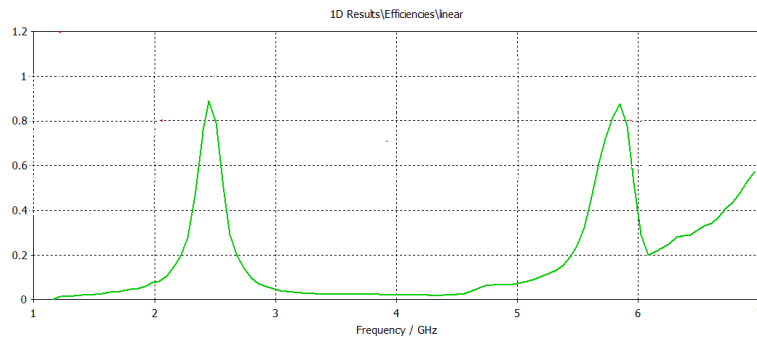


Figure 5: The efficiency course of antenna in the frequency domain.

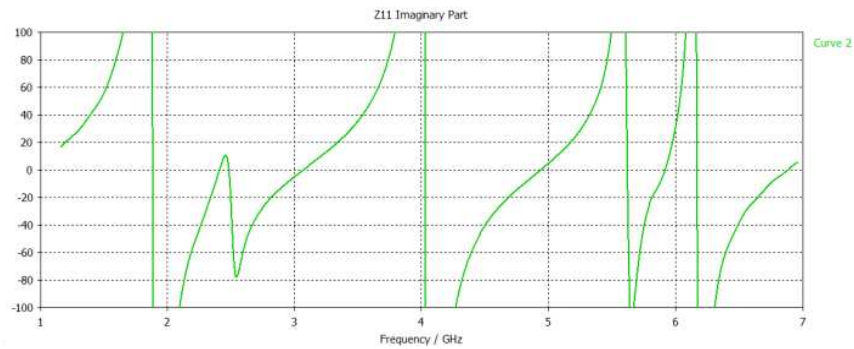


Figure 6: The input impedance course of tested antenna in the frequency domain.

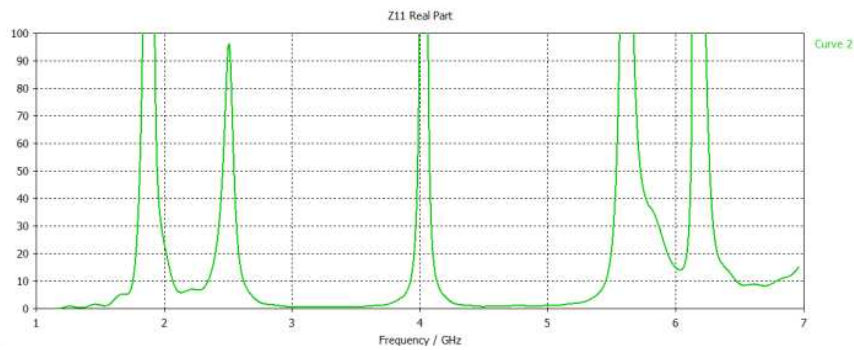


Figure 7: The input impedance course of tested antennas in the frequency domain.

in Figure 7. There were also determined input resistance and output reactance for above frequency bands (Figures 6 and 7).

Moreover for this antenna model there was determined radiation pattern in H plane for particular frequency sub-ranges (Figure 8).

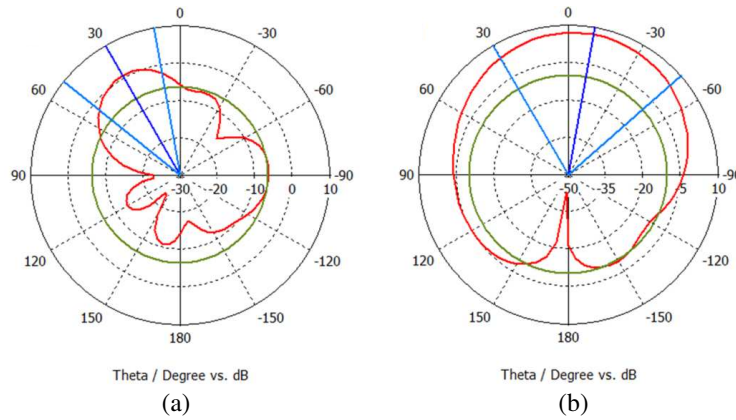


Figure 8: Normalized antenna radiation patterns for: (a) 5.8 GHz, (b) 2.4 GHz.

4. CONCLUSION

Microstrip antenna range includes frequencies covered by WLAN (2.4 GHz) as well as upper range (5725–5875 MHz) of free band **ISM** (*Industrial, Scientific, Medical*). Presented design can be used for wireless data transmission in safeguard systems. Radio monitoring cameras working at bands 2.4 and 5.8 GHz are already available on the market. These cameras enable wireless data, sound and image transmission. Device which uses presented antenna can work in two frequency bands simultaneously allowing to use frequency as required by user.

ACKNOWLEDGMENT

The research work financed from the financial funds assigned to the science in the years 2011/2013 as the development work. The research work is realized in Poland. The number of work is 4708/B/T02/2011/40.

REFERENCES

1. Turker, N., F. Gunes, and T. Yildirim, "Artificial neural design of microstrip antennas," *Turk. J. Elec. Engin.*, Vol. 14, No. 3, 445–453, Tubitak, 2006.
2. Pozar, D. M., "A reciprocity method of analysis for printed slot and slot-coupled antennas," *IEEE Trans. Antennas Propaga.*, Vol. 34, No. 12, 1439–1446, Dec. 1986.
3. Bugaj, M. and M. Wnuk, "Optimization parameters of dielectric in aperture-coupled stacked patch antenna on bandwidth," *International Conference on Microwave, Radar and Wireless Communications MIKON-2010*, 2010.

Methods of Measuring Shielding Effectiveness of Small Shielded Chambers

L. Nowosielski, M. Wnuk, R. Przesmycki, K. Piwowarczyk, and M. Bugaj

Faculty of Electronics, Military University of Technology
Gen. S. Kaliskiego 2 Str., Warsaw 00-908, Poland

Abstract— The article concerns problems connected with electromagnetic compatibility. Four methods used for measuring shielding effectiveness of small shielded chambers have been described in it. For two of them research results of a sample shielded chamber have been presented. The obtained results have been analyzed with regard to using a casing as an element protecting against undesirable electromagnetic emission.

1. INTRODUCTION

Protection of information processed by IT devices does not amount only to securing devices from interception of information directly from a device but also from interception of information contained in radiation emitted by particular devices. While using special receiving antennas and measuring receivers it is possible to intercept information processed by a particular device from the distance of a few hundred meters. It is so called an effect of compromising emanations. This effect can be prevented directly by using shielding casings or indirectly by placement of such a device in special shielded chambers. Such chambers must meet a number of requirements and provide an appropriate shielding effectiveness. Unfortunately in case of shielded chambers which dimensions are smaller than $1.5\text{ m} \times 1.5\text{ m} \times 1.5\text{ m}$ there is no determined method of measuring shielding effectiveness. Methods described for shielded chambers with dimensions larger than $1.5\text{ m} \times 1.5\text{ m} \times 1.5\text{ m}$ cannot be used for measuring shielding effectiveness of smaller chambers because of dimensions of antennas used during those measurements. Four measuring methods for determining shielding effectiveness of small shielded chambers have been described in the article. For two of the above methods the measurement results have been given.

2. METHODS OF MEASURING SHIELDING EFFECTIVENESS OF SMALL SHIELDED CHAMBERS

In the chapter below four methods of measuring shielding effectiveness of small shielded chambers have been presented:

- the method which uses broad-band measuring probes,
- the method which uses a selective measuring receiver and retuned signal generator,
- the method which uses a selective measuring receiver and Comb Generator,
- the method which uses HEMP (High Altitude Electromagnetic Pulse) generator.

The research carried out with the use of the above methods must be conducted in anechoic chambers.

2.1. The Method Which Uses Broad-band Measuring Probes

The main factor which resulted in using broad-band measuring probes (Fig. 1) for measuring attenuation was their small dimensions. In case when inner dimensions are smaller than $1.5\text{ m} \times 1.5\text{ m} \times 1.5\text{ m}$ it is harder to place a measuring antenna which will guarantee efficient work inside the chamber.

Available on the market broad-band probes are devices which are not equipped with tuned band-pass filters and unfortunately it results in the sensitivity decrease of those devices to the value of about 0.5 V/m . A sample diagram of a measuring position for measuring attenuation of small chambers is shown in Fig. 2.

In order to define the value of shielding effectiveness it is necessary to carry out measurements of electromagnetic field strength twice. First, the measurement is performed with the use of a signal transmitter and broad-band probe; both devices are placed opposite one another and with the use of the probe field strength at particular frequency is measured. Such a measurement is called standardization measurement. Next, another measurement is conducted; this time the measuring



Figure 1: Sample solutions of broad-band measuring probes.

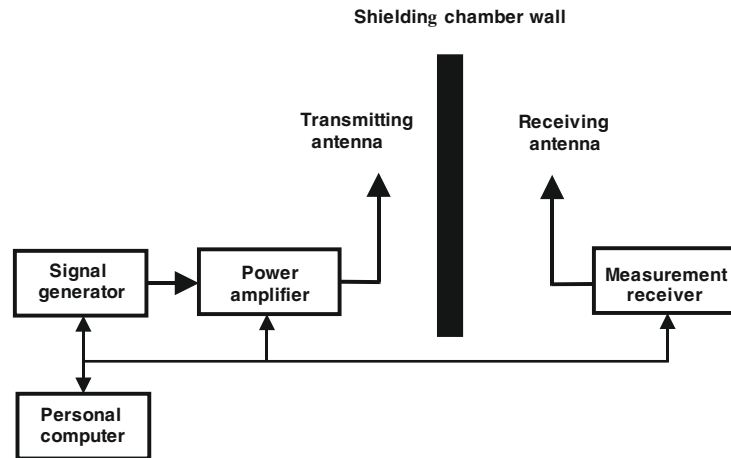


Figure 2: Block diagram of the measuring position of shielding effectiveness of small chambers with the use of broad-band probe.

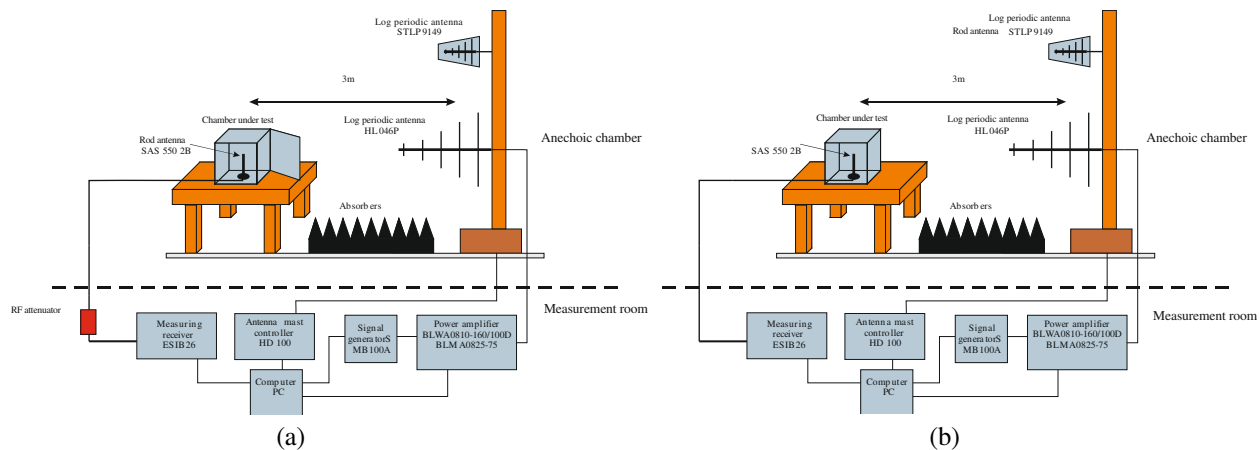


Figure 3: Block diagram of the measuring position of shielding effectiveness of small chambers with the use of selective receiver and signal generator, (a) standardization measurement, (b) basic measurement.

probe is placed in a shielding casing. This measurement is called basic measurement. Then, it is necessary to subtract measured levels of electromagnetic field strength and the obtained in that way result corresponds with attenuation of the studied shielded chamber. Because signal levels are expressed in [dB], so in a simple way we obtain the attenuation result also expressed in [dB].

2.2. The Method Which Uses a Selective Measuring Receiver and Signal Generator

Like in case of measuring attenuation with the use of broad-band measuring probe, in this method it is necessary to conduct two kinds of measurements as well. First, standardization measurements are carried out which consist in signal emission through a transmitter and signal measurement at input of a receiver at particular frequency when a receiving antenna is situated in an open shielded chamber. A distance between the transmitter and receiver is clearly defined and should correspond with a distance occurring in the second part of measurements when the receiving antenna is placed inside the shielded chamber. Next, we should proceed to carrying out basic measurement which happens analogically; however the only difference is that the receiving antenna is placed inside a closed shielding casing. By subtracting suitable values of measured signal levels we receive the result of attenuation of shielded chamber. With measuring signal levels in frequency band we obtain the course of shield attenuation in the frequency function. A sample block diagram of measuring position is presented in Fig. 3.

2.3. The Method Which Uses a Selective Measuring Receiver and Comb Generator

During conducting measurements according to methodology also described in the item below it is necessary to carry out two series of measurements with the use of a measuring signal transmitter

which role is played by Comb Generator and a measuring signal receiver. The measuring signal transmitter consists of Comb Generator, transmitting antenna and accumulator. Comb Generator is a specific kind of signal generator since it generates signal with spectrum consisting of a large amount of components of various frequencies. Spectral lines obtained in frequency & amplitude characteristic occur in equal intervals; however their amplitude is not constant and along with the increase of frequency it decreases. The measuring signal receiver consists of a set of receiving antennas, antenna commutator, measuring receiver and controlling computer.

Measurement of shielding effectiveness with the method using comb generator and selective measuring receiver amounts to performance of two measurements of signal level at input of the receiver for particular frequency. The first measurement is carried out as so called standardization measurement. Standardization measurement takes place for a specified value of signal level generated by Comb Generator located inside an open shielded chamber. The level of electromagnetic field strength is measured at the point of installation of receiving antenna connected to a measuring signal receiver. After carrying out standardization measurement it is necessary to conduct basic measurement during which Comb Generator is closed in a tested small shielded chamber. Measured values of electromagnetic field strength corresponding with particular measuring frequencies ought to be remembered by operating computer. The measurements should be performed in the same way like during standardization measurement. After subtracting recorded levels of electromagnetic field intensity corresponding with particular measuring frequencies during standardization and basic measurements we obtain the difference of levels of received signals in [dB], which is the value of attenuation contributed by a casing of a tested shielded chamber. Sample block diagrams showing the configuration used for standardization and basic measurements are presented in Fig. 4.

2.4. The Method Which Uses High Altitude Electromagnetic Pulse (HEMP) Generator

One of the most innovative solutions for the issue of increasing the measuring dynamic range of shield attenuation of small shielded chambers is using — as probing signal — high-power pulses generated by the Marx generator. This solution is practised more and more often due to high efficiency and functionality.

In order to measure the attenuation values of small shielded chambers with the method using a high altitude electromagnetic pulse generator one should have a measuring set which consists of a

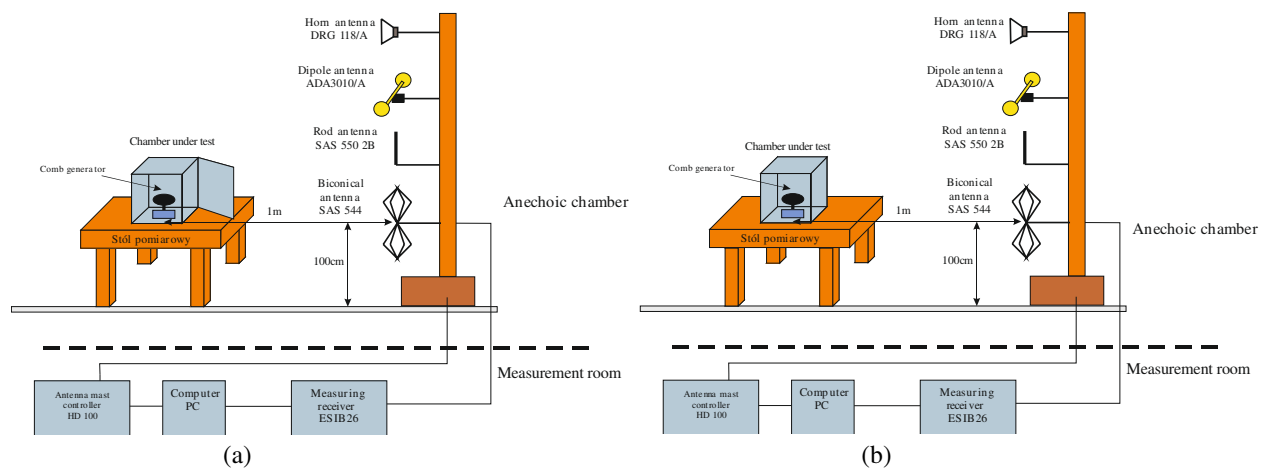


Figure 4: Block diagram of the measuring position of shielding effectiveness of small chambers with the use of a selective receiver and comb generator, (a) standardization measurement, (b) basic measurement.

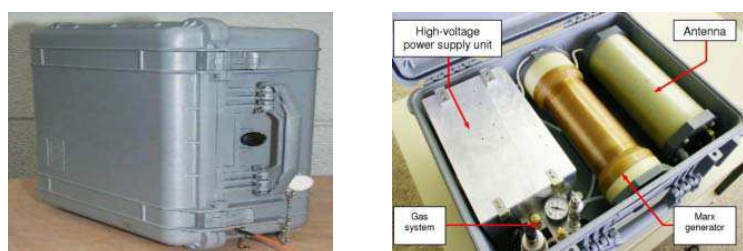


Figure 5: Structure of measuring signal transmitter.

measuring signal transmitter and a meter of electromagnetic field intensity. The measuring signal transmitter consists of the HEMP generator along with a transmitting antenna and accumulator. The set is placed in a portal case with outer dimensions not larger than $550 \times 450 \times 250$ mm. The generator must deliver high-voltage pulses with the minimal value of electric field intensity: 80 kV/m along with the maximal duration of a single pulse not exceeding 5 ns. The effect of its functioning is getting high-voltage pulse at input of a transmitting antenna at about hundreds of thousands volts for a very short period of time. The structure of the measuring signal transmitter is shown in Fig. 5.

The meter of electromagnetic field intensity consists of operating computer, oscilloscope with attenuators and sensor with matching block. For monitoring generated electromagnetic field a sensor with antenna matching unit is used which is connected by attenuators to oscilloscope with the use of coaxial cable. In the oscilloscope there comes to display of data taken from the sensor in time domain. In order to provide a correct measurement the oscilloscope must be placed in a special shielding casing which protects it against a high generated level of electromagnetic field. Software installed on operating computer, on the basis of recorded HEMP pulse in time function, calculates frequency spectrum with the use of Fourier transform.

Measuring attenuation with a method using high-power generator amounts to performance of two measurements of signal level at input of a sensor which is a part of a meter of high-power pulse level. The first measurement is carried out as so called standardization measurement. Block diagram of position for measuring attenuation (standardization measurement) with the method of high-power pulse generation is presented in Fig. 6. Standardization measurement takes place for particular value of signal level generated by high-power pulse generator. The level of electromagnetic field intensity is measured at the site of installation of a sensor along with matching block. Measured values of electromagnetic field intensity corresponding with particular measuring frequencies should be remembered by operating computer.

After performing standardization measurement it is necessary to conduct basic measurement during which the sensor with matching block is placed in a tested small shielded chamber. Block diagram of position for measuring attenuation (basic measurement) with the use of the method of high-power pulse generation is presented in Fig. 7. Basic measurement takes place for particular value of signal level generated by high-power pulse generator. The level of electromagnetic field intensity is measured at the site of installation of a sensor along with matching unit. Measurements should be carried out in the same way like during standardization measurement. Measured values of electromagnetic field intensity corresponding with particular measuring frequencies should be remembered. After subtracting recorded levels of electromagnetic field intensity corresponding with particular measuring frequencies during standardization and basic measurements we obtain the difference of levels of received signals in [dB], which is the value of attenuation contributed by a casing of a small shielded chamber.

3. DESCRIPTION OF THE STUDIED CHAMBER

In order to carry out validation of research methodologies described in items 2.2. 2.3, studies of a sample shielded chamber constructed in the form of cube being closed by adding one of walls (depending on lateral or upper configuration) have been conducted. The shielded chamber has dimensions: $0.45 \text{ m} \times 0.45 \text{ m} \times 0.45 \text{ m}$ and is made of galvanized steel sheet. In order to connect an antenna situated inside the shielded chamber on one of the walls a special panel was made which

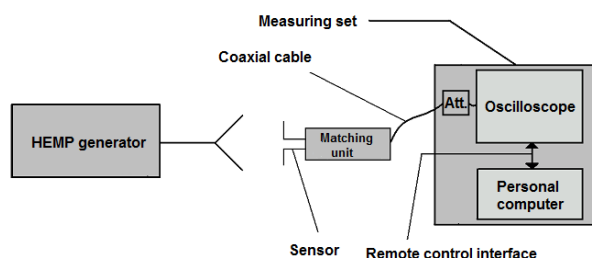


Figure 6: Block diagram for measuring attenuation (standardization measurement) with the use of the method of HEMP generation.

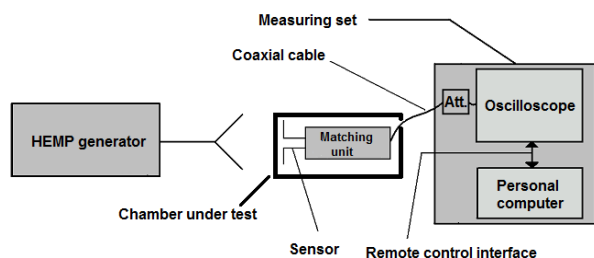


Figure 7: Block diagram for measuring attenuation (basic measurement) with the use of the method of HEMP generation.



Figure 8: View of the studied shielded chamber with terminal panel.

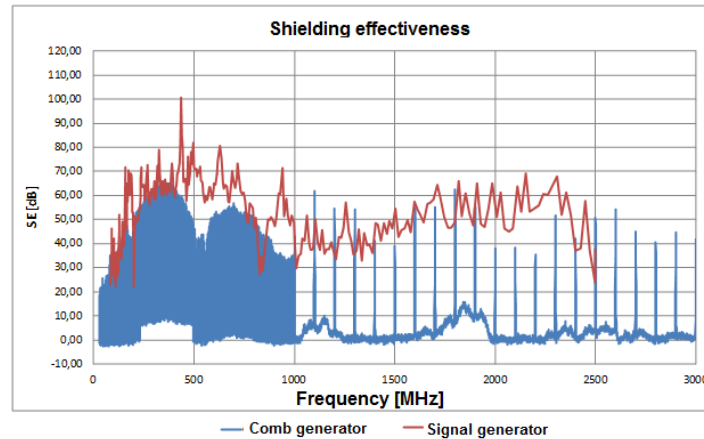


Figure 9: Value of shielding effectiveness in the function of frequency of the studied chamber.

provides connection of the antenna and receiving circuit. A view of the chamber along with the terminal panel is shown in Fig. 8. Interface panel has a special hole which allows to insert light pipe inside a shielded cubicle. On the panel there are also two outputs: of type N (female), filter VGA and filter D-Sub (9-pin).

4. RESEARCH RESULTS

In order to present measuring possibilities described in items 2.2. 2.3 measurements of shielding effectiveness of the chamber described above have been conducted. The first used methodology is the one using a selective measuring receiver and signal generator. The second one is methodology using a selective measuring receiver and Comb Generator. Specification of the obtained measuring results is shown in Fig. 9.

5. CONCLUSIONS

After making an analysis it is necessary to maintain that the most prospective methods providing the largest range of measuring dynamics of contributed attenuation are the methods using:

- selective measuring receivers,
- high altitude electromagnetic pulse generator (HEMP).

The method which uses broad-band measuring probes is the least efficient since it has too little dynamics range due to small sensitivities of field probes.

ACKNOWLEDGMENT

The research work financed from the financial funds assigned to the science in the years 2010/2012 as the development work. The research work is realized in Poland. The number of work is 0005/R/T00/2010/11, No. OR00000511.

REFERENCES

1. <http://www.ets-lindgren.com>.
2. Przesmycki, R., M. Wnuk, L. Nowosielski, and K. Piwowarczyk, "Small chambers shielding efficiency measurements," *PIERS Online*, Vol. 7, No. 3, 256–260, 2011.

3. Przesmycki, R., L. Nowosielski, M. Wnuk, and P. Skokowski, “Metodyka pomiarów skuteczności ekranowania małych komór,” *KKRRiT 08*, Poznan Polska, Oct. 6, 2011; *Przegląd Telekomunikacyjny*, 321–324, June 2011, ISSN 1230–3496.
4. Przesmycki, R., L. Nowosielski, M. Wnuk, and M. Bugaj, “Pomiar efektywności ekranowania komór ekranujących,” *KKRRiT 08*, Poznan Polska, Oct. 6, 2011; *Przegląd Telekomunikacyjny*, 325–328, June 2011, ISSN 1230–3496.

Ambient Electromagnetic Noise Environment Measurement

L. Nowosielski¹, B. Bogdan², M. Wnuk¹, R. Przesmycki¹, K. Piwowarczyk¹, and M. Bugaj¹

¹Faculty of Electronics, Military University of Technology
Gen. S. Kaliskiego 2 Str., Warsaw 00-908, Poland

²KenBIT Sp.j., Żytnia 15/22 Str., Warsaw 01-014, Poland

Abstract— The external Radio Frequency (RF) ambience establishes the minimum usable signal level for satisfactory radio communication service. Sources of the RF ambience may be naturally occurring or due to manmade sources. In order to evaluate the level of the local RF electromagnetic environment the level of the electromagnetic field strength for selected frequencies has to be measured. In the article the automated measurement system for electromagnetic field strength measurement is presented. In the system the precautions were taken to ensure that the measuring and controlling equipment does not affect the measured electromagnetic fields. The measurement system consists of the measurement receiver, antenna and personal computer. On the deck of the personal computer the dedicated software for remote control of the measurement system is running. In the article the software graphical user interface description and the algorithm for the measurement process, data collection and analysis are presented. The algorithm is based on the IEEE Std 473-1985 standard “IEEE recommended practice for an electromagnetic site survey”. The measurement results of the electromagnetic field strength in HF band in selected rural and urban areas are presented too.

1. INTRODUCTION

In some frequency ranges external noises usually prevail over individual noises of receiving radio communication and radio direction finding systems and they are often the main obstacle in radio signal reception. In order to maximize receiving sensitivity of radio communication and radio direction finding systems it is necessary to choose location characterized by as low level of environmental noises as possible. Therefore before installation of this kind of devices it is necessary to characterize environmental properties of radio engineering disturbances in a chosen location within frequency range covering operation of installed receiving systems. The environment of radio engineering disturbances consists of natural interferences (atmospheric, solar and cosmic) and those generated by human — as a result of intentional and unintentional actions — additive noises of technical character which are often called as man-made noise.

Quantitative description of fluctuation noises, both external and individual of a receiver, can be very seriously simplified and reduced to one numerical factor for the needs of analysis of the measuring system noises. This numerical factor is described below.

Let us mark tuning frequency of the receiver by f and substitute bandwidth of the whole pre-detection path in the receiver by B . A simplified methodology of analysis of the effect of external noise consists in assumption that it affects the receiver input only in narrow frequency band B . So we can accept constant value of spectral power density at the receiver input $G(f)$. Mean computational power of that noise at the receiver input is equal to:

$$P_n = GB, \quad (1)$$

On the basis of the value of noise power at the receiver input expressed by Equation (1) a notion of external noise coefficient f_a is being introduced, analogically to a well-known notion of noise coefficient of element or electronic system. We start with a general equation for fluctuation noise power:

$$P_n = kT_o B f_a, \quad (2)$$

where:

k — Boltzmann constant, equal to $1.38 \cdot 10^{-23}$ J/K,

T_o — absolute temperature in kelvins,

B — equivalent bandwidth of reference selective system in Hz,

f_a — noise coefficient, with dimension W/W and value ≥ 1 .

The Equation (2) binds with each other quantities: P_n , k , T_o and B which are directly or indirectly measurable and it is used to define noise coefficient f_a in non-logarithmic units:

$$f_a = \frac{P_n}{kT_oB} \quad (3)$$

In technical practice noise coefficient is expressed in decibels and marked symbolically with the symbol F_a .

External noise coefficient f_a is also defined by properly interpreted formula (3) and it is the measure of noise of radio channel referred to the receiver input (or to the ambience of receiving antenna). We find non-negative value $f_a(f) \geq 0$ constant in narrow frequency ambience f , but generally variable with frequency.

In further part of this study external noise coefficient will be used as the measure of evaluation of a particular location as regards the level of external noises. The values of coefficient F_a for a model area QRSL (Quiet Rural Site Line), predestined to place receiving radio communication and radio direction finding, have been determined from the dependence [2]:

$$F_a(f) = -28.6 \log_{10} f + 53.6, \quad (4)$$

whereas the values of coefficient F_a adequately for rural, suburban and urban area have been determined according to [2] on the basis of the dependence:

$$\begin{aligned} - \text{ for rural area} & & F_a(f) &= -27.7 \log_{10} f + 67.2, & (5) \end{aligned}$$

$$\begin{aligned} - \text{ for suburban area} & & F_a(f) &= -27.7 \log_{10} f + 72.5, & (6) \end{aligned}$$

$$\begin{aligned} - \text{ for urban area} & & F_a(f) &= -27.7 \log_{10} f + 76.8. & (7) \end{aligned}$$

In further part of this study a sample implementation of a measuring set for assessment of the level of external noises for a particular location and a procedure of measuring external noise coefficient F_a have been presented. Moreover sample measurement results for rural and urban areas have been shown which goal is to evaluate a given location to be used as a place of installation of receiving radio communication systems.

2. MEASURING POSITION

A measuring position includes:

- active measuring antenna SAS-550-25 working within the frequency range from 100 Hz to 60 MHz produced by the company A. H. Systems, INC,
- coaxial cable 50 Ω ,
- measuring receiver ESPI working in the frequency range from 9 kHz to 7 GHz produced by the company Rohde & Schwarz,
- personal computer (PC) with software operating a measuring process and the Ethernet interface used for remote controlling of a measuring receiver,
- Ethernet cable,
- a shielding enclosure with interface panel providing insertion to input of the measuring receiver a coaxial cable leading to output of the receiving antenna and power supply AC 230 V 50 Hz,
- supply filter AC 230 V 50 Hz of type FN2070-3-06 by Schaffner, placed inside the shielding enclosure which provides filtration of radio signals generated by the Ethernet cable and active elements of the measuring receiver inducing on power leads.

Block diagram of the measuring position is presented in Fig. 1. The photo of the measuring set is shown in Fig. 2.

A position for measuring coefficient of environment noises contains components typical for the system of measuring electromagnetic field strength. Basic components of such system are antenna and measuring receiver connected to the antenna output by coaxial cable.

The used antenna should have the measured antenna coefficients $AF(f)$ allowing to convert voltage induced at the antenna output into electric field strength at the site of antenna installation. In order to convert the signal level induced at the antenna output into the input level of the measuring receiver, after passing of signal through the coaxial cable connecting the antenna with the receiver input it is necessary to determine its transmittance $A(f)$ for particular measuring

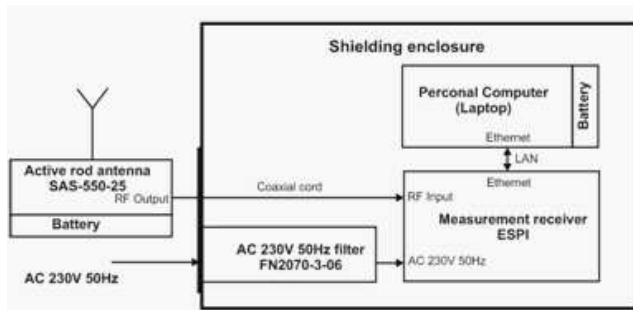


Figure 1: Block diagram of the measuring position.



Figure 2: Photo of the measuring set.

frequencies. Both antenna coefficients and transmittance of transmission line are data used by software operating the measuring process for calculations discussed in the further part of this article.

A task of the measuring receiver is detection and measurement of signal levels with radio frequencies with the use of RMS and AVG detectors. The used receiver is equipped with the Ethernet interface used for remote controlling of the receiver with the use of software installed on the PC.

An important element of the measuring position is the shielding enclosure and supply filter AC, which task is to provide separation of the measuring antenna from radiated interference signals generated unintentionally by the measuring system. The above separation is extremely important during measurements of environment noise coefficients in rural areas where measured levels of environment noise signals are repeatedly lower than the levels of interferences generated by the measuring system. The sources of particularly large disturbances generated by the measuring system are the Ethernet cable and PC used for remote controlling of the measuring receiver.

3. MEASURING PROCEDURE

An algorithm of proceeding during evaluation of a particular location to be used as the site of installation of the receiving radio communication system working in the frequency range from 1 MHz to 30 MHz has been described below. The above algorithm includes the below listed activities to be performed:

3.1. Selection of Silent Radio Frequencies

In order to conduct the above mentioned procedure, first it is necessary to make a spectral analysis of radio frequency band from 1 MHz to 30 MHz which goal is to select at least m of measuring frequencies evenly distributed in the whole analyzed band on which emissions coming from devices generating and radiating energy of radio-waves intentionally do not occur (e.g., radio communication and radio diffusion transmitters, radars). In further part of the study the above frequencies will be called 'silent frequencies'. At the above mentioned frequencies only natural interferences (atmospheric, solar and cosmic) occur as well as those generated by human unintentionally.

3.2. Measurement of Electromagnetic Field Strength at Each of Selected Measuring Frequencies

At selected silent frequencies one should measure electromagnetic field strength using the measuring set described in the previous subsection. During measurements it is necessary to take into account the value of antenna coefficients $AF(f)$ characterizing a particular measuring antenna and attenuation of coaxial cable $A(f)$ connecting antenna with input of the measuring receiver. The measurements should be performed with the detector of RMS value and AVG value. The levels $U_{AVG}(f)$ measured by the AVG detector will be used in item 5 of this measuring procedure during calculation of deviation of signal level $V_d(f)$. It is necessary to conduct n of measurements of electromagnetic field strength for each measuring frequency. With consideration that values of all components are set in the decibel measure, the value of electromagnetic field strength at the measuring site should be determined with the use of the dependence:

$$E(f) = U_{RMS}(f) + AF(f) - A(f), \quad (8)$$

where:

$AF(f)$ — antenna coefficient [dB/m],

$U_{RMS}(f)$ — value of signal level measured by measuring receiver with the detector of root-mean-square value [dB μ V],

$A(f)$ — attenuation of cable connecting measuring antenna with measuring receiver [dB].

3.3. Determining External Noise Coefficient for Each of Measuring Frequency

External noise coefficient $F_a(f)$ for each of so called ‘silent frequencies’ should be determined for every n of measured values of electromagnetic field strength, from the dependence:

$$F_a(f) = E(f) - 20 \log_{10}(f) + 95.5 - 10 \log_{10}(B), \quad (9)$$

where:

f — frequency of measured signal [MHz],

B — bandwidth of measuring receiver [Hz].

3.4. Determining Median of External Noise Coefficient for Each of Measuring Frequency

Values of external noise coefficient $F_a(f)$ determined in the above mentioned way should be subject to statistical processing. For set n of external noise coefficients for each measuring frequency it is necessary to determine median and confidence interval in which 90% of determined value $F_a(f)$ is included. The determined values of external noise coefficient $F_a(f)$ along with marked confidence intervals should be presented in a graphical form.

3.5. Determining Deviation Value of Signal Level for Each Measuring Frequency

Except the value of coefficient $F_a(f)$ for each of so called ‘silent frequencies’ it is necessary to determine so called value of the level deviation $V_d(f)$ understood as the difference between the value of signal level measured by the measuring receiver using the detector of RMS (root-mean-square) value and the detector of AVG (average) value, according to the dependence:

$$V_d(f) = U_{RMS}(f) - U_{AVG}(f). \quad (10)$$

Also in this case every set of deviation values of signal level for a particular ‘silent frequency’ should be subject to statistical processing in order to determine confidence interval in which 90% of calculated deviation values is included. The determined deviation values of signal level along with marked confidence intervals should be presented in a graphical form.

3.6. Evaluation of Particular Location

After calculating the values $F_a(f)$ and $V_d(f)$ one can decide about quality of particular location as regards the level of external noises. A good location should be characterized by the value $F_a(f)$ not larger from 3dB to 4dB than the value of coefficient $F_a(f)$ for model QRSL area. A good location should also be characterized by deviation value of the level $V_d(f)$ for signal levels measured during the day which is not larger than 3. The measurements which the algorithm has been presented above should be performed for each of four seasons. Time intervals for carrying out the measurements should cover hours from 8⁰⁰ to 12⁰⁰ (the lowest levels of interferences of technical origin) and from 20⁰⁰ to 24⁰⁰ (the highest levels of interferences of technical origin). Number of frequencies at which measurements for radio frequency band from 3 MHz to 30 MHz should be conducted is at least $m = 12$. Each series of measurements should be performed every 15 seconds for 3 minutes within 10 to 14 days.

4. RESEARCH RESULTS

In order to check operation correctness of the designed measuring position and measuring procedure, evaluation of the following three locations have been conducted: interior of anechoic shielded chamber, urban and rural area. The measurement results for these locations have been shown adequately in Figs. 3, 4 & 5. Diagrams in colours: green, yellow, orange and red mean values of external noise coefficient $F_a(f)$ adequately for: QRSL, rural area, suburban area and urban area. The diagram marked blue means values $F_a(f)$ and $V_d(f)$ for selected location. Error columns show confidence interval for significance level equal to 0.1.

Comparing levels $F_a(f)$ measured inside anechoic shielded chamber (Fig. 3) and in rural area one can state that the levels of external noises are at comparable level. The level $F_a(f)$ at frequencies

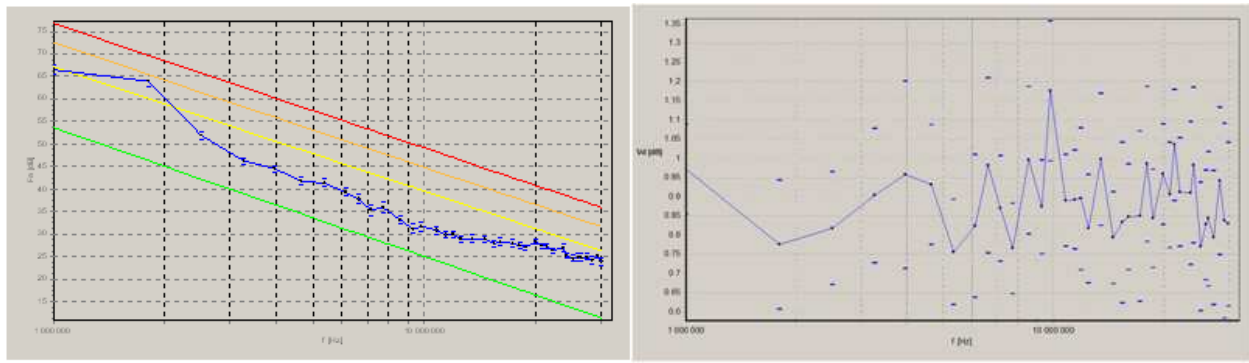


Figure 3: Values of ambient noise coefficient $F_a(f)$ and value of the level deviation $V_d(f)$ for shielded chamber.

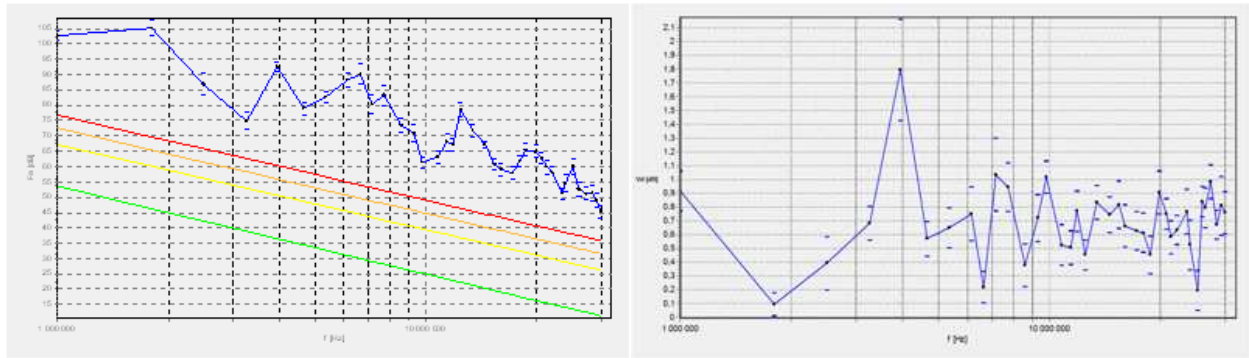


Figure 4: Values of ambient noise coefficient $F_a(f)$ and value of the level deviation $V_d(f)$ for urban area.

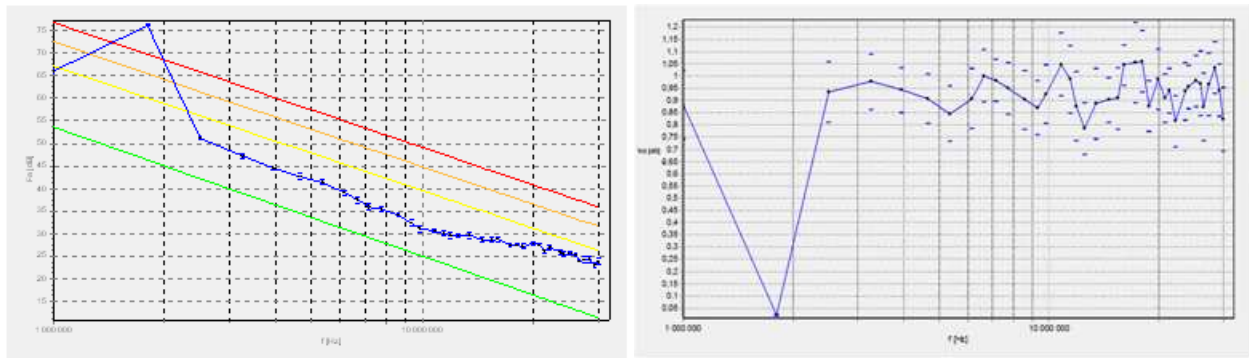


Figure 5: Values of ambient noise coefficient $F_a(f)$ and value of the level deviation $V_d(f)$ for rural area.

below 2.5 MHz seems to be disputable. In case of interior of anechoic shielded chamber a component of such frequency should not have such a significant level. The source of the above signal is emission of radiated interferences of PC operating the measuring process. The above mentioned interferences induce on power leads AC 230 V 50 Hz and find their way outside a shielding enclosure of the measuring system through a path conducted by supply filter. The above can be prevented by using supply filter AC 230 V with greater attenuation in stopband.

5. CONCLUSIONS

On the basis of the presented in Figs. 3, 4 & 5 measurement results of ambient noise coefficient $F_a(f)$ and the value of level deviation $V_d(f)$ for selected location we can state that the designed procedure and measuring set work correctly. The obtained measurement results confirm a character of electromagnetic environment chosen for the test at: interior of anechoic shielded chamber, urban and rural area.

Exceptions are signals at frequencies below 2.5 MHz for which the level of external noise coefficient exceeds assumed admissible levels for a particular location. The above phenomenon results from insufficient filtering off by the filter AC 230 V conducted interferences generated by the mea-

suring system. For prevention it is necessary to use power line filters with a greater attenuation value in stopband.

The designed procedure and measuring set can be successfully used for choosing location for radio communication and radio direction finding systems which provide the lowest level of external noises.

ACKNOWLEDGMENT

The research work financed from the financial funds assigned to the science in the years 2010/2012 as the development work. The research work is realized in Poland. The number of work is 0005/R/T00/2010/11, No. OR00000511.

REFERENCES

1. IEEE Std. 473-1985, "IEEE recommended practice for an electromagnetic site survey (10 kHz to 10 GHz)," 1985.
2. AECTP-250, *Electrical and Electromagnetic Environmental Conditions*, 2nd Edition, 2006.

The Shielding Effectiveness Measurement Using High Voltage Pulse Generator

Kazimierz Piwowarczyk, Marian Wnuk, Leszek Nowosielski,
Rafal Przesmycki, and Marek Bugaj

Faculty of Electronics, Military University of Technology
Gen. S. Kaliskiego 2 Str., Warsaw 00-908, Poland

Abstract— The article describes creation of the concept as well as the construction of laboratory stand using high-voltage pulse generator. By using the high-voltage pulse generator it was possible to perform measurements of shielding effectiveness of small chamber shielding. After preparing and creation of the laboratory stand there were series of control tests made to define the level of usability and correctness of the made researches. Tests were made based on the methodology described in the article.

1. INTRODUCTION

Due to the limited dimensions of the inner shielding of small chamber (less than $1.5\text{ m} \times 1.5\text{ m} \times 1.5\text{ m}$), it was impossible to use the methods described in the available documents of standardization. This is due to the fact that the available measurement antennas, enabling the effective working, have dimensions that unable placing them inside the small chamber shielding and consequently unable the measuring the effectiveness of shielding of these chambers.

Measurement of shielding effectiveness of shielding contributed by the chamber is reduced to perform two measurements of electric field for a given sounding frequency.

2. MEASUREMENT METHODS

Based on the methodology developed to measure the effectiveness of shielding case RACK type using selective measurement receiver and high-voltage pulse generator created the laboratory-station for measuring the effectiveness of shielding of the case RACK-type rack (basing on the equipment located in LAB-KEM WEL WAT). The list of equipment required to perform standardization and proper measurement is presented in Table 1. The equipment used for this purpose is selected basing on the laboratory equipment. Selection of an appropriate measuring system is conditioned by the existing equipment of the individual research units testing shielding effectiveness of the case RACK-type.

In order to measure the effectiveness of shielding of the case RACK-type (small chamber shielding), it was necessary to develop a model of such case. There were 2 main conditions that must have been performed for such a case: obtaining a value of shielding efficiency possible to measure

Table 1: List of measuring instruments and accessories.

	Name	Type	Serial No.
1.	Anechoic chamber	TEMPEST	-
2.	Measuring receiver	ESIB26	100195
3.	Rod antenna without amplifier	SAS 550 2B	D-69250
4.	Active antenna	HE 526	-
5.	Active antenna	HE 527	-
6.	Generator HV	-	-
7.	Control computer	-	-
8.	Controller of cameras	SI300	120080
9.	Monitor	SSM14N5U	6021242
10.	Wall camera	VC-04	0115801
11.	Tory w.cz.	-	-
12.	Control software	EMC32	-



Figure 1: Small chamber shield used as a model of the case RACK-type.



Figure 2: View of the interior of a small shielding chamber with a transit panel and Honeycomb filter.

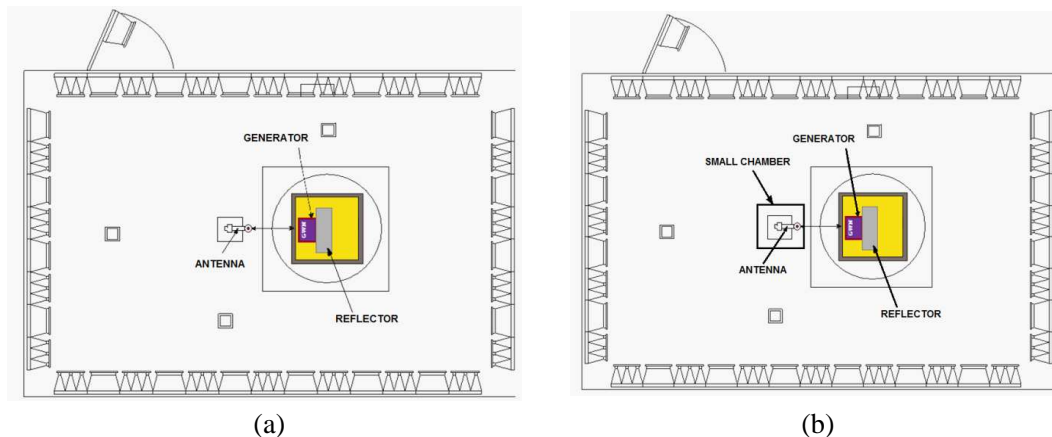


Figure 3: The location of the elements of the laboratory station during the measurement of shielding effectiveness of small shielding chambers.

(smaller than the dynamic range of developed measurement methods) and providing the geometric dimensions enabling measurement of antennas placed inside the chamber. For that purpose, there was a small chamber shield used, which simulated a case RACK-type shown on Figure 1.

On the Figure 1 there is presented the inside of the tested chamber and the panel with interfaces for connecting the measuring antenna and the honeycomb filter.

A small shielding chamber closed by the front door has following dimensions: 68/68/170 cm and is made of galvanized steel sheet 0.5 mm thick. In order to place the measurement antenna inside, there was an entry cut on the one side of the chamber for installing the panel with connections. In order to allow the exchange of air from the inside of the case there was a waveguide filter installed on one wall (Honeycomb type).

As a result of high absorption of a small shielding chamber, the intensity of the electromagnetic fields inside the chamber may be too small to be measured. Expected effectiveness of shielding of created small chamber is between 50–60 dB.

The measurement of the shielding effectiveness of the case RACK-type rack by the method using high-voltage generator and a selective measurement receiver consists of making two measurements of the value of the input signal of the receiver for a given frequency. The first measurement is a standardization measurement. The standardization measurement is made for a defined value

of the signal level generated by the high voltage generator HV inside the open shielding chamber.

The level of the intensity of the electromagnetic field is measured at the place where the receiving antenna of the measuring signal receiver is installed. After standardization measurement is made, we should make the proper measurement, during which the HV generator is closed inside tested small shielding. The measured values of the intensity of the electromagnetic field corresponding to each measuring frequencies should be recorded by the control computer.

Measurements should be made in the same way as during the standardization measurement. The measured values of the intensity of the electromagnetic field corresponding to each measuring frequencies should be recorded. After deducting the recorded levels of electromagnetic field intensity corresponding to each measuring frequencies during the standardization and proper measurement we receive the difference of the levels of the received signals [dB], which is the value of shielding effectiveness of the case of the small shielding chamber.

3. LABORATORY STAND

The measurement of the shielding effectiveness of the small shielding chambers was made inside the anechoic chamber. The location of the elements of the laboratory station inside the anechoic chamber during the standardization measurement is shown on Figure 3(a). Figure 3(b) presents the location of the elements of the laboratory station inside the anechoic chamber during the proper measurement. The block diagrams of the station measuring the shielding effectiveness of small shielding chambers are presented on Figure 4. The shielding measurement was performed twice. First time using the rod antenna, and second time using active antennas.

Figure 5 shows the laboratory stand in the anechoic chamber.

4. MEASUREMENT RESULTS

Figure 6 presents the results of the absorption of the tested shielding chamber using the rod antenna. Figure 7 presents the results of the shielding effectiveness of the tested shielding chamber

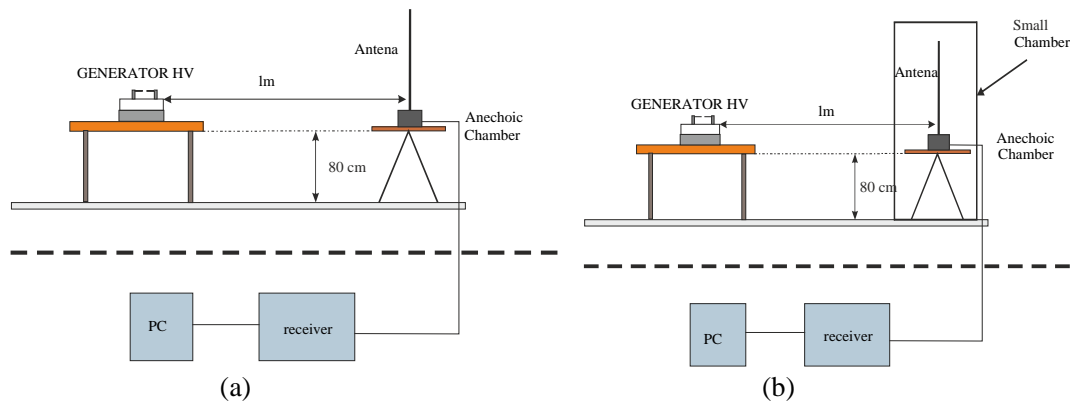


Figure 4: Block diagram of the test bench for the measurement of shielding effectiveness of small shielding chamber: (a) standardization measurement, (b) proper measurement.



Figure 5: The laboratory stand for the measurement of shielding effectiveness of small shielding chamber in the anechoic chamber: (a) standardization measurement, (b) proper measurement.

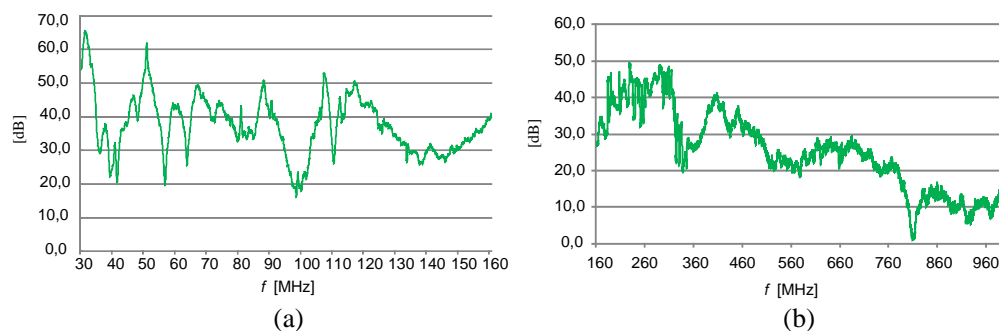


Figure 6: The shielding effectiveness levels of tested shielding chamber measured using the rod antenna.

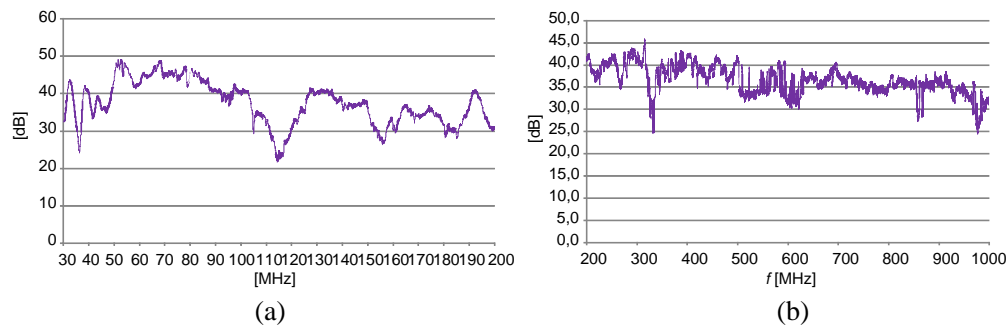


Figure 7: The shielding effectiveness levels of tested shielding chamber measured using the active antennas.

using active antennas.

5. CONCLUSIONS

Based on measurement results we can state that the laboratory stand built on the basis of Electromagnetic Compatibility Laboratory Military University of Technology equipment is working properly. The laboratory stand ensures the researches for the following level of the absorption of the small shielding chambers: 30 MHz–1 GHz and absorption level of the cases up to 40 dB.

ACKNOWLEDGMENT

The research work financed from the financial funds assigned to the science in the years 2010/2012 as the development work. The research work is realized in Poland. The number of work is 0005/R/T00/2010/11, Nr OR00000511.

REFERENCES

1. Wieckowski, T., "Badania kompatybilności elektromagnetycznej urządzeń elektrycznych i elektronicznych," Oficyna Wydawnicza Politechniki Wrocławskiej, Wrocław 2001,
2. PN-EN 55022:2006, "Information technology equipment, Radio disturbance characteristics. Limits and methods of measurement," British-Adopted European Standard, 2006.

The Algorithm of Design Multi-layer Microstrip Antenna

Kazimierz Piwowarczyk, Marian Wnuk, Leszek Nowosielski,
Rafal Przesmycki, and Marek Bugaj

Faculty of Electronics, Military University of Technology
Gen. S. Kaliskiego 2 Str., Warsaw 00-908, Poland

Abstract— The article describes the construction of a multilayer microstrip antennas and algorithm of their designing using CST STUDIO software. The idea of building microstrip antennas began in the fifties of last century. This was the first time when one observed the undesired effects of electromagnetic radiation from asymmetric stripline, also known as the microstrip line. Initially, the idea of using this phenomenon for building antennas did not arise much interest. The dynamic development of the researches of this type of structures was recorded only since the early seventies, when the microstrip antennas found many military and civilian applications.

1. INTRODUCTION

At the present time, the role of microstrip antennas in modern telecommunications and radio-electronic systems has become huge. Many advantages of these structures resulted in their very wide application.

Considering the production of antennas and their possibilities of integration with the active systems, placing the transmitter and the power line on the same side of the surface is an advantage. However, this solution has also many disadvantages. It is impossible to compatible the optimal surface both for the transmitter and the microstrip line. Considering the efficiency of the antenna, it is desirable that the permittivity of the ground is as small as possible. Then, in order to reduce the stray field of microstrip lines and reduce its geometrical dimensions, one should use the material with maximum electrical permeability. These limitations have led to creation of a new type of structure — multi-layer microstrip antenna.

2. MICROSTRIP ANTENNAS

Microstrip antenna consists of a metal bar, called the radiator, printed on a thin grounded dielectric surface (screen). In recent times increased the usage of multi-layer structures, which allow to obtain larger bandwidth of the antennas' operation.

One of the major problems of microstrip antennas is their stimulation. In the simplest cases, a single radiating element can be power supplied via the coaxial line, microstrip line, or via electromagnetic coupling. Much more interesting and practical way of powering of the multi-layer antenna is slotted power presented in Figure 1.

An example antenna made in multilayer technology can be constructed as follows. The radiating element is a rectangular patch etched on the underside of the upper layer of the laminate and stimulated through the slot cut in the shield covering the upper side of the lower layer of the laminate. The slot can be powered by asymmetrical strip line or concentric lines.

This type of antennas have the following characteristics: parameters of the laminate used to build the antenna and the power line can be chosen optimally, it is possible to achieve very low

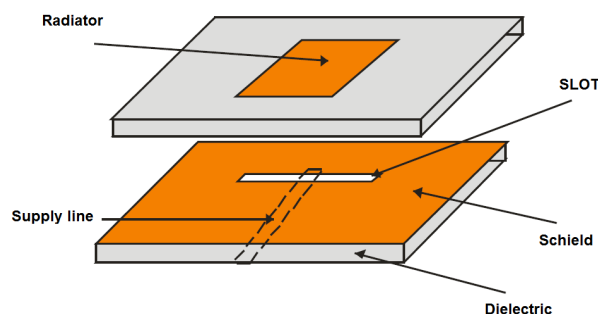


Figure 1: Example of multi-layer microstrip antenna.

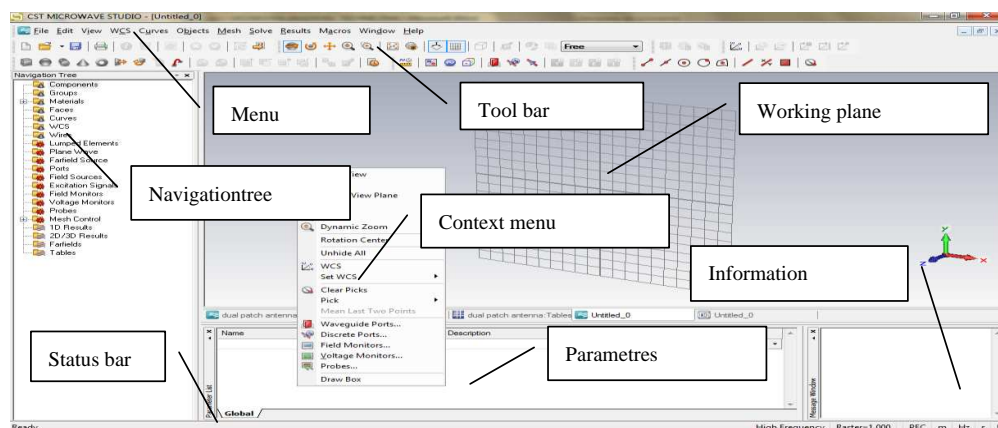


Figure 2: The main interface of CST MICROWAVE STUDIO.

levels of unwanted radiation, the need of precise composing of the package, difficult theoretical analysis, large possibilities of adjustment of the impedance.

It can be concluded that, for both classic and multi-layer antennas, the presence of the dielectric has an impact on the reduction of the dimensions of the radiating element in comparison to the option without the dielectric. One of the major disadvantage of classic strip antennas is their relatively low energy efficiency. This is mostly due to losses in the dielectric. However, in multi-layer antenna, the radiated electromagnetic wave — in a large part — is “formed” not in the dielectric but in the free space. So we can expect smaller losses.

3. THE ALGORITHM OF DESIGNING THE MICROSTRIP ANTENNA USING THE CST MICROWAVE STUDIO SOFTWARE

CST STUDIO SUITE is a powerful simulation platform of the “Computer Simulation Technology” company created for solving all the problems connected with the electromagnetic field.

The broad spectrum of available numerical methods allows you to design and optimization of the device in a wide range of frequency, from static fields to the optical range. In the current version, this environment consists of eight main modules of simulation, which, depending on the task allow developing the appropriate strategy of solving the problem.

CST MICROWAVE STUDIO (CST MWS) is a part of a simulation platform “CST STUDIO SUITE”. This application is a full-featured software package designed for electromagnetic analysis and designing at high frequencies.

3.1. The Programm Interface

After running CST MICROWAVE STUDIO user should define its design goals by selecting the appropriate model in the “Create a New Project” window. The program enables the design among others: antennas, resonators, couplers and microwave filters.

3.2. The Algorithm of Designing

After selecting the calculative model and going to the user’s main interface (Figure 2), take the pre-project activities that will help you to create an efficiently working antenna.

The process of model drawing requires the input of data for individual elements of the antenna: laminate ground plane, microstrip line, transmission line and radiator. The algorithm of creating these items by using CST MICROWAVE STUDIO is shown and described below.

3.2.1. The Input of the Basic Data

In the first stage of the project we define the units parameters (Figure 3(a)), then the size of the working plane, which is being adjusted to the size of the project (Figure 3(b)). To do this, select from the menu bar: *Edit* → *Working Plan Properties*.

3.2.2. Laminate

At the beginning you draw the surface of the antenna by selecting the sequence in the menu bar: *Objects* → *Basic Shapes* → *Brick*. In order to precisely define the location and sizing of the item, press the TAB key and enter the coordinates of three points (Figure 4(a)). It is possible to design elements of any shape. In Figure 4(b) there are shown available blocks, which the designer can use

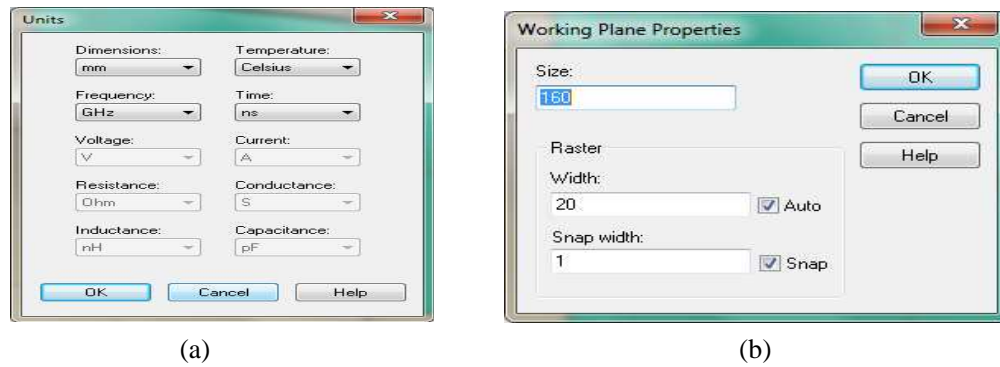


Figure 3: View of the window of defining (a) the units and (b) the working plane.

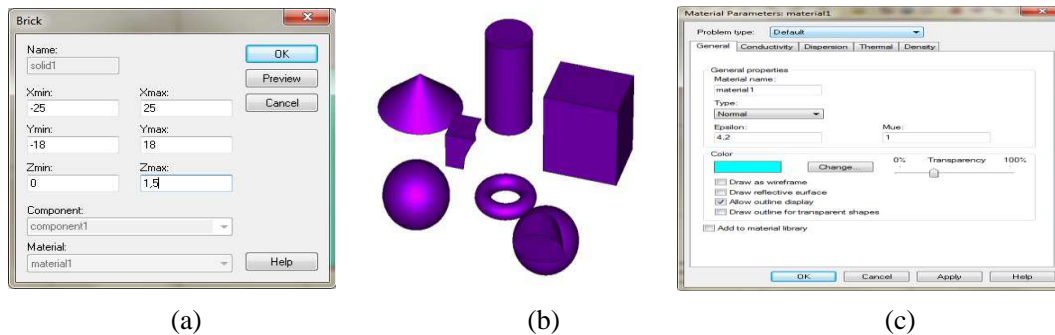


Figure 4: (a) Creating a microstrip antenna's surface, (b) block shapes available in CST MWS, (c) creation of the material parameters.

in a way described above. Each next part of the antenna created in CST MICROWAVE STUDIO (power supply units, radiator, surface and shield) is determined by using the appropriate block.

An important element of the design process in CST MICROWAVE STUDIO is definition of the material, which is used for the construction of the antenna's structure. Depending on the element (e.g., surface, microstrip line or shield) you can use metal (PEC) or create your own material by choosing the appropriate dielectric constant ϵ_t (Figure 4(c)).

3.2.3. Ground Plane

After drawing the structure of the surface, we need to define the ground plane surface. In order to do this we need to somehow 'reverse' the laminate drawn before. The easiest way is to select the command "back" from the list in the navigation bar.

There is also a much faster way of drawing the structure of the surface, using the tool 'pick face'. This method is applicable for antennas with the shield covering the entire back site of the laminate.

The next task in the process of designing an antenna is drawing its individual components. The designing of radiator and a microstrip line with a transmission line needs using the appropriate shapes. This stage of the process is the most time-consuming, and the level of the difficulty is determined by the design assumptions.

3.2.4. Microstrip Line

In order to define the shape of the microstrip line we need to use the 'Extrude' tool, located in the 'Objects' group. 'Extrude' tool allows the creation of any shape, what makes it very useful when modeling complicated elements.

When determining the points we need to adjust the coordinates of the line to the dimensions of the laminate entered before. Determination of the shape of microstrip line is done by defining the position of characteristic points. Drawing is made according to the coordinate Z . Z_{\min} parameter is determined by the thickness of the used laminate and the *height* is determined by the thickness of the etched copper.

3.2.5. Transmission Line

The process of drawing the transmission line is similar to that presented above. The “*Transform*” command allows you to perform several operations on the earlier drawn element. In addition to the application described above, the tool “*Transform*” is used for quick creation of a variety antenna’s array.

3.2.6. Radiator

By using the ‘extrude’ it is possible to draw a radiator with arbitrary shapes. This requires the coordinates of all points.

3.2.7. Defining the Power Supply Port

The last stage of the designing model is to define the power supply ports of the antenna. This is the most difficult moment for the designers. To determine the port surface, select “*Ports*” command from the navigation tree, and right-click the “*New Waveguide Port*”. Then enter the coordinates of the port and its orientation according to the local reference system.

3.2.8. Optimization

The simulation and designing process tends to get the maximum operation bandwidth, proper input impedance and low SWR multi-layer structure. The optimization process requires the determination of parameters, which are divided into two basic groups: describing and reactions. The first group can include the following antenna’s parameters:

- Permeability of each layer,
- The thickness of each layer,
- The dimensions of the radiating patch.

The second group includes:

- The operation bandwidth: B
- Standing Wave Ratio: SWR
- Input impedance of the antenna: Z

The next step in the process of optimization is defining of the optimization task.

4. CONCLUSIONS

The possibility to shorten the designing time has significantly contributed to the development of microwave antenna’s systems. Over time, appeared a number of programmers that allowed realization of projects of antenna’s systems. Starting from a simple program — Microstrip 40, to more complex ones: Antenna Magus and Zeland’s IE3D. Nowadays the most efficient, functional and effective program is the CST MICROWAVE STUDIO.

CST MICROWAVE STUDIO is a specialized program for the designing and simulation of high frequency systems. It is now one of the most popular tools, which shortens the maximum system design and optimize its performance. CST provides accurate results in calculating the structure of the antenna such as input impedance and mutual coupling of radiators. It covers all the physical phenomena occurring in the structure of the created model.

It considers the effect of plane waves, the dielectric losses and even the mutual coupling between the radiating elements of the antenna. The simulation process in CST MICROWAVE STUDIO is based on a finite difference time domain (FDTD) method.

ACKNOWLEDGMENT

The research work financed from the financial funds assigned to the science in the years 2011/2013 as the development work. The research work is realized in Poland. The number of work is 4708/B/T02/2011/40.

REFERENCES

1. Bugaj, M., “Optymalizacja struktury wielowarstwowej anteny planarnej ze wzgledu na pasmo pracy,” Rozprawa Doktorska WAT, Warszawa, 2010.
2. CST Computer Simulation Technology, CST MICROWAVE STUDIO — Workflow and Solver Overview, Darmstadt, 2007.

Tuning Fork UWB Antenna with Unsymmetrical Feed Line

A. H. M. Zahirul Alam, Md. Rafiqul Islam, and Sheroz Khan

Faculty of Engineering, International Islamic University Malaysia
P. O. Box 10, Kuala Lumpur 50728, Malaysia

Abstract— A simple planar rectangular UWB is designed with unsymmetrical feed line. It is observed that the unsymmetrical feed line plays an important role for increasing the antenna bandwidth. The rectangular planer antenna is then modified to tuning fork shaped without sacrificing the bandwidth of the antenna. By removing portion of conductive plane from the rectangular patch to makes tuning fork shaped antenna creates additional resonance, thus enhance the bandwidth of the antenna. The open space of the antenna can be utilized for placing other components. The fabricated antenna satisfies the 10-dB return loss requirement from 3.8 GHz to more than 15 GHz. The overall dimension of the antenna is $40 \times 40 \times 1.6 \text{ mm}^3$. The proposed antenna has a simple configuration and is easy to fabricate. Experimental results show that the proposed antenna could be a good candidate for UWB application.

1. INTRODUCTION

With the development of wireless technology, many systems now can operate in more than one frequency band, satellite navigation systems, wireless LANs, ultra wideband (UWB) systems and some combinations of them are examples. Their capability of operating in multiple, diverse frequency bands eventually depend on their antennas performance. To fulfill this requirement, multiple antennas are implemented in many devices, and each one covers a specific operating band or several bands. However, these antennas together occupy much space, which is at a premium in most devices, and also increase the system complexity. Such installations of multiple antennas prevent future system upgrades that require the use of currently unsupported bands. Therefore, a single antenna that has an impedance bandwidth that is wide enough to cover the operating frequency bands of multiple wireless communication systems is more desirable. Such an antenna should have stable radiation-pattern characteristics over the entire frequency range.

Commercial UWB systems require small low-cost antennas with omnidirectional radiation patterns and large bandwidth [1]. It is a well-known fact that planar monopole antennas present really appealing physical features, such as simple structure, small size and low cost. Due to all these interesting characteristics, planar monopoles are extremely attractive to be used in emerging UWB applications, and growing research activity is being focused on them.

In UWB communication systems, one of key issues is the design of a compact antenna while providing wideband characteristic over the whole operating band. Consequently, numbers of planar monopoles with different geometries have been experimentally characterized [2–5] and automatic design methods have been developed to achieve the optimum planar shape [6, 7]. Moreover, other strategies to improve the impedance bandwidth have been investigated [8].

This paper focuses on a rectangular antenna for UWB applications, which combines the rectangular-patch approach with unsymmetrical feed line tuning fork shaped, and the ground plane with partial ground conducting plane that achieves a fractional bandwidth of more than 114%.

2. ANTENNA DESIGN

The rectangular monopole antenna fed by a microstrip line is shown in Fig. 1, which is printed on a FR4 substrate of thickness 1.6 mm, permittivity 4.4, and loss tangent 0.0018. The width W_f of the microstrip feed line is fixed at 2.5 mm. The basic antenna structure consists of a rectangular patch, a feed line, and a ground plane. The rectangular patch has a width of W_p and length of L_p placed on $40 \times 40 \text{ mm}^2$ FR4 substrate. The patch is connected to a feed line of width W_f and length L_f , as shown in Fig. 1. On the other side of the substrate, a conducting ground plane of width W_{sub} and length L_{gnd} is placed. The proposed antenna is connected to a 50Ω SMA connector for signal transmission.

The antenna is initially simulated without U-shaped slot and partial ground ($L_{gnd} = L_{sub}$) for a narrowband antenna that operate at 5.5 GHz. Parametric simulation is done by varying the ground plane L_{gnd} to obtain wideband. The bandwidth of the antenna is further widening by shifting the feed line position by varying F_p . As a result of unsymmetrical feed line and rectangular patch

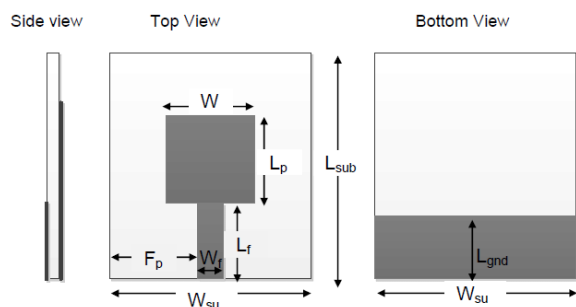


Figure 1: Geometry of the rectangular patch antenna with conductor-backed plane.

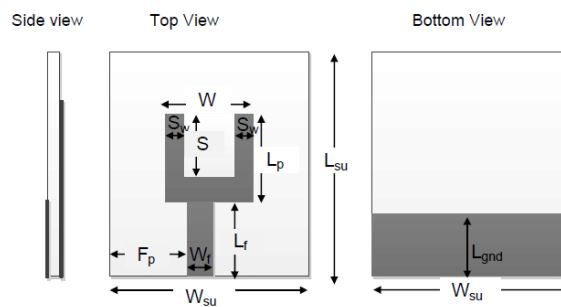


Figure 2: Geometry of proposed antenna with u-shaped slot and conductor-backed plane.

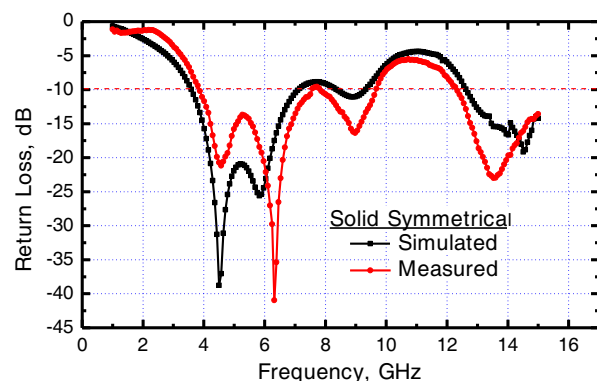


Figure 3: Symmetrical feed line rectangular patch antenna return loss with the variation of frequency.

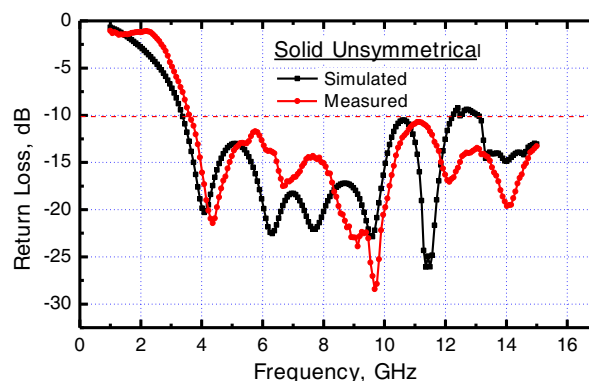


Figure 4: Unsymmetrical feed line rectangular patch antenna return loss with the variation of frequency.

gives ultra wide band response. The U-shaped slot is introduced on the rectangular patch without sacrificing bandwidth of the antenna as shown in Fig. 2.

The optimal dimensions of the designed antenna are as follows: $W_{sub} = 40$ mm, $L_{sub} = 40$ mm, $W_p = 16.6$ mm, $L_p = 12.4$ mm, $L_f = 13.6$ mm, $L_{gnd} = 12.5$ mm, $F_p = 18.7$ mm (for symmetrical fed), $F_p = 15.7$ mm (for unsymmetrical fed), $S_L = 9.9$ mm, $S_W = 2.5$ mm and $W_f = 2.5$ mm.

3. ANTENNA DESIGN

The antenna is design based on the Ansoft simulation software high frequency structure simulator (HFSS) [9]. The parametric studied have been done and optimum design antennas have been fabricated.

Figure 3 shows simulated and measured return loss of the antenna of structure as shown in Fig. 1 with symmetrical feed line. As shown in Fig. 3, the rectangular patch with symmetrical feed line antenna results simulated frequency band from 3.85 GHz to 7.15 GHz and it can be the fundamental and next higher resonant radiation band at 4.5 and 5.9 GHz, respectively. However, the frequency band is slightly shifted to measured return loss. It is also observed that lower return loss is found at higher frequency at 6.29 GHz.

It is possible to enhance bandwidth of the antenna by shifting the feed line position from the center. Fig. 4 shows the effect of feed line position shifting, as a result, additional third, fourth and fifth resonances are excited respectively, and hence the bandwidth is increased for this unsymmetrical feed line antenna. The simulated resonant frequencies are occurred at 4.02, 6.30, 7.66, 9.58 and 11.45 GHz. The frequency band of the unsymmetrical feed line antenna is 3.2 GHz to 12.2 GHz.

When the unsymmetrical feed line with rectangular patch is modified to tuning-shaped as shown in Fig. 2, there are fundamental, first and second simulated resonances at 4.39, 9.3 and 11.4 GHz, respectively as shown in Fig. 5. However, the bandwidth of both the antennas with unsymmetrical feed line is remaining almost same. However, the measured return loss is slightly different nature than that of simulated one. This may due to fabrication error, sma connector soldering effects.

The measured return loss of the fabricated three types of antennas is shown in Fig. 6. The figure

shows that the unsymmetrical feed line enhances the bandwidth of the antenna. The figure also shows that the removal of conducting part from the patch does not change the bandwidth of the antenna appreciably, however, it enhance the antenna performances in terms of return loss. The tuning fork type antenna results lower return loss compared to solid structure.

The simulated surface current distribution of the tuning fork type unsymmetrical feed line patch antenna is shown in Fig. 7 at 4.36 and 9.33 GHz.

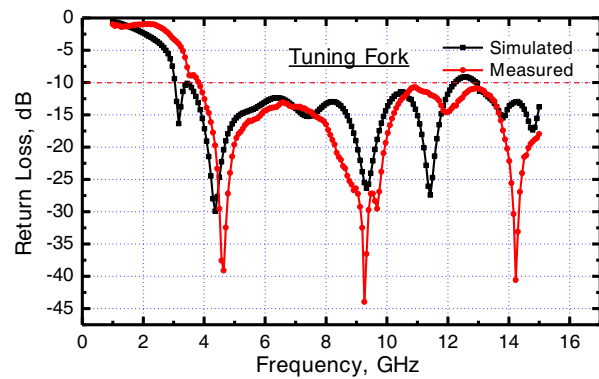


Figure 5: Unsymmetrical feed line tuning fork patch antenna return loss with the variation of frequency.

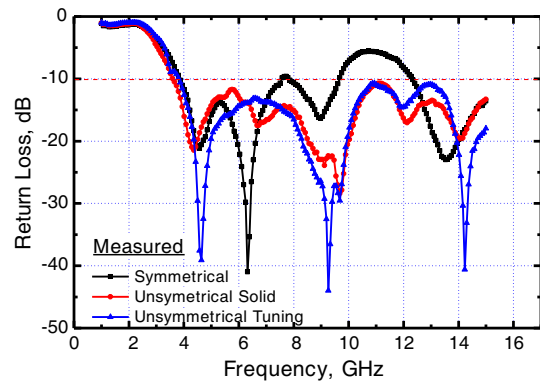


Figure 6: Measured return loss of different types of antenna.

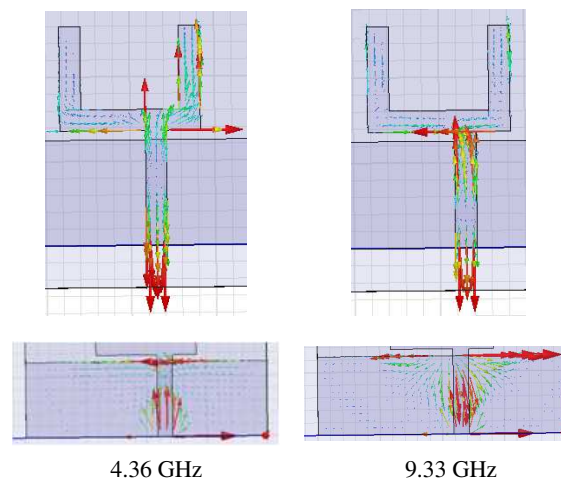


Figure 7: Simulated surface current distributions on radiating tuning fork patch and ground plane for the proposed antenna at 4.36 GHz and 9.33 GHz.

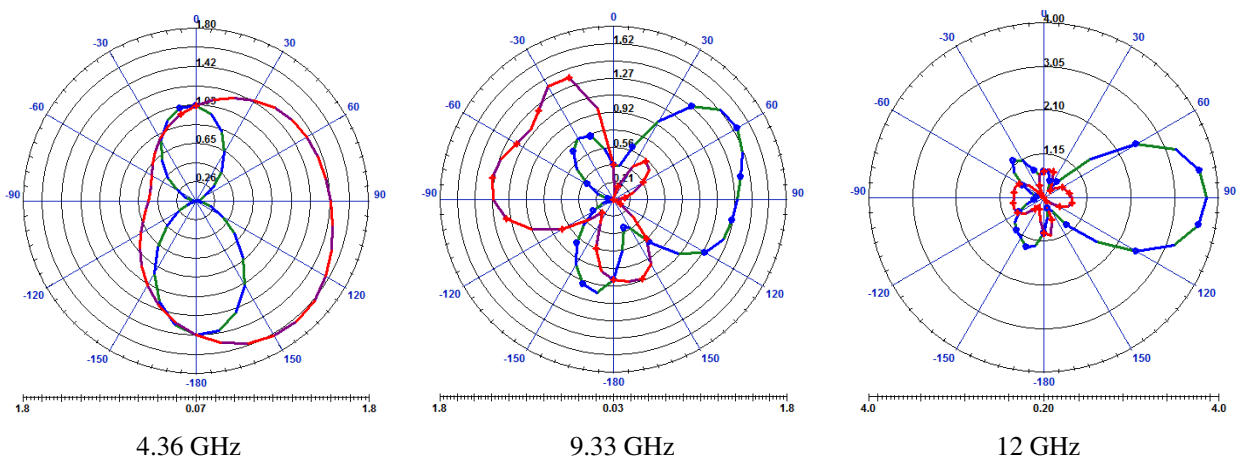


Figure 8: Simulated radiation patterns. (a) 4.36 GHz, (b) 9.33 GHz and (c) 12 GHz.

Figure 8 shows the simulated tuning fork unsymmetrical feed UWB antenna for theta cuts at 0° and 90° radiation patterns at 4.36, 9.33 and 12 GHz. The figure shows that the directivity of the antenna changes at different frequencies.

4. CONCLUSIONS

In this paper, a tuning fork unsymmetrical fed printed antenna has been proposed for UWB applications. The fabricated antenna satisfies the 10-dB return loss requirement from 3.8 to more than 15 GHz. By cutting rectangular patch to tuning fork shaped creates additional resonance and hence enhance the bandwidth of the antenna. The overall dimension of the antenna is $40 \times 40 \times 1.6 \text{ mm}^3$. The empty space on the antenna surface can be utilized for additional utilization. The proposed antenna has a simple configuration and is easy to fabricate. Experimental results show that the proposed antenna could be a good candidate for UWB application.

REFERENCES

1. Schantz, H., *The Art and Science of Ultra Wideband Antennas*, Artech House, Boston, MA, 2005.
2. Yu, C., W. Hong, L. Chiu, Z. Zhai, C. Yu, W. Qin, and Z. Kuai, "Ultrawideband printed log-periodic dipole antenna with multiple notched bands," *IEEE Trans. Antennas Propag.*, Vol. 59, No. 3, 725–732, 2011.
3. Ammann, M. J., "Impedance bandwidth of the square planar monopole," *Microw. Opt. Technol. Lett.*, Vol. 24, No. 3, 185–187, 2000.
4. Evans, J. A. and M. J. Ammann, "Planar trapezoidal and pentagonal monopoles with impedance bandwidths in excess of 10 : 1," *Proc. IEEE Antennas and Propagation Society Int. Symp.*, Vol. 3, 1558–1561, Jul. 1999.
5. Fereidoony, F., S. Chamaani, and S. A. Mirtaheeri, "UWB monopole antenna with stable radiation pattern and low transient distortion," *IEEE Antennas Wireless Propag. Lett.*, Vol. 10, 302–305, 2011.
6. Suh, S. Y., W. L. Stutzman, and W. A. Davis, "A new ultrawideband printed monopole antenna: The planar inverted cone antenna (PICA)," *IEEE Trans. Antennas Propag.*, Vol. 52, No. 5, 1361–1364, 2004.
7. Kerkhoff, A. J., R. L. Rogers, and H. Ling, "Design and analysis of planar monopole antennas using a genetic algorithm approach," *IEEE Trans. Antennas Propag.*, Vol. 2, 1768–1771, 2004.
8. Ojaroudi, M., S. Yazdanifard, N. Ojaroudi, and M. Naser-Moghaddasi, "Small square monopole antenna with enhanced bandwidth by using inverted T-shaped slot and conductor-backed plane," *IEEE Trans. Antennas Propag.*, Vol. 59, No. 2, 2011.
9. Ansoft High Frequency Structure Simulation (HFSS), Version 10, Ansoft Corporation, Pittsburgh, PA, 2005.

High Power Radiators for Ultra-wideband Electromagnetic Impulses

Vladimir M. Fedorov, Eugene F. Lebedev, Vasily Ye. Ostashev,
Vladimir P. Tarakanov, and Aleksander V. Ul'yanov

Institute for High Energy Densities of JIHT of RAS, 13/2, Izhorskaya Str., Moscow 127412, Russia

Abstract— Results of creation and diagnostics of the high power radiators for electromagnetic waves of sub-nanosecond pulses with ultra-wideband (UWB) frequency spectrum are presented in this article. The spectrum of the electromagnetic high power radiation occupies a frequency range out of 100 MHz up to 10 GHz. This electromagnetic high power radiation can be successfully used to examine on electromagnetic compatibility (EMC) of various electronic devices. One module of the multi-unit radiator was made of the UWB radiation antenna of a TEM-horn type and the high power semiconductor generator (“FID Technology”). At our laboratory were made models of compact radiators in which used generators with pulsed voltage of 10–100 kV and repetition pulses of 1–100 kHz. The synchronized radiator array can produce electromagnetic impulse waves with far-zone radiated voltage of the $V_{ER} = E(R) \cdot R = 400$ kV level. We have used experimental and computer modeling methods to investigate the non-stationary processes in a generation of the UWB radiation by the TEM-horn antennas and at propagation and receiving of the electromagnetic video-pulses.

1. INTRODUCTION

The high power semiconductor generators with high repeated sub-nanosecond pulses are developed last years and successfully used [1, 2]. The generators are applied as high power source for a radiation of electromagnetic sub-nanosecond video-pulses with ultra-wideband frequency spectrum (UWB radiation). The giga-watt-range power UWB radiators with controlled parameters can be constructed as multi-source system using the synchronized UWB radiators with semiconductor generators [3–5]. The high power UWB radiators produce electromagnetic wave pulses with high electric field of the 10 kV/m level and the widely frequency range from 30–100 MHz up to 10 GHz. Same pulsed radiation with a possible simple vary the amplitude of electromagnetic field strength and a repetition frequency of the 1–100 kHz of the pulses are very attractive to put in examinations on electromagnetic compatibility (EMC) of various electronic devices, microwave radiolocations etc [6]. As known, condition of the mutual overlapping their frequency range is required for effective EMC examinations for reliable functioning of electronic systems. The wideband frequency range of the testing electromagnetic pulse waves (“video-pulses”) is in many cases required because of testing pulses must have broad frequency range same as in electromagnetic emission which can be generated from the operated IT devices [7].

A construction of the high pulse power radiators is connected to hard problems: like the EMC of the high power sources with the triggering and control systems using low voltage pulses; realization of low jitter of delay time between the UWB radiators; compatibility of high voltage insulation and wideband frequency in the antenna unit. The electromagnetic high power radiation in the frequency range of 100 MHz–10 GHz is possible realized with using TEM-horn antennas and the high power generators with pulsed voltage of the rise time of 50 ps. Analyses of results on creation and diagnostics of the high power radiators for video-pulses of sub-nanosecond duration will be presented in this article.

2. HIGH VOLTAGE DIVIDER WITH THE $T_F = 20$ PS TRANSIT RISE TIME FOR POWER ELECTRICAL PULSES

High voltage divider of DCF3 was constructed on base of high voltage coaxial line (9 mm polythene 50 Ω cable) with direct coupler. The voltage divider which is made on base of direct coupler between two lines is had limited to measure voltage pulse of the $T_{\max} \leq 2.8 \cdot (30/L)$ ns time duration, L -cm is length of polyethylene cable. DCF3 was supplied two connectors (on input and output) of HN male type which has pulse electrical strength more 20 kV (see below on Figs. 1, 2, and 3). An application of HN coaxial connector to transport electrical pulses with rise time about 20 ps is a non trivial action. As known, high frequency signal which is being transported as symmetrical TEM-wave on coaxial line with D and d sizes (outer and inner diameters) can excite also non symmetrical modes (H_{11} type and other) of EM-traveling waves. They are being transported with different velocity compared with velocity of main TEM-wave ($\mathbf{v}_f = \mathbf{c}/\epsilon^{0.5}$). Critical wave length of the H_{11} -wave

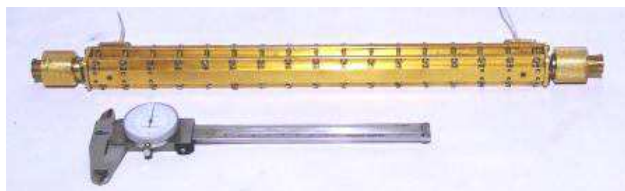


Figure 1. High voltage divider of DCF3: HN male-input/output connector, $T_f \approx 20$ ps — transient response rise time, $T_{max} = 2.8$ ns — time duration, $K_{DCF} \approx 70 : 1$ — ratio voltage, 0.7m cable length in “low voltage” channel.

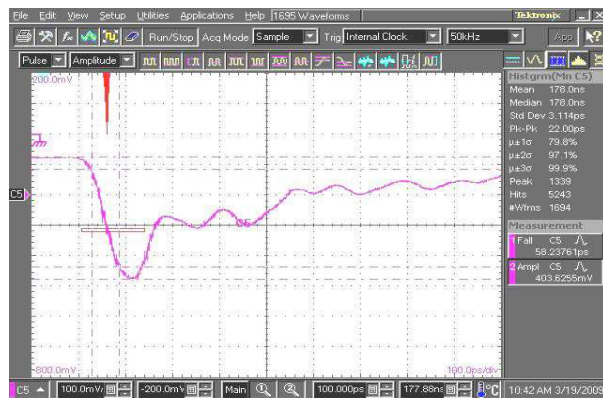


Figure 2. Display picture with voltage of $V_{pG}(t)$ — rapid leap for GIN10-50-100: $V_{pG} = 8.8$ kV — peak, $T_f = 58$ ps (0.1–0.9 levels), $V_G = 10.5$ kV total amplitude (with pedestal). Low jitter was equal 3.1 ps.



Figure 3. Gin10-50-100 [2] generated pulsed of about 10 kV (with rise time of 50–70 ps) with repetition pulses up to 100 kHz. Output feeder is HN-connector.

equals approximately $\lambda_{cr}/\epsilon^{0.5} = \pi(D + d)/2$. For HN-connector we defined $\lambda_{cr} = 3.2$ cm and $f_{cr} = 9.5$ GHz. This is conformed rise time pulse of $T_{fcr} \approx 38$ ps. Verification of HN-connector we performed using two adapters of HN-N + N-HN to transport step pulse with $T_f \approx 20$ ps — transient response rise time (examination by the 80E08 module of the Tektronix DSA8200). The result was following: HN-connector is came in useful to transport pulse with $T_f \geq 20$ ps, parasite oscillations have level less 10%.

DCF3 was used in measurements of high voltage sub-nanosecond pulse from generators of GIN10-50-100 type. In these experiments we used additionally the attenuators with the 50 dB total weakening (20 + 20 + 10 dB, each with DC-40 GHz bandwidth) in the “low voltage” channel. View of DCF3 and an example of $V_G(t)$ and GIN10-50-100 generator are shown on Figs. 1, 2, and 3.

3. EMTW SENSORS AND RECIPROCITY FOR PULSED ANTENNAS

The $\mathbf{E}(t)$ electric field in electromagnetic traveling wave (*EMTW*) is measured by few sensors: the TMA18 and TMA20-test receive antennas [8] with bandwidth at 0.3–18 GHz; and at 1–20 GHz; and linear strip transducer of LTF2 (IHED RAS). Antennas of the TMA have big effective receive aperture (cross-section of open metallic waveguides: 28×38 cm and 11×15 cm). They provide high sensitivity of $\mathbf{V}_{TMA}(t) = \mathbf{K}_{TMA} * \mathbf{E}(t)$: $\mathbf{K}_{TMA18} \approx 60$ V/(kV/m), $\mathbf{K}_{TMA20} \approx 26$ V/(kV/m). They allow to measure waves of the pulse radiation on distances more 10 m when we use the low voltage generators to excite antennas. Some defect of the TMA receive antennas for the time-domain measurement of the $\mathbf{E}(t)$ electric fields are non constant of the \mathbf{K}_{TMA} value at ultra broad frequency bandwidth (to cut down at lower frequency). At result, they produce a distortion of the $\mathbf{E}(t)$ signals approximately like distortion will be produced the “C-R” (differentiating) differential circuit. The $\mathbf{E}(t)$ signals generating at during of a limited time interval (e.g., UWB pulse radiation) may be measured by a linear strip sensor (Ch. 3 at [9]). We constructed the LTF2 sensor of like that type. Low sensitivity of the sensor is due to small receiving effective aperture (≈ 1 mm²). View of LTF2 is presented on Fig. 4.

A measurement of the LTF2 characteristics was made using own made two-electrode TEM-horn. The horn was excited by the TMG test generators: TMG30-35 (bell pulse — $V_{TMG} = 25$ V, $T_{0.5} =$

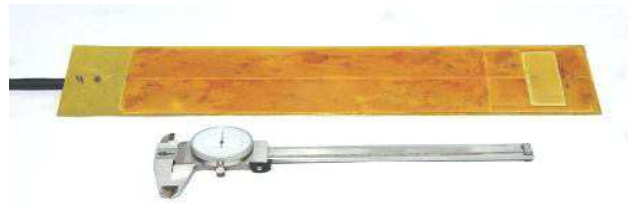


Figure 4. Linear strip transducer of LTF2 for measurement of the $\mathbf{E}(t)$ pulse electric field in TEM traveling wave. Sensor parameters: $\mathbf{T}_f \approx 20$ ps — transient response rise time; $\mathbf{T}_{\max} = 2.8$ ns — time of measured interval; $\mathbf{K}_{LTF2} = 0.4$ V/(kV/m) — sensitivity; 0.5 m — outer cable length to connect.

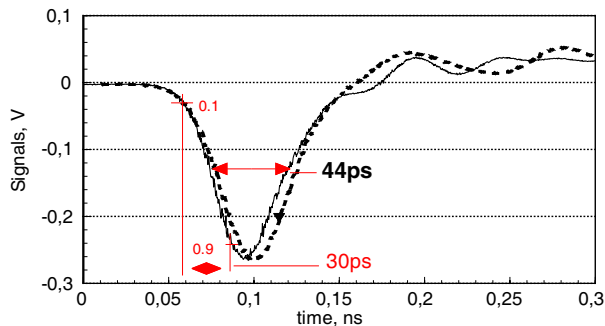


Figure 5. Shape of the $\mathbf{V}(t)_{TMG}$ — TMG30-35 (smoothed) and a voltage signal from the LTF2 sensor (dotted).

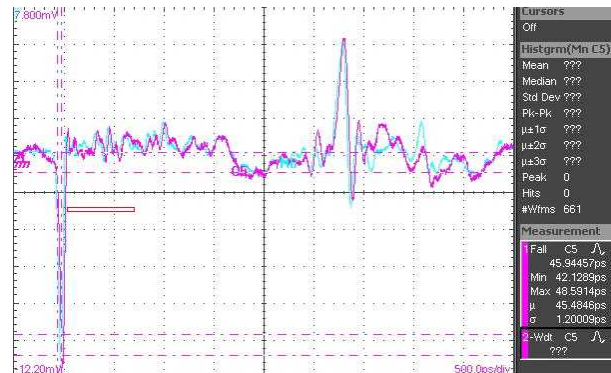


Figure 6. Application of the principle of reciprocity for the receiving and radiating antennas in a case of electromagnetic pulsed signals.

35 ps), TMG60-50 (triangle — 54 V, $\mathbf{T}_f = 57$ ps), TMG40-20 (rectangle — 33 V, $\mathbf{T}_f = 19$ ps) [8]. The TMG test generators we use as well in measurements of parameters: the voltage dividers, and angle characteristics of radiation pattern for the UWB radiators, etc. Finally, the $\mathbf{E}(t) = \mathbf{V}(t)_{TMG} / \mathbf{h}$ — electric field in electromagnetic traveling wave into a gap of the \mathbf{h} was generated. Shapes of signals of $\mathbf{E}(t)$ and $\mathbf{V}(t)_{TMG}$ are shown on Fig. 5.

The reciprocity principle is very useful attribute of a system for electromagnetic waves with the receiving antenna and the radiating antenna (for voltage linear systems). It means the received signals will be identically when we change places of the receiving and radiating antennas. The reciprocity principle for antennas in a case of harmonic oscillations is good known and widely used. In a case of pulsed signals (e.g., UWB pulse radiation) the reciprocity principle is opposite little applied up to last years [10].

We did experiments using the LTF2 sensor and the FN5 antenna (such as FN3-16 × 16 cm in the 4-th section) and this result is given on Fig. 6. Two traces on screen of DSA8200 for the receiving signals of the $\mathbf{E}(t)$ pulse radiation. Violet trace is next scene: TMG40 + FN5 (**radiator**) — 4 m distance — LTF2 (**receiver**). Blue trace: TMG40 + LTF2 (**radiator**) — 4 m distance — FN5 (**receiver**). One can see the two traces are practically identical. Plus polarity peak in two signals was generated on the LTF2 strip line end (this the LTF2 line end presents as backside antenna for forward wave).

The test result on Fig. 6 has shown success application of the principle of reciprocity for the receiving and radiating antennas in a case of electromagnetic pulsed signals. Note, it is not recognized theorem. For instance, authors of book (Chs. 1, 5 at [9]) confirm that antenna of strip line type (note, like the LTF2 sensor) is good receiving pulsed $E(t)$ -fields while this antenna will not radiate the pulsed $EMTW$ -fields. It is result of used approximate theory of two-wire line. We shall note that the reciprocity principle allows comparatively simply measure the pulse characteristics in a case of two like antennas (known method of two antennas).

4. MODELS OF THE UWB RADIATORS PRODUCED BY IHED RAS

Model M1.

The main parameters of the generator (like on Fig. 3) for excitement of radiating antenna were: amplitude — 10 kV (2 MW on 50 Ohm load), front of the pulse — 50 ... 60 ps, pulse repetition rate

— up to 10^5 Hz. The average power of generator for the 10^5 Hz repetition rate was 240 W [2]. The radiating antenna was the TEM horn type (four TEM horns connected each by two wire lines on input coaxial feeder). Input impedance of antenna is equal to nearly 50 Ohm, size of the full aperture — 16×16 cm. The view of M1 and its parameters are shown in Figs. 7, 8.

Model M3.

Figure 9. The main parameters of the generator for excitement of radiating antenna were: amplitude — 28 kV (16 MW on 50 Ohm load), front of the pulse — nearly 100 ps, FWHM — 1 ns, pulse repetition rate — up to 10^4 pps. The average power of generator consumption on maximum frequency was 300 W [2]. Antenna of radiator is of dipole type, unidirectional (with reflector) with impedance 50 Ohm. The size of aperture is equal to 50×50 cm. Choice of the such antenna size was conditioned by need to displace the energy spectrum of the radiation in low frequency area. The view of M3 is shown in Fig. 9 and its parameters — in Fig. 10.

Model G500.

The main parameters of the generator for excitement of radiating antenna were: amplitude — 3 kV, rise time — 120 ps, FWHM — 500 ps, pulse repetition rate — up to 300 kHz. The average power of generator consumption on maximum frequency was 170 W [2]. Antenna of radiator was the TEM horn type, aperture is equal to 14×27 cm. In a case of the 0.1–0.3 MHz pulse repetition rate the energy spectrum will be realized line spectrum [11]. Energy spectrum for one radiated pulse of the $E(t)$ -field at 6.6 m distance is shown on Fig. 11.

Model M8.

High power UWB radiator with total aperture of 56×56 cm sizes was built as an assembly with the 8 radiating modules (Fig. 12). Each module is made of the UWB radiating antenna unit (14×27 cm aperture) and the synchronizing pulsed power source (45 kV amplitude) that is placed into metallic screened box with $28 \times 14 \times 45$ cm sizes. Eight such models built in active antenna array with electronic device of the automatic support the synchronism. Far-field radiated voltage of this array was 455 kV and effective radiated power — nearly 7 GW. The view of M8 and measured electric field at electromagnetic wave are shown in Fig. 12.

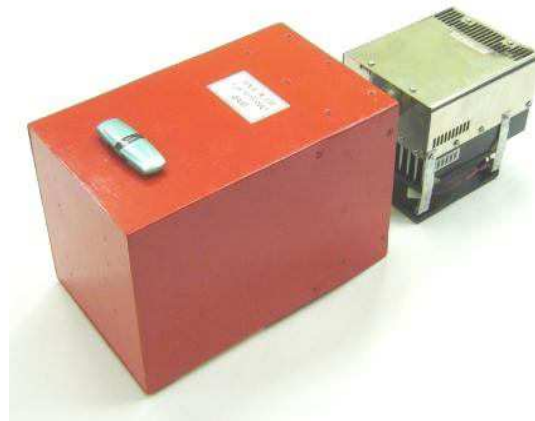


Figure 7. The view of M1: generator and antenna (aperture of 16×16 cm).

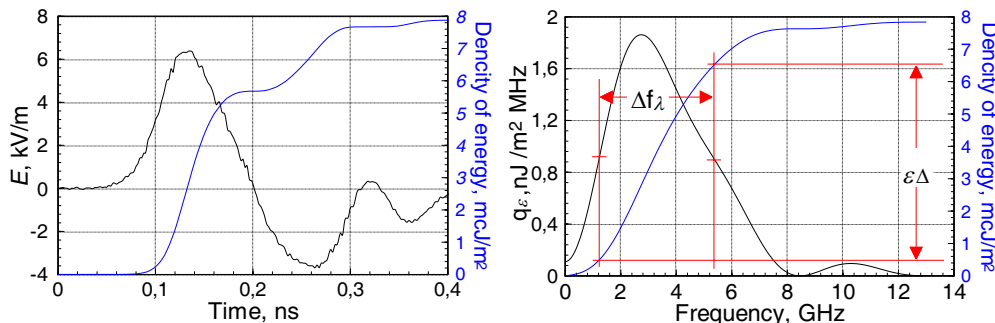


Figure 8. Model M1. Pulse of E -field strength in electromagnetic transit wave at 3 meters from antenna and energy spectrum of this pulse.



Figure 9.

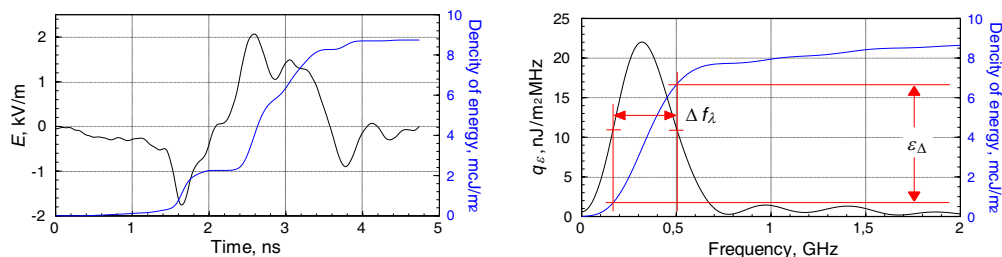


Figure 10. Model M3. Pulse of E -field strength in 7.3 m from antenna and energy spectrum of this pulse.

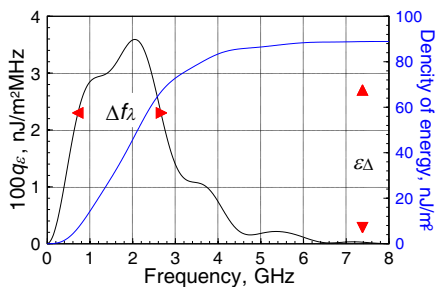


Figure 11.

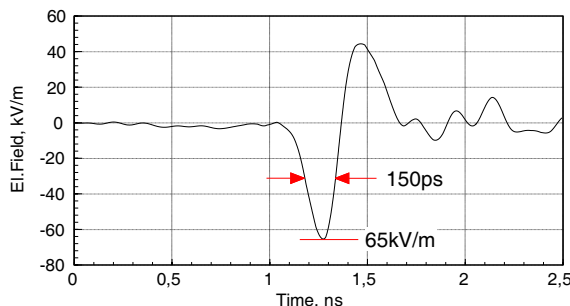


Figure 12. Model M8 and pulse of E -field strength in 7 m from antenna's aperture.

5. NON-STATIONARY PROCESSES AT PROPAGATION OF THE ELECTROMAGNETIC PULSES

Very interesting phenomenon happens when electromagnetic wave of the video-pulse comes to metallic plate with small hole (see Figs. 13, 14).

The plate with hole plays the role of the open resonator which is excited by the UWB pulse like

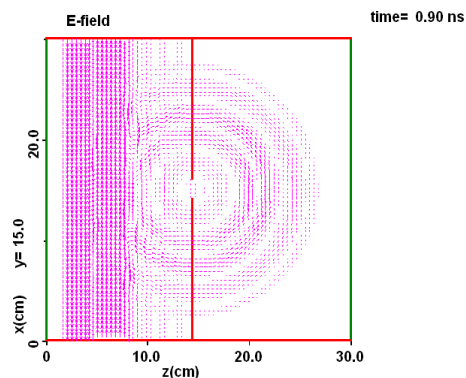


Figure 13. Picture of electric vectors for $t = 0.9$ ns from beginning process. The TEM plane wave (vertical polarization) of the video-pulse (single period of sine, $\Delta z = 6$ cm) comes from left boundary. Metallic plate ($z = 15$ cm) has hole with 2 cm diameter.

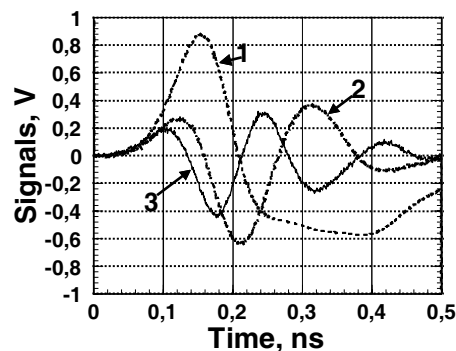


Figure 14. Wave form for the $\mathbf{E}(t)$ of the UWB pulse radiation beyond a screen with a hole (diameter of 3 cm and 1.5 cm). 1 — without screen, it uses $\mathbf{K}_1 = 1$ — signal gain factor; 2 — with 3 cm hole in metallic screen, $\mathbf{K}_2 = 20$ — signal gain factor; 3 — with 1.5 cm hole, $\mathbf{K}_3 = 80$ — signal gain factor.

shock pulse. One picture of computer simulation by code of KARAT [12] is shown in Fig. 13 and experimental results on Fig. 14. The experiments on diffraction of the UWB fast pulse radiation on hole for $D_2 = 3$ cm and $D_3 = 1.5$ cm diameters in metallic screen were provided in following conditions. AntFN3 is excited by TMG60-50. Metallic plane screen with hole is placed at 16 cm distance before AntFN3 aperture. Distance between AntFN3 and the TMA18 receive antenna is 3.3 m. The experiments confirm with the results of the computer simulation. Amount of oscillations of the $\mathbf{E}(t)$ beyond a screen is arisen for a case with smaller hole of size. Amplitude of the \mathbf{E}_{\max} beyond a screen will be proportionally a square size of the hole and the energy factor to permeability: $\mathbf{E}_{\max} \sim \mathbf{E}_0 \cdot \eta_E \cdot (D/D_0)^2$.

Given results have importance at estimation shielding characteristic of the screen with hole, as well as in experiment, when is required to localize the UWB electromagnetic wave on under investigation object.

6. CONCLUSION

Diagnostic devices (constructed by IHED RAS and successful used) for ultrafast pulses of the DCF3-high voltage divider (20 kV, $T_f = 20$ ps, $T_p \leq 2.8$ ns) and the LTF2- sensor electric field in electromagnetic traveling wave ($\mathbf{K}_{LTF2} = 0.4$ V/(kV/m), $T_f = 20$ ps, $T_p \leq 2.8$ ns) are presented and discussed. The radiators with the TEM horn antennas for high power ultrafast video-pulses (rise time of 45 ps and $FWHM$ about 70 ps) were constructed and successfully employed with far-zone radiated voltage of the $\mathbf{U}_{\text{rad}} = \mathbf{E}_{\max} \cdot \mathbf{R}$ up to 21 kV and repetition pulses up to 100 kHz. The non-stationary processes are investigated and we show they are main source for singularities at diffraction of the electromagnetic video-pulses in a hole in conductor screen.

REFERENCES

1. Efanov, V. M., V. M. Kricklenco, A. V. Komashko, and P. M. Yarin, "High voltage picosecond fid generators" *Proc. of the IEEE AP-S Intern. Symp. and UNSC/URSI and AMEREM Meetings*, 74, Albuquerque, NM, USA, July 2006.
2. "FID Technology", <http://www.fidtechnology.com>.
3. Fedorov, V. M., I. V. Grekhov, E. F. Lebedev, A. P. Milyaev, V. E. Ostashev, and A. V. Ul'ynov, "Active antenna's array with control and stabilization of regimes of synchronizing for UWB video-pulses," *Izvestiya vuzov (Physics), 14th SHCE*, Session: High Power Microwave, Vol. 11, 405, 2006, http://www.hcei.tsc.ru/conf/Proceedings_2006.
4. Ostashev, V. E., E. F. Lebedev, A. V. Ul'yanov, and V. M. Fedorov, "Radiators of powerful UWB pulses developed by AIHT of RAS," *Proc. of the 16th Intern. Symp. on High Current Electronics, 16th SHCE*, Session: High Power Microwave, 455–458, Publishing House of the IAO SB RAS, Tomsk, 2010, http://www.hcei.tsc.ru/conf/Proceedings_2010.

5. Fedorov, V. M., E. F. Lebedev, V. E. Ostashev, V. P. Tarakanov, and A. V. Ul'ynov, "Ultra-wideband TEM-Horn and high power radiators," *IEEE EMC Proc. 9th in Sump. on EM Compatibility and EM Ecology*, 394–397, St. Petersburg, Russia, 2011.
6. Zdukhov, L. N., A. P. Isaev, Yu. V. Parfenov, and B. A. Titov, "The technique of estimation of immunity of digital devices to influence of ultrashort electromagnetic pulses," *Journal of Radio Electronics*, 2011, <http://jre.cplire.ru/>.
7. Przesmycki, R., M. T. Wnuk, L. Nowosielski, K. Piwowarczyk, and M. Bugaj, "The conducted and radiated emission levels from IT devices," *PIERS Proceedings*, 77–81, Kuala Lumpur, Malaysia, March 27–30, 2012.
8. "TRIM Ltd", <http://www.trimcom.ru>.
9. Podosenov, S. A., A. A. Potapov, and A. A. Sokolov, *Impulse Electrodynamics of Wideband Radio System and Fields of Linked Structures*, 720 pages, Radiotekhnika, 2003 (in Russian).
10. Fedorov, V. M., "Reciprocity theorem and antennas of pulsed characteristics," *Proc. All-Russia 5th Conf. on Radiolocation and Wireless Communication*, 196–200, Moscow, November 21–25, 2011 (in Russian).
11. Ostashev, V. E. and A. V. Ul'ynov, "Particularities of spectral structure for video-pulses sequences," *IEEE EMC Proc. 9th in Sump. on EM Compatibility and EM Ecology*, 299–302, St. Petersburg, Russia, 2011.
12. Tarakanov, V. P., "Universal electromagnetic code KARAT," *Mathematical Simulation. Problems and Results*, 408, Nauka, 2003 (in Russian).

Two-photon Confocal and Near-field Optics of Bio-inspired Peptide Nanostructures

A. Kudryavtsev¹, E. Mishina¹, S. Lavrov¹, A. Handelman², and G. Rosenman²

¹Moscow State Institute of Radioengineering, Electronics and Automation
Prospect Vernadskogo 78, Moscow 119454, Russia

²Department of Electrical Engineering-Physical Electronics
School of Engineering, Tel Aviv University, Tel Aviv 69978, Israel

Abstract— The features of two-photon microscopy and spectroscopy application for the study of various piezoelectric nanoscale structures are presented. It is shown for peptide bio-nanotubes that the maximum second harmonic generation intensity changes along the structure. Linear microscopy reveals an axial void in the tube, unlike the SHG image is.

1. INTRODUCTION

Second-harmonic generation (SHG) is a well-known nonlinear optical process in which two incident photons of the same frequency are scattered by the nonlinear optical material into one emerging visible photon at exactly twice the energy (half the wavelength).

The particular interest to the reflected second harmonic generation is associated with a unique surface selectivity and sensitivity of the nonlinear-optical process in environments with central symmetry (which structure is invariant under inversion). It turns out that in such environments the quadratic susceptibility is identically equal to zero and there is a very strict ban on the generation of the second harmonic in the amount of substance that distinguishes the central environment from non-central symmetric one [1].

SHG microscopy is widely used in the study of various physical and biological phenomena and objects in the confocal geometry. For today, the main application of the multiphoton confocal microscopy is biology. This is related to the fact that this procedure allows one to obtain three-dimensional images of tissues by changing the laser radiation focusing; this proves to be possible because of a large radiation penetration depth at the fundamental wavelength (700–1000 nm) into biological tissues (biological transparency window).

In this paper we present the results of simultaneous studies of FF-peptide self-assembled microtubes by atomic-force, linear and nonlinear confocal and near field microscopy. Two types of structures were investigated: in-plane and z-oriented tubes on a glass substrate. (The samples were provided in Tel Aviv University).

2. SECTION 1

Novel classes of nanomaterials are represented by supramolecular bioinspired nanostructures: nanotubes, nanobelts and nanospheres which can be self-assembled from small di- and tri-peptides. The formation of nanomolecule ensembles containing crystalline building blocks is led by molecular recognition processes. Such low-dimensional highly ordered regions of building blocks create a new physical situation and provide unique physical properties based on electron-hole QC phenomena. In the case of asymmetrical crystalline structure basic physical phenomena such as linear electro-optic, piezoelectric and nonlinear optical effects described by tensors of the odd rank should be explored. Some of the crystalline structures permit the existence of spontaneous electrical polarization and observation of ferroelectricity. Crystalline arrangement of peptide nanomolecules creates highly porous nanotubes when various residues are packed into structural network with specific wettability and electrochemical properties [2].

In this work we studied diphenylalanine-based peptide nanostructures. It was shown earlier that the smallest core recognition motif of amyloid β protein, which is the basic peptide of Alzheimer peptide fibrils, is the aromatic diphenylalanine element. Basic intrinsic physical properties in these peptide nanostructures and further variation of their piezoelectric and nonlinear optical responses during the thermoinduced phase transition process using two-photon nonlinear microscopy and high resolution microscopy (confocal and near-field) have been investigated [3].

For nonlinear optical imaging, two-photon scanning microscope was developed (Figure 1). As a laser emission source, the femtosecond laser on a sapphire crystal doped with titanium ions

with a 100-MHz pulse repetition rate and a pulse width of no more than 100 fs, is used (1). The laser is intended to automatically change the operating wavelength in a range from 750 to 950 nm. The pulse energy density is of the order of 0.001 J/cm^2 . This value ensures the non-invasivity (atraumaticity) of the effect of radiation on the object under investigation, which is important for both inorganic and organic materials. Radiation is transmitted through the near-field scanning microscope (2) (WITec 300S) and then is focused on the sample by the set of lens. The spot diameter in the waist is about $0.2 \mu\text{m}$. The sample was placed on the movable table (3), which ensures precise spatial movement of the sample. After transmitting through the sample, radiation

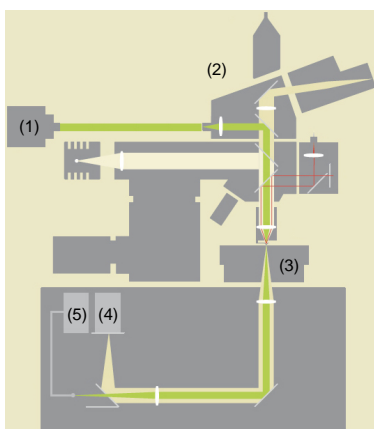


Figure 1: The diagram of the experimental setup.

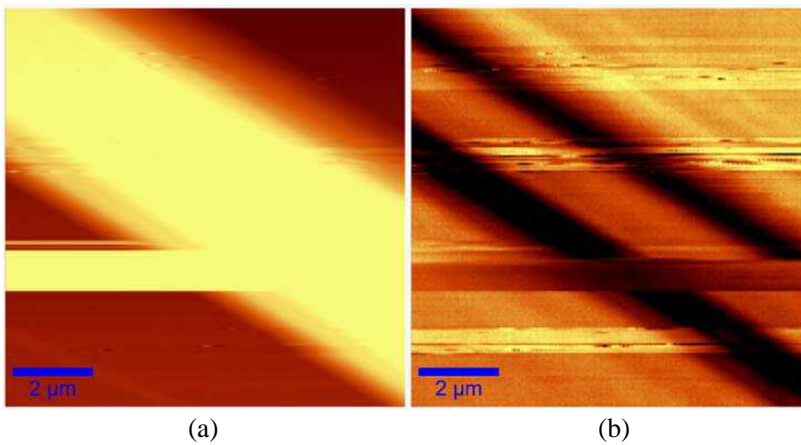


Figure 2: (a) Topography of the PNTs and (b) linear SNOM image.

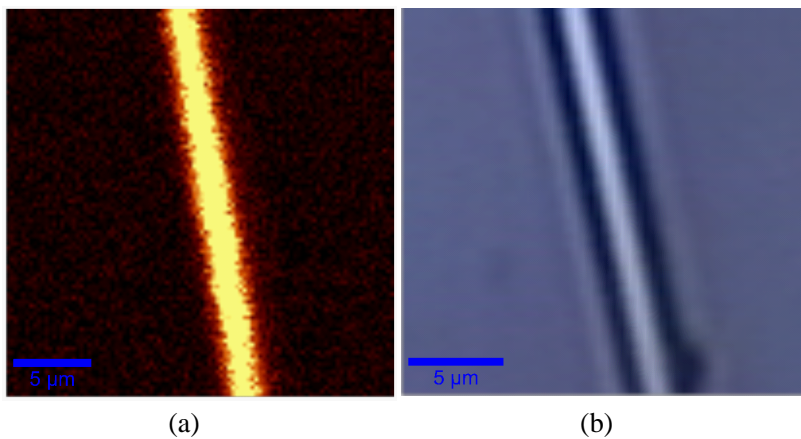


Figure 3: (a) The SHG signal and (b) CCD camera image of the first type of the nanotubes.

is focused on the photomultiplier (4). For the intermediate calibration of the device highly sensitive video camera was used.

The topography of the first type of the structures which has been obtained with the use of the experimental setup with scanning atomic force (AFM) microscope (a) and the linear optical image of the same region (b) in transmission geometry which was obtained by scanning near-field optical microscope (SNOM) is represented in Figure 2.

Nonlinear signal is represented on Figure 3(a). We showed that SHG intensity changes along the tubes, that indicates the heterogeneity of the structure. It can be seen also, that the outer diameter of the structure is about $1\ \mu\text{m}$, and the inner is about $2\ \mu\text{m}$.

As can be seen from Figure 3(b), the structure of the tube varies — on its edges radiation does not pass but the center of the tube is transparent for incidence light. This may be explained by the fact that the tubes are hollow inside, and light absorption in the centre of tube is lower than on its edges.

The confocal images of the second type of the nanotubes obtained with high-resolution CCD camera are shown on Figure 4(a). The nanotubes are several micrometers in length with the diameters ranging from 1 to $7\ \mu\text{m}$. It is clearly seen from the image that the walls of these structures are about $1\ \mu\text{m}$. In the Figure 4(b) the linear scan of the same region is shown. Due to the structure of the tubes, radiation is transmitted along the tubes without significant losses.

The SHG patterns from the same area of vertical peptide nanostructures are shown in Figure 5. These images are in consent with the linear images obtained by using of confocal and near-field microscope.

In connection with the fact that the nanotubes have different geometrical parameters, one can observe the heterogeneity of the signal of the second optical harmonic. Black spot in the middle of the image corresponds to the separate tube, which is not in inverted lens's focus. In addition there are parts of a structure with more than the others intensity. This may be explained by the fact that

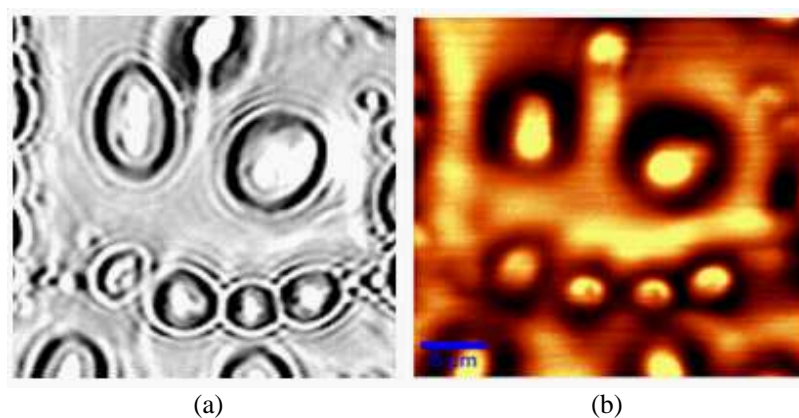


Figure 4: (a) CCD camera image and (b) its linear confocal scan of the second type of the nanotubes.

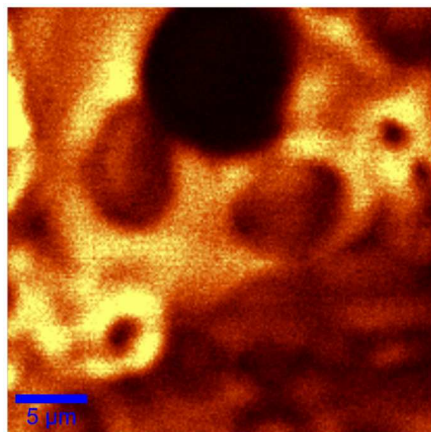


Figure 5: SHG signal of the second type of the nanotubes.

the tubes have different length and are located in the space at different heights.

3. CONCLUSIONS

Thus were defined geometrical parameters of the structures at different spatial orientations by using of such methods like atomic force microscopy and confocal microscopy. We showed the existence of second optical harmonic generation and its dependence on the parameters of the structures.

ACKNOWLEDGMENT

The work is supported by Russian Ministry of Education and Science.

REFERENCES

1. Williams, R. M., W. R. Zipfel, and W. W. Webb, “Interpreting second-harmonic generation images of collagen I fibrils,” *Applied and Engineering Physics*, Vol. 88, 1377–1386, 2005.
2. Amdursky, N., P. Beker, I. Koren, B. Bank-Srour, E. Mishina, S. Semin, T. Rasing, Y. Rosenberg, Z. Barkay, E. Gazit, and G. Rosenman, “Structural transition in peptide nanotubes,” *Biomacromolecules*, Vol. 12, 1349, 2011.
3. Kholkin, A., N. Amdursky, I. Bdikin, E. Gazit, and G. Rosenman, “Strong piezoelectric activity in peptide nanotubes,” *ACS Nano*, Vol. 4, No. 2, 610, 2010.
4. Mishina, E., S. Semin, K. Shvirkov, A. Kudriavtsev, N. Ilin, N. Sherstuk, and V. Muhortov, “Nonlinear-optical microscopy and spectroscopy of ferroelectric and multiferroic materials,” *Solid State Physics*, Vol. 54, No. 5, 2012.

Local Nonlinearities of ZnO Nanostructures

K. Shvirkov¹, A. Kedryavtsev¹, S. Lavrov¹, N. E. Sherstyuk¹,
E. D. Mishina¹, E. Rusu², and L. Kulyuk²

¹Moscow State Technical University MIREA
Vernadskogo 78, Moscow 119454, Russia

²Institute of Applied Physics, Academy of Sciences of Moldova
Str. Academiei 5, Chisinau MD-2028, Republic of Moldova

Abstract— The results of two-photon luminescence studies of zinc oxide (ZnO) microstructures consisting of microrods and microplanes are presented in this paper. When ZnO microstructure is excited by a femtosecond laser with a wavelength of 730 nm, two areas of luminescence are registered: the excitonic and impurity induced. The luminescence spectra of microstructures as function of temperature as well as the laser spot position along the structure are reported.

1. INTRODUCTION

Zinc oxide (ZnO) nano- and micro-structures have attracted enhanced interest of researchers due to their unique optical properties. ZnO possesses excitonic luminescence in the ultraviolet range that makes it very perspective cheap material for applications in optoelectronic devices [1, 2]. Recently semiconductor nanolasers based on nanorods of GaN, CdS and ZnO as well were realized [3]. The typical diameter of the rods is in the range of 50–200 nm and their length is about 2–40 microns, which makes them one of the smallest lasers today. It has been shown that even a single nanorod can work as a laser cavity with one or more modes of lasing [4]. A large refractive index contrast of ZnO nanorod regarding to the ambient air increases the quality factor of the laser cavity. In this paper, we report the radiation properties of the ZnO nanorods and nanoplanes ensembles.

2. EXPERIMENT AND RESULTS

ZnO microstructures were obtained by the MOCVD growth in a horizontal double furnace MOCVD set-up analogously to [5]. Fig. 1 shows SEM images of the obtained structures. They consist of arrays of microrods and microplanes randomly oriented along the axial axis of the whole structure.

Two-photon luminescence (TPL) experiments were performed with Ti: sapphire laser radiation (fundamental wavelength $\lambda = 730$ nm, pulse width 100 fs) focused onto a spot of about 100 μm perpendicular to the structure axial axis (see inset in Fig. 2). The sample was put in the Nitrogen cryostat in order to provide temperature measurements. Luminescence radiation from the sample was collected onto the entrance aperture of the waveguide, through which light transfer in a monochromator with small losses. The output luminescence intensity was measured by photomultiplier tube.

Figure 2 shows excitonic part of the luminescence spectrum (from 370 nm to 450 nm) of ZnO microstructure measured at different positions of the laser spot (see inset in Fig. 2). Excitation wavelength was 730 nm, the measurements were carried out at room temperature. Phonon side bands could not be resolved at room temperature although they are clearly seen at low temperature (Fig. 4). Both intensity (Fig. 2(b)) and spectrum shape are changed depending on the laser

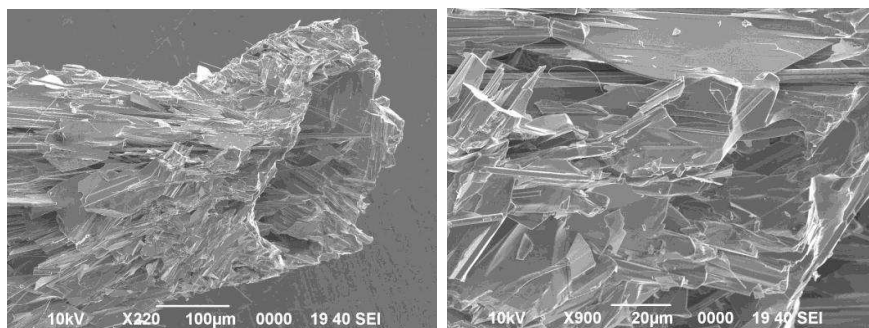


Figure 1: SEM micrographs of ZnO microstructures at different scales.

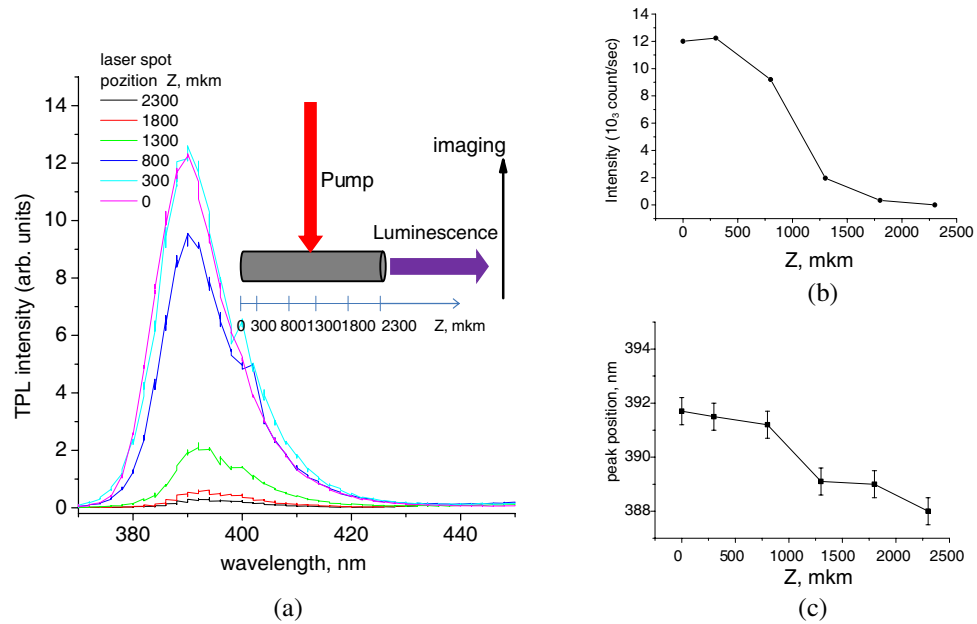


Figure 2: TPL spectra of ZnO microstructure at (a) different laser spot positions; (b) TPL intensity and (c) peak position of the center of excitonic peak as function of laser spot position; inset: geometry of TPL experiment.

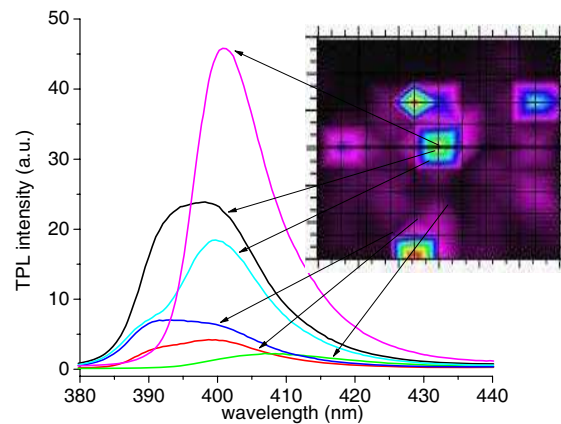


Figure 3: Scanning microscope TPL image of the sample surface.

spot position, the latter due to the different focusing conditions, the former due to the sample inhomogeneity and interplay between phonon side-bands. The same inhomogeneity which results in a quite strong change of the excitonic maximum shape is observed in TPL scanning microscopy image (Fig. 3). These studies show of inhomogeneity of the luminescence signal and hence inhomogeneity of the composition along the sample.

Complete luminescence spectra were measured at different temperatures (Fig. 4). They consist of two parts — blue excitonic part with well pronounced phonon repetitions and wide shapeless red part. Generally the red part is associated with the presence of impurities [6]. The temperature dependence of excitonic part follows ordinary exponential law (Fig. 4(a)).

The graph shows two peaks, a narrow peak corresponds to the recombination of electron-hole pairs, and the broader-transitions at impurity levels. Reduce the temperature leads primarily to an increase in the total luminescence intensity (Figs. 4(b), (c)) and the spectral resolution of the excitonic lines.

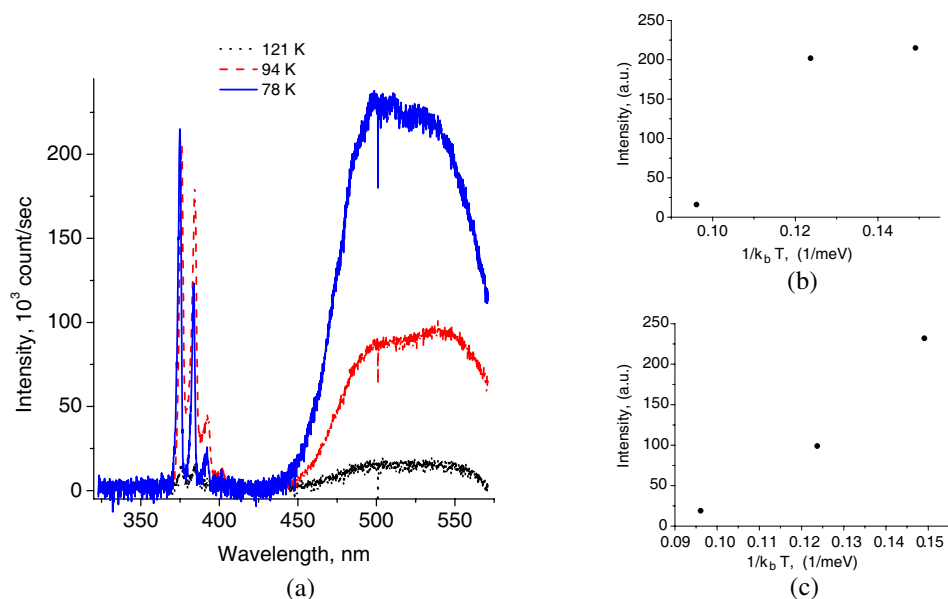


Figure 4: (a) Luminescence spectra of structures based on zinc oxide at different temperatures; Intensity of impurity peak dependence on temperature with theoretical fitting curve. (b) TPL intensity dependences on the temperature for the main excitonic peak and (c) impurity peak.

3. CONCLUSIONS

The results show that the intensity of the excitonic luminescence of zinc oxide microrods increases when the incident radiation falls close to the very edge of sample. Peak position dependence on the laser spot coordinate proves the fact of heterogeneous composition of the sample. Also showed, that a decrease of temperature leads to an increase of the TPL intensity and to the improvement of spectral resolution of the excitonic lines.

ACKNOWLEDGMENT

This work was supported by the Ministry of Education and Science of Russian Federation.

REFERENCES

1. Buinitskaya, G., L. Kulyuk, V. Mirovitskii, E. Rusua, E. Mishina, and N. Sherstyuk, "ZnO single crystal and epitaxial thin film studied by second harmonic generation and photoluminescence," *Superlattices and Microstructures*, Vol. 39, 83–90, 2006.
2. Wang, Z. L., "The new field of nanopiezotronics," *Material Today*, Vol. 10, 20–28, 2007.
3. Gruzintsev, A., G. A. Emelchenko, A. N. Redkin, V. T. Volkov, E. E. Yakimov, S. G. Romanov, and D. Visimberga, "Visualization of bound photon modes of ZnO nanorods by scanning cathodoluminescence," *FiTP*, Vol. 43, 488–492, 2009.
4. Gruzintsev, A., G. A. Emelchenko, A. N. Redkin, V. T. Volkov, E. E. Yakimov, and D. Visimberga, "The dependence of the lasing threshold of ZnO nanorods on their length," *FiTP*, Vol. 44, 1254–1259, 2010.
5. Ursaki, V. V., A. Burlacu, E. V. Rusu, V. Postolake, and I. M. Tiginyanu, "Whispering gallery modes and random lasing in ZnO microstructures," *J. Opt. A: Pure Appl. Opt.*, Vol. 11, 1–6, 2009.
6. Fang, X., Y. Bando, U. K. Gautam, T. Zhai, H. Zeng, X. Xu, M. Liao, and D. Golberg, "ZnO and ZnS nanostructures: Ultraviolet-light emitters, lasers, and sensors," *Critical Reviews in Solid State and Materials Sciences*, Vol. 34, 191–219, 2009.

Femtosecond Infrared Laser Annealing of Ferroelectric PZT Films on a Metal Substrate: Confocal and Near-field Optical Studies

N. Yu. Firsova¹, E. D. Mishina¹, S. V. Senkevich², and I. P. Pronin²

¹Moscow State Technical University of Radioengineering, Electronics and Automation (MSTU-MIREA)
Prospekt Vernadskogo 78, Moscow 119454, Russia

²Ioffe Physical-Technical Institute of the Russian Academy of Sciences
Polytekhnicheskaya 26, St-Peterburg 194021, Russia

Abstract— Ti-sapphire femtosecond laser was utilized to crystallize $\text{Pb}(\text{Zr}_{0.54}\text{Ti}_{0.46})\text{O}_3$ (PZT) film on platinized silicon substrate. Second harmonic generation was used to in-situ monitor of the annealing process and to confirm a non-centrosymmetric perovskite ferroelectric phase of the irradiated area. The images of the film surface after laser exposure were obtained by confocal optical microscopy.

1. INTRODUCTION

Along with conventional crystallization performed by furnace annealing, ferroelectrics are frequently annealed by the illumination with excimer laser light [1, 2]. Using the UV irradiation efficient absorption of light provides heating of the films on a substrate which results in annealing and subsequent crystallization.

Laser annealing is attractive because the light can be absorbed selectively and has high-power density and short heating time. The temperature ramp-up rate of laser annealing is higher than that provided with rapid thermal process (RTP) by a factor of 10^8 times. Therefore, it can provide sufficient thermal energy to the thin film of a ferroelectric precursor and transform it into the perovskite phase without causing any ablation and chemical decomposition. By this procedure the bulk of the material as well as a substrate keep low temperature, which is very important for multilayer structures and semiconductor back-end process.

The application of ultrashort pulse lasers for a controlled material processing has been an active area of fundamental and applied research due to the unique properties of this method. When an ultrashort laser pulse interacts with a solid target, the electrons are heated to a high temperature by the absorption of laser energy. Facilitated by electron-phonon interactions, the hot electrons transfer energy to the lattice. For the femtosecond laser pulse, the energy is transferred to the electrons on a time scale much faster than the transfer time of this energy to the lattice of the material and then the time of further propagation of heat along the sample surface. The latter results in a much smaller lateral thermal damage or heat-affected zone if compared with longer pulses impact.

High energy femtosecond laser radiation is used for processing both the opaque and transparent materials, for their ablation and nanostructuring [3, 4] as well as for interaction with biological tissues [5, 6].

Low energy femtosecond laser radiation is used for nondestructive characterization of both types of materials, organic and non-organic. Application of femtosecond radiation of intermediate power range is less developed although it may provide precise rapid heating or annealing of different materials, followed by re-crystallization.

Ultrashort pulsed laser irradiation was frequently used for the re-crystallization of amorphous-silicon (a-Si) films. Different techniques were applied to clarify the mechanism of re-crystallization. Pump-probe experiments [7] revealed that the phase transition is mediated by a short-lived non-thermal lattice disorder. Alternative mechanism is a crystallization through a molten liquid layer whose properties and transient behavior differ from normal thermal melting. Phase transformation of a titanium dioxide crystal from rutile to anatase under irradiation by a femtosecond laser was studied by Raman spectroscopy [8]. In transparent dielectrics, periodic micro-structures were reported to be formed in the bulk of lithium niobate under ultrashort pulse laser irradiation [9].

In this paper we present the results of femtosecond laser annealing of PZT thin films, using laser wavelength that falls down into the transparency range of PZT. Second harmonic generation was used to in-situ monitor of the annealing process and to confirm a non-centrosymmetric perovskite ferroelectric phase of the irradiated area.

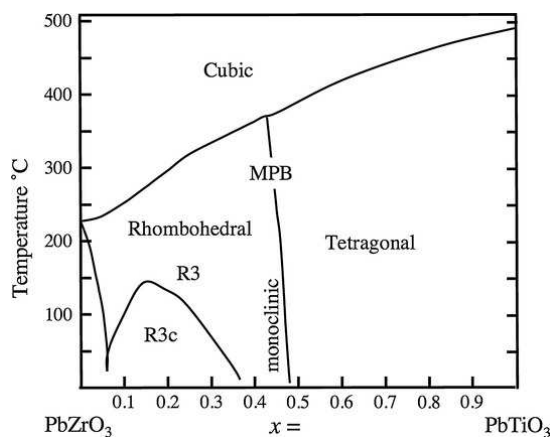


Figure 1: Schematic phase diagram of $\text{Pb}(\text{Zr}_{1-x}\text{Ti}_x)\text{O}_3$.

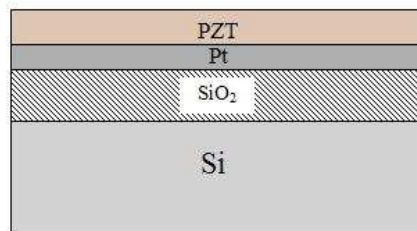


Figure 2: Scheme of the sample layers.

2. INVESTIGATED STRUCTURE

In the system of solid solutions of PZT the range of concentrations of Zr (Ti) near the morphotropic phase boundary (MPB), separating the rhombohedral (with a high content of zirconium ions) and tetragonal (with a high content of titanium ions) modification of the ferroelectric phase is the most interesting area (Figure 1). It is well known that many physical properties undergo extremes around MPB. We used a target of rhombohedral $\text{Pb}(\text{Zr}_{0.54}\text{Ti}_{0.46})\text{O}_3$ composition, as well as composition, containing additional 10 mol% lead oxide: $\text{Pb}(\text{Zr}_{0.54}\text{Ti}_{0.46})\text{O}_3 + 10\% \text{PbO}$. The multilayer system (Figure 2) consists of silicon (Si) substrate (300 μm thickness) with a layer of oxide (SiO_2) (300 nm thickness). Platinum (Pt) film (80 nm thickness) is deposited on oxide layer. PZT layer (300 nm thickness) in above the platinum film. Thermally conductive contact is attached to the bottom Si substrate to draw off heat from the multilayer system.

$\text{Pb}(\text{Zr}_{0.54}\text{Ti}_{0.46})\text{O}_3$ films of 300 nm thickness were deposited by RF magnetron sputtering. Because of low substrate temperature (nearly 150°C) X-ray study showed quasi amorphous structure of the pre-annealed films.

3. EXPERIMENT DETAILS

For annealing, radiation of titanium-sapphire laser was used with pulse duration of 100 fs, wavelength in a range of 800 nm, repetition rate of 100 MHz and average power up to 2.5 W. Incident radiation falls onto the spot of about 100 μm at 45° incidence; its polarization could be varied by a half-wave plate. Only two parameters, power and annealing were found to influence on the properties of annealed film.

The annealing process was monitored in situ by second harmonic generation (SHG) in reflection geometry, which was detected by photomultiplier tube (PMT) and photon counting system. In order to cut fundamental radiation color BG39 filters were used. Monitoring was performed in two ways. First of all, in situ SHG intensity was measured as function of time during annealing. Secondly, after the heating was stopped laser pulse of much lower energy was used to scan along the annealed area. Figure 3 shows the experimental setup providing laser annealing, in-situ SHG detection the annealing process and ex-situ SHG scanning of the annealed areas.

4. RESULTS AND DISCUSSION

4.1. Second Harmonic Generation

SHG technique of detection the annealing process is based on the changing of symmetry of the film from centrosymmetric (amorphous) to non-centrosymmetric (perovskite). The SHG intensity behavior during annealing is shown in Figure 4, inset. At time zero SHG intensity is very small and determined by surface and quadrupole contributions [10] from centrosymmetric quasi-amorphous film.

At the same time power dependence of the SHG signal at saturation follows classical power (quadratic) law. It means that the SHG signal is generated in ferroelectric phase only and this ferroelectric phase is stable under further illumination.

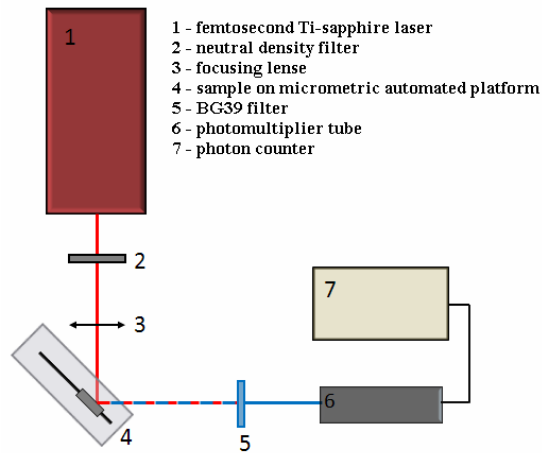


Figure 3: Setup providing laser annealing, in-situ SHG detection the annealing process and ex-situ SHG scanning of the annealed areas.

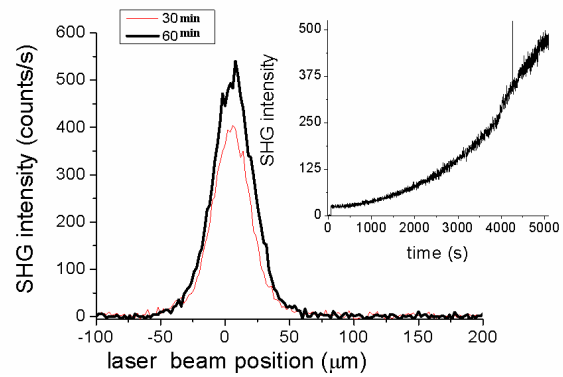


Figure 4: Time dependence of SHG intensity during the annealing process for pulse power density 10 GW/cm^2 .

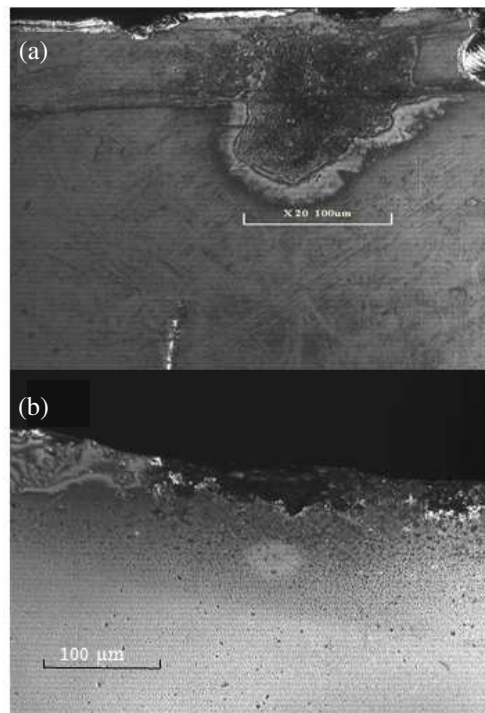


Figure 5: Confocal microscopy images of (a) focusing area, (b) the film after 10 min annealing.

4.2. Confocal Microscopy

Figure 5 shows images of laser exposed areas (average power 700 mW; (a) focusing; (b) 10 min) of the film obtained by confocal optical microscopy. The feature of the use of femtosecond laser is the high degree of radial uniformity of single-mode Gaussian beam, and therefore the temperature profile is also spatially homogeneous, and therefore the region of crystallization also represents an area of regular symmetrical shape (Figure 5(b)) After annealing the film during 10 min destruction of the surface is not observed. The spot on Figure 5(b) represents irregular shape which is associated with a slight movement of sample during focusing.

5. CONCLUSIONS

The results of the present work showed the possibility of local regions of ferroelectric phase formation in the body of the amorphous PZT film under femtosecond laser radiation exposure. Second

harmonic generation, which is measured with spatial resolution of 20 μm reveals strong enhancement of SHG intensity over the spot area with Gaussian-like shape. Used in this work scanning technique (also based on SHG) allowed not only to detect the transition to the ferroelectric phase, but also evaluate the diameter of the resulting structure. The diameter of the annealed regions according to the SHG scanning results was equal to 50 microns, which agrees with the assessment by confocal optical microscopy.

ACKNOWLEDGMENT

Parts of this work were supported by the Russian Foundation for Basic Research, and the Ministry of Education and Science of Russian Federation (Center of Collective Users UNO “Electronics”).

REFERENCES

1. Zhu, Y., J. Zhu, Y. J. Song, and S. B. Desu, “Laser-assisted low temperature processing of $\text{Pb}(\text{Zr}, \text{Ti})\text{O}_3$ thin film,” *Appl. Phys. Lett.*, Vol. 73, 1958, 1998.
2. Lai, S. C., H.-T. Lue, K. Y. Hsieh, S. L. Lung, R. Liu, T. B. Wu, P. P. Donohue, and P. Rumsby, “Extended-pulse excimer laser annealing of $\text{Pb}(\text{Zr}_{1-x}\text{Ti}_x)\text{O}_3$ thin film on LaNiO_3 electrode,” *J. Appl. Phys.*, Vol. 96, 2779, 2004.
3. Gattass, R. R. and E. Mazur, “Femtosecond laser micromachining in transparent materials,” *Nat. Photonics*, Vol. 2, 219–225, 2008.
4. Dausinger, F., F. Lichtner, and H. Lubatschowski, Ed., *Femtosecond Technology for Technical and Medical Applications*, Springer, 2004.
5. Juhasz, T., Z. Nagy, M. Sarayba, and R. M. Kurtz, “Femtosecond lasers in ophthalmology: Clinical applications in anterior segment surgery,” *Proc. SPIE*, Vol. 7589, 758904, 2010.
6. Yanik, M. F., H. Cinar, H. N. Cinar, A. D. Chisholm, Y. Jin, and A. Ben-Yakar, “Neurosurgery: Functional regeneration after laser axotomy,” *Nature*, Vol. 432, 822–822, 2004.
7. Choi, T. Y., D. J. Hwang, and C. P. Grigoropoulos, “Ultrafast laser-induced crystallization of amorphous silicon films,” *Opt. Eng.*, Vol. 42, No. 11, 3383–3388, 2003.
8. Yang, J. Y., H. L. Ma, G. H. Ma, B. Lu, and H. Ma, “Phase transformation at the surface of TiO_2 single crystal irradiated by femtosecond laser pulse,” *Appl. Phys. A*, Vol. 88, 801–804, 2007.
9. Nejadmalayeri, A. H. and P. R. Herman, “Rapid thermal annealing in high repetition rate ultrafast laser waveguide writing in lithium niobate,” *Optics Express*, Vol. 15, No. 17, 10842, 2007.
10. Epperlein, D., B. Dick, G. Marowsky, and G. A. Reider, “Second-harmonic generation in centro-symmetric media,” *Appl. Phys. B*, Vol. 44, 5–10, 1987.

Optical Properties of Fotonnokristallicheskih Structures Based on Single-crystal GaAs

A. U. Dobritsky, N. A. Ilyin, T. V. Nikonorova, N. E. Sherstyuk, and E. D. Mishina

Moscow State Institute of Radio-Engineering, Electronics and Automation

Prospect Vernadskogo 78, Moscow 119454, Russia

Abstract— Photonic crystals (PhC) offer wide opportunities for creation of small-type components, which allow to downsize the existing integrated circuits. The operation of these devices is based on the presence of photonic bandgap. Size and period of photonic crystal determine effective range of wavelength for the concrete functional element. The creation of PhC structures on the basis of functional materials with the characteristics being switched by external electric/magnetic field allow to manage the propagation parameters of electromagnetic field inside them.

The majority of research in the sphere of PhC waveguides is based on the modeling of their characteristics. Herewith 2 models are used: model of dielectric channels in air and model of ordered group of holes in functional material. The advantage of the first model waveguides lies in the fact that they are single-mode. The literature also offers variants of calculation of deflecting and bisected waveguides. But such a configuration of the waveguide does not provide the acceptable level of losses for the creation of actually functioning prototypes, working in the optical range. PhC structures, based on the second model are much more diverse and allow to create waveguides of more complicated construction, for example, optical T- and Y-couplers, interferometers and so on.

This work presents the result of the systematical research using the method of numerical simulation of transmission spectra for PhC waveguides with different type of ordering and their characterization by scanning near-field optical microscopy (SNOM).

The modeling of the characteristics of 2D PhC structures was carried out with the help of software package CST StudioSuite. The following parameters were used for modeling: wavelength of 900–2000 nm, ratio of period of the structure to wavelength $0.24 \leq a/\lambda \leq 0.42$; ratio of hole diameter to period $0.5 \leq d/a \leq 0.9$. Photonic crystals based on silicon and gallium arsenide with quadratic and hexagonal ordering were investigated.

1. INTRODUCTION

This article presents the results of numerical modeling and experimental investigation of optical properties of semiconductor two-dimensional photonic crystals, depending on the parameters of the structures. The study also presented the distribution of the electromagnetic field in the photonic crystal-waveguide structure on depending on the parameters of the structure and the emission wavelength. In this paper we carried out a comparative study of spectral properties of two-dimensional photonic crystals based on GaAs, with different type of ordering. The simulation of the spatial distribution of electromagnetic fields in waveguide structures based on semiconductor FC, as well as provided evaluation of the influence of the type of order on the main parameters of the transmission structures. The simulation was performed in the software environment CST Microwave Studio 2010, using the method of FIT (method of eventual integration). The detailed description of the methodology can be found, for example, in [1, 2].

2. EXPERIMENTS AND RESULTS

Theoretical study and modeling of parameters of the distribution of electromagnetic fields in photonic crystal (FC) of two-dimensional structures based on semiconductor materials in a large number of papers [3–6]. Among them, special attention is paid to systems containing FC-waveguide elements and structures, because it is such a system have the most ample opportunities for practical applications.

Most theoretical research examines two types of waveguide structures. The first type includes FC-structures, which represent an ensemble of parallel plates of the functional material (e.g., dielectric) separated by a layer of air (model “rod-in-air”) [3, 4]. The advantage of these structures lies in the fact that the waveguide, which is a “missed” some elements of FK-structure is a single-mode. However, such structures are quite difficult for practical implementation. The second type

of waveguide photonic-structures is an ensemble of holes (usually cylindrical) with a square or hexagonal ordering, made in the semiconductor or dielectric plate. In this geometry, the waveguide can be, theoretically, any form of [5], in this case can be realized compared with other types of structures of radiation losses [5].

Numerical calculations and simulations carried out for such structures, which show that at certain ratios of dimensional parameters of the structure (the period of FC, the size of the holes, etc.) and the emission wavelength can be determined by a relatively narrow range of wavelengths for which the basic parameters of the transmission/reflection depends on the type of ordering FC uncritical way. Nevertheless, for most of the investigated FC conditions of electromagnetic field distribution in the structure to a large extent depend on the parameters of the structure and geometry of the FC selection.

In order to study the model was chosen, which is an ordered ensemble of vertical air-filled cylindrical holes in a uniform layer of the semiconductor GaAs. For the calculation were chosen structure with hexagonal and square ordering with a ratio of a period and wavelength λ in the range of $0.28 \leq a/\lambda \leq 0.3$ and hole diameter of $0.5A \leq d \leq 0.95a$. As a functional material used single-crystal gallium arsenide. For the calculation we used the data on the dispersion of the dielectric constant of GaAs [6]. From the data sheet shows that pure single-crystal gallium arsenide opaque for the entire visible spectrum, and the maximum transmission accounts for the wavelength interval 1.7, . . . , 10 m.

One of the important parameters of the model is the depth of the holes. At the initial stage of the research for this parameter is used the value $h = 2$ m, which corresponds to an average depth of the holes in the actual structures fabricated by focused ion beam etching. In calculating the parameters of the field distribution in the sample plane, depending on the depth of the holes, it was shown that under the model used for any value of $h \leq 2$ m, the field distribution in the XY plane of the same. Consequently, for the numerical simulation, you can use smaller values of the depth of the holes, which is significantly (at times) reduces the calculation time.

Waveguide two-dimensional FC of this type can be formed by the “passing” of one period of the structure by etching. In accordance with [10], electromagnetic radiation with a wavelength corresponding to the forbidden photonic zone in such a structure should be extended only along the waveguide. Fig. 1 shows the results of a study of the distribution parameters of the electromagnetic field with a wavelength of 1550 nm in the forward waveguide, made in the FC structures with a square (Fig. 1) and hexagonal (Fig. 2) ordering with a period $a = 450$ nm and hole diameter $d = 290$ nm.

The intensity of the transmitted electromagnetic wave is calculated based on the following considerations. The result of numerical simulation using CST Microwave Studio software is the dependence of the real $\text{Re}(E_i)$ and imaginary $\text{Im}(E_i)$ parts of the i -th component ($i = x, y, z$) of the electric field on the coordinate. The electric field is defined as $E = Ae^{i\omega t}$, where the A -amplitude

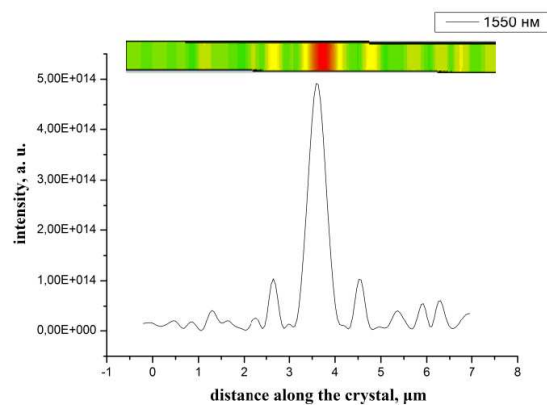


Figure 1: The results of numerical modeling of photonic-crystal structures of the transmission containing the waveguide, in the case of square order.

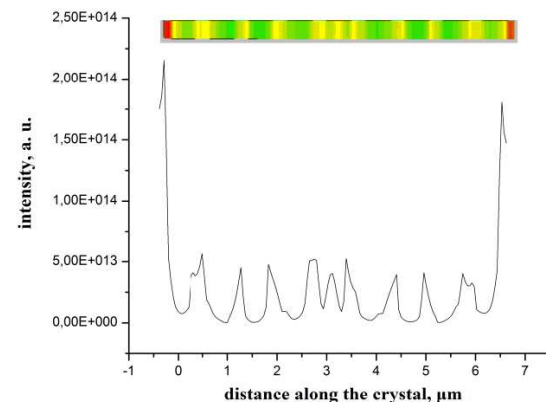


Figure 2: The results of numerical modeling of photonic-crystal structures of the transmission containing the waveguide, in the case of hexagonal order.

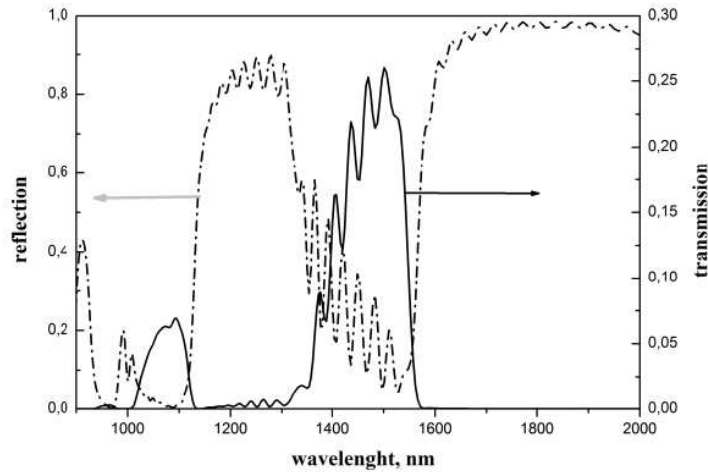


Figure 3: Calculated reflection and transmission spectra of two-dimensional photonic crystal based on GaAs with a period of 450 nm and 290 nm diameter holes of the hexagonal ordering.

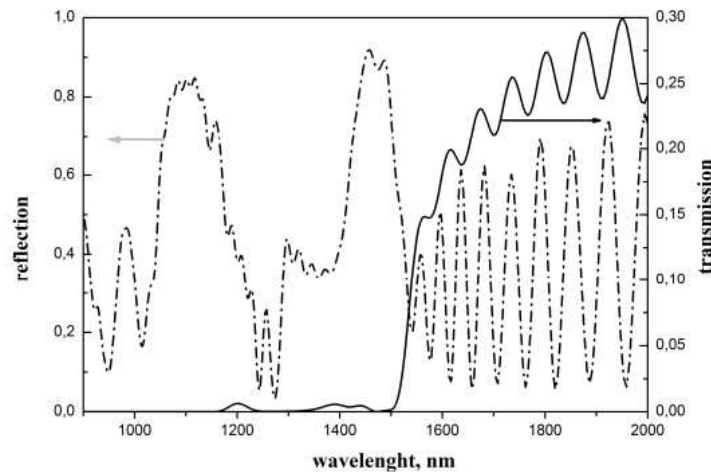


Figure 4: Calculated reflection and transmission spectra of two-dimensional photonic crystal based on GaAs with a period of 450 nm and 290 nm diameter holes of the square ordering.

of the electric field, which is calculated by the formula:

$$A = \sqrt{E_x^2 + E_y^2 + E_z^2} \quad (1)$$

which, in turn, $E_i = \sqrt{\text{Re}(E_i)^2 + \text{Im}(E_i)^2}$.

The intensity of the transmitted electromagnetic wave is proportional to the square of the amplitude of the electric field $I \sim A^2$.

As shown in the figure, the structure of FC-square-ordering to ensure good transmission of selected wavelengths, while the FC structure with hexagonal ordering does not let this light, even in the waveguide. Similar studies conducted for the zigzag waveguides, have shown that they provide an even lower transmittance than the straight waveguide, the parameters of the transmission is almost independent of the length of the waveguide. It should be noted that these waveguides are often multi-mode, which reduces the efficiency of light propagation in the waveguide due to the fact that higher-order modes are easily excited by local heterogeneity in the structure. The influence of the same factor explains the large losses of radiation passing through the structure.

The simulation results of transmission and reflection spectra of photonic crystals with different types of ordering are shown in Fig. 2. In the transmission of GaAs (0, 9, ..., 15 mm) photonic crystal with a square type ordering (Fig. 3) has investigated the wavelength range of two-photon

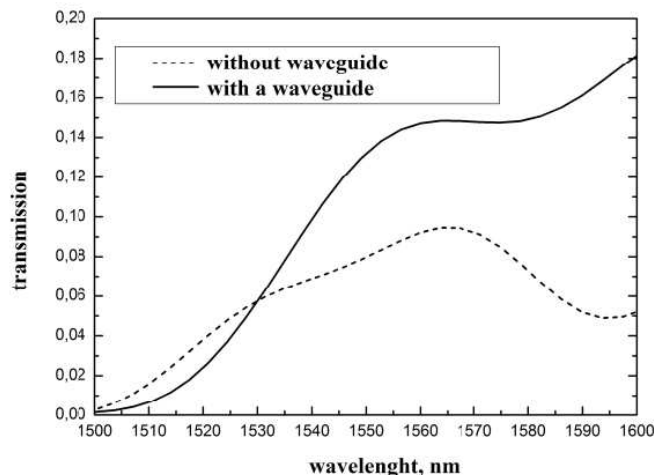


Figure 5: Transmission spectra of photonic-crystal structures with a square type of order ($a = 450$ nm, $d = 290$ nm) containing FC-waveguide (solid line), and structures without FC-waveguide (dotted line).

band gap (PBG): 1049, ..., 1177, ..., 1417 nm and 1514 nm. PBG estimated from the width of the absorption edge in the spectrum of FC. For the FC with a hexagonal type of order (Fig. 4) also observed two-photon forbidden zone: in 1134, ..., 1309 nm and 1600, ..., 2000 nm. As can be seen from a comparison of the spectra, the type of ordering FC has a critical influence on the form and position of the band gap. To identify patterns of change in the position of the band gap, were calculated transmission and reflection spectra of FC with a fixed period when the diameter of the holes of the photonic crystal. By increasing the diameter of the hole position of PBG for both types of ordering is shifted to shorter wavelengths. In addition, the width increases and the PBG.

Investigation of the transmission spectra of photonic-crystal structures containing a straight waveguide, showed that the presence of the structure of the waveguide does not significantly modify the transmittance in the entire range, except for the 15 corresponding to the boundary of the PBG (Fig. 5). The inclusion of a waveguide in the photonic-crystal structure leads to a reduction of losses in this area more than 1.5 times. For the FC-type structures with hexagonal ordering of the numerical simulation of the spectral parameters did not show significant effect on transmission in the presence of the waveguide structure, which is consistent with the data presented in Fig. 1.

For experimental verification of the method of calculation model focused ion beam etching were fabricated photonic-crystal structure with a square order, and the period of the structure of 450 nm and 290 nm diameter holes (inset in Fig. 6). The size of the structure was 25×25 mm. FC structures were based on single-crystal wafer of gallium arsenide width of 70 microns. The effective thickness of the structure (depth of hole) was 2 mm. In addition, in the FC structures were etched technological holes that allow to draw waveguides to ensure that the input light into the structure and read the transmitted radiation, close to the photonic-crystal structure.

As a radiation source tunable laser with 1500–1600 nm. Input radiation in photonic-crystal waveguide is carried out using a modified optical fiber with a diameter of the outlet of the order of 1 mm. The use of such fibers are allowed to provide the most accurate positioning of the input fiber relative to FC-waveguide, thus reducing the loss of intensity when you enter into the structure.

To evaluate the efficiency of transmission system, where the input and output waveguides used modified, was used to measure the intensity of the radiation receiver taken, the distance between the waveguides. The measurements were performed in air, in the wavelength range 1500–1600 nm. It was shown that with increasing distance between the waveguides is modified from 0 to 30 micron radiation losses increase more than 1.3 times. Thus, the use of a modified fiber as the receiver (output) is inappropriate. To receive radiation was used a standard optical fiber is Corning SMF-28 10/125 diameter of 125 microns, ensuring minimal loss of radiation at the reception.

The sample input and output fibers were attached to the multikoordinatnyh independent platforms that provide linear movement increments of less than 1 micron. The combination of fiber and the sample was carried out using an optical microscope with a magnification of 200 times.

The size of the waveguide core, which receives the optical signal is equal to 10 microns. In this

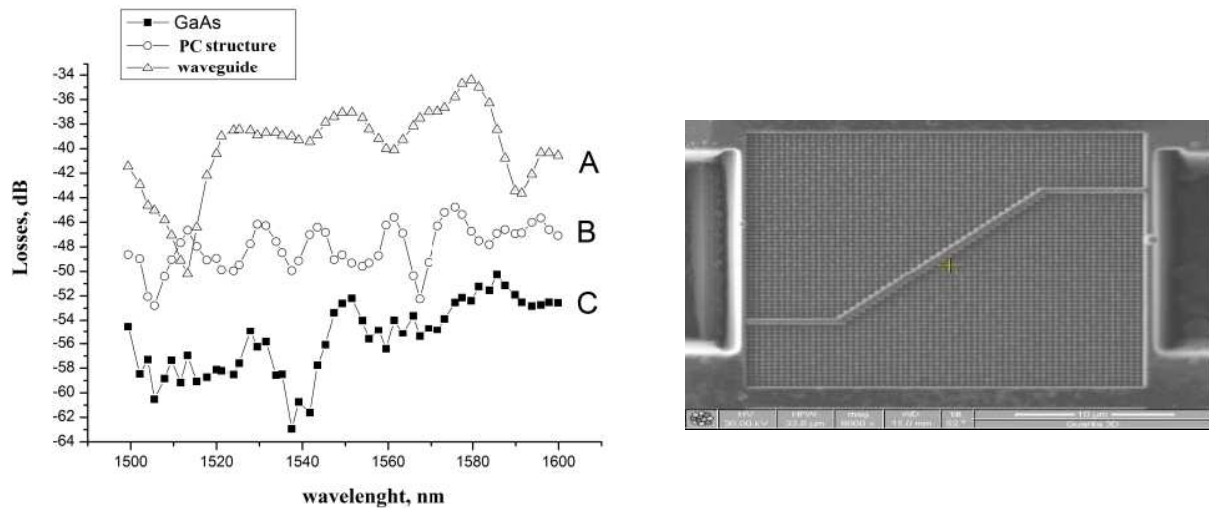


Figure 6: Investigation of waveguide transmission FK-type structure with a square ordering. The inset — the image of the structure obtained by electron microscopy. The size of the structure of 25×25 mm, period 450 nm, 290 nm diameter holes.

configuration, we measured the loss of radiation with a wavelength in the range 1500–1600 nm, while passing through the structure in three areas: in the FC-waveguide (A) photonic crystal (B) and in “pure” GaAs material away from the FC structure (C) (Fig. 6). It is shown that radiation losses in photonic-crystal waveguide is much lower than in the field of photonic crystal and, moreover, a single crystal GaAs.

3. CONCLUSIONS

Thus, the FIT method were analyzed by the spectral properties of photonic-crystal structures containing a waveguide with hexagonal and square ordering. As shown, the properties of structures with the given parameters of FC essentially depend on the type of ordering. One of the main causes significant losses of the radiation range of telecommunications in these structures may serve as a multimode photonic-crystal waveguide.

REFERENCES

1. Yee, K., “Numerical solution of initial boundary value problems involving Maxwell’s equations in isotropic media,” *IEEE Transactions on Antennas and Propagation*, Vol. 14, 302–307.
2. Clemens, M. and T. Weiland, “Discrete electromagnetism with the finite integration technique,” *Progress In Electromagnetics Research*, Vol. 32, 65–87, 2001.
3. Fan, S. H., S. G. Johnson, J. D. Joannopoulos, et al., “Waveguide branches in photonic crystals,” *J. Opt. Sci. Am. B*, Vol. 18, 162–165, 2001.
4. Zhou, Z. Y., X. Y. Huang, R. Vanga, and R. Li, “Tunable photonic crystals based on ferroelectric and ferromagnetic materials by focused ion beam,” *Chinese Optics Letters*, Vol. 5, No. 12, 693, 2007.
5. Mingaleev, S. F., M. Schillinger, D. Hermann, and K. Busch, “Tunable photonic crystal circuits: Concepts and designs based on single-pore infiltration,” *Optics Letters*, Vol. 29, No. 24, 2858–2860, 2004.
6. Palik, E. D., *Handbook of Optical Constants of Solids*, Academic Press, Inc., Orlando, Florida, 1985.

Novel Bow-tie Bandpass Filter Design Using Multiple Radial Stubs

Z. Y. Fu, K. M. Lum, and W. T. Koh

School of Science and Technology, SIM University, Singapore

Abstract— A novel bow-tie bandpass filter (BPF) design using multiple radial stubs is presented in this paper. The proposed topology consists of seven radial stubs arranged in periodic angular orientation, a L-shape microstrip line and a pair of U-shape coupling arms. The centre frequency of the proposed BPF is 2.8 GHz. A pair of radial stubs with arc size of 20° and 35° respectively is introduced. Three identical pairs of radial stub are positioned at 45 degrees interval, diagonally on the exterior vicinity of the right-angle bend of the L-shape microstrip line. A single radial stub is integrated within the interior vicinity right-angle bend. It should be noted that the seven radial stubs are open-ended. $50\ \Omega$ input and output ports are placed at the centre of the U-shape coupling arm, namely coupling arm 1 and 2 respectively. The radial stub provides low impedance and it is physically shorter compare with the equivalent transmission line. In addition, radial stub gives a wider bandwidth response in comparison with the corresponding quarter-wave transmission line. Hence, by implementing the proposed BPF using multiple pairs of radial stubs, it allows wider bandwidth to be achieved. The proposed BPF is fabricated on a single layer FR4 substrate with relative permittivity of 4.7, loss tangent of 0.027 and a thickness of 1.6 mm. Overall dimension of the prototyped BPF is 37 mm by 37 mm. The best matched measured return loss S_{11} is obtained at 2.78 GHz with value less than -30 dB. The passband insertion loss S_{21} is approximately -1 dB and the stopband lower and upper attenuation rate are greater than 40 dB/GHz and 20 dB/GHz respectively. The simulation and measurement results are presented and discussed.

1. INTRODUCTION

Bandpass filters are widely being implemented in many wireless application, where only a particular band of frequency that is required to filtered out from a range of mixed signals. In many modern microwave communication system microstrip bandpass filters is required as it will further improved the performance for in-of-band responses, out-of-band responses, reduced in size of filter, high in rejection and low in insertion losses.

Filter is fabricated and designed base on the most common standard printed circuit technologies in order to keep the manufacturing cost of the filter low. The filter should design to target on reduction in the size of the filter and improve on the filter performance. Many had studied to improve and enhance on the performance using different kind of filter [1–6]. Filters using stub-loaded structure have a good selectivity for transmission zero that is close to the passband. Hence radial stub is being implemented in this proposed bandpass filter design. The proposed configuration seems particularly suitable for integration with multilayer transceiver antenna modules [7–11] and localization applications [12–16].

2. BANDPASS FILTER DESIGN AND CONCEPT

The filter design topology as shown in Fig. 1 is arranged on the top conductor layer laid on a FR4 dielectric substrate. A $50\ \Omega$ microstrip feedline is connected to the coupling arm 1 and 2 where coupling arm 1 is the input and coupling arm 2 is the output. It is detailed in [17] that radial angles greater than 180° have the disadvantage of requiring section of transmission line to access the radial stub, and the advantage of greater bandwidth. From Gianni [18], it reported measurement data comparing 180° stubs to three 60° stubs. The three 60° stubs configuration yielded approximately 20% wider bandwidth. Hence, in this paper, a BPF using multiple radial stubs is presented as radial stub is used widely as it gives a wider bandwidth compare to an open stub quarter wave resonator. The specification of the proposed 2.8 GHz BPF is being presented in Table 1. The key dimensional data of the filter are shown in Fig. 2.

3. SIMULATION AND MEASUREMENT RESULT

The simulated insertion loss S_{21} response is shown below in Fig. 3. It is observed that by reducing the length of L_3 as shown in Fig. 2, a broader passband bandwidth at -10 dB is presented. Hence, a L_3 value of 10.7 mm is selected to be used in the proposed BPF design.

Table 1: Design specification of proposed bandpass filter.

Key Parameters	Values
Centre Frequency	2.8 GHz
Return Loss, S_{11}	< -10 dB
Insertion Loss, S_{21}	> -2 dB
Passband Bandwidth at -10 dB	500 MHz
Stopband Rejection	> 20 dB

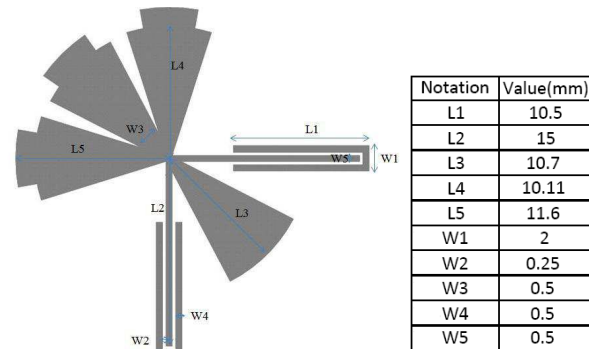
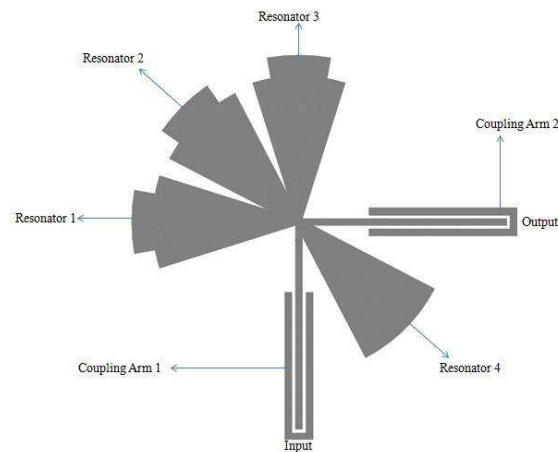


Figure 1: Design topology of proposed bandpass filter.

Figure 2: Key dimensional data of proposed bandpass filter.

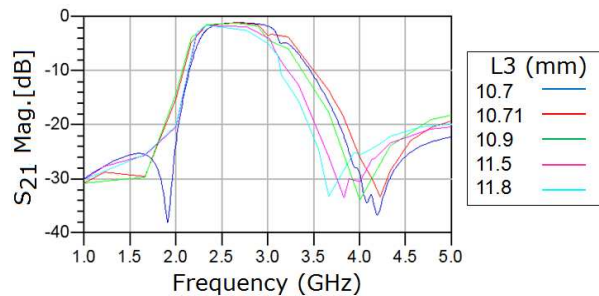


Figure 3: Simulated S_{21} response of proposed bandpass filter using various lengths of L_3 .

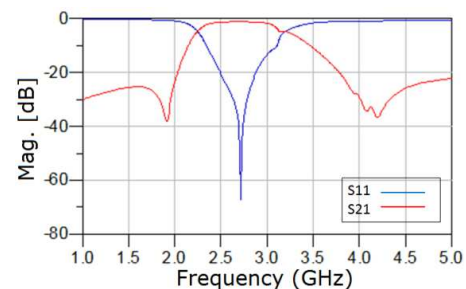


Figure 4: Simulated S_{11} and S_{21} response of proposed bandpass filter using 10.7 mm for L_3 .

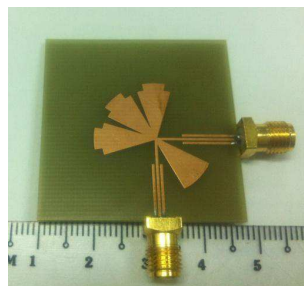


Figure 5: Photos of fabricated proposed bandpass filter.

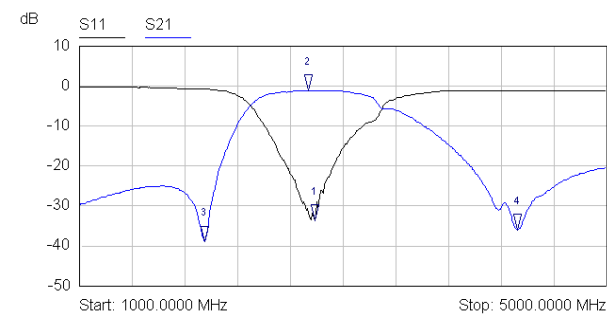


Figure 6: Measured S_{11} and S_{21} response of proposed bandpass filter.

As shown in Fig. 4, the best matched simulated return loss S_{11} is observed at 2.7 GHz with a value less than -60 dB. The insertion loss S_{21} at 2.7 GHz is greater than -1 dB with a -10 dB bandwidth of 1.3 GHz. The stopband attenuation is more than 30 dB.

Table 2: Comparison of simulated and measured result.

Key Parameters	Simulation Results	Measurement Results
Center Frequency (GHz)	2.7	2.78
Return Loss, S_{11} (dB)	-67.15	-33.8
Insertion Loss, S_{21} (dB)	-1.17	-1.21
Passband Bandwidth at -10 dB (GHz)	1.3	1.4
Stopband Rejection (dB)	> 30	> 30

The proposed BPF design was prototyped using FR4 dielectric substrate which has a dielectric constant of 4.7, loss tangent of 0.027 and a thickness of 1.6 mm. Fig. 5 presents the fabricated BPF. Measurement is done using network analyzer and the measured S_{11} and S_{21} response are shown in Fig. 6.

The best measured return loss S_{11} is obtained at 2.78 GHz with a value less than -30 dB and the insertion loss S_{21} is approximately -1.2 dB. The stopband rejection is greater than 30 dB and the -10 dB passband bandwidth is 1.4 GHz. Comparison between the simulated and measured result is presented in Table 2. It is clearly evident that the simulated and measured response presents reasonably good agreement.

4. CONCLUSION

A unique bow-tie radial stub bandpass filter design is proposed in this paper. By using the radial stubs, a wide passband response can be easily achieved. The proposed BPF is validated through simulation and practical measurement and can be employed for high data rate digital signalling application such as mobile broadband, metropolitan area network (MAN), mobile phone and image rejection filtering.

REFERENCES

- Hong, J.-S. and M. J. Lancaster, *Microstrip Filters for RF/Microwave Applications*, John Wiley & Sons, Inc., 2001.
- Wong, C. Y. and K. M. Lum, "Miniaturized multilayered bandpass filter using microstrip hairpin resonator for C-band application," *PIERS Proceedings*, 602–605, Kuala Lumpur, Malaysia, Mar. 27–30, 2012.
- Lim, P. L. and K. M. Lum, "A novel bandpass filter design using E-shaped resonator and dual square-loop defected ground structure," *PIERS Proceedings*, 610–614, Kuala Lumpur, Malaysia, Mar. 27–30, 2012.
- Lim, Y. T. and K. M. Lum, "A stepped impedance comb-line filter design using defective ground structure for wireless applications," *PIERS Proceedings*, 598–601, Kuala Lumpur, Malaysia, Mar. 27–30, 2012.
- Lee, M. L. and K. M. Lum, "Multilayered miniaturized hairpin resonator for bandpass filter design," *PIERS Proceedings*, 593–597, Kuala Lumpur, Malaysia, Mar. 27–30, 2012.
- Lek, K. C. and K. M. Lum, "Stepped impedance key-shaped resonator for bandpass and bandstop filters design," *PIERS Proceedings*, 588–592, Kuala Lumpur, Malaysia, Mar. 27–30, 2012.
- Lum, K. M., "A novel radiation enhancement technique for multilayer microwave circuits," *PIERS Proceedings*, 578–582, Kuala Lumpur, Malaysia, Mar. 27–30, 2012.
- Lum, K. M., C. Laohapensaeng, and C. E. Free, "A novel traveling-wave feed technique for circularly polarized planar antennas," *IEEE Micro. and Wireless Components Letters*, Vol. 15, No. 3, 180–182, Mar. 2005.
- Lum, K. M., T. Tick, C. Free, and H. Jantunen, "Design and measurement data for a microwave CP antenna using a new travelling-wave feed concept," *European Microwave Conf.*, Paris, France, Oct. 2005.
- Lum, K. M. and C. Free, "A novel traveling-wave feed technique for circularly polarized planar microstrip antennas," *IEEE Antennas and Propag. International Symposium*, Vol. 2A, 250–253, Oct. 2005.

11. Lum, K. M. and C. E. Free, “A novel dual circularly polarized planar and multi-layer LTCC antenna arrays using traveling-wave feed system,” *IEEE Trans. Micro. Theory Tech.*, Vol. 54, No. 6, 2880–2886, Jun. 2006.
12. Seow, C. K. and S. Y. Tan, “Localisation of mobile device in multipath environment using bi-directional estimation,” *Electronics Letters*, Vol. 44, No. 7, 485–487, Mar. 2008.
13. Seow, C. K. and S. Y. Tan, “Non-line-of-sight unidirectional mobile localisation in multipath environment,” *Electronics Letters*, Vol. 44, No. 2, 141–142, Jan. 2008.
14. Tai, C. S., S. Y. Tan, and C. K. Seow, “Robust non-line-of-sight localisation system in indoor environment,” *Electronics Letters*, Vol. 46, No. 8, 593–595, Apr. 2010.
15. Seow, C. K. and S. Y. Tan, “Localization of omni-directional mobile device in multipath environments,” *Progress In Electromagnetics Research*, Vol. 85, 323–348, 2008.
16. Seow, C. K. and S. Y. Tan, “Non-line-of-sight localization in multipath environments,” *IEEE Transactions on Mobile Computing*, Vol. 7, No. 5, 647–660, May 2008.
17. Wadell, B. C., *Transmission Line Design Handbook*, Artech House, Inc., 1991.
18. Giannini, F., et al., “A very broadband matched termination utilizing non grounded radial line,” *17th European Microwave Conference Proceedings*, 1027–1031, 1987.

Ultra-wideband Bandpass Filter Using Symmetrical Step-impedance Resonators

C. G. Tan and K. M. Lum

School of Science and Technology, SIM University, Singapore

Abstract— This paper presents a compact ultra-wideband (UWB) bandpass filter (BPF) using symmetrical step-impedance resonators (SSIR). The operating frequency range is chosen to fall within the lower UWB spectrum of 3.1 GHz to 5 GHz. The passband has a centre frequency is 4 GHz. The proposed BPF generates a single passband located at the desired frequency through a single filter circuitry. The highly selective passband effect is obtained by the step-impedance resonators configuration in a similar topology as the classical comb filter. The proposed step-impedance topology consists of several microstrip sections: a main $50\ \Omega$ T-shape transmission line and a fork-shape SSIR cascaded with a shunt stub. A ring resonator with an inner circular aperture is further integrated at the end terminate of the two shunt stubs. Within the step-impedance configuration, the topology and position of the fork-shape SSIR is critically important in achieving the desired passband response. The proposed compact ultra-wideband bandpass filter is prototyped using FR4 substrate with a dielectric constant of 4.7, thickness of 1.6 mm, and loss tangent of 0.027. The fabricated structure has a miniature dimensional size of 35 mm by 39 mm. The best matched return loss S_{11} is observed at 4.22 GHz with value less than -20 dB. The passband insertion loss S_{21} is greater than -1.5 dB. Attenuation is greater than 14 dB for the lower and upper stopband respectively. The passband bandwidth is around 1.1 GHz at -10 dB level. The measured filter response showed good agreement with the simulation results. Both simulation and measurement data are presented and discussed.

1. INTRODUCTION

Since the release of ultra-wideband (UWB) in 2002 by Federal Communications Commission (FCC) for communication applications [1], remarkable research interests in the analysis and design of various UWB devices have been investigated. Planar transmission structures such as microstrip line are widely used due to its low cost, low loss, compact size, and ease of implementation. Therefore, microstrip is commonly used to design UWB filter.

Different type of filter configurations such as hairpin resonator, step-impedance resonator (SIR), ring resonator, short & open circuit stub have been analyzed in the past [2–6]. The ring resonator has the key benefit of almost free radiation loss, and structural ability to elimination of parasitic components which are normally induced at the open and short circuited of the resonator. SIR has been found advantageous in designing microstrip bandpass filter. One of the key attribute is that it allows its resonant frequencies to be tuned by adjusting its structural parameters. In this paper, an UWB BPF using SIR is presented with bandwidth of focus at lower UWB region of interest from 3.1 GHz to 5 GHz. The proposed configuration is suitable for integration with multilayer transceiver antenna modules [7–11] and localization applications [12–16].

2. ULTRA-WIDEBAND BANDPASS FILTER DESIGN

Table 1 presents the design specification of the proposed BPF. As shown in Fig. 1, the proposed BPF includes a main $50\ \Omega$ T-shape transmission line and a fork-shape SSIR cascaded with a shunt stub. A ring resonator with an inner circular aperture is further integrated at the end terminate of the two shunt stubs. Within the step-impedance configuration, the topology and position of

Table 1: Design specifications of proposed BPF.

Parameter	Value
Centre Frequency	4 GHz
Passband Bandwidth, $f_{-10\text{ dB}}$	> 1 GHz
Return Loss, S_{11}	< -20 dB
Insertion Loss, S_{21}	> -1 dB
Stopband Attenuation (L_{AS})	> 10 dB

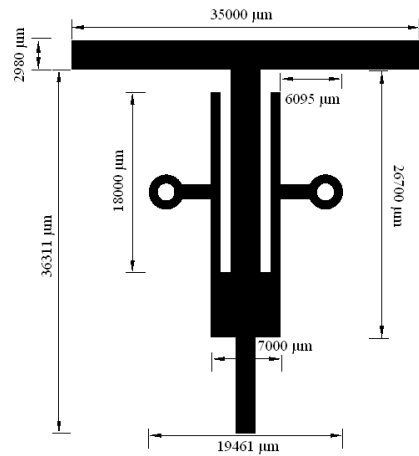
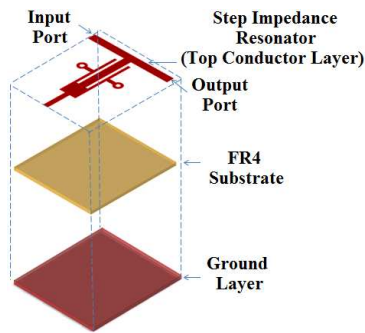


Figure 1: Design configuration of proposed BPF.

Figure 2: Key dimensional data of proposed BPF.

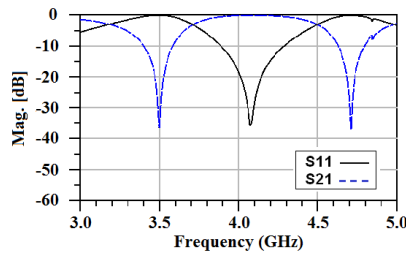


Figure 3: Simulated S_{11} and S_{21} response of proposed BPF.

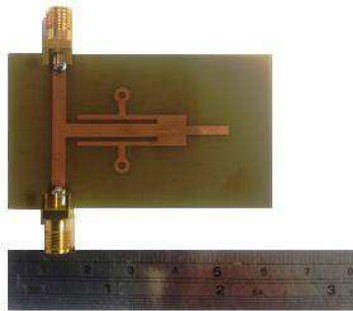


Figure 4: Photograph of fabricated proposed BPF.

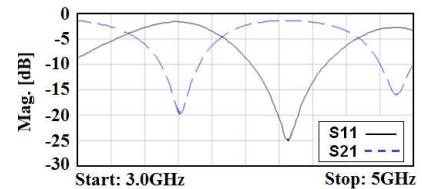


Figure 5: Measured S_{11} and S_{21} response of proposed BPF.

Table 2: Comparison of simulation and measurement response of proposed BPF.

Parameter	Simulated Results	Measured Results
Centre Frequency (GHz)	4.06	4.22
Return Loss, S_{11} (dB)	-35	-25
Passband Insertion Loss, S_{21} (dB)	-0.08	-1.3
Passband Bandwidth at -10 dB Level (GHz)	0.95	1.1
Stopband Attenuation (dB)	> 30	> 14

the fork-shape SSIR is critically important in achieving the desired passband response. Fig. 2 illustrated the key dimensional data of the proposed BPF.

3. SIMULATED AND MEASURED RESULTS OF BANDPASS FILTER

The simulated filter response of the proposed BPF is shown in Fig. 3. The best matched return loss S_{11} is obtained at 4.06 GHz with a value of -35 dB. The corresponding passband insertion loss S_{21} is around -0.08 dB with a -10 dB bandwidth of approximately 950 MHz. The lower and upper stopband rejection is greater than 30 dB respectively.

The fabricated BPF is shown in Fig. 4. The overall dimensional size is 35 mm by 39 mm. Measurement is done using Network Analyzer. As depicted in Fig. 5, the best matched return loss S_{11} is obtained at 4.22 GHz with a value of -25 dB. The measured insertion loss S_{21} is around -1.3 dB and the passband bandwidth at -10 dB level is approximately 1.1 GHz. The lower and upper stopband rejection is greater than 14 dB.

4. CONCLUSION

In this paper, a new BPF with step-impedance resonator was proposed. Simulation and measurement results have shown reasonably good matching return loss S_{11} at values below -20 dB, and passband insertion loss, S_{21} above -1.52 dB. Broad passband bandwidth at -10 dB level is also obtained. The proposed filter can be used for multilayer ultra-wideband transceiver systems.

REFERENCES

1. Federal Communications Commission, "Revision of Part 15 of the commission's rules regarding ultra-wideband transmission systems," Tech. Report, ET-Docket 98-153, FCC02-48, Apr. 2002.
2. Lek, K. C. and K. M. Lum, "Stepped impedance key-shaped resonator for bandpass and bandstop filters design," *PIERS Proceedings*, 588–592, Kuala Lumpur, Malaysia, Mar. 27–30, 2012.
3. Lee, M. L. and K. M. Lum, "Multilayered miniaturized hairpin resonator for bandpass filter design," *PIERS Proceedings*, 593–597, Kuala Lumpur, Malaysia, Mar. 27–30, 2012.
4. Lim, Y. T. and K. M. Lum, "A stepped impedance comb-line filter design using defective ground structure for wireless applications," *PIERS Proceedings*, 598–601, Kuala Lumpur, Malaysia, Mar. 27–30, 2012.
5. Lim, P. L. and K. M. Lum, "A novel bandpass filter design using E-shaped resonator and dual square-loop defected ground structure," *PIERS Proceedings*, 610–614, Kuala Lumpur, Malaysia, Mar. 27–30, 2012.
6. Wong, C. Y. and K. M. Lum, "Miniaturized multilayered bandpass filter using microstrip hairpin resonator for C-band application," *PIERS Proceedings*, 602–605, Kuala Lumpur, Malaysia, Mar. 27–30, 2012.
7. Lum, K. M., "A novel radiation enhancement technique for multilayer microwave circuits," *PIERS Proceedings*, 578–582, Kuala Lumpur, Malaysia, Mar. 27–30, 2012.
8. Lum, K. M., C. Laohapensaeng, and C. E. Free, "A novel traveling-wave feed technique for circularly polarized planar antennas," *IEEE Micro. and Wireless Components Letters*, Vol. 15, No. 3, 180–182, Mar. 2005.
9. Lum, K. M., T. Tick, C. Free, and H. Jantunen, "Design and measurement data for a microwave CP antenna using a new travelling-wave feed concept," *European Microwave Conf.*, Paris, France, Oct. 2005.
10. Lum, K. M. and C. Free, "A novel traveling-wave feed technique for circularly polarized planar microstrip antennas," *IEEE Antennas and Propag. International Symposium*, Vol. 2A, 250–253, Oct. 2005.
11. Lum, K. M. and C. E. Free, "A novel dual circularly polarized planar and multi-layer LTCC antenna arrays using traveling-wave feed system," *IEEE Trans. Micro. Theory Tech.*, Vol. 54, No. 6, 2880–2886, Jun. 2006.
12. Tai, C. S., S. Y. Tan, and C. K. Seow, "Robust non-line-of-sight localisation system in indoor environment," *Electronics Letters*, Vol. 46, No. 8, 593–595, Apr. 2010.
13. Seow, C. K. and S. Y. Tan, "Non-line-of-sight localization in multipath environments," *IEEE Transactions on Mobile Computing*, Vol. 7, No. 5, 647–660, May 2008.
14. Seow, C. K. and S. Y. Tan, "Non-line-of-sight unidirectional mobile localisation in multipath environment," *Electronics Letters*, Vol. 44, No. 2, 141–142, Jan. 2008.
15. Seow, C. K. and S. Y. Tan, "Localization of omni-directional mobile device in multipath environments," *Progress In Electromagnetics Research*, Vol. 85, 323–348, 2008.
16. Seow, C. K. and S. Y. Tan, "Localisation of mobile device in multipath environment using bi-directional estimation," *Electronics Letters*, Vol. 44, No. 7, 485–487, Mar. 2008.

Dual-band Bandpass Filter Design Using Stub-loaded Resonators

W. T. Koh and K. M. Lum

School of Science and Technology, SIM University, Singapore

Abstract— A novel dual-band bandpass filter (BPF) using stub-loaded resonators (SLR) is presented. The proposed filter consists of a pair of independent open-ended square loops arranged in an adjacent manner with each other. Thus, allowing electromagnetic coupling configuration to be established. In addition, an open-ended microstrip stub is integrated into each respective square loop to achieve the dual-band characteristics at 2 GHz and 4 GHz. The resonant frequencies of the even-mode can be flexibly controlled by tuning the length of the open-ended stub whilst the odd-mode resonant frequencies stay constant. Two microstrip transmission lines with $50\ \Omega$ characteristic impedance act as the input and output feedlines respectively. The proposed dual-band BPF is implemented on a FR4 substrate with dielectric constant of 4.6, loss tangent of 0.027 and thickness of 1.6 mm. It has an overall dimensional size of 53.5 mm by 32.1 mm. The best measured matching return loss S_{11} for the first passband is observed at 2.21 GHz with a value less than -10 dB. The corresponding passband response S_{21} is approximately -1.76 dB with an upper and lower stopband attenuation of more than 20 dB/GHz. Additionally, the best measured matching return loss S_{11} for the second passband is observed at 3.81 GHz with a value less than -10 dB. The corresponding passband response S_{21} is approximately -2.88 dB with a lower and upper stopband rejection rate of more than 10 dB/GHz and 30 dB/GHz respectively. It is also observed that three transmission zeros with more than 30 dB attenuation are realized. Both simulation and measurement results are presented and discussed.

1. INTRODUCTION

Filters play an important role in many radio frequency and microwave applications. As wireless applications increase in popularity in recent years, dual-band filters have become key components at the front end of modern communication systems. A bandpass filter allows signals of frequencies within a certain range and rejects (attenuates) unwanted signals outside that range. As proposed previously [1], a dual-band bandpass filter (BPF) was achieved by combining two bandpass filters designed for two different passband, with the drawback of a large circuit area twice that of a single-band filter and additional combining networks. Thus, an integrated filter with dual-band response is desired. A dual-band filter can be realized by using a stepped-impedance resonator (SIR) [2–6].

A dual-band bandpass microstrip filter using stub-loaded resonator (SLR) is presented in this paper. The concept of the proposed dual-band filter are discussed and analyzed. In order to establish the validity of the proposed technique, a prototype filter was fabricated and tested. Data are presented that compare the measured and simulated performance of this filter. The proposed configuration seems particularly suitable for integration with multilayer transceiver antenna modules [7–11] and localization applications [12–16].

2. DUAL-BAND BANDPASS FILTER DESIGN AND CONCEPT

Design specifications of the proposed dual-band BPF are highlighted in Table 1 and the layout is presented in Fig. 1. The dual-band BPF consists of a pair of independent open-ended square loops arranged in an adjacent manner with each other. Thus, allowing electromagnetic coupling configuration to be established. In addition, an open-ended microstrip stub is integrated into each respective square loop to achieve the dual-band characteristics at 2 GHz and 4 GHz. Two microstrip transmission lines with $50\ \Omega$ characteristic impedance are fed to the proposed dual-band BPF to act as the input and output feedlines respectively.

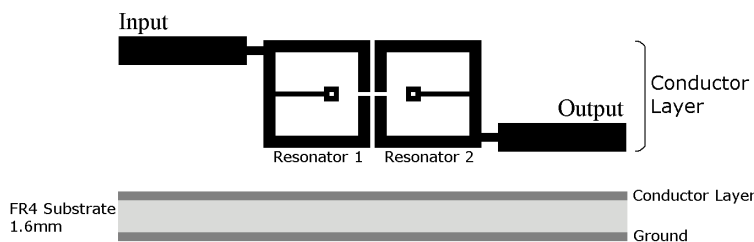


Figure 1: Design configuration of proposed dual-band bandpass filter.

Table 1: Design specifications of dual-band bandpass filter.

Parameter	Value
Centre Frequency 1, f_1	2 GHz
Centre Frequency 2, f_2	4 GHz
Return Loss, S_{11}	< -10 dB
Passband Insertion Loss, S_{21}	> -3 dB
Passband Bandwidth at -10 dB	500 MHz
Stopband attenuation	> 30 dB

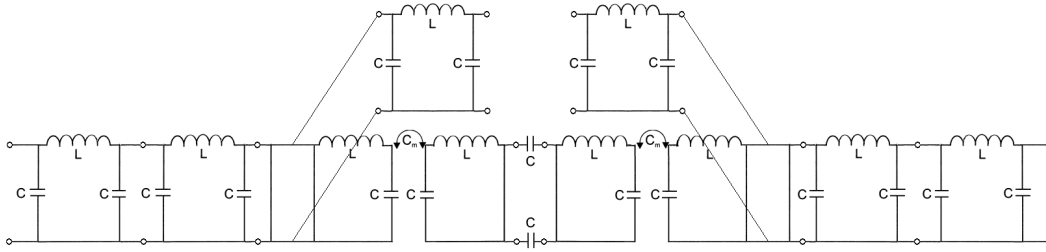


Figure 2: Equivalent circuit of proposed dual-band bandpass filter.

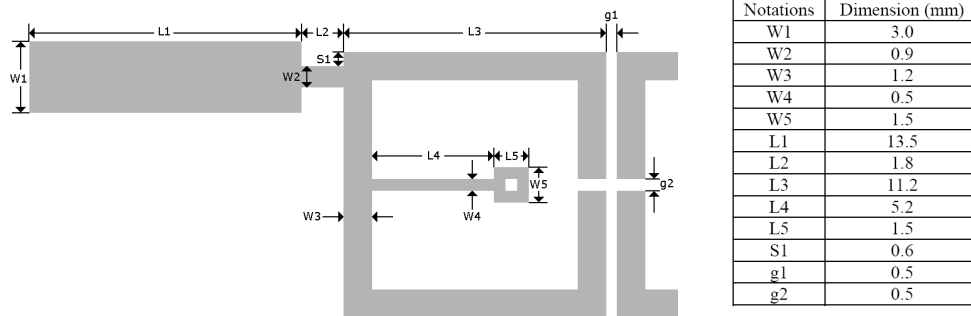


Figure 3: Key dimensional data of stub-loaded resonator.

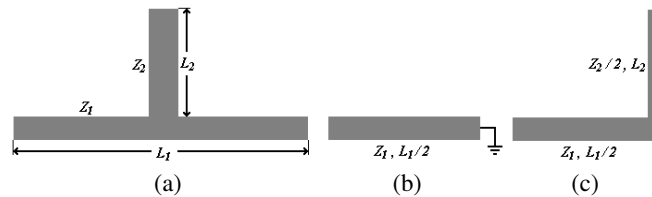


Figure 4: (a) Structure of proposed SLR, (b) odd-mode equivalent circuit, and (c) even-mode equivalent circuit.

Figure 2 illustrates the equivalent circuit of proposed dual-band bandpass filter and Fig. 3 detailed the dimensional data of the stub-loaded resonator. The following section will detail the concept of the stub-loaded resonators (SLR).

A half-wavelength microstrip resonator is shown in Fig. 4(a). Z_1 , L_1 , Z_2 and L_2 denote the characteristic impedances and lengths of the resonator and open stub, respectively. As the SLR is symmetrical in structure, odd- and even-mode analysis can be adopted.

For odd-mode resonance of the SLR, the horizontal plane behaves as an electric wall which there is a voltage null along the middle of the SLR. The equivalent circuit is shown in Fig. 4(b). The odd-mode resonant frequencies can be expressed as

$$f_{odd} = \frac{(2n-1)c}{2L_1\sqrt{\varepsilon_{eff}}} \quad (1)$$

where $n = 1, 2, 3, \dots$, c is the speed of light in free space, and ε_{eff} denotes the effective dielectric constant of the substrate. It can be observed that the odd-mode resonant frequencies of the SLR

are not affected by the loaded stub. For the even-mode resonance of the SLR, the horizontal plane behaves as a magnetic wall which there is no current flow. The equivalent circuit is shown in Fig. 4(c). The even-mode resonant frequencies can be expressed as

$$f_{\text{even}} = \frac{nc}{(L_1 + 2L_2)\sqrt{\epsilon_{\text{eff}}}} \quad (2)$$

where $n = 1, 2, 3, \dots$. It can be observed that the even-mode resonant frequencies can be controlled by varying the length L_2 of the added stub. In order to validate the theoretical principles presented above, full-wave simulations are carried out. The length L_1 is 40 mm with stub length $L_2 = 2.7$ mm, 3.7 mm, 4.7 mm, 5.7 mm and 6.7 mm, respectively. As shown in Fig. 5, varying the length L_2 results in a shift in the even-mode resonant frequency while the odd-mode resonant frequency stays constant.

3. SIMULATION AND MEASUREMENT RESULT

Figure 6 illustrates the simulated result of the proposed dual-band BPF. The best matching responses are observed at 2.17 GHz and 3.69 GHz with a return loss S_{11} value of less than -10 dB. The corresponding passband insertion losses S_{21} are approximately -2.1 dB and -3.2 dB for the first and second passband respectively. The -10 dB bandwidth of both passband are 530 MHz and 600 MHz respectively. A FR4 substrate with dielectric constant of 4.7 and a thickness of 1.6 mm was used to prototype the proposed dual-band BPF. Fig. 7 shows the fabricated dual-band BPF.

Measurements are taken using network analyzer. The measured results are shown in Fig. 8. The best matching responses are observed at 2.21 GHz and 3.81 GHz. The measured insertion losses of the first and second passband are -1.76 dB and -2.88 dB respectively with return losses of less than -10 dB. Three transmission zeros with more than -30 dB attenuations are observed. The

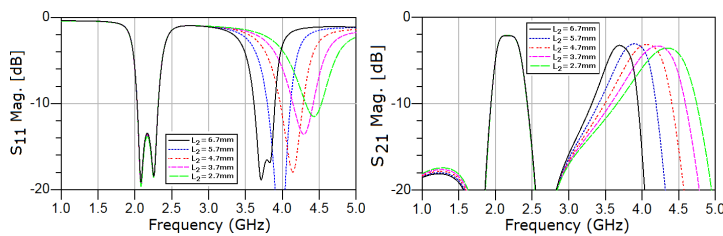


Figure 5: S_{11} and S_{21} response with respect to different stub length L_2 .

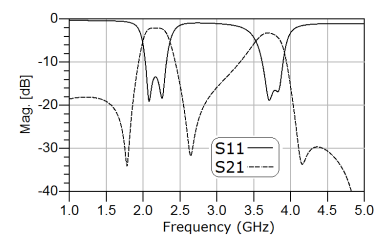


Figure 6: Simulated result of proposed dual-band bandpass filter.

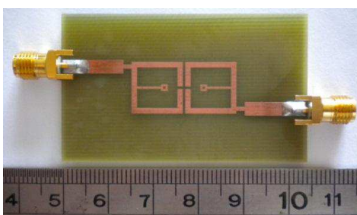


Figure 7: Fabricated dual-band bandpass filter.

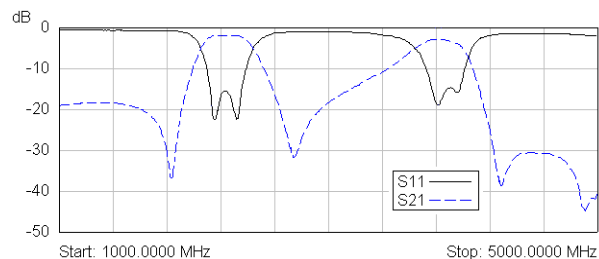


Figure 8: Measured result of proposed dual-band bandpass filter.

Table 2: Simulation and measurement results of proposed dual-band bandpass filter.

Parameter	Simulated results		Measured results	
	Passband 1	Passband 2	Passband 1	Passband 2
Centre Frequency (GHz)	2.17	3.69	2.21	3.81
Return Loss, S_{11} (dB)	-12.7	-16.3	-14.3	-13.2
Passband Insertion Loss, S_{21} (dB)	-2.1	-3.2	-1.76	-2.88
Stopband Attenuation (dB)	> 29	> 28	> 29	> 28
Passbands $BW_{-10\text{dB}}$ (MHz)	530	600	530	660

–10 dB bandwidth of both passband are 530 MHz and 660 MHz respectively. Table 2 detailed the simulation and measurement results.

4. CONCLUSION

In this paper, a dual-band bandpass microstrip filter using stub-loaded resonator (SLR) has been proposed and implemented. Good agreement is found between the simulated and measured responses. The best matched return loss is obtained at values below –10 dB with insertion loss above –3 dB. The stopband attenuation rate is greater than 20 dB with a –10 dB passband bandwidth of greater than 500 MHz. The proposed filter can be used for bluetooth headset and WiMAX applications.

REFERENCES

1. Tsai, L.-C. and C.-W. Huse, “Dual-band bandpass filters using equal length coupled-serial-shunted lines and Z-transform techniques,” *IEEE Trans. Microwave Theory Tech.*, Vol. 52, No. 4, 1111–1117, Apr. 2004.
2. Lek, K. C. and K. M. Lum, “Stepped Impedance key-shaped resonator for bandpass and bandstop filters design,” *PIERS Proceedings*, 588–592, Kuala Lumpur, Malaysia, Mar. 27–30, 2012.
3. Lee, M. L. and K. M. Lum, “Multilayered miniaturized hairpin resonator for bandpass filter design,” *PIERS Proceedings*, 593–597, Kuala Lumpur, Malaysia, Mar. 27–30, 2012.
4. Lim, Y. T. and K. M. Lum, “A stepped impedance comb-line filter design using defective ground structure for wireless applications,” *PIERS Proceedings*, 598–601, Kuala Lumpur, Malaysia, Mar. 27–30, 2012.
5. Lim, P. L. and K. M. Lum, “A novel bandpass filter design using E-shaped resonator and dual square-loop defected ground structure,” *PIERS Proceedings*, 610–614, Kuala Lumpur, Malaysia, Mar. 27–30, 2012.
6. Wong, C. Y. and K. M. Lum, “Miniaturized multilayered bandpass filter using microstrip hairpin resonator for C-band application,” *PIERS Proceedings*, 602–605, Kuala Lumpur, Malaysia, Mar. 27–30, 2012.
7. Lum, K. M., “A novel radiation enhancement technique for multilayer microwave circuits,” *PIERS Proceedings*, 578–582, Kuala Lumpur, Malaysia, Mar. 27–30, 2012.
8. Lum, K. M., C. Laohapensaeng, and C. E. Free, “A novel traveling-wave feed technique for circularly polarized planar antennas,” *IEEE Micro. and Wireless Components Letters*, Vol. 15, No. 3, 180–182, Mar. 2005.
9. Lum, K. M., T. Tick, C. Free, and H. Jantunen, “Design and measurement data for a microwave CP antenna using a new travelling-wave feed concept,” *European Microwave Conf.*, Paris, France, Oct. 2005.
10. Lum, K. M. and C. Free, “A novel traveling-wave feed technique for circularly polarized planar microstrip antennas,” *IEEE Antennas and Propag. International Symposium*, Vol. 2A, 250–253, Oct. 2005.
11. Lum, K. M. and C. E. Free, “A novel dual circularly polarized planar and multi-layer LTCC antenna arrays using traveling-wave feed system,” *IEEE Trans. Micro. Theory Tech.*, Vol. 54, No. 6, 2880–2886, Jun. 2006.
12. Seow, C. K. and S. Y. Tan, “Localisation of mobile device in multipath environment using bi-directional estimation,” *Electronics Letters*, Vol. 44, No. 7, 485–487, Mar. 2008.
13. Tai, C. S., S. Y. Tan, and C. K. Seow, “Robust non-line-of-sight localisation system in indoor environment,” *Electronics Letters*, Vol. 46, No. 8, 593–595, Apr. 2010.
14. Seow, C. K. and S. Y. Tan, “Non-line-of-sight unidirectional mobile localisation in multipath environment,” *Electronics Letters*, Vol. 44, No. 2, 141–142, Jan. 2008.
15. Seow, C. K. and S. Y. Tan, “Non-line-of-sight localization in multipath environments,” *IEEE Transactions on Mobile Computing*, Vol. 7, No. 5, 647–660, May 2008.
16. Seow, C. K. and S. Y. Tan, “Localization of omni-directional mobile device in multipath environments,” *Progress In Electromagnetics Research*, Vol. 85, 323–348, 2008.

Bandstop Filter Design Using Cascaded Step-impedance Resonators with Defected Ground Structure

L. F. Lim and K. M. Lum

School of Science and Technology, SIM University, Singapore

Abstract— This paper presents a bandstop filter (BSF) design with a centre frequency of 3 GHz using cascaded step-impedance resonator (CSIR) with defected ground structure (DGS). The proposed design consists of two single-plane conductor layers. The top conductor layer comprises six microstrips square-patch periodically cascaded in series with microstrip transmission lines, thus forming the cascaded step-impedance resonator structure. The input and output ports are terminated with $50\ \Omega$ characteristic impedance. The DGS is laid in the bottom conductor layer beneath the cascaded microstrip resonator. Integration of the DGS in the BSF design topology allows the flexibility in varying the characteristics response of the cascaded step-impedance resonator structure in the top conductor layer. Furthermore, it helps to eliminate unwanted harmonic frequencies and increases the effective permittivity which, eventually lead to the enhancement of the desire stopband filter response. It is to be noted that high accuracy of alignment for the CSIR and DGS structures laid in the top and bottom conductor layers are critically important in achieving the desired stopband response. The proposed BSF is prototyped using FR4 substrate with a relative permittivity of 4.6 and a thickness of $1600\ \mu\text{m}$. The overall dimension is 68 mm by 14.85 mm. The best measured return loss S_{11} is observed at 3.18 GHz with a value greater than $-3\ \text{dB}$ and the corresponding stopband insertion loss S_{21} is approximately $-15\ \text{dB}$. The lower and upper attenuation of the stopband response is greater than 10 dB. Both simulation data and measurement results are evaluated and discussed for the proposed BSF.

1. INTRODUCTION

Electromagnetic bandgap (EBG), derived from photonic bandgap (PBG) structure, has been accepted widely to perform microwave frequency experiments [1]. Its purpose is to reduce unwanted affected bands and harmonics so that it inhibits the propagation of electromagnetic waves at a particular frequency band in millimeter/micrometer [2]. In spite of the fact that EBG structure may not be able to prohibit the wave propagation perfectly, it does not have additional interference to propagate in the existing bandgap.

Similar to the PBG structure, defected ground structure (DGS) that etched a pattern in the ground plane, changes the characteristics of the transmission line controlled by the DGS layout topology. It also helps to eliminate the unwanted frequency rejection and enhance the performance. Numerous filter designs using SIR and DGS approaches have been proposed in the past [3–9]. In this paper, the proposed BSF design is configured using square patches resonators and spiral DGS design. The proposed configuration can be integrated with multilayer transceiver antenna modules [10–14] and localization applications [15–19].

2. BANDSTOP FILTER DESIGN AND CONCEPT

The proposed BSF design consists of two single-plane conductor layers. Fig. 1 presents the configuration of the proposed BSF design. The top conductor layer comprises the main microstrip line

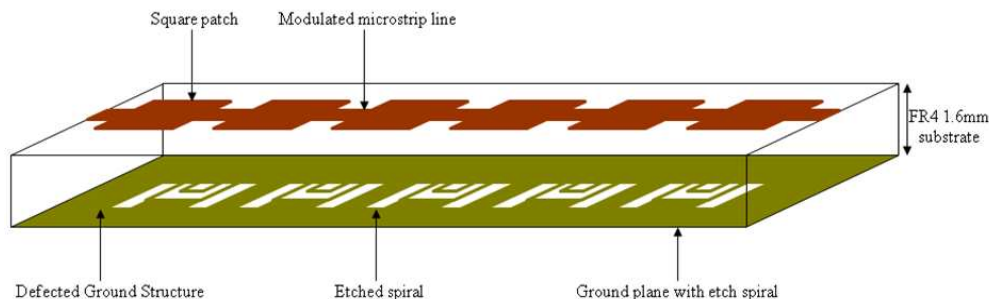


Figure 1: Configuration of proposed BSF design.

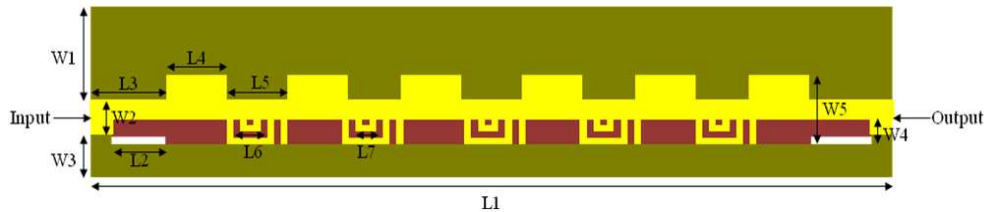
and an array of six microstrip square-patch periodically positioned. The spiral DGS is located on the bottom conductor layer. Design specifications of the BSF design is shown in Table 1.

Figures 2 and 3 present the key dimensional data and equivalent circuit of the proposed BSF design respectively.

3. SIMULATION AND MEASUREMENT RESULTS OF BANDSTOP FILTER

As shown in Fig. 4, the best matching simulated response is observed at 3.2 GHz with return loss S_{11} value greater than -1 dB. The corresponding stopband insertion loss S_{21} is approximately -26 dB. The lower and upper stopband attenuation is greater than 20 dB respectively. Stopband bandwidth at -10 dB level is 390 MHz. Fig. 5 presents the prototyped BSF design using FR4 substrate with relative permittivity of 4.6 and a thickness of $1600 \mu\text{m}$. The overall dimension is 68 mm by 14.85 mm.

Measurement is done using network analyzer. As presented in Fig. 6, the best measured return loss S_{11} is observed at 3.18 GHz with a value greater than -3 dB and the corresponding stopband insertion loss S_{21} is approximately -15 dB. The lower and upper attenuation of the stopband response is greater than 10 dB respectively. Stopband bandwidth at -10 dB level is 850 MHz. Comparison of the simulation and measurement results are shown in Table 2. Slight different in the results maybe attributed by the accuracy of the CSIR and DGS.



Notation	Dimension in μm	Notation	Dimension in μm
L1	68000	L7	2000
L2	5000	W1	8417
L3	6500	W2	2933
L4	5000	W3	3500
L5	5000	W4	1966
L6	3000	W5	5000

Figure 2: Dimensional data of proposed BSF design.

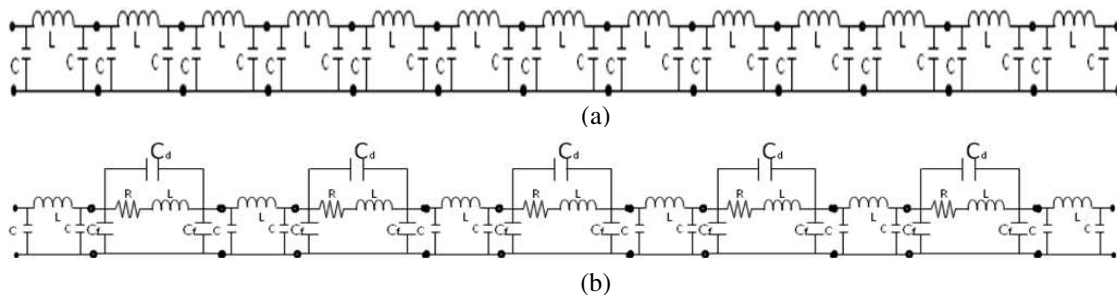


Figure 3: Equivalent circuit of BSF design (a) square patches, (b) spiral DGS.

Table 1: Design specifications of proposed bandstop filter.

Key Parameters	Values
Centre Frequency	3 GHz
Return loss, S_{11}	> -3 dB
Stopband Insertion loss, S_{21}	< -2 dB
Stopband Bandwidth at -10 dB	> 500 MHz
Stopband Attenuation	> 10 dB

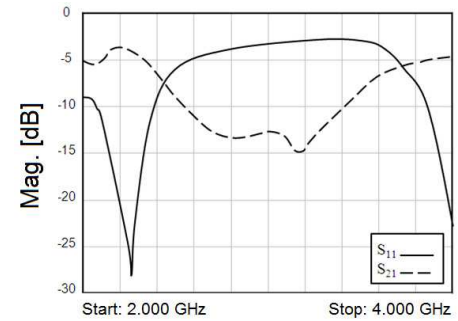
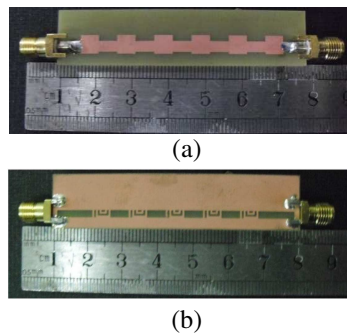
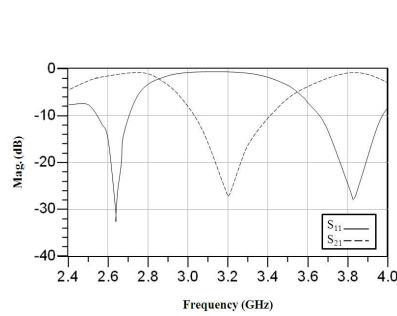


Figure 4: Simulated S_{11} and S_{21} response of proposed BSF design.

Figure 5: Fabricated BSF (a) top conductor layer, (b) bottom conductor layer.

Figure 6: Measured S_{11} and S_{21} response of proposed BSF design.

Table 2: Comparison of simulation and measurement results of proposed BSF design.

Parameter	Simulated Results	Measured Results
Centre Frequency (GHz)	3.2	3.18
Return Loss, S_{11} (dB)	> -1	> -3
Stopband Insertion loss, S_{21} (dB)	-26	-15
Stopband Bandwidth at -10 dB (MHz)	390	85
Lower and Upper Stopband attenuation (dB)	> 20	> 10

4. CONCLUSION

The concept of a new bandstop filter design using cascaded step-impedance resonators with defected ground structure had been verified via simulation and measured results. The measured results presented close resemble with the simulation results. The stopband rejection can be improved with better technique to obtain good alignment accuracy between the two conductor layers. The proposed filter can be used for WiMAX applications.

REFERENCES

1. Yablonovitch, E., "Photonic band-gap structures," *J. Opt. Amber. B. Opt. Phys.*, Vol. 10, 283–295, Feb. 1993.
2. Rahmat-Samii, Y. and H. Mosallaei, "Electromagnetic bandgap structures: Classification, characterization and applications," *Proc. 11th Int. Conf. Antennas and Propagation*, 560–564, Manchester, UK, Apr. 17–20, 2001.
3. Ng, K. X. and K. M. Lum, "Compact lowpass filter design using cavity resonator and ladder-shaped defected ground structure," *PIERS Proceedings*, 606–609, Kuala Lumpur, Malaysia, Mar. 27–30, 2012.
4. Lau, J. W. and K. M. Lum, "Novel M-shaped defected ground structure for spurious suppressed dual mode bandpass filter design," *PIERS Proceedings*, 583–587, Kuala Lumpur, Malaysia, Mar. 27–30, 2012.
5. Lim, Y. T. and K. M. Lum, "A stepped impedance comb-line filter design using defective ground structure for wireless applications," *PIERS Proceedings*, 598–601, Kuala Lumpur, Malaysia, Mar. 27–30, 2012.
6. Wong, C. Y. and K. M. Lum, "Miniaturized multilayered bandpass filter using microstrip hairpin resonator for C-band application," *PIERS Proceedings*, 602–605, Kuala Lumpur, Malaysia, Mar. 27–30, 2012.
7. Lek, K. C. and K. M. Lum, "Stepped impedance key-shaped resonator for bandpass and bandstop filters design," *PIERS Proceedings*, 588–592, Kuala Lumpur, Malaysia, Mar. 27–30, 2012.
8. Lim, P. L. and K. M. Lum, "A novel bandpass filter design using E-shaped resonator and dual square-loop defected ground structure," *PIERS Proceedings*, 610–614, Kuala Lumpur, Malaysia, Mar. 27–30, 2012.

9. Lee, M. L. and K. M. Lum, “Multilayered miniaturized hairpin resonator for bandpass filter design,” *PIERS Proceedings*, 593–597, Kuala Lumpur, Malaysia, Mar. 27–30, 2012.
10. Lum, K. M., “A novel radiation enhancement technique for multilayer microwave circuits,” *PIERS Proceedings*, 578–582, Kuala Lumpur, Malaysia, Mar. 27–30, 2012.
11. Lum, K. M. and C. Free, “A novel traveling-wave feed technique for circularly polarized planar microstrip antennas,” *IEEE Antennas and Propag. International Symposium*, Vol. 2A, 250–253, Oct. 2005.
12. Lum, K. M. and C. E. Free, “A novel dual circularly polarized planar and multi-layer LTCC antenna arrays using traveling-wave feed system,” *IEEE Trans. Micro. Theory Tech.*, Vol. 54, No. 6, 2880–2886, Jun. 2006.
13. Lum, K. M., C. Laohapensaeng, and C. E. Free, “A novel traveling-wave feed technique for circularly polarized planar antennas,” *IEEE Micro. and Wireless Components Letters*, Vol. 15, No. 3, 180–182, Mar. 2005.
14. Lum, K. M., T. Tick, C. Free, and H. Jantunen, “Design and measurement data for a microwave CP antenna using a new travelling-wave feed concept,” *European Microwave Conf.*, Paris, France, Oct. 2005.
15. Seow, C. K. and S. Y. Tan, “Non-line-of-sight localization in multipath environments,” *IEEE Transactions on Mobile Computing*, Vol. 7, No. 5, 647–660, May 2008.
16. Seow, C. K. and S. Y. Tan, “Localization of omni-directional mobile device in multipath environments,” *Progress In Electromagnetics Research*, Vol. 85, 323–348, 2008.
17. Seow, C. K. and S. Y. Tan, “Localisation of mobile device in multipath environment using bi-directional estimation,” *Electronics Letters*, Vol. 44, No. 7, 485–487, Mar. 2008.
18. Seow, C. K. and S. Y. Tan, “Non-line-of-sight unidirectional mobile localisation in multipath environment,” *Electronics Letters*, Vol. 44, No. 2, 141–142, Jan. 2008.
19. Tai, C. S., S. Y. Tan, and C. K. Seow, “Robust non-line-of-sight localisation system in indoor environment,” *Electronics Letters*, Vol. 46, No. 8, 593–595, Apr. 2010.

Concept of Image Based Non-line-of-sight (NLOS) Localization in Multipath Environments

Si Wen Chen, Chee Kiat Seow, and Kai Wen

School of Electrical and Electronic Engineering, Nanyang Technological University, Singapore

Abstract— Current bidirectional localization schemes are able to locate a mobile device using Line-of-Sight (LOS) or Non-Line-of-Sight (NLOS) Time-of-Arrival (TOA) and Angle-of-Arrival (AOA) information measured at both the mobile device and reference device. This information is used to derive line of possible mobile device position (LPMD). The intersection points of LPMDs are used to estimate mobile position. However these algorithms do not work well in a dense multipath environment with high levels of TOA and AOA measurement noise. In addition, these techniques require at least two single bounce reflection paths to locate the mobile position. This paper explores the feasibility of using multiple image theory to obtain the image point of the NLOS single bounce multipath to perform NLOS localization and overcome the abovementioned limitations. Simulation results have shown that there are few variance shape of image point with various combinations of TOA and AOA variance noises. With the discovery of these variance shapes in the image point, it opened up new method and possibility to perform NLOS localization in a more effective and accurate way.

1. INTRODUCTION

Wireless localization is an important area that receives significant research interest recently. It is required in many sensor network applications, such as transportation systems, personal tracking and navigation [1–3]. Conventional LOS schemes fail to work when there are insufficient RDs in LOS with the MD or when the signals are dominated by NLOS paths [4, 5]. Several NLOS mitigation techniques [6, 7] have been suggested to identify and discard NLOS signals. These techniques are, however, will not perform satisfactorily as they generally require the number of LOS RDs to be more than the number of NLOS RDs.

With the popularity of Multiple Input Multiple Output (MIMO) system using antenna array [8, 9], Non Line of Sight localization (NLOS) techniques have been proposed to tackle the problem of insufficiency of LOS path. In NLOS schemes, NLOS information, like those of one bounce scattering, is not discarded but used to complement LOS information in determining MD position. So far, NLOS information that is contained within one bounce scattering paths can be used to assist LOS paths [10, 11]. However, these methods do not work well in environments when multipath becomes too dominant and distances traveled by multiple-bounce reflection paths become comparable with those of one-bounce reflection, causing weighting factors of multiple-bounce LPMDs to be comparable with those of one-bounce. Also, these methods is unable to locate

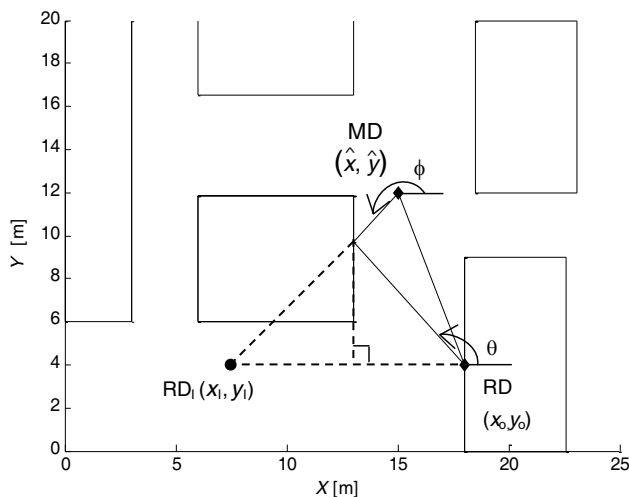


Figure 1: Geometrical depiction of the image point RD.

MD relying only one signal path and the accuracy will be deteriorated when the TOA and AOA measurement noises become larger.

In this paper, we use multiple image theory to get the image point of NLOS single path reflection path to perform NLOS localization. Most importantly, the concept of image brings the opportunity to improve the robustness and accuracy of NLOS localization. Our simulation results have also shown the shape of image point with various combinations of TOA and AOA variance noises.

2. CONCEPT OF IMAGE POINT

As shown in Fig. 1, RD with known location coordinate (x_o, y_o) has a measured angle θ for one bounce scattering path and MD with estimation coordinate (\hat{x}, \hat{y}) has a measured angle ϕ . The distances measured at RD and MD are equal to d and r respectively. σ_d, σ_r and $\sigma_\theta, \sigma_\phi$ are the standard deviations of TOA and AOA measured at RD and MD respectively that are followed by Gaussian distribution. From the figure, we can observe that the image point RD_I is in symmetry with RD with regards to the reflection surface. To calculate the image point RD_I , we can change one bounce scattering path to LOS path. As such, when the MD keeps moving around the environment, through constructing the image point we are able to change multiple bounce reflection paths to single bounce reflection and based on the bidirectional NLOS localization scheme [10], we still can leverage on the multiple bounce reflection paths to do the localization.

To evaluate the performance of our proposed scheme, the following three scenarios will be illustrated:

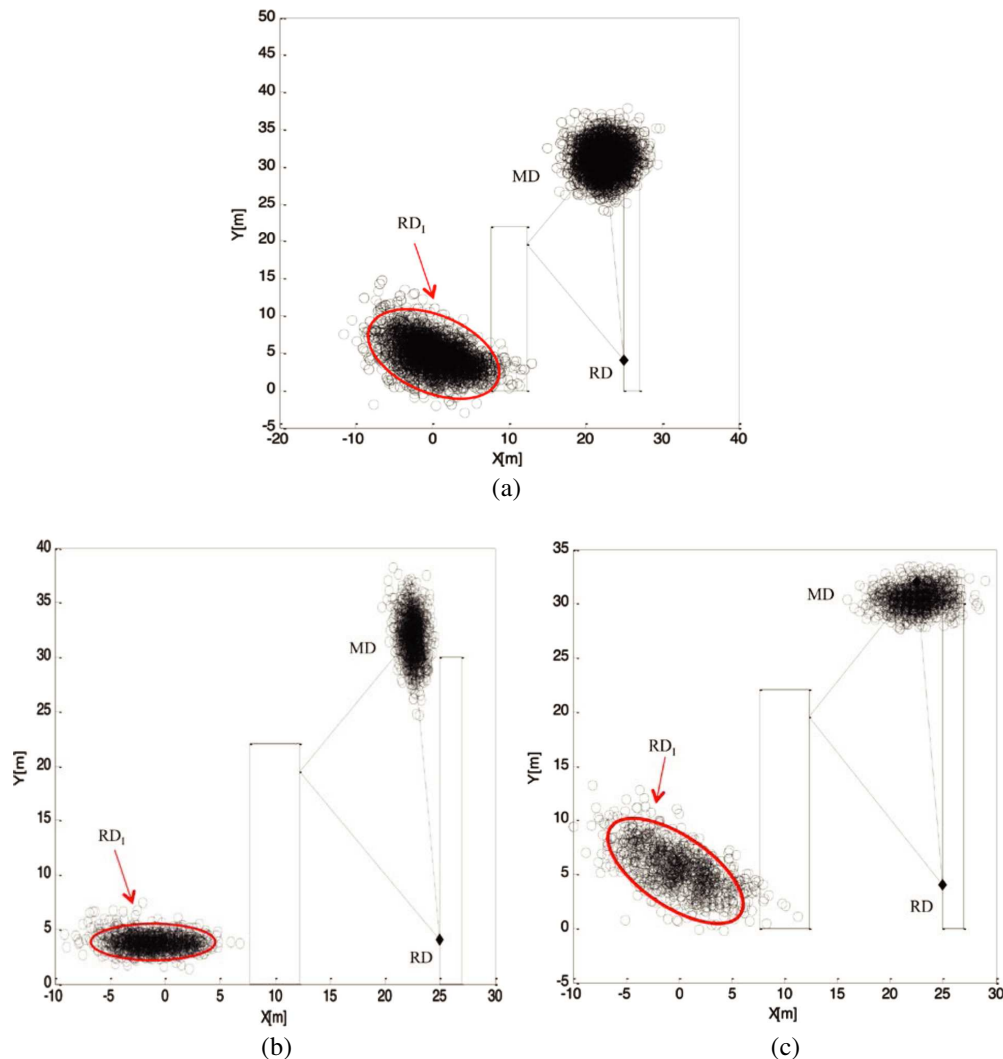


Figure 2: Scatterplot of the estimated image point RD_I . (a) Case A — $\sigma_d = \sigma_r = 3$ m, $\sigma_\theta = \sigma_\phi = 6^\circ$. (b) Case B — $\sigma_d = \sigma_r = 3$ m, $\sigma_\theta = \sigma_\phi = 2^\circ$. (c) Case C — $\sigma_d = \sigma_r = 1$ m, $\sigma_\theta = \sigma_\phi = 6^\circ$.

- Case A. $\sigma_d = \sigma_r = 3$ m, $\sigma_\theta = \sigma_\phi = 6^\circ$
- Case B. $\sigma_d = \sigma_r = 3$ m, $\sigma_\theta = \sigma_\phi = 2^\circ$
- Case C. $\sigma_d = \sigma_r = 1$ m, $\sigma_\theta = \sigma_\phi = 6^\circ$

Measurement data metrics (AOA and TOA) were measured by using ray tracing methodology proposed in [12–14]. One RD was positioned in the environment at (25, 4) and the mobile device was placed at (22.5, 32). There are two signal paths between RD and MD, LOS path and one bounce reflection path.

It is observed from the simulation results, as illustrated in Fig. 2, that the shape of the estimated image point RD_I is always an ellipse under the above three cases. Thus we are able to make use this character to develop novel method for NLOS localization.

3. CONCLUSIONS

A novel approach to introduce the concept of image for NLOS localization has been proposed. The shape of image was tested and shown to be an ellipse under various conditions. Moreover, by exploring the image we can create new method for NLOS localization.

REFERENCES

1. Patwari, N., J. N. Ash, S. Kyperountas, A. O. Hero III, R. L. Moses, and N. S. Correal, “Locating the nodes: Cooperative localization in wireless networks,” *IEEE Signal Processing Mag.*, Vol. 22, 54–69, Jul. 2005.
2. Sayed, A. H., A. Tarighat, and N. Khajehnouri, “Network-based wireless location: Challenges faced in developing techniques for accurate wireless location information,” *IEEE Signal Processing Mag.*, Vol. 22, 24–40, Jul. 2005.
3. Reed, J. H., K. J. Krizman, B. D. Woerner, and T. S. Rappaport, “An overview of the challenges and progress in meeting the E-911 requirement for location services,” *IEEE Commun. Mag.*, 30–37, Apr. 1998.
4. Jiang, L. and S. Y. Tan, “A simple geometrical-based AOA model for mobile communication systems,” *IEE Electronics Letters*, Vol. 40, No. 19, 1203–1205, Sep. 2004.
5. Jiang, L. and S. Y. Tan, “Geometrical-based statistical channel model for outdoor and indoor propagation environments,” *IEEE Trans. Vehicular Technology*, Vol. 56, No. 6, 3587–3593, Nov. 2007.
6. Cong, L. and W. H. Zhuang, “Nonline-of-sight error mitigation in mobile location,” *IEEE Trans. Wireless Commun.*, Vol. 4, 560–572, Mar. 2005.
7. Chan, Y. T., W. Y. Tsui, H. C. So, and P. C. Ching, “Time-of-arrival based localization under NLOS conditions,” *IEEE Trans. Veh. Tech.*, Vol. 55, 17–24, Jan. 2006.
8. Lum, K. M., C. Laohapensaeng, and C. E. Free, “A novel traveling-wave feed technique for circularly polarized planar antennas,” *IEEE Micro. and Wireless Components Letters*, Vol. 15, No. 3, 180–182, Mar. 2005.
9. Lum, K. M. and C. E. Free, “A novel dual circularly polarized planar and multi-layer LTCC antenna arrays using traveling-wave feed system,” *IEEE Trans. Micro. Theory Tech.*, Vol. 54, No. 6, 2880–2886, Jun. 2006.
10. Seow, C. K. and S. Y. Tan, “Non-line-of-sight localization in multipath environments,” *IEEE Trans. Mobile Computing*, Vol. 7, No. 5, 647–660, May 2008.
11. Chen, S. W., S. Y. Tan, and C. K. Seow, “Peer-to-peer localization in urban and indoor environments,” *Progress In Electromagnetic Research B*, 339–358, 2011.
12. Ang, T. W., S. Y. Tan, and H. S. Tan, “Analytical methods to determine diffraction points on multiple edges and cylindrical scatterers in UTD ray tracing,” *Microwave and Optical Technology Letters*, Vol. 22, No. 5, 304–309, Sep. 1999.
13. Tan, S. Y. and H. S. Tan, “Modelling and measurements of channel impulse response for an indoor wireless communication system,” *IEE Proceedings Microwaves, Antennas and Propagation*, Part H, Vol. 142, No. 5, 405–410, London, Oct. 1995.
14. Tan, S. Y., M. Y. Tan, and H. S. Tan, “Multipath delay measurements and modelling for inter-floor wireless communications,” *IEEE Trans. Vehicular Technology*, Vol. 49, No. 4, 1334–1341, Jul. 2000.

An Eigenvalue Hybrid FEM Formulation for Three Dimensional Open Cavities

C. L. Zekios¹, P. C. Allilomes¹, A. V. Kudrin², and G. A. Kyriacou¹

¹Microwaves Lab., Department of Electrical and Computer Engineering
Democritus University of Thrace, Xanthi, Greece

²Department of Radiophysics, University of Nizhny Novrogod, Russia

Abstract— A non-linear hybrid finite element formulation, for the three dimensional eigenvalue analysis of open cavities is proposed. The infinite solution domain is truncated using a separation surface- S_f . Inside the surface- S_f the electromagnetic field is formulated employing the finite element technique. Outside the surface- S_f the infinite free space domain is modeled through an “infinite” sum of spherical harmonics. The two field expressions, the numerical inside (subdomain-II) the fictitious surface and the analytical one outside (subdomain-I) are bind together by enforcing the “exact” field continuity conditions strictly following a vector Dirichlet-to-Neumann map formalism. Thus, the “transparency” of the fictitious surface is ensured. The overall procedure ends up to a nonlinear eigenvalue problem for the unknown resonant wavenumber k_r . For the solution of the nonlinear eigenvalue problem the Regula Falsi method is considered. The solution procedure is based on the initial values provided from the resonances of an equivalent closed cavity. The validity of the method is tested against the results of a commercial simulator and is verified through a comparison with results presented in the bibliography.

1. INTRODUCTION

The analysis and design of open-radiating cavities is one of the most active research fields in electromagnetics. Numerous attempts towards this direction have been published but most of them employ the deterministic approach, namely the electromagnetic simulation in the presence of a specific excitation-source. Moreover, most of the computerized techniques able to solve cavity problems in a unified manner are based on numerical techniques such as the finite element (FE) and the finite difference (FD) methods. The eigenfrequency of open-radiating cavities exploiting all the advantages of the source-free problems analysis, namely the stability and physical insight of the structure, constitutes a challenge in this research field. Thus, a numerical analysis tool capable of computing the eigenfrequencies and the corresponding modal fields (eigenvectors) of arbitrary open cavities will significantly contribute to the design and particularly to devise novel antennas and various electromagnetic structures. The idea is to bind together the efficiency and the robustness of the numerical technique (in our work the FE) for the physically bounded area with an appropriate method for the description of the field in the semi-infinite domain.

Several techniques have been developed for the implementation of FEM in the deterministic analysis of such cases. For this purpose FEM is hybridized rendering the open/unbounded solution domain to an equivalent closed one, using an artificial-mathematical separation surface. The hybridization of FEM with Moment Method (FEM-MoM), e.g., [1] and FEM with Boundary Elements (FEM-BEM), e.g., [2], where in both techniques an integral equation is formulated for the unknown equivalent current densities defined over the artificial separation surface. One quite different procedure is that of Unimoment introduced by Mei [3] and Bymoment technique introduced by Cangellaris [4]. Aiming at the eigenanalysis of a structure is important to ensure a “perfect transparency” for the fictitious separation surface, since a slight scattering from this may give rise to spurious modes which can not be distinguished from the true solutions. Even the “Perfect Matching Layer, PML” is proved to yield spurious solutions called “Berenger modes”. MoM and BEM are indeed proved to offer an almost “exact transparency”. However, both of them suffer from a problem of “fictitious internal resonances” when it is formulated based on either the Electric field (EFIE) or Magnetic field (MFIE) integral equation. It was proved by Prof. Harrington group [5] that both electric and magnetic field continuity should be enforced over the fictitious separation surface (uniqueness theorem overcome), through the Combined Electric-Magnetic (CFIE) field integral equation, in order to ensure “exact transparency” and avoid spurious internal resonances. However, this is exactly equivalent to enforce the field continuity through the Dirichlet-to-Neumann (DtN) map formalism and this is the approach adopted within our effort. Besides that MoM and BEM suffer from a field singularity when integrating at observation points on or near the surface

where the equivalent current densities are defined. Hence, in order to avoid these problems as well as to avoid the necessity of complicated Green's functions asked by MoM, a field expansion into a superposition of spherical harmonics is employed for the infinite free space domain. Explicitly, the 3-D solution domain in the generalized case is enclosed within a fictitious spherical surface S_f . For the field solution inside the surface- S_f the formulation is applied based on a tetrahedral edge elements discretization. Thus, being able to model arbitrary shaped radiating 3D structures. The field outside- S_f is expressed by an in principle “infinite” series of spherical harmonics given by the analytical solution of the field wave equation in free space, which in turn obey the Sommerfeld radiation condition. The final formulation is obtained by imposing the field continuity conditions across the fictitious surface and exploiting the orthogonality properties of the spherical harmonics. The final nonlinear eigenproblem is solved using the Regula Falsi technique [6] and employing the eigenvalues of the corresponding closed cavity as an initial guess.

2. FORMULATION

The general geometry of Figure 1 is considered which is actually an open-radiating cavity enclosed inside the fictitious spherical surface noted as S_f . Our goal is to derive a hybrid finite element (FEM) formalism able to estimate the complex eigenfrequencies and ultimately to formulate an eigenproblem for the characteristic modes in particular the eigencurrents flowing on the metallic parts.

Aiming at a general formulation the electromagnetic behaviour within the enclosed region (II) is characterized by the electric field vector wave equation, which for a source free region tensor permittivity ($\bar{\epsilon}_r$) and permeability ($\bar{\mu}_r$) material loading reads [7]:

$$\nabla \times \bar{\mu}_r^{-1} \cdot \nabla \times \bar{E} - k_0^2 \bar{\epsilon}_r \bar{E} = 0 \quad (1)$$

Applying the standard Galerkin procedure to Eq. (1) the following weak formulation can be derived [7]:

$$\iiint_V (\nabla \times \bar{T}) \cdot \bar{\mu}_r^{-1} \cdot (\nabla \times \bar{E}) dV - k_0^2 \iiint_V \bar{T} \cdot (\bar{\epsilon}_r \bar{E}) dV - jk_0 \oint_S \bar{T} \cdot (\hat{n} \times \bar{H}) dS = 0 \quad (2)$$

where $k_0 = \omega/c$ is the free space wavenumber, \bar{T} is the vector weighting function and V denotes the bounded space of region (II), which is enclosed by the artificial spherical surface- S_f . The artificial surface S_f is introduced in order to truncate the semi-infinite solution domain of Figure 1 and it is of highly importance to be “transparent” to the field solution. This “transparency” is realized by enforcing on the fictitious boundary both the electric and magnetic field continuity conditions between the finite element method solution in region (II) and the field expansion in region (I). The accurate enforcement of the field continuity conditions is ensured by strictly following a vector Dirichlet-to-Neumann mapping mathematical formalism, e.g., [10].

For the unbounded part of the solution domain (region-I), since the medium is homogeneous and source free, the field can be expressed as a superposition of radial TE^r and TM^r modes, or

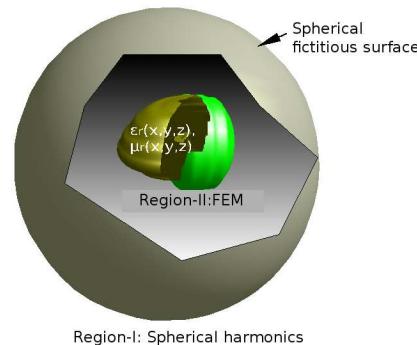


Figure 1: A three dimensional open cavity.

equivalently an infinite expansion of the well known spherical eigenfunctions for the electric and the magnetic field components respectively [8]:

$$E_r^I = \frac{1}{j\omega\mu_0\epsilon_0} \cdot \sum_{l=0}^{\infty} \left(\sum_{m=-l}^l k_0^2 \cdot a_{lm} \cdot \left(h_l^{(2)}(k_0 r) + h_l^{(2)}(k_0 r) \right) \cdot P_l^{|m|}(\cos(\theta)) \cdot e^{jm\phi} \right) \quad (3)$$

$$H_r^I = \frac{1}{j\omega\mu_0\epsilon_0} \cdot \sum_{l=0}^{\infty} \left(\sum_{m=-l}^l k_0^2 \cdot f_{lm} \cdot \left(h_l^{(2)}(k_0 r) + h_l^{(2)}(k_0 r) \right) \cdot P_l^{|m|}(\cos(\theta)) \cdot e^{jm\phi} \right) \quad (4)$$

The terms a_{lm} and f_{lm} are unknown weighting factors of the magnetic and the electric potential respectively, the $P_l^{|m|}$ are the Legendre functions and the $h_l^{(2)}(k_0 r)$ are the spherical Hankel functions of order l .

Following the DtN formalism this expansion is established from the Dirichlet data enforced along the fictitious surface- S_f . Since the electric field wave equation is considered in region-II, the Dirichlet data are comprised of the electric field values. Hence, the tangential electric field values defined by FEM along the fictitious surface are considered as known Dirichlet data. In turn the tangential electric field continuity must be enforced along S_f to yield summation equations with unknowns the weighting coefficients of the expansion (3)–(4) in the outer region:

$$\hat{r} \times \bar{E}^{\text{exp}}|_{r=r_c} = -\hat{r} \times \bar{E}^{\text{FEM}}|_{r=r_c} \quad (5)$$

Exploiting the orthogonality properties of the functions $e^{jm\phi}$ and $P_l^{|m|}$ the weighting factor a_{lm} and f_{lm} can be given in a compact symbolic form as:

$$a_{lm} \propto \left(\dots \int_0^{2\pi} \int_0^\pi E_\theta^{\text{FEM}} \cdot P_l^{|m|}(\cos(\theta)) \cdot \sin^2(\theta) \cdot e^{jm\phi} d\theta d\phi \right. \\ \left. + (\dots) \int_0^{2\pi} \int_0^\pi E_\phi^{\text{FEM}} \cdot P_l^{|m|}(\cos(\theta)) \cdot \sin^2(\theta) \cdot e^{jm\phi} d\theta d\phi \right] \quad (6)$$

$$f_{lm} \propto \left(\dots \int_0^{2\pi} \int_0^\pi E_\theta^{\text{FEM}} \cdot P_l^{|m|}(\cos(\theta)) \cdot \sin^2(\theta) \cdot e^{jm\phi} d\theta d\phi \right. \\ \left. + (\dots) \int_0^{2\pi} \int_0^\pi E_\phi^{\text{FEM}} \cdot P_l^{|m|}(\cos(\theta)) \cdot \sin^2(\theta) \cdot e^{jm\phi} d\theta d\phi \right] \quad (7)$$

According now to the second step of the DtN formalism the field in the outer region is differentiated in order to establish the DtN map, so as to obtain the Neumann data along the fictitious surface. This differentiation is actually provided by the electric field curl equation itself, to yield the magnetic field expressions in the outer region as well as along the fictitious surface S_f . For this reason the coefficients a_{lm} and f_{lm} obtained above are substituted back into the expression of the tangential magnetic field to yield the following formal Dirichlet to Neumann map:

$$H_\theta^I \propto \sum_{l=0}^{\infty} \left(\sum_{m=-l}^l (\dots) \int_0^{2\pi} \int_0^\pi E_\theta^{\text{FEM}} \cdot P_l^{|m|}(\cos(\theta)) \cdot \sin^2(\theta) \cdot e^{jm\phi} d\theta d\phi \right. \\ \left. + (\dots) \int_0^{2\pi} \int_0^\pi E_\phi^{\text{FEM}} \cdot P_l^{|m|}(\cos(\theta)) \cdot \sin^2(\theta) \cdot e^{jm\phi} d\theta d\phi \right) \quad (8)$$

$$H_\phi^I \propto \sum_{l=0}^{\infty} \left(\sum_{m=-l}^l (\dots) \int_0^{2\pi} \int_0^\pi E_\theta^{\text{FEM}} \cdot P_l^{|m|}(\cos(\theta)) \cdot \sin^2(\theta) \cdot e^{jm\phi} d\theta d\phi \right. \\ \left. + (\dots) \int_0^{2\pi} \int_0^\pi E_\phi^{\text{FEM}} \cdot P_l^{|m|}(\cos(\theta)) \cdot \sin^2(\theta) \cdot e^{jm\phi} d\theta d\phi \right) \quad (9)$$

So, the magnetic field of the outer expansion is written in terms of the ‘FEM-discretized’ electric field.

The third DtN step asks for the enforcement of the normal derivatives of the electric field being continuous along the S_f . This herein reads as requiring the tangential components of the magnetic field expansion to be equal to that of the FEM description along the surface:

$$-\hat{r} \times \overline{H}^{FEM}|_{r=r_c} = \hat{r} \times \overline{H}^{\text{exp}}|_{r=r_c} \quad (10)$$

These tangential magnetic field components are identical to the field derivatives occurring in the surface integral of the FEM mesh formulation (2). So the surface integral serves also the coupling of the two field expressions. The resulting eigenproblem expression can be written in a matrix form as:

$$A(k_0)[e] = 0 \quad (11)$$

The major difficulty of the presented technique is the solution of the nonlinear problem (11). In our case the final nonlinear eigenvalue problem is treated by means of the regula falsi technique presented by Hager in [6], in combination with the Implicitly Restarted Arnoldi Method (IRAM) [9]. The regula falsi algorithm linearly interpolates the nonlinear eigenvalue problem between two given points σ and μ . Subsequently, this new “linearized” eigenvalue problem is solved and the eigenvalue with the smaller magnitude provides us with a new μ . This procedure is repeated until a convergence is reached. The regula falsi algorithm can find with acceptable precision only the eigenvalue and its corresponding eigenvector that is closer to. Also, if the unknown eigenvalue is far from the interval spanning from σ to μ the procedure is quite slow, as it needs a lot of iterations to reach the convergence. To overcome the above drawbacks, it would be very convenient if an initial guess of the eigenvalue spectrum was available. This initial guess of the spectrum is provided by the eigenvalues of the closed cavity.

3. NUMERICAL RESULTS

The proposed method is currently under validation. In this paper the results of a cavity backed patch antenna (Figure 2) are presented. The patch is 4 [cm] \times 3 [cm] and it is recessed in a 8 [cm] \times 6 [cm] \times 0.1 [cm] cavity, that is homogeneously filled with dielectric $\epsilon_r = 2.0$. A discretization of 10983 tetrahedrals was initialized for the volume of the structure, while the surface of the metallic patch was discretized by 2768 triangles. In Table 1 the numerical evaluation of the first two resonant frequencies is depicted. The first 3 values appearing in the table are spurious modes, which are actually under consideration. To validate our results the commercial electromagnetic simulator HFSS was used. However, HFSS doesn't support an eigenanalysis for open radiating structures,

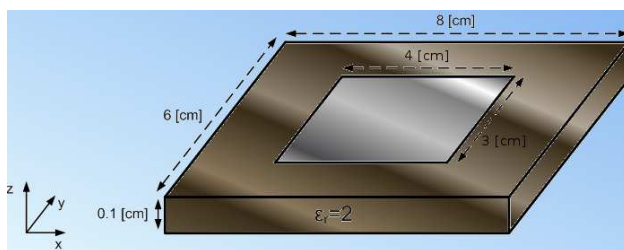


Figure 2: A cavity backed patch antenna geometry.

Table 1: Cavity backed patch antenna resonant frequencies.

	proposed technique f [GHz]	HFSS f [GHz]
1	0.11	-
2	0.11	-
3	0.11	-
4	2.78	2.81
5	4.79	4.80

thus a simulation procedure of a plane wave scattering on the patch was adopted for a frequency sweep from 1 [GHz] to 20 [GHz]. The patch antenna seems to efficiently radiate at 2.8 [GHz] and 4.8 [GHz] with both simulation procedures, the proposed and the HFSS. These frequencies were indeed identified as resonances by adding an excitation port to extract the antenna input impedance. Parallel resonances are identified at frequency points where the real part of the input impedance becomes maximum.

4. CONCLUSION

A non-linear eigenanalysis scheme for 3D open radiating structure based on a hybrid FEM and a spherical harmonics expansion is formulated. The separation surface transparency is ensured by following a Dirichlet-to-Neumann mathematical formalism. The next step refers to the exploitation of the methodology to devise for novel antenna structures especially through a Characteristic mode eigenanalysis.

ACKNOWLEDGMENT

This work was financially supported by the Greek Ministry of Education, Lifelong Learning and Religious Affairs through the research project THALIS Design Techniques for Digitally Controlled RF-Microwave Structures Appropriate for Software Defined-Cognitive Radio (RF-EIGEN-SDR).

REFERENCES

1. Yuan, X., "Three dimensional electromagnetic scattering from inhomogeneous objects by the hybrid moment and finite element method," *IEEE Trans. on Microwave Theory and Techniques*, Vol. 38, 1053–1058, Aug. 1990.
2. Lynch, D. R, K. D. Paulsen, and J. W. Strohbehn, "Hybrid element method for unbounded electromagnetic problems in hyperthermia," *Int. Journal for Num. Meth. in Eng.*, Vol. 23, 1915–1937, Jun. 1986.
3. Mei, K., "Unimoment method of solving antenna and scattering problems," *IEEE Trans. on Ant. and Propagat.*, Vol. 22, 760–766, Nov. 1974.
4. Cangellaris, A., and R. Lee, "The bymoment method for two-dimensional electromagnetic scattering," *IEEE Trans. on Ant. and Propagat.*, Vol. 38, 1429–1437, Sep. 1990.
5. Harrington, R. F. and J. R. Mautz, "Theory of characteristic modes for conducting bodies," *IEEE Trans. on Ant. and Propagat.*, Vol. 19, 622–628, 1971.
6. Hager, P., "Eigenfrequency analysis. Fe-adaptivity and nonlinear eigen-problem algorithm," Ph.D. Thesis, Dept. Struct. Mech., Chalmers University of Technology, Geteborg, 2001.
7. Zhu, Y. and A. C. Cangellaris, *Multigrid Finite Element Methods for Electromagnetic Field Modeling*, Wiley Interscience, N.Y., 2006.
8. Balanis, C. A., *Advanced Engineering Electromagnetics*, Edition I, Wiley, N.Y., 1989.
9. Sorensen, D. C., "Implicit application of polynomial filters in a k-step arnoldi method," *SIAM J. Matrix Analysis and Applications*, Vol. 13, No. 1, 357–385, 1992.
10. Allilomes, P. C. and G. A. Kyriacou, "A nonlinear finite-element leaky-waveguide solver," *IEEE Trans. on Microwave Theory and Techniques*, Vol. 55, No. 7, 1496–1510, Jul. 2007.

A Mode Matching Methodology for the Analysis of Circular Waveguides Loaded with Infinite and Finite Periodic Structures

Dimitris G. Makris, Spyros J. Lavdas, Christos S. Lavranos, and George A. Kyriacou

Microwaves Lab., Department of Electrical and Computer Engineering

Democritus University of Thrace, Xanthi 67100, Greece

Abstract— A mode matching methodology for the analysis of periodically loaded circular waveguides is proposed. Our present effort is focused on infinite periodic waveguides employing two different approaches. The first one is similar to the so called transfer matrix technique, where classical mode matching is employed to analyze the discontinuities involved within a unit cell. In turn periodic boundary conditions are enforced between the input and output ports of the unit cell. The resulting system of equations is formulated as an eigenproblem and solved for the Floquet wavenumbers. A more rigorous approach is also under development where the field within the unit cell is expressed directly as a Floquet expansion. While the methodology is general, it is herein applied particularly for the study of periodical irises in which complementary split ring resonators (CSRRs) are etched.

1. INTRODUCTION

Periodic structures have been examined and investigated widely, due to their importance in design and implementation of a plethora of microwave devices, mainly microwave filters. The early analysis was based on approximate-analytical techniques and the resultant deviations were regulated with mechanical moving elements. The usage of complex geometries and anisotropic material loadings, offers excellent potential. Additionally electromagnetic band gap (EBG) applications, where the periodic structure is designed to prevent the wave propagation either at certain frequencies (frequency band gap) or in certain directions (space gap or space selective propagation), have been acquired a special attention, particularly in recent years.

In this paper, we will examine a circular waveguide loaded with infinite or finite periodic structures. These are mainly comprised of irises etched on diaphragms or corrugations and we will try to investigate their propagation characteristics. Particular effort is devoted to periodic structure loaded with periodically repeated split ring resonators (SRR), printed on dielectric diaphragms, which presents negative refraction phenomena and constitutes a popular physical realization of left handed (LH) medium. Explicitly, LH behavior is expected when circular waveguide is operated below cutoff and this phenomenon will be examined herein in order to be verified for both infinite and finite periodic SRRs sections. Usually such structures are analyzed and designed by usage of advanced numerical methods. However, the increasing demand for accurate prediction of wave propagation behavior and the electrically large dimensions of such structures, render the numerical simulation, time consuming or almost impossible.

Floquet theorem has been used to tackle this problem, but this is possible if only the periodic structure extends infinitely. Then the analysis is restricted to the determination of only one spatial period-cell. The electromagnetic field in one cell is related with electromagnetic field of the next or the previous cell by an exponential function. Hence, periodic boundary conditions are enforced on the unit cell's periodic surfaces in order to introduce the periodicity into the formulation. Initially the infinitely extended circular waveguide is divided into unit cells. The unit cell internal structure is composed of discontinuities and uniform (geometrically) circular waveguide sections. Each discontinuity is analyzed with the aid of a Mode Matching Technique (MMT). Electromagnetic fields at the terminal cross sections of each uniform unit cell section are correlated by known expressions [5]. Finally the Floquet theorem, by mean of periodic boundary conditions, at the ports of the unit cell, is used in combination with previous expressions in order to derive a classical eigenvalue problem which is solved for the Floquet wavenumbers.

2. FORMULATION

The unit cell of the periodic structure as shown in Fig. 1(a), is composed of a split ring iris waveguide between two regular circular waveguide sections. The eigenanalysis of a regular circular waveguide is very well established. Also the eigenanalysis of a Split Ring Iris (SRI) waveguide has accomplished in our previous work [3]. Hence the eigenfunctions and the related propagation constants in each

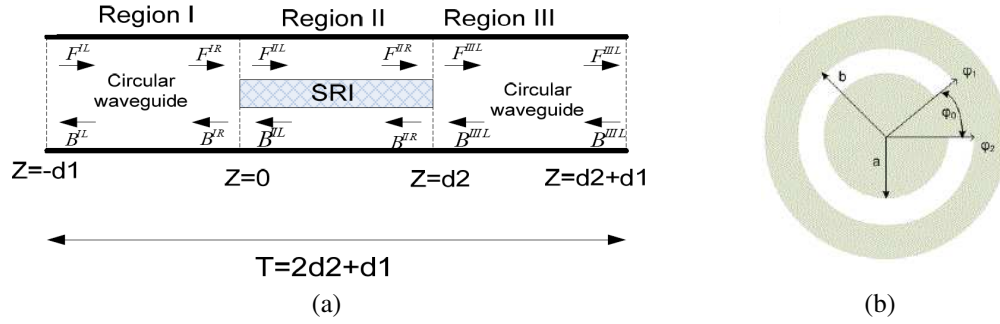


Figure 1: (a) Spatial unit cell of the periodic structure. (b) Cross section of the Split Ring Iris (SRI) waveguide.

uniform section of the unit cell are readily available. As described in the introduction a mode matching technique will be first employed in order to model the unit cell (spatial period) with the aid of a Generalized Scattering Matrix. In turn periodic boundary conditions will be imposed at its input and output ports and the resulting system will be formulated as an eigenproblem for the Floquet wavenumbers.

Imposing mode matching (MMT) at $z = 0$, namely imposing boundary conditions for the transverse electric and magnetic fields and using the modes orthogonality relation, the propagating and reflected (scattered) waves amplitudes can be related to each other in the following manner:

$$[d_U] [F^{IR} + B^{IR}] = [A_0] [F^{ILL} + B^{ILL}] \quad \text{and} \quad [B_0] [F^{IR} - B^{IR}] = [d_Q]^* [F^{ILL} - B^{ILL}] \quad (1)$$

where d_U , d_Q are diagonal matrices with elements the integrals defined after utilizing the orthogonality relations [1]:

$$\int_{S_1} \left(\vec{e}_p^I \times \vec{h}_q^{I*} \right) \cdot \hat{z} dS = U_p \cdot \delta_{pq} \quad \text{and} \quad \int_{S_2} \left(\vec{e}_q^{II} \times \vec{h}_p^{II*} \right) \cdot \hat{z} dS = Q_q \cdot \delta_{pq} \quad (2)$$

where δ_{pq} is the Kronecker delta function and Q_q , U_p defined as

$$Q_q, U_p = \begin{cases} 2 & \text{for propagating modes} \\ 2j & \text{for evanescent } TE \text{ modes} \\ -2j & \text{for evanescent } TM \text{ modes} \end{cases}$$

$A_0 B_0$ are mode coupling matrices with elements the coupling integrals between the two regions:

$$A_{pq} = \int_{S_1} \left(\vec{e}_q^{II} \times \vec{h}_p^{I*} \right) \cdot \hat{z} dS \quad \text{and} \quad B_{qp} = \int_{S_1} \left(\vec{e}_q^{II*} \times \vec{h}_p^I \right) \cdot \hat{z} dS \quad (3)$$

Detailed expressions for the circular waveguide eigenfunctions e and h are given in [2, 4], while those for an infinitely extended split ring waveguide are given in our previous work [3] and with more details in the diploma thesis [6]. Then, the reflected and propagating waves amplitudes can be related with equivalent voltages and currents in the following manner [5]:

$$[V^{IR}] = [F^{IR} + B^{IR}]; [I^{IR}] = [F^{IR} - B^{IR}] \quad \text{and} \quad [V^{ILL}] = [F^{ILL} + B^{ILL}]; [I^{ILL}] = [F^{ILL} - B^{ILL}] \quad (4)$$

The combination of (1), (4) will lead to a relationship between voltage and current coefficients in the left and right side of discontinuity at $z = 0$:

$$[V^{IR}] = [R_0] \cdot [V^{ILL}] \quad \text{and} \quad [T_0] \cdot [I^{IR}] = [I^{ILL}] \quad (5)$$

In the same way we can extract a relationship between voltage and current amplitudes in the left and right side of discontinuity at $z = d_2$:

$$[R_0] \cdot [V^{IIR}] = [V^{IILL}] \quad \text{and} \quad [I^{IIR}] = [T_0] \cdot [I^{IILL}] \quad (6)$$

where

$$[R_0] = [d_U]^{-1} \cdot [A_0] \quad \text{and} \quad [T_0] = [d_Q^*]^{-1} \cdot [B_0] \quad (7)$$

The voltage and current coefficients in the left and right side of each unit cell's uniform section are correlated as follows [5]:

REGION I

$$[V^{IR}] = [C_{d1}] [V^{IL}] - [S_{d1}] [I^{IL}] \quad \text{and} \quad [I^{IR}] = [-S_{d1}] [V^{IL}] + [C_{d1}] [I^{IL}] \quad (8)$$

REGION II

$$[V^{IIL}] = [C_{d2}] \cdot [V^{IIR}] + [S_{d2}] \cdot [I^{IIR}] \quad \text{and} \quad [I^{IIL}] = [S_{d2}] \cdot [V^{IIR}] + [C_{d2}] \cdot [I^{IIR}] \quad (9)$$

REGION III

$$[V^{IIIL}] = [C_{d1}] \cdot [V^{IIIR}] + [S_{d1}] \cdot [I^{IIIR}] \quad \text{and} \quad [I^{IIIL}] = [S_{d1}] \cdot [V^{IIIR}] + [C_{d1}] \cdot [I^{IIIR}] \quad (10)$$

where

$$\begin{aligned} [C_{d1}] &= \text{diag}([\cosh(\gamma_p \cdot d1)]) & [C_{d2}] &= \text{diag}([\cosh(\gamma_q \cdot d2)]) \\ \text{and } [S_{d1}] &= \text{diag}([\sinh(\gamma_p \cdot d1)]) & [S_{d2}] &= \text{diag}([\sinh(\gamma_q \cdot d2)]) \end{aligned} \quad (11)$$

After suitable algebraic manipulations of (5), (6), (9) we derive that:

$$[V^{IR}] = [Z_1] [I^{IR}] + [Z_2] [I^{IIIL}] \quad \text{and} \quad [V^{IIIL}] = [Z_3] [I^{IR}] + [Z_4] [I^{IIIL}] \quad (12)$$

where

$$\begin{aligned} [Z_1] &= [R_0] [C_{d2}] [S_{d2}^{-1}] [T_0] & [Z_2] &= ([R_0] [S_{d2}] - [R_0] [C_{d2}] [S_{d2}^{-1}] [C_{d2}]) [T_0] \\ [Z_3] &= [R_0] [S_{d2}^{-1}] [T_0] & [Z_4] &= [R_0] [S_{d2}^{-1}] [C_{d2}] [T_0] \end{aligned} \quad (13)$$

The combination of (8), (9), (12) will lead to a relationship between voltage and current coefficients at the left of region I and right of region III, (Fig. 1(a)):

$$([C_{d1}] + [Z_1] [S_{d1}]) [V^{IL}] - ([S_{d1}] + [Z_1] [C_{d1}]) [I^{IL}] = [Z_2] [S_{d1}] [V^{IIIR}] + [Z_2] [C_{d1}] [I^{IIIR}] \quad (14)$$

$$- [Z_3] [S_{d1}] [V^{IL}] + [Z_3] [C_{d1}] [I^{IL}] = ([C_{d1}] - [Z_4] [S_{d1}]) [V^{IIIR}] + ([S_{d1}] - [Z_4] [C_{d1}]) [I^{IIIR}] \quad (15)$$

Floquet Theorem states that in a periodic system for a given mode of propagation at a steady state, the fields at one cross section differ from those one period (or an integer multiple periods) away by only a complex exponential constant. Hence, the usage of Floquet theorem, in the sense of periodic boundary conditions leads to the correlation of voltages and currents between region I and region III, (Fig. 1(a)):

$$\left. \begin{aligned} [F^{IIIR}] &= [e^{\gamma T}] [F^{IL}] \\ [B^{IIIR}] &= [e^{\gamma T}] [B^{IL}] \end{aligned} \right\} \left. \begin{aligned} [F^{IIIR} + B^{IIIR}] &= [e^{\gamma T}] [F^{IL} + B^{IL}] \\ [F^{IIIR} - B^{IIIR}] &= [e^{\gamma T}] [F^{IL} - B^{IL}] \end{aligned} \right\} \begin{aligned} [V^{IIIR}] &= [\lambda_F] [V^{IL}] \\ [I^{IIIR}] &= [\lambda_F] [I^{IL}] \end{aligned} \quad (16)$$

where

$$[\lambda_F] = [e^{\gamma T}] \quad (17)$$

is a diagonal matrix with elements the Floquet exponentials, which are actually the eigenvalues to be sought numerically. Eventually the Floquet propagation constants γ , through these exponentials, are the unknowns and describe the propagation characteristics of the periodic structure.

The combination of (14)–(17) leads to a linear system with unknowns the vector and current coefficients at the left of the region I:

$$([C_{d1}] + [Z_1] [S_{d1}] + [Z_2] [S_{d1}] [\lambda_F]) [V^{IL}] - ([S_{d1}] + [Z_1] [C_{d1}] + [Z_2] [C_{d1}] [\lambda_F]) [I^{IL}] = 0 \quad (18)$$

$$(- [Z_3] [S_{d1}] - [C_{d1}] [\lambda_F] + [Z_4] [S_{d1}] [\lambda_F]) [V^{IL}] + ([Z_3] [C_{d1}] - [S_{d1}] [\lambda_F] + [Z_4] [C_{d1}] [\lambda_F]) [I^{IL}] = 0 \quad (19)$$

Equations (21) and (22) describe a homogeneous system of equations, which has a non trivial solution only when the determinant of its coefficients is zero:

$$\begin{vmatrix} ([C_{d1}] + [Z_1] [S_{d1}] - [Z_2] [S_{d1}] [\lambda_F]) & -([S_{d1}] + [Z_1] [C_{d1}] + [Z_2] [C_{d1}] [\lambda_F]) \\ (- [Z_3] [S_{d1}] - [C_{d1}] [\lambda_F] + [Z_4] [S_{d1}] [\lambda_F]) & ([Z_3] [C_{d1}] - [S_{d1}] [\lambda_F] + [Z_4] [C_{d1}] [\lambda_F]) \end{vmatrix} = 0 \quad (20)$$

This determinant explicitly defines the eigenproblem which, after simple manipulations, can be formulated into a characteristic equation:

$$A\lambda_F^2 + B\lambda_F + C = 0 \quad (21)$$

where

$$\begin{aligned} A &= Z_2 (S_{d1}^2 - C_{d1}^2), & B &= -2Z_2 S_{d1} Z_3 C_{d1} + 2Z_4 S_{d1} Z_{d1} C_{d1} - 2C_{d1} S_{d1} + Z_4 (C_{d1}^2 + S_{d1}^2) - Z_1 S_{d1}^2 \\ C &= (Z_3 - Z_1) C_{d1}^2 - Z_3 C_{d1}^2 \end{aligned} \quad (22)$$

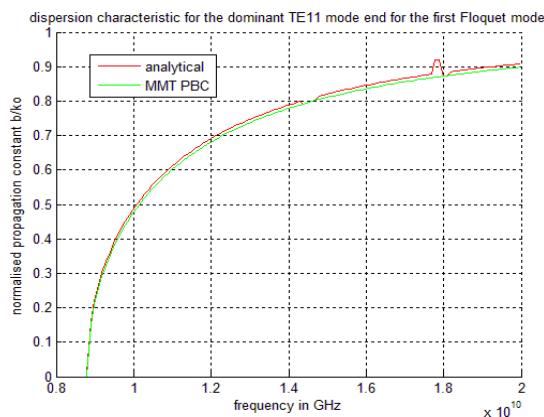


Figure 2: Dispersion characteristic for the dominant TE_{11} mode and the first Floquet mode in a uniform circular waveguide with radius a .

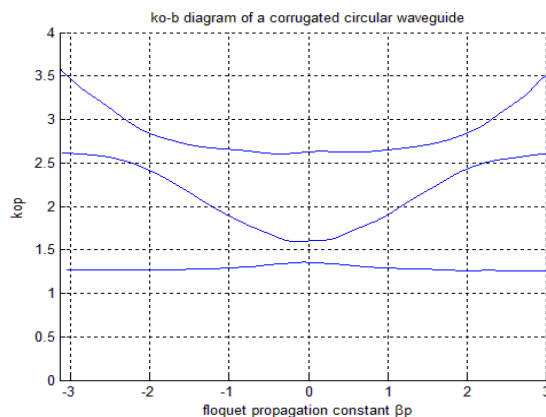


Figure 3: Dispersion characteristic for the first three Floquet modes for a corrugated circular waveguide with $r_1/r_o = 0.7$, $d_1 = 4$ mm, $d_2 = 5$ mm.

3. NUMERICAL RESULTS

In order to validate the present methodology an air filled circular waveguide, for which an analytical solution is available, is first analyzed as periodic structure by choosing an arbitrary length (p) as a unit cell. The results for the dominant mode (TE_{11}) dispersion curve are depicted in Fig. 2 against the corresponding analytical values and are almost identical (as expected). More important results are extracted from a corrugated circular waveguide as one can see in Fig. 3, where the normalized free space wavenumber (k_0p) versus the normalized Floquet wavenumber (βp) is presented. One may observe that the expected spectral band-stop (band-gap) and pass-band indeed appear. A variety of interesting results, including those for the periodic split-ring irises, will be presented at the symposium, along with suggestions for further work on periodic waveguides loaded with anisotropic media.

4. CONCLUSIONS

A periodic mode matching technique for circular waveguides is elaborated and particularly applied to periodically repeated irises on which Complementary Split Ring resonator are etched. While this effort is focused on the “infinite periodicity” the mode matching is readily offered for finite periodic structures by exploiting the Floquet expansion in the periodic section. This constitutes our next task along with a more rigorous eigenanalysis where the Floquet expansion will be directly incorporated within the unit cell.

ACKNOWLEDGMENT

This work was financially supported by the Greek Ministry of Education, Lifelong Learning and Religious Affairs through the research project THALIS Design Techniques for Digitally Controlled RF-Microwave Structures Appropriate for Software Defined-Cognitive Radio (RF-EIGEN-SDR).

REFERENCES

1. Barybin, A. A., “Modal expansions and orthogonal complements in the theory of complex media waveguide excitation by external sources for anisotropic and bianisotropic media,” Vol. 19, 241–300, 1998.
2. Marcuvitz, N., *Waveguide Handbook*, Peter Peregrinus Ltd., 1986.
3. Economou Filandras, P. A., A. P. Orphanides, C. Lavranos, and G. A. Kyriacou, “Mode matching analysis of split ring irises inserted in a circular waveguide,” *Mediterranean Microwave Symposium (MMS-08)*, Damascus, Syria, 2008.
4. Uher, J., J. Bornemann, and U. Rosenberg, *Waveguide Components for Antenna Feed Systems: Theory and CAD*, Artech House, 1993.
5. Pozar, D., *Microwave Engineering*, John Wiley, 2005.
6. Economou Filandras, P. A., Diploma Thesis, Democritus University of Thrace Department of EECE, Available Online at <http://microwaves.ee.duth.gr/>.

Using the Eigenfunction Expansion Technique for Analysis of the Electrodynamic Characteristics of a Loop Antenna Located on the Surface of a Magnetized Plasma Column

A. V. Kudrin¹, T. M. Zaboronkova², and A. S. Zaitseva¹

¹University of Nizhny Novgorod, Russia

²Technical University of Nizhny Novgorod, Russia

Abstract— The electrodynamic characteristics of a circular loop antenna located on the surface of an axially magnetized plasma column are studied using the eigenfunction expansion technique. The antenna has the form of an infinitesimally thin, perfectly conducting narrow strip coiled into a ring and is excited by a time-harmonic given voltage. The problem is reduced to a system of integral equations for the current. It is shown that solutions of these equations can be obtained in analytical form in the case where the column is filled with a resonant magnetoplasma.

1. INTRODUCTION

Much previous work on the electrodynamic characteristics of a loop antenna immersed in a magnetoplasma refers to the case where the plasma parameters are independent of the spatial coordinates (see, e.g., [1, 2] and references therein). In the past decade, a substantial degree of interest has been shown in the characteristics of loop antennas in inhomogeneous plasma media [3]. Of special interest is the case where the antenna is operated in the presence of an axially magnetized cylindrical plasma column. It is the purpose of the present work to find the electrodynamic characteristics of a circular loop antenna located on the surface of a column filled with a resonant magnetoplasma. By resonant magnetoplasma, we mean a cold collisionless magnetized plasma in which the refractive index of one of the characteristic modes tends to infinity at a certain angle between the wave vector and an external dc magnetic field [1–3].

2. FORMULATION OF THE PROBLEM

Consider an antenna having the form of an infinitesimally thin, perfectly conducting narrow strip of half-width d coiled into a circular loop of radius a ($d \ll a$). The antenna is located coaxially on the surface of a uniform circular plasma column aligned with the external dc magnetic field \mathbf{B}_0 (see Figure 1) which is parallel to the z axis of a cylindrical coordinate system (ρ, ϕ, z) . It is assumed that the column is surrounded by a homogeneous isotropic medium with dielectric permittivity $\varepsilon_{out} = \varepsilon_0 \varepsilon_a$, where ε_0 is the permittivity of free space. The medium inside the column is described by a general dielectric tensor with the following nonzero elements: $\varepsilon_{\rho\rho} = \varepsilon_{\phi\phi} = \varepsilon_0 \varepsilon$, $\varepsilon_{\rho\phi} = -\varepsilon_{\phi\rho} = -i\varepsilon_0 g$, and $\varepsilon_{zz} = \varepsilon_0 \eta$. The elements ε , g , and η of the plasma dielectric tensor are functions of the angular frequency ω , and expressions for them can be found elsewhere [3].

The antenna is excited by a time-harmonic ($\sim \exp(i\omega t)$) voltage which creates an electric field with the only nonzero azimuthal component E_ϕ^{ext} in a narrow angular interval (gap) $|\phi - \phi_0| \leq \Delta \ll \pi$ on the surface of the strip (i.e., at $\rho = a$ and $|z| < d$):

$$E_\phi^{ext}(a, \phi, z) = \frac{V_0}{2a\Delta} [U(\phi - \phi_0 + \Delta) - U(\phi - \phi_0 - \Delta)] [U(z + d) - U(z - d)]. \quad (1)$$

Here, $V_0 = \text{const}$ is a constant amplitude of the given voltage, U is a Heaviside function, and Δ is the angular half-width of the gap centered at $\phi = \phi_0$.

We restrict ourselves to consideration only of the case where the magnetoplasma inside the column is resonant. For such a plasma, the diagonal elements ε and η of the dielectric tensor should have opposite signs [3]. For definiteness, in what follows we will be discussing the case where $\varepsilon > 0$ and $\eta < 0$, which is encountered in many important applications [2, 3].

3. INTEGRAL EQUATIONS FOR THE ANTENNA CURRENT

We represent the excitation field E_ϕ^{ext} in the form

$$E_\phi^{ext} = \sum_{m=-\infty}^{\infty} A_m \exp(-im\phi), \quad (2)$$

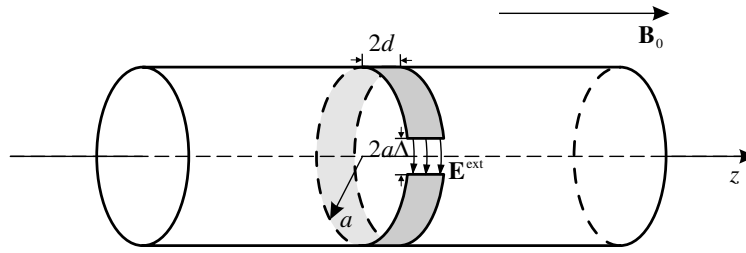


Figure 1: Geometry of the problem.

where

$$A_m = \frac{V_0}{2\pi a} \frac{\sin(m\Delta)}{m\Delta} \exp(im\phi_0). \quad (3)$$

The density \mathbf{J} of the electric current excited on the antenna by the field (1) can be sought as

$$\mathbf{J} = \phi_0 I(\phi, z) \delta(\rho - a), \quad (4)$$

where $|z| < d$, δ is a Dirac function, and $I(\phi, z)$ is the surface current density which admits the following representation:

$$I(\phi, z) = \sum_{m=-\infty}^{\infty} I_m(z) \exp(-im\phi). \quad (5)$$

To find $I(\phi, z)$, we express the azimuthal (E_ϕ) and longitudinal (E_z) components of the electric field excited by the current (4) in terms of unknown quantities $I_m(z)$ and then use the boundary conditions on the surface of the plasma column ($\rho = a$ and $-\infty < z < \infty$) along with the boundary conditions on the antenna surface ($\rho = a$ and $|z| < d$):

$$E_\phi + E_\phi^{ext} = 0, \quad E_z = 0. \quad (6)$$

After some lengthy algebra, the azimuthal and longitudinal components of the antenna-excited electric field at $\rho = a$ can be written as

$$\begin{bmatrix} E_\phi(a, \phi, z) \\ E_z(a, \phi, z) \end{bmatrix} = \sum_{m=-\infty}^{\infty} \exp(-im\phi) \int_{-d}^d \begin{bmatrix} K_m(z - z') \\ k_m(z - z') \end{bmatrix} I_m(z') dz'. \quad (7)$$

Here,

$$K_m(\zeta) = \sum_n \frac{2\pi a}{N_{m,n}} E_{\phi;m,n}^2(a) \exp(-ik_0 p_{m,n} |\zeta|) + \frac{ik_0}{2\pi} \int_0^\infty \frac{q}{p(q)} \sum_{l=1}^2 \sum_{k=1}^2 \frac{B_{mk}^{(l)}}{\Delta_m^{(l)}} \left[J_{m+1}(Q_k) + \alpha_k m \frac{J_m(Q_k)}{Q_k} \right] \exp(-ik_0 p(q) |\zeta|) dq, \quad (8)$$

$$k_m(\zeta) = \text{sgn}\zeta \left\{ \sum_n \frac{2\pi a}{N_{m,n}} E_{\phi;m,n}(a) E_{z;m,n}(a) \exp(-ik_0 p_{m,n} |\zeta|) + \frac{i}{2\pi a \eta} \int_0^\infty \frac{q}{p(q)} \sum_{l=1}^2 \sum_{k=1}^2 \frac{B_{mk}^{(l)}}{\Delta_m^{(l)}} n_k Q_k J_m(Q_k) \exp(-ik_0 p(q) |\zeta|) dq \right\}, \quad (9)$$

where J_m is a Bessel function of the first kind of order m , $k_0 = \omega/c$ is the wave number in free space, $E_{\phi;m,n}(\rho)$ and $E_{z;m,n}(\rho)$ are functions describing the distributions of eigenmodes over the transverse coordinate ρ of the azimuthal and longitudinal electric-field components of eigenmodes that are guided by the column and have the azimuthal and radial indices m and n , respectively ($m = 0, \pm 1, \pm 2, \dots$ and $n = 1, 2, \dots$), $N_{m,n}$ are the norms of the eigenmodes, $p_{m,n}$ are the eigenmode propagation constants normalized to k_0 , and $p(q) = (\epsilon_a - q^2)^{1/2}$ is the normalized propagation constant of the characteristic mode of the medium surrounding the column for the transverse wave number $q = k_\perp/k_0$ (it is assumed that $\text{Im}p(q) < 0$). Expressions for the fields and norms of the eigenmodes

supported by a magnetized plasma column as well as their dispersion properties are discussed in [3]. Other quantities in Equations (8) and (9) are written as

$$\begin{aligned}
 B_{m1}^{(l)} &= Z_0 \frac{k_0 a}{Q_1 J_m(Q_1)} \left[\frac{\eta}{\varepsilon_a} n_2 J_m^{(2)} \mathcal{H}_m^{(l)} + \frac{\eta}{\varepsilon_a} p \frac{m}{Q^2} \tilde{J}_m^{(2)} - n_2 (\mathcal{H}_m^{(l)})^2 + \frac{p^2 m^2}{\varepsilon_a Q^4} n_2 \right], \\
 B_{m2}^{(l)} &= Z_0 \frac{k_0 a}{Q_2 J_m(Q_2)} \left[-\frac{\eta}{\varepsilon_a} n_1 \tilde{J}_m^{(1)} \mathcal{H}_m^{(l)} - \frac{\eta}{\varepsilon_a} p \frac{m}{Q^2} J_m^{(1)} + n_1 (\mathcal{H}_m^{(l)})^2 - \frac{p^2 m^2}{\varepsilon_a Q^4} n_1 \right], \\
 \Delta_m^{(l)} &= (-1)^l \left\{ n_2 \left[\frac{\eta}{\varepsilon_a} J_m^{(1)} J_m^{(2)} - \left(J_m^{(1)} + \frac{\eta}{\varepsilon_a} J_m^{(2)} \right) \mathcal{H}_m^{(l)} \right] \right. \\
 &\quad \left. - n_1 \left[\frac{\eta}{\varepsilon_a} \tilde{J}_m^{(1)} \tilde{J}_m^{(2)} - \left(\tilde{J}_m^{(2)} + \frac{\eta}{\varepsilon_a} \tilde{J}_m^{(1)} \right) \mathcal{H}_m^{(l)} \right] \right. \\
 &\quad \left. + (n_2 - n_1) \left[(\mathcal{H}_m^{(l)})^2 - \frac{p^2 m^2}{\varepsilon_a Q^4} \right] + \frac{\eta}{\varepsilon_a} p \frac{m}{Q^2} \left[J_m^{(1)} + \tilde{J}_m^{(1)} - J_m^{(2)} - \tilde{J}_m^{(2)} \right] \right\}, \quad l = 1, 2, \\
 \alpha_k &= -1 + \frac{p^2(q) + q_k^2(p(q)) - \varepsilon}{g}, \quad n_k = -\frac{\varepsilon}{p(q)g} \left[p^2(q) + q_k^2(p(q)) + \frac{g^2}{\varepsilon} - \varepsilon \right], \\
 Q_k &= k_0 a q_k(p(q)),
 \end{aligned} \tag{10}$$

where

$$\begin{aligned}
 J_m^{(1)} &= \frac{J_{m+1}(Q_1)}{Q_1 J_m(Q_1)} + m \frac{\alpha_1}{Q_1^2}, \quad J_m^{(2)} = \frac{J_{m+1}(Q_2)}{Q_2 J_m(Q_2)} - m \frac{\beta_2}{Q_2^2}, \\
 \tilde{J}_m^{(1)} &= \frac{J_{m+1}(Q_1)}{Q_1 J_m(Q_1)} - m \frac{\beta_1}{Q_1^2}, \quad \tilde{J}_m^{(2)} = \frac{J_{m+1}(Q_2)}{Q_2 J_m(Q_2)} + m \frac{\alpha_2}{Q_2^2}, \\
 \mathcal{H}_m^{(l)} &= \frac{H_{m+1}^{(l)}(Q)}{Q H_m^{(l)}(Q)} - \frac{m}{Q^2}, \quad \beta_k = 1 + \frac{p(q)}{n_k}, \quad Q = k_0 a q, \quad k = 1, 2,
 \end{aligned} \tag{11}$$

$$q_k(p) = \frac{1}{\sqrt{2}} \left\{ \varepsilon - \frac{g^2}{\varepsilon} + \eta - \left(\frac{\eta}{\varepsilon} + 1 \right) p^2 - \left(\frac{\eta}{\varepsilon} - 1 \right) (-1)^k [(p^2 - P_b^2)(p^2 - P_c^2)]^{1/2} \right\}^{1/2},$$

$$P_{b,c} = \left\{ \varepsilon - (\eta + \varepsilon) \frac{g^2}{(\eta - \varepsilon)^2} + \frac{2\chi_{b,c}}{(\eta - \varepsilon)^2} [\varepsilon g^2 \eta (g^2 - (\eta - \varepsilon)^2)]^{1/2} \right\}^{1/2},$$

$\chi_b = -\chi_c = -1$, Z_0 is the impedance of free space, and $H_m^{(1)}$ and $H_m^{(2)}$ are Hankel functions of the first and second kinds, respectively. In the above formulas, q_1 and q_2 are the transverse wave numbers of two characteristic modes of a magnetoplasma for $p = p(q)$. The propagation constants $p = p_{m,n}$ of eigenmodes of the plasma column are found as roots of the equation $\Delta_m^{(2)}(p) = 0$. Thus, Equations (8)–(11) represent the kernels $K_m(\zeta)$ and $k_m(\zeta)$ in the form of expansion in terms of the discrete- and continuous-spectrum waves of the plasma column [3]. Such a representation significantly facilitates the analysis of properties of these kernels.

Using the boundary conditions (6) for the tangential components of the electric field on the antenna surface and allowing for Equations (2), (3), and (7), we obtain the integral equations

$$\int_{-d}^d K_m(z - z') I_m(z') dz' = -A_m, \tag{12}$$

$$\int_{-d}^d k_m(z - z') I_m(z') dz' = 0 \tag{13}$$

for the complex amplitudes of the angular harmonics $I_m(z)$ of the surface current density, where $|z| < d$.

4. SOLUTION OF THE INTEGRAL EQUATIONS

The kernels $K_m(\zeta)$ and $k_m(\zeta)$ of integral Equations (12) and (13) can be represented as the sums of singular and regular parts:

$$K_m(\zeta) = K_m^{(s)}(\zeta) + K_m^{(r)}(\zeta), \quad k_m(\zeta) = k_m^{(s)}(\zeta) + k_m^{(r)}(\zeta).$$

The singular parts $K_m^{(s)}(\zeta)$ and $k_m^{(s)}(\zeta)$ tend to infinity for $\zeta \rightarrow 0$, whereas the regular parts $K_m^{(r)}(\zeta)$ and $k_m^{(r)}(\zeta)$ remain finite in this limit and can be taken at $\zeta = 0$ if the antenna is so narrow that the following conditions take place:

$$d \ll a, \quad d \ll a|\eta/\varepsilon|^{1/2}, \quad k_0 d \ll 1, \quad (k_0 d)^2 \max\{|\varepsilon_a|, |\varepsilon|, |g|, |\eta|\} \ll 1. \quad (14)$$

The singular parts of the kernels can be written as

$$K_m^{(s)}(\zeta) = \sum_{n=n^*}^{\infty} \frac{2\pi a}{N_{m,n}} E_{\phi;m,n}^2(a) \exp(-ik_0 p_{m,n}|\zeta|) - iZ_0 \frac{k_0^2 a}{2} \int_0^{\infty} J_{m+1}^2(k_0 a q) \exp(-k_0 q|\zeta|) dq \\ + iZ_0 \frac{m^2}{\pi k_0 a^2} \frac{\varepsilon_a}{|\varepsilon\eta|} \int_0^{\infty} \frac{\mathcal{I}_m^2(k_0 a q)}{q U_m(q)} \exp\left(-k_0 \sqrt{-\frac{\varepsilon}{\eta}} q|\zeta|\right) dq, \quad (15)$$

$$k_m^{(s)}(\zeta) = \operatorname{sgn} \zeta \left\{ \sum_{n=n^*}^{\infty} \frac{2\pi a}{N_{m,n}} E_{\phi;m,n}(a) E_{z;m,n}(a) \exp(-ik_0 p_{m,n}|\zeta|) \right. \\ \left. + Z_0 \frac{m}{\pi a} \frac{\varepsilon_a}{|\varepsilon\eta|} \sqrt{-\frac{\varepsilon}{\eta}} \int_0^{\infty} \frac{\mathcal{I}_m^2(k_0 a q)}{U_m(q)} \exp\left(-k_0 \sqrt{-\frac{\varepsilon}{\eta}} q|\zeta|\right) dq \right\}. \quad (16)$$

Here,

$$U_m(q) = \mathcal{I}_{m+1}^2(k_0 a q) + \varepsilon_a^2 |\varepsilon\eta|^{-1} \mathcal{I}_m^2(k_0 a q),$$

where \mathcal{I}_m is a modified Bessel function of the first kind of order m . The quantity n^* in Equations (15) and (16) is a certain large positive integer such that the propagation constants of eigenmodes with the radial indices $n > n^*$ can be approximated as $p_{m,n} = \mu_n^{(m+1)} \sqrt{-\varepsilon/\eta} \xi (k_0 a)^{-1}$, where $\mu_n^{(m+1)}$ is the n th zero of the Bessel function J_{m+1} and ξ is a certain quantity depending on the ratio $|\varepsilon_a/\eta|$. It can be shown that in the case $|\varepsilon_a/\eta| \ll 1$, $\xi \simeq 1$. Expressions for $K_m^{(r)}(\zeta)$ and $k_m^{(r)}(\zeta)$, which are very cumbersome, can be derived in an evident manner, and are not given here for the sake of brevity.

Under conditions (14), the singular parts of the kernels are represented as

$$K_m^{(s)} = iZ_0 \frac{k_0}{2\pi} \left\{ \ln \frac{|\zeta|}{2a} + \psi\left(m + \frac{3}{2}\right) + \gamma \right. \\ \left. - \frac{4im^2}{(k_0 a)^2 \sqrt{|\varepsilon\eta|}} \left[\ln \frac{|\zeta|}{2a} + \ln\left(\pi \sqrt{-\frac{\varepsilon}{\eta}}\right) + \gamma + \psi\left(2n^* + m + \frac{3}{2}\right) + i\frac{\pi}{2} \right] \right. \\ \left. - \frac{\varepsilon_a}{|\varepsilon\eta|} \frac{4m^2}{(k_0 a)^2 (1 + \varepsilon_a^2 |\varepsilon\eta|^{-1})} \left[\frac{1}{2} \ln \frac{|\zeta|}{2a} + \frac{1}{2} \ln \sqrt{-\frac{\varepsilon}{\eta}} + \gamma + \psi\left(m + \frac{1}{2}\right) \right] \right\}, \quad (17)$$

$$k_m^{(s)}(\zeta) = -\frac{2m}{\zeta(1 + \varepsilon_a^2 |\varepsilon\eta|^{-1})} \left[\ln \sqrt{-\frac{\varepsilon}{\eta}} + 2\psi\left(m + \frac{1}{2}\right) + 2\gamma \right], \quad (18)$$

where $\gamma = 0.5772\dots$ is Euler's constant and $\psi(z) = d \ln \Gamma(z) / dz$ is the logarithmic derivative of a gamma function. As a result, integral Equations (12) and (13) are transformed as follows:

$$\int_{-d}^d I_m(z') \ln \frac{|z - z'|}{2a} dz' = -\alpha_m \frac{2\pi i A_m}{Z_0 k_0} - S_m \int_{-d}^d I_m(z') dz', \quad (19)$$

$$\int_{-d}^d m \frac{I_m(z')}{z - z'} dz' = 0, \quad (20)$$

where

$$\begin{aligned}\alpha_m &= -\frac{i(k_0a)^2\sqrt{|\varepsilon\eta|}}{m^2[4-2i(1+\varepsilon_a^2/|\varepsilon\eta|)^{-1}\varepsilon_a/\sqrt{|\varepsilon\eta|}]+i(k_0a)^2\sqrt{|\varepsilon\eta|}}, \\ S_m &= \frac{i\alpha_m}{(k_0a)^2\sqrt{|\varepsilon\eta|}} \left\{ -\frac{4im^2\varepsilon_a}{(1+\varepsilon_a^2/|\varepsilon\eta|)^{-1}\sqrt{|\varepsilon\eta|}} \left[\frac{1}{2} \ln \sqrt{-\frac{\varepsilon}{\eta}} + \gamma + \psi\left(m + \frac{1}{2}\right) \right] \right. \\ &\quad + 4m^2 \left[\ln\left(\pi\sqrt{-\frac{\varepsilon}{\eta}}\right) + \psi\left(2n^* + m + \frac{3}{2}\right) + \gamma + i\frac{\pi}{2} \operatorname{sgn}\varepsilon \right] \\ &\quad \left. + i(k_0a)^2\sqrt{|\varepsilon\eta|} \left[\psi\left(m + \frac{3}{2}\right) + \gamma - \frac{2i\pi}{Z_0k_0} K_m^{(r)}(0) \right] \right\}.\end{aligned}\quad (21)$$

When deriving Equation (20), we took into account the relation $k_m^{(r)}(0) = 0$. It can be shown that the solutions of Equations (19) and (20) are the main terms of the asymptotics of exact solutions to initial integral Equations (12) and (13) under conditions (14). It is a straightforward matter to verify that the solution to Equation (19) with the logarithmic kernel automatically satisfies the singular integral Equation (20) with the Cauchy kernel [2]. This fact allows us to consider only Equation (19). The solution to Equation (19) can be found using the techniques discussed in [2] and has the form

$$I_m(z) = \frac{2i}{Z_0k_0\sqrt{d^2-z^2}} \frac{A_m\alpha_m}{\ln(4a/d) - S_m}.\quad (22)$$

Substituting Equation (22) into (5), we obtain the following formula for the linear current density $I(\phi, z)$:

$$I(\phi, z) = \frac{iV_0}{Z_0\pi k_0a\sqrt{d^2-z^2}} \sum_{m=-\infty}^{\infty} \frac{\sin(m\Delta)}{m\Delta} \frac{\alpha_m}{\ln(4a/d) - S_m} \exp[-im(\phi - \phi_0)].\quad (23)$$

Despite the divergence of $I(\phi, z)$ for $|z| \rightarrow d$, which corresponds to the well-known Meixner condition at the edge, the total current $I_\Sigma(\phi)$ in the cross section $\phi = \text{const}$, yielded by integration of $I(\phi, z)$ over z between $-d$ and d , is finite. Upon calculation of $I_\Sigma(\phi)$, one can find the antenna input impedance $Z = V_0/I_\Sigma(\phi_0)$.

5. CONCLUSION

In this paper, we have developed a method for finding the solution to the problem of the current distribution and input impedance of a strip loop antenna located on the surface of an axially magnetized plasma column in an isotropic medium and operated in the resonant frequency band of a magnetoplasma. The solution is based on using the eigenfunction expansions of kernels of the integral equations for the current, describes its distribution both along and across the strip, and makes it possible to study the electrodynamic characteristics of such an antenna as functions of its parameters as well as the parameters of the plasma column.

ACKNOWLEDGMENT

This work was supported by the RFBR (Project No. 12-02-00747-a), the Government of the Russian Federation (Contract No. 11.G34.31.0048), the Russian Federal Program ‘‘Scientific and Education Personnel of the Innovative Russia’’ (Contract Nos. P313 and 02.740.11.0565), and the Greek Ministry of Education through the project THALIS (RF-EIGEN-SDR).

REFERENCES

1. Zaboronkova, T. M., A. V. Kudrin, and E. Yu. Petrov, ‘‘Toward the theory of a loop antenna in an anisotropic plasma,’’ *Radiophys. Quantum Electron.*, Vol. 41, No. 3, 236–246, 1998.
2. Kudrin, A. V., E. Yu. Petrov, and T. M. Zaboronkova, ‘‘Current distribution and input impedance of a loop antenna in a cold magnetoplasma,’’ *Journal of Electromagnetic Waves and Applications*, Vol. 15, No. 3, 345–378, 2001.
3. Kondrat’ev, I. G., A. V. Kudrin, and T. M. Zaboronkova, *Electrodynamics of Density Ducts in Magnetized Plasmas*, Gordon and Breach, Amsterdam, 1999.

A Characteristic Mode Eigenanalysis Exploiting FEM Features

R. Maximidis¹, C. L. Zekios¹, P. C. Allilomes¹, A. V. Kudrin², and G. A. Kyriacou¹

¹Microwaves Lab., Department of Electrical and Computer Engineering
Democritus University of Thrace, Xanthi, Greece

²Department of Radiophysics, University of Nizhny Novgorod, Russia

Abstract— A new technique of complex impedance matrix calculation based on finite element method (FEM), in contrast to the established use of Method of Moment (MoM) is proposed. The infinite solution domain is truncated with the introduction of a fictitious surface- S_f . For the field solution inside the surface- S_f the applied formulation is based on the finite element technique, being able to model inhomogeneous arbitrary shaped radiating 3D structures. The field solution in the semi-infinite domain outside S_f is expressed by an in principle infinite series expansion of spherical harmonics. The two solutions are bind together by enforcing the “exact” field continuity conditions strictly following a vector Dirichlet to Neumann map formalism. The overall procedure ends up to a final system with sole unknown the surface current distribution flowing over the metallic surfaces. This system defines the impedance matrix $[Z]$ and it is formulated and solved as a characteristic mode eigenproblem. Namely, separating the complex impedance matrix into a real $[R]$ and imaginary $[X]$ part, yields a real eigenproblem of the form $[X][I] = \lambda[R]$ is formulated and solved.

1. INTRODUCTION

The current work aims at the development of a numerical tool for the electromagnetic simulation and design of digitally controlled and multifunctional multiple input multiple output (MIMO) antennas integrated on the devices chassis and/or package utilizing Characteristic Mode theory. Several researchers already exploit characteristic modes for the antenna design, but their work is limited to geometries described by the Method of Moments (MoM), namely depending on the availability of the corresponding Green’s functions. Usually, only simple metallic surfaces of canonical shapes in free space are efficiently considered.

Characteristic mode eigenanalysis concerns the actual electric current densities flowing on the outer surface of possibly radiating objects as well as equivalent electric or magnetic current densities resulting from the adoption of a field (Loves) equivalence principle. According to [1], characteristic modes are real current modal distributions that correspond to the eigenvectors of a particular weighted eigenvalue equation, which involves the real and imaginary parts of the body impedance matrix. Thus, characteristic modes can be numerically computed for conducting bodies of arbitrary shape and since they comprize a set of orthogonal functions, they can be used to expand the total current on the surface of the body. One main drawback to the wide utilization of characteristic modes until now was the almost exclusive need of the Moment Method (MoM) for their extraction. The main MoM limitation factor lies in its dependence in the availability of the Greens functions corresponding to the particular structure. On the other hand the numerical evaluation of Greens functions (especially in its dyadic form) is as complex as the simulation of the entire structure and has to be repeated for every possible position and orientation of any elementary dipole source. To stress the complexity of the above procedure it is worth mentioning that usually its more preferable to calculate the Greens functions utilizing eigenfunctions expansions. It is obvious that this leads us to a closed loop, since it is not possible to define the eigenfunctions through Greens functions, which are by nature more complex and assume the eigenfunctions knowledge.

The novelty of the proposed research is a new technique of complex impedance matrix calculation based on Finite Element (FEM) method with similarities to Finite Element Tearing and Interconnect (FETI) (e.g., Zhao) [2], in contrast to the established use of MoM. The basic idea is as follows: If the structure is analyzed solving the electric field vector wave equation, then at the boundary of the solution domain (or on all the metallic surfaces) current densities are defined through the tangential magnetic field. The three dimensional solution domain is actually divided in a finite and semi-infinite domain by a fictitious surface S_f . Outside the surface S_f the field is expressed in an infinite sum of spherical harmonics known from the analytical solution of the wave equation in free space. This expansion satisfies the radiation condition of the studied structure. Inside surface S_f the field is established with the aid of finite element technique. The solution

domain is discretized by tetrahedral edge elements to exploit their flexibility for the description of any arbitrary geometry. The two solutions are bind together through the surface integral of the FEM weak form and following the Dirichlet to Neumann map formalism described in the next section. The final system is manipulated in such a way that the internal field distribution is obliterated ending up to a system with sole unknown the desired surface current distribution. This system indeed defines the impedance matrix $[Z]$ and is of the same form as defined as an eigenvalue problem $[Z][I] = 0$. This, eventually, will be formulated and solved as a characteristic mode eigenproblem. Namely, separating the complex impedance matrix into a real $[R]$ and imaginary $[X]$ parts, a real eigenproblem of the form $[X][I] = \lambda[R]$ is formulated and solved according to [1]. The use of FEM allows the eigenanalysis of complex structures loaded with inhomogeneous and/or anisotropic media, such as the chassis, or the frame package of mobile devices which can even be curved for conformal integration to the devices.

2. FORMULATION

Let us assume the general geometry of Figure 1. It is an open cavity (a chassis, or the frame package of a mobile device) enclosed inside a fictitious spherical surface noted as S_f . The goal of this work is to end up to a final matrix, the impedance matrix of the analyzed structure to form and solve the characteristic mode eigenproblem. The novelty of the proposed research is to replace the established MoM technique with the FEM technique to exploit the advantages of the second one handling any arbitrary structure versus the rigidness and stiffness of the MoM with complex structures. Thus, initially the problem is manipulated in such a way that the impedance matrix can be retrieved to apply the characteristic mode theory.

The electromagnetic behaviour within the enclosed region (I) the electric field wave equation for a source free region tensor permittivity ($\bar{\epsilon}_r$) and permeability ($\bar{\mu}_r$) materials reads:

$$\nabla \times \bar{\mu}_r^{-1} \cdot \nabla \times \bar{E} - k_0^2 \bar{\epsilon}_r \bar{E} = 0 \quad (1)$$

Applying the standard Galerkin procedure to Eq. (1) the following weak formulation can be derived [3]:

$$\iiint_V (\bar{\nabla} \times \bar{T}) \cdot \bar{\mu}_r^{-1} \cdot (\bar{\nabla} \times \bar{E}) dV - k_0^2 \iiint_V \bar{T} \cdot (\bar{\epsilon}_r \bar{E}) dV - jk_0 \oint_S \bar{T} \cdot (\hat{n} \times \bar{H}) dS = 0 \quad (2)$$

where $k_0 = \omega/c$ is the free space wavenumber, \bar{T} is the vector weighting function and V denotes the space of region (II), which is enclosed by the artificial spherical surface- S_{f_i} . This actually offers the means to connect the two solution between the inner and outer regions through the accurate enforcement of the field continuity conditions. These are ensured by strictly following Dirichlet-to-Neumann mapping mathematical formalism. In the outer region (I), since the medium is homogeneous and source free, the field is expanded in terms of radial TE^r and TM^r modes, or equivalently in an infinite expansion of the well known eigenfunctions for the electric and the

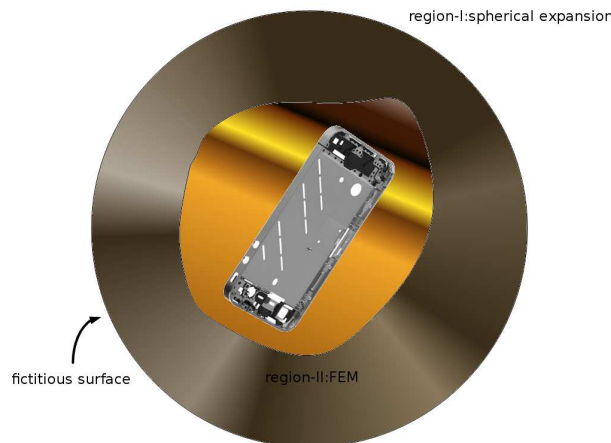


Figure 1: A three dimensional open cavity.

magnetic field components respectively [4]:

$$E_r^I = \frac{1}{j\omega\mu_0\epsilon_0} \cdot \sum_{l=0}^{\infty} \left(\sum_{m=-l}^l k_0^2 \cdot a_{lm} \cdot \left(h_l^{(2)}(k_0 r) + h_l^{(2)'}(k_0 r) \right) \cdot P_l^{|m|}(\cos(\theta)) \cdot e^{jm\phi} \right) \quad (3)$$

$$H_r^I = \frac{1}{j\omega\mu_0\epsilon_0} \cdot \sum_{l=0}^{\infty} \left(\sum_{m=-l}^l k_0^2 \cdot f_{lm} \cdot \left(h_l^{(2)}(k_0 r) + h_l^{(2)'}(k_0 r) \right) \cdot P_l^{|m|}(\cos(\theta)) \cdot e^{jm\phi} \right) \quad (4)$$

The terms a_{lm} and f_{lm} are unknown weighting factors of the magnetic and the electric potential respectively, the $P_l^{|m|}$ are the Legendre functions and the $h_l^{(2)}(k_0 r)$ are the second type spherical Hankel functions of order l .

Following the DtN formalism the outer expression is written in terms of the inner/numerical expansion (Dirichlet data) enforcing the electric field continuity over the surface- S_f . The coefficients a_{lm} and f_{lm} are defined exploiting the orthogonality properties of the functions $e^{jm\phi}$ and $P_l^{|m|}$. Thus, the weighting factor a_{lm} and f_{lm} can be given in a compact form as:

$$a_{lm} \propto (\dots) \int_0^{2\pi} \int_0^\pi E^{FEM} \cdot P_l^{|m|}(\cos(\theta)) \cdot \sin^2(\theta) \cdot e^{jm\phi} d\theta d\phi \quad (5)$$

$$f_{lm} \propto (\dots) \int_0^{2\pi} \int_0^\pi E^{FEM} \cdot P_l^{|m|}(\cos(\theta)) \cdot \sin^2(\theta) \cdot e^{jm\phi} d\theta d\phi \quad (6)$$

According now to the second step of the DtN formalism the Neumann data are being established. The field in region-I is differentiated in order to establish the DtN map, so as to obtain the Neumann data along the separation surface. This differentiation is actually provided by the electric field curl equation itself. For this reason the coefficients a_{lm} and f_{lm} obtained above, are substituted back into the expression of the tangential magnetic field to yield the following formal Dirichlet to Neumann map:

$$H^I \propto (\dots) \int_0^{2\pi} \int_0^\pi E^{FEM} \cdot P_l^{|m|}(\cos(\theta)) \cdot \sin^2(\theta) \cdot e^{jm\phi} d\theta d\phi \quad (7)$$

The third step of DtN asks for the enforcement of the electric field normal derivatives continuity along the surface S_f . This herein reads as requiring the tangential components of the magnetic field expansion to be equal to that of the FEM field description along the separation surface. So the surface integral of FEM in Eq. (2) can be derived by exploiting the DtN map given by the expansion of Eq. (7) and using the continuity of the magnetic field. As it occurs the surface integral serves the coupling of the two field expressions and thus, the radiation condition is actually introduced in the functional of FEM. The resulting expression, after some algebraic manipulations can be brought in a matrix form as:

$$A(k_0)[e] = 0 \quad (8)$$

The next step is to retrieve magnetic field components tangential to the structure metallic surfaces, or equally to modify the matrix in a such a way that the characteristic mode theory can be applied. For this purpose the system matrix A should be subdivided into four parts, to be written as:

$$\begin{bmatrix} A_{ii}(k_0) & A_{is}(k_0) \\ A_{si}(k_0) & A_{ss}(k_0) \end{bmatrix} \begin{bmatrix} e_i \\ e_s \end{bmatrix} = 0 \quad (9)$$

where the subscripts 'i' and 's' denote the internal and metallic surface edges of the mesh respectively. Solving the system of Eq. (9) for e_s a final form can be derived with the only unknown the surface degrees of freedom. Thus, the desired $[Z]$ matrix can be expressed as:

$$\left[A_{ss}(k_0) - A_{si}(k_0) \cdot A_{ii}^{-1}(k_0) \cdot A_{is}(k_0) \right] \begin{bmatrix} e_s \end{bmatrix} = 0 \quad (10)$$

$$\begin{bmatrix} Y(k_0) \end{bmatrix} \begin{bmatrix} e_s \end{bmatrix} = 0 \quad (11)$$

where $[Y(k_0)] = [A_{ss}(k_0) - A_{si}(k_0) \cdot A_{ii}^{-1}(k_0) \cdot A_{is}(k_0)]$ and $[Z(k_0)] = [Y(k_0)]^{-1}$. According now to the characteristic mode theory the matrix $[Z]$ is split into its real $[R]$ and imaginary $[X]$ part forming the eigenproblem:

$$[X][I]_n = \lambda_n[R][I]_n \quad (12)$$

This real generalized eigenproblem represents the so called characteristic modes. Its real eigenvalues λ_n offer a unique physical insight, since their values define the radiation effectiveness of the corresponding eigenfunction-eigencurrent. In general the eigenvalues λ_n range from $-\infty$ to $+\infty$ and provide us with different information about the physical behavior of the characteristic modes. Eigenvalues that tend to zero represent a characteristic mode resonance (this is the optimum radiator), while eigenvalues that tend to ∞ represent an internal resonance mode. Thus it is of critical importance to track the moving trace of each eigenvalue while the structure is being analyzed at different frequencies to get dispersion curves of the form $\lambda_n - f$. The zero crossing of these curves represents the eigencurrents resonances at which the structure behave as an optimal radiator. Besides that, the eigencurrents distribution offer the knowledge for their excitation providing operation at multiple frequencies and/or multiple polarization which can in principle being excited simultaneously if necessary.

3. NUMERICAL RESULTS

A cavity backed patch antenna (Figure 2) is studied in two steps. Firstly a characteristic mode eigenanalysis of the single patch (a plane in the free space) is elaborated, while in turn a total characteristic mode eigenanalysis of the structure is adopted. The patch is 4 [cm] \times 3 [cm] and it is recessed in a 8 [cm] \times 6 [cm] \times 0.1 [cm] cavity, that is homogeneously filled with dielectric $\epsilon_r = 2.0$.

For the volume of the structure a discretization of 10983 tetrahedrals was initialized, while the surface of the metallic patch was discretized by 2768 triangles. The proposed method is currently under validation.

For the first simulation procedure both the classical characteristic mode eigenanalysis (based on Method of Moments, MoM) and the proposed characteristic mode eigenanalysis (based on a FEM matrix) was elaborated. The patch seems to resonate for both techniques at 3.75 [GHz], Table 1. However, the proposed technique presents some spurious modes due to the ill-conditioning of the constructed matrix.

For the second step the simulation of the whole cavity backed antenna was elaborated. In Table 2 the numerical evaluation of the two first resonant frequencies is introduced. The first 3 values appearing in the table are spurious modes, which are actually under consideration. To

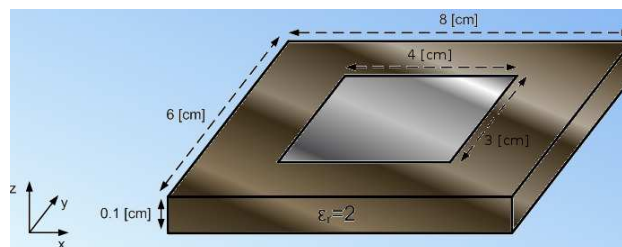


Figure 2: A cavity backed patch antenna geometry

Table 1: Resonant frequencies of a rectangular patch antenna 4 [cm] \times 3 [cm].

	proposed technique f [GHz]	MoM f [GHz]
1	0.11	-
2	0.11	-
3	0.11	-
4	3.71	3.75
5	4.95	5.00

Table 2: Cavity backed patch antenna resonant frequencies.

	proposed technique f [GHz]	HFSS f [GHz]
1	0.11	-
2	0.11	-
3	0.11	-
4	2.78	2.81
5	4.79	4.80

validate our results the commercial electromagnetic simulator HFSS was used. However, HFSS doesn't support an eigenanalysis for open radiating structures, thus a simulation procedure of a plane wave scattering on the patch was adopted for a frequency sweep from 1 [GHz] to 20 [GHz]. The patch antenna seems to efficiently radiate at 2.8 [GHz] and 4.8 [GHz] with both simulation procedures, the proposed and the HFSS.

4. CONCLUSION

A FEM based methodology is formulated providing the complex impedance matrix open-radiating three dimensional structures. This offers the means to circumvent the Moment Method necessity for the knowledge of arbitrary structures Green's functions, thus sometimes the proposed method is known as "numerical Green's functions evaluation". A lot of effort is still necessary in order to establish this methodology running various tests and especially to specialize its usage in the formulation and solution of various types of Characteristic modes eigenanalysis. This effort starts from this work focusing on the electric eigencurrents flowing along the metallic surfaces, but it can be readily extended to equivalent magnetic eigencurrents flowing on material surfaces/interfaces and ultimately to challenging complicated surfaces of metals with slots printed on curved media which may require both electric and magnetic eigencurrents.

ACKNOWLEDGMENT

This work was financially supported by the Greek Ministry of Education, Lifelong Learning and Religious Affairs through the research project THALIS Design Techniques for Digitally Controlled RF-Microwave Structures Appropriate for Software Defined — Cognitive Radio (RF-EIGEN-SDR).

REFERENCES

1. Harrington, R. F. and J. R. Mautz, "Theory of characteristic modes for conducting bodies," *IEEE Trans. on Antennas and Propagation*, Vol. 19, 622–628, 1971.
2. Zhao, K., "A domain decomposition method for solving electrically large electromagnetic problems," *Doctoral Thesis*, Ohio State University, 2007.
3. Zhu Y. and A. C. Cangellaris, *Multigrid Finite Element methods for Electromagnetic Field Modeling*, Wiley Interscience, NY, 2006.
4. Balanis, C. A., *Advanced Engineering Electromagnetics*, 1st Edition, Wiley, NY, 1989.

Computational Efficient Solution of Maxwell's Equations for Lamellar Gratings

I. Semenikhin¹, M. Zanucoli², V. Vyurkov¹, E. Sangiorgi², and C. Fiegna²

¹Institute of Physics and Technology RAS, Moscow 117218, Russia

²ARCES-DEIS University of Bologna and IUNET, Cesena (FC) 47521, Italy

Abstract— In this work, a new implementation of the analytic modal method (AMM) based on an improved and computationally efficient approach to calculate the eigenvalues and corresponding eigenfunctions of the Helmholtz equation is presented. In case of TE polarization the computational time is remarkably reduced by adopting the perturbation approach. The portion of the computation time required to calculate eigenfunctions in case of TE polarization become almost negligible when a large number of eigenfunctions in the expansion is used. In case of TM polarization we use the pseudospectral method to calculate an initial guess solution for eigenvalues which are subsequently refined by Newton's method. The proposed improved AMM allows to calculate the electromagnetic field in arbitrary stack of lamellar gratings.

1. INTRODUCTION

Over the past three decades, a large number of algorithms have been developed to solve Maxwell's equations for the analysis of diffraction gratings and other periodic structures. Among them, the algorithms based on eigenmode expansion are widely used. According to these methods, the simulation domain is divided into layers featuring parallel interfaces within which the permittivity varies only in the plane of the layer and is constant along the perpendicular direction allowing the separation of variables (Fig. 1). Within each layer the eigenmodes of the electromagnetic field are calculated and the general solution is then expressed by means of an eigenmode expansion. The expansion coefficients can be calculated by applying proper boundary conditions. Several implementations of this general approach have been proposed for the two-dimensional (2-D) case [1–11], for which the dielectric constant within each parallel layer depends only on one spatial coordinate and, in order to obtain the eigenmodes, the one-dimensional Helmholtz equation has to be solved.

Most proposed implementations differ only by a set of basis functions, through which the eigenfunctions are expressed. However, disregarding the attained accuracy level such approaches merely approximate the eigenfunctions of the Helmholtz equation. For example the Rigorous Coupled-Wave Analysis method (RCWA) [1] uses complex Fourier series expansion. The Polynomial expansion modal method (PEMM) [2] and the modal method by Gegenbauer polynomial expansion (MMGE1) [3] exploit the Legendre/Chebyshev polynomials and the Gegenbauer polynomials respectively. In [4, 5] the eigenfunctions are expressed by the B-splines and in [6, 7] the pseudospectral method for the Chebyshev polynomials (PSMM) is adopted. On the other hand the form of the exact eigenfunctions for piecewise constant permittivity can be explicitly written, consequently the only problem that remains is to find the corresponding eigenvalues. In [8, 9] the analytic modal method (AMM) has been proposed and the solution for a simple rectangular grating has been derived through the roots of the transcendental equation by using the theory of analytic functions. Subsequently in [10], another method, which involves the solution of differential equations in order to calculate the roots, has been presented; in such approach the initial condition corresponds to

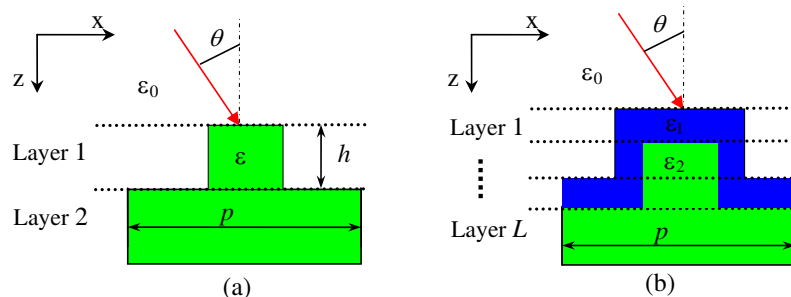


Figure 1: The grating configurations discussed in Section 3: one period is depicted.

that of the counterpart grating featuring real dielectric constant, for which the solution can be straightforwardly determined. This method has been already extended in order to be applied to multi-groove gratings [11].

In this work, we present a new implementation of AMM, exploiting an improved and computationally efficient approach to calculate the eigenvalues. In case of TE polarization an initial guess solution is obtained by applying the perturbation theory for adjacent levels, then the solution is refined by means of modified Newton's method. These approaches considerably reduce the computational time. In the case of TM polarization we use the pseudospectral method to calculate an initial guess solution. The implementation of AMM proposed in this work allows the general approach to calculate arbitrary stack of lamellar gratings.

The remainder of this paper is organized as follows. The implementation of the proposed approach is described in detail in Section 2, in which the TE and the TM polarizations are discussed separately. Finally, in Section 3 the application of the improved AMM to a metal grating featuring a rectangular groove profile is presented, showing that the proposed implementation features a remarkably reduced computational time with respect to the FMM in case of TE -polarization.

2. IMPLEMENTATION

In case of TE polarization the electric field at each s -th layer satisfies the following equation:

$$\frac{\partial^2 E_y}{\partial z^2} + \frac{\partial^2 E_y}{\partial x^2} = -k_0^2 \varepsilon_s(x) E_y, \quad E_x = E_z = 0, \quad (TE) \quad (1)$$

where $\varepsilon_s(x)$ is the relative dielectric constant of the s -th layer, $k_0^2 = (2\pi)^2 \lambda^{-2}$ and λ is the wavelength of the incident radiation. The relative permeability is set equal to unity. The incident wave is described by $E_y^{inc} = e^{ik_0 n_0 (x \sin(\theta) + z \cos(\theta))}$, where θ is the angle of incidence of the radiation with respect to the normal to the device plane (Fig. 1). After separating the variables in Eq. (1), the solution of such equation within each s -th layer can be written as:

$$E_y(x, z) = \sum_n \left(c_{s,n}^+ e^{ik_0 \sqrt{\kappa_s^n} z} + c_{s,n}^- e^{-ik_0 \sqrt{\kappa_s^n} z} \right) \psi_s^n(x), \quad (2)$$

where κ_s^n and $\psi_s^n(x)$ are, respectively, the eigenvalues and eigenfunctions, of the one-dimensional Helmholtz equation:

$$\frac{\partial^2 \psi_s(x)}{k_0^2 \partial x^2} + \varepsilon_s(x) \psi_s(x) = \kappa_s \psi_s(x). \quad (3)$$

Dividing the s -th layer into J regions, within which the permittivity is spatially uniform, the solution of Eq. (3) for each j -th region ($j = 1, \dots, J$) can be written in the form:

$$\psi_{s,j}(x) = a_{s,j} e^{ik_0 \sqrt{\varepsilon_{s,j} - \kappa_s} x} + b_{s,j} e^{-ik_0 \sqrt{\varepsilon_{s,j} - \kappa_s} x}, \quad (4)$$

where the coefficients $a_{s,j}$, $b_{s,j}$ are determined by assuming the continuity of the function $\psi_s(x)$ and of its first derivative at the boundaries x_j of these regions:

$$\begin{aligned} a_{s,1} e^{ik_0 \sqrt{\varepsilon_{s,1} - \kappa_s} x_1} + b_{s,1} e^{-ik_0 \sqrt{\varepsilon_{s,1} - \kappa_s} x_1} &= a_{s,2} e^{ik_0 \sqrt{\varepsilon_{s,2} - \kappa_s} x_1} + b_{s,2} e^{-ik_0 \sqrt{\varepsilon_{s,2} - \kappa_s} x_1} \\ \sqrt{\varepsilon_{s,1} - \kappa_s} \left(a_{s,1} e^{ik_0 \sqrt{\varepsilon_{s,1} - \kappa_s} x_1} - b_{s,1} e^{-ik_0 \sqrt{\varepsilon_{s,1} - \kappa_s} x_1} \right) &= \sqrt{\varepsilon_{s,2} - \kappa_s} \left(a_{s,2} e^{ik_0 \sqrt{\varepsilon_{s,2} - \kappa_s} x_1} - b_{s,2} e^{-ik_0 \sqrt{\varepsilon_{s,2} - \kappa_s} x_1} \right) \\ \dots & \\ a_{s,J} e^{ik_0 \sqrt{\varepsilon_{s,J} - \kappa_s} p} + b_{s,J} e^{-ik_0 \sqrt{\varepsilon_{s,J} - \kappa_s} p} &= e^{ik_0 n_0 p \sin(\theta)} (a_{s,1} + b_{s,1}) \\ \sqrt{\varepsilon_{s,J} - \kappa_s} \left(a_{s,J} e^{ik_0 \sqrt{\varepsilon_{s,J} - \kappa_s} p} - b_{s,J} e^{-ik_0 \sqrt{\varepsilon_{s,J} - \kappa_s} p} \right) &= e^{ik_0 n_0 p \sin(\theta)} \sqrt{\varepsilon_{s,1} - \kappa_s} (a_{s,1} - b_{s,1}) \end{aligned} \quad (5)$$

In the last two equations of Eq. (5), the Floquet conditions are applied at the boundary of the period: $E_y(x+p, z) = e^{ik_0 n_0 p \sin(\theta)} E_y(x, z)$, where $n_0 = \sqrt{\varepsilon_0}$ is the refraction index of the environment. The values κ_s for which the system of Eq. (5) has a nonzero solution, i.e., the determinant of the system of Eq. (5) is equal to zero, are the eigenvalues of Eq. (3). It should be noted that the determinant of the system of Eq. (5) can be calculated exploiting a number of arithmetic operations in the order of J only. We enumerate the set of values κ_s^n , $n = 1, \dots, \infty$, in descending order of the real part κ_s^n .

Thus, for large absolute values of κ_s^n the increase in the number n , corresponds to an increase in magnitude of the second derivative (the number of oscillations) of the eigenfunction $\psi_{s,j}^n$ in Eq. (3). The number of functions N in Eq. (2) depends on the required accuracy of $E_y(x, z)$.

In case of homogeneous layers it is possible to write:

$$\kappa_s^n = \varepsilon_s - (n_0 \sin(\theta) + n\lambda/p)^2, \quad n = 0, \pm 1, \pm 2, \dots, \quad (6)$$

Therefore $a = 1$, $b = 0$ and the eigenfunction $\psi_s^n(x)$ has the form:

$$\psi_s^n(x) = e^{ik_0 n_0 x \sin(\theta) + i2\pi n x/p}. \quad (7)$$

In the most general case, we have to find N roots of the equation $F(\kappa_s^n) = 0$, in descending order of the real part κ_s^n , where the function F denotes the determinant of Eq. (5). After that, coefficients $a_{s,j} b_{s,j}$ can be calculated for every κ_s^n by solution of the system of Eq. (5). If the Newton's method is adopted in order to find the roots $F(\kappa_s^n)$, it always converges to the correspondent roots, depending upon the initial guess solution. However, if any root κ_s^n , $n < N$ in the calculation is not included, all further increase in the number of functions in Eq. (2) may be not effective, because it does not improve the accuracy better than some constant value that depends on the order of magnitude of the multiplier in brackets in Eq. (2) corresponding to the non considered eigenfunctions $\psi_s^n(x)$. Therefore, the initial guess must be chosen very accurately. To find the initial guess we adopt the method of perturbation theory for adjacent levels. As unperturbed system we choose the system featuring the uniform permittivity which is independent of the coordinates. We assume the value of this permittivity equal to the environment dielectric constant. According to the first-order perturbation theory $\kappa_s^n \approx \kappa_0^n + \delta\kappa_s^n$, where κ_0^n is defined by Eq. (6) and $\delta\kappa_s^n$ is the appropriate eigenvalue of the matrix \mathbf{B} which is calculated by means of the eigenfunctions corresponding to κ_0^n and of the eigenvalues closest to κ_0^n :

$$B_{l,m} = \int_0^p \psi_0^{l*} (\varepsilon_s(x) - \varepsilon_0) \psi_0^m dx = \frac{1}{i2\pi(m-l)} \sum_{j=1, \dots, J} \varepsilon_s^j \left(e^{i2\pi(m-l)x_j/p} - e^{i2\pi(m-l)x_{j-1}/p} \right) - \varepsilon_0 \delta_{l,m}, \quad (8)$$

where ψ_0^m is the eigenfunction corresponding to κ_0^m . The required number of unperturbed states M which are used to calculate \mathbf{B} can be determined by comparing the approximate eigenvalue with that refined by Newton's method. If the difference is within an order of magnitude or greater than the distance between nondegenerate eigenvalues close to κ_0^n , the number of required states M have to be increased. Generally, when the values κ_0^n are several times larger than the maximum variation of $\varepsilon_s(x)$ in the s -th layer no more than three unperturbed states are required. On the other hand, in order to purify the root κ_0^n , only few iterations of Newton's method are necessary. Therefore the computation time required to find the eigenfunctions become negligible in comparison with other operations especially when a relatively large number of eigenfunctions in the expansion are adopted. In order to avoid the convergence of Newton's method to the previously calculated closed values κ_s^l , the root κ_0^n of the function $F(\kappa_s^n) / \prod_l (\kappa_s^n - \kappa_s^l) = 0$ can be found. With the aim of determining the coefficients $c_{s,n}^+$, $c_{s,n}^-$, the continuity conditions for $E_y(x, z)$ and $\partial E_y(x, z)/\partial z$ are assumed at the boundary of the layer s :

$$\begin{aligned} & \sum_{n=1, \dots, N} \left(c_{s-1,n}^+ e^{ik_0 \sqrt{\kappa_{s-1}^n} z_s} + c_{s-1,n}^- e^{-ik_0 \sqrt{\kappa_{s-1}^n} z_s} \right) \psi_{s-1}^n(x) \\ &= \sum_{n=1, \dots, N} \left(c_{s,n}^+ e^{ik_0 \sqrt{\kappa_s^n} z_s} + c_{s,n}^- e^{-ik_0 \sqrt{\kappa_s^n} z_s} \right) \psi_s^n(x) \\ & \quad \sum_{n=1, \dots, N} \left(c_{s-1,n}^+ e^{ik_0 \sqrt{\kappa_{s-1}^n} z_s} - c_{s-1,n}^- e^{-ik_0 \sqrt{\kappa_{s-1}^n} z_s} \right) \sqrt{\kappa_{s-1}^n} \psi_{s-1}^n(x) \\ &= \sum_{n=1, \dots, N} \left(c_{s,n}^+ e^{ik_0 \sqrt{\kappa_s^n} z_s} - c_{s,n}^- e^{-ik_0 \sqrt{\kappa_s^n} z_s} \right) \sqrt{\kappa_s^n} \psi_s^n(x). \end{aligned} \quad (9)$$

By multiplying Eq. (9) by $e^{-i2\pi m x/p}$, $m = 1, \dots, N$ and by integrating analytically over x it is possible to obtain a system of linear equations relating the coefficients $c_{s-1,n}^+$, $c_{s-1,n}^-$ and $c_{s,n}^+$, $c_{s,n}^-$.

By means of simple algebraic manipulations this system can be reduced to the form:

$$\begin{pmatrix} \mathbf{c}_s^+ \\ \mathbf{c}_{s-1}^- \end{pmatrix} = \mathbf{S}^{(s-1 \rightarrow s)} \begin{pmatrix} \mathbf{c}_{s-1}^+ \\ \mathbf{c}_s^- \end{pmatrix}. \quad (10)$$

The coefficients \mathbf{c} of Eq. (2) can be found by properly combining the \mathbf{S} matrices of all layers and by applying the boundary condition at the superstrate and at the substrate.

In case of *TM* polarization the equation for the magnetic field at each s -th layer is given by:

$$\frac{\partial^2 H_y}{\partial z^2} = -\varepsilon_s(x) \frac{\partial}{\partial x} \left(\frac{1}{\varepsilon_s(x)} \frac{\partial H_y}{\partial x} \right) - k_0^2 \varepsilon_s(x) H_y, \quad H_x = H_z = 0, \quad (TM). \quad (11)$$

Formulas similar to those of Eqs. (2)–(7), (9) and (10) derived for the *TE* case are valid also for *TM*; the only difference is that the corresponding first derivatives of H_y divided by the dielectric constant need to be equated with, i.e., $(1/\varepsilon) \cdot \partial H_y / \partial z$ at the boundaries between layers and $(1/\varepsilon) \cdot \partial H_y / \partial x$ at the boundaries between regions featuring different dielectric constant within each layer. However, in contrast to the *TE* polarization, the method of perturbation theory in this case is not suitable therefore in order to find approximate eigenvalues we adopt the pseudospectral method proposed in [6] in which the number of collocation points are $2N$ where N is the number of modes. The accuracy of the approximate values obtained by this method is suitable to allow the convergence of the Newton's method to the correct root by exploiting only few iterations.

3. NUMERICAL RESULTS

As example of application of the method discussed this paper, the structure considered in [3–6] has been adopted. In particular we consider a metal grating featuring a rectangular groove profile with periodicity $p = 1 \mu\text{m}$, height h equal to the periodicity and width of the rectangular profile equal to half period (Fig. 1(a)). The dielectric permittivity of the lattice material and of the external environment are $\varepsilon = (0.22 + 6.71i)^2$ and $\varepsilon_0 = 1$, respectively. The wavelength λ of the incident field forming an angle of incidence $\theta = 30^\circ$ is equal to $1 \mu\text{m}$. In Fig. 2(a) is reported a comparison of the relative accuracy of the diffraction efficiency of the minus-first reflected order R_{-1} obtained by means of the presented method and by the FMM for the same number of the expansion modes in *TE* case. As reference value we use $R_{-1} = 0.7342788519301$, obtained by AMM with the number of eigenmodes $N = 2001$. It is worth noting that to purify the eigenvalues by the Newton's method we use quad precision. The computation time required to find the eigenfunctions in case of AMM was more than ten times smaller than that required by FMM case for $N = 2001$. In Fig. 2(b) the relative accuracy of the zero reflected order R_0 for *TM* case is presented. As reference value, we use $R_0 = 0.8484817$, obtained with the number of eigenmodes $N = 3001$. For a given number of expansion modes the time required by AMM in case of *TM*-polarization is longer than that for FMM, but it is compensated by better accuracy as shown in Fig. 2(b), therefore we can use a much smaller number of modes in practical applications.

The second example of the proposed method is the investigation of the relative accuracy of the reflectance for the structure of Fig. 1(b) in which the groove ($\varepsilon_2 = (3.73 + 0.009i)^2$) is covered by

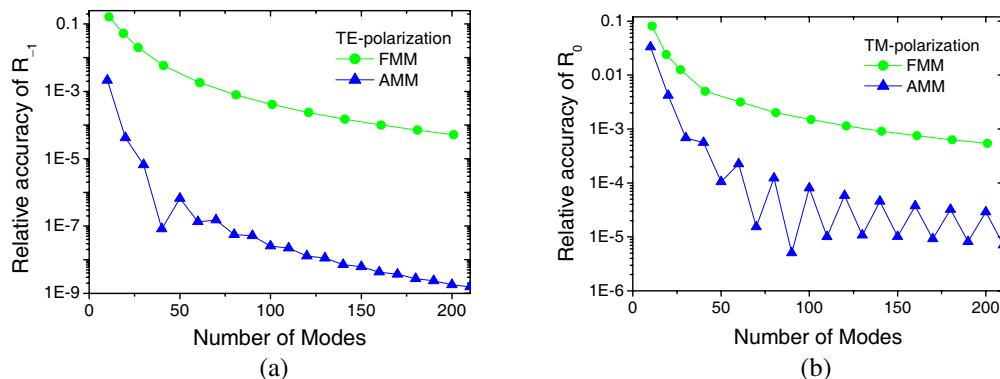


Figure 2: The relative accuracy of the diffraction efficiencies for the structure of Fig. 1(a) at $\lambda = 1 \mu\text{m}$ obtained by adopting the presented AMM method and by using the FMM as function of the number of the expansion modes in (a) *TE* and (b) *TM* case.

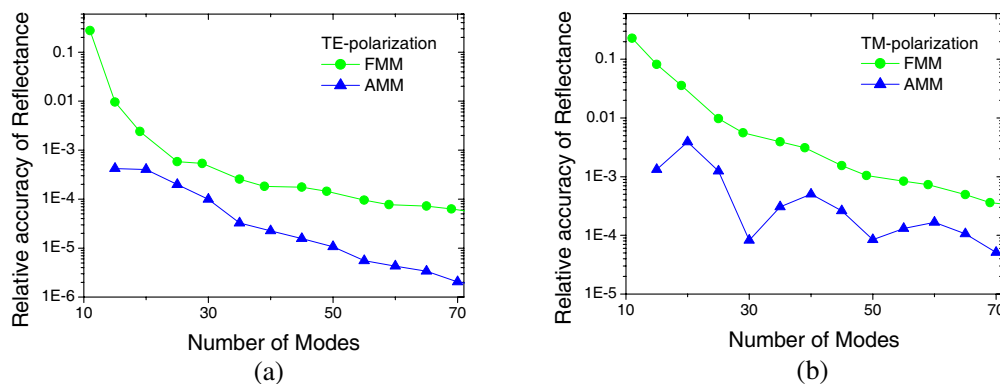


Figure 3: The relative accuracy of the reflectance for the structure of Fig. 1(b) at $\lambda = 0.75 \mu\text{m}$ obtained by adopting the presented AMM method and by using the FMM as function of the number of the expansion modes in (a) TE and (b) TM case.

a layer ($\epsilon_1 = 1.54^2$), $0.1 \mu\text{m}$ -thick (Fig. (1b)) The wavelength λ of the incident field forming an angle of incidence $\theta = 0^\circ$ is equal to $0.75 \mu\text{m}$. A comparison of the relative accuracy of reflectance obtained by means of the presented method and by the FMM is shown in Fig. 3 for (a) TE and (b) TM case. As reference value, we use $R = 0.0382332181758$ for TE -case and $R = 0.07481724$ for TM , obtained with the number of eigenmodes $N = 2001$.

4. CONCLUSIONS

A new implementation of analytic modal method (AMM) has been presented. It allows to remarkably reduce the computational time in case of TE polarization by adopting the perturbation approach and proposes a robust algorithm to calculate eigenvalues in case of TM polarization. The presented implementation of AMM allows to formulate a general approach to calculate arbitrary stacks of lamellar gratings for TE and TM polarizations.

REFERENCES

1. Moharam, M. G., et al., "Formulation for stable and efficient implementation of the rigorous coupled-wave analysis of binary gratings," *Opt. Soc. Am. A*, Vol. 12, No. 5, 1068–1076, 1995.
2. Morf, R. H., "Exponentially convergent and numerically efficient solution of Maxwell's equations for lamellar gratings," *J. Opt. Soc. Am. A*, Vol. 12, No. 5, 1043–1056, 1995.
3. Edee, K., "Modal method based on subsectional Gegenbauer polynomial expansion for lamellar gratings," *J. Opt. Soc. Am. A*, Vol. 28, No. 10, 2006–2013, 2011.
4. Granet, G., A. L. Bakonirina, R. Karyl, A. M. Armeanu, and K. Edee, "Modal analysis of lamellar gratings using the moment method with subsectional basis and adaptive spatial-resolution," *J. Opt. Soc. Am. A*, Vol. 27, No. 6, 1303–1310, 2010.
5. Armeanu, A. M., K. Edee, G. Granet, and P. Schiavone, "Modal method based on spline expansion for the electromagnetic analysis of the lamellar grating," *Progress In Electromagnetics Research*, Vol. 106, 243–261, 2010.
6. Song, D., L. Yuan, and Y. Y. Lu, "Fourier-matching pseudospectral modal method for diffraction gratings," *J. Opt. Soc. Am. A*, Vol. 28, No. 4, 613–620, 2011.
7. Chiou, Y.-P., W.-L. Yeh, and N.-Y. Shih, "Analysis of highly conducting lamellar gratings with multidomain pseudospectral method," *J. Lightwave Technol.*, Vol. 27, No. 22, 5151–5159, 2009.
8. Botten, L. C., M. S. Craig, R. C. McPhedran, J. L. Adams, and J. R. Andrewartha, "The finitely conducting lamellar diffraction grating," *Opt. Acta*, Vol. 28, No. 8, 1087–1102, 1981.
9. Botten, L. C., M. S. Craig, R. C. McPhedran, and J. L. Adams, "Highly conducting lamellar diffraction gratings," *Opt. Acta*, Vol. 28, No. 8, 1103–1106, 1981.
10. Tayeb, G. and R. Petit, "On the numerical study of deep conducting lamellar diffraction gratings," *Optica Acta*, Vol. 31, No. 12, 1361–1365, 1984.
11. Miller, J. M., J. Turunen, E. Noponen, A. Vasara, and M. R. Taghizadeh, "Rigorous modal theory for multiply grooved lamellar gratings," *Opt. Commun.*, Vol. 111, 526–535, 1994.

Analytical Study of Surface and Leaky Waves on a Grounded Magnetized Plasma Slab

Xenofon M. Mitsalás¹, Alexander V. Kudrin², and George A. Kyriacou¹

¹Microwaves Laboratory, Department of Electrical and Computer Engineering
Democritus University of Thrace, Xanthi, Greece

²Department of Radiophysics, University of Nizhny Novgorod, Russia

Abstract— Leaky wave along with surface wave eigenmodes excited on a grounded magnetized plasma are considered. The structure of interest refers to magnetized semiconductors at cryogenic temperatures. A homogeneous magnetization is assumed with the DC-biasing magnetic field parallel to the substrate, but normal to the direction of propagation. While the characteristics of surface waves are extensively studied in the past and especially by Seshadri et al., the possibility of leaky waves is not well examined and constitutes the original contribution of the present effort. The characteristic equation is first obtained analytically and in turn investigated numerically. The important non-reciprocal phenomena due to the non-even expression of the characteristic equation are verified regarding the surface waves while roots are then sought herein in the leaky modes regime. The conditions enabling backward waves and particularly their unidirectional nature are indeed challenging since they enable numerous novel applications, thus particular attention is devoted to them.

1. INTRODUCTION

The propagation of electromagnetic waves within and around a dielectric slab including the radiation characteristics when leaky waves are excited has been extensively studied as it is involved in important practical applications. The majority of these investigations pertain to the case of a slab of isotropic dielectric. A complete survey of the relevant literature may be found in the work of Oliner and Tamir [1], who have given a comprehensive treatment of the electromagnetic field of a source-excited, isotropic plasma slab.

When ferrite or plasma materials are subject to constant magnetic field they exhibit anisotropic permeability $\bar{\mu}_r$ and permittivity $\bar{\epsilon}_r$ respectively. These tensors depend on both the biasing magnetic field and the operating frequency. This dependence enables their dynamic control through the *dc* current of an electromagnet which generates the biasing constant magnetic field H_{DC} . These features offered by ferrites are extensively used in microwave waveguides, stripline and microstrip devices.

In contrary to the above there was only a limited use of magnetized plasma in microwave devices. In antenna applications there was a considerable research effort because these antennas were embedded in magnetized plasma in their operating environment, as for example in satellite communications and nuclear fusion. The evolution in the solid state plasma technology enables its application in microwave devices and printed antennas. “Perfect” semiconductors are known to behave as “solid state plasma” at cryogenic temperatures. Their practical exploitation is postponed until recently that cryogenic technology advancement made the operation of these devices attainable.

Our previous effort directed toward the solution of a canonical problem of a grounded slab filled with anisotropic plasma [3]. A lot of interesting phenomena regarding the excitation of surface and leaky waves in the grounded plasma region and the radiating space wave are involved in the scattered field expressions. The dependence of the modes turn-on/off conditions from the plasma parameters and especially the magnetizing *dc* field are of particular importance. A lot of these surface wave phenomena on grounded plasma slabs have been studied by Seshadri [2]. Besides this, higher order modes of this grounded structure are expected to become leaky waves. These waves offer non-reciprocal features in their radiation mechanisms. All these type of modes are indeed involved in the mathematical formulation [3] and are required for the evaluation of the field and especially the radiation of the structure. The study of all of those modes and particularly leaky waves constitutes the original contribution of the present effort.

2. FORMULATION OF THE PROBLEM

2.1. Definition of the Problem

The geometry to be studied is shown in Fig. 1. It consists of a grounded magnetized solid state plasma slab, where both the lower conducting ground plane and the plasma substrate are assumed extending to infinity. The biasing *dc* magnetic field is assumed parallel to the ground plane and along the *y*-axis.

2.1.1. Simplifications of Maxwell Equations

Considering wave propagation along the *z*-axis like $e^{-jk_0\lambda z}$ results in a simplification of the wave equation by substituting $\frac{\partial}{\partial z} = -jk_0\lambda$. For relative simplicity reasons the analysis is restricted to the case when no variation of the field in the also infinite *y*-direction is assumed, resulting to the simplification $\frac{\partial}{\partial y} = 0$. Moreover, the magnetized cold plasma ($\vec{H}_{dc} = H_0\hat{y}$) relative permittivity tensor is also given in [2] and the original references cited in [3]:

$$\vec{\epsilon}_r = \begin{bmatrix} \epsilon_{r1} & 0 & j\epsilon_{r2} \\ 0 & \epsilon_{r3} & 0 \\ -j\epsilon_{r2} & 0 & \epsilon_{r1} \end{bmatrix} \quad \text{where } \epsilon_{r1} = \frac{\Omega^2 - R^2 - 1}{\Omega^2 - R^2}, \quad \epsilon_{r2} = \frac{R}{\Omega(\Omega^2 - R^2)}, \quad \epsilon_{r3} = 1 - \frac{1}{\Omega^2} \quad (1a)$$

And

$$\Omega = \frac{\omega}{\omega_p}, \quad R = \frac{\omega_c}{\omega_p}, \quad \omega_p^2 = \frac{Ne^2}{m\epsilon_0} = \frac{\gamma Ne}{\epsilon_0}, \quad \omega_c = -\frac{e\mu_0 H_0}{m} = -\gamma\mu_0 H_0, \quad k_p = \frac{\omega_p}{c} \quad (1b)$$

The plasma frequency is symbolized as ω_p and its gyromagnetic frequency as ω_c . Also, *e* and *m* are the charge and the mass of an electron, $\gamma = \frac{e}{m}$ is the magneto-mechanic or gyromagnetic ratio (gyroelectric ratio could be more appropriate for magnetized plasmas) and ϵ_0 , μ_0 are the free space permittivity and permeability. Also, *N* is the average density of electrons.

2.1.2. General Solutions of the Wave Equations

In the geometry of the problem shown in Fig. 1, the region $-\infty < z < +\infty$, $-\infty < y < +\infty$ and $-\alpha < x < \alpha$, is filled with uniform plasma and the rest of half-space $x > \alpha$ is vacuum. The wave equation for the magnetic field for the plasma region $-\alpha \leq x \leq \alpha$ can be written as:

$$\left[\frac{\partial^2}{\partial x^2} + k_0^2 \left(\frac{\epsilon_{rq}}{\epsilon_{r1}} - \lambda^2 \right) \right] H_y = 0 \quad (2)$$

where $k_0 = \omega\sqrt{\mu_0\epsilon_0}$ the free space wavenumber, $\epsilon_{rq} = \epsilon_1^2 - \epsilon_{r2}^2$ and the transverse effective permittivity is $\epsilon_{reff} = \frac{\epsilon_{rq}}{\epsilon_{r1}}$. The general solution of (2) takes the form:

$$H_y = B_p(\lambda) \cosh(k_0 u_p x) + C_p(\lambda) \sinh(k_0 u_p x) \quad \text{for } -\alpha \leq x \leq \alpha \quad (3a)$$

where

$$u_p = \sqrt{\lambda^2 - \epsilon_{reff}} = \sqrt{\lambda^2 - \frac{\epsilon_{rq}}{\epsilon_{r1}}} \quad \text{and} \quad \text{Re}(u_p) \geq 0 \quad (3b)$$

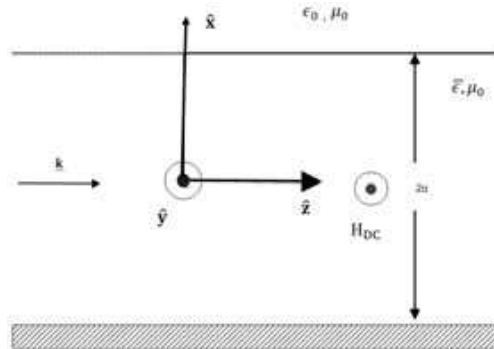


Figure 1: Geometry of the magnetized grounded plasma slab.

The transverse field components can also be expressed by expanding the Maxwell rotational equations and using the above simplifications:

$$E_x = \frac{\zeta_0}{\epsilon_{rq}} \left\{ \lambda \epsilon_{r1} H_y - \frac{\epsilon_{r2} \partial H_y}{k_0 \partial x} \right\} \quad \text{and} \quad E_z = j \frac{\zeta_0}{\epsilon_{rq}} \left\{ \lambda \epsilon_{r2} H_y - \frac{\epsilon_{r1} \partial H_y}{k_0 \partial x} \right\} \quad (4)$$

where $\zeta_0 = \sqrt{\frac{\mu_0}{\epsilon_0}} = 120\pi\Omega$ the free space characteristic impedance.

Substituting the general solution into (3)–(4) the transverse components in the plasma region $-\alpha \leq x \leq \alpha$ read:

$$E_x = \frac{\zeta_0}{\epsilon_{rq}} \{ [\lambda \cdot \epsilon_{r1} \cdot B_p(\lambda) - \epsilon_{r2} u_p C_p(\lambda)] \cosh(k_0 u_p x) + [\lambda \cdot \epsilon_{r1} \cdot C_p(\lambda) - \epsilon_{r2} \cdot u_p \cdot B_p(\lambda)] \sinh(k_0 u_p x) \} \quad (5a)$$

$$E_z = j \frac{\zeta_0}{\epsilon_{rq}} \{ [\lambda \cdot \epsilon_{r2} \cdot B_p(\lambda) - \epsilon_{r1} u_p C_p(\lambda)] \cosh(k_0 u_p x) + [\lambda \cdot \epsilon_{r2} \cdot C_p(\lambda) - \epsilon_{r1} \cdot u_p \cdot B_p(\lambda)] \sinh(k_0 u_p x) \} \quad (5b)$$

The remaining field components vanish ($E_y = H_x = H_z = 0$ and $D_x = 0$) due to the assumption of the absence of propagation in the y -direction, ($\frac{\partial}{\partial y} = 0$). The general solution for the air region can be obtained by substituting in Equations (2)–(5) its characteristics ($\epsilon_{r1} = \epsilon_{r3} = 1$, $\epsilon_{r2} = 0$). Besides, this solution must also obey the radiation condition at infinity, so for the air region $x \geq \alpha$, we have:

$$H_y = A_p(\lambda) \cdot e^{-k_0 u_0 (x-\alpha)} \quad \text{for } x \geq \alpha \quad \text{with } u_0 = \sqrt{\lambda^2 - 1} \quad \text{and} \quad \text{Re}(u_0) \geq 0, \quad (6)$$

$$E_x = -\frac{1}{j\omega\epsilon_0} \frac{\partial H_y}{\partial z} = \zeta_0 \cdot \lambda \cdot H_y \quad \text{and} \quad E_z = \frac{1}{j\omega\epsilon_0} \frac{\partial H_y}{\partial x} = j\zeta_0 u_0 \cdot H_y \quad (7)$$

2.1.3. Boundary Conditions

The quantities $A_p(\lambda)$, $B_p(\lambda)$ and $C_p(\lambda)$ can be estimated by enforcing the boundary conditions. For the tangential electric and magnetic field components on the ground plane ($x = -\alpha$) and their continuity at the plasma — air interface at $x = \alpha$:

$$E_z(x = -\alpha, \lambda) = 0 \quad \text{and} \quad E_z(x = \alpha^-, \lambda) = E_z(x = \alpha^+, \lambda) \quad (8a)$$

$$H_y(x = \alpha^-) = H_y(x = \alpha^+) \rightarrow B_p(\lambda) \cosh(k_0 u_p \alpha) + C_p(\lambda) \sinh(k_0 u_p \alpha) = A_p(\lambda) \quad (8b)$$

Equation (8b) and the expression resulting from (8a) are substituted back to yield:

$$B_p(\lambda) = \frac{\epsilon_{rq} u_0 A_p(\lambda)}{2 [(\lambda \epsilon_{r2})^2 - (\epsilon_{r1} \cdot u_p)^2]} \cdot \left(\frac{\lambda \epsilon_{r2}}{\cosh(k_0 u_p \alpha)} + \frac{\epsilon_{r1} \cdot u_p}{\sinh(k_0 u_p \alpha)} \right) \quad (9a)$$

$$C_p(\lambda) = \frac{\epsilon_{rq} u_0 A_p(\lambda)}{2 [(\lambda \epsilon_{r2})^2 - (\epsilon_{r1} \cdot u_p)^2]} \cdot \left(\frac{\epsilon_{r1} \cdot u_p}{\cosh(k_0 u_p \alpha)} + \frac{\lambda \epsilon_{r2}}{\sinh(k_0 u_p \alpha)} \right) \quad (9b)$$

$$H_y(x = \alpha^-) = \frac{\epsilon_{rq} u_0 A_p(\lambda)}{2 [(\lambda \epsilon_{r2})^2 - (\epsilon_{r1} \cdot u_p)^2]} \cdot [2\lambda \epsilon_{r2} + 2\epsilon_{r1} u_p \coth(2k_0 u_p \alpha)] \quad (9c)$$

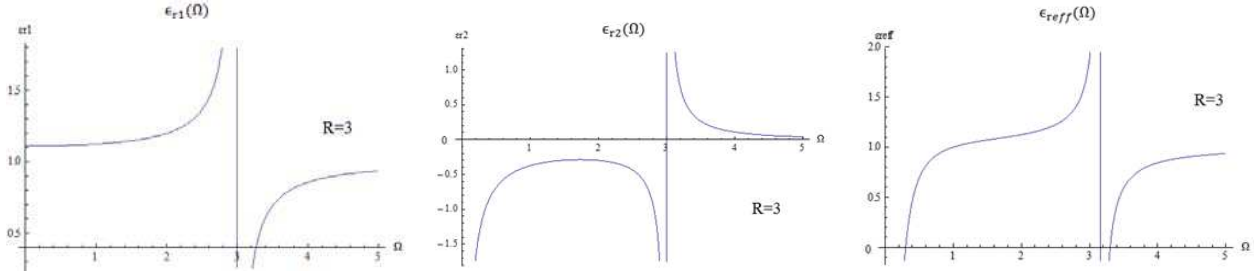
Reformulating the above expressions yields the characteristic equation

$$F(\lambda) = \left(1 - \frac{\lambda^2}{\epsilon_{r1}} - \frac{\epsilon_{r2}}{\epsilon_{r1}} \lambda u_0 \right) \tanh(k_0 u_p 2\alpha) - u_0 u_p = 0 \quad (10)$$

The above characteristic equation involves two branch points at $u_0 = 0$ or $\lambda = \pm 1$. Note that $u_p = 0$ constitutes a removable singularity of the form $cu_p \cdot \coth(cu_p) = cu_p / \tanh(cu_p) \rightarrow 1$ as $u_p \rightarrow 0$.

3. DISPERSION CURVES FOR THE WAVES

The behavior of plasma tensor properties ϵ_{r1} , ϵ_{r2} and ϵ_{reff} as a function of the normalized frequency Ω is presented graphically in Fig. 2. Observing Fig. 2, it is obvious that there are frequency bands


 Figure 2: Plasma tensor entries ϵ_{r1} , ϵ_{r2} and ϵ_{reff} as a function of the normalized frequency Ω .

where the entries of the permittivity tensor and ϵ_{reff} become negative as:

$$0 < \epsilon_{reff} < 1 \quad \text{for} \quad \Omega_1 < \Omega < 1 \quad \text{and} \quad \Omega_3 < \Omega < +\infty \quad (11a)$$

$$1 < \epsilon_{reff} < +\infty \quad \text{for} \quad 1 < \Omega < \Omega_2 \quad (11b)$$

$$-\infty < \epsilon_{reff} < 1 \quad \text{for} \quad 0 < \Omega < \Omega_1 \quad \text{and} \quad \Omega_2 < \Omega < \Omega_3 \quad (11c)$$

where

$$\Omega_1 = \frac{-R + \sqrt{R^2 + 4}}{2}, \quad \Omega_2 = \sqrt{R^2 + 1}, \quad \Omega_3 = \frac{R + \sqrt{R^2 + 4}}{2} \quad (11d)$$

It was elegantly clarified by Seshadri [2] and exploited herein that the roots of the characteristic equation (modes) can be classified in four cases, which are identified below along with the corresponding characteristic equations:

$$\begin{aligned} \text{case 1:} \quad & \lambda^2 \leq 1, \quad \lambda^2 \leq \epsilon_{reff}, \quad u_p = j|u_p|, \quad u_0 = j|u_0| \\ & \implies \left(1 - \frac{\lambda^2}{\epsilon_{r1}} - j \frac{\epsilon_{r2}}{\epsilon_{r1}} \lambda |u_0| \right) \tan(k_0 |u_p| 2\alpha) - j |u_0| |u_p| = 0 \end{aligned} \quad (12a)$$

$$\begin{aligned} \text{case 2:} \quad & \lambda^2 \leq 1, \quad \lambda^2 \geq \epsilon_{reff}, \quad u_p = |u_p|, \quad u_0 = j|u_0| \\ & \implies \left(1 - \frac{\lambda^2}{\epsilon_{r1}} - j \frac{\epsilon_{r2}}{\epsilon_{r1}} \lambda |u_0| \right) \tanh(k_0 |u_p| 2\alpha) - j |u_0| |u_p| = 0 \end{aligned} \quad (12b)$$

$$\begin{aligned} \text{case 3:} \quad & \lambda^2 \geq 1, \quad \lambda^2 \leq \epsilon_{reff}, \quad u_p = j|u_p|, \quad u_0 = |u_0| \\ & \implies \left(1 - \frac{\lambda^2}{\epsilon_{r1}} - \frac{\epsilon_{r2}}{\epsilon_{r1}} \lambda |u_0| \right) \tan(k_0 |u_p| 2\alpha) - |u_0| |u_p| = 0 \end{aligned} \quad (12c)$$

$$\begin{aligned} \text{case 4:} \quad & \lambda^2 \geq 1, \quad \lambda^2 \geq \epsilon_{reff}, \quad u_p = |u_p|, \quad u_0 = |u_0| \\ & \implies \left(1 - \frac{\lambda^2}{\epsilon_{r1}} - \frac{\epsilon_{r2}}{\epsilon_{r1}} \lambda |u_0| \right) \tanh(k_0 |u_p| 2\alpha) - |u_0| |u_p| = 0 \end{aligned} \quad (12d)$$

The cases 1, 2 represent leaky modes, since Equations (12a), (12b) do not have any real roots and both of them correspond to a fast wave ($\beta < k_0$). Explicitly in this case the phase velocity $v_p = \omega/\beta$ becomes higher than the speed of light in vacuum $c = \omega/k_0$. The cases 3 and 4 correspond to surface waves where the characteristic Equations (12c), (12d) have real roots with $\beta/k_0 > 1$.

The real roots λ of the characteristic equation in the case of the grounded anisotropic plasma slab were obtained numerically for three values of the involved parameter. By adopting Seshadri [2] symbolism and since the frequency Ω and the wave number λ of the surface wave are respectively proportional to Ω and $\Omega\lambda$ the dispersion diagram are plotted as Ω vs $\Omega\lambda$, and these plots are depicted in Fig. 3. In each case, the results are given for three values of the thickness parameter b , namely $b = k_0 2\alpha = 10, 1$ and 0.1 . For forward propagating modes the dispersion curves tend asymptotically to $\Omega = R = 0.5$, while the reverse propagating waves tend asymptotically to $\Omega = 1$. It is interesting to notice the negative slope in Fig. 3(c) which identifies a backward.

For a validation of the employed root searching method our results are compared to those of Seshadri [2], for the case in Fig. 3(b). Since Seshadri [2] assumed an $e^{-j\omega t}$ dependence instead of $e^{+j\omega t}$ herein, a mirror image of his results is identical to ours as shown in Fig. 4.

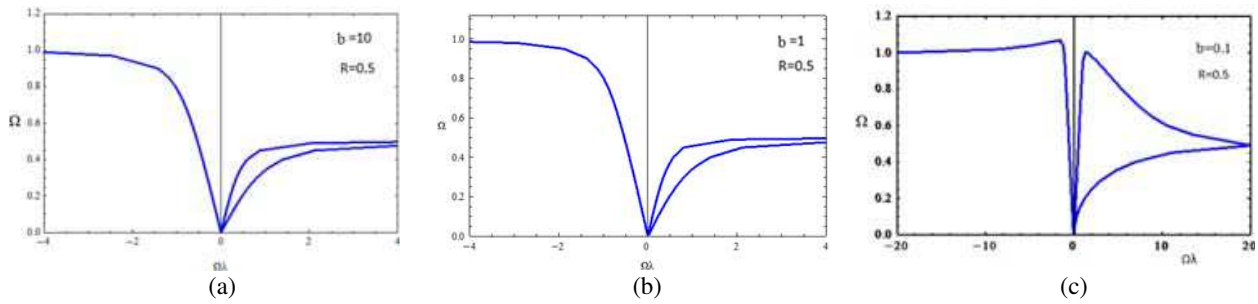


Figure 3: Dispersion curves for the surface waves.

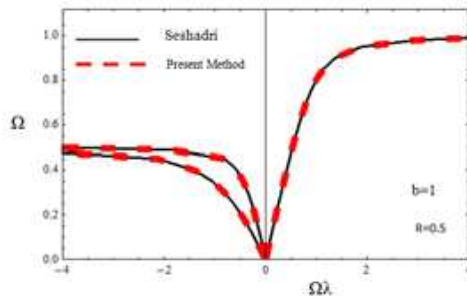


Figure 4: Comparison of results for the case of Fig. 3(b).

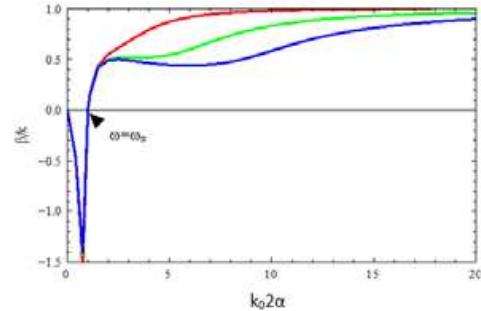


Figure 5: Leaky wave dispersion curves for the grounded isotropic plasma ($R = 0$).

Although the surface modes exist above $\beta/k_0 = 1$, leaky waves did not exist above these cutoffs. The leaky modes existed throughout the frequency spectrum. Especially for the case of a grounded isotropic plasma slab ($R = 0$), three lower order leaky modes were depicted in Fig. 5, for constant normalized plasma frequency $k_p 2\alpha = 1$. The normalized phase constants monotonically tend to unity, as $k_0 2\alpha$ is increased. Below the plasma frequency the normalized phase constants have negative values, meaning reverse propagation (Fig. 5).

In the case of a grounded anisotropic plasma slab, considering $\lambda = \beta - j\alpha$, the characteristic equation yields the following dispersion curves (Figs. 6–7) for leaky waves. For forward (Fig. 6) and the reverse (Fig. 7) propagating modes the dispersion curves tend asymptotically to $\beta/k_0 = 1$, as the frequency is increased.

4. FIELD CALCULATION

It is by now well understood that leaky waves are not improper modes but they are rather inhomogeneous (attenuated) waves propagating at a specific angle (θ) with respect to the air-dielectric interface. It is along this specific direction that they were found to exhibit maximum radiation-leakage, namely this the direction of beam maximum. This direction is defined by the leaky mode complex propagation constant, e.g., Jasik [4, p. 16–7] as:

$$\cos \theta = \frac{\beta_z}{\beta} = \frac{\beta_z}{\sqrt{\beta_z^2 + \beta_{tr}^2}} \tag{13}$$

where $\beta_z = \text{Re}(\lambda)$ and $B_{tr} = \text{Re}(|u_0|)$ which are defined below Equation (6) and calculated from the solution of the characteristic equation. The corresponding roots are substituted in the field expressions of H_y in the Equation (3a) and the field intensity in the transverse x -direction is plotted in Fig. 8.

According to Seshadri [2] waves propagating in the positive z -direction are expected to concentrate their energy in the plasma-air interface at $x = \alpha$ in the frequency range of $\sqrt{R^2 + 1} < \Omega < \infty$, as shown in Fig. 9. An example of a such waves is given in Fig. 9, where the power of the wave is concentrated at the air-plasma interface.

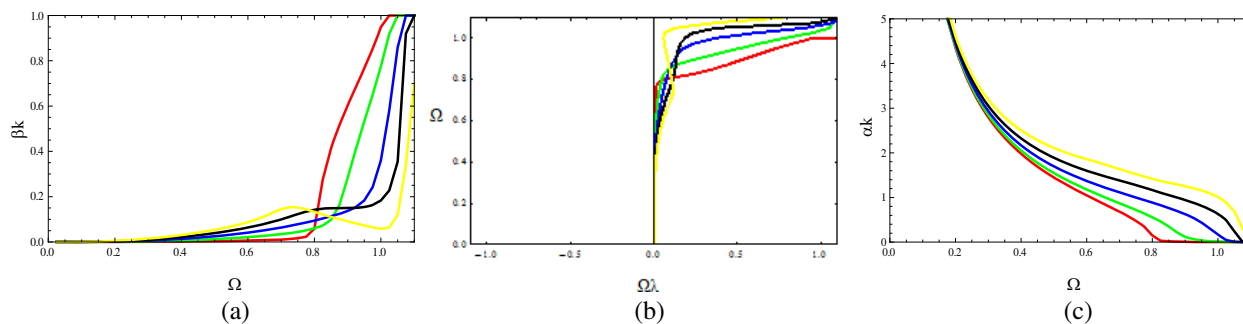


Figure 6: Dispersion curve of phase constant, (a) as a function of β/k_0 vs Ω and (b) as Ω vs $\Omega\lambda$ and (c) of attenuation constant vs frequency in positive z direction for $b = 10$.

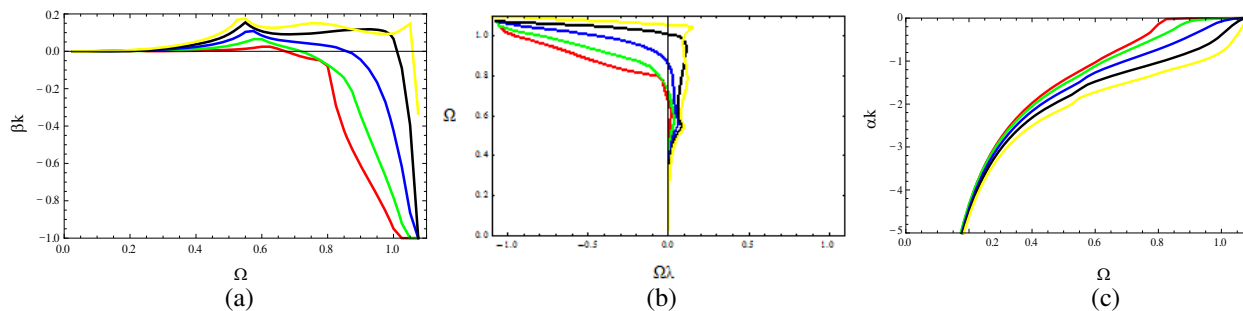


Figure 7: Dispersion curve of phase constant (a) as a function of β/k_0 vs Ω and (b) as Ω vs $\Omega\lambda$ and (c) of attenuation constant vs frequency in negative z direction for $b = 10$.

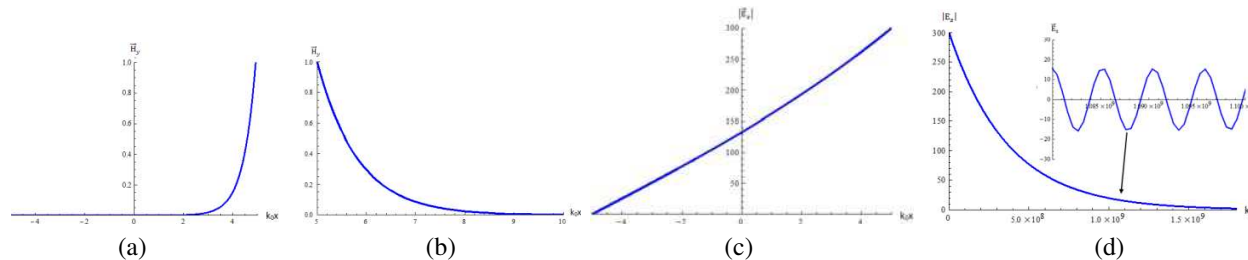


Figure 8: Magnetic and electric field intensity vs the transverse x -direction for a plasma slab with $R = 0.5$, $\Omega = 0.9$ and normalized thickness $b = k_0 2\alpha = 10$: (a) surface mode ($\lambda = -1.57823$) inside the slab, (b) surface mode outside the slab, (c) leaky mode ($\lambda = 0.60425 - j0.00808815$) inside the slab, (d) leaky mode outside the slab $\theta \approx 52.8270^\circ$.

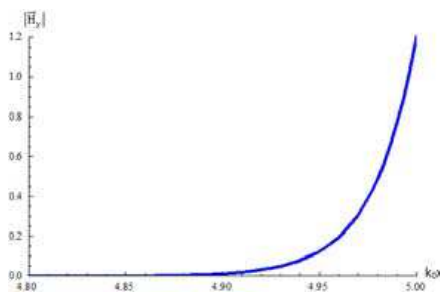


Figure 9: Total magnetic field $H_t = H_y$ of a unidirectional wave vs the transverse x -direction for a plasma slab, with $R = 0.5$ and normalized thickness $b = k_0 2\alpha = 10$, traveling in the positive x -direction ($\lambda = 0.0822583 - j0.494844$) for $\Omega = 1.12$.

5. CONCLUSIONS

A geometry of a grounded plasma slab is considered in the present effort. Important non-reciprocal and unidirectional wave propagation phenomena are involved as a result of the magnetized plasma anisotropy. The characteristic equation is obtained and solved numerically for both surface and leaky wave modes. The permittivity tensor dependence on frequency yields extraordinary phenomena including backward and unidirectional wave propagation. The next step of this work aims at the complete understanding of these phenomena in the leaky wave regime as well as in the already studied surface wave regime. The ultimate task is to exploit these type of modes for the analysis and design of novel structures (non-reciprocal) printed on magnetized plasma substrate.

ACKNOWLEDGMENT

This work was financially supported by the Greek Ministry of Education, Lifelong Learning and Religious Affairs through the research project THALIS Design Techniques for Digitally Controlled RF-Microwave Structures appropriate for Software Defined-Cognitive Radio (RF-EIGEN-SDR).

REFERENCES

1. Oliner, A. A. and T. Tamir, "Backward waves on isotropic slab," *J. Appl. Phys.*, Vol. 33, 231–233, Jan. 1962.
2. Seshadri, S. R. and W. F. Pickard, "Surface waves on an anisotropic plasma sheath," *IEEE Trans. on Microwave Theory and Techniques*, 529–541, 1964.
3. Kyriacou, G. A., "Wiener-hopf analysis of planar canonical structures loaded with longitudinally magnetized plasma biased normally to the extraordinary wave propagation," *Progress In Electromagnetics Research B*, Vol. 5, 1–34, 2008.
4. Jasik, H., *Antenna Engineering Handbook*, Mc Graw Hill, 1961.
5. Berral, R. R., F. Mesa, and F. Medina, "Appropriate formulation of the characteristic equation for open nonreciprocal layered waveguides with different upper and lower half spaces," *IEEE Trans. on Microwave Theory and Technology*, Vol. 53, No. 5, May 2005.

Radiation Efficiency of a Circular Loop Antenna with Pulsed Excitation in a Magnetoplasma Containing a Cylindrical Density Nonuniformity

A. V. Kudrin¹, N. M. Shmeleva¹, N. V. Yurasova¹, and T. M. Zaboronkova²

¹University of Nizhny Novgorod, Russia

²Technical University of Nizhny Novgorod, Russia

Abstract— Energy radiation characteristics of a pulsed loop antenna placed coaxially in a cylindrical density nonuniformity that is surrounded by a uniform cold magnetoplasma are studied. An expression for the radiated energy is derived and its distribution over the spatial and frequency spectra of the excited waves is analyzed. Numerical results referring to the case where the frequency spectrum of the current is concentrated in the whistler range are reported. It is shown that the presence of a cylindrical nonuniformity with enhanced plasma density can lead to a significant increase in the energy radiated from a pulse-excited loop antenna compared with the case where the same source is immersed in the surrounding uniform magnetoplasma. It is found that in the resonant part of the whistler range, the predominant contribution to the radiated energy is ensured by slightly leaky modes that are guided by such a nonuniformity and can be separated from the continuous part of the spatial spectrum of the excited waves.

1. INTRODUCTION

Over the past decade, there has been shown a substantial degree of interest in the excitation of electromagnetic radiation in a magnetoplasma containing magnetic-field-aligned density nonuniformities commonly known as density ducts (see, e.g., [1] and references therein). Such plasma structures consisting of density enhancements or depletions, or combinations thereof can arise near electromagnetic sources in a magnetoplasma due to various nonlinear effects [2, 3] and are capable of guiding electromagnetic waves in some frequency ranges. Much previous theoretical work on the subject is focused on studying the radiation characteristics of monochromatic sources immersed in density ducts [1]. However, there exists a very little theory of the radiation from nonmonochromatic sources operated in the presence of field-aligned plasma density nonuniformities.

It is the purpose of the present work to study the energy radiation characteristics of a pulsed circular loop antenna located in an enhanced-density duct that is surrounded by a uniform cold magnetoplasma such as exists in the Earth's ionosphere. The emphasis will be placed on the case where the frequency spectrum of the antenna current is concentrated in the whistler range which plays an important role in many promising applications [1–3].

2. BASIC FORMULATION

Consider a circular loop antenna placed coaxially in a cylindrical duct of radius a . The duct is aligned with the z axis of a cylindrical coordinate system (ρ, ϕ, z) . Parallel to this axis is a uniform dc magnetic field $\mathbf{B}_0 = B_0 \mathbf{z}_0$. The plasma density is equal to \tilde{N} inside the duct, and to N_a in the ambient uniform plasma surrounding the duct. The electric current density of the antenna is specified as

$$\mathbf{J}(\mathbf{r}, t) = \phi_0 I_0 \delta(\rho - b) \delta(z) \chi(t), \quad (1)$$

where I_0 is the amplitude of total current, b is the antenna radius ($b < a$), δ is a Dirac function, and $\chi(t)$ is a dimensionless function describing the current behavior in time. The function $\chi(t)$ has the maximum value equal to unity and is assumed nonzero in the time interval $0 < t < \tau$, where τ is the current pulse duration. The plasma is assumed collisionless, and is described by the permittivity tensor

$$\boldsymbol{\varepsilon} = \epsilon_0 \begin{pmatrix} \varepsilon & -ig & 0 \\ ig & \varepsilon & 0 \\ 0 & 0 & \eta \end{pmatrix}, \quad (2)$$

where ϵ_0 is the electric constant. For a monochromatic signal with a time dependence of $\exp(i\omega t)$, the tensor elements ε , g , and η in the case of a two-component magnetoplasma can be written as [1]

$$\varepsilon = \frac{(\omega^2 - \omega_{\text{LH}}^2)(\omega^2 - \omega_{\text{UH}}^2)}{(\omega^2 - \omega_{\text{H}}^2)(\omega^2 - \Omega_{\text{H}}^2)}, \quad g = \frac{\omega_p^2 \omega_{\text{H}} \omega}{(\omega^2 - \omega_{\text{H}}^2)(\omega^2 - \Omega_{\text{H}}^2)}, \quad \eta = 1 - \frac{\omega_p^2}{\omega^2},$$

where Ω_H , ω_H , ω_{LH} , ω_p , and ω_{UH} are the ion and electron gyrofrequencies, the lower hybrid frequency, the electron plasma frequency, and the upper hybrid frequency, respectively.

The total energy W radiated from a current $\mathbf{J}(\mathbf{r}, t)$ with duration τ is obtained as

$$W = - \int_0^\tau dt \int_V \mathbf{J}(\mathbf{r}, t) \cdot \mathbf{E}(\mathbf{r}, t) d\mathbf{r}, \quad (3)$$

where integration with respect to the spatial coordinates is performed over the volume V occupied by the source current, and $\mathbf{E}(\mathbf{r}, t)$ is the total electric field excited by the source. We emphasize that this field comprises not only the nonradiative part, which is predominant near the source, but also the radiative part responsible for the outgoing energy transport. To evaluate W , we need to express $\mathbf{E}(\mathbf{r}, t)$ in terms of the source current. To do this, it is convenient to use the Laplace transforms of these quantities as functions of time. Throughout this paper, we use the following convention for the definition of the Laplace transform and its inverse:

$$\begin{aligned} f(\omega) &= \int_0^\infty f(t) \exp(-i\omega t) dt, \quad \text{Im}\omega = -\sigma < 0, \quad \sigma = \text{const}; \\ f(t) &= \frac{1}{2\pi} \int_{-i\sigma-\infty}^{-i\sigma+\infty} f(\omega) \exp(i\omega t) d\omega. \end{aligned} \quad (4)$$

Here, σ is a real-valued positive constant and ω is a complex-valued quantity such that $\omega = \text{Re}\omega - i\sigma$.

For a source with current (1), only the azimuthal electric-field component $E_\phi(\mathbf{r}, t)$ is required to evaluate W . It can be shown that the Laplace-transformed quantity $E_\phi(\mathbf{r}, \omega)$ is given by the formula [1, 4]

$$\begin{aligned} E_\phi(\mathbf{r}, \omega) &= \sum_n a_{s,n}(\omega) E_{\phi;s,n}(\rho, \omega) \exp(-ih_{s,n}z) \\ &+ \sum_\alpha \int_0^\infty a_{s,\alpha}(k_\perp, \omega) E_{\phi;s,\alpha}(\rho, k_\perp, \omega) \exp(-ih_{s,\alpha}z) dk_\perp, \end{aligned} \quad (5)$$

where $E_{\phi;s,n}(\rho, \omega)$ and $E_{\phi;s,\alpha}(\rho, k_\perp, \omega)$ are the azimuthal components of the vector wave functions describing the radial distribution of the electric fields of eigenmodes (discrete-spectrum waves) and continuous-spectrum waves of the duct, respectively, at a fixed frequency ω ; $a_{s,n}(\omega)$ and $a_{s,\alpha}(k_\perp, \omega)$ are the excitation coefficients of the corresponding waves; n is the eigenmode radial index ($n = 0, 1, \dots$); $h_{s,n}$ is the longitudinal wave number of an eigenmode with the index n ; k_\perp is the transverse (with respect to \mathbf{B}_0) wave number in the ambient uniform magnetoplasma; the functions $h_{s,\alpha}(k_\perp, \omega)$ stand for the longitudinal wave numbers of the ordinary ($\alpha = o$) and extraordinary ($\alpha = e$) waves of the ambient magnetoplasma; and the subscript s designates the wave propagation direction ($s = +$ and $s = -$ correspond to waves propagating in the positive and negative directions of the z axis, respectively). Expressions for $h_{s,\alpha}(k_\perp, \omega)$, as well as for the vector functions describing the fields of the discrete- and continuous-spectrum waves are given in [1].

Using the well-known technique based on Lorentz's reciprocity theorem, which was developed for finding the excitation coefficients of open guiding systems in a magnetoplasma [1, 4], we can write

$$\begin{aligned} a_{\pm,n}(\omega) &= 2\pi b I_0 \chi(\omega) N_n^{-1}(\omega) E_{\phi;\mp,n}^{(T)}(b, \omega), \\ a_{\pm,\alpha}(k_\perp, \omega) &= 2\pi b I_0 \chi(\omega) N_\alpha^{-1}(k_\perp, \omega) E_{\phi;\mp,\alpha}^{(T)}(b, k_\perp, \omega). \end{aligned} \quad (6)$$

Here, $\chi(\omega)$ is the Laplace transform of the source function $\chi(t)$, the superscript (T) denotes fields taken in a medium described by the transposed dielectric tensor $\boldsymbol{\varepsilon}^T$, and $N_n(\omega)$ and $N_\alpha(k_\perp, \omega)$ are the normalization quantities that are deduced from the orthogonality relations for the discrete- and continuous-spectrum waves (see [1] for details).

Substituting the inverse Laplace transform of $E_\phi(\mathbf{r}, \omega)$ into Eq. (3) and performing integration with respect to the spatial coordinates and time, we obtain

$$W = -I_0 b \int_{-i\sigma-\infty}^{-i\sigma+\infty} d\omega \chi(-\omega) E_\phi(\mathbf{r}, \omega)|_{\rho=b, z=0}. \quad (7)$$

The integration path in Eq. (7) is symmetric about the imaginary ω axis. Passing to integration over the right-hand part of this path, for which $\text{Re } \omega > 0$, and then making the limiting transition $\sigma \rightarrow 0$, we get the resulting expression

$$W = \int_0^\infty d\omega (-I_0^2) 4\pi b^2 \chi(-\omega) \chi(\omega) \text{Re} \left[\sum_n N_n^{-1}(\omega) E_{\phi; -s, n}^{(T)}(b, \omega) E_{\phi; s, n}(b, \omega) + \sum_\alpha \int_0^\infty N_\alpha^{-1}(k_\perp, \omega) E_{\phi; -s, \alpha}^{(T)}(b, k_\perp, \omega) E_{\phi; s, \alpha}(b, k_\perp, \omega) dk_\perp \right]. \quad (8)$$

It is to be stressed that integration with respect to ω in Eq. (8) is performed over the positive real frequency semi-axis. Note that only the regions of integration over positive k_\perp values for which the functions $h_{s, \alpha}$ are purely real make nonzero contributions, along with the propagated eigenmodes, to the radiated energy W given by Eq. (8).

We examine the case where the temporal behavior of the source current is taken as a pulse whose filling comprises a few half-periods of a monochromatic oscillation:

$$\chi(t) = \sin(\omega_0 t) [H(t) - H(t - \tau)]. \quad (9)$$

Here, $H(t)$ is a Heaviside function, $\tau = kT/2 = \pi k/\omega_0$ is the signal duration ($k = 1, 2, \dots$), and ω_0 is the frequency corresponding to a given period $T = 2\pi/\omega_0$.

3. NUMERICAL RESULTS

The quantity W was evaluated numerically for plasma parameters chosen to be typical of the Earth's ionosphere: the ambient plasma density $N_a = 10^6 \text{ cm}^{-3}$ and the external static magnetic field $B_0 = 0.5 \text{ G}$. With these values, the ambient plasma had the electron plasma frequency $\omega_p = 5.6 \times 10^7 \text{ s}^{-1}$, the electron gyrofrequency $\omega_H = 8.8 \times 10^6 \text{ s}^{-1}$, and the effective ion gyrofrequency $\Omega_H = 200 \text{ s}^{-1}$. It was assumed that the source radius $b = 2.5 \text{ m}$, the duct radius $a = 5 \text{ m}$, and $\tilde{N} > N_a$. For the source function $\chi(t)$ described by Eq. (9), we choose the parameter ω_0 such as to satisfy the condition $\omega_{\text{LH}} < \omega_0 \ll \omega_H$, which corresponds to the resonant part of the whistler range [1]. Here, the lower hybrid frequency $\omega_{\text{LH}} = (\omega_H \Omega_H)^{1/2}$. The upper hybrid frequency is given by $\omega_{\text{UH}} = (\omega_p^2 + \omega_H^2)^{1/2}$. Calculations show that in the case considered, the dominant contribution to the radiated energy is ensured by the continuous-spectrum waves. Neglecting the contribution of the discrete-spectrum waves, we can reduce the radiated energy to the form

$$W = I_0^2 \int_0^\infty d\omega \sum_\alpha \int_{Q_\alpha} w_\alpha(q, \omega) dq. \quad (10)$$

Here, $q = k_\perp/k_0$ and $p_{s, \alpha} = h_{s, \alpha}/k_0$, where k_0 is the wave number in free space. The symbol Q_α ($\alpha = 1, 2$) in Eq. (10) denotes the regions of positive q values for which the functions $h_{s, \alpha}$ are purely real.

It turns out that in the resonant part of the whistler range, the energy going to the continuous-spectrum waves is determined by slightly leaky modes. Their contributions to the radiated energy can be separated from the $\alpha = e$ term in Eq. (10). The leaky modes have complex longitudinal wave numbers $h = k_0(p' - ip'')$. The fields of such modes can be obtained by appropriately deforming the path of integration over k_\perp in Eq. (5) [1, 2]. The continuous-spectrum waves corresponding to $\alpha = o$ do not contribute to the radiated energy in the whistler range.

As an example, Fig. 1 shows the quantity $w_e(q, \omega)$ as a function of the frequency ω and the dimensionless transverse wave number q for source (9) if $\omega_0 = 1.9 \times 10^5 \text{ s}^{-1}$, $\tilde{N}/N_a = 30$, and $k = 5$. Note that the dashed line in the figure displays the frequency dependence of the boundary below which the normalized transverse wave numbers q of the outward-radiating part of the leaky-mode fields cannot be found [1, 2]. The discrete nonoverlapping traces in the region above the dashed line, which correspond to sharp crests of $w_e(q, \omega)$, show the individual contribution of leaky modes to the radiated energy.

Results of numerical calculation of the total energy radiated from the loop antenna are shown in Fig. 2 for the previously chosen values of ω_p , ω_H , Ω_H , a , and b . The closed circles in the figure indicate the total energy radiated from the source with time dependence (9) for $\omega_0 = 1.9 \times 10^5 \text{ s}^{-1}$

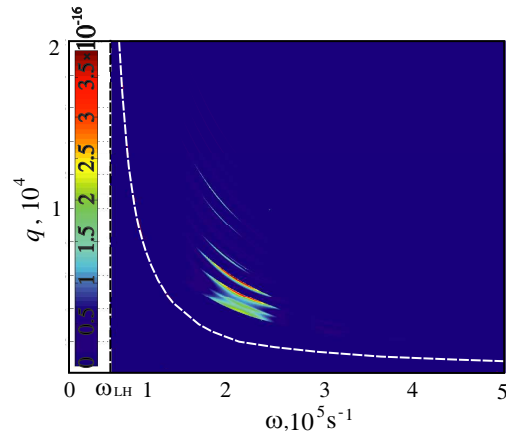


Figure 1: Distribution $w_e(q, \omega)$ over the spatial and frequency spectra (in JA^{-2}s) of the energy radiated from source (9) to the continuous-spectrum waves for $\alpha = e$, $k = 5$, $\tilde{N}/N_a = 30$, $\omega_0 = 1.9 \times 10^5 \text{ s}^{-1}$, $\omega_p = 5.6 \times 10^7 \text{ s}^{-1}$, $\omega_H = 8.8 \times 10^6 \text{ s}^{-1}$, $\Omega_H = 200 \text{ s}^{-1}$, $a = 5 \text{ m}$, and $b = 2.5 \text{ m}$.

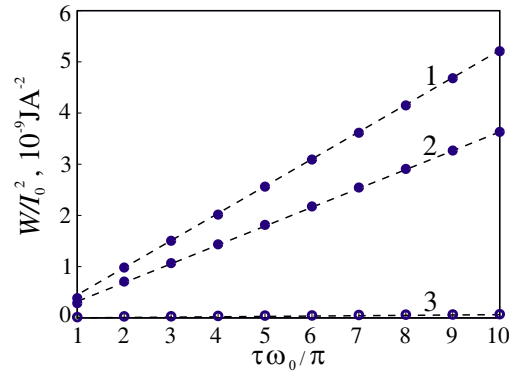


Figure 2: The total radiated energy as a function of the signal duration for $\tilde{N}/N_a = 30$ (1), $\tilde{N}/N_a = 10$ (2), and $\tilde{N}/N_a = 1$ (3). The values of ω_0 , ω_p , ω_H , Ω_H , a , and b are the same as in Fig. 1.

and various values of \tilde{N}/N_a and $k = \tau\omega_0/\pi$. The open circles in Fig. 2 show the radiated energy when the loop antenna is immersed in the surrounding uniform magnetoplasma.

It follows from Fig. 2 that the presence of a duct with enhanced density can lead to a significant increase in the energy radiated from a pulsed loop antenna compared with the case where the same source is immersed in the surrounding uniform magnetoplasma. Another important implication of the numerical results is that the radiated energy in the case where the current pulse is described by Eq. (9) obeys the relation $W = \bar{P}_{\text{rad}}\tau$ with a fairly good accuracy. Here, \bar{P}_{rad} is the time-averaged power radiated from the source possessing a time-harmonic current with the frequency ω_0 . It is important that such behavior is observed for the current containing even a few half-periods of a monochromatic oscillation, when the parameter k is moderately small, and is related to the features of excitation of whistler-mode waves by the loop antenna in a magnetoplasma. As the characteristic frequency ω_0 is increased, while remaining in the resonant frequency range, the energy spectrum becomes wider and the marks representing the radiated energy approach the dependence $W = \bar{P}_{\text{rad}}\tau$ for somewhat higher values of k . Nevertheless, the resonant part of the whistler range continues to give the predominant contribution to the radiation until the characteristic frequency ω_0 is located in this spectral interval.

4. CONCLUSION

In this paper, we have studied the radiation characteristics of a pulsed loop antenna located in an enhanced-density duct in a magnetoplasma modeled upon the Earth's ionosphere. A notable increase in the energy radiated from such an antenna has been found to occur in the whistler range due to the presence of the duct. It has been shown that the radiated energy of a loop antenna whose current pulse contains only a few half-periods of a monochromatic oscillation with the frequency lying in the resonant part of the whistler range is very close to the product of the

current duration by the time-averaged radiated power of the corresponding monochromatic source. The results obtained can be useful in interpreting the data of space and laboratory experiments on electromagnetic wave excitation by pulsed sources in a magnetoplasma containing magnetic-field-aligned density nonuniformities of natural or artificial origin.

ACKNOWLEDGMENT

This work was supported by the Russian Foundation for Basic Research (Project No. 12-02-00747-a), the Government of the Russian Federation (Contract No. 11.G34.31.0048), the Russian Federal Program “Scientific and Education Personnel of the Innovative Russia” (Contract Nos. P313 and 02.740.11.0565), and the Greek Ministry of Education through the project THALIS (RF-EIGEN-SDR).

REFERENCES

1. Kondrat'ev, I. G., A. V. Kudrin, and T. M. Zaboronkova, *Electrodynamics of Density Ducts in Magnetized Plasmas*, Gordon and Breach, Amsterdam, 1999.
2. Kostrov, A. V., A. V. Kudrin, L. E. Kurina, G. A. Luchinin, A. A. Shaykin, and T. M. Zaboronkova, “Whistlers in thermally generated ducts with enhanced plasma density: Excitation and propagation,” *Phys. Scr.*, Vol. 62, No. 1, 51–65, 2000.
3. Kudrin A. V., L. E. Kurina, and E. Yu. Petrov, “Ionization formation of plasma inhomogeneity by the near-zone field of a magnetic-type source in a magnetized plasma,” *Journal of Experimental & Theoretical Physics*, Vol. 92, No. 6, 969–978, 2001.
4. Kudrin A. V., E. Yu. Petrov, G. A. Kyriacou, and T. M. Zaboronkova, “Electromagnetic radiation from sources embedded in a cylindrically stratified unbounded gyrotropic medium,” *Progress In Electromagnetics Research B*, Vol. 12, 297–331, 2009.

Eigenanalysis for Lossy or Open Periodic Structures Incorporating the Floquet Field Expansion

Spyros J. Lavdas, Panagiotis Tsompanis, Christos S. Lavranos, and George A. Kyriacou

Microwaves Lab., Department of Electrical and Computer Engineering
Democritus University of Thrace, Xanthi 67100, Greece

Abstract— The present work aims at an eigenanalysis methodology for lossy or open periodic structures incorporating the Floquet field expansion within the FDFD formulation. For that case, a β -eigenvalue problem is formulated but this leads to a non linear eigenvalue problem. Different eigenvector — eigenvalue transformations are currently tried in order to remove the nonlinearity. Periodic structures resulting to negative refractive index comprised of magnetized ferrite slabs and dipole arrays are considered as particular examples.

1. INTRODUCTION

The unique electromagnetic features of periodic structures attracted a huge research interest during the last decades. These features enabled the development of novel metamaterials and were exploited in frequency selective surfaces, phased arrays and numerous electromagnetic bandgap applications. The analysis and design of such structures have received particular attention which is almost exclusively directed toward the deterministic numerous simulations. Namely, an electromagnetic simulation of periodic structure excited by a specific source. Even though this analysis served as a very useful tool, it does not offer the required physical insight, while it does not provide any means to devise novel structures. On the other hand, an eigenanalysis reveal the physical behavior of the structure. In particular, the resulting eigenfunctions can be exploited to devise novel features and enable multifunctionality of periodic structures. Besides, a variety of microwave applications and in particular conformal antennas with their beamforming networks, require a simulation tool capable of handling periodic structures loaded with inhomogeneous and anisotropic media.

An appropriate eigenanalysis for the three-dimensional waveguiding periodic structures was developed in our previous work [1], which was able to handle anisotropic media. For this analysis a Finite Difference Frequency Domain (FDFD) method was employed in orthogonal Curvilinear Coordinates Yee type mesh [2]. At this first attempt the eigenvalue problem was formulated and solved for the eigenfrequencies (ω -formulation) or the wavenumber. Namely, the range of a real valued (ignoring losses or radiation) Floquet wavenumber was defined and scanned in an iterative solution procedure. This procedure yields the Bloch diagrams. However this kind of ω -formulation is restricted to closed periodic structures, since we assume the propagation constant to be real.

The present work aims at an eigenanalysis methodology for lossy or open periodic structures incorporating the Floquet field expansion within the FDFD formulation. The ω -formulation of such geometries requires the knowledge of the range of values for the phase and especially attenuation constants which are the unknowns to be sought. For that case, a β -eigenvalue problem is formulated and solved for the complex propagation constants (eigenvalues) with the Arnoldi iterative Algorithm. The periodicity of the structure is accounted through the incorporation of Floquet Field Expansion within the FDFD formulation. The boundary conditions are in turn imposed on the remaining surfaces of the unit cell and especially at the interface with free space, where an artificial-separation absorbing boundary is introduced. For that case, the Absorbing Boundary Conditions (ABCs) or the Perfect Matching Layers (PML) are usually assumed but this approach results to unwanted spurious eigenvalues, the so-called Berenger modes. One of the future tasks of this research aims at overcoming this drawback through exact-global truncation techniques. The main difficulty encountered in the β -formulation is that the eigenproblem becomes non linear and this constitutes the main drawback of the presented approach. However, due to the important applications that can be supported, it worth to deal with this complexity.

2. GEOMETRY OF THE PROBLEM

For the establishment of the proposed method a particular geometry was considered. Specifically, we suggest an eigenanalysis technique for the study and design of a structure that is loaded periodically with a dipole array built on a magnetized ferrite in order to synthesize a double negative metamaterial (DNG). A technique based on the Finite-Difference in Frequency Domain method

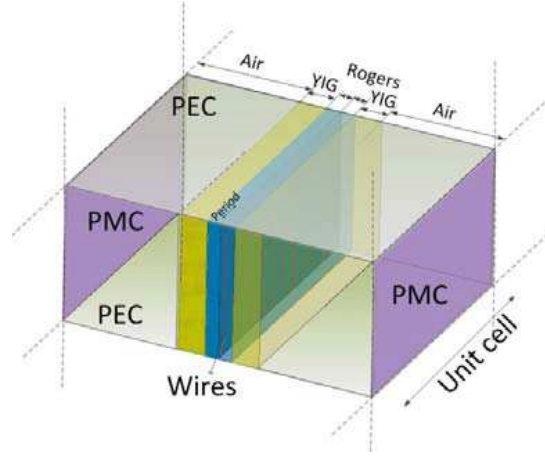


Figure 1: Geometry of the unit cell for the dipole array-magnetized ferrite DNG metamaterial utilized in “deterministic” simulations. The assumed boundary conditions related to field symmetries are also presented.

incorporating the Floquet Field Expansion was utilized. Hence, the high order Floquet harmonics, that can possibly manifest the negative refraction properties of a periodic structure, were also taken into consideration. Indeed the eigenanalysis reveal the physical behavior of the structure, since all of the excited eigenmodes supported by this periodic structure can be estimated. In particular, the resulting eigenfunctions can be exploited to devise novel features and enable multifunctionality of the periodic structures that construct DNG metamaterials. As explained above, herein we aim at the design of an artificial DNG metamaterial that is consisted of a non conducting ferrimagnetic medium, in order to provide negative permeability, and a dipole array, in order to ensure a negative permittivity (Fig. 1). However, the interaction between the ferrimagnetic and the wire array, which possibly destroys the negative permittivity of the wire, can be overcome by maintaining an air gap between ferrimagnetic and wires (Fig. 1). The usual approach for the analysis of infinite periodic structures which is based on the discretization of a unit cell was followed herein. Alternatively, commercial electromagnetic simulators (deterministic approach) are utilized to obtain some solutions to validate the proposed method. For this purpose, the symmetries of the electric and magnetic field as established in the study of metamaterials, e.g., [3], were exploited, to avoid the complications related to absorbing boundary conditions. Namely, perfect electric (PEC) walls were assumed at the two unit cell boundaries which are normal to the electric field (or normal to the electric dipoles) as shown in Fig. 1. Likewise, perfect magnetic walls (PMC) were imposed at the two unit cell boundaries normal to the magnetic fields (usually these were parallel to the split ring array). Recall that there is no need for periodic boundary conditions since we have incorporated the Floquet Expansion into the FDFD formulation according to our previous work [1].

3. FORMULATION

The proposed 3-D FDFD scheme aims at the formulation of an eigenvalue problem in Cartesian coordinates (x, y, z) for the propagation constant of a waveguiding structure as shown in Fig. 1. The whole analysis starts from Maxwell curl equations for the electric and magnetic fields in the frequency domain (i.e., assuming time harmonic dependence). The decoupling of Maxwell’s equations lead to the following wave equations:

$$(\bar{\epsilon})^{-1} \left\{ \vec{\nabla} \times \left[(\bar{\mu})^{-1} \vec{\nabla} \times \vec{E} \right] \right\} - \omega^2 \vec{E} = 0 \quad (1)$$

$$(\bar{\mu})^{-1} \left\{ \vec{\nabla} \times \left[(\bar{\epsilon})^{-1} \vec{\nabla} \times \vec{H} \right] \right\} - \omega^2 \vec{H} = 0 \quad (2)$$

The form of wave Equations (1)–(2) is appropriate for discretization with the aid of a Finite Difference Grid [2], where the involved cross product operators are formulated in a matrix form. In this manner all operations are reduced to simple matrix multiplications. The form of these operators depends on the approach used for the discretization of the fields. This method adopts the main characteristic of every finite-difference grid, which is the direct global discretization. Moreover, the solution domain is discretized to form a rectangular mesh, according to Yee’s mesh [2]. Both eigenvalue problems are equivalent regarding the calculation of the propagation constant of the

propagating mode. However, the type of the formulated eigenvalue problem is depends on the application of the boundary conditions in conjunction with the Floquet Theorem.

Floquet Theorem [4] is a spatial transform or actually a Fourier's series since the electric/magnetic field of lossless periodic structures is a spatial periodic function. Hence, the electric and magnetic fields are expressed as:

$$E_{(x,y,z)} = \sum_{n=-\infty}^{n=+\infty} C_{n_E} e^{-j\beta_n z} \quad \text{and} \quad H_{(x,y,z)} = \sum_{n=-\infty}^{n=+\infty} C_{n_H} e^{-j\beta_n z} \quad (3)$$

where $C_{n_{E,H}}$ are called Floquet coefficients:

$$C_{n_E} = \frac{1}{p} \int_0^p E_{(x,y,z)} e^{j\beta_n z} dz \quad \text{and} \quad C_{n_H} = \frac{1}{p} \int_0^p H_{(x,y,z)} e^{j\beta_n z} dz \quad (4)$$

and β_n is the Floquet wavenumber which is equal to:

$$\beta_n = \beta_0 + \frac{2n\pi}{p} \quad (5)$$

n stands for the index of Floquet harmonics and β_0 is the propagation constant corresponding to the fundamental harmonic ($n = 0$). According to Equations (1)–(5) the wave equation (e.g., electric field) is formulated as follows:

$$(\bar{\epsilon})^{-1} \left\{ \vec{\nabla} \times \left[(\bar{\mu})^{-1} \vec{\nabla} \times \sum_{n=-\infty}^{n=+\infty} \left(\int_{z=0}^{z=period} \vec{E} e^{+j\beta_n Z} dz \right) e^{-j\beta_n Z} \right] \right\} - \omega^2 \sum_{n=-\infty}^{n=+\infty} \left(\int_{z=0}^{z=period} \vec{E} e^{+j\beta_n Z} dz \right) e^{-j\beta_n Z} = 0 \quad (6)$$

The discretized form of the latter equation requires linear interpolation between the adjacent nodes of the electric field towards the periodicity of the structure in order to calculate the integrals (Floquet Coefficients) of the latter eigenvalue problem (Equation (6)). The complexity of the current eigenvalue is abruptly increased by the linear interpolation, thus formulating a non-linear eigenvalue problem:

$$\begin{aligned} & (\bar{\epsilon})^{-1} \left\{ \vec{\nabla} \times \left[(\bar{\mu})^{-1} \vec{\nabla} \times \left(\vec{E} e^{-j\beta_0 Z} \sum_{n=-\infty}^{n=+\infty} \left(\frac{e^{-j2n\pi \frac{z}{p}}}{j(\beta_0 + \frac{2n\pi}{p})} (e^{+j\beta_0 P} - 1) \right) \right) \right] \right\} \\ & - \omega^2 \vec{E} e^{-j\beta_0 Z} \sum_{n=-\infty}^{n=+\infty} \left(\frac{e^{-j2n\pi \frac{z}{p}}}{j(\beta_0 + \frac{2n\pi}{p})} (e^{+j\beta_0 P} - 1) \right) = 0 \end{aligned} \quad (7)$$

The solution of the above non-linear eigenvalue problem for the propagation constant offers a great physical insight as well as provides the means to devise novel structures, especially open DNG structures. This type of eigenanalysis is able to simulate surface waves even leaky ones with significant accuracy since the eigenvalue, propagation constant, could be a complex quantity which is derived by the solution of the previous eigenvalue problem (Equation (7)). Due to the significance of these solutions, we are working towards the elimination of this nonlinearity by implementing different eigenvector or eigenvalue transformations.

4. PRELIMINARY NUMERICAL RESULTS

Since the proposed method is currently under a series of validation tests only some preliminary results obtained using commercial simulations for the periodic structure of Fig. 1 are presented herein. By the symposium time we expect results from the proposed method to be compared against these reference results. The analysis of periodic structure of Fig. 1 led to a negative refractive index that is located on the center of an X-band waveguide simulations are carried out with the Ansoft's High Frequency Structure Simulator (HFSS). The simulation of the DNG metamaterial transmission properties under the incidence of plane waves is achieved through a planar waveguide system with a cross section of 22.86 mm × 10.16 mm. Namely, the dimensions and the properties of the composite (periodic structure) are shown in the following Table 1.

The electromagnetic parameters retrieval method that was proposed by Smith et al. [5] was used in order to calculate the effective parameters (ε , μ , n) of the whole periodic structure. According to the previous method, the required parameters can be retrieved by using the S -parameters. The final set of equations used in present work is:

$$\varepsilon_{eff} = \frac{n_{eff}}{Z_{eff}}, \quad \mu_{eff} = n_{eff} \cdot Z_{eff},$$

$$n_{eff} = \pm \frac{c}{2\pi \cdot f \cdot L} \cos^{-1} \left(\frac{1 - S_{11}^2 + S_{21}^2}{2S_{21}} \right), \quad Z_{eff} = \pm \sqrt{\frac{(1 + S_{11})^2 - S_{21}^2}{(1 - S_{11})^2 - S_{21}^2}} \quad (8)$$

According to (4)–(5) the diagram of Fig. 2(a) is extracted, where the refractive index is negative in the frequency region from 8.8 to 9.6 GHz and in a small band around 8.35 GHz. Moreover, in Fig. 2(b) the S_{21} parameter at the previous frequency range is shown. In addition, the negative

Table 1: Dimensions and inner properties of proposed periodic structure.

WR-90 X-Band Waveguide		Properties of the Inner media: YIG $\varepsilon_r = 13.8$, $\mu_r = 1$, 1 mm, $4\pi Ms = 1830$ G, $\Delta H = 22$ Oe, Conductivity = 1000 S/m
x -size	10.16 mm	Air: $\varepsilon_r = 1.0006$, $\mu_r = 1.0000004$
y -size	22.86 mm	Rogers RT/Duroid 5880: $\varepsilon_r = 2.2$, $\tan \delta = 0.0009$, 0.254 mm
z -size	18.096 mm	
Copper wires: $\varepsilon_r = 1$, $\mu_r = 0.999991$, width = 0.2 mm (z -axis), thickness = 0.018 mm (y -axis) Periodic distance between copper wires = 1.308 mm		

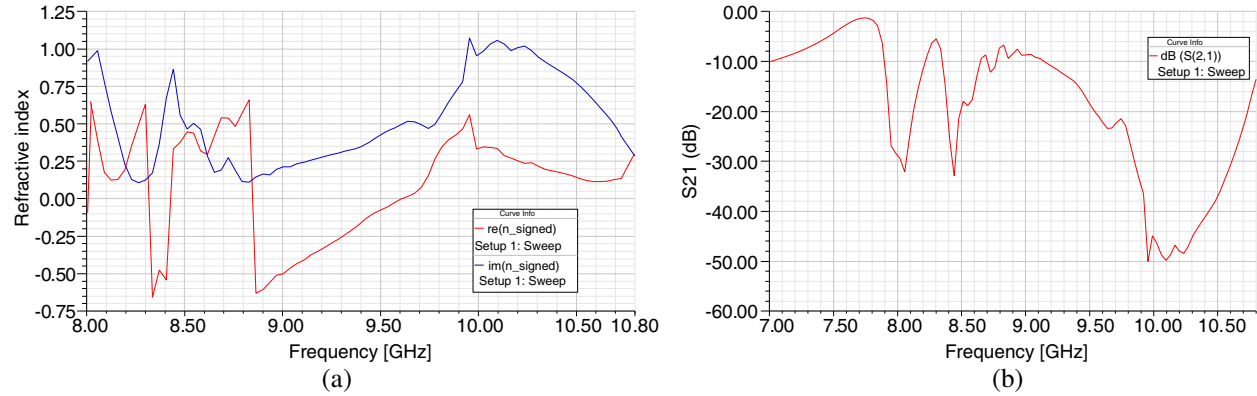


Figure 2: (a) The refractive index real and imaginary part versus frequency. (b) The magnitude (in dB) of S_{21} parameters for the proposed periodic structure.

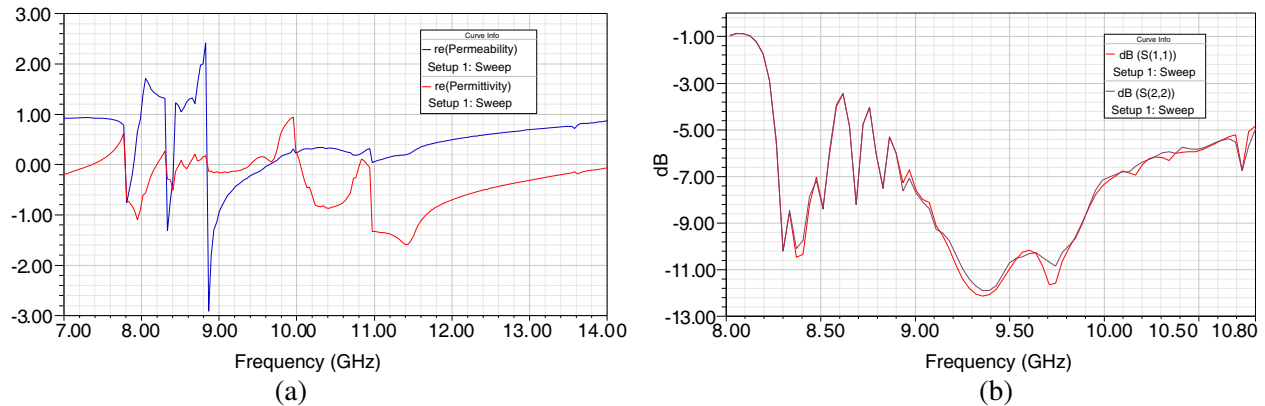


Figure 3: (a) Permeability (μ) and permittivity (ε) for the proposed periodic structure. (b) The magnitude (in dB) of S_{11} and S_{22} parameters for the proposed periodic structure.

refractive index is also verified by the negative values of permeability (μ) and permittivity (ε) at the same frequency range, as it is illustrated in Fig. 3(a). Recall, that Smith et al. state at the fact, that the Equation (8) are valid for homogeneous and symmetric inhomogeneous unit cells only if $S_{11} = S_{22}$, which is indeed fulfilled as shown in the diagram of Fig. 3(b).

5. CONCLUSIONS

The formulation of an eigenproblem for the complex Floquet wavenumber of periodic structures involving full tensor anisotropic media is tried herein by incorporating the Floquet expansion within a curvilinear FDFD scheme. This approach yields a challenging nonlinear eigenvalue problem which could be formulated to an equivalent linear one through eigenvalue or eigenvectors transformations. For this purpose we are trying to learn from analytical approaches already proposed for photonic periodic structures.

ACKNOWLEDGMENT

This work was financially supported by the Greek Ministry of Education, Lifelong Learning and Religious Affairs through the research project THALIS Design Techniques for Digitally Controlled RF-Microwave Structures Appropriate for Software Defined-Cognitive Radio (RF-EIGEN-SDR).

REFERENCES

1. Lavdas, S., C. Lavranos, and G. A. Kyriacou, "Periodic structures eigenanalysis incorporating the floquet field expansion," *Proceedings of the ICEAA 2011 Conference*, Torino, Italy, 2011.
2. Przybyszewski, P., "Fast finite difference numerical techniques for the time and frequency domain solution of electromagnetic problems," Ph.D. Dissertation, Gdansk, Poland, 2001.
3. Orten, P. Y., "Numerical analysis, design and two port equivalent circuit models for split ringresonator arrays," Master Thesis, Midle East University, February 2010.
4. Zhang, K. and D. Li, *Electromagnetic Theory for Microwaves and Optoelectronics*, 2nd Edition, Chapter 7, Springer, 2008.
5. Smith, D. R., D. C. Vier, T. Koschny, and C. M. Soukoulis, "Electromagnetic parameter retrieval from inhomogeneous metamaterials," *Physical Review E*, Vol. 71, 036617, 2005.

The Use of the Wigner Distribution Function for Defining the Concept of Quasi-point Source, and the Application of this Concept to the Restoration of Defocused Images

L. R. Berriel-Valdos¹, J. F. Aguilar¹, I. J. Orlando-Guerrero², R. Ortiz-Sosa¹,
S. Mejía-Romero¹, and J. E. A Landgrave³

¹Instituto Nacional de Astrofísica, Óptica y Electrónica, Pue., México

²Univ. de la Cañada (UNCA), Oax, México

³Centro de Investigaciones en Óptica, Gto., México

Abstract— We introduce the concept of quasi-point source (QPS) by means of the sampled Wigner distribution function (WDF), as applied to the detected image of a small incoherent disc object. A QPS is realized when the WDF of such image is always positive within the extended bandwidth corresponding to this function. To substantiate this concept, we employed a conventional microscope with Köhler illumination. We made use of a QPS to obtain an estimation of the defocused point spread function of an specific optical system. This function was employed next to construct the corresponding Wiener filter, in order to restore defocused images of extended objects.

1. INTRODUCTION

In a diffraction limited optical system (OS), with a circular exit pupil, the image of a point object obeys the well known Airy intensity distribution. The Fourier transform, or spectrum, of this function is the optical transfer function (OTF) of the OS, which in this case, of an aberration free system, is circularly symmetric, real, and positive inside its bandwidth. A quasi-point source (QPS) is an object with an image that follows closely the Airy pattern [1, 2]. If, according to an appropriate likeness criterion, the resemblance is insufficient, we regard the source as an extended object [2]. Otherwise, the object can be considered as a QPS, and the spectrum of its image can be expected to be real and positive, and a good estimation of the OTF inside the relevant bandwidth.

Apart from the finite size of the source, another factor that diminishes the likeness of the source image from the Airy pattern is the resolution of the detector, which typically is a CCD. The noise and the detection threshold of the CCD also contribute to lessen the resemblance [3]. These experimental facts traduce in source images with asymmetric central lobes and lacking the well known rings of an Airy pattern. The question naturally arises: can this image be of any use to justify the concept of a QPS?

In this work, we propose a criterion based on the WDF of the source image to establish if this can be taken as the image of a QPS. The criterion is the following: an object can be regarded a QPS if the WDF of the average intensity of a set of images of such object, evaluated at the origin of spatial coordinates, is positive for all frequencies within the extended bandwidth (EBW) corresponding to the WDF, which is four times the bandwidth of the OS working with coherent illumination [4]; otherwise, if the WDF assumes negative as well as positive values throughout the EBW, we can conclude that the object will be resolved by the OS, and will act, therefore, like an extended source.

Following this criterion, we can select a QPS to generate out-of-focus images, and obtain from them the defocused OTF of the OS. It is possible to use this latter function to produce a Wiener filter, and restore with it the defocused image of a whole scene [5].

2. THEORY

In an optical system operating with incoherent illumination and including a CCD detector, the average intensity of a set of detected images [3], $\bar{g}_n(x, y)$, of an object $o(x, y)$ is given by the equation

$$\bar{g}_n(x_i, y_j) = h(x_i, y_j) * o(x_i, y_j) + \bar{n}(x_i, y_j), \quad (1)$$

where (x_i, y_j) are rectangular coordinates, and the functions $h(x_i, y_j)$ and $\bar{n}(x_i, y_j)$ represent the intensity point spread function (IPSF) and the average noise, respectively. The sub-indices $i = 0, \dots, M - 1$ and $j = 0, \dots, N - 1$ designate the pixels in the CCD, $M \times N$ being the total number

of them. In the absence of noise, from Eq. (1) follows that the image of an ideal point source, $o(x, y) = \delta(x, y)$, is the sampled Airy pattern

$$g(r_{i,j}) = h(r_{i,j}) = \left\{ \frac{J_1 \left[\frac{2\pi}{\lambda} NA \cdot r_{i,j} \right]}{\frac{\pi}{\lambda} NA \cdot r_{i,j}} \right\}^2, \quad (2)$$

where $J_1(\dots)$ is the Bessel function of the first kind and first order, $r_{i,j} = \sqrt{x_i^2 + y_j^2}$ is the radial coordinate, NA the numerical aperture of the system, and $\bar{\lambda}$ the mean wavelength.

In general, the spectrum of the image $\bar{g}_n(x_i, y_j)$ is given by

$$\bar{G}_\eta(u_k, v_m) = H(u_k, v_m) O(u_k, v_m) + \bar{\eta}(u_k, v_m), \quad (3)$$

where $H(u_k, v_m)$ is the OTF and $\bar{\eta}(u_k, v_m)$ is the spectrum of the average noise. In general, $\bar{G}_\eta(u_k, v_m)$ is a complex valued function. From $\bar{G}_\eta(u_k, v_m)$ or $\bar{g}_n(x_i, y_j)$ is not always possible to decide whether the object is a QPS or not. For this end, a more useful approach would be to compute the *WDF* of $\bar{g}_n(x_i, y_j)$ at the origin of spatial coordinates, $W_{\bar{g}_n}(x'_i = 0, y'_j = 0; u_k/2, v_m/2)$. In terms of the image average intensity distribution

$$W_{\bar{g}_n}(0, 0; u_k/2, v_m/2) = \sum_{i=0}^{M-1} \sum_{j=0}^{N-1} \bar{g}_n(x_i, y_j) \bar{g}_n(-x_i, -y_j) e^{-j2\pi(u_k \frac{x_i}{M} + v_m \frac{y_j}{N})}. \quad (4)$$

Since the bandwidth of this function is twice the bandwidth of $H(u_k, v_m)$, we refer to it as the EBW. Knowing this, the criterion for resolution that we propose is

$$W_{\bar{g}_n}(0, 0; u_k/2, v_m/2) > 0, \quad \sqrt{u_k^2 + v_m^2} \leq 4w, \quad (5)$$

where w is the coherent cut-off frequency of the system. In words: if the inequality in Eq. (5) holds, the OS does not resolve the object and this can be considered a *QPS*; otherwise, if the function in Eq. (4) assumes negative as well as positive values, the object is resolved and can be considered an extended source. Eq. (5) states, therefore, the positivity condition for the *WDF* on which our criterion for resolution rests.

Once the positivity condition [Eq. (5)] is verified for $\bar{g}_n(x_i, y_j)$ throughout the EBW, we remove the central peak in its spectrum, $\bar{G}_\eta(u_k, v_m)$, caused by the background noise of the CCD. With this we increase the contrast of the image average intensity $\bar{g}_n(x_i, y_j)$, and get a better estimation for the IPSF, $\hat{h}(x_i, y_j)$. By means of a simple Fourier transformation of $\hat{h}(x_i, y_j)$ we obtain the corresponding estimation for the OTF, $\hat{H}(u_k, v_m)$. By slightly defocusing a QPS, we can similarly obtain an estimation of the IPSF and the OTF for the defocused OS, $\hat{h}_d(x_i, y_j)$ and $\hat{H}_d(u_k, v_m)$, and with the latter create a Wiener filter

$$\hat{F}(u_k, v_m) = \frac{\hat{H}_d^*(u_k, v_m)}{|\hat{H}_d(u_k, v_m)|^2 + \alpha}, \quad (6)$$

where α is a constant, and the symbol $*$ stands for complex conjugation. To demonstrate the relevance of the concept of a QPS, we will use this filter to restore a defocused image of an extended object, consisting of a set of latex spheres with a nominal diameter of 10 μm .

3. EXPERIMENTAL RESULTS

In our experiment the OS was a conventional, transmission bright field microscope, equipped with Köhler illumination and a $4\times$ (0.1) objective lens. The images were captured with a SONY XCL-5000 CCD camera, which has $2048\text{H} \times 2050\text{V}$ pixels and a pixel pitch of 3.45 μm . For their acquisition we employed a PCI-142924 frame grabber from National Instruments. The average image of the QPS was obtained from 20 images of the object, which was a pinhole of 0.8 μm in nominal diameter. Fig. 1(a) shows the average image of the pinhole, $\bar{g}_n(x_i, y_j)$, in 100×100 pixels.

Fig. 1(b) shows the modulus of the corresponding spectrum in 1024×1024 pixels. The bandwidth of the spectrum, or OTF (if the object is a QPS) is delimited by the circle with the dotted-line. In Fig. 1(c), on the other hand, we display the function $|W_{\hat{g}}(0, 0; u_k/2, v_m/2)|$. We can readily notice that this function has no zeros inside the EBW, bounded by the circle with the dotted-line. Fig. 1(d) shows the profile of the previous image along the u_k coordinate, the function $|W_{\hat{g}}(0, 0; u_k/2, 0)|$. This is clearly positive within the limits of the EBW, shown here with two vertical dotted lines.

Figure 2(a) shows the defocused image of the pinhole which serves for an estimation of the defocused IPSF. The image of a set of spheres, with the same amount of defocus than the pinhole, is shown in Fig. 2(b). The spectrum of this image is multiplied by the appropriate Wiener filter [Eq. (6)], and the fast Fourier transform of this product is subsequently computed to obtain the restored image [Fig. 2(c)]. For the sake of comparison, in Fig. 2(d) we present the in-focus image of the sample.

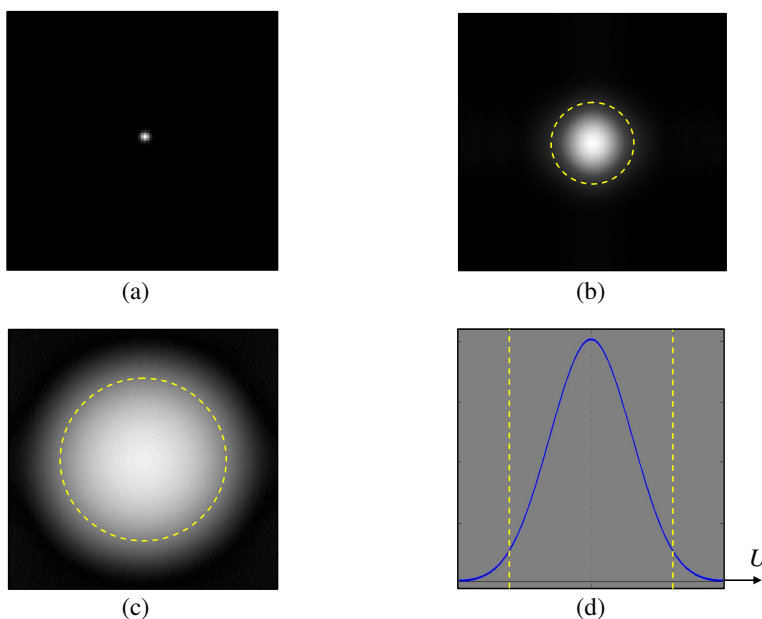


Figure 1: (a) Average image, (b) image spectrum, (c) modulus of the WDF, and (d) profile of the WDF.

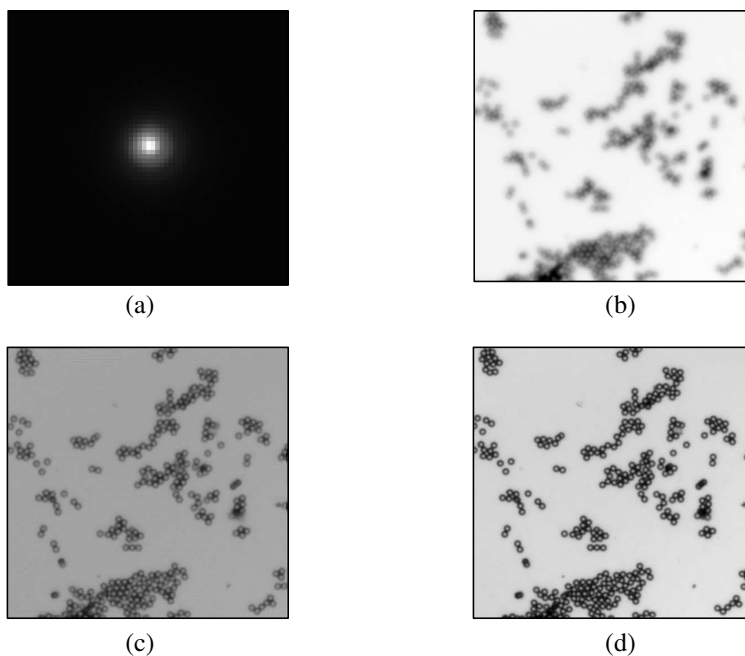


Figure 2: (a) Defocused image of the pinhole, (b) defocused image of the sample, (c) restored image, and (d) in-focus image of the sample.

4. CONCLUSION

The criterion advanced here to decide whether an object is a QPS or not was verified with microscope images obtained with low magnification and low numerical aperture objectives, although preliminary encouraging results, including restoration of defocused images, have also been obtained with objectives of higher magnification and NA . Our results are certainly repeatable for objectives with magnifications $4\times$ and $NA = 0.1$, using CCDs with a background noise below 5% of their maximum recordable intensity [6].

REFERENCES

1. Weinstein, W., "Images of incoherently illuminated bright and opaque disks," *J. Opt. Soc. Am.*, Vol. 45, 1006–1007, 1955.
2. Singer, W., M. Totzek, and H. Gross, *Handbook of Optical Systems, Vol. 2: Physical Image Formation*, Herbert Gross, Ed., Wiley-VCH, Weinheim, 2005.
3. Ronchi, V., "Resolving power of calculated and detected images," *J. Opt. Soc. Am.*, Vol. 51, 458–460, 1960.
4. Wigner, E., "On the quantum correction for thermodynamic equilibrium," *Phys. Rev.*, Vol. 40, 749–759, 1932.
5. Wiener, N., *The Extrapolation, Interpolation, and Smoothing of Stationary Time Series*, Wiley, New York, 1949.
6. Ortiz-Sosa, R., L. R. Berriel-Valdos, J. F. Aguilar, J. Carranza-Gallardo, I. J. Orlando-Guerrero, and S. Mejía-Romero, "Optical-digital restoration of out-of-focus color images detected in microscopy," *Proc. SPIE*, Vol. 8011, 801184-6, 2011.

The Interaction of Electromagnetic Waves from Sheets of Spherical Nano-elements Meshed on Concentric Spherical Shells

T. Sengor

Yildiz Technical University, Istanbul 34220, Turkey

Abstract— Possibilities creating nano-structures providing unnatural electromagnetic characteristics are given. Co-rings in nano-metric dimensions lying on different azimuth and/or equatorial planes are defined as nano-element providing such possibilities. These nano-elements are meshed on concentric spherical shells. The interaction of electromagnetic wave with both of nano element and meshed spherical surface are studied. For an example, the necessary configurations for both of the electromagnetically effective cloaking and the optically effective cloaking (invisibility) are given for this purpose.

1. INTRODUCTION

Possibilities creating nano-structures providing unnatural electromagnetic characteristics are given. Co-rings in nano-metric dimensions lying on different azimuth and/or equatorial planes are defined as nano-element providing such possibilities. These nano-elements are meshed on concentric spherical shells. The interaction of electromagnetic wave with both of nano element and meshed spherical surface are studied. For an example, the necessary configurations for both of the electromagnetically effective cloaking and the optically effective cloaking (invisibility) are given for this purpose [1–3].

The loops are used at meta-material applications, frequently. The using of circular loop combinations on spherical substrates is offered in this paper to consider in both of artificial material studies and cloaking applications. The array combinations of the couples of semi-cross ring balls on dispersive chiralic substrates generate chirality values higher than the chiralities of natural chiral materials besides providing almost zero permittivity and almost zero permeability and negative chirality.

The using of circular loop combinations on non-planar substrates is offered in this paper to consider in both of artificial material studies and cloaking applications [3]. Two basic combinations are used: i) Parallely located circular loop lying on latitude circles on a spherical core. We call this element smooth ring ball. ii) Intersecting circular loop lying on meridian circles on a spherical core. We call this element cross ring ball. The circular loop is located on a spherical core having the radius a , that is sufficiently small. The magnitudes of the currents on the circular loops must be sufficiently large. These necessary conditions give a chance to generate TM_θ waves, which we call principal wave. Additionally, using of materials having time independent permittivity and θ -independent permeability brings the property of TE_ϕ waves to the previous TM_θ waves. We call the last TM_θ - TE_ϕ waves secondary wave. The arrangements at the circumstance of the ring balls bring the property of TM_r waves to the waves under the discussion. The last property enforces to bring the behaviour of TE_θ waves to the principal wave; therefore the principal wave gains the property of TEM_θ waves. The last property enforces adding the behaviour of TM_ϕ waves to the principal wave. So the wave under the discussion gains the property of TEM_ϕ waves. After all, the use of suitably built up layers of almost zero epsilon material and/or perfectly conducting material brings the behaviour of TE_r waves to the waves under the discussion. The final wave is gained a propagation characteristic fitting on the propagation characteristics of $TEM_{\theta\phi}$ waves and almost TEM_r waves.

The above said characteristic gives a way to produce suitable objects with spherical shapes in nanometer scale; those change the RCS of objects and therefore provide us to built structures demonstrating effective electromagnetic cloaking property. We call this structure effective electromagnetic cloaking device.

2. THE COMPONENT CASE

The smooth ring ball and the cross ring ball are illustrated at Figure 1. The current density is given at Table 1 for several ring ball configurations, where the δ is the Dirac's distribution and a is the radius of the spherical substrate. The u is the unit step function.

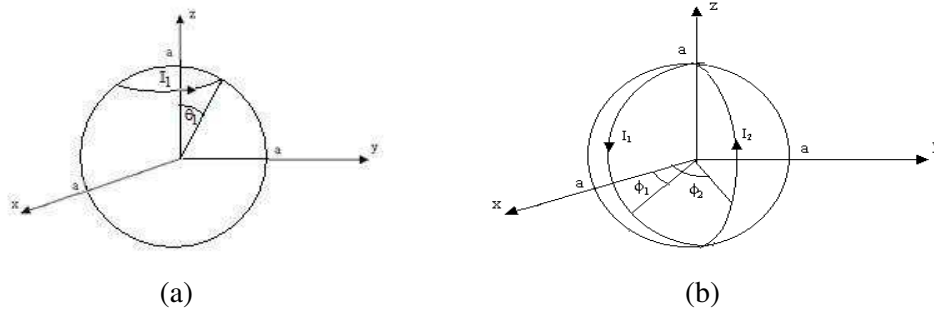


Figure 1: (a) The smooth ring ball: parallelly located loop lying on latitude circle of a spherical core. (b) The cross ring ball: intersecting two semi-loops located on meridian circles of a spherical core.

Table 1: The definitions of current densities induced on the several configurations of ring balls on spherical substrate.

Cross ring ball	$J_\theta = \frac{1}{a} I_1 [\delta(\phi - \phi_1) - \delta(\phi - \phi_1 - \pi)] \delta(r - a) [u(\theta) - u(\theta - \pi)]$
A couple of cross ring balls	$J_\theta = \{I_1 [\delta(\phi - \phi_1) - \delta(\phi - \phi_1 - \pi)] - I_2 [\delta(\phi - \phi_2) - \delta(\phi - \phi_2 - \pi)]\} \times \frac{1}{a} \delta(r - a) [u(\theta) - u(\theta - \pi)]$
Semi-cross ring ball	$J_\theta = \frac{1}{a} I_1 \delta(\phi - \phi_1) \delta(r - a) [u(\theta) - u(\theta - \pi)]$
A couple of semi-cross ring balls	$J_\theta = \frac{1}{a} \{I_1 \delta(\phi - \phi_1) - I_2 \delta(\phi - \phi_2)\} \delta(r - a) [u(\theta) - u(\theta - \pi)]$
Smooth ring ball	$\vec{J} = \vec{e}_\theta \frac{1}{a} I_1 \delta(\theta - \theta_1) \delta(r - a) [u(\phi) - u(\phi - 2\pi)]$
Semi-smooth ring ball	$\vec{J} = \vec{e}_\theta \frac{1}{a} I_1 \delta(\theta - \theta_1) [u(\phi) - u(\phi - \pi)] \delta(r - a)$
A couple of smooth ring balls	$\vec{J} = \vec{e}_\theta \frac{1}{a} [I_1 \delta(\theta - \theta_1) - I_3 \delta(\theta - \theta_2)] [u(\phi) - u(\phi - 2\pi)] \delta(r - a)$
A couple of semi-smooth ring balls	$\vec{J} = \vec{e}_\theta \frac{1}{a} [I_1 \delta(\theta - \theta_1) - I_2 \delta(\theta - \theta_2)] [u(\phi) - u(\phi - \pi)] \delta(r - a)$
Multiple cross ring balls	$J_\theta = \frac{1}{a} \sum_n I_n [\delta(\phi - \phi_n) - \delta(\phi - \phi_n - \pi)] \delta(r - a) [u(\theta) - u(\theta - \pi)]$

3. THE FORMULATION OF THE PROBLEM

The conditions those are given in section 1 bring the equations below:

$$\sin \theta \frac{\partial E_\phi}{\partial \theta} + \cos \theta E_\phi + r \sin \theta \frac{\partial(\mu H_r)}{\partial t} = 0 \quad (1a)$$

$$\sin \theta \frac{\partial E_\phi}{\partial \theta} + \cos \theta E_\phi - \sigma r \sin \theta E_r - r \sin \theta \frac{\partial(\varepsilon E_r)}{\partial t} = 0 \quad (1b)$$

$$E_\phi - r \frac{\partial(\mu H_\theta)}{\partial t} = 0, \quad E_\theta - \frac{\partial(E_r)}{\partial \theta} + r \frac{\partial(\mu H_\phi)}{\partial t} = 0 \quad (1c)$$

$$H_\phi + \sigma r E_\theta + r \frac{\partial(\varepsilon E_\theta)}{\partial t} = 0, \quad H_\theta - \frac{\partial(H_r)}{\partial \theta} - \sigma r E_\phi - r \frac{\partial(\varepsilon E_\theta)}{\partial t} = 0 \quad (1d)$$

The principal wave TM_θ generates TE_ϕ wave under the condition below:

$$\frac{\partial \mu}{\partial t} = 0, \quad \frac{\partial \varepsilon}{\partial t} = 0, \quad \frac{\partial^2 \mu}{\partial t \partial \theta} = 0 \quad (2)$$

The conditions (2) provide the generation of secondary wave; i.e., TM_θ - TE_ϕ . The Equation (1a) gives $H_r \equiv H_r(r, \phi)$, which gives $E_\theta \equiv 0$ due to the radiation condition for $t \rightarrow \infty$ and $\forall r \in [0, \infty)$, when the conditions at (2) are provided. So we get $H_\phi \equiv 0$, from (1d). After substituting these results at (1b) and (1c) we get

$$\frac{\partial(\varepsilon E_r)}{\partial t} = -\sigma E_r \quad (3)$$

therefore the nonzero components of the field are below, only:

$$E_r \equiv E_r(r, \theta, \phi, t), \quad H_r \equiv H_r(r, \phi) \quad (4)$$

The solution of (3) is below:

$$E_r = \frac{1}{\varepsilon} e^{-(\sigma/\varepsilon)t} e^{C(r, \theta, \phi)} \quad (5)$$

4. THE GLOBAL INVISIBILITY CONDITIONS FOR EM AND/OR OPTICAL CLOAKING

The Equations (1a)–(1d) gives

$$H_r = -(1/r)R(r)\frac{\partial F(\phi)}{\partial \phi} \cos(\omega t) \tag{6}$$

However, H_r is time independent due to (4); therefore, the functions R and F should provide the conditions of $R(r) \equiv 0$ and/or $(\partial F/\partial \phi) \equiv 0$. So we get $H_r \equiv 0$. The only non zero component remains as E_r . The solution at (5) gives the conditions below for almost invisibility and global invisibility, respectively:

$$i) \sigma \gg \varepsilon, \quad ii) \sigma \equiv 0 \text{ and/or } \varepsilon \rightarrow \infty.$$

5. ALMOST INVISIBILITY BUCKLER DESIGN FOR ELECTROMAGNETICALLY CLOAKING

The suitable configured spherical substrate involving conducting rings (see Figure 2) enforces the scattered field to propagate with a propagation characteristic fitting on the propagation characteristics of $TEM_{\theta\phi}$ waves and almost TEM_r waves if the diameter of the substrate is around 1 nm;

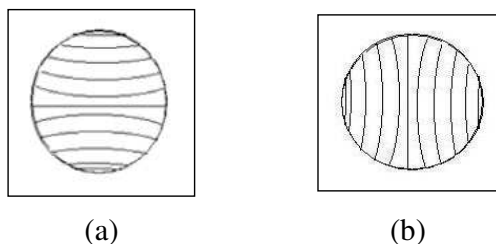


Figure 2: The Spherical EM Cloaking Nano-Elements: cloaking balls. (a) Horizontal cloaking ball: horizontally located loops lying on latitude circles on a spherical core. (b) Vertical cloaking ball: vertically located loops lying on latitude circles on a spherical core.

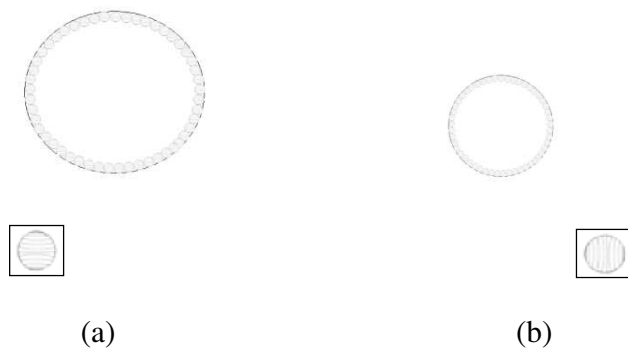


Figure 3: The EM buckler configurations. (a) Horizontal outer buckler. (b) Vertical inner buckler.

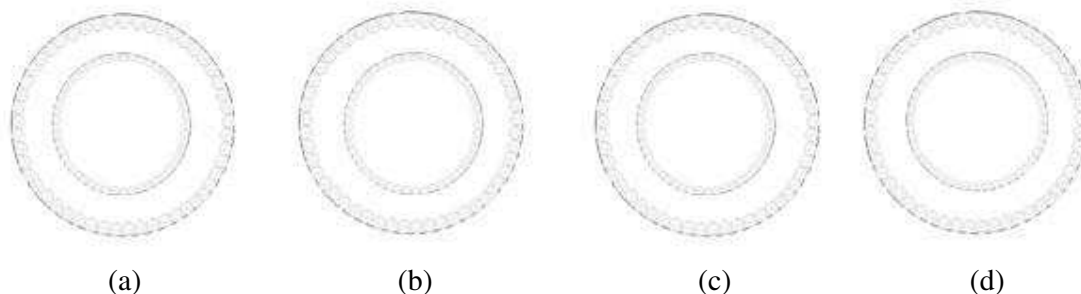


Figure 4: The EM outer-inner buckler configurations. (a) Horizontal outer-Horizontal inner buckler. (b) Horizontal outer-Vertical inner buckler. (c) Vertical outer-Vertical inner buckler. (d) Vertical outer-Horizontal inner buckler.

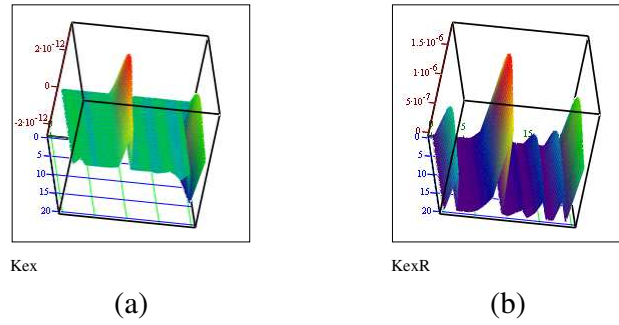


Figure 5: Radial component of electric field. (a) The modulus. Axes: blue- ω , green- t , red- $|\mathbf{E}_r|$. (b) $\text{Re} \{\mathbf{E}_r\}$. Axes: blue- ω , green- t , red- $\text{Re} \{\mathbf{E}_r\}$. $\varepsilon_\infty = 1.5$, $\varepsilon_s = 3.0$, $\delta_e = 2 \text{ rad/s}$, $\mu_s = 3.0$, $\mu_\infty = 1.5$, $a = 1 \text{ nm}$, $0 \leq \mu \ll 1 \text{ H/m}$, $0 \leq \mu \ll 1 \text{ F/m}$, $I_1 = I_2 = 1 \text{ pa}$, $\delta_h = 2 \text{ rad/s}$, $\delta_c = 1.9 \text{ rad/s}$.

therefore the using of the cloaking balls provide a suitable way to built global EM cloaking device for the waves of $f < 3 \times 10^{17} \text{ Hz}$. The cloaking balls are collated on a sphere enclosing the object that will be hid (see Figures 3 and 4).

If the diameter of cloaking ball is less than 10^{-10} m then realization of the global optical cloaking is possible.

6. SOLUTIONS AND RESULTS

The array combinations of the couples of semi-cross ring balls on dispersive chiralic substrates generate chirality values higher than the chiralities of natural chiral materials besides providing almost zero permittivity and almost zero permeability and negative chirality. The spherical substrate with the characteristics below is taken [2–5]:

$$\mathbf{B}(\mathbf{r}, t) = \mu(t) * \mathbf{H}(\mathbf{r}, t) + \left\{ \frac{\partial[\chi(t)\varepsilon(t)\mu(t)]}{\partial t} \right\} * \mathbf{E}(\mathbf{r}, t) + \sigma(t) * \mathbf{E}(\mathbf{r}, t) \quad (7)$$

$$\mathbf{D}(\mathbf{r}, t) = \varepsilon(t) * \mathbf{E}(\mathbf{r}, t) - \left\{ \frac{\partial[\chi(t)\varepsilon(t)\mu(t)]}{\partial t} \right\} * \mathbf{H}(\mathbf{r}, t) - \sigma^m(t) * \mathbf{H}(\mathbf{r}, t) \quad (8)$$

$$\chi(t) = \alpha \left(\frac{1}{\eta} \right) u(t) (\omega_p^2 / v_0) \left[v_0 \cos(v_0 t) - \left(\frac{v}{2} \right) \sin(v_0 t) \right] \exp(-vt/2) \quad (9)$$

The scattering of Gaussian pulse from a couple of semi-cross ring ball is depicted in Figure 5, where $\omega_{0e} = 2\pi 15 \times 10^9 \text{ rad/s}$, $\omega_{0c} = 2\pi 15 \times 10^9 \text{ rad/s}$, $-10^{10} < \chi < 10^{10}$, $\theta_1 \approx \theta_2 \approx 0.0177772 \times 10^{-3} \text{ rad}$, $\omega_{0h} = 2\pi 15 \times 10^9 \text{ rad/s}$.

REFERENCES

1. Sengor, T., "The interaction of electromagnetic waves from single sheet of spherical nano-elements meshed on spherical shell," *Proc. of 6th Nanoscience and Nanotechnology Conf.*, Cesme, Turkey, June 15–18, 2010.
2. Sengor, T., "Properties of a non-planar metamaterial elements: Ring resonators on a spherical substrate," *Proceedings of The First International Congress on Advanced Electromagnetic Materials in Microwaves and Optics, Metamaterials 2007 Congress*, Rome, Italy, October 22–26, 2007.
3. Sengor, T., "Analytical theory of effective global cloaking processes: Designing the spherical EM cloaking nano-element," *Proceedings of NATO Advanced Research Workshop, META'10, International Conference on Metamaterials, Photonic Crystals and Plasmonics*, Cairo, Egypt, February 21–25, 2009.
4. Sengor, T., "State approach in artificial materials development in electromagnetics," *PIERS Proceedings*, 568, Pisa, Italy, March 28–31, 2004.
5. Sengor, T., "The state space approach and modified state equations solution in dispersive chiral media," *Proc. of XXVIIIth General Assembly of the Intern. Union of Radio Science*, India, ND, October 23–29, 2005.

Quantum Electrodynamical Interaction Mechanisms in Simple Atoms

T. Sengor

Yildiz Technical University, Istanbul 34220, Turkey

Abstract— This study suggests semi-analytical considerations for quantum electrodynamical interaction mechanisms in simple atoms displaying computational processes to perform the task with sufficient accuracy and sensibility. The analytical frame is, basically, an extension of the Frequency Depended Finite Difference Method in Time Domain, E(FD)²TD. The E(FD)²TD scheme is transferred on a state space algorithm to provide the possibility of the application of the method on atomic and/or molecular structures.

1. INTRODUCTION

This paper involves a study suggesting semi-analytical considerations for quantum electrodynamical interaction mechanisms in simple atoms displaying computational processes to perform the task with sufficient accuracy and sensibility. The analytical frame is, basically, an extension of the Frequency Depended Finite Difference Method in Time Domain, E(FD)²TD. The E(FD)²TD scheme is transferred on a state space algorithm (see [1] for the interpretation of the method) to provide the possibility of the application of the method on atomic and/or molecular structures. The interaction of an electron and an electromagnetic field considered applying some modification to the total Hamiltonian, first for this purpose in an E(FD)²TD scheme. Second, the interaction of a proton and an electromagnetic field is considered in a similar way. Later, the He⁺⁽⁻⁾ and H⁺⁽⁻⁾ ions interacting with an external electromagnetic wave is studied by doing some modifications on the process. These modifications are obtained by re-manipulating the equation of total Hamiltonian including the electromagnetic field to get the state equations and suitable variables with appropriate matrix presentations. This approach is used first in [1–6], systematically.

2. SCATTERING OF GAUSSIAN ELECTROMAGNETIC WAVE FROM A HYDROGEN-LIKE ATOMIC PAIR

A gaussian pulse source with following details is applied for studying the wave scattering from the simple atomic structure:

```

if SourceType == 2
lambda0 = lambda; % central wavelength of pulse
freq0 = cc/lambda0; % central frequency of pulse
omega0 = 2.0*pi*freq0;
rtau = 1.5e-15; % input ('Enter the half-width value at 1/e of the Gaussian pulse [sec] (default: 1.5e-15):');
tau = rtau/dt; % half-width value at 1/e in # timesteps
delay = 3*tau; % time delay in # timesteps
source = zeros(1, nmax);
for n = 1 : nmax
source(n) = Eo*sin(omega0*(n-delay)*dt)*exp(-((n-delay) 2/tau 2));
end
end

```

The state equation formalism is applied on the alternate approaches generated by alterations of FDTD approaches.

3. SOLUTION OF RELATIVISTIC DIRAC'S EQUATION

The simulation results are illustrated in Figure 1 for the H⁺⁽⁻⁾ ionic pair. The near field effect of the scattering is contraction of equiphase surfaces; however, far field effect is displayed as multiple expansion processes which never allow the reshaping of equiphase surfaces to bring the original waveform of the pulse. This characteristic may be potentially used to generate suitable detection algorithms for detecting the undetectable things.

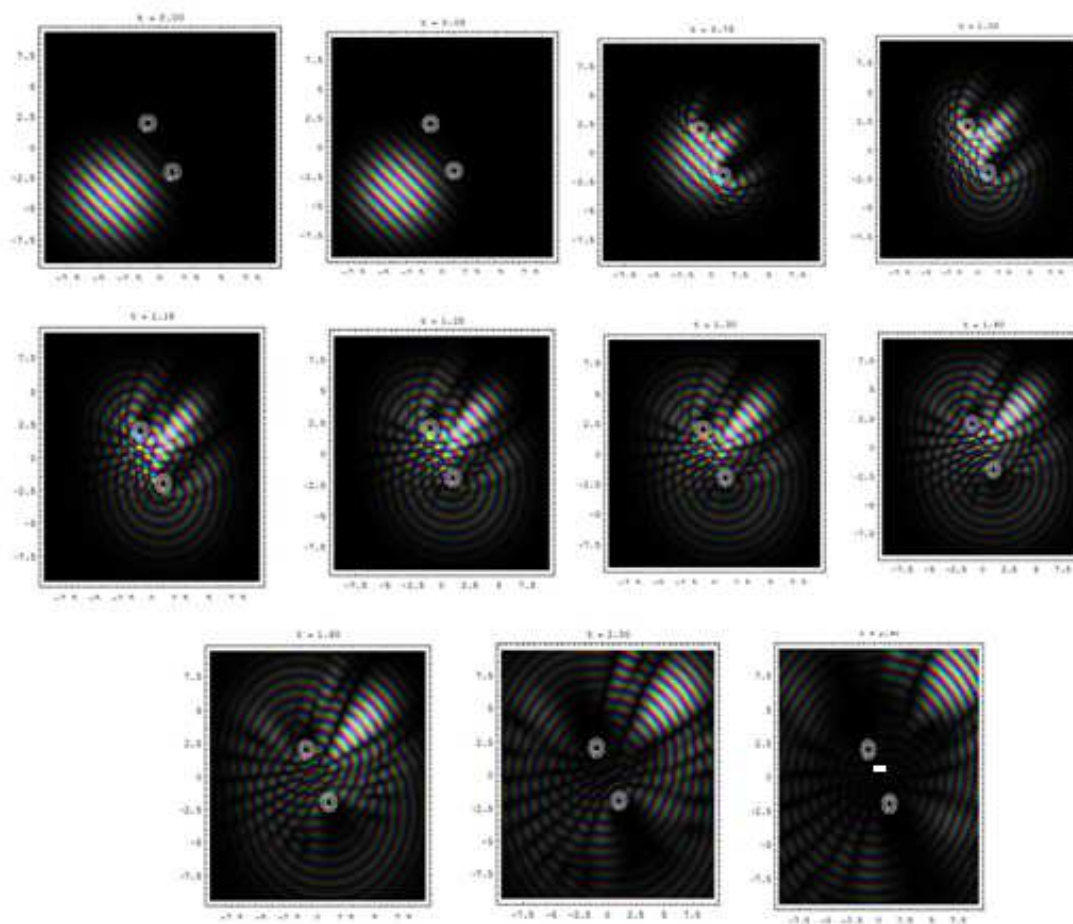


Figure 1: Scattering of Gaussian electromagnetic wave from hydrogen-like atomic pair.

4. CONCLUSIONS

The quantum electrodynamical interaction mechanisms in simple atoms are studied with semi-analytical computational processes. Potential application processes of the used structure are discussed.

REFERENCES

1. Sengor, T., "Inversion algorithm for chiralic materials," *Proceedings of Progress In Electromagnetics Research Symposium*, Invited Paper, The Electromagnetics Academy, Cosmosquare International Education and Training Center, Osaka, Japan, July 18–24, 2001.
2. Sengor, T., "The interaction of electromagnetic waves from single sheet of spherical nano-elements meshed on spherical shell," *Proceedings of 6th Nanoscience and Nanotechnology Conference*, Çeşme, İzmir, NanoTR6, June 15–18, 2010.
3. Sengor, N. S. and T. Sengor, "Chiralic circuits," *Proceedings of Progress In Electromagnetics Research Symposium*, Invited Paper, The Electromagnetics Academy, Cosmosquare International Education and Training Center, Osaka, Japan, July 18–24, 2001.
4. Sengor, T., "State approach in artificial materials development in electromagnetics," *Proceedings of Progress In Electromagnetics Research Symposium*, Invited Paper, 568, The Electromagnetics Academy (USA), University of Pisa, Pisa, Italy, March 28–31, 2004.
5. Sengor, T., "The state space approach and modified state equations solution in dispersive chiral media," *Proceedings of XXVIIIth General Assembly of the International Union of Radio Science*, URSI GA 2005, Abstracts Book, COM2-01430-2005, Conference CD, URSI New Delhi 2005, Paper No. COM2-01430-2005, New Delhi, India, October 23–29, 2005.
6. Sengor, T., "A chiralic circuit element and its use in a chiralic circuit," *Complex Computing-Networks, Brain-like and Wave-oriented Electrodynamical Algorithms*, Springer Proceedings in Physics, Vol. 104, Part 1, 203–209, 2006.

Inflective Nano-antenna

T. Sengor

Yildiz Technical University, Istanbul 34220, Turkey

Abstract— In this paper, an antenna structure at nano scale, overcoming the difficulties of including capacitive elements in integrated electronic circuits and devices is developed. The element is based on the wave phenomena around the inflection points on discontinuities of the field. Inflective coordinates are used to overcome the difficulties coming from the inflection points. The simplest case of such discontinuities is created by joining one end point of a convex semi-circular thin wire with one end point of a convex semi-circular thin wire where all the end points of both wires trace the same line. The inflective nano-antenna is a extra thin and short wire with an inflection point and has a time varying potential distribution. The deviations of potential of inflective element depend on spatial coordinates on inflective wire.

1. INTRODUCTION

The inflection points still raise some critical problems in electromagnetic phenomena. There are some results related to these problems, to name some: diffraction from S-shaped discontinuities [1], diffraction from the edged concave-convex boundaries [2], and smooth targets with inflection points [3, 4]. These works use some approximations and focus on the uniformization of physical optics. The first paper requires a radius of curvature that is relatively large at every point on the surface but gives more compact solution than the solution given in the second paper. The second paper describes an asymptotic, high frequency solution for the scattering from a concave-convex shaped boundary with an edge. This second paper requires that the associated reflected ray caustic with transition regions of two points of inflection do not come close together. The authors' PO based uniform analysis fails near grazing angles of incidence on the reflecting boundaries with points of inflection. The third and fourth papers have used PO approximations. Therefore, it is clear that the influence of inflection points on electromagnetic field still has some open questions. A recent paper aimed to open the analytical insights behind the inflection points when the solutions of the basic field equations are asked [5]. This last paper describes inflective circular cylindrical coordinates and derives the essential analytical expressions for the solution of problems with inflection points. The evaluation is due to the new defined inflective series obtained by applying the extracted separation method, which is defined here. The extracted separation method comes with some modifications on extended separation method in [5, 6]. In view of the above comments, this paper aims to extend the analytical perspectives of [5–8] for the wave phenomena around inflection points in nano-scale and studying to design useful metamaterial structures.

The most simple inflection point can be arranged by two semi-cylinders that are placed side by side as in Fig. 1(a). Here the curves L_i^{ra} and L_i^{la} are the upper and lower halves of cylinders with radii a . When the points on such curves are coordinated by repeating the curve $L_i^a \triangleq L_i^{la} \cup L_i^{ra}$ without changing the inflection point $O(0, 0)$ as in Fig. 1(b), it is seen that the trajectory obtained is more versatile than using the common cylindrical coordinate lines. However, if we use the weighted inflective circular cylindrical coordinates x^1 and x^2 of point P then the separations of the differential equations arising from field calculations become possible. These coordinates are defined as

$$x^1 \equiv q\rho/\cos\phi, \quad x^2 \equiv p\phi, \quad x^3 \equiv z \quad (1)$$

where p and q are finite real numbers other than zero [5]. The distance ρ and angle ϕ are usual circular cylindrical coordinates of P (see Fig. 1(c)). We call weight parameters p and q .

To address the essential mathematical analysis we deal with the scalar wave and consider the solution of Helmholtz's equation.

2. THE WAVES IN INFLECTIVE COORDINATES

Let Ψ be a scalar, and time independent wave function then a wave propagation problem can be solved by extending the usual separation method in inflective coordinates. If Ψ is written as $\Psi(x^1, x^2) = X_1(x^1)X_2(x^2)$ on $x^3 \equiv 0$, then Helmholtz's equation gives the first and second terms

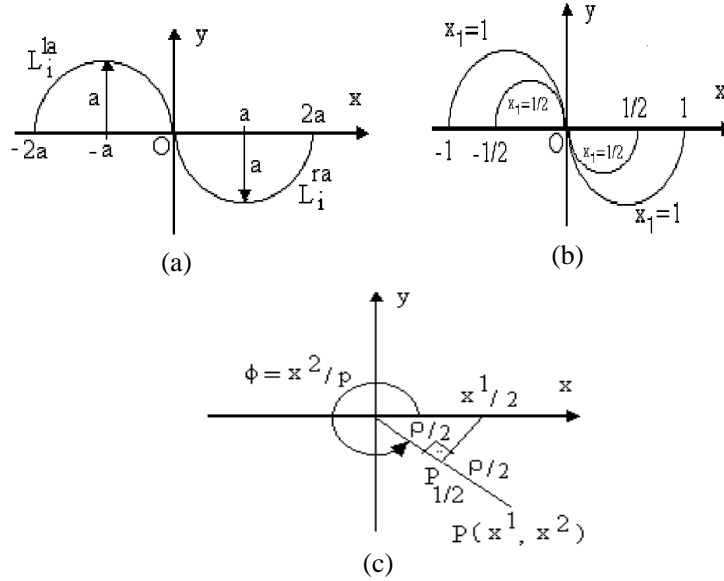


Figure 1: Inflective circular cylindrical coordinates system. (a) Simplest inflection point. (b) More versatile trajectory. (c) Relation with circular coordinates of P .

of u are only the functions of x^1 and x^2 , respectively. So we may write [8]

$$X_1'' - (x^1)^3 X_1' + (\kappa_1 x^1/q)^2 X_1 = 0 \tag{2}$$

$$X_2'' - X_2' \frac{1}{p} \text{seng}(x^2/p) + X_2 (2\kappa_2/q)^2 \frac{1}{p^2} [s_c(x^2/p)]^2 = 0 \tag{3}$$

3. THE CHARGES MOVING AROUND INFLECTIVE POINTS

If

$$\Psi(x, y, z, t) \rightarrow \text{Re} \left\{ e^{-i\omega t} \tilde{\Psi}(x, y, z,) \right\} \tag{4a}$$

then

$$\nabla^2 \Psi - \frac{1}{c^2} \frac{\partial^2 \Psi}{\partial t^2} = \frac{m_0^2 c^2}{\hbar^2} \Psi \rightarrow \nabla^2 \tilde{\Psi} + \left(k^2 - \frac{m_0^2 c^2}{\hbar^2} \right) \tilde{\Psi} = 0 \tag{4b}$$

After long calculations the above mentioned inflective series X_1 , X_2 and X_3 bring three independent solutions of the Relativistic Schrödinger Equation of free particle moving around an inflection point for cylindrical symmetric cases.

At the case of zero mass at rest

$$m_0 = 0 \Rightarrow \text{Photon} \tag{5a}$$

$$\nabla^2 \Psi - \frac{1}{c^2} \frac{\partial^2 \Psi}{\partial t^2} = 0 \rightarrow \nabla^2 \tilde{\Psi} + k^2 \tilde{\Psi} = 0 \tag{5b}$$

So again, the inflective series X_1 and X_2 define two independent solutions for the photon moving around an inflection point for cylindrical symmetric cases.

The electron sharing processes are suitable for considering them as inflective nano-antenna structures. These structures are analyzed between neighbor atoms in simple atomic systems using quantum electrodynamics. The critical pass and transition structures are derived by considering Casimir-Polder potential and van der Waals force and Forster energy transfer. The structures involving triggering that transition mechanisms are suitable to design extra high density and fast data storage processes. The fields on the nanometer scale bring useful applications in both the optical communication and computing. The high resolution optical microscopy and high-density optical data storage and electromagnetic cloaking and optical invisibility and several meta-material applications. From this point of view, this paper aims bringing some possible new sights and

solutions to atom-photon-electron-proton interactions in the optical near-field and their potential applications [8–11].

Green functions are used with the external perturbation on the Hamiltonian in time dependent particles system. A geometric approach is considered to explain the interaction processes. A brief description of the geometric method is given below, which is explained with electron transitions.

4. CONCLUSIONS

The wave phenomenon is studied near inflection points at nano scale. The analytical essentials are derived for the solution of Helmholtz's equation when inflective boundaries are included. The evaluation is obtained by the extracted separation method. The results are given by nano-scale manipulations for inflective wave series.

REFERENCES

1. Kempel, L. C., J. L. Volakis, T. B. A. Senior, S. S. Locus, and K. M. Mitzner, "Scattering by S-shaped surfaces," *IEEE Transactions on Antennas and Propagation*, Vol. 41, No. 6, 701–708, 1993.
2. Pathak, P. H. and M. C. Liang, "On a uniform asymptotic solution valid across smooth caustics of rays reflected by smoothly indented boundaries," *IEEE Transactions on Antennas and Propagation*, Vol. 8, No. 8, 1192–1203, 1990.
3. Ikuno, H. and L. B. Felsen, "Complex ray interpretation of reflection from concave-convex surfaces," *IEEE Transactions on Antennas and Propagation*, Vol. 36, No. 9, 1260–1271, 1988.
4. Ikuno, H. and L. B. Felsen, "Complex rays in transient scattering from smooth targets with inflection points," *IEEE Transactions on Antennas and Propagation*, Vol. 36, No. 9, 1272–1280, 1988.
5. Sengor, T., "Contribution of inflection points to field," *Electronics Letters*, Vol. 34, No. 16, 1571–1573, Aug. 6, 1988.
6. Sengor, T., *Static Field near Inflection Points*, Helsinki Univ. Tech. Electromagnetics Lab. Rept., 350, Jan. 2001.
7. Sengor, T., "Contribution of inflection points to waves," *Electronics Letters*, Vol. 35, No. 19, 1593–1594. Sep. 16, 1999.
8. Sengor, T., *Waves near Inflection Points*, Helsinki Univ. Tech. Electromagnetics Lab. Rept., 351, Jan. 2001.
9. Sengor, T., "Designing the nano-elements for global EM cloaking and optical invisibility," *International Conference on Nanomaterials and Nanosystems*, Istanbul, Turkey, Aug. 10–13, 2009.
10. Sengor, T., "The interaction of electromagnetic waves from single sheet of spherical nano-elements meshed on spherical shell," *NanoTR6*, Cesme, Turkey, Jun. 15–18, 2010.
11. Sengor, T., "Quantum electrodynamical interaction mechanisms among atoms in simple compounds," *CPC IX*, Cesme, Turkey, Oct. 14–16, 2010.

A Novel Proximity Measurement System Using Microwave Antennas

Yongjae Lee, Boris L. Sheikman, and Steven Y. Go

General Electric Corporation, USA

Abstract— In this paper, a novel approach for making proximity measurements using a microwave antenna system in an industrial setting is presented. The proposed technique is demonstrated by designing and building two differently sized antennas. Each antenna was placed inside its own mechanical housing in order to match the form and fit of a standard industrial eddy current sensor head. Matching the form and fit of currently accepted industrial dimensions will reduce the amount of redesign of the sensor mounts to accommodate the new system. Both of the differently sized antennas were designed to electrically resonate at a specific frequency. The first antenna was designed to resonate at ~ 3 GHz and the second antenna was designed to resonate at ~ 5.8 GHz. A vector network analyzer (VNA) is used to create the excitation signals and to monitor return loss changes as the observed target's displacement to the antennas is varied. Additionally, a linear stage from Thor Labs was used to carefully and repeatedly step a flat metal target away from the sensor head with the embedded antenna. This new system showed an extended measurement range compared to the conventional proximity measurement technologies. The microwave antenna system was able to measure a distance equal to at least $1 \times$ the diameter of the probe tip. Also, good sensitivity, i.e., significant return loss change (> 1 dB/mm), was obtained as the observed target displacement is varied. Furthermore, it showed great immunity to variations in permeability across a selection of metal targets. For example, at a fixed target displacement, the S_{11} variation between the different target materials was $< 5\%$. A commercial software package, Ansys' HFSS, was utilized for the design, modeling, and analysis of the overall microwave antenna system. The modeling results matched the performance of the prototypes to within 3%. Future work in the areas of temperature stability, materials, and signal processing methodologies is also presented.

1. INTRODUCTION

Numerous proximity measurement technologies [1–5] have been well demonstrated and widely applied in various industrial settings. Each of those technologies has at least one significant disadvantage to overcome. Eddy current technology [3, 4] is extremely sensitive to the permeability of the target material because it measures H (magnetic) field change due to the opposing H fields created by eddy currents on the metallic surface. Compensating for this sensitivity typically requires surface treatment of the target to be measured. Eddy current probes also have a limited measurement range which is approximately equal to about a half of the diameter of the probe or less. In a typical installation, the probe needs to be gapped at half of the full measurement range of the probe, which is a quarter of diameter of sensor head to the target [7]. Applications requiring additional range require either a bigger probe or additional smaller probes which results in increased cost. Other techniques such as ultrasonic [1] and optical sensor [6] are also costly and sensitive to contamination and changes to the dielectric through which it measures. LVDT (Linear Variable Differential Transformer) sensors require direct contact with the target and a lot of space for installation.

To alleviate and overcome these limitations, a novel proximity measurement approach is proposed. It utilizes an antenna operating in the near field range as a sensing element. Fig. 1 shows a system level block diagram of the microwave proximity system.

It is composed of three functional blocks which are:

- 1) The antenna as a sensing element,
- 2) The RF (Radio Frequency) transceiver for generating the current that will be used to excite the antenna, and
- 3) A signal processing system that will generate an output signal which is proportionate to the proximity.

The antenna in this instance was a 2D planar structure on a substrate. A copper radiating element was on the top surface and a grounding pattern was on the bottom surface. The RF transceiver system feeds an excitation signal to the antenna which causes the creation of an electromagnetic field that couples to the target. Electromagnetic energy is near-field coupled to the target. The coupling strength varies with the displacement of the target to the antenna. More or less coupling to the target will vary the impedance of the antenna. When the antenna's impedance

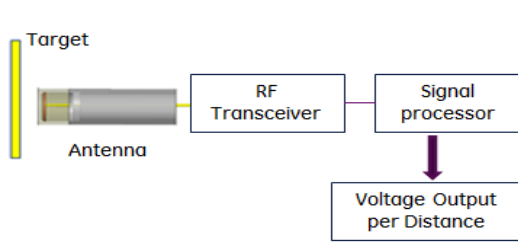


Figure 1: Schematic of microwave proximity measurement system.

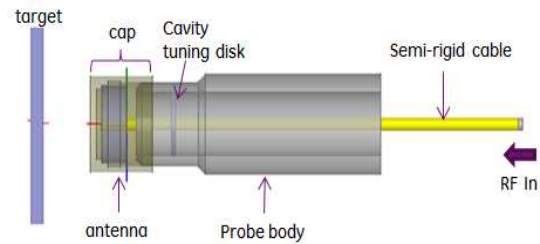


Figure 2: Profile view of the antenna assembly model.

changes from its nominal value, e.g., 50 Ohms, a reflection of the excitation signal is sent back to the RF transceiver from within the antenna structure and cable. A directional coupler is used to route the reflected signal to a signal processing system which will create a new signal that is proportional to the proximity. Power detectors and additional support circuitry are utilized for converting the reflected RF signal into a linear proximity voltage output. The output voltage can then be fed into control systems, data displays, data recorders, etc. in real time. Feasibility of the proposed system is examined by testing a prototype antenna operating at microwave frequency range with multiple target materials at various proximities.

This paper is organized as follows. An overview of the design and analysis of the antenna, measurement of the antenna performance, and modeling validation is given in Section 2. Section 3 presents the microwave proximity sensor's immunity to electrical run out. Section 4 will go into a discussion of future work.

2. MODELING/MEASUREMENT OF MICROWAVE ANTENNA

2.1. Modeling Validation of Antenna

Given the limited form factor of the antenna for practical industrial applications, we first investigated many different antenna types and geometries. The design procedure starts by creating various antenna types and patterns followed by integrating them with the other sensor assembly components as shown in Fig. 2 (cable, probe body, probe cap, antenna substrate, tuning disc, etc.) including a target to measure the proximity to. We utilized a commercial software package, ANSYS HFSS, for generating the 3D model and for the EM analysis [8]. The sensing element is 24.13 mm in diameter and it is encapsulated with a probe cap of 25.40 mm in diameter. These dimensions match the industry standard Bently Nevada 3300XL 25 mm probe head. The full sensor assembly was prototyped and tested using a network analyzer with an accurately controlled linear stage from Thor Labs for modulating the target proximity. Scattering parameters (S_{11}) or return loss changes were monitored as the target moves away along the axial direction of the antenna assembly.

Figure 3 presents both measured and simulated results of an antenna operating at ~ 3 GHz. Good agreement is obtained between the simulated and the measured data with 3% error. This modeling validation provided us with a high degree of confidence in the software for the design and analysis of antennas operating in the near field region. In the example dataset below, a significant S_{11} change is observed as the target displacement changes from 20 mm to 26 mm and we see that the dynamic range is ~ 10 dB, which is equates to > 1.5 [dB/mm] of antenna sensitivity. We refer to this scalar, [dB/mm], as *sensitivity*.

Note that the total measuring range of this 25 mm example is shown to be at least 26 mm. This is in contrast to the typical 12 mm range of an eddy current probe of similar diameter such as the previously mentioned Bently Nevada 3300XL 25 mm system.

2.2. Measurement of 8 mm Antenna Assembly

After proving the feasibility of the system with a 25 mm diameter antenna, the size of the sensor head was scaled down to see if the operation and the aforementioned advantages of the technology are maintained. The most popular sensor diameter in industrial applications is 8 mm. A small diameter allows users to minimize the physical intrusion into a system requiring proximity measurement. For example, a power plant operator who wants to install a proximity sensor in their gas turbine would now only need to drill an 8 mm hole in the shroud vs. a 25 mm hole. The selected operating frequency range was 5.785–5.815 GHz to utilize the free ISM (Industrial, Scientific, and Medical) band [9]. A two-arm spiral antenna [10] was selected as a basic antenna structure. The structure

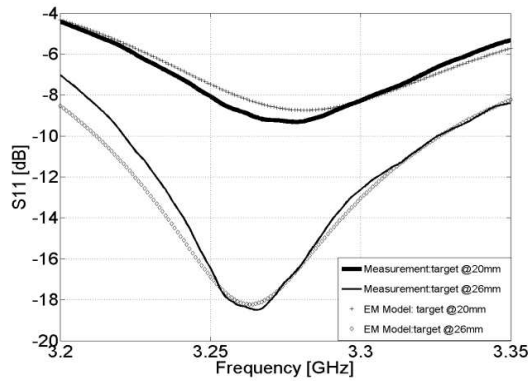


Figure 3: Comparison of measurement and simulation results from 25 mm antenna prototype for the target displacement sweep test.

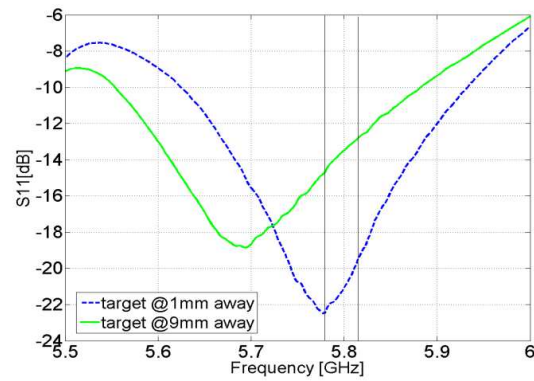


Figure 4: S_{11} measurement results in network analyzer as target displacement varied from 1 mm to 9 mm in 1 mm steps.

was optimized to provide an efficient radiating E field pattern that enables coupling to the target and good proximity measurement performance. Rogers 6010 [11] with a high dielectric constant (nominal $\epsilon_r = 10.2$) was chosen for the antenna substrate. The spiral is connected to a semi rigid co-axial cable that runs through the length of the sensor body and the antenna substrate is encapsulated with molded plastic (nominal $\epsilon_r = 3.2$). A metal disk in the sensor body spaced a certain distance ($\sim \lambda/4$) back from the antenna was carefully designed for creating a tuned cavity. Fig. 4 shows S_{11} measurement results of the 8 mm sensor assembly with target displacement at 1 mm and 9 mm. The average S_{11} change over the displacement range was calculated as ~ 1.0 [dB/mm] @ 5.8 GHz. The result implies the antenna has freedom to be placed any distance away from the target within 9 mm without sacrificing its sensitivity performance. This range of 8 mm from 1 mm to 9 mm is an improvement over a similar sized eddy current probe system such as the industry standard Bently Nevada 3300XL 8 mm system which has a measurement range of approximately 2 mm.

3. IMMUNITY TO ELECTRICAL RUNOUT

Immunity to electrical run out is a critical issue in the realm of proximity measurements [14]. Consider the case where the target is a rotating shaft spinning at 3600 RPM that connects a turbine to an electrical generator. Dynamic forces will cause this shaft to vibrate. Measuring this vibration gives an indication of the performance of the bearings supporting the shaft, the generator's electrical windings, etc.. Electrical run out is the distortion of a proximity signal measured by an eddy current sensor caused by inconsistencies in the permeability the metal target at different locations around the shaft. This distortion can either add to or subtract from the actual proximity signal and this results in false readings. The final proximity values may be higher than the actual amount and a plant operator may be shutting down his machine for safety's sake when there is no real need to do so. When the final proximity value is less than the actual amount then the plant operator may be operating his machinery in a dangerous state. The total amount of electrical run out could range from $3 \mu\text{m}$ such as in AISI 4140 steel to 30 or even $40 \mu\text{m}$ in precipitation hardened 17-4PH steel. These values may seem small but it is important to note that industrial plant operators set shutdown parameters within $25 \sim 50 \mu\text{m}$ of nominally allowed vibration level.

In both cases above, the permeability variations lead to erroneous diagnostic conclusions. Both the microwave and the eddy current sensor heads have a small radiating antenna inside that radiates both an E (electric) and H (magnetic) field. When the E field radiating out of the antenna in the sensor head contacts the target, a near field coupling affect occurs and energy radiating from the antenna in the sensor head is propagated over the target surface. Changing the distance between the target and the sensor head will in turn change the coupling, making it stronger or weaker. When the H field contacts the target, an RF current is induced on the target surface and this current will flow on the surface according to the resistivity of the material. This causes the creation of eddy currents. Higher or lower permeability will dramatically increase or decrease the amplitude of the eddy currents. Since the eddy current sensors are H field dominant, this effect would have a major impact in the operation of an eddy current based sensor.

Table 1: S_{11} difference between three different target materials.

Materials	S_{11} @ 5.8 GHz	Relative Permeability
Aluminum	-19.76 dB	1.00
Brass	-20.74 dB	1.05
Stainless Steel	-19.99 dB	100

Table 2: Additional cable length effect on the return loss of antenna at ~ 3.3 GHz.

No Extra Cable	4' Cable Added	16' Cable Added
-6.3 dB	-8.0 dB	-12.6 dB

Inside the microwave sensor head is a radiating antenna that is designed to be E field dominant. The H field coming from the antenna in the sensor head is very small and can be considered insignificant compared to the strength of the E field. Any H field affects, such as eddy currents, are overwhelmed by the E field coupling effects. Assuming that the antenna inside the sensor head is a well-designed and efficient E field radiator, the distance between the sensor head and the target will have the greatest effect on the near field coupling and the resulting proximity measurement. Any variation in the coupling caused by differences in the conductivity of target is also negligible in comparison because there is sufficient conductivity in various metals to facilitate the propagation of E field current.

Table 1 shows the measured S_{11} return loss value at 5.8 GHz for aluminum, brass, and stainless steel targets at the same position along with the material's relative permeability. As shown, there is no significant S_{11} difference between each metal, which shows that the microwave system is immune to electrical run out. The variation is due to the instance to instance variation in setting up one target material and then removing it for another to make the next measurement.

4. DISCUSSION AND FUTURE WORK

To better understand and to maximize the antenna's performance, we conducted two studies on the influence of cabling in the proximity measurement system. The first study quantified the amount of signal degradation due to long cable lengths. In a real world field installation, adding extra cable length between the antenna and signal processing system is typically unavoidable due to a lack of space in and near the area where the sensor is mounted. We selected two different cable lengths, 4 ft and 16 ft. Each cable was inserted between the RF calibration point on a VNA (Vector Network Analyzer) and the antenna. Table 2 shows the change in S_{11} magnitude at the resonance frequency of the antenna as the inserted cable length increases. Note that the antenna size used for this study was 25 mm in diameter.

Longer lengths of cable increased the amount of signal loss to the antenna which in turn degrades the sensitivity of the proximity measurement system. With less power entering the antenna, the system will not be able to radiate enough meaningful power to the target whose proximity is being measured. Likewise, any reflected signal will see its own reduction in strength as it travels back to the signal processing system. The additional capacitance, inductance, and other electrical properties of the cable overwhelm the same properties in the antenna. This implies that the sensor needs to be excited with as short of a cable as possible from the RF source. To remedy this issue, it is possible to incorporate a de-embedding technique [12, 13] to compensate for the degraded performance. Beyond intricate feeding methods and high end cables, it may be possible to monitor phase and frequency values rather than magnitude [14].

The second study was the effect of temperature variation on the cable. A high quality Temp Flex 063-2501 RF cable [16] was temperature cycled in an oven. The first end of the cable was connected to a VNA so that S_{11} data can be gathered on the cable. From there, the cable was looped around inside the oven before exiting to an ambient 25°C environment where it was connected to the 25 mm version of a microwave proximity sensor. It was observed that the return loss magnitude would vary with the change in temperature. Figure 5 shows the swings in S_{11} magnitude from 0°C to 180°C and the frequency was swept from 3 GHz to 6 GHz.

These changes occurred because the dielectric properties of the cable shifted. For example, the

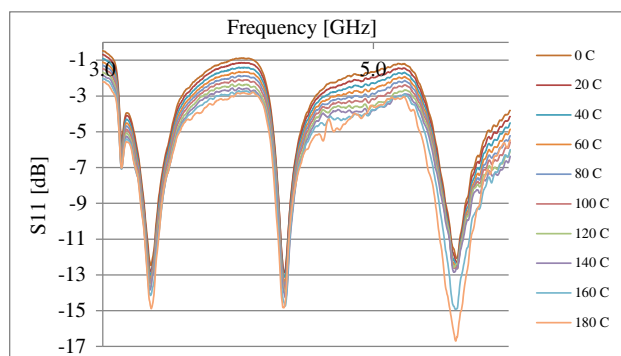


Figure 5: S_{11} measurement results in network analyzer as the temperature of the cable is cycled from 0°C to 180°C.

Teflon dielectric in the cable would expand and contract and the cable, which was initially a 50 Ohm component, experienced an impedance change. When the cable would contract then it no longer sat in the same position covering the center conductor near the jacks. There are several areas of potential additional research remaining. First, different dielectrics in the cable should be tested over temperature. For example, it is known in the industry that mineral based dielectrics (i.e., SiO_2) offer better stability than traditional PTFE (i.e., Teflon). Second, it is possible to incorporate a compensation system in the signal processing system. Monitoring phase and resonant frequency data could indicate what the temperature is and the system could then compensate for it. Lastly, it may be possible to build a sensor head with materials whose temperature affects cancel each other out. Third, the target re-radiates the energy at a different phase. Although the re-radiated energy levels are very small, they can create multipath reflection paths which may couple back to the sensor head and interfere with the proximity measurement. It is important to understand these reflections and how to filter out the unwanted phase information in the reverse reflected signal coming out of the power directional coupler.

5. CONCLUSIONS

A proximity measurement technique using near field effects in a microwave antenna was presented. The prototype system showed excellent sensitivity, extended measuring range, and immunity to electrical run out. Good validation of EM model with measured results was also obtained. Although more work needs to be done to resolve cabling issues and harsh environment effect compensation algorithms, a proper implementation of the proposed system would be a viable way to overcome major drawbacks of traditional proximity measurement methods.

REFERENCES

1. Canali, C., G. Cicco, B. Morten, M. Prudenziati, and A. Taroni, "A temperature compensated ultrasonic sensor operating in air for distance and proximity measurements," *IEEE Trans. Industrial Electronics*, Vol. 29, No. 4, 336–341, 1982.
2. Bowers, W. and D. Olson, "A capacitive probe for measuring the clearance between the piston and the cylinder of a gas piston gauge," *Review of Scientific Instruments*, Vol. 81, No. 3, 035102–035102-7, 2010.
3. McClurg, G., "Nondestructive eddy current testing," *IEEE Trans. Industrial Electronics*, Vol. 11, 20–26, 1959.
4. Xin, J., N. Lei, L. Udpa, and S. Udpa, "Nondestructive inspection using rotating magnetic field eddy-current probe," *IEEE Trans. Magnetics*, Vol. 47, No. 5, 1070–1073, 2011.
5. Novak, J. and I. Feddema, "A capacitance-based proximity sensor for whole arm obstacle avoidance," *IEEE Robotics and Automation Proceedings*, Vol. 2, 1307–1314, 1992.
6. Wang, Y., Y. Cheng, L. Shyu, and C. Chang, "Fabry-Pérot interferometer utilized for displacement measurement in a large measuring range," *Review of Scientific Instruments*, Vol. 81, No. 9, 093102–093102-3, 2010.
7. Hansen, C. H. and S. D. Snyder, *Active Control of Noise and Vibration*, Chapman & Hall, New York, 1997.
8. <http://www.ansoft.com/products/hf/hfss/>.
9. http://www.access.gpo.gov/nara/cfr/waisidx_10/47cfr18.10.html.

10. Nakano, H., T. Igarashi, R. Suzuki, Y. Iitsuka, and J. Yamauchi, “Consideration on radiation from an unbalanced-mode spiral antenna,” *ISAPE, Int. Symp. Antennas, Propagation and EM Theory*, 211–214, 2008.
11. <http://www.rogerscorp.com/acm/products/12/RT-duroid-6002-6202-6006-6010-PTFE-Ceramic-Laminates.aspx>.
12. Vanhille, K., D. Filipovic, C. Nichols, and D. Fontaine, “Balanced low-loss Ka-band μ -coaxial hybrids,” *IEEE MTT-S Int. Microwave Symp.*, 1157–1160, 2007.
13. Fischer, T., M. Spang, and M. Albach, “Easy de-embedding of symmetrical coax-to-microstrip transitions,” *IEEE Workshop Signal Propagation on Interconnects*, 1–4, 2008.
14. Billington, S. and J. Geisheimer, “Method and system for calibration of a phase-based sensing system,” US Patent 6,856,281, Feb. 15, 2005.
15. Yu, Y., P. Du, and T. Yang “Investigation on contribution of conductivity and permeability on electrical runout problem of eddy current displacement sensor,” *IEEE MTC*, 1–5, 2011.
16. <http://www.sanyu-usa.com/assets/files/Temp-Flex/T7-PDF.pdf>.

Microwave Bandpass Filter Using Cascaded Bow-tie Resonators

S. B. Sng, K. M. Lum, and L. F. Lim

School of Science and Technology, SIM University, Singapore

Abstract— A microwave bandpass filter (BPF) using cascaded bow-tie resonators is presented. The centre frequency of the proposed BPF is 3 GHz. Two open-ended bow-tie resonators are positioned near the input and output feedlines respectively. Four short-ended bow-tie resonators are cascaded in series along the main transmission line which comprises eleven sub-section using microstrip. A VIA hole with radius of 600 μm is integrated in the four short-ended bow-tie resonators topology to facilitate the shorting effect. The bow-tie configuration is a simple assembly between the imaginary images of two triangular patches. It provides the flexibility in controlling the resonating frequency and passband bandwidth via its bow-shape microstrip topology. In addition, it is well known that bow-tie structures are able to provide wider bandwidth response. A 50 Ω microstrip line is being used for the input and output port respectively. FR4 substrate with relative permittivity of 4.6, thickness of 1.6 mm and a loss tangent of 0.027 is being used to fabricate the proposed BPF design. The dimensional size of the prototyped BPF is 15.7 cm by 4.4 cm. The best matched measured return loss S_{11} at the centre frequency of the passband response is observed at 3.25 GHz with a value less than -10 dB and the corresponding passband insertion loss S_{21} is greater than -3 dB. The lower and upper stopband rejection is more than 30 dB. The passband bandwidth is approximately 3.3 GHz at -10 dB level. Simulation and measurement response of the proposed BPF are presented and discussed.

1. INTRODUCTION

As space for communication device is always a limitation, microstrip designed filters size must be compact. This prompt numbers of researchers to propose different configuration of filters design without compromising the filter performance [1]. There are numerous existing BPF configurations that utilize step impedance resonators (SIR) [2–6]. In present day, among these different BPF configurations, bow-tie patches resonators have been used in communication devices due to the simple designing procedures and space saving advantages compare to the rectangular patches design resonators. In this paper, a new BPF using bow-tie patches resonators will be discussed. The proposed configuration is suitable for integration with multilayer transceiver antenna modules [7–11] and localization applications [12–16].

2. BANDPASS FILTER DESIGN AND CONCEPT

A single conductor layer is laid on the dielectric substrate. It consists of the main transmission line which comprise eleven microstrip sub-section and six bow-tie resonators. VIA hole of diameter 600 μm is used to short the four smaller bow-tie resonators. The bow-tie resonator is integrated to improve the effective capacitance of the overall configuration. Fig. 1 and Table 1 present the design configuration and specification of the proposed BPF design. Fig. 2 details the key dimensional data of the proposed BPF.

3. SIMULATION AND MEASUREMENT RESULT

The simulated S_{11} and S_{21} response of the proposed BPF are shown in Fig. 3. The S_{11} value at the centre frequency 3.1 GHz of the passband response, has a value less than -15 dB. The corresponding S_{21} response is greater than -1 dB. The lower and upper stopband rejection is greater than 50 dB

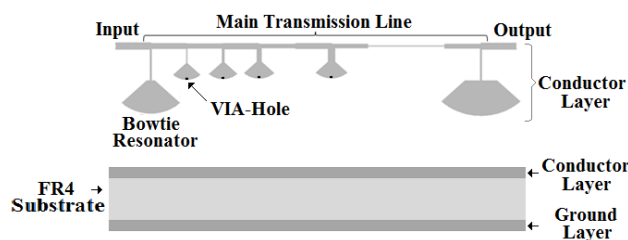
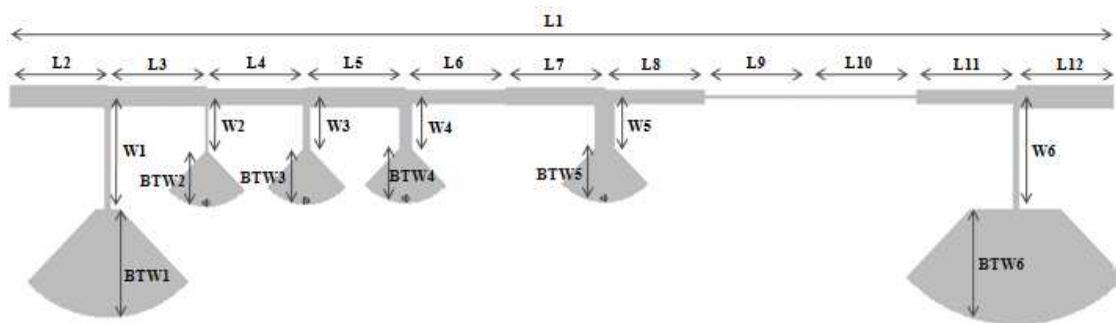


Figure 1: Design configuration of BPF.



Notation	Value (mm)	Notation	Value (mm)	Notation	Value (mm)
L1	149.95	L9	14.31	W5	6.45
L2	13.35	L10	14.24	W6	14.29
L3	13.44	L11	13.57	BTW1	13.93
L4	13.53	L12	13.35	BTW2	7.09
L5	13.43	W1	14.30	BTW3	7.00
L6	13.61	W2	7.01	BTW4	6.95
L7	13.48	W3	6.80	BTW5	7.02
L8	13.61	W4	6.59	BTW6	14.91

Figure 2: Key dimensional data of proposed BPF.

Table 1: Design specifications of proposed BPF.

Key Parameters	Values
Passband Centre Frequency	3 GHz
Passband Return Loss, S_{11}	< -10 dB
Passband Insertion Loss, S_{21}	> -3 dB
Passband Bandwidth at -10 dB	> 2 GHz
Stopband Rejection	> 30 dB

Table 2: Comparison of simulation and measurement response.

Key Parameters	Simulated	Measured
Passband Centre Frequency (GHz)	3.1	3.25
Passband Return Loss, S_{11} (dB)	< -15	< -10
Passband Insertion Loss, S_{21} (dB)	> -1	> -3
Lower and Upper Stopband Rejection (dB)	> 50	> 30
Passband Bandwidth at -10 dB Level (GHz)	3	3.3

respectively. The passband bandwidth at -10 dB level is 3 GHz. Fig. 4 presents the fabricated proposed BPF using FR4 substrate with a dielectric constant of 4.6 and thickness of $1600 \mu\text{m}$. The overall size of the prototyped BPF is 15.7 cm by 4.4 cm. Measurement was carried out using network analyzer.

The measured S_{11} and S_{21} response of the BPF are shown in Fig. 5. The S_{11} value at the centre frequency 3.25 GHz of the passband response, has a value less than -10 dB. The corresponding S_{21} response is greater than -3 dB. The lower and upper stopband rejection are greater than 30 dB respectively. The passband bandwidth at -10 dB level is 3.3 GHz. Table 2 tabulated the comparison between the simulation and measurement response of the proposed BPF. The slight difference in the response maybe attributed by the accuracy of the alignment between the bow-tie resonators and the VIA holes.

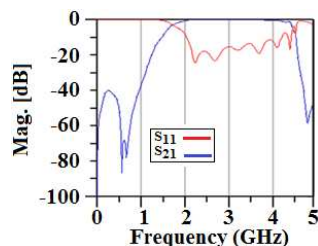


Figure 3: Simulated S_{11} and S_{21} response of proposed BPF.

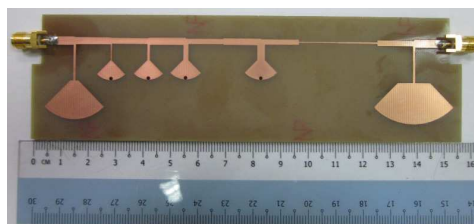


Figure 4: Fabricated topology on conductor layer.

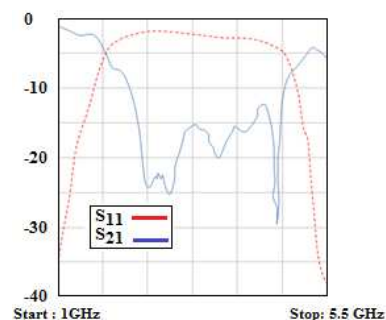


Figure 5: Measured S_{11} and S_{21} response of proposed BPF.

4. CONCLUSION

A new 3 GHz bandpass filter is proposed in this paper and there is close resemblance between the simulated and measured filter response. Broad passband bandwidth is achieved at -10 dB level and the filter displays reasonably acceptable return loss, insertion loss and stopband rejection. The proposed filter can be used for multilayer microwave transceiver systems.

REFERENCES

- Hong, J.-S. G. and M. J. Lancaster, *Microstrip Filters for RF/Microwave Applications*, John Wiley & Sons, Inc., 2001.
- Lek, K. C. and K. M. Lum, "Stepped impedance key-shaped resonator for bandpass and bandstop filters design," *PIERS Proceedings*, 588–592, Kuala Lumpur, Malaysia, Mar. 27–30, 2012.
- Lee, M. L. and K. M. Lum, "Multilayered miniaturized hairpin resonator for bandpass filter design," *PIERS Proceedings*, 593–597, Kuala Lumpur, Malaysia, Mar. 27–30, 2012.
- Lim, Y. T. and K. M. Lum, "A stepped impedance comb-line filter design using defective ground structure for wireless applications," *PIERS Proceedings*, 598–601, Kuala Lumpur, Malaysia, Mar. 27–30, 2012.
- Lim, P. L. and K. M. Lum, "A novel bandpass filter design using E-shaped resonator and dual square-loop defected ground structure," *PIERS Proceedings*, 610–614, Kuala Lumpur, Malaysia, Mar. 27–30, 2012.
- Wong, C. Y. and K. M. Lum, "Miniaturized multilayered bandpass filter using microstrip hairpin resonator for C-band application," *PIERS Proceedings*, 602–605, Kuala Lumpur, Malaysia, Mar. 27–30, 2012.
- Lum, K. M., "A novel radiation enhancement technique for multilayer microwave circuits," *PIERS Proceedings*, 578–582, Kuala Lumpur, Malaysia, Mar. 27–30, 2012.
- Lum, K. M., C. Laohapensaeng, and C. E. Free, "A novel traveling-wave feed technique for circularly polarized planar antennas," *IEEE Micro. and Wireless Components Letters*, Vol. 15, No. 3, 180–182, Mar. 2005.
- Lum, K. M., T. Tick, C. Free, and H. Jantunen, "Design and measurement data for a microwave CP antenna using a new travelling-wave feed concept," *European Microwave Conf.*, Paris, France, Oct. 2005.
- Lum, K. M. and C. Free, "A novel traveling-wave feed technique for circularly polarized planar microstrip antennas," *IEEE Antennas and Propag. International Symposium*, Vol. 2A, 250–253, Oct. 2005.
- Lum, K. M. and C. E. Free, "A novel dual circularly polarized planar and multi-layer LTCC antenna arrays using traveling-wave feed system," *IEEE Trans. Micro. Theory Tech.*, Vol. 54, No. 6, 2880–2886, Jun. 2006.
- Seow, C. K. and S. Y. Tan, "Localization of omni-directional mobile device in multipath environments," *Progress In Electromagnetics Research*, Vol. 85, 323–348, 2008.
- Tai, C. S., S. Y. Tan, and C. K. Seow, "Robust non-line-of-sight localisation system in indoor environment," *Electronics Letters*, Vol. 46, No. 8, 593–595, Apr. 2010.

14. Seow, C. K. and S. Y. Tan, "Localisation of mobile device in multipath environment using bi-directional estimation," *Electronics Letters*, Vol. 44, No. 7, 485–487, Mar. 2008.
15. Seow, C. K. and S. Y. Tan, "Non-line-of-sight localization in multipath environments," *IEEE Transactions on Mobile Computing*, Vol. 7, No. 5, 647–660, May 2008.
16. Seow, C. K. and S. Y. Tan, "Non-line-of-sight unidirectional mobile localisation in multipath environment," *Electronics Letters*, Vol. 44, No. 2, 141–142, Jan. 2008.

A New Small and Low-cost Wideband PIFA with Corrugations Based on Digital Dividend

C. D. Nikolopoulos, K. D. Stravoskoufis, and C. N. Capsalis
 Division of Information Transmission Systems and Material Technology
 School of Electrical and Computer Engineering
 National Technical University of Athens, Greece

Abstract— A broadband and low cost planar inverted F antenna (PIFA) with corrugations suitable for applications in the frequency gap of Digital Dividend (698–862 MHz) is designed in this paper. Present mobile terminal antennas are expected to show increased bandwidth as well as low-loss impedance matching while maintaining low-profile geometry. A custom Genetic Algorithm (GA) is used in order to optimize the proposed antenna's parameters regarding resonant frequency and radiation pattern. The optimized antenna exhibits small size (dimensions 13.6×12.1 cm), satisfactory directivity for mobile terminal applications of 3 dBi over an operation bandwidth of 180 MHz around the central frequency of 790 MHz. Simulation results and parameters range are exposed below followed by the according radiation pattern and variation of the simulated VSWR.

1. INTRODUCTION

Now days more than ever the modern society has become dependent on radio spectrum and the demand for new wireless communications services in the so-called area of Digital Dividend [1, 2] make the necessity present to form a wideband antenna based on this area (698–862 America & Asia, 790–862 Europe). WC-07 made positive steps towards making spectrum available for future LTE deployments. In particular, WRC-07 began the process of migrating broadcast spectrum in the 698–862 MHz band to mobile applications. For that reason a lot of effort is carried out to optimize a structure in the central frequency of 790 MHz. Exploiting corrugations scheme we optimize the new antenna, suitable to operate from channel 52 to 69 (corresponding frequencies 698–862 MHz). The present mobile terminal antenna is expected to show increased bandwidth (180 MHz) as well as low-loss impedance matching ($VSWR = 1.48$). The optimized structure consists of a conductive top plate lying over a finite sized ground plane which is interconnected through a wire (feeding wire) and a second element as shorting strip [3, 4], as depicted in Fig. 1. The radiation characteristics and performance of a PIFA can be adjusted by altering the dimensions of the feeding wire and sorting element or the size and contour of the top and ground plane, so a custom Genetic Algorithm (GA) is used in order to optimize the antenna parameters regarding resonant frequency [5–7].

The optimized antenna exhibits satisfactory directivity for mobile terminal applications of 3 dBi over an operational bandwidth of 180 MHz, corresponding to a percentage of 22.8%. After the optimization procedure, a corrugation scheme employed in the edges of the antenna to improve its characteristics as explained later and presented in Fig. 2. Simulation results and parameters range are exposed below followed by the according radiation pattern and variation of the simulated VSWR.

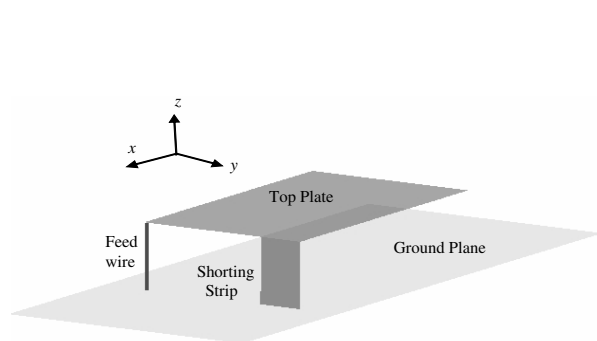


Figure 1: Structure of a normal PIFA.

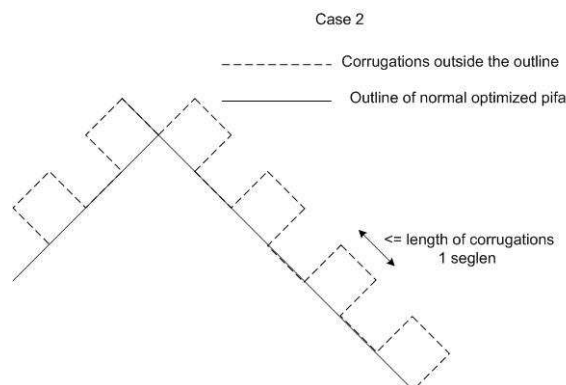


Figure 2: Corrugations scheme outside the outline of the single PIFA.

2. DESIGN AND OPTIMIZATION OF THE CROSS PIFA

The structure under consideration is depicted in Fig. 1. Simulation and analysis of the proposed antenna architecture were made feasible with the aid of SNEC software package. SNEC is a hybrid MoM-UTD (Method of Moments-Uniform Theory of Diffractions) antenna and electromagnetic simulation program. The MoM primitives available in the code are wire segments, whereas the UTD primitives supported are dielectrically coated plates and elliptical cylinders [8, 9]. The MoM is used in order to calculate the radiation pattern and input impedance of wire structured antennas. In our cases the ground and PIFA elements metal plates are simulated using a grid of wires as depicted in Fig. 1(b). The user-defined dimensions for each component of this structure are given in terms of the number of wire segments instead of their physical values. Taking into consideration the fact that the segment length is a fraction of the wavelength λ at the simulation frequency, the electrical size of the PIFA remains constant with the variation of the operating wavelength. This concept ensures compatibility via the handling of this PIFA structure with the SNEC design procedure. In Fig. 1 the SNEC implementation of the PIFA is depicted. In order to find an optimum PIFA structure with perfect impedance matching and adequate operational bandwidth, the method of GAs is applied. GAs are search methods based on the principles and concepts of natural selection and evolution (crossover, mutation) [8–11]. A GA is capable of facing multi-variable problems, such as the design and synthesis of antennas, where a set of performance conditions (e.g., input impedance) should be satisfied. In the optimization procedure described herein, the GA module incorporated in SNEC was utilized. In Table 1, the range of variation of each component parameter participating in the optimization procedure is depicted.

The objective function (OF) deployed to obtain desired input impedance level is expressed as:

$$OF = (VSWR_{DES}/VSWR)^2 \quad (1)$$

where $VSWR_{DES}$, $VSWR$ are the desired and computed values, respectively. The constraint of $VSWR_{DES}$ was set equal to 1. The simulation frequency was set to be 790 MHz. The total population consists of 250 generations with 60 chromosomes per generation. The selection method was population decimation, while adjacent fitness pairing was the mating scheme. The crossover point was chosen randomly and each chromosome was divided at a gene level. The mutation probability was equal to 0.15 [8,9]. As previously stated, Table 1 describes the variation of the parameters that took part in the GA optimization procedure. The proposed PIFA dimensions are expressed in terms of the number of segments. Each segment length was selected to be equal to $seglen = 0.01\lambda$. The results of the optimization implementation are exhibited in Table 1. The desired impedance bandwidth is determined by the band of frequencies where the value of the reflection coefficient at the feed point is less than -10 dB, corresponding to a VSWR with a value of no more than 2, when a characteristic impedance of 50Ω is considered.

Corrugations until now are used for improving directivity [12–14] and reducing the size of an antenna [12], without degrading or upgrading the antenna bandwidth. In our case we propose to use corrugations along the antenna edges, to improve the antenna characteristics such as operational bandwidth and impedance matching [15–19]. The scheme of corrugations is simulated using wire segments and the antenna architecture in SNEC implementation is depicted in Fig. 3. These corrugations are employed to the standard optimized PIFA, previously demonstrated, in both

Table 1: Genetic Algorithm parameters range and results. (Wavelength equal to $\lambda_0 = 0.379$ m corresponding to an operating freq. of 790 MHz.

Element	Range of Variation	Step	Results
Length of top plate (UpLen)	$0.01\lambda_0-0.15\lambda_0$	$0.01\lambda_0$	$0.05\lambda_0$
Width of top plate (UpWid)	$0.01\lambda_0-0.15\lambda_0$	$0.01\lambda_0$	$0.12\lambda_0$
Length of ground plane (UpLen + addx)	$UpLen + (0.01\lambda_0-0.15\lambda_0)$	$0.01\lambda_0$	$UpLen + 0.13\lambda_0$
Width of ground plane (UpWid + addy)	$UpWid + (0.01\lambda_0-0.15\lambda_0)$	$0.01\lambda_0$	$UpWid + 0.04\lambda_0$
Height of wires/shorting strips	$0.01\lambda_0-0.06\lambda_0$	$0.01\lambda_0$	$0.05\lambda_0$
Width of shorting strips	$0.01\lambda_0-0.15\lambda_0$	$0.01\lambda_0$	$0.01\lambda_0$

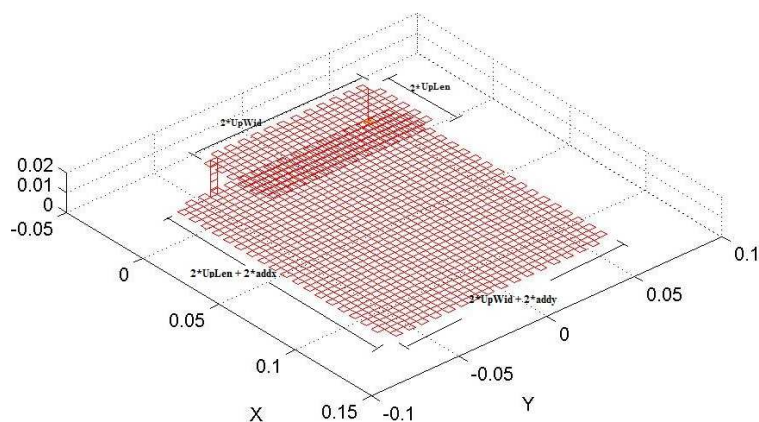


Figure 3: Implementation and analysis of the corrugated PIFA using wire segments and the SNEC platform.

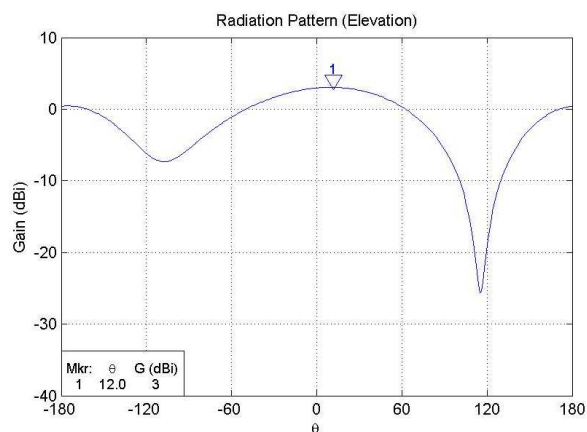


Figure 4: Radiation pattern of the optimized Corrugated PIFA at 790 MHz.

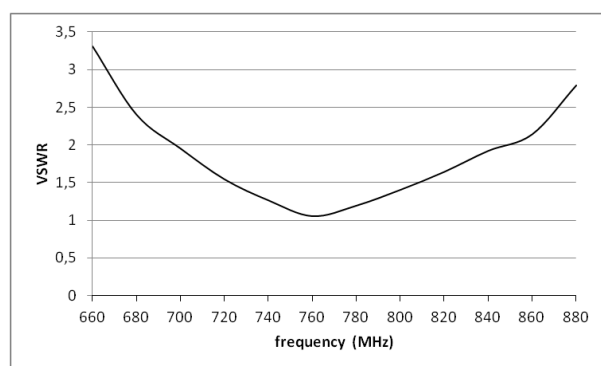


Figure 5: VSWR of optimized Corrugated PIFA at 790 MHz.

top plate and down plane. The length and width of these patches is 1 seglen. The number of corrugations could vary according to the dimensions of the structure and the length of the patch.

3. NUMERICAL RESULTS

The optimized normal PIFA exhibits impedance matching at 790 MHz ($VSWR = 1.48$) and an operational bandwidth of 180 MHz. Also in Fig. 2, it is depicted that the simulated array demonstrates a main beam with a 3 dB-beamwidth of 90° and a gain of 3 dBi at 790 MHz. It should be noted that these values are maintained through the entire 180 MHz operating bandwidth of the proposed structure, thus making the achieved beamwidth and gain quite satisfactory. As previously stated, Table 1 describes the variation of the parameters that took part in the GA optimization procedure and the respective radiation pattern is depicted in Fig. 4. The proposed array dimensions are expressed in terms of the number of segments (physical dimensions 13.6×12.1 cm). Each segment length was selected to be equal to $0.01 * \lambda$. The results of the optimization implementation are exhibited also in Table 1. The desired impedance bandwidth is determined by the band of frequencies where the value of the reflection coefficient at the feed point is less than -10 dB, corresponding to a VSWR with a value of no more than 2, when a characteristic impedance of 50Ω is considered. In Fig. 5, the variation of simulated VSWR around the frequency band of 790 MHz is plotted.

4. CONCLUSION

In this paper, we proposed a standard optimized PIFA structure with corrugations, which has better antenna-characteristics and performance compared to a basic PIFA, for new wireless communications services in the so-called area of Digital Dividend. The operational bandwidth performance was optimized using the technique of the genetic algorithms and a corrugation scheme was implemented in order to broaden the bandwidth in limited height so that can be adjusted in any mobile-portable

handsets. The PIFA with corrugations exhibits a significantly wider bandwidth compared with the single PIFA configuration. The proposed structure has constant electrical dimensions (physical size depends only on the wavelength) and consequently their radiation and operational properties are independent of the frequency of operation. Moreover, the suggested configuration provides a wide impedance bandwidth for use in mobile communications applications and can be used as internal antenna or access point at several frequency bands in an efficient manner.

REFERENCES

1. Cordeiro, C., K. Challapali, and D. Birru, "IEE 802.22: An introduction to the first wireless standard based on cognitive radios," *Journal of Communications*, Vol. 1, No. 1, 38–47, April 2006.
2. Karimi, H. R., M. Fenton, G. Lapierre, and E. Fournier, "European harmonized technical conditions and band plans for broadband wireless access in the 790–862 MHz digital dividend spectrum," *Proceedings of IEEE DySPAN 2010*, April 2010.
3. Waterhouse, R., *Printed Antennas for Wireless Communications*, John Wiley & Sons, Inc., 2007.
4. Nikolopoulos, C. D., C. I. Tsitouri, T. D. Dimousios, and C. N. Capsalis, "A compact single feed, low cost broadband switched-beam antenna for mobile wimax applications," *PIERS Proceedings*, 85–88, Marrakesh, Morocco, March 20–23, 2011.
5. Virga, K. L. and Y. Rahmat-Samii, "Low-profile enhanced-bandwidth PIFA antennas for wireless communications packaging," *IEEE Trans. Microwave Theory Tech.*, Vol. 45, No. 10, 1879–1888, October 1997.
6. Abedin, M. F. and M. Ali, "Modifying the ground plane and its effect on planar inverted-F antennas (PIFAs) for mobile phone handsets," *IEEE Antennas Wireless Propagation Letters*, Vol. 2, 226–229, 2003.
7. Shackelford, A. K., K.-F. Lee, and K. M. Luk, "Design of small-size wide-bandwidth microstrip-patch antennas," *IEEE Antennas and Propagation Magazine*, Vol. 45, 75–83, February 2003.
8. "SuperNec v. 2.4 MOM technical reference manual," Available at: <http://www.supernec.com/manuals/snmomtrm.htm>.
9. Fourie, A. and D. Nitch, "SuperNEC: Antenna and indoor-propagation simulation program," *IEEE Antennas and Propagation Magazine*, Vol. 42, No. 3, 31–48, June 2000.
10. Rahmat-Samii, Y. and E. Michielssen, *Electromagnetic Optimization by Genetic Algorithms*, John Wiley & Sons, Inc., 1999.
11. Goldberg, D. E., *Genetic Algorithms in Search, Optimization, and Machine Learning*, Addison-Wesley Publishing Company, Inc., 1989.
12. Abbosh, A. M., "Miniaturization of planar ultrawideband antenna via corrugation," *IEEE Antennas and Wireless Propagation Letters*, Vol. 7, 685, 2008.
13. Desrumaux, L., M. Lalande, V. Bertrand, J. Andrieu, and B. Jecko, "Increase of the gain of a miniature ultra wide band antenna using short-circuit wires," *International Journal on Communications Antenna and Propagation*, Vol. 1, No. 1, 8–12, February 2011.
14. Bialkowski, M. E. and Y. Wang, "A size-reduced exponentially tapered slot antenna with corrugations for directivity improvement," *Asia Pacific Microwave Conference, APMC 2009*, 2482, December 2009.
15. Nikolopoulos, C. D. and C. N. Capsalis, "The impact of corrugations in optimized planar inverted F antennas (Pifa's)," *International Journal on Communications antenna and Propagation, IRECAP*, Vol. 2, No. 1., February 2012.
16. Teniente-Vallinas, J., R. Gonzalo-Garcia, and C. del-Rio-Bocio, "Ultra-wide band corrugated gaussian profiled horn antenna design," *IEEE International Symposium on Antennas and Propagation Society*, Vol. 2, 316, August 2001.
17. Ge, Y., K. P. Esselle, and T. S. Bird, "A compact E-shaped patch antenna with corrugated wings," *IEEE Transactions on Antennas and Propagation*, Vol. 54, No. 8, August 2006.
18. James, G. L., "Analysis and design of TEI I-to-HE1 1 corrugated cylindrical waveguide mode converters," *IEEE Trans. Microwave Theory Tech.*, Vol. 29, No. 10, 1059–1066, October 1981.
19. Mikhnev, V. and P. Vainikainen, "Wideband tapered-slot antenna with corrugated edges for GPR applications," *33rd European Microwave Conference*, Vol. 2, 727, Munich, October 2003.

Extraction of Distance-dependent Rain Rate Distributions for Satellite Links Calculation

S. C. Leong

Defence Science & Technology Agency, Singapore

Abstract— A new distance dependent point rainfall rate, $R_{0.01}$, originally defined by ITU to be only dependent on location, has been established to take into account the finite rain cell size effect on the rain/link attenuation cumulative distribution curves for a one-way simplex satellite communication link. With modified $R_{0.01}$ rainfall rates, a more accurate link budget calculation can be computed as compared to the traditional dual or single rain fade calculations. Using this methodology, 6 dB of link margin improvement as compared to a dual rain fade calculation can be achieved for a typical satellite communication link between median distances in Singapore at Ku band 99.99% availability.

1. INTRODUCTION

Satellite communication links are known to be severely attenuated by rain. In tropical countries, such as Singapore, where rainfall at 0.01% exceedance reaches 149 mmhr^{-1} [1], a single path attenuation due to rainfall at Ku (12 GHz) band can easily reach 20 dB for satellite links. This places the upper limit for total link availability to 99.99% for current fade mitigation techniques having equivalent dynamic range. Typical satellite communication link budgets use either single uplink or downlink fades to determine link margins and satellite transponder bandwidth/power requirements. This methodology results in under-provisioning of transponder bandwidth for small regions, such as Singapore, where both uplink and downlink may suffer simultaneous fades from a localized rain cell. On the other hand, considering a dual rain fade link budget calculation results in unrealistic link requirements, especially at higher frequencies.

This paper addresses the issue of finite rain cell size on the overall rainfall and link attenuation cumulative distribution (CDF) curves as a function of separation distance between 2 arbitrary locations in Singapore. To establish separation distance between 2 locations as a variable in the rainfall distribution curves, joint statistics such as correlation coefficient of rainfall, extracted from 13 years of weather radar data are used. Section 2 describes the weather radar data processing and methodology for obtaining the rainfall CDF curves in accordance to ITU-R P. 618-10 specifications [2]. Section 3 provides a statistical analysis of rainfall information for locations with different separation distance. Section 4 proposes a modification of the single point rainfall distribution curve to estimate the distance dependent rainfall distribution curve. In Section 5, a link budget calculation methodology is established to calculate the overall link carrier to noise ratio for a simplex link. Improvement in link margin is also computed for median distance locations in Singapore using a sample link.

2. DATA PROCESSING

Weather radar data, which contained spatial information of rainfall over Singapore, are acquired from Singapore Meteorological Service [3]. The data are in the form of raster images and provide cross sectional rainfall values 70 km from Changi, located at 103.97°E , 1.3512°N . The data collection characteristics are as shown in Table 1. Weather radar information has been cited in numerous literature to be a reliable and accurate source of rainfall information. However, because of the different sampling intervals provided and the need for 1-min integration time rain statistics defined by ITU-R, a suitable τ -min to 1-min conversion methodology described in [4] is adopted. Subsequently, the 1-min integration time rate rates is used to compute the various distribution curves described in the following sections.

3. STATISTICAL ANALYSIS

To observe how the rainfall rates are correlated with separation distances, we used the Pearson product moment correlation coefficient, ρ , to compute the 1-min integrated rainfall value for a series of 80 randomly selected locations in Singapore. ρ , measures the linear dependence correlation between the two variables R_1 and R_2 for the rainfall rates at the 2 locations, respectively, and is

Table 1: Weather radar data duration and availability. The non-availability of data in 2010 is due to an upgrade of the weather radar system.

Duration	Data Availability	Sampling Interval
May 1999–Jan. 2010	93.8%	4 min
May 2010–Apr. 2012	93.4%	5 min

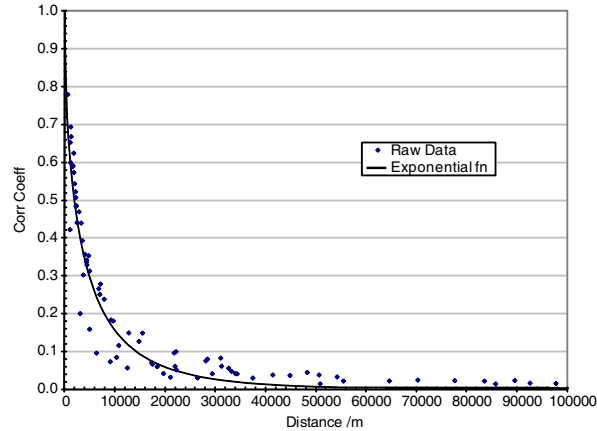
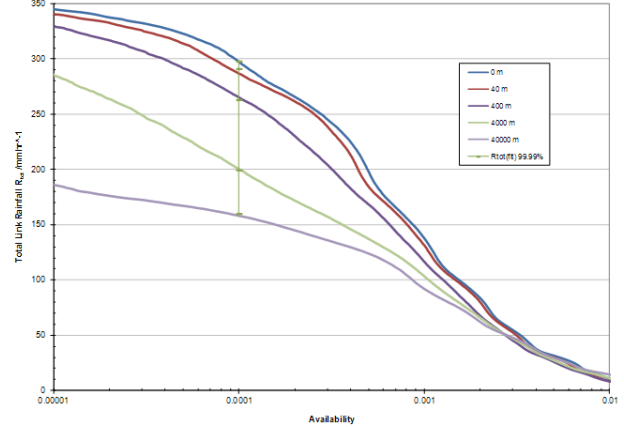


Figure 1: Dependence of correlation coefficient on separation distance between 2 random locations.


 Figure 2: Overall rainfall, R_{tot} , CDF as a function of distance. The vertical line with bars is the fitted R_{tot} function. 99.99% availability is equivalent to 0.0001 on the horizontal axis.

defined in Equation (1). $Cov(\cdot)$ and $Var(\cdot)$ are the covariance and variance functions, respectively. The numerical distance between the 2 locations is determined using the haversine [5] formula.

$$\rho = \frac{Cov(R_1, R_2)}{\sqrt{var(R_1) var(R_2)}} \quad (1)$$

$$\rho_{fit} = \exp(-\alpha D^\beta) \quad (2)$$

Figure 1 shows the correlation coefficients as a function of separation distance generated from random pairs of locations. The correlation coefficient and distance relationship can be approximately fitted using the Levenberg-Marquardt algorithm by the exponential function defined in Equation (2) with empirical constants, $\alpha(6.596 \times 10^{-3})$, $\beta(6.1182 \times 10^{-1})$, and separation distance, D . Correlation coefficient tends to unity for distances close to 0 km as similar rainfall rates occur at the same location within a rain cell. The variation of ρ at low separation distances is small and follows the exponential fit closely, indicating that the rainfall values at the 2 locations are highly correlated. Highly correlated values at 2 locations are possible within a rain cell, where the rise and fall of rainfall are “tracked” as the rain cell moves along the direction of the 2 location axis. Variation in ρ increases from 3 to 30 km, indicating that the 2 locations are possibly in new rain cells but still have positive correlation. ρ is also observed to be positive and close to 0 for distances close to 100 km.

4. DERIVATION OF DISTANCE DEPENDENT RAINFALL CUMULATIVE DISTRIBUTION CURVES

In practical link budget computations, the uplink and downlink are treated as independent and separate. The overall link availability is decomposed into an equivalent product of uplink and downlink availability. Each of these uplink and downlink availabilities will map to an equivalent atmospheric attenuation, contributed mainly by physical rain phenomenon. Rain attenuation is dependent on frequency of transmission but independent of separation distance between the transmit and receive locations. Subsequently, the overall link budget calculation for this worst case dual rain fade condition is performed. This way of computing the link budget is hereafter referred

Table 2: Salient parameters used in the link budget calculation.

Tx and Rx Antenna Sizing: 10 m, 0.65% efficiency	Satellite longitude: 85°
Tx and Rx coupling loss: 0.5 dB, 0.5 dB	Satellite effective G/T: 6 dBK ⁻¹
Tx and Rx pointing loss: 2.61 dB, 1.92 dB	Satellite transponder SFD: -90 dBWm ⁻²
Tx power: 10 W	Satellite effective EIRP: 50 dB
Tx and Rx polarization: HLP, VLP	Atmospheric losses: ITU-R 618-10 [2]
Carrier: 2 Msym/s, 2 MHz RF, 2-PSK	Transponder C/IM: 25 dB
Carrier frequencies: Ku: 14 GHz U/L, 12 GHz D/L,	LNA noise temp: 40 K
Ka: 30 GHz U/L, 20 GHz D/L	Antenna noise temp: 40 K
Tx and Rx C/ACI, C/ASI, C/XPI: 25 dB, 25 dB, 25 dB	Tx and Rx locations: 103.75°E, 1.3667°N

to as *typical*. The dual rain fade link budget calculation results in high transponder power and bandwidth utilization.

This method of calculating the link budget has a few fundamental issues. First, although different uplink and downlink availabilities ratio can be made mathematically equivalent to the overall link availability, physically, the links do not suffer attenuation in that ratio. Second, when the transponder is operating with sufficient back-off and in the linear region, the uplink and downlink are not two independent separate links but are part of the overall link.

As indicated in the rainfall statistical analysis in Section 2, rainfall at the same location is completely correlated and equivalent. The uplink to downlink attenuation ratio is typically higher than unity because of higher losses at higher frequencies. Consequently, the overall attenuation is limited only by the uplink availability and clear sky (uncorrelated rain conditions) at downlink for separation distances beyond 30 km.

To formulate the overall link attenuation, we attempt to first determine the overall rainfall, R_{tot} , at uplink and downlink locations. Figure 2 shows the CDF curve for the overall rainfall for 50 pairs of randomly generated locations. At separation distances close to 0 km, R_{tot} tends to twice the point rainfall rate. At separation distances close to 40 km, R_{tot} tends to the long term point rainfall rate. Relationship between R_{tot} and separation distance is established using the curve fitting Equation (3). At 0.01% exceedance, $R_{tot}|_{avail} = 298 \text{ mmhr}^{-1}$, $a = 0.92541$, $b = -3.24091$. The same empirical fitting function can be used at different exceedance value.

$$R_{tot(fit)} = \frac{R_{tot}|_{avail}}{4} [3 - \tanh(a(\lg(D + b)))] \quad (3)$$

5. APPLICATION OF DISTANCE DEPENDENT RAINFALL CDF CURVES TO LINK BUDGET CALCULATION

In a link budget calculation, it is desirable to accurately correlate the entire link $C/(N + I)$ CDF to the rainfall CDF. N and I components refer to the thermal noise and interference contributions, respectively. To achieve this, we used a simplex data link with the parameters defined in Table 2 and the ITU-R link loss model to first calculate the attenuation figures at each time interval. The attenuation algorithms described in [6] include physical phenomenon models, such as rain, clouds, atmosphere, scintillation, faraday, and depolarization. Sufficient transponder operating power back-off is assumed.

We assume the ITU attenuation model is deterministic with 0.01% exceedance, $A_{0.01}$, [2] defined for each rainfall value, $r_{u/d}$ on uplink or downlink. The discrete cumulative density function, $p_{C/(N+I)}(y)$, for $C/(N + I)$ is defined in Equation (4). [7] x_{ui} is the probability of having an attenuation value a_{uri} in the uplink path. $g(\cdot)$ is the link budget calculation based on the uplink and downlink attenuations. M is set at 500 to allow sufficient quantization resolution of $C/(N + I)$ on $g(a)$. The $C/(N + I)$ CDF curve shown in Figure 3 (for Ku band) and Figure 4 (for Ka band) can be obtained by performing a numerical summation of the probability density function. This

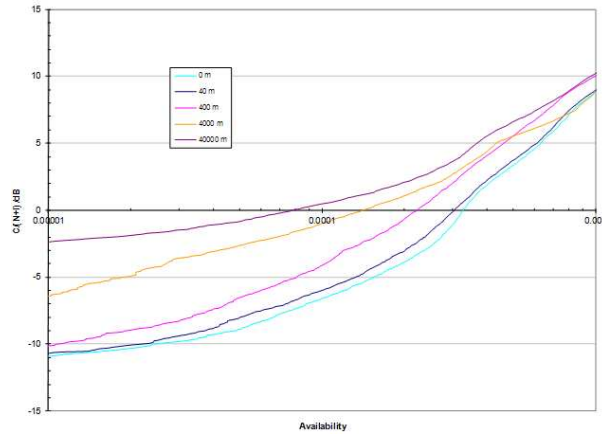
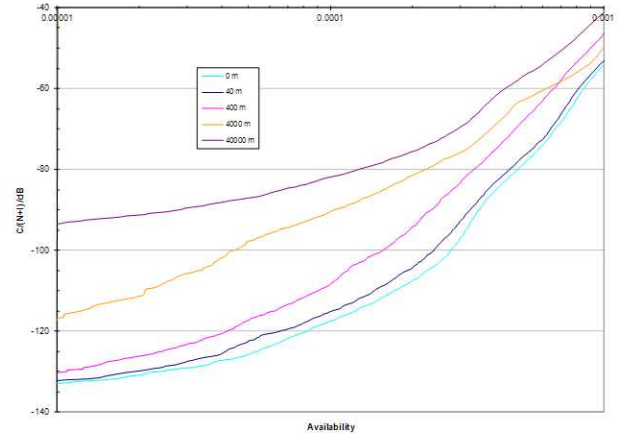

 Figure 3: Ku band total link $C/(N+I)$ CDF as a function of distance.

 Figure 4: Ka band total link $C/(N+I)$ CDF as a function of distance.

 Table 3: Comparison of Ku and Ka band $C/(N+I)$ values obtained using the accurate, typical, and proposed link budget methodologies for exceedance at 0.01%. $R_{0.01}$ for a single point is 149 (298/2) mmhr⁻¹.

Separation Dist, D/m	R_{tot} at 0.01% exceedance	Ku $C/(N+I)$ /dB (Accurate)	Ku $C/(N+I)$ /dB (Typical)	Ka $C/(N+I)$ /dB (Accurate)	Ka $C/(N+I)$ /dB (Typical)	Partition Ratio, PR	Rain at Uplink, $r_u/$ mmhr ⁻¹	Rain at Downlink, $r_d/$ mmhr ⁻¹	Ku $C/(N+I)$ dB (Proposed)	Ka $C/(N+I)$ dB (Proposed)
0	298	-6.71	-7.05	-117.7	-122.6	0.999	149.0	149.0	-7.05	-122.6
40	285	-5.94	-7.05	-115.2	-122.6	0.954	145.9	139.1	-6.08	-119.2
400	250	-4.00	-7.05	-108.3	-122.6	0.765	141.6	108.4	-3.90	-111.5
4000	193	-0.96	-7.05	-90.5	-122.6	0.339	144.2	48.8	-0.69	-96.1
40000	157	0.49	-7.05	-82.1	-122.6	0.075	146.1	10.9	0.73	-84.7

way of computing the link budget is hereafter referred to as *accurate*.

$$p_{C/(N+I)}(y) = \sum_{i=1}^M \sum_{j=1}^M x_{ui} x_{dj} \delta(g(a_{uri}, a_{drj})) \quad (4)$$

$$PR = \frac{r_d}{r_u} = \frac{1}{2} [1 - \tanh(a(\lg(D+b)))] \quad (5)$$

With the rainfall and $C/(N+I)$ cumulative distribution functions, we estimate $C/(N+I)$ by partitioning the total rainfall into the individual uplink and downlink using the same relationship derived in Equation (3) with modified scaling and translation factors defined in Equation (5). In this new proposed method, the final $C/(N+I)$ is calculated with the partitioned rainfall value and the $A_{0.01}$ rain attenuation is computed individually for the uplink and downlink. Table 3 is a comparison of $C/(N+I)$ figures obtained using the accurate, typical and proposed link budget methodologies. It can be seen that the proposed method provides better estimates with the distance variable dependence whereas the typical model does not. The deviation of the proposed system is qualitatively related to the link budget non-linearities. These include the additional system noise due to rain, intermodulation interference dependence on carrier back-off, and asymmetrical impact of rain on uplink and downlink thermal noise.

With well correlated $C/(N+I)$ to total rainfall values, we can estimate the savings in transponder bandwidth. The median distance between 2 locations in Singapore is 18.8 km. Therefore, the difference in typical worst case and proposed $C/(N+I)$ calculations is about 6 dB and 32 dB at Ku and Ka bands, respectively, at 99.99% availability. This translates to about 3 times more bandwidth for this 2 MHz carrier example at Ku band.

6. CONCLUSION

Rainfall correlation coefficient for pairs of locations as a function of distance apart is extracted from 13 years of weather radar data for Singapore. Statistical results demonstrate a monotonically decrease in rainfall values correlation coefficient with increasing separation distances for each location pair in Singapore. This suggests that co-located transmit and receive locations ($D < 3$ km) should utilize dual-rain fade link budget calculations without compromising on accuracy whereas transmit and receive locations located with distances more than 3 km apart should use modified rainfall distribution curves. A new proposed link budget calculation utilizes rainfall value partitioning on the uplink and downlink to determine the overall link $C/(N + I)$ figures as a function of separation distance. Using this proposed methodology for calculating link budget at Ku and Ka bands, it can provide an additional 6 dB of link margin for median locations in Singapore at 99.99% availability. As this methodology provides distance dependent interpolation only on the rainfall distribution curves, it will be applicable to any monotonically non-linear and linear functions such as link attenuation.

REFERENCES

1. Leong, S. C. and Y. C. Foo, "Singapore rain rate distributions," *6th Int. Conf. on Information, Comms and Signal Processing*, 1–5, Dec. 2007.
2. ITU-R, "Propagation data and prediction methods required for the design of Earth-space telecommunication systems," Recommendation ITU-R P.618-9, Geneva, 2011.
3. Meteorological Service Singapore, 2011, http://www.weather.gov.sg/wip/c/portal/layout?p_Lid=PUB.1023.5.
4. Leong, S. C., W. J. Loh, Y. J. Chen, P. H. Yip, and B. T. Koh, "Evaluation of site diversity effectiveness using weather radar data for singapore," *PIERS Proceedings*, 620–625, Kuala Lumpur, Malaysia, Mar. 27–30, 2012.
5. Sinnott, R. W., "Virtues of the harvesine," *Sky and Telescope*, Vol. 68, No. 2, 159, 1984.
6. ITU-R Propagation Models Software Library, Sep. 2010, <http://logiciel-ls.cnes.fr/PROPA/en/usermanual.pdf>.
7. Vuong, X. T. and S. T. Vuong, "Satellite link margin and availability issues," *IEEE Trans. on Broadcasting*, Vol. 43, No. 2, Jun. 1997.

A Method of PCI Planning in LTE Based on Genetic Algorithm

Hao Sun, Nan Li, Yanlei Chen, Jiangbo Dong, Na Liu, Yunbo Han, and Wei Liu
China Mobile Design Institute, Beijing, China

Abstract— Physical Cell ID (PCI) planning is one of the most important steps in whole Long Term Evolution (LTE) network planning and construction. It is difficult to improve the QoS of Network by some traditional methods, such as antenna adjustment in LTE system. Assigning PCI reasonably is able to decrease interference and increase operation rate and performance of the network. A PCI planning system is presented in this paper. This system would analyze the interference of LTE system and build up an interference matrix. Then this system would use genetic algorithm to adjust the distribution of PIC to minimize the interference. Finally a PCI plan scheme would be given by this system.

1. INTRODUCTION

Physical Cell ID (PCI) is one of the most important cell's identifier in the wireless network of LTE system. Therefore, PCI planning is one of the most important steps in LTE network planning and construction. To assign and use PCI reasonably could reduce interference and increase resource utilization and QoS of the LTE system. PCI in LTE only has 168 groups, 504 in total [1], which is not enough for needs of LTE commercial networks.

The main idea of genetic algorithms is that adaptable individuals in the group have more chance to hybrid in order to inherit good characteristics. In this way, the group as a whole could adapt to the environment. Genetic algorithm starts with a problem which could have potential results. Then, based on the principle of survival of the fittest, the problem would get the best approximate solution by the evolution of each generation. In each generation, the most adaptable individuals are picked to produce new population presenting new by combination, crossover and mutation with the genetic operators. This procedure would lead to evolution of the population to much more adaptable as in the nature. The best individual though decoding in the latest population could seem as the best approximate solution of the problem [2].

LTE network needs not only well Reference Signal Receive Power (RSRP), but also high Signal to Interference plus Noise Ratio (SINR). If PCI could not be planned well, it will cause high interruption of Reference Signal (RS). Then this situation would cause black hole of signal coverage. A method of PCI planning based on genetic algorithm is presented in this paper to assign PCI reasonably for LTE networks. This method could improve the PCI plan result to increase the QoS of LTE network.

2. PRINCIPLES

The theoretical basis of genetic algorithm is schema theorem and building block assumptions. The basic follow of genetic algorithm is shown as Figure 1 [3].

Schema theorem has the character of low order, short length and average fitness of the mode of degree higher than the population means fitness in the offspring. A schema could contain many strings, and different strings could link to each other through schema. The string operator in the genetic algorithm is essentially a mode of operation.

Statistics researches show that to obtain optimal feasible solution in random search should make sure that the sample of better feasible solutions must grow exponentially.

2.1. Mathematical Modeling

There are two ways of string and binary encoding in genetic algorithm. Binary encoding method is used in this paper. The result of this problem is presented by an $n * m$ two-dimensional matrix F . Figure 2 shows that different antenna numbers in LTE system would get different matrix F . Every element in this matrix is presented as f_{ij} , which the value is 1 or 0. When PCI j is assigned to cell i , $f_{ij} = 1$, otherwise $f_{ij} = 0$. In order to satisfy the demand vector, we need to make $\sum_{j=1}^m f_{ij} = d_i$, which d_i is cell i 's PCI demand, n is number of cell, m is the number of usable frequency [4].

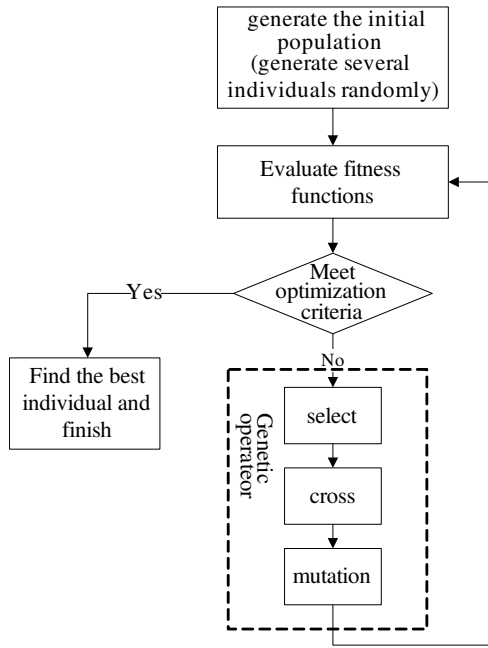


Figure 1: Follow of genetic algorithm.

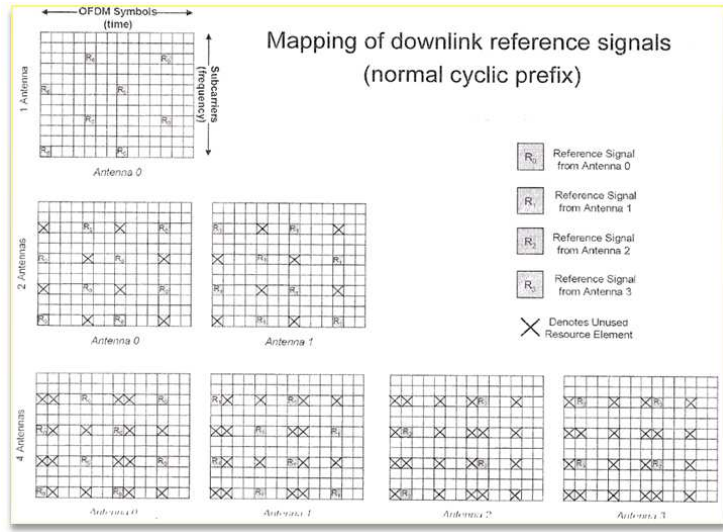


Figure 2: Mapping of downlink reference signals.

2.2. Initial Population

There are two ways to initial population generally, one is random generation, which is used for the situation of solution to the problem without any prior knowledge, and another one is to transfer some prior knowledge to a group of essential requirements, then choose the population randomly from the results which meet the requirement. In order to get the optimal solution faster, the second way is used to initial population in this paper [5].

3. SYSTEM REALIZATIONS

Genetic algorithm is packaged in this paper to realize the function of automatic plan for each cell's PCI in LTE.

3.1. Theory of Automatic PCI Plan

There are several factors needed to consider during PCI code plan, such as PBCH, PDCCH and so on. In this system, user could choose one or multiple channels as the considerations during PCI plan. As known, the different channel has different parameter. For example, PBCH uses initial parameter

$$C_{Init} = N_{ID}^{Cell}, \tag{1}$$

which N_{ID}^{Cell} is PCI of this cell. PDCCH uses initial parameter

$$C_{Init} = \lfloor n_s/2 \rfloor * 2^9 + N_{ID}^{Cell}, \tag{2}$$

which n_s is number of timeslot in frame, N_{ID}^{Cell} is PCI of this cell. PCFICH uses initial parameter

$$C_{Init} = (\lfloor n_s/2 \rfloor + 1) * (2 * N_{ID}^{Cell} + 1) * 2^9 + N_{ID}^{Cell}, \tag{3}$$

which n_s is number of timeslot in frame, N_{ID}^{Cell} is PCI of this cell.

Correlation of scrambling code in LTE is calculated by $R_{ab} = \frac{1}{N} \sum_{i=1}^N a_i \cdot b_i$. Considering the delay of LTE system, an improved method is used as follows:

$$R_{ab} = \frac{1}{N} \sum_{i=1}^N a_M \cdot b_i, \quad M = \begin{cases} N, & (i+m) \bmod N = 0 \\ (i+m) \bmod N, & (i+m) \bmod N \neq 0 \end{cases} \tag{4}$$

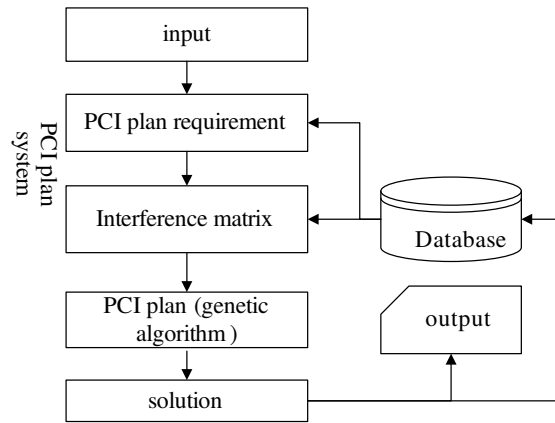


Figure 3: Construction of PCI plan system.

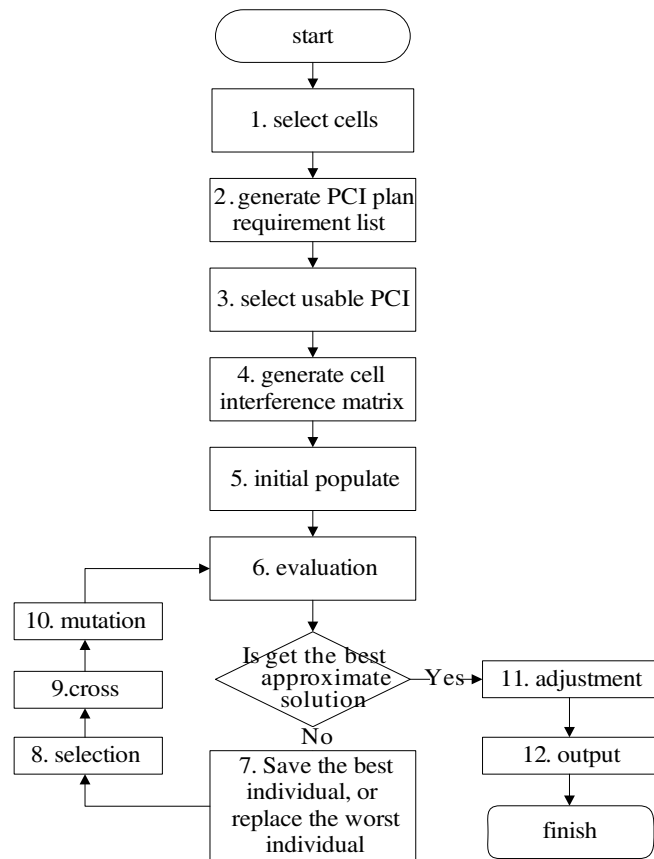


Figure 4: Flow of PCI plan algorithm.

3.2. PCI Automatic Plan

PCI plan module is used for assisting LTE network plan and optimizes and gets best solution of PCI plan. System would obtain cell information, such as frequency, and measurement report, etc. before PCI planning. Then system would assign PCI for cells in order to reduce the interference of the whole LTE network as far as possible. At last, the system would output the solution for users. PCI plan module is shown in Figure 3, which, the flow of PCI plan algorithm is shown in Figure 4.

4. SIMULATION RESULT OF PCI PLAN

All the algorithm and method introduced above are coded with C# and used in LTE plan tool ANPOP. This PCI plan system also needs Geographic Information System (GIS) as an addition condition. In this section, we use RS and PBCH's SINR to evaluate the effect of PCI plan method based on genetic algorithm by compare with the simulation result of manual and automatic PCI plan.

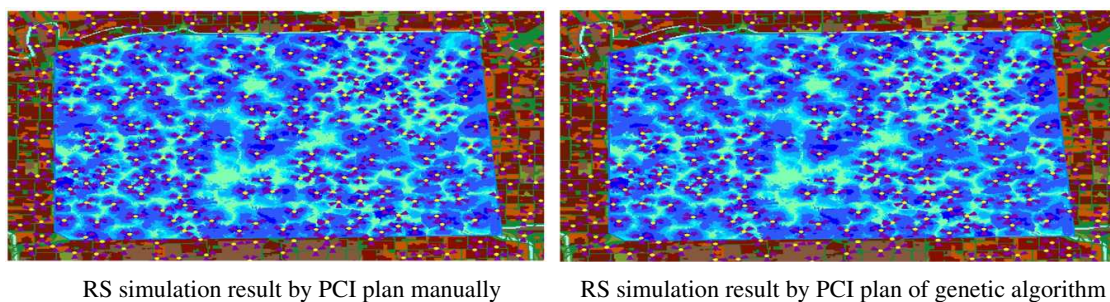
At the same time, Monte Carlo (MC) simulation is also launched in this paper. Assuming there are 5 UEs every cell, service type is Full Buffer FTP. The result of MC shows as follows:

Manual PCI plan, average cell throughput is 16.3Mbps, average cell edge throughput is 0.43 Mbps;

Automatic PCI plan using genetic algorithm, average cell throughput is 20.1 Mbps, average cell edge throughput is 0.65 Mbps.

To compare the two results, we could know that, using the second method could increase cell throughput 23.3%, and cell edge throughput 51.2%.

According to the results above, the algorithm mentioned in this paper could reduce same frequency disturbance and improve SINR coverage of the network, and also could increase the throughput of the LTE network.



RS SINR	Area (km ²)	Percentage (%)	RS SINR	Area (km ²)	Percentage (%)
$-15.0 \leq X < -10.0$	0.025	0.1	$-15.0 \leq X < -10.0$	0.000	0.0
$-10.0 \leq X < -3.0$	4.988	13.6	$-10.0 \leq X < -3.0$	0.025	0.1
$-3.0 \leq X < 5.0$	4.187	11.4	$-3.0 \leq X < 5.0$	4.988	13.6
$5.0 \leq X < 10.0$	8.137	22.2	$5.0 \leq X < 10.0$	4.187	11.4
$10.0 \leq X < 20.0$	15.330	41.8	$10.0 \leq X < 20.0$	8.137	22.2
$20.0 \leq X < 40.0$	4.016	10.9	$20.0 \leq X < 40.0$	15.330	41.8
$40.0 \leq X$	0.000	0.0	$40.0 \leq X$	4.016	10.9

Figure 5: Simulation results of RS's SINR.

5. CONCLUSIONS

From the simulation result above, we could get the conclusion that assigning PCI reasonably is able to effectively reduce the interference in LTE system, especially in the case of constructing network using the same frequency, and to improve coverage and QoS of the network. As a result, PCI plan algorithm presented in this paper is suitable for multi-antenna LTE system.

ACKNOWLEDGMENT

Especially thanks to my lovely wife; I cannot finish this paper without her support.

REFERENCES

- 3GPP, "Evolved universal terrestrial radio access (E-UTRA); Physical channels and modulation (release 8)," *3GPP TS 36.211*, 72–74, Dec. 2009.
- Shen, J. and S. Suo, *3GPP Long Term Evolution (LTE) Technical Principle and System Design*, Posts & Telecom Press, Beijing, 2010.
- Ngo, C. Y. and V. O. K. Li, "Fixed channel assignment in cellular radio networks using a modified genetic algorithm," *IEEE Transactions on Vehicular Technology*, Vol. 47, No. 1, 163–172, 1998.
- 3GPP, "Evolved universal terrestrial radio access (E-UTRA); Radio resource control (release 8)," *3GPP TS 36.331*, 75–76, Dec. 2010.
- Wang, X. P. and L. M. Cao, *Genetic Algorithm — Theory, Application and Software Implementation*, Xi'an Jiaotong University Press, Xi'an, 2003.

Investigation of Adaptive Multi-antenna Switching Strategy in TD-LTE Systems

Wei Liu, Kaikai Liu, Nan Li, Jiangbo Dong, Na Liu, Yanlei Chen,
Hao Sun, and Yunbo Han

China Mobile Design Institute, Beijing, China

Abstract— Multi-antenna technology can be implemented in several modes. This paper introduces Spatial Diversity (SD), Spatial Multiplexing (SM) and Adaptive Multi-Antenna Technology. It compares capacity performance and application scenarios of SD and SM. Then, it gives capacity gain of Adaptive Multi-Antenna Technology under different channel conditions and analysis the reason why it can enhance the capacity performance. Factors and Notes are proposed when adaptive multi-antenna switching strategy applied to the actual.

1. INTRODUCTION

LTE (Long Term Evolution) can provide high-speed wireless business experience, the rate is several times higher than 3G. A report which is released by GSA says the 218 operators in 81 countries around the world have invested in LTE networks. From 2008, China began to deploy TD-LTE research industry and set up a special TD-LTE working group to carry out TD-LTE key technology research and validation.

One of the key technologies of TD-LTE is a multi-antenna technology, refers to using multiple antennas at the sender or the receiver. Multi-antenna technology available spatial diversity gain, spatial multiplexing gain and interference suppression gain. It can improve coverage, capacity and stability of the system, and does not increase the cost of wireless communication systems. Multi-antenna technology can be divided into spatial diversity, spatial multiplexing and beamforming. Spatial diversity and spatial multiplexing known as multiple input multiple output (MIMO) technology. This paper studies the spatial diversity and spatial multiplexing principle, verify the capacity of performance and application scenarios. And then, it gives the effect and the reason for adaptive multi-antenna technology to enhance system capacity. Finally, factors and notes are proposed when adaptive multi-antenna switching strategy applied to the actual.

2. MIMO RESEARCH

2.1. Basic Principle

2.1.1. Spatial Diversity

Spatial diversity introduces the signal redundancy in the space in order to achieve the purpose of diversity. The basic sending technology of spatial diversity in TD-LTE is Space Frequency Block Code (SFBC). It means that data stream is joint encoding in the sending end to reduce the BER caused by channel fading and noise [1].

2.1.2. Spatial Multiplexing

Spatial multiplexing refers to send different data streams in the same time-frequency resources of each antenna, and the receiver uses interference suppression to decode for the purpose of increasing the system capacity while do not increase the frequency resources at the same time [2].

2.2. Capacity Analysis

Spatial diversity can obtain the diversity gain and coding gain, while it is not sensitive for the signal to noise ratio (SNR), channel correlation, terminal moving speed. So it can use higher modulation and coding scheme (MCS) in the poor radio channel environment (such as low SNR, high channel correlation, high terminal speed), and then increase the stability and coverage of the link. Spatial multiplexing can enhance the transmission capacity of the system and meet user demand for high-speed transfer of data in the good channel environment (such as high SNR, low channel correlation and low terminal speed).

In order to verify the capacity performance of spatial diversity and spatial multiplexing, we choose 6 data collection point at different antenna directions (normal, 30 degrees, 60 degrees) in a TD-LTE cell, these data collection point are divided into near point, mid-point and far point based on the distance between the point and base station, the cell radius is about 290 meters, near

point, mid-point and far point from the base station are: 55 m, 150 m, 245 m. Doing FTP download service respectively in the 6 data collection point with a same TD-LTE terminal to get the capacity performance of TD-LTE single-cell single-user conditions, the data collection point throughput are shown in Table 1:

Table 1: Spatial diversity, spatial multiplexing mode capacity performance comparison.

throughput /Mbps	Normal near point	Normal mid-point	Normal far point	30 degree Mid-point	30degree Far point	60 degree Near point
Spatial diversity	25.19	25.32	24.57	25.02	24.53	25.29
spatial multiplexing	48.78	27.7	12.92	28.05	12.02	48.56

The above data can be seen:

- (1) At near point, mid-point in antenna different directions, the throughput of spatial multiplexing mode is higher than that of spatial diversity mode, the increase is respectively about 92.83%, 10.75%.
- (2) At far point in antenna different directions, the throughput of spatial diversity mode is higher than that of spatial multiplexing mode, the increase is about 97.12%.

2.3. Applications Scenarios

The realization of the principle and test data of spatial diversity, spatial multiplexing show that: when the radio channel is poor (corresponding to the data collection point in the far point), spatial diversity mode reflects better capacity characteristics; when the radio channel is good (corresponding to the data collection point in the near point, mid-point), spatial multiplexing mode reflects better capacity characteristics.

Radio signal in the environment of dense urban, indoor coverage will be frequent reflection, resulting in the fading characteristics are more independent between more space channel, so that the spatial multiplexing effect is more pronounced; multipath components is less in the suburbs, rural areas, the correlation between space channel is larger, and therefore more suitable for space diversity.

3. ADAPTIVE MIMO AND SWITCHING STRATEGY

3.1. Adaptive MIMO

Spatial diversity and spatial multiplexing have their own performance characteristics and application scenarios. When building networks, channel environment and moving speed that users in is keeping changing, no matter what kind of technology used alone can't best to play out the performance of the system. Adaptive MIMO is a multi-antenna technology that can switch between spatial diversity and spatial multiplexing according to system configuration, wireless channel environment and other factors. Adaptive can maximum improve the system performance. In order to validate the enhancement effect of system capacity performance caused by adaptive MIMO, we set system antenna mode as adaptive MIMO. Then we can get testing data of single cell and single user at original data select point.

From the figure we can see that the following rules:

- (1) Adaptive MIMO can get better enhance effect of capacity of performance at near point in antenna different directions. Compared with spatial diversity and spatial multiplexing, throughput increased 92.9% and 0.8% respectively in average;
- (2) Adaptive MIMO did not fully reflect the enhancement effect of capacity performance at mid-point in antenna different directions. Compared with spatial diversity and spatial multiplexing, throughput increased 44.2% and 31.8% respectively at normal mid-point, but the lowest throughput at 30 degrees mid-point;
- (3) From the data at far point in antenna different directions, adaptive MIMO did not reflect the capacity performance improvements, compared with spatial diversity, the throughput reduced 47% in average.

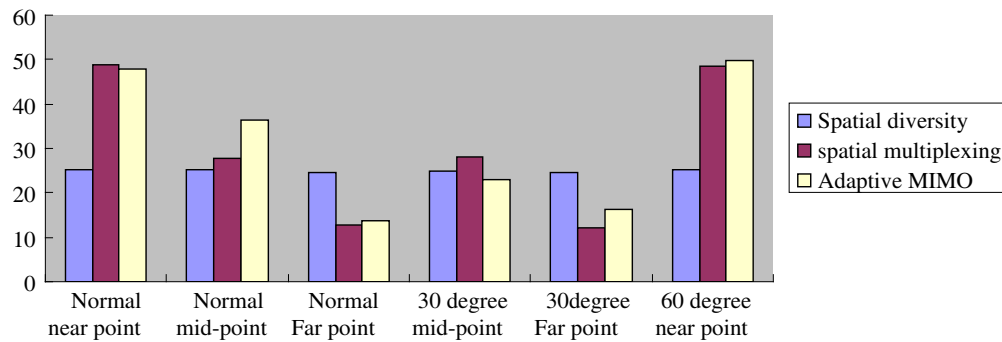


Figure 1: Spatial diversity, spatial multiplexing and adaptive MIMO.

Table 2: Adaptive capacity performance.

throughput /Mbps	Normal near point	Normal mid-point	Normal far point	30 degree Mid-point	30degree Far point	60 degree Near point
Adaptive MIMO	47.74	36.5	13.64	23.01	16.3	49.68

The above validation results are not fully fit with the theoretical analysis. Research on wireless network environment, adaptive MIMO method found that the essence of adaptive MIMO technology is to use some switching strategy. According to the users' current wireless channel environment to make users choose spatial diversity mode or spatial multiplexing mode to transfer data. Most optimized switching strategy should be able to do real-time response to users' current wireless channel environment and switch between spatial diversity and spatial multiplexing fast and accurately. It reflects respective performance advantage of two multi-antenna mode and to the largest extent can improve the system performance. So, adaptive MIMO technology performance depends on switching strategy. The deviation of the above test data and theoretical explained current switching strategy in practical applications has room for further optimization.

3.2. Switching Strategy

According to research, adaptive MIMO switching strategy needs to consider the following factors:

- (1) Users movement speed. High speed gives priority to the spatial diversity mode.
- (2) Wireless channel quality. System gives channel quality indicator when users corrected it.
- (3) Wireless channel correlation. It is measured by the user reported to the RI values.
- (4) User BLER. Maintain a steady decrease of the user BLER.

3.3. Note in the Practical Application

Through a combination on factors that need to be considered in the adaptive MIMO switching strategy and an in-depth analysis of test data, we can summarize the following matters.

3.3.1. Avoid Frequent Switching

When switching between spatial Diversity and spatial multiplexing, system side will not do switching control until all data in buffer sent. This process will directly influence the terminal throughput. So, adaptive MIMO should try to avoid frequent switching. We found that under the conditions of adaptive MIMO terminal happened frequent switch (6 times) between spatial diversity and spatial multiplexing through in-depth analysis on 30 degree far point in Section 3.1. In TD-LTE system, base station choose suitable modulation coding mode (MCS) to adapt to channel the real-time conditions change through a terminal feedback CQI. The following picture shows the record of MCS used by terminal, the blue line represents the MCS value of TB0, green line represents the MCS value of TB1, the green line appears means that the switch for the spatial multiplexing mode.

As can be seen from the graph, the sharp fluctuations of the MCS, at this time statistical terminal is BLER 9.3%. Sharp fluctuations of the values of the MCS can indirectly explain channel quality change quickly of that point. System side switches between spatial diversity and spatial multiplexing frequently in order to adapt to different channel quality. Eventually lead to the decline of throughput. To avoid frequent switching problem, system side can improve by setting up reasonable hysteresis parameters. Switching hysteresis parameters refers to take an average of COI/RI

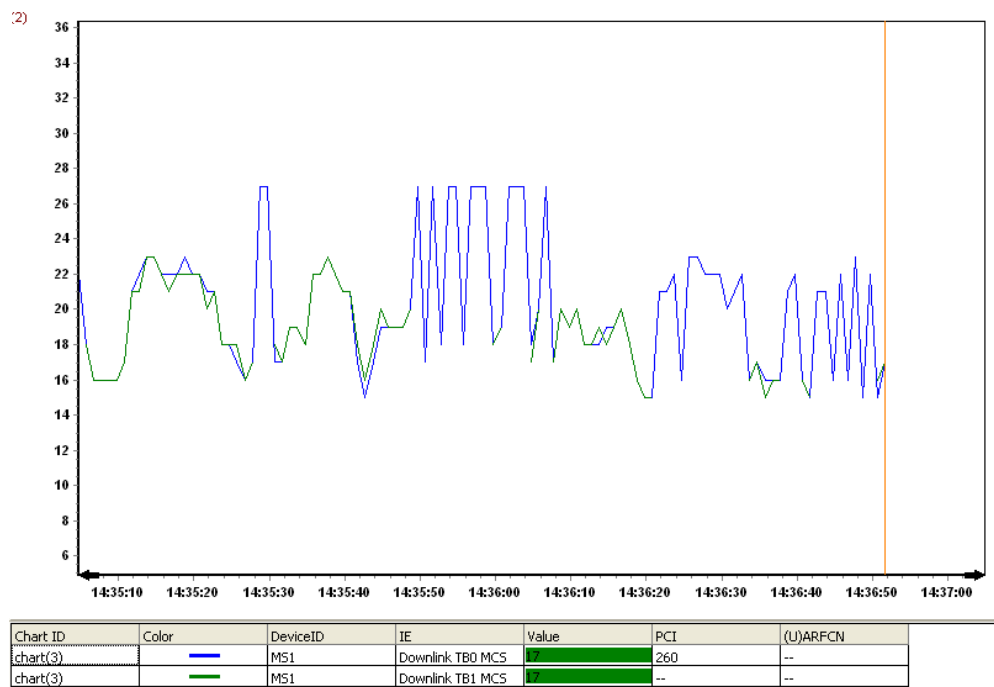


Figure 2: The frequent switching between spatial diversity, spatial multiplexing.

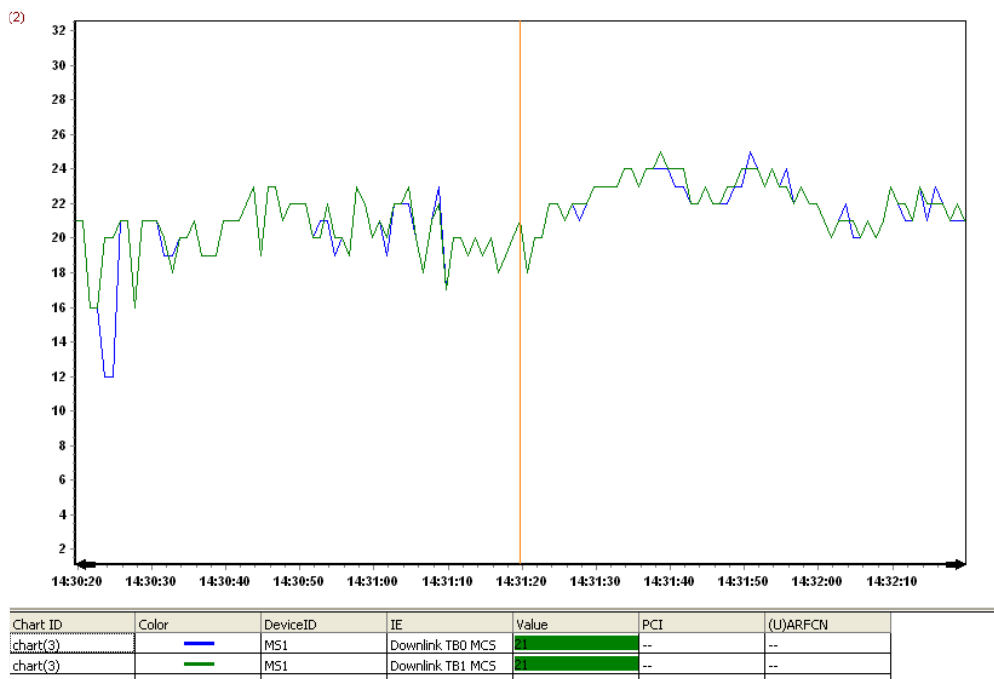


Figure 3: MCS record plan in normal far point at the terminal.

values reported by terminal in a certain period of time averaged as the final side of the system can refer to the channel quality parameters, and set the average as channel quality parameter that can be referred by final system side. Switching hysteresis is generally private parameters of manufacturer and key parameters of maximum upgrading system capacity performance and ensuring the stability of the terminal business. Corresponds to the system side parameter configuration, we recommend increase switching hysteresis parameters suitable to avoid frequent switching problem. But at the same time, it may reduce the capacity of the performance in other wireless channel environment.

3.3.2. Spatial Multiplexing Should Be Timely Back to Spatial Diversity Mode

Through making a deep analysis of the data on far point in Section 3.1, we can conclude that the reason for adaptive MIMO throughput lower is that there is no time to switch to the spatial diversity mode when terminal stays in spatial multiplexing mode, and current interference has more serious. The following picture shows the record of MCS used by terminal.

As can be seen from the graph, terminal in this moment don't happen frequently switching, and continuously stay in spatial multiplexing mode. So, the throughput in adaptive MIMO mode is equal to the throughput in spatial multiplexing mode. The BLER value reached 18.11%, contrary to the principle of switching strategy that make users maintain the BLER steady decline. RI value represents channel correlation, further research find that RI reported by terminal at that point remains 2, indicating that the correlation of the channel is lower. And in theory, RI is appropriate for spatial multiplexing mode. But at this point in the terminal neighbor cell list can see multiple adjacent cell signal, and the lower of SINR means interface is serious. Meanwhile, we observed that in the condition of spatial diversity mode BLER is only 2%. It means wireless environment condition at that point is more suitable for spatial diversity mode. Therefore, the system should set RI probability threshold, that is when the probability of $RI = 2$ is more than X , we choose spatial multiplexing. When the probability of $RI = 2$ is more than Y , we choose spatial diversity. Generally, X and Y are private parameters of manufacturers. Corresponds to the system side parameters configuration, it is recommended that adjust the Y value appropriate to avoid the problems of higher BLER and no obvious ascension of throughput caused by spatial multiplexing mode not back to spatial diversity in time.

4. CONCLUSIONS

This paper introduces basic principle, capacity performance and application scenarios of spatial diversity and spatial multiplexing two kind of multi-antenna technology through analysis data in TD-LTE network. This paper also describes the reasons and effects that the adaptive MIMO can increase system capacity and performance and give notes of switching strategy of adaptive MIMO in the practical application.

- (1) Can reduce the effect of system performance caused by frequent switching through setting the switching hysteresis parameters.
- (2) Can avoid the effect of system performance caused by higher BLER value through adjusting probability threshold Y when $RI = 2$.

At last, proposed to continue to start from the switching strategy algorithm, as a means to further improve the system performance of TD-LTE network.

REFERENCES

1. Zhang, L. Z. and D. N. C. Tse, "Diversity and multiplexing: A fundamental tradeoff in multiple antenna channels," *IEEE Transactions on Information Theory*, Vol. 49, No. 5, 1073–1096, 2003.
2. Golden, G. D., C. J. Foschini, R. A. Valenzuela, et al., "Detection algorithm and initial laboratory results using V-blast space-time communication architecture," *Electronics Letters*, Vol. 35, 1, 14–16, 1999.
3. Zhang, W. X., H. L. Hu, and Y. Yang, "Based on collaborative cover green wireless network technology," *Zhongxing Communication Technology*, Vol. 16, No. 6, 04–07, 2010.

Fractal Labyrinths: Physics and Fractional Operators

A. A. Potapov and V. I. Grachev

Kotel'nikov Institute of Radio Engineering and Electronics, Russian Academy of Sciences, Russia

Abstract— Is basic information about the processes of anomalous diffusion, Levy flights and fractal labyrinths. It is shown, that the mathematics of fractional operators is a basic machine description of complex technical and natural systems with fractal structures.

1.

In the world around us there are a lot of objects, a description of which does not fit into a rigid framework of Euclidean lines and surfaces. With the advent of fractals their description has become a reality, at the same place in the physics of the processes described by the fractal medium nontraditional areas of mathematics. Here is just one example [1]. The average square of the distance to which is removed from the initial point randomly wandering particle (with equal probability in any direction) is proportional to the time, if we are talking about a normal, continuous medium. In a fractal environment that is not so. Here it is obvious that the particle will be randomly wandering away from the launch pad is slower, because not all areas are available for it. The average square of the distance for the fractal medium is proportional to some fractional power of time, index which is related to the fractal dimension of the medium. This means, in particular, that the diffusion in a fractal environment is not as in a conventional, continuous medium. Many obstacles (bottlenecks, steep turns and dead ends) hampers the promotion of particles and slow diffusion. Hence, the fractional rates in the different dependencies.

Slowing diffusion of fractals so much that it ceases to satisfy the classical Fick's law, and — as a consequence — the diffusion equation. Does not save the situation and attempt to enter a variable diffusion coefficient, which depends on the concentration of particles. There is arise a new, integro-differential equation containing a new unusual object — derivative (in time) of fractional order, associated with the fractal dimension of the medium. Another example — in the field of telecommunications, namely, the Internet — a labyrinth of the fractal structure with portals.

The purpose of this paper — to draw attention to exotic fractal labyrinths and the theory of fractional calculus. Moreover, these questions are interesting and new research directions.

2.

In recent years, intensively developing methods for the synthesis of fractal artificial composites and metamaterials, such as, for example, fractal antennas subminiature, fractal structure in photon and magnon crystals, fractal modeling of impedance and fractional operators, percolation synthesis, fractal labyrinths, Cantor blocks, etc. [2–8]. Fractal labyrinths are quite common in nature and technology. These should include: transport and communication networks, systems of collection and distribution of resources and information, river systems, the system of blood circulation, lightning discharges, etc.. The fractal nature of the geometry of these systems determines the specifics of their dynamical behavior and transport properties. *Fractal labyrinth* — *connected topological structure with a fractal dimension $d_f > 1$ and the scaling nature of the conducting channels.*

3.

The description of such systems does not fit into the traditional framework of differential equations of integer order. More precisely these processes and objects quantitatively describes by the operators of fractional integro-differentiation $D^\alpha[f(t)]$, where $-1 < \alpha < 1$ [9–11]. Physically, the operators of fractional integration play a role unique “filters” that emit only those components that are localized on the fractal (fractional) sets the process under investigation. The presence in the equations of fractional derivative taken interpreted as a reflection of the special properties of the process/system — memory, or nonMarkovian (heredity). It should be noted that recently in the scientific world are intensively discussed fractal objects and processes that are negative and complex fractional powers.

4.

Fractal labyrinths and processes in them can be described by operators with a real exponent. In this diffusion — anomalous diffusion is described by fractional diffusion equation FDE (Fractional Diffusion Equation) [2, 3, 11–13]:

$$\frac{\partial W}{\partial t} = {}_0D_t^{1-\alpha} K_\alpha \frac{\partial^2}{\partial x^2} W(x, t), \quad (1)$$

where $W(x, t)$ — probability density function that depends in general on the particular geometry of the interaction; K_α — the generalized diffusion coefficient and the operator ${}_0D_t^{1-\alpha} = \frac{\partial}{\partial t} {}_0D_t^{-\alpha}$ for $0 < \alpha < 1$ — the Riemann-Liouville operator, defined by the integral relation [2, 3, 11, 12]:

$${}_0D_t^{1-\alpha} W(x, t) = \frac{1}{\Gamma(\alpha)} \frac{\partial}{\partial t} \int_0^t dt' \frac{W(x, t')}{(t-t')^{1-\alpha}} \quad (2)$$

— direct continuation of the multiple integral Cauchy problem for an arbitrary complex α with $\text{Re}(\alpha) > 0$. Fractional derivative is set with fractional integration and then — the usual differentiation according to the formula

$${}_t D_t^\beta f(t) = \frac{d^n}{dt^n} {}_t D_t^{\beta-n} f(t)$$

with $\text{Re}(\beta) > 0$, the natural number n satisfies the inequality $n \geq \text{Re}(\beta) > n - 1$.

Thus, the integro-differential nature of the Riemann-Liouville fractional operator ${}_0D_t^{1-\alpha}$ according to (2), with the integral kernel $M(t) \propto t^{\alpha-1}$ ensures the non-Markovian nature of the subdiffusive process, defined by the FDE (1).

Indeed, calculating the mean squared displacement can be inferred from the FDE (1) through integration over $\int d(x) \cdot x^2$, leading to $(d/dt) \langle x^2(t) \rangle = {}_0D_t^{1-\alpha} 2K_\alpha = 2K_\alpha t^{\alpha-1} / \Gamma(\alpha)$.

Rewriting the FDE (1) in the equivalent form

$${}_0D_t^\alpha W - \frac{t^{-\alpha}}{\Gamma(1-\alpha)} W_0(x) = K_\alpha \frac{\partial^2}{\partial x^2} W(x, t), \quad (3)$$

the initial value $W_0(x)$ is seen to decay with the inverse power-law form $(t^{-\alpha} / \Gamma(1-\alpha)) W_0(x)$, and not exponentially fast as for standard diffusion [11, 12]. Note that in the limit $\alpha \rightarrow 1$, the FDE (1) reduces to Fick's second law, as it should.

The generalized diffusion constant K_α which appears in the FDE (1), is defined by $K_\alpha \equiv \sigma^2 / \tau^\alpha$ in terms of the scales σ and τ , leading to the dimension $[K_\alpha] = cM^2c^{-\alpha}$.

The use of fractional operators also provides the relatively straightforward way of calculating the moments. Being very simple for the continuous time random walk approach in force-free diffusion, this advantage is obvious in such cases where a non-linear external force acts upon the test particle. Thereby, integration over the underlying fractional equation produces an ordinary fractional differential equation from which the moments can be inferred.

5.

A generalized diffusion equation of fractional order model is constructed using a continuous time random walk, when events are subject to the general transport statistics [12]. In this case the probability density function of the jump length $\lambda(x) = \int_0^\infty dt \psi(x, t)$ and waiting time $w(t) = \int_{-\infty}^\infty dx \psi(x, t)$

is, that is, $\lambda(x)dx$ is the probability of the length of the jump in the interval $(x, x+dx)$, and $w(t)dt$ — the probability of waiting time in the interval $(t, t+dt)$. Then the processes in the model are determined by the characteristic time of expectation $T = \int_0^\infty dt w(t)t$ and variance of the length of

the jump $\sum^2 = \int_{-\infty}^\infty dx \lambda(x)x^2$. The process of continuous time random walk can be described by the corresponding generalization of the basic equation.

In Fourier-Laplace space, probability density function $W(x, t)$ be at the point x at time t obeys the algebraic relations

$$W(k, u) = \frac{1 - w(u)}{u} \frac{W_0(k)}{1 - \psi(k, u)}, \quad (4)$$

where $W_0(k)$ denotes the Fourier transform of the initial condition $W_0(x)$.

The case of finite characteristic waiting time T and diverging jump length variance Σ^2 can be modelled by a Levy distribution for the jump length, i.e.,

$$\lambda(k) = \exp(-\sigma^\mu |k|^\mu) \approx 1 - \sigma^\mu |k|^\mu \quad (5)$$

for $1 < \mu < 2$, corresponding to the asymptotic behavior

$$\lambda(x) \approx A_\mu \sigma^{-\mu} |x|^{-1-\mu} \quad (6)$$

for $|x| \gg \sigma$.

Due to the finiteness of T , this process is of Markovian nature. Substituting the asymptotic expansion from Eq. (5) into the relation (4), one obtains $W(k, u) = \frac{1}{u + K^\mu |k|^\mu}$, from which, upon Fourier and Laplace inversion, the FDE

$$\frac{\partial W}{\partial t} = K^\mu {}_{-\infty}D_x^\mu W(x, t). \quad (7)$$

is inferred. Here ${}_{-\infty}D_x^\mu$ is fractional Weyl operator. The generalised diffusion constant is $K^\mu \equiv \sigma^\mu / \tau$ and carries the dimension $[K^\mu] = cm^\mu s^{-1}$. The Fourier transform of the propagator can be readily computed, obtaining $W(k, t) = \exp(-K^\mu t |k|^\mu)$, which is but the characteristic function of a centred and symmetric Levy distribution, and as such used to generate Levy flights [12].

In Fig. 1, a computer simulation [12] of a Levy flight is shown on the right, in comparison to the trajectory of a walk with finite jump length variance Σ^2 , for the same number of steps.

From Fig. 1 shows that whereas both trajectories are statistically self-similar, the Levy walk trajectory possesses a fractal dimension, characterising the island structure of clusters of smaller steps, connected by a long step.

Due to the asymptotic property (6) of the jump length probability density function, very long jumps may occur with a significantly higher probability than for an exponentially decaying probability density function like the formerly employed Gaussian jump length probability density function. The scaling nature of the jump length probability density function, as expressed by Eq. (6), leads to the clustering nature of the Levy flights, i.e., local motion is occasionally interrupted by long sojourns, on all length scales. That is, one finds clusters of local motion within clusters. In fact, the Levy flight trajectory can be assigned a fractal dimension $d_f = \mu$. Contrarily, the trajectory drawn on the left of Fig. 1, with $\Sigma^2 < \infty$, fills the two-dimensional space completely, and features no distinguishable clusters, as all jumps are of about the same length.

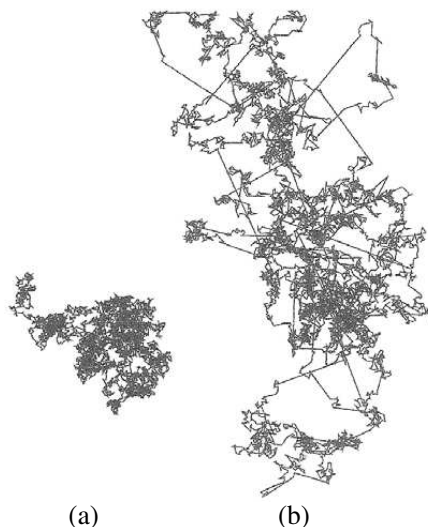


Figure 1: Comparison of the trajectories of (a) a Brownian or subdiffusive random walk and (b) a Levy walk with index $\mu = 1.5$. Both walks are drawn for the same number of steps (approx. 7000).

6.

Thus, both the case of particle dynamics in fractal labyrinths are essential — these being the Riemann-Liouville operator ${}_0D_t^\alpha$ for $t_0 = 0$, and the Weyl operator ${}_{-\infty}D_x^\mu$ for $t_0 = -\infty$ (mathematically, the expression ${}_0D_t^\alpha f(t) = \frac{1}{\Gamma(\alpha)} t^{\alpha-1} * f(t)$ is a Laplace convolution, whereas ${}_{-\infty}D_x^\mu f(x) = \frac{1}{\Gamma(\mu)} x^{\mu-1} * f(x)$ represents a Fourier convolution). Therefore, Laplace and Fourier transformations will be a useful tool in solving fractional order differential and integrodifferential equations.

7.

In conclusion, we can say that a model for the transport dynamics in physical systems based on stochastic walk are still the same, and have become a joint venture of mathematicians, physicists, chemists, engineers, biophysicists, etc.. The extension of random walk theory to incorporate generalised statistics which no longer follow the central limit theorem, and hereditary effects violating the Markovian nature of early days random walks [13, 14], has created a very rich tool, rich enough to be able to describe all features of complex systems.

REFERENCES

1. Danilov, Y. A., *Prekrasny Mir Nauki, (The Wonderful World of Science)*, Collection, Compiled by A. G. Shadtina, V. I. Sanyuk and D. Trubetskoy, Eds., 384, Traditsiya Publication, Progress, Moscow, 2008.
2. Potapov, A. A., *Fraktaly v Radiofizike i Radiolokatsii, (Fractals in Radiophysics and Radiolocation)*, 664, Logos Publication, Moscow, 2002.
3. Potapov, A. A., *Fraktaly v Radiofizike i Radiolokatsii: Topologiya Vyborki, (Fractals in Radiophysics and Radiolocation: Topology of Sample)*, 848, Universitetskaya Kniga Publication, Moscow, 2005.
4. Potapov, A. A., “Fraktalnye anteny, impedansy i radiopogloschayushchie pokrytiya — ‘Umnye’ materialy,” (Fractal antennas impedance and the radio-absorbing coating — A ‘smart materials’),” *Proc. 1st Intern. Conf. ‘Nanostrukturnye Materialy-2008’ (Nanostructured Materials-2008: Belarus-Russia-Ukraine)*, 532, Nauka Publication, Minsk, Belarus, 2008.
5. Potapov, A. A., “Fraktaly, skeling, drobnye operatory — Primenenie v nanotekhnologiyakh? (Fractals, scaling, fractional operators — Applications in nanotechnology?),” *Proc. 1th Conf. Nanotechnological Society of Russia (NtSR)*, 5, NIYaU-MIFI Publication, Moscow, 2009, <http://ntsr.info/nor/bulletin/seminars/index.php?ID=1601>.
6. Iudin, D. I. and V. Y. Trakhtengerts, *Fraktalnye Labirinty: Strukturnaya Dinamika (Fractal Labyrinths: A Structural Dynamics)*, 360–377, Nelineynye Volny, IPF RAS, N. Novgorod, 2007.
7. Feder, E., *Fractals*, 254, Mir Publication, Moscow, 1991.
8. Hunt, A. G. and R. Ewing, *Percolation Theory for Flow in Porous Media*, 319, Springer, Berlin, Heidelberg, 2009.
9. Oldham, K. B. and J. Spanier, *The Fractional Calculus*, 234, Academic Press, NY, 1974.
10. Hilfer, R., *Applications of Fractional Calculus in Physics*, 472, World Scientific, Singapore, 1999.
11. Uchaykin, V. V., *Metod Drobnnykh Proizvodnykh, (The Method of Fractional Derivatives)*, 512, Artishok Publication, Ul’yanovsk, 2008.
12. Metzler, R. and J. Klafter, “The random walk’s guide to anomalous diffusion: A fractional dynamics approach,” *Phys. Rep.*, Vol. 339, 1–77, 2000.
13. Zaslavsky, G. M., *Gamiltonov Khaos i Fraktal’naya Dinamika, (Hamiltonian Chaos and Fractal Dynamics)*, 472, “Regulyarnaya i khaoticheskaya dinamika”, Izhevsky Institut Komp’yuternykh Issledovaniy Publication, NIZ, Izhevsk, Moscow, 2010.
14. Gnedenko, B. V. and A. N. Kolmogorov, *Predel’nye Raspredeleniya Dlya Sum Nezavisimyykh Sluchaynykh Velichin, (Limit Distributions for Sums of Independent Random Variables)*, 264, Gostekhizdat Publication, Leningrad, Moscow, 1949.

A Compact Ultra Wideband EBG Antenna with Band Notched Characteristics

S. Raghavan, Ch. Anandkumar, A. Subbarao, M. Ramaraj, and R. Pandeewari
National Institute of Technology, Tiruchirappalli-620015, India

Abstract— A compact ultra wideband antenna fed by microstripline is presented. The antenna has a size of 30 mm × 35 mm. The antenna is excited by hexagonal shaped tuning stub. It provides bandwidth ranging from 3.1 GHz to 10.2 GHz. A single EBG cell is placed near the feedline which provides band-stop characteristic in frequency range 3.3–4.2 GHz to avoid interference from WiMAX band. The antenna can be easily integrated with radio frequency circuit for low cost. Details of antenna are presented with parametric study. The bandwidth is varied by varying the width, height of hexagonal shaped structure and ultrawide bandwidth is obtained. The antenna has stable radiation pattern in operating bandwidth and it has good radiation efficiency. The fundamental parameters return loss, VSWR, radiation pattern are obtained, which meet standard specifications. Method of moments based IE3D simulator is used to analyze antenna.

1. INTRODUCTION

Ultra wideband communication (UWB) systems have received great attraction in wireless world. It is popularly used technology in radar and remote sensing. Ultra wideband technology provides promising solutions for future communication systems due to excellent immunity to multi path interference, large bandwidth and high speed data rate. A bandwidth from 3.1 GHz to 10.6 GHz is allocated for UWB systems by Federal Communication Commission (FCC) in 2002. From then, the design of UWB antenna became challenging task for engineers in UWB systems. One major issue in UWB is the design of compact size and wide band antenna [1]. Several UWB antennas have been studied for UWB applications [2, 3]. Planar monopole antenna [4, 5] is popular for UWB applications due to small size and stable radiation pattern. Microstrip-fed antennas are useful for microwave communications due to low profile, light weight and low cost of manufacturing.

Due to interference of worldwide interoperability for microwave access (WiMAX) band (3.3–3.6 GHz) in UWB frequency range, it is necessary to provide band-notched characteristic in WiMAX frequency band. The conventional methods to provide band notched design are cutting slots in patch [6] and embedding quarter-wavelength tuning stub in circular ring monopole [7]. The adjustment of band-notched design is not easy in these designs. To overcome this, electromagnetic-bandgap (EBG) structures have become popular. In our paper, a single EBG cell is placed near the feedline and it uses bandgap property of EBG structure to provide notched band in frequency range 3.3–4.2 GHz.

In this paper, we have proposed a novel microstrip-fed monopole antenna which covers entire UWB band. An EBG cell avoids the interference from WiMAX band. The antenna is of hexagonal shaped. It provides stable radiation pattern and high radiation efficiency. The antenna geometry is introduced in Section 2. The antenna parameters return loss, radiation characteristics are discussed in Section 3. Conclusions are given in Section 4.

2. ANTENNA DESIGN

The antenna is constructed with low cost FR4 substrate with relative permittivity $\epsilon_r = 4.4$ and thickness $h = 0.8$ mm with loss tangent $\tan \delta = 0.002$. It has compact size of 30 mm × 35 mm. The antenna consists of hexagonal patch which is feed by microstrip line. The truncated ground plane has dimension of 30 mm × 15 mm and is presented in green region as shown in Figure 1. The various configuration parameters of antenna are $W = 30$ mm, $W_1 = 14.1$ mm, $W_2 = 5.7$ mm, $W_3 = 10$ mm, $W_4 = 1.6$ mm, $L = 35$ mm, $L_1 = 15$ mm, $L_2 = 5.7$ mm, $T = 0.3$ mm, $g = 0.3$ mm. An EBG cell with via is placed near microstrip fed line with a size of $W_2 \times L_2$ as shown in Figure 1. The fabricated antenna is presented in Figure 2.

3. RESULTS AND DISCUSSION

The proposed antenna was simulated and optimized using Zeland IE3D simulator. The return loss curve for the proposed antenna is presented in Figure 3. The return loss curve shows that the proposed antenna achieves an impedance bandwidth ranging from 3.1 GHz to 10.2 GHz for return

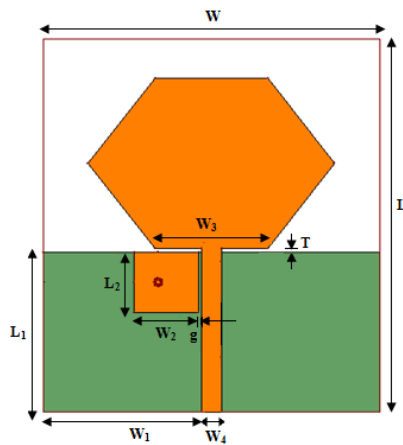


Figure 1: Structure of proposed antenna.

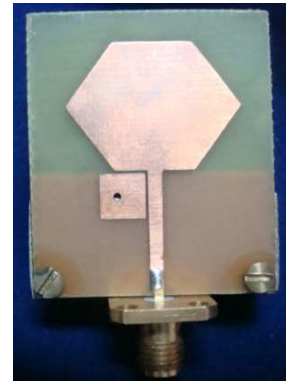


Figure 2: Photo of fabricated antenna.

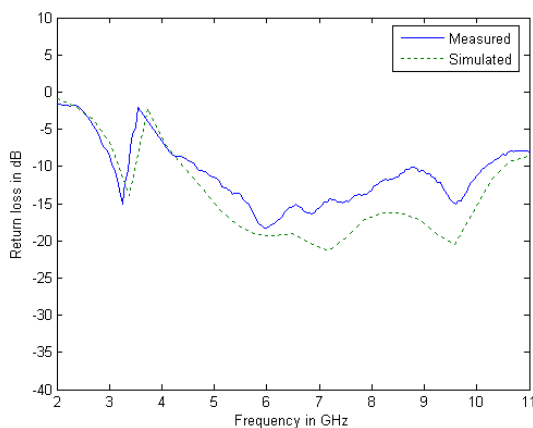


Figure 3: Return loss of proposed antenna against frequency.

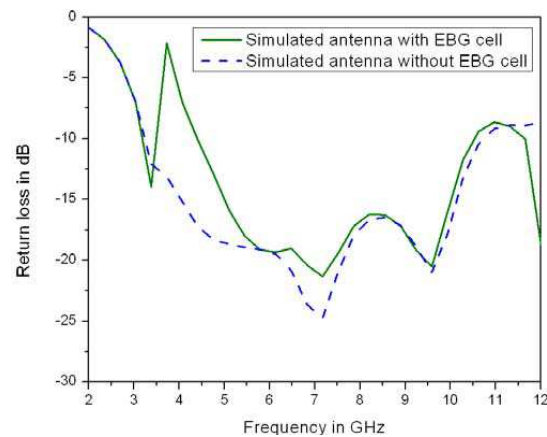


Figure 4: Return loss of proposed antenna with and without EBG cell.

loss below -10 dB. An EBG cell avoids WiMAX band from 3.3 GHz to 4.2 GHz in UWB width and also provides better impedance matching.

Parametric study is important to analyze the characteristics of an antenna. Hence, the critical parameters are performed to examine the effect of various design parameters on various characteristics of antenna. In this configuration, one parameter is varied keeping all other parameters constant. The return loss characteristics of antenna with and without EBG cell is shown in Figure 4. It is evident that the EBG cell is responsible for rejection of interfering WI-MAX band.

3.1. Effect of Height L_2 of EBG Cell on Return Loss

The effect of height L_2 on the EBG antenna is shown in Figure 5. As L_2 increases from 5.2 mm to 6.2 mm, the centre frequency of notched band decreases from 4.1 GHz to 3.4 GHz and resonant frequencies slightly effected. Hence, this parameter has more effect on centre frequency of notched band.

3.2. Effect of Intrusion Depth ' T ' on Return Loss

The variation of return loss for various values of intrusion depth ' T ' is shown in Figure 6. When T increases from 0.3 mm to 1.3 mm, the impedance matching is effected. The impedance matching is poor in the frequency range of 7.4–9.4 GHz at $T = 1.3$ mm. This is mainly due to changes in inductances and capacitance produced by change in electromagnetic coupling between ground plane and patch. The resonating frequencies change rapidly, when T changes. Hence it can be concluded that intrusion depth T has more effect on impedance matching and resonating frequencies.

3.3. Radiation Pattern and Gain

The antenna has reasonably good radiation pattern and almost constant gain in the operating band. Far field radiation characteristics were also studied. The Figure 7 shows radiation patterns in E and H -planes at 3.2 GHz, 5.9 GHz and 9.6 GHz. The radiation patterns are omni directional

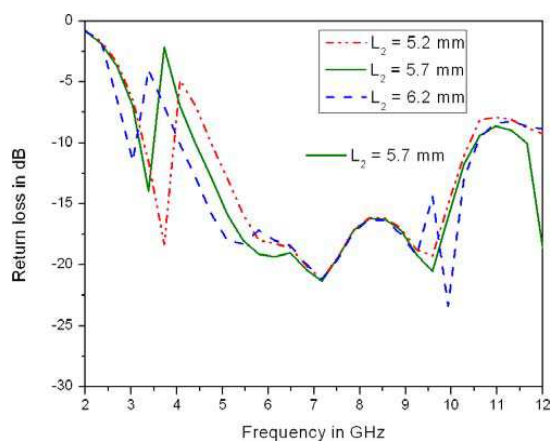


Figure 5: Effect of height L_2 of EBG cell on return loss.

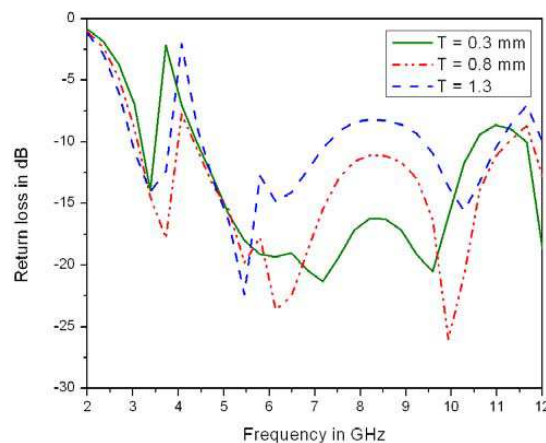


Figure 6: Effect of intrusion depth ' T ' on return loss.

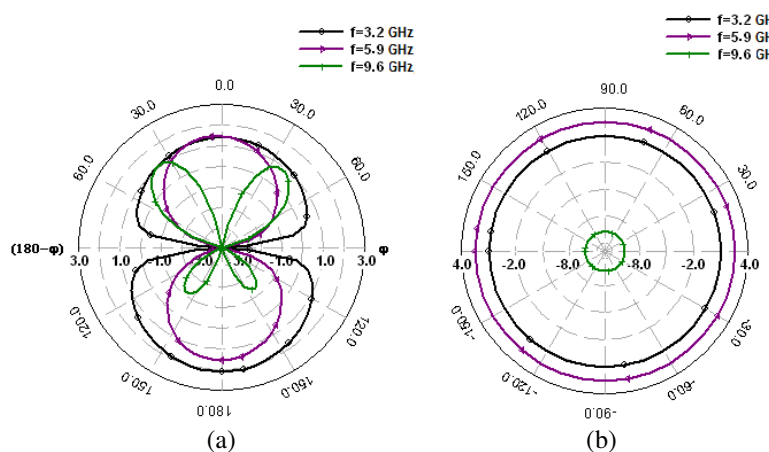


Figure 7: Simulated radiation pattern at 3.2 GHz, 5.9 GHz, 9.6 GHz in (a) E -plane, (b) H -plane.

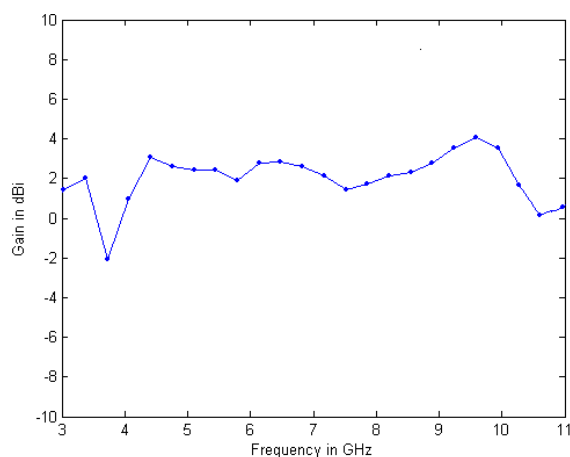


Figure 8: Simulated gain of antenna against frequency.

in H -plane and bi-directional in E -plane. The different frequencies in the operating bandwidth show similar radiation patterns. Hence, stable radiation patterns have been obtained for proposed antenna.

The gain of antenna varies from 1.8 dBi to 4.1 dBi as shown in Figure 8 and it has maximum value of 4.1 dBi at 9.5 GHz. The antenna has high radiation efficiency over the operating bandwidth and it has highest radiation efficiency of 92% at 4.5 GHz. The antenna has highest antenna efficiency of 91% at 4.5 GHz. Group delay of antenna is less than 1 nano second expect in notched-band, which

provides linear phase response.

4. CONCLUSIONS

A compact microstrip-fed antenna with single EBG cell is presented for UWB applications. The microstrip-fed UWB antenna is simulated and experimentally verified. The EBG cell is used to avoid interference from WiMAX. The results show that the antenna has simulated bandwidth of 3.1–10.2 GHz with notched band of 3.3–4.2 GHz. It has constant gain and stable radiation pattern over the entire operating frequency band. The group delay of antenna provides linear phase response. The antenna has highest radiating efficiency of 92% at 4.5 GHz. The antenna is also useful for radio communications.

ACKNOWLEDGMENT

The authors gratefully acknowledge Defence Research and Development Laboratory (DRDL) Hyderabad, India, for help with antenna measurements and sincerely thankful to the Reviewers.

REFERENCES

1. Koohestani, M. and M. Golpour, “U-shaped microstrip patch antenna with novel parasitic tuning stubs for ultra wideband applications,” *IET Trans. Antennas Propag.*, Vol. 4, No. 7, 938–946, 2010.
2. Zhang, G. M., J. S. Hong, B. Z. Wang, Q. Y. Qin, J. B. Mo, and D. M. Wan, “A novel multi folded UWB antenna fed by CPW,” *Journal of Electromagnetic Waves and Applications*, Vol. 21, No. 14, 2109–2119, 2007.
3. Qu, S.-W., J.-L. Li, and Q. Xue, “A band notched ultra wideband printed monopole antenna,” *IEEE Antennas and Wireless Propagation Letters*, Vol. 5, 495–498, 2006.
4. Jacob, K. F., M. N. Suma, R. K. Raj, M. Joseph, and P. Mohanan, “Planar branched monopole antenna for UWB applications,” *Microwave and Optical Technology Letters*, Vol. 49, No. 1, 45–57, 2007.
5. Ahmed, O. and A. R. Sebak, “A printed monopole antenna with two steps and a circular slot for UWB applications,” *IEEE Antennas and Wireless Propagation Letters*, Vol. 7, 411–413, 2008.
6. Zhang, M., X. Zhou, J. Guo, and W. Yin, “A novel ultrawideband planar antenna with dual band-notched performance,” *Microwave and Optical Technology Letters*, Vol. 52, No. 1, 90–92, 2010.
7. Gao, Y., B. L. Ooi, and A. P. Popov, “Band-notched ultra-wideband ring-monopole antenna,” *Microwave and Optical Technology Letters*, Vol. 48, No. 1, 125–126, 2006.

A Continues 360° CMOS Phase Shifter for 60 GHz Phased Array Applications

H. Aliakbari¹, A. Abdipour¹, A. Mohammadi¹, and R. Mirzavand²

¹Microwave/mm-wave & Wireless Communication Research Lab
Radio Communications Center of Excellence, Electrical Engineering Department
Amirkabir University of Technology, Iran

²Institute of Communications Technology and Applied Electromagnetics
Amirkabir University of Technology, Iran

Abstract— The overall designing of one 90 nm CMOS reflective-type phase shifter for the first three channels in 60 GHz band is described. The performance investigation is based on full wave electromagnetic analysis and optimization. The simulation predicts a phase tuning range of 360° as a function of control voltage with an average insertion loss of 5.5 dB over all phase states. The linearity of the phase shifter makes it suitable for the phased array transmitter because it is the output stage of the power amplifier rather than the phase shifter that saturates first so it won't decrease the overall efficiency of the transmitter.

1. INTRODUCTION

The 60 GHz band is of much interest since the wide 7 GHz allocated unlicensed bandwidth which has been divided in three channels enable multi-Gb/s wireless transmission over typical indoor distances [1]. High path loss in MMW wireless transmitter systems leads to use Phased array configuration transmitter (Figure 1(a)) in which the signals transmitted by the multiple antennas can be added up coherently in a certain direction. Furthermore, RF phase shift is of interest due to the smaller number of physical circuit elements [2]. Passive RF phase shifters are proper selection for transmitter phased arrays due to their lower power consumption, higher linearity and lower cost in comparison with active phase shifters [3] but also their insertion loss is high in this band due to the dielectric loss and metal resistivity. Nowadays designing low-loss phase shifters with an analog 360° phase shifting, especially in a low cost CMOS technology is challenging in RF phased array architecture. This paper presents a 360° continues CMOS phase shifter with an acceptable insertion loss over all phase states. At the end of the paper comparison of this work and the recent 60 GHz phase shifters is given.

2. DESIGN OF REFLECTION-TYPE PHASE SHIFTER

The structure of reflection type phase shifter is shown in Figure 1(b). The input signal is divided into two 90° out of phase signals by a quadrature hybrid. These signals reflect from a pair of reflective loads in through and coupled ports and combine in phase at the quadrature isolated port. The phase of the RTPS can be controlled by varying the impedance of the reflective load [4]. The

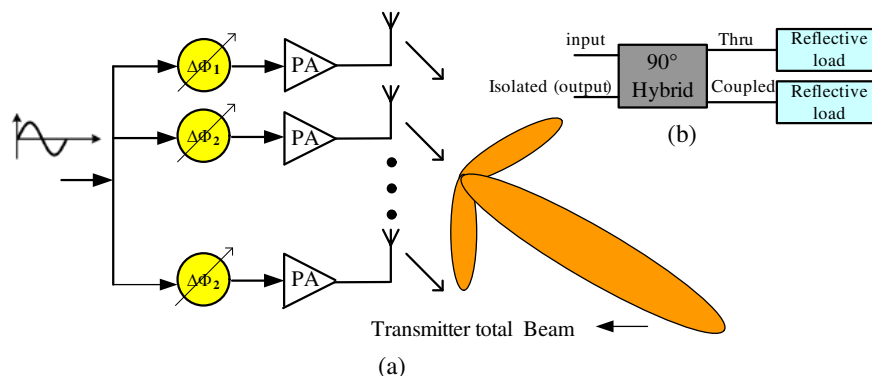


Figure 1: (a) phased array transmitter. (b) RTPS structure.

absolute value of the phase variation of the reflection coefficient is given by:

$$\Delta\phi = 2 \left| \arctan \left(\frac{Z_{\max}}{Z_0} \right) - \arctan \left(\frac{Z_{\min}}{Z_0} \right) \right|. \quad (1)$$

2.1. Design of CMOS Multilayer Quadrature Coupler

The current CMOS technology is based on conductive silicon substrates. A 3-dB CMOS quadrature coupler which use broadside coupling between lines and is isolated from silicon is utilized in RTPS structure (Figure 2). Two top metal layers are used in an offset parallel-coupled strip line structure. The bottom metal completely eliminates the electric field that penetrated through the lossy silicon substrate. The top metal layers are used since this will minimize the resistive coupling to the substrate to reduce the loss as much as possible. The closed form expressions for tight coupling are derived in [5]. The maximum coupling from input port to the through port occurs when the coupling length is one quarter-wavelength, i.e., $\Theta = \Pi/2$. For the miniaturization of the coupler the lines are meandered and also rectangular corners have been avoided in the symmetric structure in order to avoid field crowding effects at high frequencies. By inserting the passivation layer

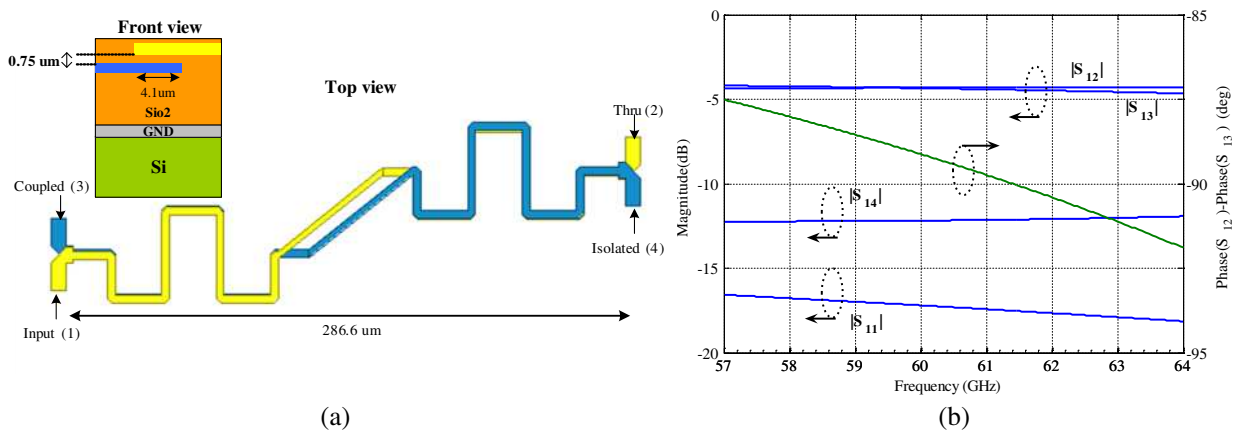


Figure 2: (a) layout of the broad side CMOS Coupler and (b) full-wave simulated S -parameters as a function of frequency.

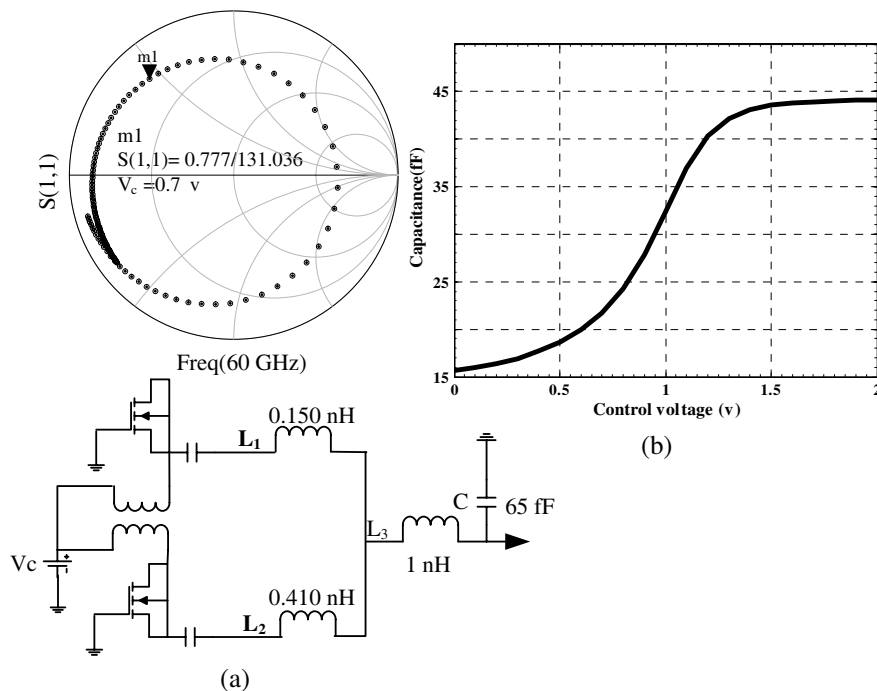


Figure 3: (a) The proposed reflective load. (b) Capacitance of the NMOS varactor.

the radiation loss will decrease. An EM optimization of the strip width and offset resulted in an acceptable insertion loss ($-4.3 \text{ dB} \pm 0.2 \text{ dB}$) and phase shift ($-90^\circ \pm 2^\circ$) in the desired frequency band. Port isolations of higher than 12 dB and return losses of higher than 16 dB were simulated.

2.2. Design of Reflective Terminations

The total phase shift capability of the RTPS can be controlled by optimizing the impedance of the reflective load. Varactors can be implemented by applying a variable voltage between the gate and drain/source of a CMOS transistor in which the source and drain terminals are connected together. The transistor model used in this paper is based on 90 nm CMOS BSIM4. The maximum phase shift can be increased by connecting two different loads with overlapping resonances in parallel (L_1 and L_2). The inductor values are approximately chosen to enable a resonance at high bias voltage (v_c) associated with maximum capacitance of the varactor (L_1) and a resonance at low bias voltage associated with minimum capacitance of the varactor (L_2). A simple LC network (L_3 and C) is added to decrease the magnitude variations of the reflection. For taking the elements parasitic into account the inductors were designed using the rule of thumb dimension described in [6] and implemented in schematics using a 2-II model [7]. High frequency parasitics of the MIM capacitors are taken in to account by using equivalent circuit [8] in schematic.

By taking the parasitic in to account, due to the large insertion loss, the overall phase shift of the phase shifter will be limited. The schematic of the optimized reflective load is shown in Figure 3.

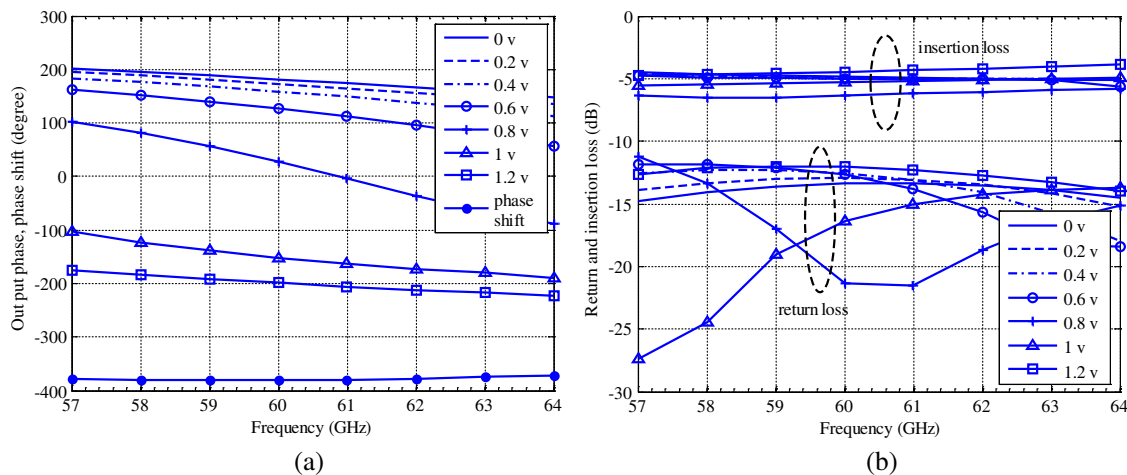


Figure 4: (a) Full-wave simulated output phase versus frequency for various varactor control voltages and (b) S -parameters versus frequency for different control voltages.

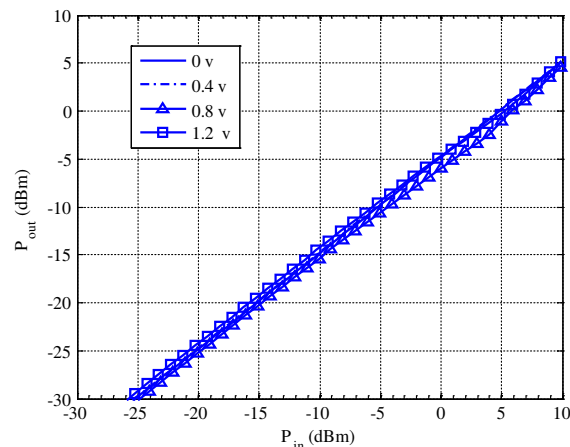


Figure 5: Output power versus input power at various control voltages.

Table 1: Survey of 60 GHz phase shifter designs.

Ref.	Type	Phase shift	Power consumption	Insertion loss(dB)
[3]	CMOS/Vector modulation	360°/4 bit	72 mW (active)	N/A
[9]	CMOS/RTPS (single ended)	90°/Cont's	~ 0 mW (passive)	6.25 ± 1.75
[10]	SiGe/RTPS (single ended)	180°/Cont's	~ 0 mW (passive)	5.85 ± 1.65
[11]	CMOS/Varactor-loaded transmission_line (differential)	180°/4 bit	~ 0 mW (passive)	-9.4 ± 3.1
This Work	CMOS/RTPS (single ended)	360°/Cont's	~ 0 mW (passive)	5.5 ± 1.2

3. RTPS PERFORMANCE

Figure 4(a) depicts that the phase varies linearly over 57–64 GHz frequency range. At each frequency the 360° phase shift is obtained by changing the control voltage.

Figure 4(b) shows that the RTPS has an acceptable average insertion loss of 5.5 dB at all phase states furthermore the return loss of the phase shifter is more than 11 dB over the entire bandwidth. The linearity of the designed phase shifter in different control voltages is investigated by the aid of harmonic balance analysis. Figure 5 shows the linearity of the phase shifter which is suitable for phased array transmitters due to their high linearity requirement.

4. CONCLUSIONS

The design and performance of an analog 360° passive phase shifter, suitable for 60 GHz phased array transmitters, has been reported. The reported reflective phase shifter is consisting of a quadrature hybrid and reflective loads. The EM simulation predicts continuous 360° phase shift from 57 to 64 GHz by varying the applied bias voltage of CMOS varactors which have been used in the optimized Reflective loads.

To the authors' knowledge, this is the first reported 360° RTPS in CMOS technology with an acceptable insertion loss at 60 GHz band.

Table 1 compares the current work with the similar works.

REFERENCES

1. IEEE, IEEE 802.15WPAN Task Group 3c (TG3c), Sep. 2009, <http://www.ieee802.org/15/pub/TG3c.html>.
2. Koh, K.-J., J. W. May, and G. M. Rebeiz, "A millimeter-wave 16-element phased-array transmitter in 0.18- μm SiGe BiCMOS technology," *IEEE J. Solid-State Circuits*, Vol. 44, No. 5, 1498–1509, 2009.
3. Alalusi, S. and R. Brodersen, "A 60 GHz phased array in CMOS," *Proceedings of IEEE Custom Integrated Circuits Conference*, 393–396, Sep. 2006.
4. Ellinger, F., R. Vogt, and W. Bächtold, "Compact reflective type phase shifter MMIC for C-band using a lumped element coupler," *IEEE Transactions on Microwave Theory and Techniques*, Vol. 49, 913–917, 2001.
5. Shelton, J. P., "Impedances of offset parallel-coupled strip transmission lines," *IEEE Transactions on Microwave Theory and Techniques*, Vol. 14, 7–15, 1966.
6. <http://smirc.stanford.edu/spiralCalc.html>.
7. Dickson, T. O., et al., "30–100 GHz inductors and transformers for millimeter-wave (Bi)CMOS integrated circuits," *IEEE Transactions on Microwave Theory and Techniques*, Vol. 53, 123–133, 2005.
8. Ytterdal, T., Y. Cheng, and T. Fjeldly, *Device Modeling for Analog and RF CMOS Circuit Design*, Wiley, England, 2003.
9. Fakharzadeh, M., et al., "CMOS phased array transceiver technology for 60 GHz wireless applications," *IEEE Transactions on Antennas and Propagation*, Vol. 58, 1093–1104, 2010.
10. Tsai, M. D. and A. Natarajan, "60 GHz passive and active RF-path phase shifters in silicon," *RFIC Dig. Tech. Papers*, 223–226, 2009.
11. Yu, Y., et al., "A 60 GHz digitally controlled phase shifter in CMOS," *Proceedings 34th Eur. Solid-State Circuits Conf. (ESSCIRC'08)*, 250–253, Sep. 2008.